An Observational Study of Astrophysical Black Hole Candidates and Gamma Ray Bursts

by

Robert Edward Rutledge

Submitted to the Department of Physics
in partial fulfillment of the requirements for the degree of

Doctor of Philosophy

at the

MASSACHUSETTS INSTITUTE OF TECHNOLOGY

Oct 1996
[February 1997]

Author .....
Department of Physics
October 11, 1996

Certified by .....
Walter H. G. Lewin
Professor of Physics
Thesis Supervisor

Accepted by .....
George Koster
Chairman, Graduate Thesis Committee

An Observational Study of Astrophysical Black Hole Candidates and Gamma Ray Bursts

by

Robert Edward Rutledge

Submitted to the Department of Physics
on October 11, 1996, in partial fulfillment of the
requirements for the degree of
Doctor of Philosophy

Abstract

Analyzing the 2-20 keV data of ten black hole candidates (BHCs; 1354-64, 1826-24, 1630-47, LMC X-1, LMC X-3, GS 2000+25, GS 2023+33, GS 1124-68, Cyg X-1, and GX 339-4) observed with *Ginga*, we produce color-color-diagrams and simultaneous power density spectra (PDS) in three energy ranges (2.3–4.6 keV; 4.6–9.2 keV; and 9.2–18.4 keV). The result of this study is a phenomenological description of the behavior of BHCs, including the strength, energy dependence, and frequency dependence of the continuum variability (0.001–64 Hz) as a function of the spectral hardness ratio (9.2–18.4/2.3–4.6 keV), which spans four orders of magnitude between these ten sources. We relate the so-called Low-State (LS), High-State (HS) and Very High State (VHS) behavior to this hardness ratio. The presence, centroid frequency and width of the 3-10 Hz QPO observed from GS 1124-68 and GX 339-4 are related to this hardness ratio and to the transition between Low-State and High-State.

In the second part of this thesis, we examine the durations of gamma-ray bursts (GRBs) as a function of peak flux. By fitting log-normal models to bright and dim GRB-sample duration distributions, and requiring the factor by which the centroid increases to be equal to the factor by which the FWHM increases between the bright and dim burst duration distributions (as expected from a cosmological origin) we derive 3σ limits on this factor of $\sim$0.95–1.9 (using data kindly provided by J. Norris et al.) and 0.7–1.5 (using data from the 3B BATSE Catalog). Application of Kolmogorov-Smirnov tests indicate that this factor is constrained with 3σ upper-limits in the range of $<$1.8–2.5, depending on data selection criteria.

We find no significant monotonic correlation between GRB peak-flux and duration. We present a method which, in principle, can extract the peak-flux – absolute red shift relationship of GRBs in a cosmological scenario. Using this method we find the non-physical result that median values of the resulting red shift distributions are less than 0 for the faintest GRBs, which increase with increasing burst peak flux to approximately 0 for brighter bursts. This non-physical result is due to the large log-normal width of the GRB duration distribution.

We compare GRB peak-flux distributions to those expected from standard-

We compare GRB peak-flux distributions to those expected from standard-candle cosmological distributions (both evolving and non-evolving). The peak-flux distribution is consistent with a non-evolving GRB population, for standard cosmologies in which Ω_0 is unconstrained. The evolution in the number of GRBs per unit volume per unit time of the form $\propto (1+z)^p$ is constrained, with the exponent p <2. The evolution in GRB peak luminosity of the form $\propto (1+z)^l$ is constrained, with the exponent $l < 2$.

Thesis Supervisor: Walter H. G. Lewin
Title: Professor of Physics

ACKNOWLEDGMENTS

The support and assistance of many people have helped make this work possible. I am indebted to my X-ray collaborators, Brian Vaughan, Michiel van der Klis, Jan van Paradijs, Yasuo Tanaka, Kasuhisa Mitsuda, Tadayasu Dotani, for their extensive aid and parallel analysis which greatly enhanced the scope and depth of this thesis. I am also indebted to my collaborators of the gamma-ray band, in particular Chip Meegan, Chryssa Kouveliotou, Jerry Fishman, Tom Koshut, John Horack, Bob Mallozzi and Jon Hakkila for their conversations, and for providing data prior to its publication.

I am grateful to Jay Norris and Robert Nemiroff, for making available to me data-products of their gamma-ray burst duration analyses, painstakingly obtained, which were used in this thesis.

I am also indebted to Kazumi Asai and Ryuichi Fujimoto who greatly aided in the use of the computers at ISAS.

I am grateful for the kind hospitality showed me during my visits to their institutions: Tom Koshut, Kim Fields, Bob Mallozzi, Brian Vaughan, Tim Oosterbroek, Sacha Prins, John Telting, Erik Kuulkers, Chris Otani, Yasuo Tanaka, Jan van Paradijs, Chryssa Kouveliotou, and Jerry Fishman.

Fellow graduate students at MIT are, in large part, responsible for the development of one's scientific ability, which result in enduring attachment of collegial respect. I have been greatly fortunate to have been touched by many, some in the briefest and yet memorable and important ways. gene magnier, Casey Inman, and Matt Kowitt were patient and kind. Jeff Kommers, Derek Fox, and Patrick Wojdowski asked tough questions, and are great and good friends. And there were many others: Jon Woo, Dave Buote, Una Hwang, Eric Gaidos, Taotao Fang, Chris Moore, Charlie Katz, Sera Markoff, Shep Doelman, Keith Gendreau, Bruce Grossan, Chris Becker, Andy Silber, Don Smith, and Bob Shirey.

Bohdan Paczyński was generous in his hospitality during my brief visit to Princeton, and I am grateful for his useful comments on the paper which resulted in Chapter 9.

My parents, Richard and Norma Rutledge, have been a source of enormous love, support, and confidence. My brother Steve and I have made AT&T wealthy. My brother and sisters Bill, Mary, Joyce and Susan have all come to my aid over the many years.

My apartment-mate, collaborator, and friend Lam Hui (Super-man) is deserving of my highest esteem for clarifying my thinking on a great number and breadth of issues.

During my six years of living in Cambridge, I have benefitted from the friendship of many. Kendra and Peter Siembab, my touchstones. Damon and Amy Korb, who turned me around when I needed turning. Jennifer Harris and Matt Edstrom, both ready with encouragement and kind words. The MIT/Wellesley Toons, with whom I sang. Eva Man, who opened her home to me during my last weeks in Cambridge. Charolette Iverson, who also opened her home to me during my final days here. Wally Siembab and his wife Elizabeth, for New Year's Eve, every year. My USC mentor Dean Joan Schaefer, whose friendship and advice gave birth to my love for academia. Robin Dennis, for unbeatable career advice. Shuk-San Lee, for her films, and her friendship. and Tara Silvestri, who broadened my educational vision.

I am indebted to my thesis committee members, George Clark and Alan Guth, for their guidance, questions, and especially their patient reading of the manuscript, providing comments which resulted in clearer writing throughout.

Finally, there is my advisor, Walter Lewin. I know that he is highly regarded by undergraduates for his inspiring teaching, and is respected by his colleagues for this enormous talent, which I have seen active many times. He is an even better graduate advisor.

This work was supported by the National Aeronautics and Space Administration's Graduate Student Research Program under grant NGT-51369.

DECLARATION

I declare that this thesis is the result of my own work apart from where explicit reference is made to the work of others.

Some of the work contained in this dissertation has been published in refereed scientific journals, or in conference proceedings.

Several results in Chapter 8 are due to be published in the 3rd Huntsville Gamma-Ray Burst conference proceedings, in three separate papers. These include: 1) early results of the log-normal distribution model fits of the 3B BATSE catalog durations; 2) early results of the non-parametric tests for correlation between gamma-ray burst peak flux and duration using the 3B BATSE catalog; 3) description of the simple galactic halo model, with a one-to-one correlation between burst luminosity and duration to account for the broad dispersion in durations and the (postulated) correlation between peak-flux and duration; 4) the comment on the recent result by Kouveliotou et al. (1996), which, if confirmed, indicates the first observational indication of a finite-width gamma-ray burst luminosity function.

The analysis of Chapter 9 exploring the gamma-ray burst peak-flux distribution consistency with non-evolving and evolving populations in standard cosmology has been published in *Monthly Notices of the Royal Astronomical Society* (MNRAS), vol. 276, p. 753.

Contents

List of Figures

List of Tables

Table 0.1: Glossary of Acronyms

%rms	per cent root-mean-square amplitude of variability
ASM	All-Sky Monitor (on *Ginga*)
BB	Broad Band (or, continuum)
BHC	Black Hole Candidate
CCD	Color Color Diagram
dof	degrees of freedom
FFT	Fast Fourier Transform
FOV	Field of View
GBD	Gamma-ray Burst Detector (on *Ginga*)
GC	Galactic Center
GRB	Gamma Ray Burst
HID	Hardness – Intensity Diagram
HS	High State
ISAS	Institute for Space and Astronautical Science (Sagamihara,Japan)
LAC	Large Area Counter (on *Ginga*)
LAD	Large Area Detector (on BATSE)
LC	Light Curve
LS	Low State
PDS	Power Density Spectra
PE	persistent emission
PHD	Pulse Height Distribution
QPO	Quasi-Periodic Oscillations
SAA	South Atlantic Anomaly
VHS	Very High State

Chapter 1

Introduction

Two separate problems are discussed in this thesis: Stellar Black Holes and Gamma-ray Bursts (GRBs). The two phenomena are (distinct) interests of the author, and are treated separately.

1.1 Organization

This thesis is divided into three parts.

Part I is a study of the correlated X-ray spectral and fast-timing characteristics of black hole candidates (BHCs) observed with the X-ray satellite *Ginga*. The goal of this study is to quantify the behavior of these objects using identical analyses to provide a global BHC phenomenology, to compare behavior between sources, to identify that which is peculiar in this class, and to facilitate future observational classification of behavior of these and other sources. Chapter 2 provides historical and observational background on black holes in general, and stellar black hole candidates in particular; Chapter 3 describes the data which are used in this study – its acquisition, primary selection and corrections; Chapter 4 contains the spectral analyses of the BHCs – the color-color diagrams and hardness-intensity diagrams; Chapter 5 contains the timing study of the BHCs, which was done with the knowledge of source spectral states found in Ch. 4; and Chapter 6 contains the discussion and conclusions regarding the BHC analyses.

Part II is comprised of analyses of gamma-ray burst (GRBs) durations as a function of peak-flux, using the 3B BATSE catalog durations and durations obtained with a different technique by Norris et al. (1994; 1995). In Chapter 7 we provide a short observational overview, and describe the BATSE instrument, with which all the GRB data in this thesis were obtained; Chapter 8 contains analyses of the duration–peak-flux correlation; and Chapter 9 investigates the permissible cosmological populations of GRBs, assuming non-evolving source populations, as well as source populations which evolve in either peak-luminosity or in frequency density as a function of red shift.

In Part III, we provide a summary of conclusions drawn from the BHC and GRB analyses (Chapter 10), and appendices.

Part I

Black Hole Candidates

Chapter 2

Black Hole Candidate Background

2.1 Where Have We Been?

The history of stellar-mass black hole candidates (BHCs) has been recently reviewed (Tanaka & Lewin 1995). We touch upon some of the historical aspects of the study of black holes in this chapter, with a focus on X-ray observations. Much of our discussion is based upon the historical treatments by Luminet (1992) and Lewin (1994) and the review by Van der Klis (1995).

2.2 Early Ideas

The earliest theoretical predictions of objects from which light could not escape due to gravity were made in the context of Newtonian gravitational theory. As early as 1783, in an article read to the Royal Society and published later in *Philosophical Transactions*, John Michell combined the ideas of finite light velocity (known to be ~300,000 km/s since Roemer's observations of Jupiter's moons in 1676) with that of escape velocity in the Newtonian gravitational theory. He deduced that a body with the density of the sun, but with a diameter 500 times larger, would have an escape velocity equal to the speed of light, and, therefore, that corpuscles of light would be unable to escape from its surface. In 1796, Pierre Simon Laplace published similar comments in his *Exposition du système du monde*. These comments were

largely forgotten when the corpuscular theory of light, advocated by Newton, was discredited by Young's interference experiments.

Within a month after the publication by Einstein of his equations of General Relativity (GR), Karl Schwarzschild formulated the solution of a gravitational field surrounding a sphere in a vacuum. This formulation, however, contained a mathematical singularity at a distance $r = 2GM/c^2$, corresponding to 3.0 km/$M_\odot$. This singularity was thought to be a flaw in the theory, until it was shown by David Finkelstein during the 1950's that the singularity disappeared under certain coordinate transformations – and therefore was due to the choice of coordinates. (In fact, Eddington had also shown that this was the case some time earlier.) The mathematical singularity was avoided, but the behavior of space and time near $r = 2GM/c^2$ remained – that surface about a spherical body is one of infinite red shift, from within which no photon can be detected at an infinite distance.

Advances in nuclear physics and quantum mechanics had a profound impact on stellar theory. Discovery of the mass-limit of a zero-temperature stellar-body supported against its own gravity by electron degeneracy pressure led to the prediction that such bodies could not be self-supporting for masses greater than $\sim$1.4 $M_\odot$ (Chandrasekhar 1935; Landau 1932).

Chadwick's discovery of the neutron in 1932 led to a suggestion by Zwicky and Baade that zero-temperature non-rotating stars more massive than the "Chandrasekhar limit" could support themselves against gravitation by neutron degeneracy pressure (Baade & Zwicky 1934). The theory of neutron stars was developed further by Oppenheimer & Serber (1938), Oppenheimer & Volkoff (1939), and Tolman (1939). According to Weinberg (1972), neutron stars had also been discussed by Landau (1932). It was calculated that a zero-temperature star of mass greater than 3.0 $M_\odot$ could not support itself against gravity, and must collapse. Neutron stars are the most massive objects known to be supported against gravitational collapse by Fermi degeneracy pressure; "cold" stars which are more massive are destined to collapse, with nothing to support them against the force of gravity.

2.3 Observational Discoveries

The discussion in the previous section outlines the state of knowledge in 1962 about the end-state of the evolution of massive stars, when the first extra-solar X-ray source – Sco X-1 – was discovered (Giacconi & et al. 1962). The discovery of a radio pulsar by J. Bell (Hewish et al. 1967) confirmed the existence of neutron stars, theoretically predicted thirty years earlier. The discovery of the Crab radio pulsar as an X-ray pulsar tied the two phenomena together (Fritz & et al. 1969; Bradt et al. 1969). The observation of coherent pulsations is now considered to be an unmistakable observational signature of a spinning neutron star. The expectation that black holes would also manifest themselves by some unmistakable phenomenology seemed natural.

In 1972, two groups (Webster & Murdin 1972; Bolton 1972) found the mass of a new, highly variable X-ray source – Cyg X-1 – to be $\gtrsim 7$ $M_\odot$ and therefore possibly a black hole. Soon after this, results from the X-ray satellite *Uhuru* provided conclusive evidence that other compact X-ray sources are also binary systems (*e.g.* Schreier & et al. 1972); observations of Doppler-shifts of X-ray pulsation frequencies caused by orbital motion unambiguously identified the X-ray binaries as strongly magnetized ($> 10^{12}$ G) neutron-stars.

However, it was observed that some X-ray binaries pulsed, but others did not. While the pulsations were an unambiguous signature of a neutron star, the non-pulsing sources could either be black holes or neutron stars with weak magnetic fields. The difficulty in observationally distinguishing between neutron stars and black holes was alleviated somewhat when X-ray bursts were discovered (Grindlay et al. 1976; Belian et al. 1976). Within a few years, the X-ray bursts were understood to come from flashes of thermonuclear burning of He on the surfaces of neutron stars (for a recent review, see Lewin et al. 1993). These bursts were never observed from X-ray pulsars, resulting in the dictum "Bursters don't pulse and pulsars don't burst", as well as (and more importantly) a second unambiguous signature of a neutron star, which was exclusive of the first signature.

Also in 1975, the recurrent transient A 0620-00 was discovered. Initially very

bright in the X-rays (50-crab), it declined over a period of hundreds of days (Elvis et al. 1975 ; see also references in Tanaka & Lewin 1995). In quiescence, optical measurements of the radial motion of the counterpart placed a firm lower limit (3σ) on the mass of the compact object of 3.2 $M_\odot$ (McClintock & Remillard 1986). As with Cyg X-1, the mass function was the important observational characteristic which convinced observers that the source is likely to be a black hole.

By the early 1980's, the observational challenge in classifying X-ray binaries was to distinguish between neutron-star sources and black-hole sources. The "Smoking Gun" phenomena of X-ray pulsations and thermonuclear flash X-ray bursts clearly identified some of the neutron-star sources. White & Marshall (1984), in searching for the "Smoking Gun" of black holes, suggested instead that all sources which have "ultra-soft" energy spectra should be considered *potential* black holes – black hole candidates (BHCs). However, the ultra-soft spectrum also is found in several neutron star binaries (*e.g.* 4U 0142+61, Cir X-1; see Van Paradijs 1995).

In 1985, another observational clue which helped in the classification came to light. Intensity dependent quasi-periodic oscillations (QPO) were discovered in GX 5-1 (Van der Klis et al. 1985). Subsequent study by numerous observers, followed by a more global study found those of the class of sources known as Low-Mass X-ray Binaries (White et al. 1995) thought to contain neutron stars can be divided phenomenologically by their correlated X-ray timing and spectral behavior into two separate groups: the so-called "Z" sources and "Atoll" sources (see Hasinger and Van der Klis 1989 and references therein). The Z-sources are characterized by their strong QPO, which has complex, but phenomenologically understood,[1] correlations with intensity and spectrum. This has reinforced the theory that these sources are accretion driven neutron-star binary sources with moderate magnetic-fields, the interaction of which with the accretion disk is responsible for their QPO properties. The Atoll sources are those which have no QPO, and show broad noise properties which are also dependent on their spectral state; atoll sources tend to be X-ray burst sources

[1]The term "phenomenologically understood", in this sense, means that the complex and regular phenomenology has been described, and is reasonably complete.

as well, although two (of six) Z-sources also burst (see Van der Klis 1995 for a review of Z- and Atoll sources).

The epoch when the Japanese X-ray satellite *Ginga* flew (1987-1991) saw the long-term observation of three X-ray transients (GS 1124-68, GS 2000+25, and GS 2023+33). Such transients have an occurrence rate of $\sim$1/year/full sky. They typically brighten to X-ray fluxes of $\gtrsim$few times that of the Crab on the timescale of a few days, and then decrease in X-ray flux with an exponential time-scale of $\sim$35-40 days (Tanaka 1992). A second increase near 40-80 days is also observed, followed by a continued decrease on the same exponential timescale. All three transients observed with *Ginga* have been optically identified, and their mass functions are determined, indicating that they are BHCs (the mass function of GS 1124-683 is 3.1$\pm$0.4, Remillard et al. 1992 ; GS 2023+33 is 6.26$\pm$0.31, Casares et al. 1992 ; GS 2000+25 is 5.02 $\pm$0.46, Casares, Charles and Marsh 1995, see also Beekman et al. 1996).

2.4 The "State" Nomenclature

There exists a nomenclature which contains a useful basis for discussing and comparing the behavior of X-ray sources identified as BHCs. This nomenclature is based on the idea of "states", which is based on the observation that at any given time each BHC occupies one of at least two to three states which have different spectral, timing and intensity properties. We review this nomenclature and its development, because it provides the prevalent framework under which the properties of BHCs are currently understood.

Tananbaum et al. (1972) first invoked the idea of BHC "states" (described as "pre-" and "post-transition" states) to explain *Uhuru* observations of Cyg X-1, in which in less than one month, the 2-6 keV flux dropped by a factor of 4, the 6-10 keV flux remained constant, and the 10-20 keV flux increased by more than a factor of 2.

Markert et al. (1973) named several states observed in the newly discovered source GX 339-4 "high", "low", and "off", in reference to their intensities measured with *OSO-7*, and the indication that the high state was spectrally softer than the low

state. However, no connection was drawn with Cyg X-1, as the source exhibited no evidence of variability on timescales between 3min–13 days.

Of historical interest is how the "high" and "low" state nomenclature came to be applied to BHCs. In the first paper showing a transition in the BHC Cyg X-1 (Tananbaum et al. 1972), only a "transition" is mentioned, with no reference to "high" or "low" states – although the transition described was from a "high" to a "low" state as now defined. Markert et al. (1973) seemed to use the "high" and "low" state nomenclature first, in reference to GX 339-4, which they did not consider to be a BHC (the change in intensity and spectrum are similar, but no variability was observed). However, by 1975 when the next Cyg X-1 transition was observed, the "high" and "low" state nomenclature had been adopted, apparently in the announcement IAU Circular (Gursky et al. 1975), and in the subsequent X-ray papers (Sanford et al. 1975; Heise et al. 1975 though not by Holt et al. 1975). The similarity between GX 339-4 and Cyg X-1 was somehow seen, but the connection was not drawn in the literature. Thus, with the second outburst of Cyg X-1, the description of "high" (intensity) for the more X-ray luminous, soft, and less variable state, and the "low" (intensity) for the less X-ray luminous, spectrally hard, and larger variability state (Gursky et al. 1975; Sanford et al. 1975; Heise et al. 1975; Holt et al. 1975; Eyles et al. 1975) was adopted.

The connection between Cyg X-1 and GX 339-4 was first made by Samimi et al. (1979), who pointed out that both had bi-modal spectral behavior; Cir X-1 was also pointed to, and had been discussed previously as having a similar spectrum (Forman et al. 1976; Jones 1977). It was later shown that Cir X-1 is a neutron star system, as thermonuclear-flash X-ray bursts were detected from it (Tennant et al. 1986b; Tennant et al. 1986a); it thus became the first source mis-identified as a BHC on the basis of spectral/timing property comparisons.

White & Marshall (1984) produced color-color diagrams (CCD) of *HEAO 1* data which showed LMC X-3 and LMC X-1 (as well as several other sources) to have spectra similar to GX 339-4 and Cyg X-1 in their high states. On this basis, it was suggested that these sources be considered potential black holes – that is, black hole

candidates (BHCs).

With the launch of *Ginga* in 1987 came a spate of discoveries, which greatly strengthened the state paradigm. Cyg X-1, GX 339-4, GS 2023+33, GS 1826-24, and GS 1124-683 were each seen to have simultaneously a strong power-law X-ray energy spectrum and "flickering" variability, which took the form of a power-density spectrum which was constant below some frequency, and decreased with power-law dependency on frequency above this frequency (Belloni & Hasinger 1989; Tanaka 1992; Miyamoto et al. 1992; Miyamoto et al. 1992). It was also found that in a high-state of GS 1124-68 (Dotani 1992; Miyamoto et al. 1994; Takizawa et al. 1996) and GX 339-4 (Makishima & Miyamoto 1988; Dotani 1988; Kitamoto 1989; Miyamoto et al. 1989; Ebisawa 1991; Miyamoto et al. 1991), these sources gave very strong, highly peaked quasi-periodic oscillations in the 3-10 Hz frequency range. As GX 339-4 exhibited the QPO while at its brightest (1-37 keV) state ever observed, the state where QPO are observed from GX 339-4 has been called the Very High State (Miyamoto et al. 1991). The name has also been applied to the state when QPO have been observed from GS 1124-68, which also occurs while the source is near its peak 1-20 keV intensity.

Miyamoto et al. (1994) have shown that the power spectral density (that is, the variability) of GS 1124-68 at 0.3 Hz (arbitrarily chosen) increases with an increasing fraction of source luminosity being due to the power-law energy spectral component, once the fraction due to the power-law energy spectral component is greater than 10%; below 10%, the power spectral density at 0.3 Hz is a constant.

2.5 The Present Observational Situation

At the present time, we are still searching for the "Smoking Gun" of black holes – an observational signature which unambiguously identifies a black hole. The first step in the search for this "Smoking Gun" has been classifying sources as BHCs.

There are several observational signatures for a BHC. The first, and clearest, method is to optically identify the counterpart, and determine the mass function of the compact object by measuring the period and radial velocity of the binary companion.

A mass function which indicates a compact object mass >3.0 $M_\odot$ is sufficient to classify the individual object as a BHC. There are no instances of compact X-ray objects which have been demonstrated to have mass >3.0 $M_\odot$ which have also been demonstrated to be a neutron star. Second, if the combined spectral and timing behavior of a source is similar to that seen either as the canonical high-state or low-state behavior, then such an object may be classified a BHC. However, there are several examples of sources which qualify on the basis of their combined spectral and timing behavior alone which have been demonstrated to be neutron star binaries (*e.g.* Cir X-1, 1608-522).

2.6 How Has The Present Sample Been Identified as BHCs

The present sample consists of 10 BHCs. Six of these were identified due to their mass-functions: Cyg X-1, GS 1124-68, GS 2023+33, GS 2000+25, LMC X-1, and LMC X-3. The remaining four were identified on the basis of their combined spectral and timing behavior: 1630-47, 1826-24, GX 339-4, and 1354-64.

Details about the numerous characteristics of each of these ten sources has been recently reviewed (Tanaka & Lewin 1995).

2.7 Summary

There are two independent spectral components in BHCs: 1) an ultra-soft component, which is well described by the Disk Black-Body model (Mitsuda et al. 1984), which has little intensity variability associated with it; and 2) a power-law component, which is associated with strong (~30%) short-timescale (0.01-64 Hz) variability associated with it. When the ultra-soft component is dominant, little or no intensity variability is observed from the source. When the power-law energy spectral component is dominant, the source shows strong variability. There exists a high-intensity (2-10 keV) state in two sources — GX 339-4 and GS 1124-68 – in which strong QPO

are observed. While these QPO are observed, there are periods when either the "flickering" power density spectrum (PDS) shape is present, or when the power-law shape is present (Miyamoto et al. 1994).

The present framework of "states" is at times confusing, due in part to its historical reliance upon source intensity as the determinant of source behavior ("high" and "low" refer to high intensity and low intensity). In addition to the incomparability of source luminosities due to large uncertainties in the distances to various sources, the anti-correlation of the 1-10 keV flux and 20-300 keV flux observed in Cyg X-1 (Zhang et al. 1996) implies that high intensity in one band is low intensity in another band, and perhaps that source luminosity is a constant (W. Cui, private communication). As other observations of similar behavior in other sources has been reported previously (cf. Tanaka & Lewin 1995), a shift has occurred in the thinking of workers in which "high" largely means "spectrally soft" (or, ultra-soft energy spectral component) and "low" largely means "spectrally hard" (or, power-law energy spectral component), and implies the attendant variability properties of each component.

Perhaps a more useful approach is to connect the high/low state properties to observed spectral behavior in a quantitative fashion. This has already been done for neutron star LMXBs, the result of which has been the phenomenological ordering of those sources into two distinct classes: Z-sources, and atoll sources (Hasinger & Van Der Klis 1989). This phenomenological ordering has provoked theory on the production of their attendant phenomena, and has permitted comparison of these sources with others which are likely to be similar in behavior (Van der Klis 1994a; Van der Klis 1994b; Van der Klis 1995).

2.8 The Proposed Work

Currently, our best understanding of the behavior of BHCs is based on the classification of their state. Investigators of BHCs must first address the question, What state is it in? before moving on to discuss other observational issues.

As a structure for phenomenologically characterizing BHCs, the "state" paradigm

lacks quantitative value. For example, Cyg X-1 may be observed in the high-state. One might well ask, how high? There currently exists no gradation of states, no formal quantitative test to determine if a particular source occupies a state or not, and "how much" it occupies a state.

In the absence of a basis for quantitative gradation, at times qualitative gradation is substituted, with the declaration of new states to describe previously unseen behavior, or to elaborate on old behavior which, in consideration of different parameters, shows added complexity not observed in other sources. This procedure would attach a new "state" title to each new phenomenon. By deriving quantitative measures to the spectral and variability properties of BHCs, we may discover fine distinctions of behavior which may deepen our understanding of the underlying physics.

The use of the "state" nomenclature is useful to categorize phenomena which are shared by several sources. However, if a particular source demonstrates a peculiarity which defies simple classification, the declaration of a new state does not typically convey the relationship between the new and previously known behaviors. Instead, an approach which quantifies the behavior of the source in such a way that its relation to other behavior is transparent would be more useful.

In fact, such an approach has already been used – the combined use of color-color diagrams and the contemporaneous timing behavior of each source. This approach has quite successfully revealed regularities in the complex QPO and broad-band timing behavior of GS 1124-68 (Takizawa et al. 1996) and GX 339-4 (Miyamoto et al. 1991; Belloni et al. 1996) while these sources occupied their respective Very High States. Following this work, it was found that the Very High State, in which strong QPO is found, can have PDS (apart from the QPO) which are like the low-state (flat-topped with a single power-law) or which are like the high state (single power-law) (Miyamoto et al. 1993). In a similar vein, it has been shown that, as the fraction of the total intensity due to the power-law spectral component increases above 10%, the %rms variability (at an arbitrary frequency) also increases (Miyamoto et al. 1994). Again, by examining the spectral state (the ratio of the hard-component to the total

intensity), the variability behavior of GS 1124-68 was demonstrated to be correlated to the strength of the hard-component, which had been long suspected.

More generally, this approach has been used to untangle correlated timing and spectral/intensity behavior of non-pulsing neutron-star Low-Mass X-ray Binaries (LMXBs). Following this, it has become clearer what the accretion rate is during various states. More detailed theory on the spectral and timing behavior has been produced, as well as proposals for the relationship between the behavior of neutron-star LMXBs and that of BHCs, pulsars, and the peculiar source Cir X-1 (Van der Klis 1994a; see Van der Klis 1995 for review).

We have undertaken a study of the 10 BHCs observed with the *Ginga* LAC, with the aim of obtaining quantitative descriptions of recurrent spectral and variability phenomena. We have examined the source spectral state, as characterized by its location on a CCD, and attendant contemporaneous timing properties. Our goal is to tie the various states of BHCs – "high", "low", "very high" "high-to-low transition", and others – to specific positions on the CCD. One might expect that the location of a BHC on the CCD would be predictive of its timing behavior, as has been shown to be true of Z- and Atoll sources.

Chapter 3 describes the Large Area Counter (LAC) on the *Ginga* satellite, and the data selection and preparation methods. Chapter 4 shows the resulting intensity histories, hardness-intensity diagrams (HIDs), color-color-diagrams (CCDs), as well as the full combined CCDs of all sources. Chapter 5 will show the timing studies of each of the individual sources as a function of their contemporaneous color. Chapter 6 provides an overview of the results, with a discussion. Conclusions are summarized in Chapter 10.

Chapter 3

The X-ray Data

3.1 The *Ginga* Satellite

All X-ray data on black hole candidates (BHCs) in this thesis were obtained by the Large Area Counter (LAC) on the the *Ginga* satellite, which has been fully described (Turner et al. 1989). We repeat here the salient features of this instrument, as regards instrument capabilities and data acquisition.

The Japanese *Ginga* satellite was launched Feb 5 1987 from Kagoshima Space Center in the southern Japanese province Honshu, and operated until it re-entered the atmosphere in December 1991. On it were three principal scientific research instruments: the Gamma-ray Burst Detector (designed to search for Gamma-ray Bursts), an All-Sky Monitor (ASM) which provided long-term monitoring of bright X-ray sources and searched for X-ray transients, and the LAC.

The LAC instrument is shown in Fig. 3-1 (Turner et al. 1989). It was composed of eight identical, sealed collimated gas proportional counters, providing a geometric area of 4000 cm^2. The nominal energy range of these proportional counters was 1.5-37 keV, divided into 64 non-energy-independent channels. The collimators at the front of these detectors limited the field of view to an oval of 1°x2° full-width at half-maximum response. The satellite could be oriented to point the LAC in any direction on the sky between 50° and 130° from the solar direction (although typically the sun was kept $> 90°$ to avoid solar X-ray contamination).

The data acquisition modes available to the on-board computer (OBC) operate under the constraint of limited satellite telemetry bandwidth. One OBC mode is specified for each observation, which determines both the energy and time resolution of the telemetered data; if one used N energy channels and a time-resolution of M samples/sec, then the required telemetry (bits/sec) scales as N×M. Thus, providing greater accuracy in energy required lower time-resolution, and vice-versa.

Table 3.1: *Ginga* Data Modes

Mode	# Energy Channels	Time Resolution		
		High	Medium	Low
MPC1	48	500ms	4s	16s
MPC2	48	62.5ms	500ms	2s
MPC3	12	7.8ms	62.5ms	250ms
PC-H	1	1.9ms	15.6ms	62.5ms
PC-L	1	0.98ms	7.8ms	31.3ms

Table adapted from (Turner et al. 1989), Table 2

The available observation modes (shown in Table 3.1) are called MPC1, MPC2, MPC3, and PC. MPC1&2 permit division of the nominal energy range into 48 energy channels; MPC3 provides 12; PC provides 2. In each of these modes, there are three time-resolution options ("high", "medium", or "low"); these are commonly referred to as the bit-rate of the observing mode ("high", "medium" and "low" bit-rate).

The PC data provide the highest time-resolution, while only offering two energy channels, "H" and "L" (high and low). The low-energy channel has higher time-resolution than the high-energy channel, typically by a factor of two.

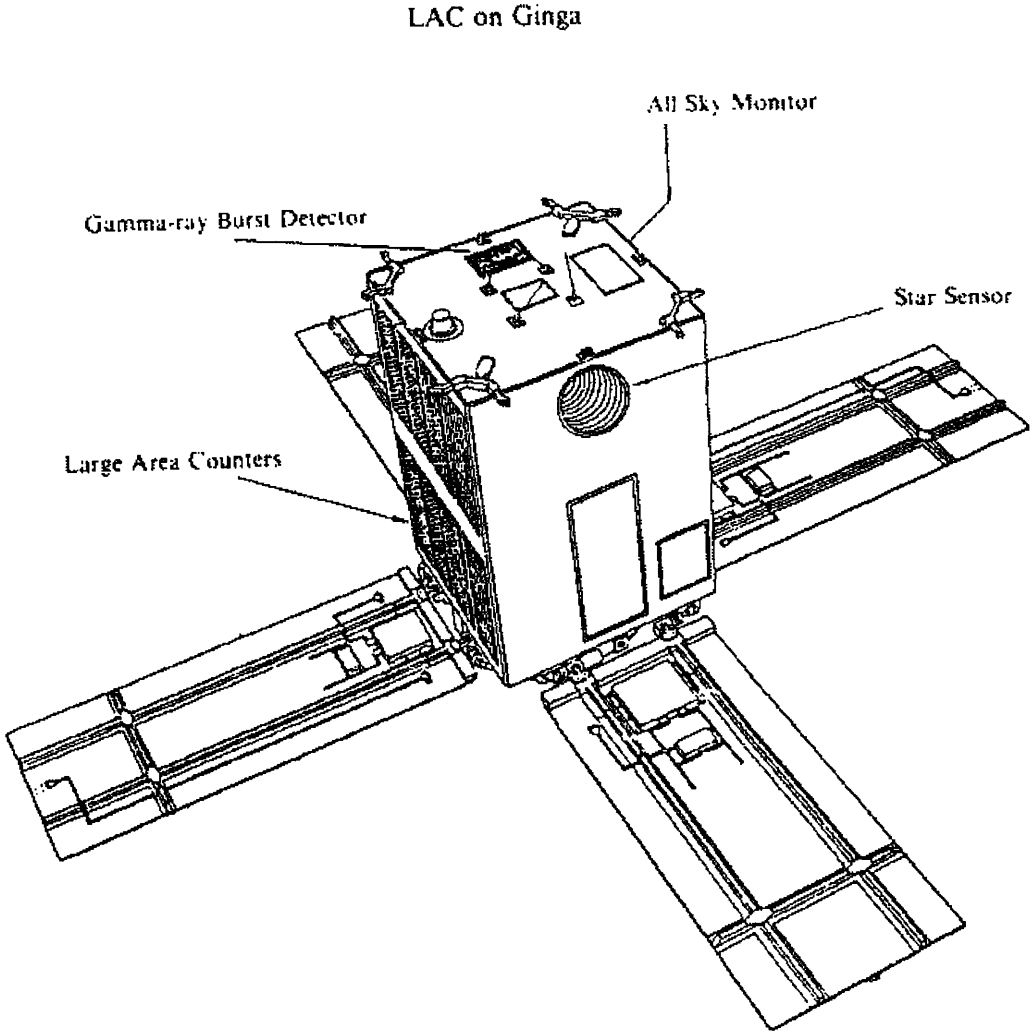

Figure 3-1: **Schematic of the Ginga Satellite.** The location of the Large Area Counters is indicated. From Turner (1989).

3.1.1 The LAC Background Counts

The most detailed study of the LAC background was performed by Hayashida (1989). We repeat here the important features.

The internal background varies by a factor of two during a single orbit and by approximately 25% over the 37-day precession period of the satellite. A typical background count-rate is roughly 75-150 counts/s in the 1.5-37 keV energy range. This background is due to several sources: a) the cosmic X-ray background; b) geomagnetically trapped charged particles; c) fluorescent line features (at 3.1, 4.8, 6.4, and 22.0 keV); d) radio-active decay of isotopes with characteristic half lives of 5.5min, 41min, and 8hr following a passage through the South Atlantic Anomaly.

The Adopted Background Subtraction Method

Hayashida et al. (1989) describes the several methods which may be used to produce a model spectrum of the background. These methods make use of several observational parameters, including:

- **SUD count-rate**: the count-rate of X-ray like events whose energy deposit exceeds the upper-level energy discriminator (typically 37 keV, or 60 keV).

- **MID count-rate**: the count-rate of a middle-layer of the LAC, which has a low (~5%) efficiency for X-ray detection in the 1-5 keV range, but is sensitive to the internal background, and in particular to the 3 and 5 keV fluorescent line features.

- **PIM count-rate**: the count-rate in detector wires which are screened from direct illumination, but are otherwise similar to the wires in the detector, and therefore provides a good estimation of the non-source background count-rate.

- **COR**: the cut-off geo-magnetic rigidity, the amount of momentum/unit charge required for a particle to penetrate to the spacecraft's position in the geomagnetosphere from infinity.

- **Time since SAA Passage**: required to model the decaying count-rate of radio-activated isotopes produced during passage through the SAA.

- **recent off-source observations**: an observation of a near-by field which contains only cosmic X-ray background can provide an estimation of the non time-variable X-ray background in the region of the object of interest.

The energy spectra of BHCs can have hard power-law "tails" which can extend to high energies (>50-500 keV). As such, we cannot make use of methods which estimate the non-X-ray background using the SUD count-rate; the BHCs contributed significantly to the SUD count-rate, causing an over-estimation of the background count-rate, and therefore an over-subtraction of the background count-rate.

While for a few observations, we could use a recent off-source observation to estimate the background, such off-sources observations are usually not available, particularly for the transient sources where short observations were employed for monitoring purposes, requiring time out from the planned observations (which programmatically must be minimized).

For the data which are discussed in the present work, we employed a background subtraction method which makes use only of the satellite position (i.e. geomagnetic latitude) and the "MID" count-rate, as is provided in the package of data-reduction programs at ISAS as the card "BGD590ML".

3.2 Data Preparation – Corrected and Uncorrected Data

The data seletected were obtained from the archives of *Ginga* kept on the FACOM computer at the Institute for Space and Astronautical Science (ISAS; Sagamihara, Japan). Originally, the data were taken during planned, pointed observations of these sources. These observations were planned by different observers with different observational objectives. Thus, the data were taken in a variety of observing modes, with different energy resolution and time resolution, and under different observing

conditions. We first selected data which suit our observational needs.

We applied the following criteria to select data of sufficient quality to insure they are not contaminated by events unrelated to the source properties:

- source elevation (angle between the earth limb and the source) $> 5\,\mathrm{deg}$
- contiguous observing time must be > 128 s
- multi-channel energy resolution is necessary, and thus PC data (with only two energy bands) were not obtained for these analyses.
- geo-magnetic rigidity > 9 GeV; rigidity, which is a function of the spacecraft position in the earth's magnetosphere, is a measure of the momentum per unit charge required for a particle to penetrate the magnetosphere to the spacecraft's location
- the telemetry must have been perfectly relayed (*i.e.* no a-synchronous bits, indicating telemetry dropout during relay between the satellite to ground station)

Using these criteria, we selected data which were obtained during the observations listed in Table B.1. Data which met the above criteria from these observations were then prepared as a timing file, which was inspected for "spikes" (see Sec 3.3), which were systematically (although not completely) excluded from the data. Finally, a timing file was produced, preserving both the original time resolution and energy resolution. These data are what we will refer to throughout this work as the "raw data".

Following data selection, the data were pre-processed using the standard analysis programs available on the FACOM computer at ISAS (Sagamihara, Japan). For each source, observation lists were produced and the data which met the above criteria were extracted from the *Ginga* data archive. These data were then rebinned in time (to 4 s or 16 s), and pre-processed. During pre-processing, the data were dead-time corrected, background subtracted using a method similar but not identical to Hiyashida's method 2 (Hayashida et al. 1989), which was selected as a compromise between uniformity and accuracy for observations of BHCs, and aspect corrected. This

yielded data with 4-16s time resolution and 5-20 energy bins below 20 keV, which represented the true counts flux of the source (not corrected for energy response) in counts sec^{-1}.

Following pre-processing, the data were transported to MIT for further selection and analysis. The light-curve and integrated X-ray pulse height distribution (PHD, or "counts-spectrum") over the duration of the contiguous observation were analyzed for signs of poor background subtraction; observations which showed signs of poor background subtraction (either over- or under-subtraction) were excluded from further analysis.

To identify over- or under-subtracted data, we use the >20 keV range, where the signal/noise is the lowest, and thus, the effects of poor subtraction will be most evident. If the there is no discernible effect in the counts-spectrum in this range, then it is certain that the magnitude of under- or over- subtraction will not be measurable (i.e. in the noise) in the energy ranges used in the present work.

If two or more energy bins above 10 keV had count-rates which were more than 4 σ below 0, then the background was considered to have been over-subtracted and the full observational period was excluded from further analysis. An example of an over-subtracted counts-spectrum is shown in Fig. 3-2a.

The counts spectrum was visually inspected for signs of under-subtraction in the high-energy (>20 keV) range. Two features which signal under-subtraction are: 1) the spectrum flattens at high energy (> 20 keV), becoming nearly constant; and 2) the presence of the 22 keV silver line. An example of an under-subtracted counts-spectrum is shown in Fig. 3-2b.

Significant amounts (~30%) of data from 4 of the 10 BHCs were not usable (see Table 4.1). The major cause of data exclusion was poor background subtraction, which resulted in the exclusion of a total of 270 ksec of data.

We include a complete list from which all data which were used in this thesis were selected in Sec. B.1.

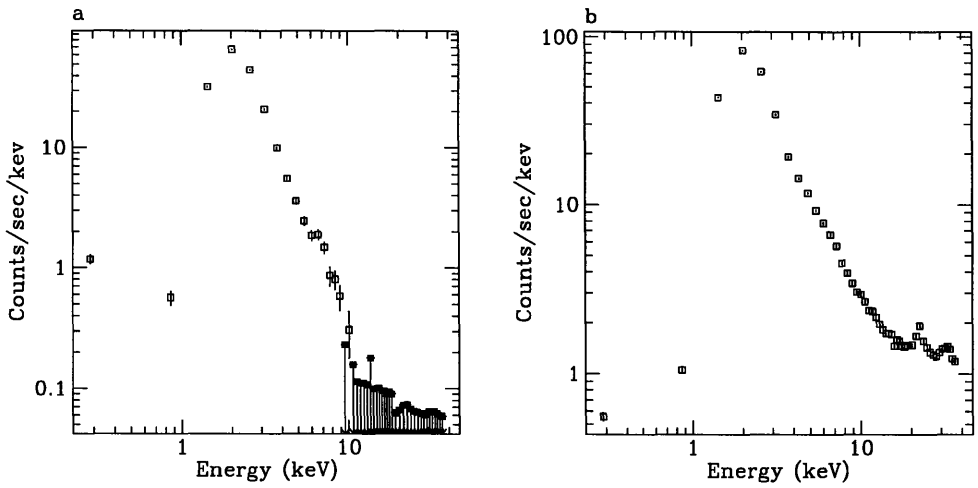

Figure 3-2: **Examples of of Poor Background Subtraction.** Panel *a* is a case where the data were over-subtracted, resulting in count-rates which are significantly below zero (shown here as 1 σupper-limits). Panel *b* is a case where the data are under-subtracted, as can be seen by the flattening of the spectrum at high energies, and the presence of the 22.0 keV Silver line.

3.3 SPIKES

At various times during the observations, events which we call "spikes" can be seen in the data. There are at least two different kinds of spikes. The first is easily identified, as it occurs near the beginning or the end of an observational period, as the high-voltage of the instrument is switched on or off, to exclude operation in the South-Atlantic-Anomaly (a geographic region of low geo-magnetic field and resulting high particle background). The second come during the middle of observations, and are typically due to a single high-energy particle which penetrates the detector and leaves a stream of ions in its wake.

We show an example of this second kind of spike in Fig. 3-3. In the bottom left panel is a typical spike light-curve. Spikes are usually constrained to a few $\times$ 8-msec time bins (here, the spike occupies 3-8 msec time bins near t=103.4 sec), during which the count-rate increases to saturation, as here). In the top panels, we show the counts-spectra which were obtained in the three time-bins. We see that in the t=0 msec time-bin, most of the counts occurred above 10 keV; in the t=7.8 msec time-bin, the counts are evenly spread over all observed energies; and in the t=15.6msec time-bin, the counts are largely below 10 keV. For comparison, in the fourth panel, we include a raw counts spectrum of the source + background obtained during a 100-s period.

This type of event can be excluded from being astrophysical, by separating the data by detector module (of which there are eight in the LAC), and examining the count-rates individually. Typically, these events are due to particles which penetrate the detector, leaving a stream of ions in their wake. Many of this type of event were seen with *Ginga*. We did not systematically inspect the individual module count-rates for these events. Rather, because they are so common, we systematically excluded from analysis all periods where the distinctive intensity profile of the spike was observed. It remains as an interesting and perhaps fruitful project to inspect all the spikes which were observed during these observations with the full *Ginga* database.

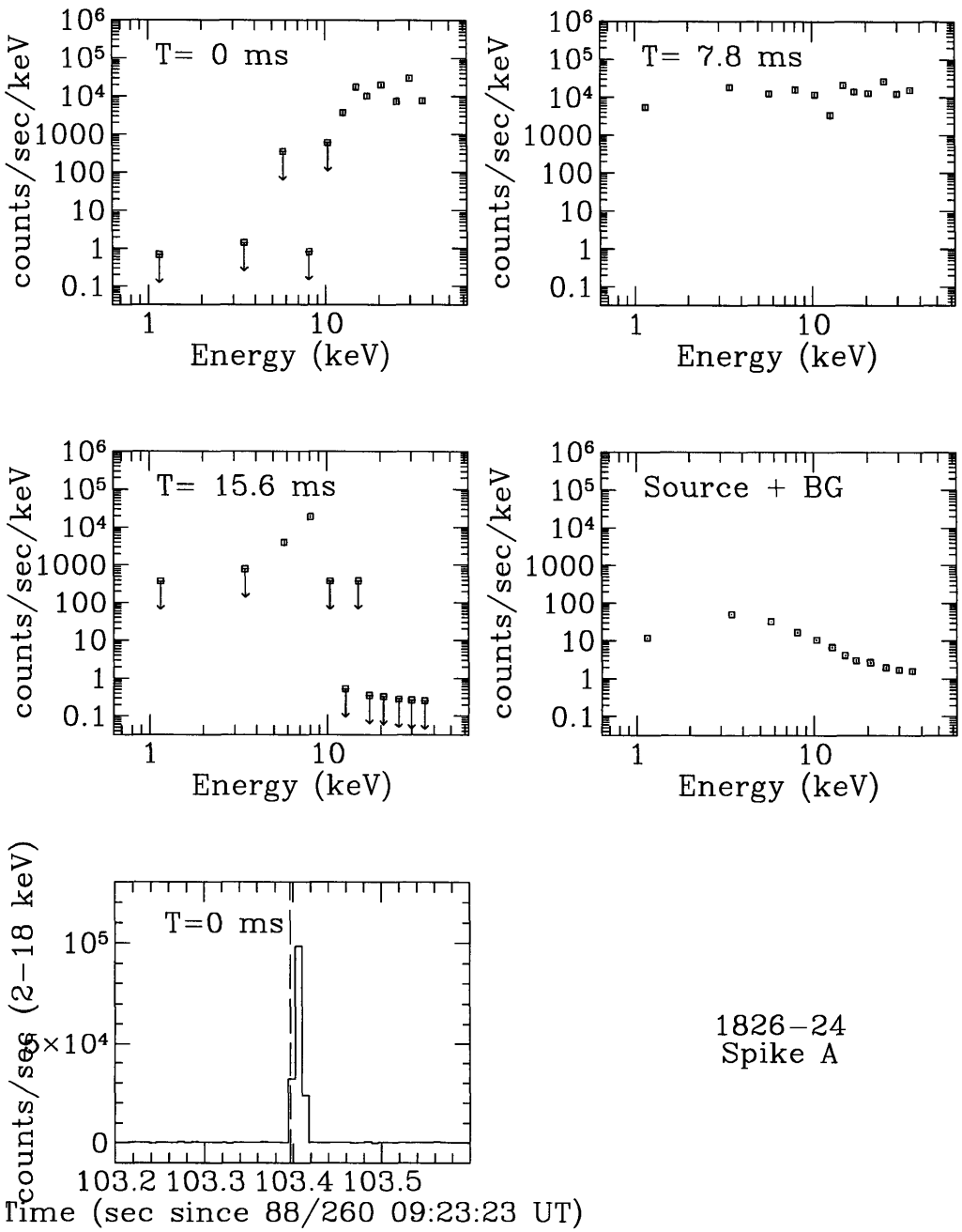

Figure 3-3: **1826-24: Spike A** The counts spectrum from the raw data of the three time-bins of Spike A from 1826-24 (T=0, 7.8ms, and 15.6ms). In these three spectra, we subtracted the source+background spectrum, and show only the excess counts. For comparison, we show a counts spectrum of the source plus background, from 100 s of data in the same observational period. The bottom panel is the light-curve of this spike, which shows that the spike clearly takes up three 7.8ms time-bins.

During preliminary data preparation, we scanned the 1-37 keV light-curves for spikes and excluded them from the final raw and corrected data files. However, not all spikes were found, and several made their way into the timing files, and thus had to be excluded during analysis.

3.4 High Energy (> 10 keV) Electron Events

In the process of investigating high energy spectral variability, several transient ($\lesssim$50 sec) high energy (> 10 keV) events were identified, which do not fit the general description of "spikes". These events came during observations of LMC X-1 and 1354-64, which led us to perform a more general search through the data.

For the seven events discussed here, simultaneous light-curves were produced showing the *Ginga* LAC count-rates, simultaneously with the ASM and GBD count-rates (T. Dotani, private communication). It was found that the events observed in the *Ginga* LAC had simultaneous events observed in the ASM and GBD. As these detectors do not have over-lapping FOVs, the source of the counts must have been omni-directional, the simplest cause of which are electrons trapped in the earth's magnetic field.

Based on the weight of the evidence here, we concluded that these events are due to particles, trapped in the earth's magnetosphere, injected there from nuclear reactors borne on satellites (see the dedicated issue of *Science* April, 1989 for several articles describing SMM observations of these events). As few observations of these events below 100 keV have been reported, we provide a description of the general search for these events, the events themselves, and at the end of this section, our reasons for concluding these events are due to electrons from orbiting nuclear reactors.

3.4.1 Description of Search For High Energy Events

We performed a search for high energy events in the corrected and raw data.

Light-curves of all corrected data were produced in the highest available time resolution (typically 4s or 16s) in four energy ranges: Low Energy Range (=2.3–4.6 keV), Medium Energy Range(=4.6–9.2 keV), High Energy Range(=9.2–18.4 keV), and 18.4–36.7 keV. Also, light-curves in the same energy ranges were produced of the raw data for all sources, using time resolution of 0.5 s and 16 s.

The light-curves were scanned by eye for events which showed a sudden rise in the count-rate in the High Energy Range and 18.4–36.7 keV range, with little or no

excess count-rate in the Low Energy Range or Medium Energy Range, which lasted for over 1 second. In a more quantifiable manner, "sudden rise" indicates an increase in the source intensity in the relevant energy range which represents a strong deviation from the continuum PDS properties – thus distinguishing these events from simple "flickers" in the source intensity. Events which satisfied these criteria were used to produce counts spectra, and were compared with counts spectra of the persistent emission from earlier in the observation to examine the spectral properties of the event.

Candidate events in the corrected data were sometimes found in data taken in MPC3 data mode (12 energy channels). To corroborate such events, we used the corresponding raw (high time resolution) data, if available, to investigate the time-profile. In our original data selection criteria, many (but not all) of these events qualify as "spikes", and were thus summarily excluded from the raw-data which was prepared for analysis at ISAS in Japan.

The goal of these criteria is to identify spectrally hard, transient events, and distinguish them from the time-averaged intensity variability properties, and also the ubiquitous instrumental "spikes" (see 3.3).

A total of 7 events which satisfied these criteria were found during observations of two of the ten sources: LMC X-1 and 1354-64. We describe these events in detail in this section.

3.4.2 High Energy (>10 keV) Electron Events During Observations of LMC X-1

Four events, identified by eye, were found in 16 ksec of observations of LMC X-1, where a sudden, transient change in the 9.2-36.7 keV count-rate occurred. The energy spectra of these events were considerably harder than the emission before and after, usually only apparent above 10 keV. In three of the cases (events 1, 2, & 3), the occurrence of the burst was accompanied by a change in the persistent emission spectrum (before the burst, compared to after the burst). In event 1, the PE became

softer after the burst, while for events 2 & 3 the PE became spectrally *harder* after the burst. We give the details of the occurrences of the events in Table 3.2. The four events each typically last for $\sim$ 50 s.

Table 3.2: Event Information During LMC X-1 Observations

Event Number	Time (UT)	Wide Ratio (before)	Wide Ratio (after)
1	87/113 02:54:39	0.061±0.002	0.052 ±0.002
2	87/113 04:39:11	0.051 ±0.001	0.047 ±0.004
3	87/113 06:16:47	0.047 ±0.002	0.063 ±0.004
4	87/197 10:43:52	0.018 ±0.001	0.018 ±0.002

In Figs. 3-4–3-7, we show the light-curves of these events in four energy ranges (Low Energy Range, Medium Energy Range, High Energy Range, and 18.4–36.7 keV), as well as a hardness ratio. The events are most noticeable in the energy ranges above 10 keV, and not at all noticeable below 10 keV. In event 1 (Fig. 3-4), the count-rate in the 18.4-37.6 keV energy range is lower following the event than prior to the event, indicating spectral softening. In event 3, (Fig. 3-6), the count-rate in the 18.4-37.6 keV energy range is *higher* following the event than prior to the event, indicating spectral hardening. In the other two events (Figs. 3-5 & 3-7) there is no measurable change in the source spectrum between before and after the event. To quantify this, we took the average Wide Ratio integrated from time=0 during each observation period to $\sim$100 s before the time peak count-rate in the 18.4–37.6 keV band, and compared it to the Wide Ratio, averaged from 100 seconds after the time peak count-rate in the 18.4–37.6 keV band to the end of each observation period (see Table 3.2). Event 1 shows an appreciably *softened* spectrum, while event 3 shows an appreciably *hardened* spectrum, and events 2 & 4 show no change.

In Fig. 3-8, we compared the counts spectra observed during the event to an average persistent emission (PE) spectrum. The event spectrum is integrated for 48 s around each event, while the PE spectra was integrated from before the events observation periods in each of the 4 observations, for a total of 2700 s. The counts spectra are nearly identical below 5 keV, with increasing deviations at increasing

energies. Above 15 keV, the event counts spectrum is almost flat, indicating an extremely hard tail.

For events 1, 2 and 3, the data were acquired with 16 second time resolution; thus, we gain no additional information from showing the raw data, as the corrected data also have 16 s time resolution. For event 4, the data were acquired with 0.5 second time resolution. In Fig. 3-9 we re-binned the data to 2-second time resolution, and show the 9.2–36.7 keV light-curve, the 2.3–9.2 keV lightcurve, and the integrated counts spectrum during the event compared to a spectrum integrated during the PE. The event structure is observable in the 9.2–36.7 keV light-curve; the event begins with a fast rise ($<$ 2 seconds) with a spike of 4-6 seconds duration, which is followed by approximately 30 seconds of excess emission. During this same time, no excess emission is evident in the 2.3–9.2 keV range.

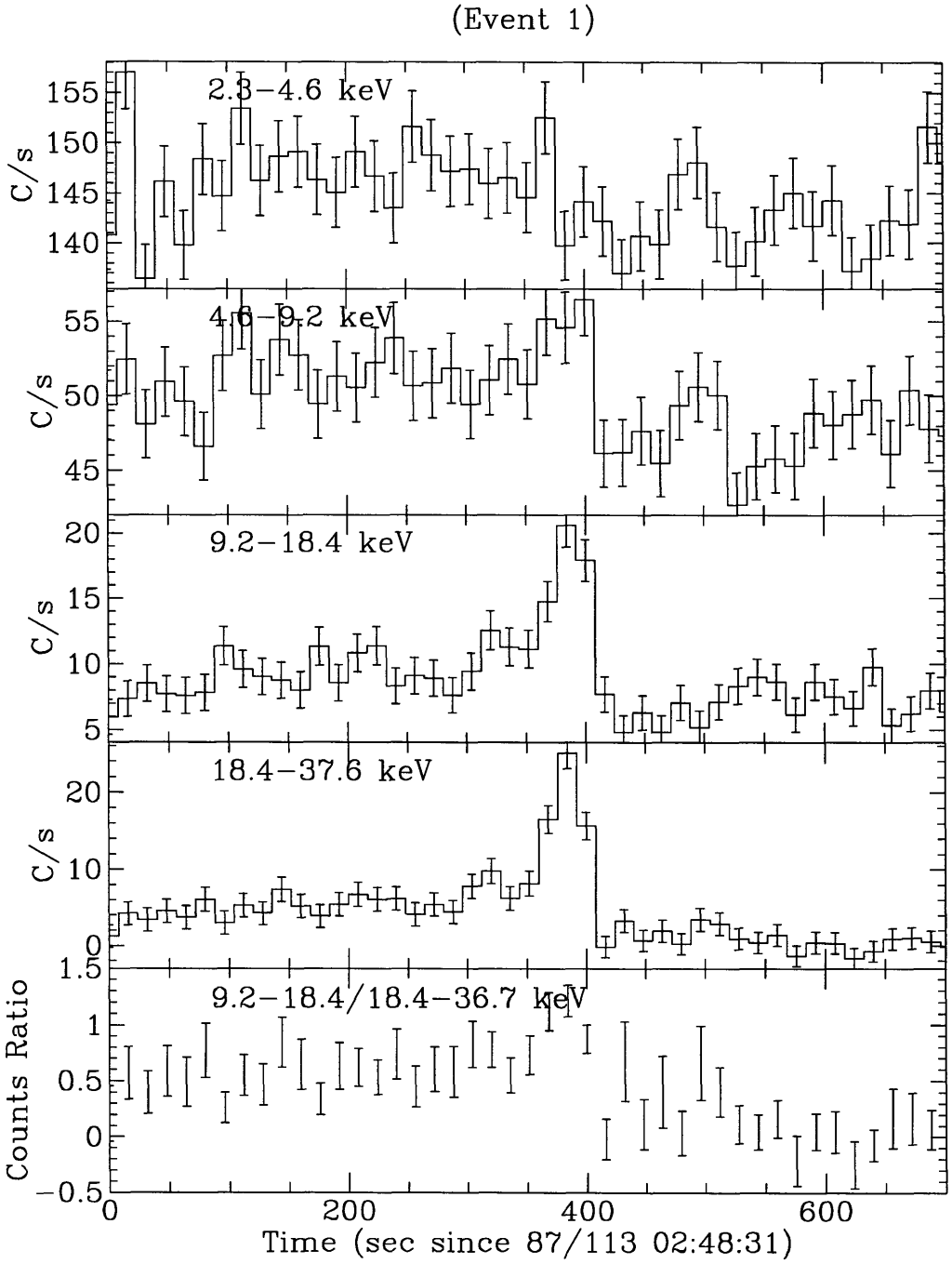

Figure 3-4: **LMC X-1 High Energy Spike LC and Wide Ratio (Event 1)** Corrected light curves in four energy ranges (marked in each panel) and the hardness ratio (9.2–18.4 keV/18.4–36.7 keV) during the high-energy spike. Error bars are 1 σ. The time resolution is 16 s.

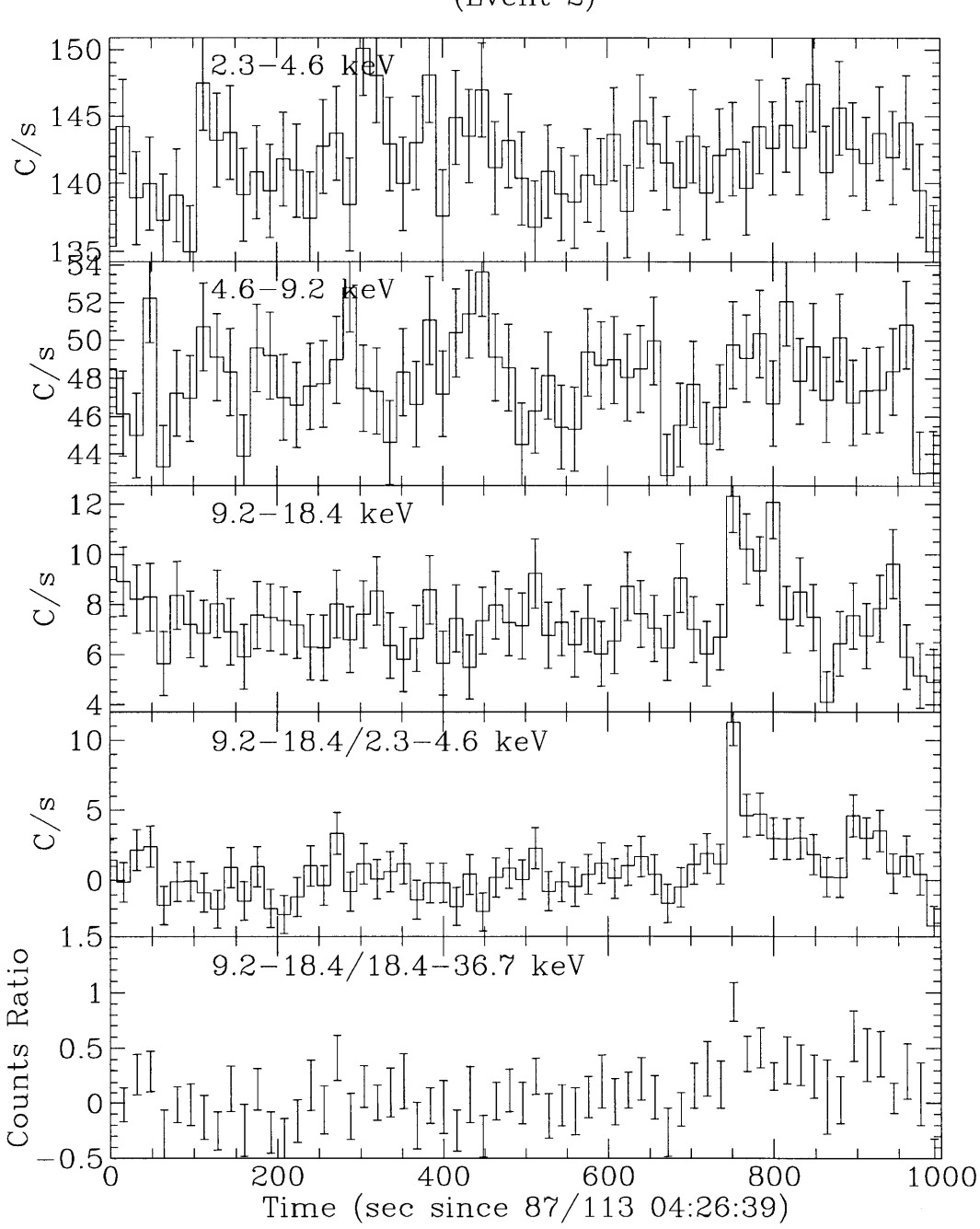

Figure 3-5: **LMC X-1 High Energy Spike LC and Wide Ratio (Event 2)** Corrected light curves in four energy ranges (marked in each panel) and the hardness ratio (9.2–18.4 keV/18.4–36.7 keV) during the high-energy spike. Error bars are 1 σ. The time resolution is 16 s.

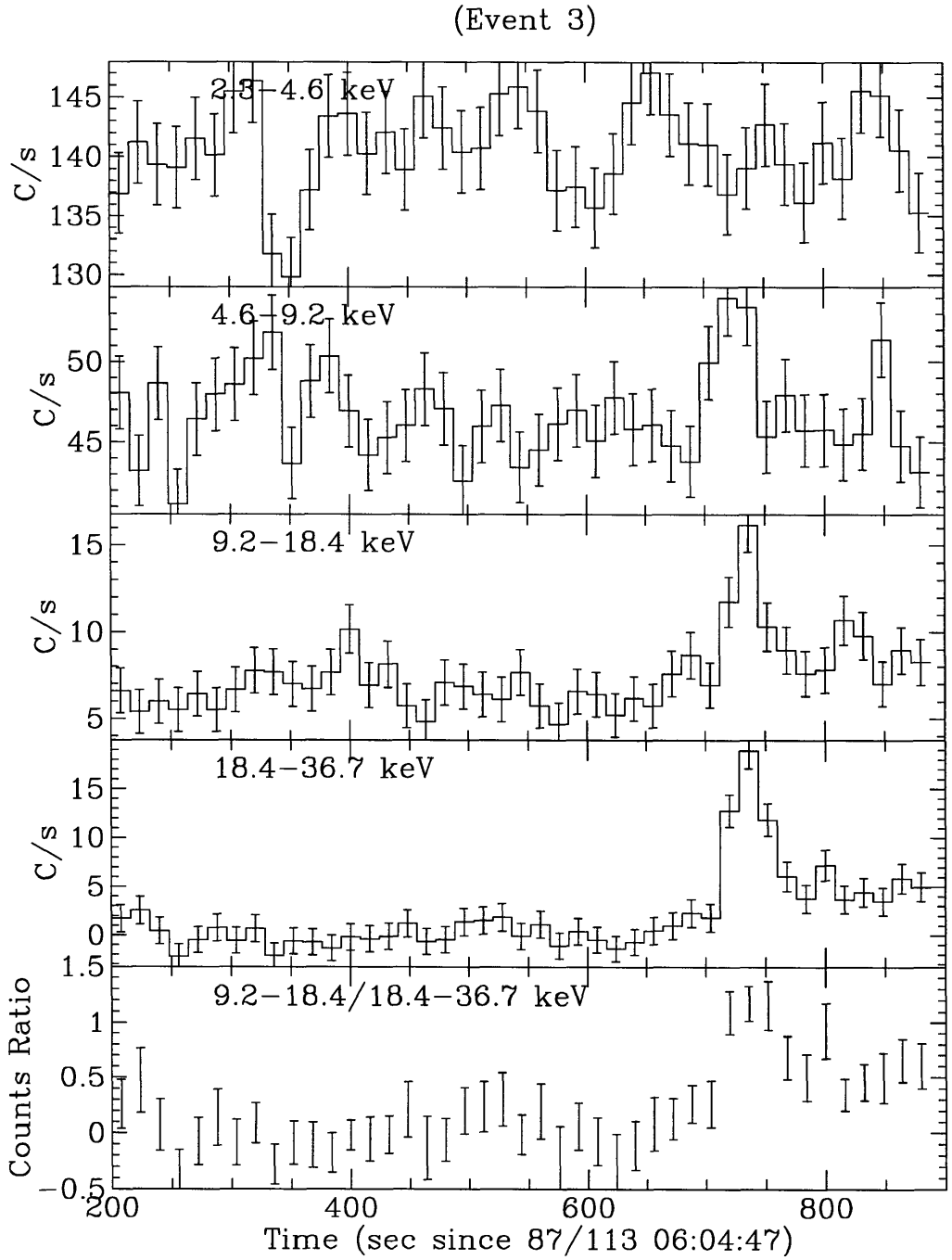

Figure 3-6: **LMC X-1 High Energy Spike LC and Wide Ratio (Event 3)** Corrected light curves in four energy ranges (marked in each panel) and the hardness ratio (9.2–18.4 keV/18.4–36.7 keV) during the high-energy spike. Error bars are 1 σ. The time resolution is 16 s.

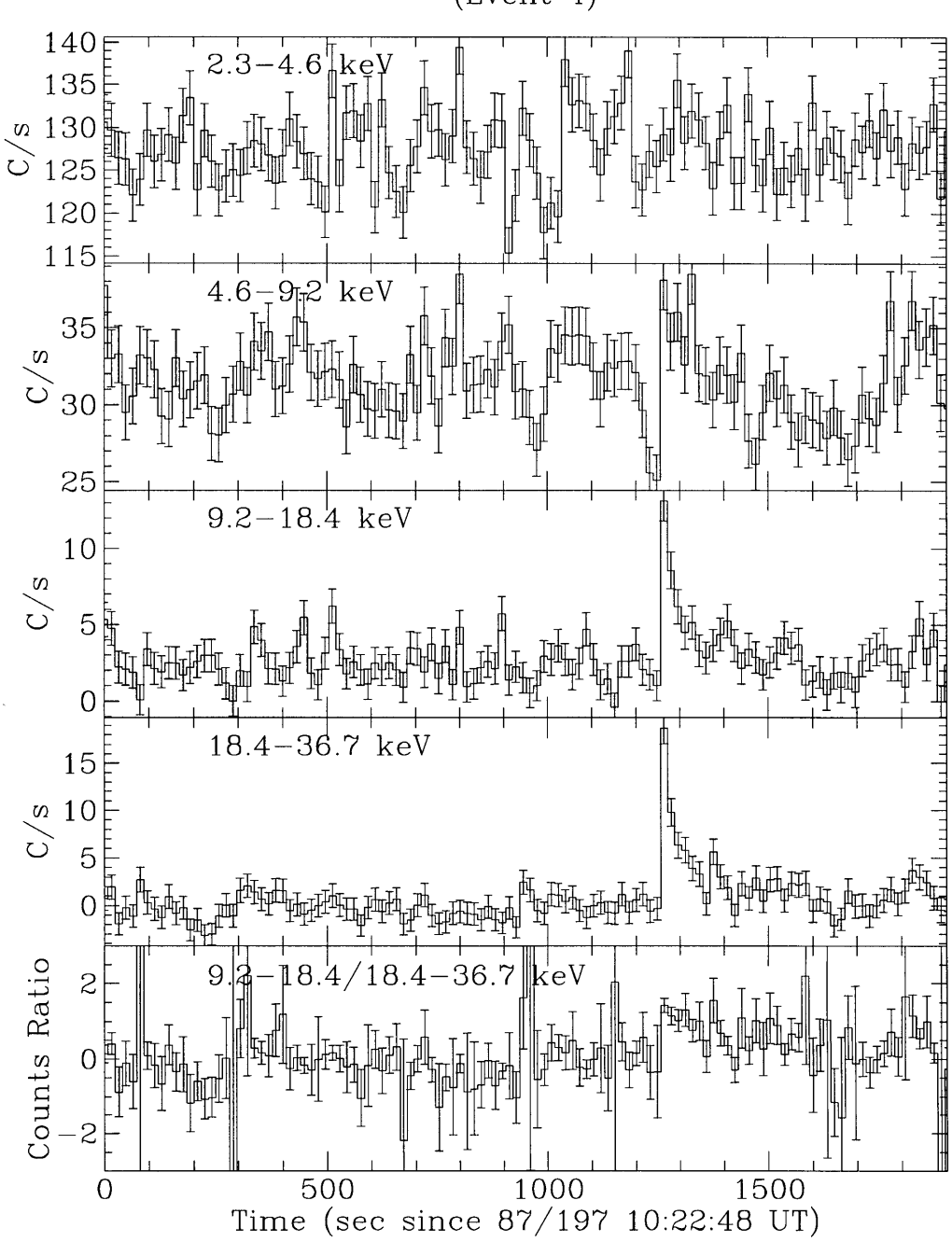

Figure 3-7: **LMC X-1 High Energy Spike LC and Wide Ratio (Event 4)** Corrected light curves in four energy ranges (marked in each panel) and the hardness ratio (9.2–18.4 keV/18.4–36.7 keV) during the high-energy spike. Error bars are 1 σ. The time resolution is 16 s.

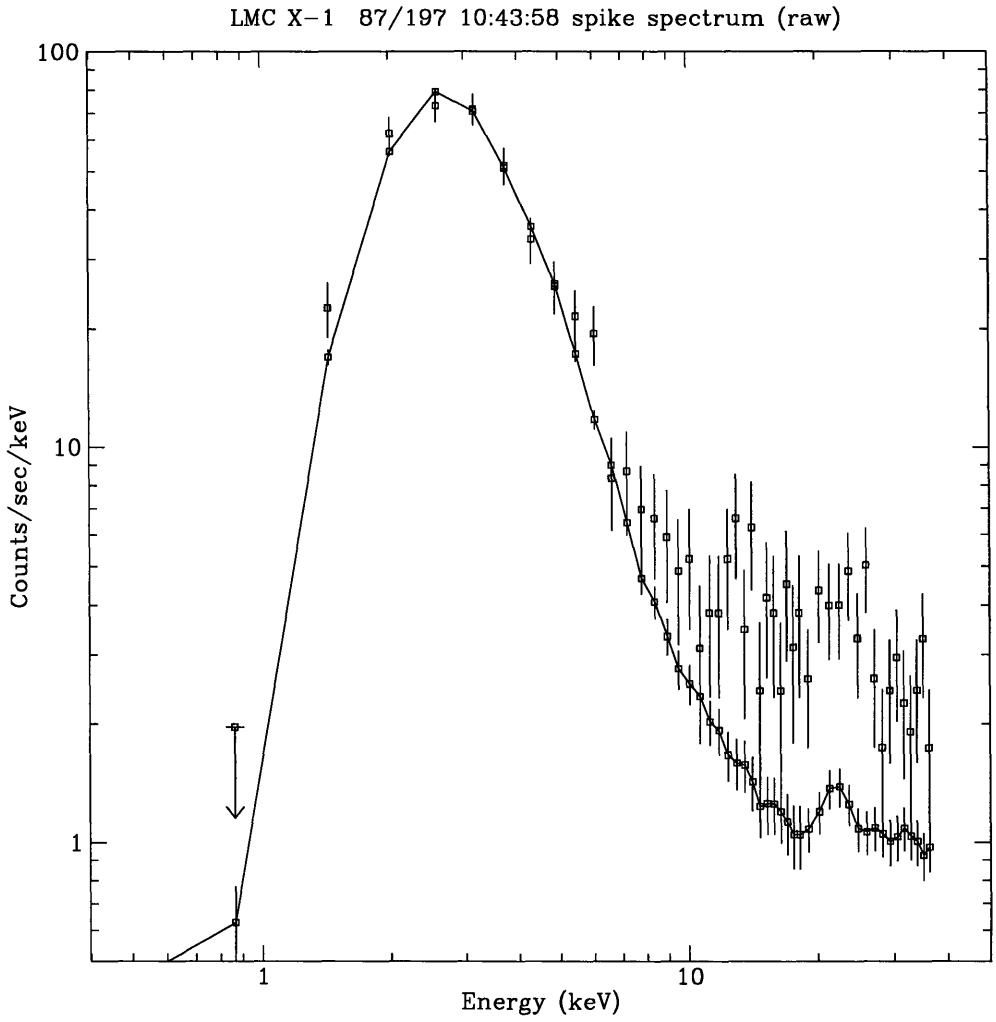

Figure 3-8: **LMC X-1 Observation High Energy Event Integrated Spectrum** Corrected summed counts spectrum from all four events, and the persistent emission spectrum (connected points) averaged from 2700 sec divided among the four observations. Error-bars are 1 σGaussian errors, and upper-limits are 2 σ. The two spectra are nearly identical below 5 keV, with deviation in the 10-30 keV range; the events are much harder than the persistent emission.

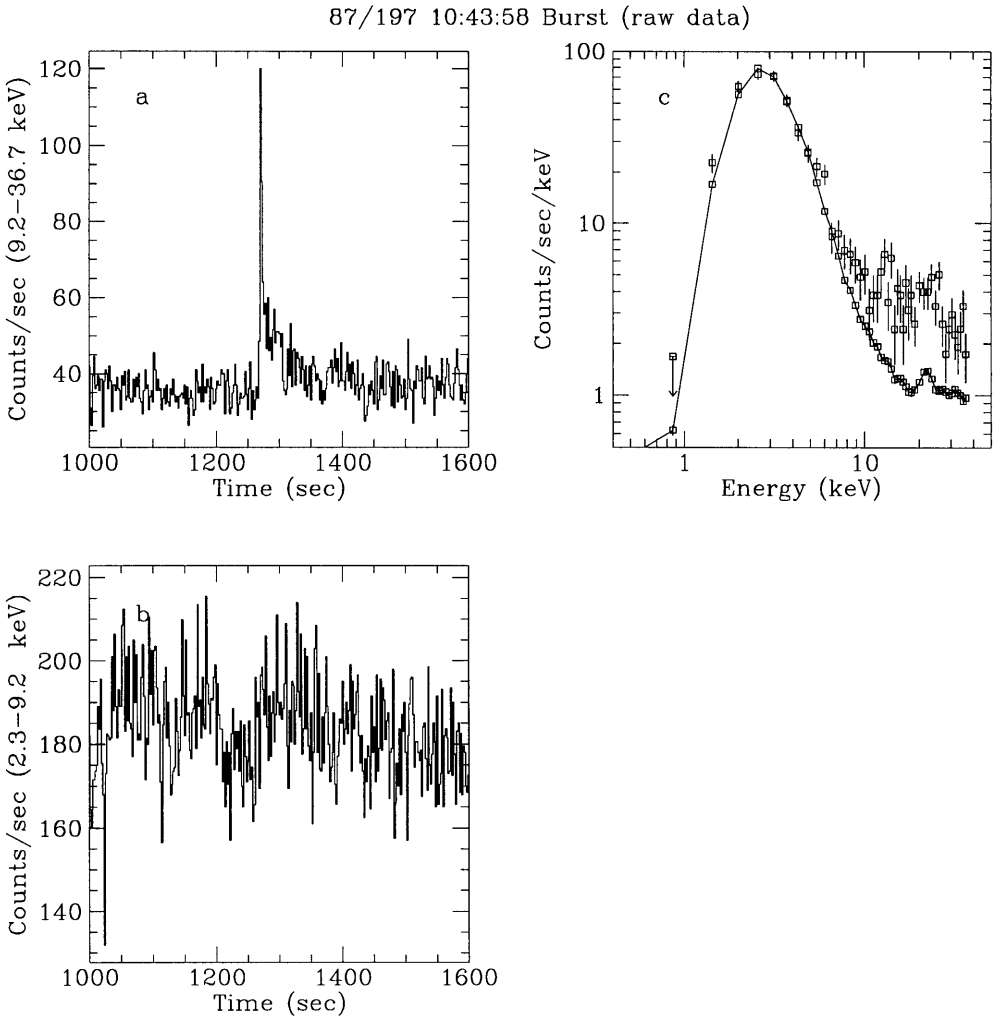

Figure 3-9: **LMC X-1 Observation High Energy Event – Raw Data (Event 4) (a)** The 9.2–36.7 keV raw count-rate (uncorrected for deadtime, background, or aspect) from event 4. The time resolution is 2 s. **(b)** The raw counts spectrum taken from Time=1269-1274 s (unconnected points) compared with the raw counts spectrum taken from time=600-1200 s (connected points). Upper limits are 2σ. The spectrum taken during the burst shows excess counts at energies $\gtrsim$7 keV. **(c)** The 2.3–9.2 keV raw count-rate (uncorrected for deadtime, background, or aspect) from event 4. The time resolution is 2 s. No excess emission is evident in this energy range.

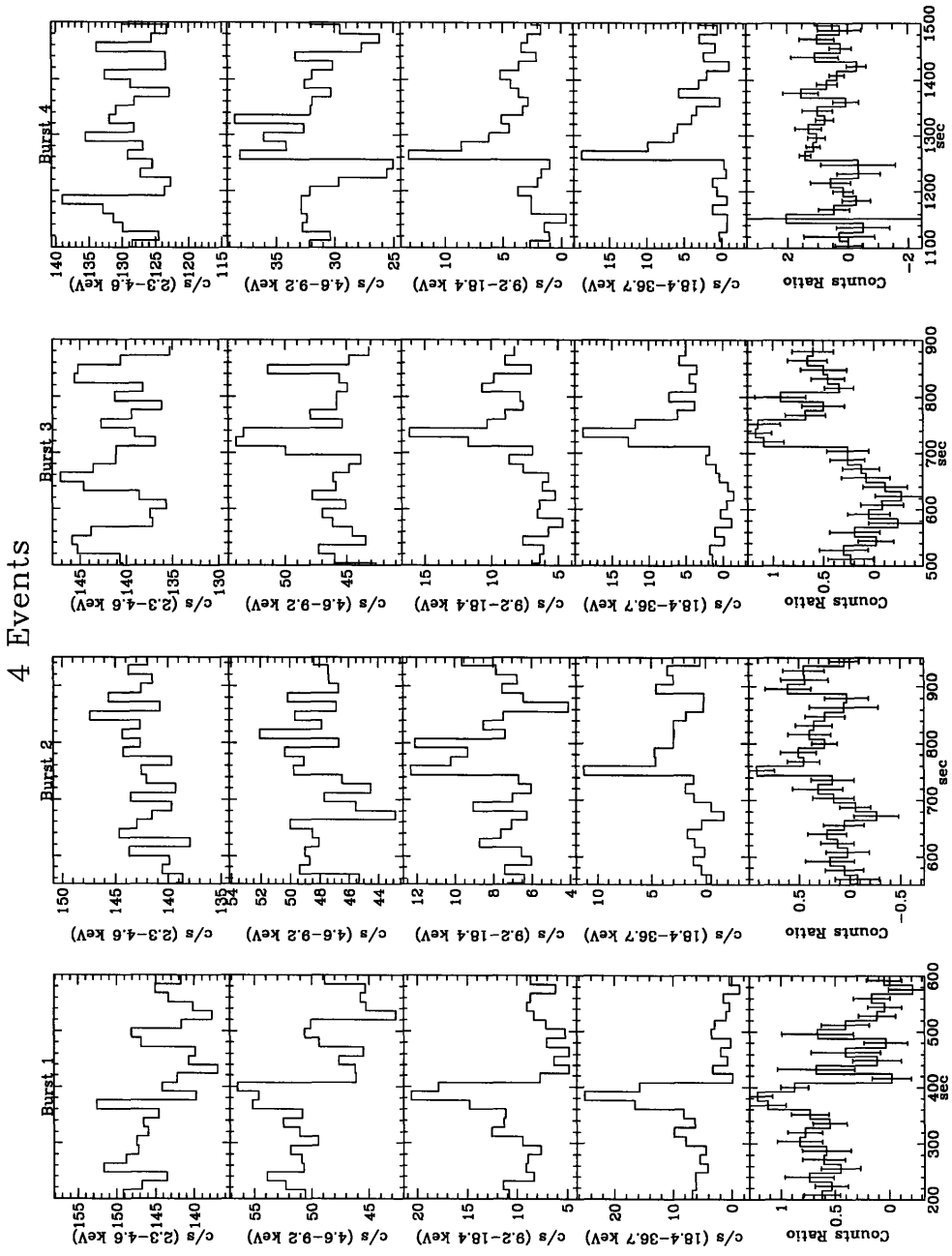

Figure 3-10: **LMC X-1 Observation Event Light Curves** The raw light-curves of all four events found in the data of LMC X-1, in (top panel) 2.3–4.6 keV, (second panel) 4.6–9.2 keV, (third panel) 9.2–18.4 keV, (fourth panel) 18.4-36.7 keV; and (bottom panel) the hardness ratio 18.4–36.7 keV/9.2–18.4 keV. Each lightcurve covers 400 s. The hardness ratio (18.4–36.7 keV/9.2–18.4 keV) *decreases* after event 1, while it *increases* after event 2 and 3.

3.4.3 High Energy (>10 keV) Events During Observations of 1354-64

Table 3.3: Event Information During 1354-64 Observations

Event Number	Time (UT)
1	87/194 10:29:48
2	87/194 12:07:40
3	87/194 10:33:10

Similar to that which we did for the events observed during observations of LMC X-1, we provide light-curves and counts spectra of the events observed during observations of 1354-64. The three events identified are listed, with observation times, in Table 3.3. The events 1 & 2 appear roughly similar in their intensity profiles (see Figs. 3-11 & 3-13), while event 3 is considerably longer (~50 s vs. 5 s; Fig. 3-15) and of lower significance, being not identified in the 0.5 s lightcurves, but easily picked out in the 16 s time-resolution lightcurves. This is easier to see in Fig. 3-17, where we show the shortened lightcurves of all three events.

In Figs. 3-12, 3-14, and 3-16, we show the figures of the counts spectrum of each of these three events, along with counts spectrum derived from during the same observational period. In each of the three events, the counts spectra are identical below ~7 keV, while above this value the counts-spectrum of the events show considerable excess count-rate all the way up three 37 keV. In the next section, we fit these counts spectra to extract power-law model parameters.

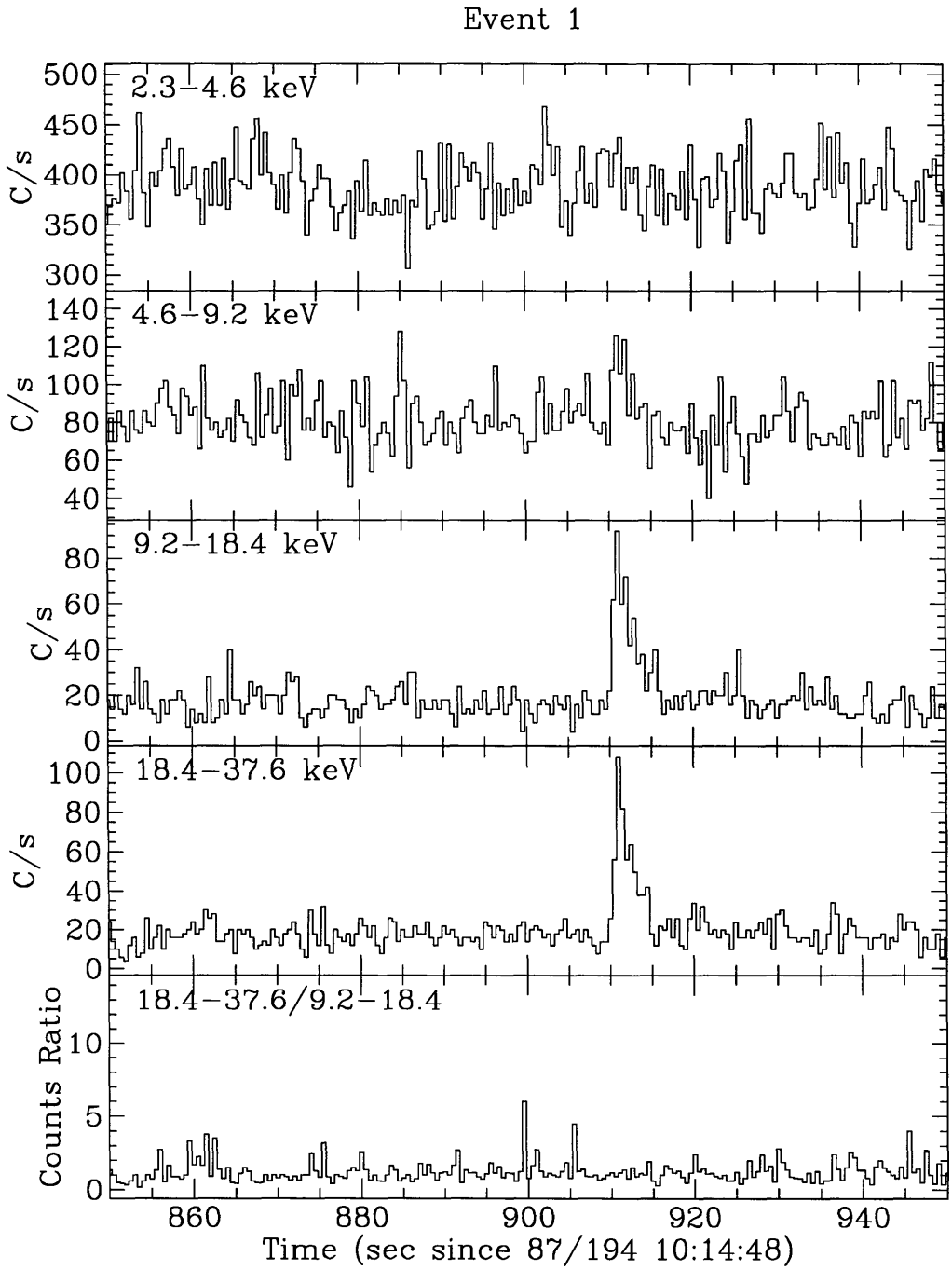

Figure 3-11: **1354-64 High Energy Spike LC and Wide Ratio (Event 1)** Raw light curves in four energy ranges (marked in each panel) and the hardness ratio (18.4–37.6 keV/9.2–18.4 keV) during the high-energy spike. Error bars are 1 σ. The time resolution is 0.5 s.

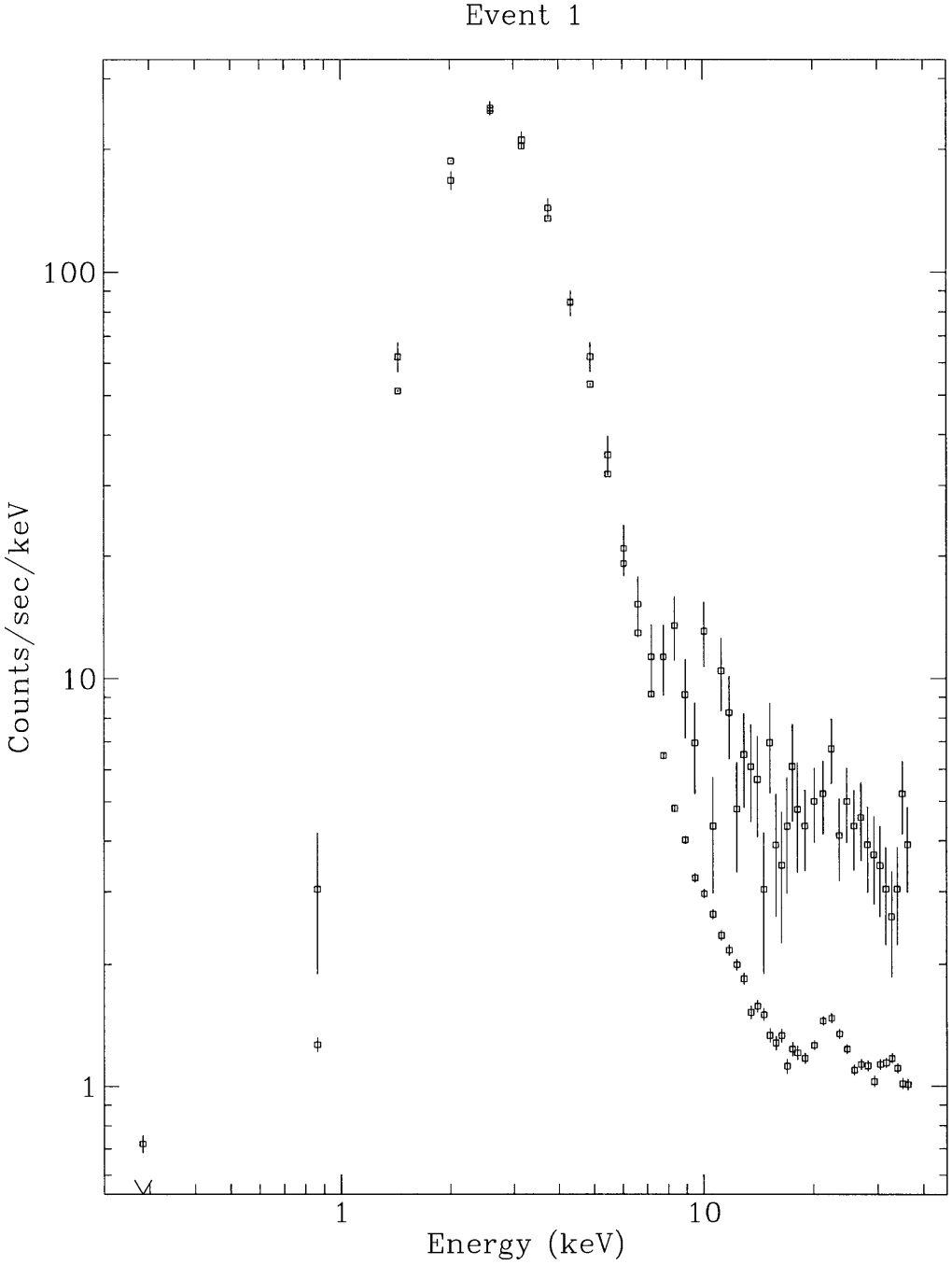

Figure 3-12: **1354-64 Counts Spectrum of Event 1** The counts-spectrum (raw data) of Event 1 observed from 1354-64, including ~4 seconds of data; we show the 1σ error bars for these data. The points (open squares) are the counts-spectrum from a 900 s observation period during the same observation period. There is an excess of counts above the persistent emission above ~5 keV.

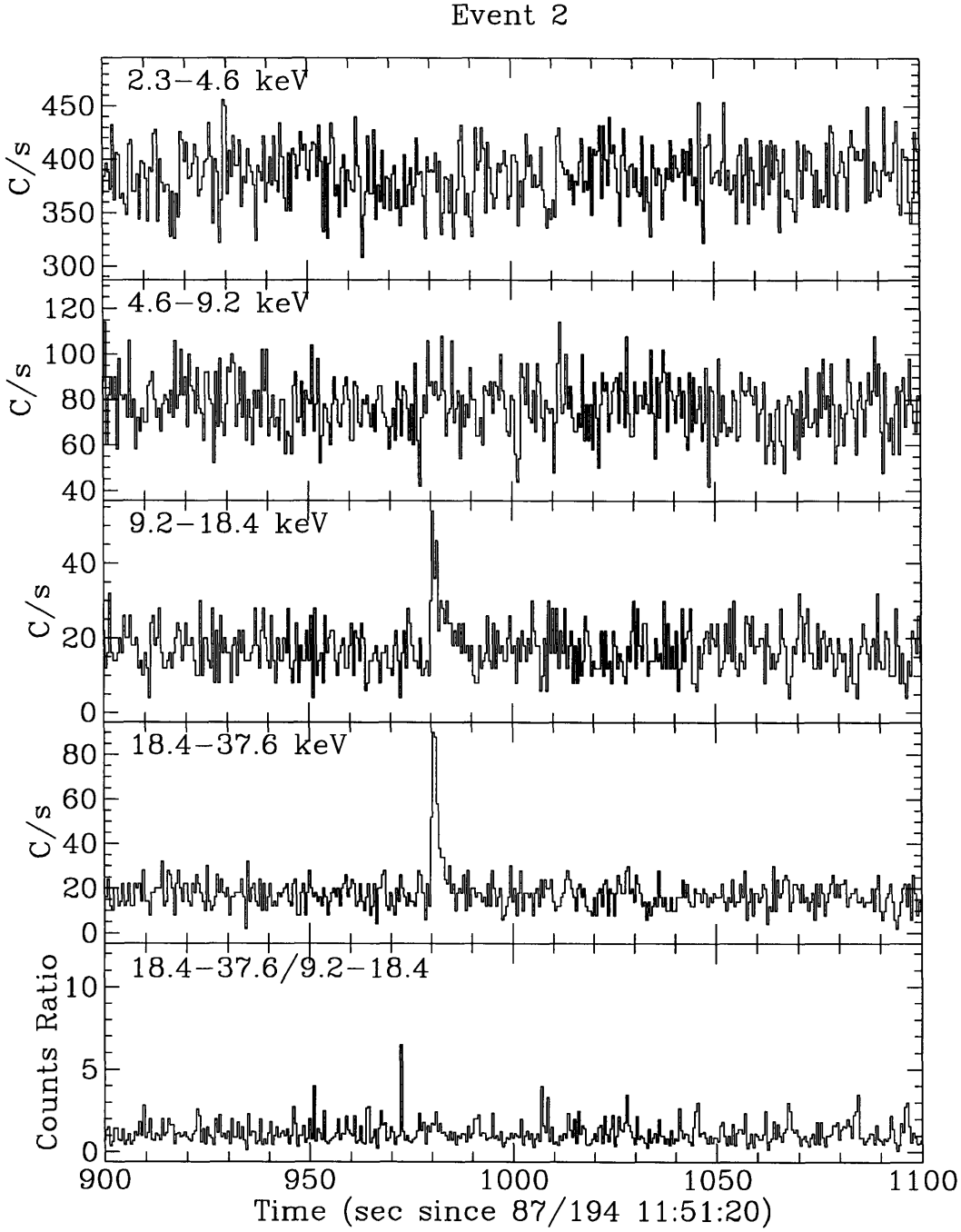

Figure 3-13: **1354-64 High Energy Spike LC and Wide Ratio (Event 2)** Raw light curve in four energy ranges (marked in each panel) and the hardness ratio (18.4–37.6 keV/9.2-18.4 keV) during the high-energy event. Error bars are 1 σ. The time resolution is 0.5 s.

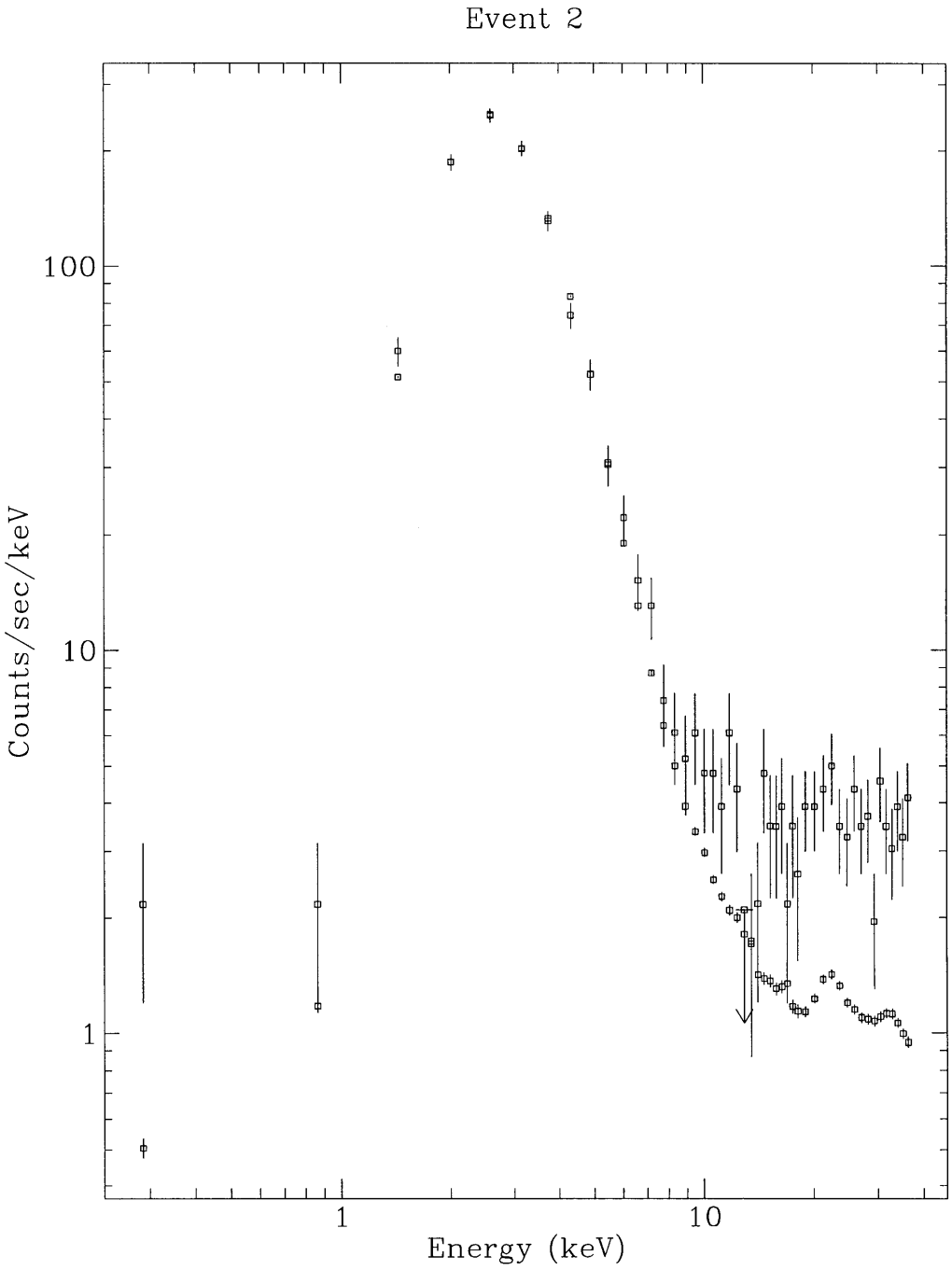

Figure 3-14: **1354-64 Counts Spectrum of Event 2** The counts-spectrum (raw data) of Event 2 observed from 1354-64, including ~4 seconds of data; we show the 1σ error bars for these data. The points (open squares) are the counts-spectrum from a 900 s observation period during the same observation period. There is an excess of counts above the persistent emission above ~5 keV.

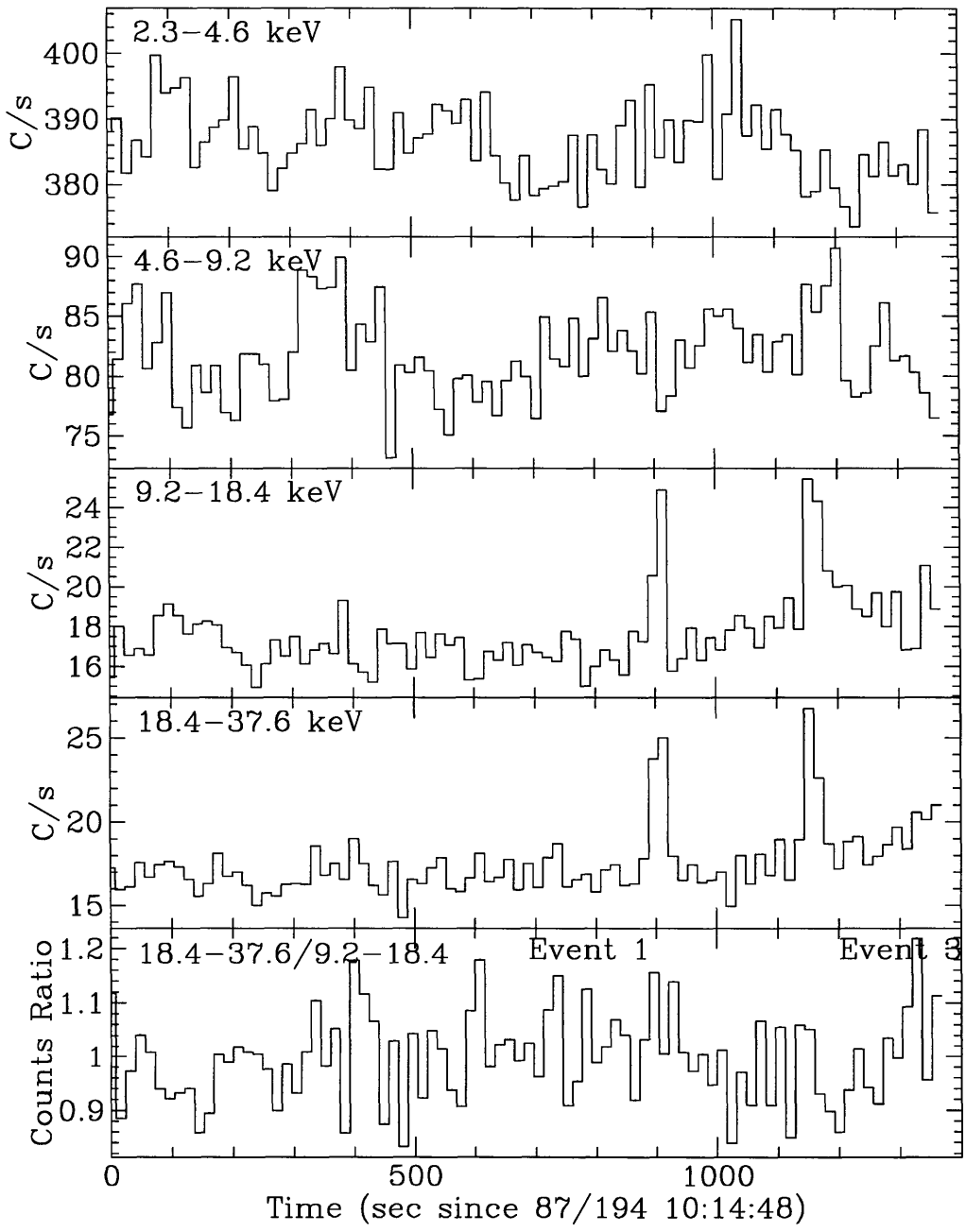

Figure 3-15: **1354-64 High Energy Spike LC and Wide Ratio (Event 3)** Raw light curve in four energy ranges (marked in each panel) and the hardness ratio (18.4–37.6 keV/9.2–18.4 keV) during the high-energy event. Error bars are 1 σ. The time resolution is 16 s. In the bottom panel, we indicate the occurrence of Event 1 just previous to Event 3. Here, at 16 s time resolution, the events are of similar significance; however, at 0.5 s time resolution (see Fig. 3-11) Event 1 is easily identified, while Event 3 does not appear above the persistent emission.

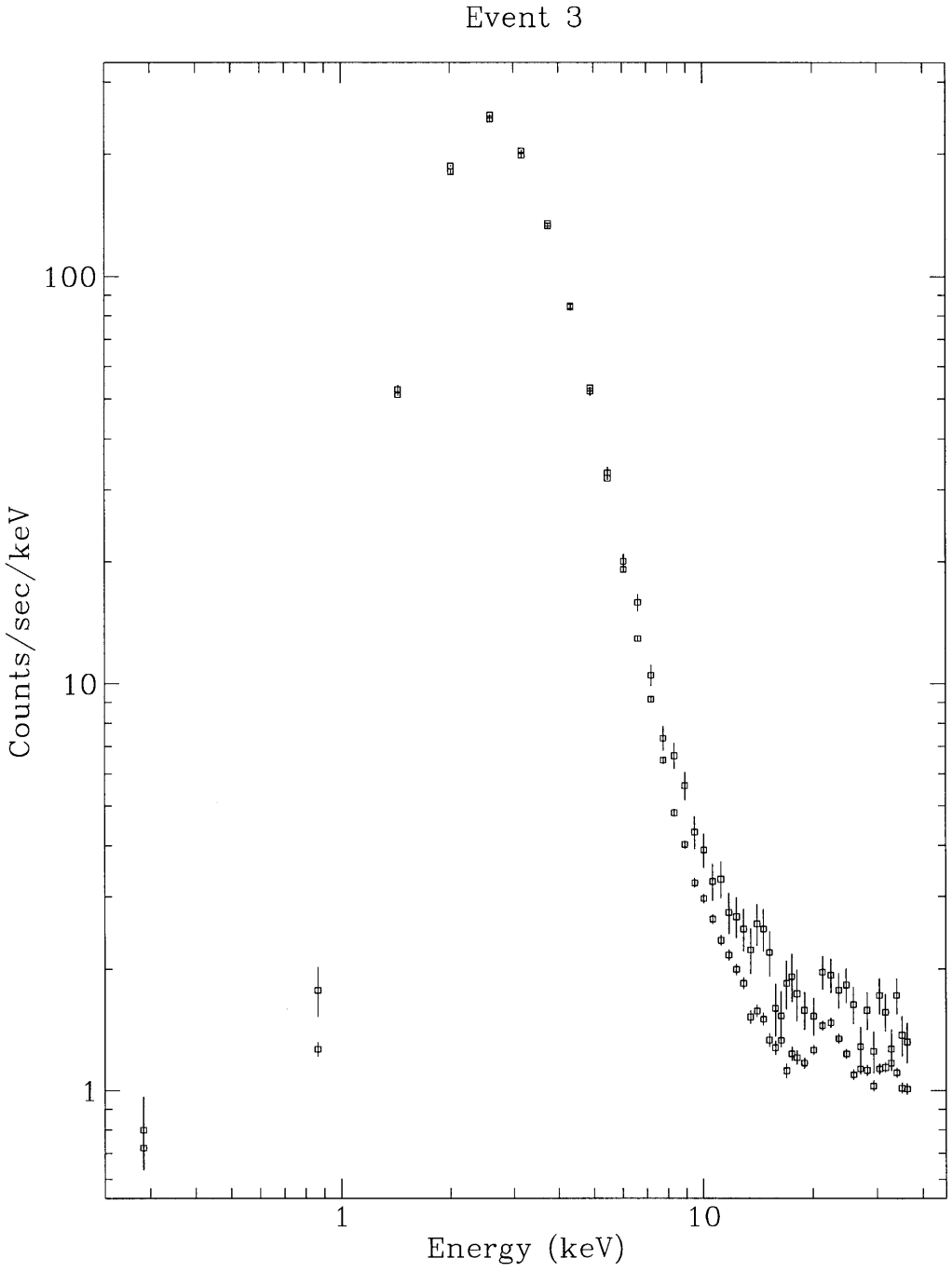

Figure 3-16: **1354-64 Counts Spectrum of Event 3** The counts-spectrum (raw data) of Event 3 observed from 1354-64, including ~50 seconds of data; we show the 1σ error bars for these data. The points (open squares) are the counts-spectrum from a 900 s observation period during the same observation period. There is an excess of counts above the persistent emission above ~5 keV.

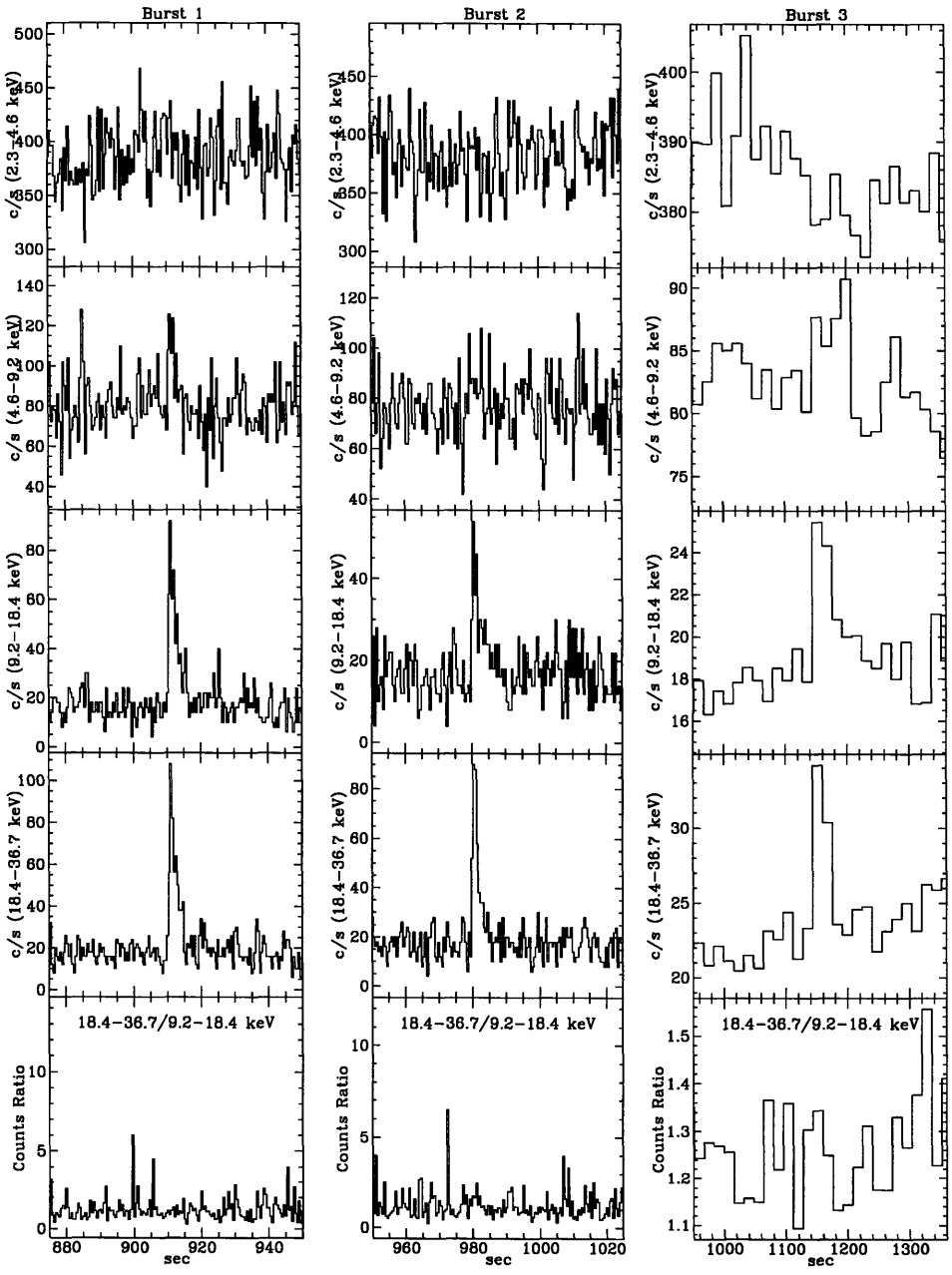

Figure 3-17: **1354-64 Observation Event Light Curves** The raw light-curves (uncorrected for background, deadtime, or aspect) of all three events found in the data of 1354-64 data, in (top panel) 2.3–4.6 keV, (second panel) 4.6–9.2 keV, (third panel) 9.2–18.4 keV, (fourth panel) 18.4-36.7 keV; and (bottom panel) the hardness ratio 18.4–36.7 keV/9.2–18.4 keV. The light-curves of event 1 and event 2 are shown with 0.5s time resolution with 75 s of coverage, while that of event 3 is 16 s with 410 s of coverage. The coarser time resolution for event 3 is used, because on a 0.5 s timescale the excess is not obvious. The counts-ratio during all the events are consistent with no change in the spectrum (in the 9.2-36.7 keV range). The events are clearly spectrally harder (9.2-36.7 keV/2.3-9.2 keV) than the persistent emission.

3.4.4 Counts Spectra

We produced model fits to the acquired counts spectra for LMC X-1 and 1354-64. We used the program XSPEC (Arnaud 1995) with its several utility programs, plus a program for converting the ASCII data into an XSPEC readable file kindly provided by J. Woo. In our fits, we added an additional 1% of the counts/channel to account for systematics, and we ignored channels 1-2 and 48.

We fit a multi-color disk black body, plus a power-law model together with a smeared edge Fe line and galactic absorption to the LMC X-1 data. The fits were fair, with χ^2_ν values in the range 1.0-2.0. For the PE alone, the photon index was 2.4 $\pm$0.1 (90% confidence), consistent with previous results (Ebisawa 1991). For the events plus PE , the photon index was measured to be -0.5 $\pm$0.07, accompanied by large changes in other spectral parameters, which indicates that the event emission does not have the same spectrum as the PE. We fit a single power-law to the difference spectrum (the PE spectrum subtracted from the PE + events spectrum). The photon index for the difference spectrum was -1.90 $\pm$0.16; the spectrum of the events is *inverted* in the energy range 2-37 keV. The normalization of this photon index is (1.1 $\pm$1.3) $\times 10^{-6}$ phot $cm^{-2}sec^{-1}kev^{-1}$ at 1 keV).

We fit a galactic absorption model, disk black-body, and power-law model to 1354-64. The fits in general were poor with $\chi^2_\nu \sim$2.4–3.4. The photon index for the PE alone was 2.8 $\pm$0.1, consistent with previous results (Tanaka & Lewin 1995). For the events+PE (all counts-spectra taken together), the photon index was 0.28 $\pm$0.12, which indicates that the event emission does not have the same spectrum as the PE power-law tail. For the difference spectrum, the best fit photon index was -1.85 $\pm$0.33 (normalized with (8.6 $\pm$17.7)10^{-6} phot $cm^{-2}sec^{-1}kev^{-1}$ at 1 keV).

The uncertainty normalization for the power-law component of the difference spectrum is overestimated by our fitting routine; the significant data are in the 10-37 keV range, while the data below 10 keV provide almost no constraint. Thus, the uncertainty should be taken as a percentage calculated at some higher energy. Conservatively taking 10 keV, for α=1.86, this drops the uncertainty in the difference spectra power-law normalization by a factor of $\sim$70.

3.4.5 Candidate Events in Cyg X-1 and GX 339-4

The present search produced two events which we consider to be candidate events, but which we were not able to confirm. These events we identified by eye in the corrected data. In the 16 s time-resolution intensity profiles, these cannot be differentiated from the aforementioned "spikes", which are due to instrumental effects, and were systematically excluded in the production of raw-data.

In Table 3.4, we give the source-name and time of the event we find satisfy the following criteria:

- Significant excess in count-rate in the 9.4–18.4 keV and, separately, 18.4–36.7 keV energy ranges in a 16 s bin, with only marginal (if any) significant excess count-rate in the 2.3–4.6 keV and 4.6–9.2 keV energy ranges.

- Energy spectrum which is consistent with an increased count-rate across the 10-36.7 keV energy range, not due to an instrumental effect, identifiable by spectral features which have widths less than the instrument energy resolution.

Confirmation of these candidate events can be provided by analysis of the raw-data in higher time-resolution, to confirm that the event is not restricted to a single time-bin.

Table 3.4: List of Candidate High Energy Events

Source	Time[a] (UT)
Cyg X-1	87/219 14:58:10
GX 339-4	91/253 20:12:30

[a] Times are approximate, to within 60 seconds

3.4.6 Comparison of the *Ginga* Events With SMM Events

We describe our reasons for classifying these events as due to particles in the earth magnetosphere, most likely deposited by nuclear reactors on board the COSMOS-class Russian satellites. Events caused by these satellites, detected in the 0.3-7 MeV

detectors and particle detectors of the SMM satellite, are described in the dedicated issue of *Science* (Rieger & et al. 1989; Share et al. 1989; Hones & Higbie 1989) previously mentioned.

First, two of the events observed during the LMC X-1 observation were separated by 98 minutes (events 2 and 3); 96 minutes after the second of these two, a previously unidentified (due to low significance) excess is visible in the light-curve. These two events both occurred as the satellite rigidity was falling, approximately near 12.6-13.0 GeV/c^2. The first LMC X-1 event occurred while the rigidity was rising, again past the rigidity in the range 12.6–13.0 GeV/c^2.

Also, two events observed during the 1354-64 observation were separated by 98 minutes. This is very close to the 96-min orbital period of *Ginga*, the difference possibly due to the difference between precession cycles of both satellites.

Chapter 4

Energy Spectral Study

4.1 Why Use Colors?

The overall goal of the combined study of 10 BHCs is to establish a single observational framework, which will lend a descriptive basis to which all BHCs can be compared. In selecting the observational parameters on which to establish this framework, it is essential to be able to use low S/N data in procuring these parameters, and to maximize the amount of useful data and therefore observational coverage.

We selected spectral color as our primary spectral indicator. First, the use of spectral color has the advantage over the use of source intensity alone by being independent of the distance to the source. Intensity scales with the square of the source distance. Thus, a large uncertainty in the distance to the source results in a much larger uncertainty in the source luminosity, the physically meaningful parameter; moreover, some of the sources under study have distances uncertain by a factor of several. The spectral color avoids this uncertainty, as it is the ratio of counts in one energy band to that in another energy band, and is independent of distance.

Second, the source color is easily calculated. One need not correct for the energy-independent aspect efficiency or the energy independent dead time factor (see Sec. A.2 for a brief description) as one must do to retrieve the source intensity. Background count-rates must be subtracted from each energy band, but this is the only major correction which must be made to produce spectral color. In addition,

the spectral color does not require fitting to a spectral function to extract spectral parameters, and thus is computationally simple, and therefore lends itself well to the analyses of large amounts of data.

Third, if the detector response is stable, a source which is observed while in a specific spectral state (say, a black-body with kT=3.0 keV, for example) will have the same spectral color whenever it is observed in the identical spectral state. However, it should be noted that the value of the spectral color does not correspond uniquely to a specific spectral state – the same spectral color could correspond to a black-body of kT=3.0 keV, or a Comptonized spectrum of kT=10.0 keV, depending on the detector response. Or, if the spectral function is dependent on more than one parameter, one can always find a locus of the spectral parameters which will produce the same spectral color – although such a situation may be physically contrived. Thus, while spectral color has one-to-many correspondence to the intrinsic source spectrum it may be expected that spectral evolution in a source results in changes to the spectral color.

Fourth, the spectral color is sensitive to small changes in the spectral state. By integrating all counts over a broad spectral band, one decreases the fractional uncertainty (ideally) by $1/\sqrt{N}$, where N is the number of counts; in practice, additional uncertainty is introduced by the data correction, but these are often small.

Finally, source color has been successfully used in the phenomenological description of non-pulsing neutron-star Low-Mass X-ray Binaries (LMXBs) (Hasinger & Van Der Klis 1989). By examination of the source behavior in a color-color diagram in conjunction with fast-timing properties, each LMXB falls into one of two categories: Z-sources, which are thought to have strong magnetic fields, and Atoll sources, which are thought to have relatively weak magnetic fields.

Thus, because spectral colors are independent of source distance, easily calculated without detailed spectral fitting or corrections, sensitively indicate spectral evolution in the source, and have been previously successful in divining source phenomenology, we have chosen to make use of them as the measurable parameter of interest in the present study.

4.2 Selection of Energy Ranges Used in this Study

The energy ranges used for this study were selected with the following considerations in mind. First and foremost, the same energy ranges must be used for all 10 sources. Thus, the selected energy ranges must be available in a majority of the observations, from all sources.

Second, the selected energy ranges used must provide enough signal to noise that the count-rates and spectral colors are $>4\sigma$ above 0 (data which do not meet this criteria are excluded from the analysis). Third, the energy ranges must span physically interesting parameter space. Fourth, the energy ranges must be such that data can be selected from all observing modes (MPC1, MPC2, MPC3) of *Ginga*.

On the basis of these criteria we selected four energy ranges for use in this study, which we define here:

- Low Energy Range: 2.3–4.6 keV
- Medium Energy Range: 4.6–9.2 keV
- High Energy Range: 9.2–18.4 keV
- Intensity Range: 2.3–18.4 keV

These are the lower- and upper- limits of the energy channels (provided by the *Ginga* LAC data formatting routines at ISAS) which are to be used in this study. In practice, the energy bins produced by the *Ginga* OBC are roughly 1.15 keV in width; the intrinsic energy resolution of *Ginga* LAC is 18 $(6keV/E)^{1/2}$%; thus, these energy "limits" are only approximate. However, the energy response of the *Ginga* LAC did not change appreciably during its lifetime, and therefore the actual energy ranges will be the same, independent of the observation time and source observed, permitting comparison between the various sources.

4.2.1 Definition of the Colors Used in this Study

We define, for use in this study, hardness ratios ("colors") which will be used in the spectral investigation of this study. Historically, the term "spectral colors" is taken

from optical astronomy, where it describes the difference between two optical energy pass-band magnitudes (*e.g.* $V-I$ or $B-V$). As optical magnitudes are proportional to the logarithm of the detected flux in a defined energy pass-band, a "color" is proportional to the logarithm of the ratio of two different energy pass-bands.

In X-ray astronomy, the term "color" has come to mean the simple ratio of the detected flux in two different energy pass-bands (not the logarithm of this). X-ray colors do not represent the detailed X-ray energy spectrum in a transparently absolute manner; *a priori* knowledge of the source energy spectrum is required to extract model parameters from a CCD. However, one can compare multiple measurements of the same color from the same or different sources, and make the qualitative statement that the source is spectrally *harder* (indicating a greater fraction of source photons at higher energies) or *softer* (indicating a lessor fraction of source photons at higher energies) during particular measurements, in comparison with others. This is of particular use for investigations requiring knowledge of the energy spectrum on timescales too short to produce a high signal-to-noise energy spectrum.

Traditionally, hardness ratios place the counts in the higher-energy spectral band in the numerator, and those in the lower energy spectral band in the denomenator. Thus, harder spectra produce a higher hardness ratio. We follow this convention.

The colors which we use in this study, and the terms by which we will refer to them are:

- Soft Ratio: (Medium Energy Range) / (Low Energy Range)
- Wide Ratio: (High Energy Range) / (Low Energy Range)
- Hard Ratio: (High Energy Range) / (Medium Energy Range)

To produce a color, it is not necessary to correct for:

- detector response: as the detector response does not change between measurements, the color will remain constant for a constant spectrum. In this case, the ratio is taken of the number of *counts* above background (not photons). One can use the detector response to extract spectral parameters from the CCD.

- energy-independent detector dead-time: for *Ginga*, the detector dead-time is energy independent; thus, the correction factor due to deadtime is the same for all energy ranges and, because the color is the ratio of two energy bands, the energy-independent detector deadtime correction factor divides out.

- energy-independent aspect correction: the aspect corretion for *Ginga* (Turner et al. 1989) is mildly dependent upon energy. In the X-direction, the 90% efficiency contour is at 0.15 degrees from the detector normal in the 1.2-2.9 keV band, while it is at 0.17 degree in > 4.0 keV; the 10% efficiency contour is at 0.90 deg and 0.86 degrees in the 1.2–2.9 keV and > 4.0 keV bands, respectively. Thus, the energy dependent aspect corrrection is small. Throughout, we have neglected it. This may introduce discrepancies in the color at the level of a few percent between observations made with vastly different aspect efficiencies.

In practice, we use the corrected data (see Sec. 3.2), which include corrections or aspect, deadtime, and background.

4.3 Light Curves, Color-Color Diagrams and Hardni Intensity Diagrams

Light curves (LCs), color-color diagrams (CCDs) and hardness-intensity diagrams (HIDs) provide a basis for comparison between the various sources. We do not *a priori* know which spectral color or what combination of spectral colors will provide the most useful information for comparison. Therefore, our approach is to be exploratory – to look at all possible combinations of intensity and spectral hardness, to divine behaviors which multiple sources have in common.

4.3.1 Data Preparation and Selection

We describe in this section the data selection procedures and analysis used to produce the light curves (LCs), color-color diagrams (CCDs) and hardness-intensity diagrams (HIDs).

To produce LCs, CCDs, and HIDs, only corrected data were used, as the systematic effects associated with raw data would, for most of the data, dominate possible observational effects.

Using only corrected data, prepared as described in Section 3.2, the counts and their corresponding uncertainties were integrated over continuous 128s periods in the four energy ranges of interest (Low Energy Range, Medium Energy Range, High Energy Range, and Intensity Range). Often, near the ends of observations, there were data remaining of interval less than 128s, which we included. For each datum, the starting time of the integration is noted, for use in the production of light-curves and for comparison with the simultaneous raw-data timing properties.

After the count-rates and their corresponding uncertainties were found, we then calculated the Hard Ratio, Wide Ratio, and Soft Ratio, as defined in Section 4.2.1, and their corresponding uncertainties. Data of low significance were not used in further analysis. Data are considered to be low significance if, integrated over 128s, either the Hard Ratio, Soft Ratio, Wide Ratio or intensity measure was $< 4\ \sigma$ greater than 0. This resulted in the exclusion of a total of 39.9 ksec of data for all sources. See Table 4.1 for a breakdown by source.

As described in Sec 3.2, data which had improperly subtracted background were excluded from further analysis. After selecting data for significance and background subtraction, a total of 627 ksec of data was useable for analysis. See Table 4.1 for a breakdown by source.

4.3.2 The CCDs/HIDs and LCs

In this section, we present the resulting Color-Color Diagrams (CCDs), Hardness-Intensity Diagrams (HIDs) and Light-Curves (LCs) of each source individually, and for the CCDs taken together.

For each individual source, the LCs, HIDs, and CCDs are shown in Figs. 4-1 – 4-10. At the top of each figure, in panel *(a)*, is the 2.3–18.4 keV light-curve, beginning at an arbitrary time (typically, that of the first datum), and ending after the last datum. These LCs therefore can cover anywhere from a fraction of a day, to several

Table 4.1: BHC Data Excluded for Spectral Analysis, by source

Source	Poor Background (ksec)	Low Significance [a] (ksec)	Usable Data (ksec)
1354-64	23.6	0.3	13.6
1630-47	<0.1	<0.1	34.5
1826-24	0.3	<0.1	8.7
Cyg X-1	9.5	<0.1	109.8
GS 1124-68	102	0.2	76.8
GS 2000+25	27.0	3.6	113.6
GS 2023+33	2.3	13.6	152.5
GX 339-4	57.0	<0.1	85.1
LMC X-3	47.0	17.4	20.0
LMC X-1	0.7	11.4	21.6

[a] Has either the Hard Ratio, Soft Ratio, Wide Ratio, or Intensity Range at a significance level below 4 σ

years. They do not optimally show the detailed intensity variations during individual observations. They are included in this fashion to show the intensity range covered by the source and the observation periods which are used in the present analysis. They also provide visual familiarity with the the source's intensity variations, and permit easy separation between the more persistent sources and the transient sources. In the upper-right-hand corner of each panel, we list two values: the amount of data (in ksec) which was used in the figures on that page, and the amount of data which was selected plus data which did not pass the significance requirements.

In the second row of each figure are the HIDs – these show the Soft Ratio (panel *b*), Wide Ratio (panel *c*) and Hard Ratio (panel *d*) vs. the 2.3–18.4 keV intensity. On each point is included its 1-σ error bar.

In the bottom row of each figure are the CCDs. These show the Hard Ratio vs. Soft Ratio (panel *e*), Hard Ratio vs. Wide Ratio (panel *f*), and Wide Ratio vs. Soft Ratio (panel *g*) – all possible combinations of the three counts ratios.

In each of these panels, the limits used were selected for the specific source on that page, complicating comparison between sources, but showing in the greatest detail possible the behavior of the particular source.

In Fig. 4-1, we show the LC, CCDs, and HIDs of transient 1354-64. The selected data all came within ~1 day, during which the source showed moderate intensity and spectral variability, as can be seen in the LCs and CCDs. Examination of the HIDs and CCDs shows that, with one exception, these are largely scatter-plots, showing little or no correlation between colors themselves or color with intensity. The exception is panel *f*, the Hard Ratio vs. Wide Ratio, in which the two colors show strong correlation. While this may not be surprising due to the fact that Hard Ratio and Wide Ratio share the High Energy Range band, the source shows considerably greater correlation in this CCD than in those showing the Hard Ratio vs. Soft Ratio and the Wide Ratio vs. Soft Ratio, in spite of the fact that both those CCD color pairs also share an energy band.

In Fig. 4-2, we show the LC, CCDs, and HIDs of the persistent source 1630-47. The data come from three separate observational periods spanning almost one year in time. In this period, 1630-47 varied in the 2.3–18.4 keV intensity by ×2-3 (~70–200 c/s), and showed moderate spectral variability. In the HIDs, 1630-47 shows a positive correlation between intensity and hardness. In the CCDs, 1630-47 shows evolution along a single locus, consistent with positive correlation between all hardness ratios.

In Fig. 4-3 we show the LC, CCDs and HIDs of the persistent source 1826-47. The observations used took place during a seven day period, during which the 2.3–18.4 keV intensity varied by ~75% (200-350 c/s). In the HIDs and CCDs, moderate spectral variability is indicated, with hardness ratios varying by ~20-60%. The variabiliity is largely uncorrelated, except in the CCDs of Hard Ratio vs. Wide Ratio (panel *f*) and Wide Ratio vs. Soft Ratio (panel *g*), in which a positive correlation between the two colors is plain.

In Fig. 4-4 we show the LC, CCDs and HIDs of the persistent source Cyg X-1. The three observations used took place over a 3.8 year period; most of the factor of two variability in the 2.3–18.4 keV intensity takes place during short-term (~1 day) observational periods. In the HID's we see that the data separates into two individual states, which overlap in intensity, but not in spectral hardness. In the Soft Ratio vs. intensity HID (panel *b*), there is a spectrally hard state (Soft

Ratio$\sim$1.0) which, at higher intensities, is roughly constant in hardness, but which at lower intensities "flares" in hardness by 50%– increasing the hardness ratio, but never dropping below the constant value. There is also a spectrally soft state (Soft Ratio $\sim$0.55) which remains roughly constant in hardness during changes in the Intensity Range count-rate $\gtrsim \times 2$. The HID showing Wide Ratio vs. Intensity Range count-rate is similar to the Soft Ratio vs. Intensity Range HID. In the Hard Ratio vs. Intensity Range HID (panel *d*), larger Hard Ratio variability is evident for the low-count-rate soft-state than the other two colors, while less variability in Hard Ratio than in the other two colors is evident for the lower-count-rate hard state.

In the CCDs (panels *e, f, g*), spectral variability in Cyg X-1 is shown to be strongly positively correlated. The softer data reflects the behavior we see already in the HIDs: in the soft state, the Hard Ratio varies almost independently of the Soft Ratio and Wide Ratio; in the hard state the the Hard Ratio becomes more strongly correlated with the Soft Ratio and Wide Ratio. The behavior of the Wide Ratio and Soft Ratio shows that the two are strongly postively correlated.

In Fig. 4-5 we show the LC, CCDs and HIDs of the transient GS 1124-68. The observations were made during the first 200 days while the source was in outburst. The LC follows that of the canonical BHC X-ray transient – an intensity rise in a few days, followed by an exponential decay, with a secondary hump near time=80 d. During these observations, the source varied in intensity by over two orders of magnitude. The spectral hardness changes appreciably – more than any other source in this study; the Wide Ratio – the most variable of the three hardness ratios in this source, changes by four orders of magnitude (between 0.0004 and 0.4; this is more plain in Fig. 4-25).

The HIDs of GS 1124-68 show complicated behavior, compared, for example, to Cyg X-1. Before time=20 days, the source shows a negative correlation between 2.3–18.4 keV intensity and spectral hardness, as can be seen in all three HIDs. During observations between time =20-90 days, the correlation changes sign – the intensity and spectral hardness are positively correlated. Finally, during observations between time=150-200, the energy spectrum of GS 1124-68 is considerably harder, and shows

no strong correlated behavior, little spectral variation within single observation periods, but significant spectral variation between observations.

The CCDs of GS 1124-68 show that, over the large range of colors which are covered, the colors are strongly correlated, most tightly when the source is spectrally soft. In the Hard Ratio vs. Soft Ratio CCD, this correlation is roughly linear, while in the CCDs of Hard Ratio vs. Wide Ratio and Wide Ratio vs. Soft Ratio, the correlations have power-law character. In the Hard Ratio vs. Wide Ratio data, this power-law is roughly Hard Ratio $\propto$ (Wide Ratio)$^{0.62}$, while in the Wide Ratio vs. Soft Ratio data, the power law is roughly Wide Ratio$\propto$ (Soft Ratio)$^{2.65}$.

Thus, we may speak of GS 1124-68 of having at least three distinct phases in its evolution: 1) days 0-20, spectral hardness is anti-correlated with intensity; 2) days 20-80, spectral hardness is correlated with intensity; 3) days 150–200 complex spectral behavior with little correlation to changes in intensity.

In Fig. 4-6, we show the LC, CCDs and HIDs of the transient GS 2000+25. The observations were made over 230 days while the source was in outburst. During this period, the 2.3–18.4 keV count-rate spanned four orders of magnitude.

In the HIDs, GS 2000+25 goes through complex behavior. No simple tracks are observed in the data used; the source is spectrally soft at high count-rates, and becomes spectrally harder at low count-rates. The CCDs show evidence of correlation between colors, in particular in the Hard Ratio vs. Wide Ratio and Wide Ratio vs. Soft Ratio CCDs; however, there are several periods when the source lies somewhat away from the correlated locus.

In Fig. 4-7, we show the LC, CCDs and HIDs of the transient GS 2023+33. The observations made over a 450 day period while the source was in outburst and when it had largely returned to quiescence, spanning four orders of magnitude in count-rate (10–10^5 c/s in the Intensity Range). The HIDs show that, at high 2.3–18.4 keV intensity, the source was very strongly spectrally variable, even while the source was spectrally harder than any other BHC in the present study. At lower count-rates, the spectral variability decreased, and the source remained roughly spectrally constant at the softest level achieved during the high count-rate epoch.

The CCDs show, largely, strongly correlated spectral colors, which lie upon a single locus, with the exception of a large amount of variabilty which makes the source harder than the locus.

In Fig. 4-8, we show the LC, CCDs and HIDs of the persistent source GX 339-4. Of the persistent sources in the present study, GX 339-4 has the largest Intensity Range count-rate variability (30 c/s –7×10^3 c/s), over the ~1200 days spanned by the four obsevational periods and, for that reason, it is often referred to as a transient source. Unlike Cyg X-1, most of the intensity variability of GX 339-4 occurs between observations, not within them (that is, on timescales longer than the ~day observaional period).

The HIDs of GX 339-4 show moderate spectral variability within the observations. The mean hardness of each remains roughly constant, although there are some considerable excursions and discontinuities in the HIDs within single observational periods – for example, in the Hard Ratio near 100 c/s in panel *d*. At the highest count-rate, the spectral color drops measurably in all HIDs.

In the CCDs, the spectral colors are positively correlated, and show some interesting behavior. Also, the CCDs show resolved clouds of points in the spectrally harder regions, indicating that the spectra could be locally uncorrelated while being globally correlated.

In Fig. 4-9, we show the LC, CCDs and HIDs of the persistent source LMC X-1. The 2.3–18.4 keV count-rate varies by ~50% (150–220 c/s) during three observational periods over ~160 days.

During this period, the spectral variability is modest, but measureable and, according to the HIDs, correlated with intensity. The CCDs also indicate correlated spectral evolution. In panel *e* and *g*, two positions on the CCDs seem most occupied, with a stream of points between them.

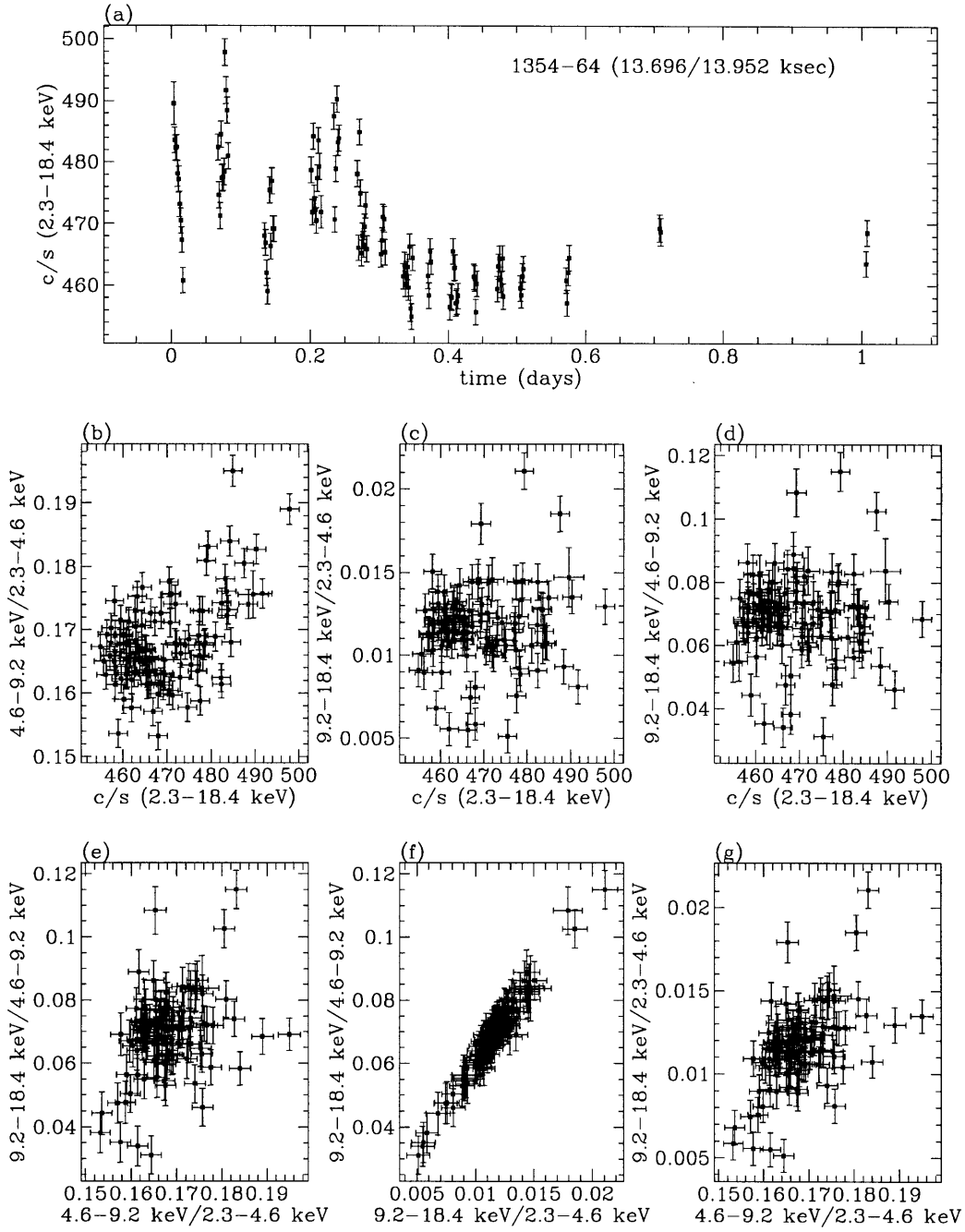

Figure 4-1: **LC/CCDs/HIDs of 1354-64**
Each point represents 128 s of data. 1 σ error bars are on each point. Data have been corrected for background, deadtime, and aspect. *(a):* 2-18 keV light curve (time=0 at 87/194 02:13:12). In the upper-right-hand corner is the amount of time in ksec of (usable data/usable data+low significance data). *(b):* HID, Intensity Range count-rate vs. Soft Ratio. *(c):* HID, Intensity Range count-rate vs. Wide Ratio. *(d):* HID, Intensity Range count-rate vs. Hard Ratio. *(e):* CCD, Hard Ratio vs. Soft Ratio. *(f):* CCD, Hard Ratio vs. Wide Ratio. *(g):* CCD, Soft Ratio vs. Wide Ratio.

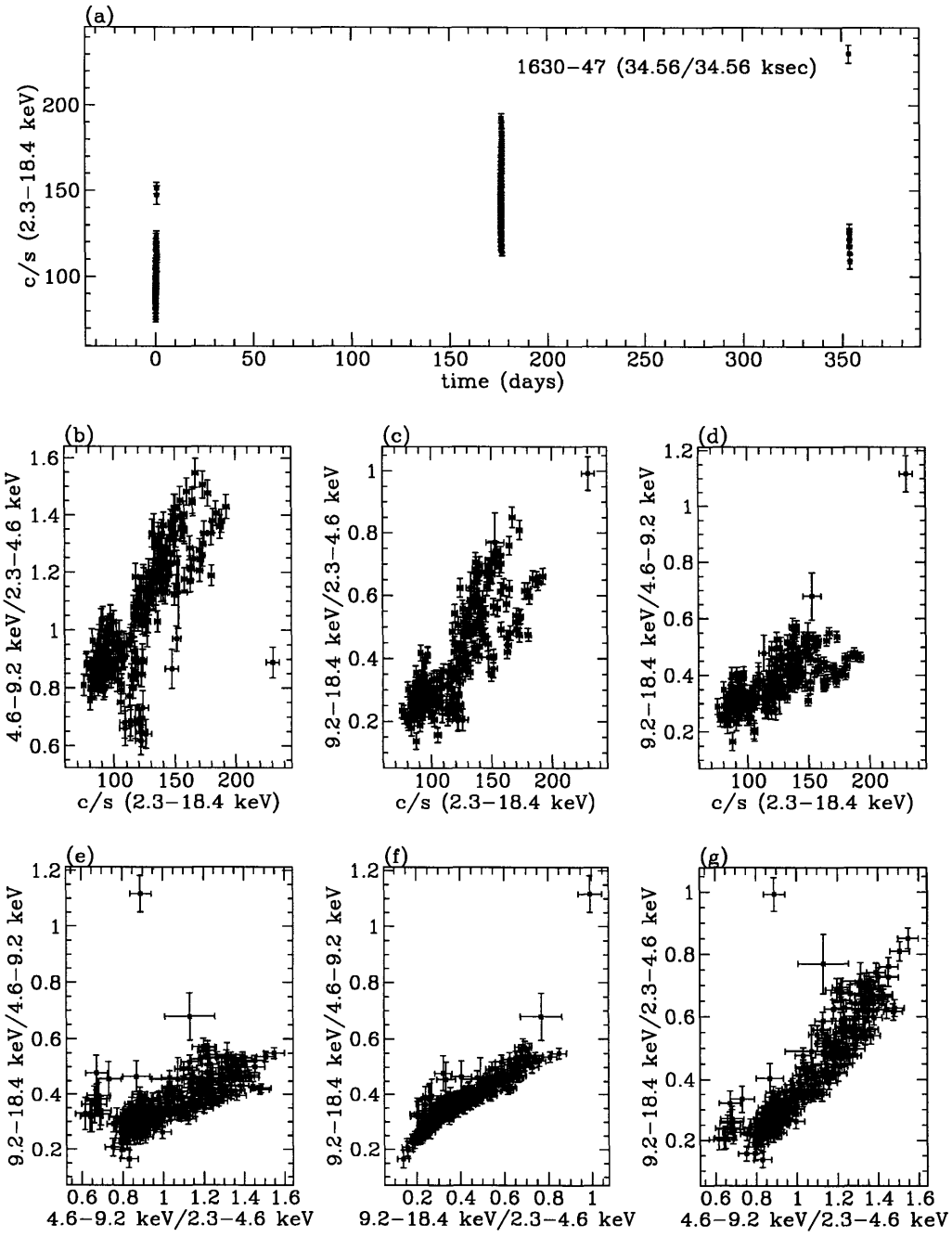

Figure 4-2: **LC/CCDs/HIDs of 1630-47**

Each point represents 128 s of data. 1 σ error bars are on each point. Data have been corrected for background, deadtime, and aspect. *(a):* 2-18 keV light curve (time=0 at 87/290 06:22:40). In the upper-right-hand corner is the amount of time in ksec of (usable data/usable data+low significance data). *(b):* HID, Intensity Range count-rate vs. Soft Ratio. *(c):* HID, Intensity Range count-rate vs. Wide Ratio. *(d):* HID, Intensity Range count-rate vs. Hard Ratio. *(e):* CCD, Hard Ratio vs. Soft Ratio. *(f):* CCD, Hard Ratio vs. Wide Ratio. *(g):* CCD, Soft Ratio vs. Wide Ratio.

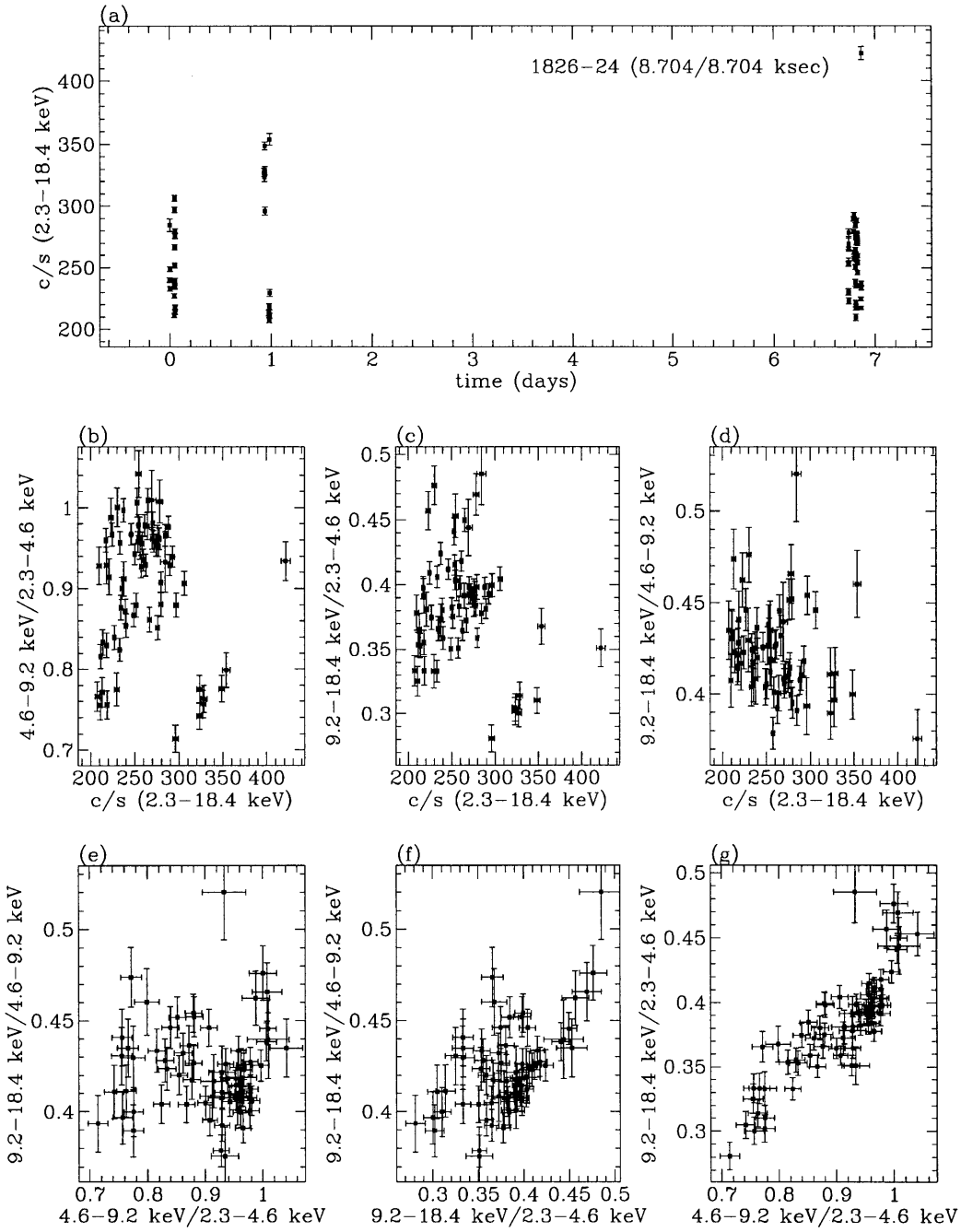

Figure 4-3: **LC/CCDs/HIDs of 1826-24**
Each point represents 128 s of data. 1 σ error bars are on each point. Data have been corrected for background, deadtime, and aspect. *(a):* 2-18 keV light curve (time=0 at 88/253 14:14:51). In the upper-right-hand corner is the amount of time in ksec of (usable data/usable data+low significance data). *(b):* HID, Intensity Range count-rate vs. Soft Ratio. *(c):* HID, Intensity Range count-rate vs. Wide Ratio. *(d):* HID, Intensity Range count-rate vs. Hard Ratio. *(e):* CCD, Hard Ratio vs. Soft Ratio. *(f):* CCD, Hard Ratio vs. Wide Ratio. *(g):* CCD, Soft Ratio vs. Wide Ratio.

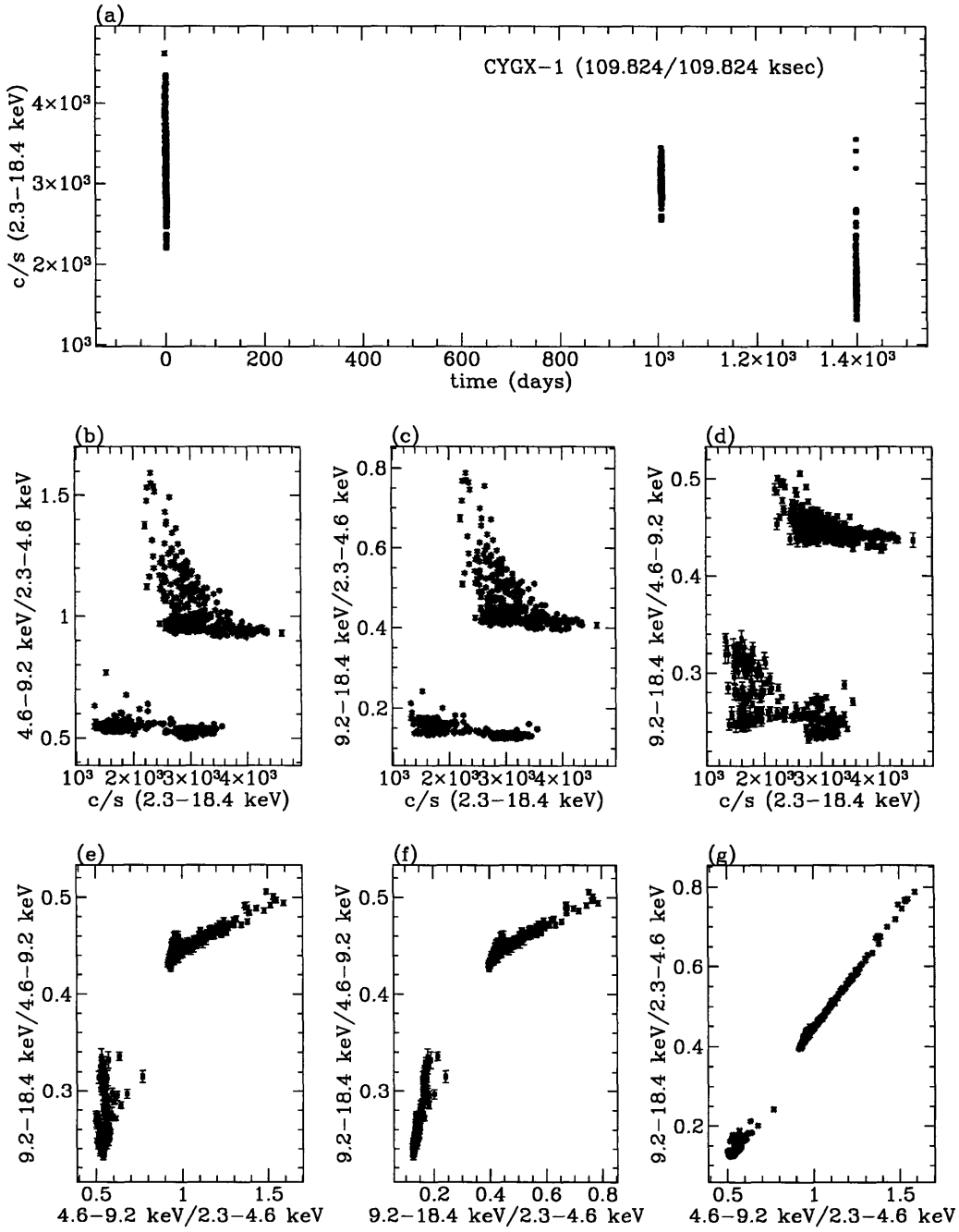

Figure 4-4: **LC/CCDs/HIDs of Cyg X-1**

Each point represents 128 s of data. 1 σ error bars are on each point. Data have been corrected for background, deadtime, and aspect. *(a):* 2-18 keV light curve (time=0 at 87/217 11:41:18). In the upper-right-hand corner is the amount of time in ksec of (usable data/usable data+low significance data). *(b):* HID, Intensity Range count-rate vs. Soft Ratio. *(c):* HID, Intensity Range count-rate vs. Wide Ratio. *(d):* HID, Intensity Range count-rate vs. Hard Ratio. *(e):* CCD, Hard Ratio vs. Soft Ratio. *(f):* CCD, Hard Ratio vs. Wide Ratio. *(g):* CCD, Soft Ratio vs. Wide Ratio.

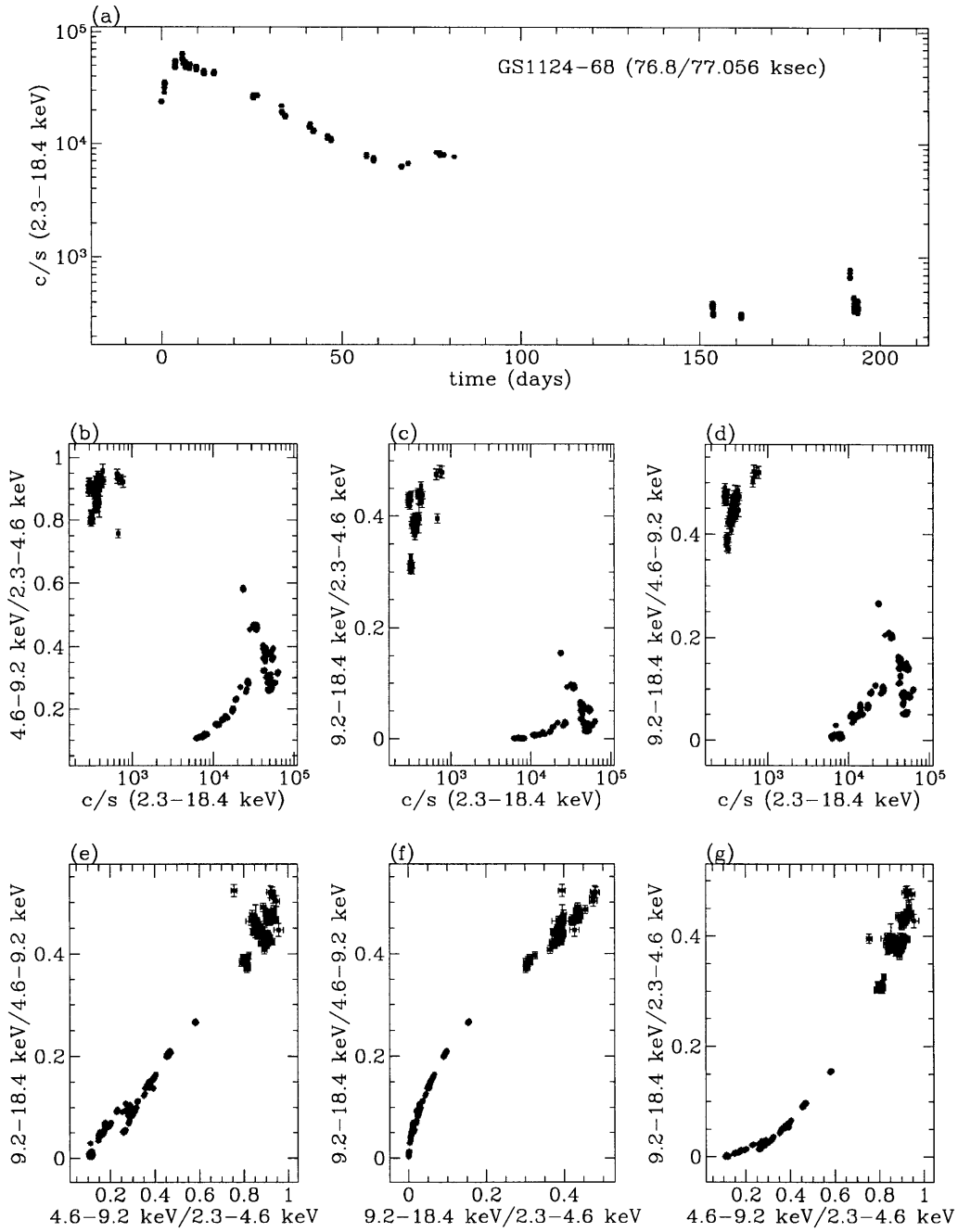

Figure 4-5: **LC/CCDs/HIDs of GS 1124-68**

Each point represents 128 s of data. 1 σ error bars are on each point. Data have been corrected for background, deadtime, and aspect. *(a):* 2-18 keV light curve (time=0 at 91/011 00:55:04). In the upper-right-hand corner is the amount of time in ksec of (usable data/usable data+low significance data). *(b):* HID, Intensity Range count-rate vs. Soft Ratio. *(c):* HID, Intensity Range count-rate vs. Wide Ratio. *(d):* HID, Intensity Range count-rate vs. Hard Ratio. *(e):* CCD, Hard Ratio vs. Soft Ratio. *(f):* CCD, Hard Ratio vs. Wide Ratio. *(g):* CCD, Soft Ratio vs. Wide Ratio.

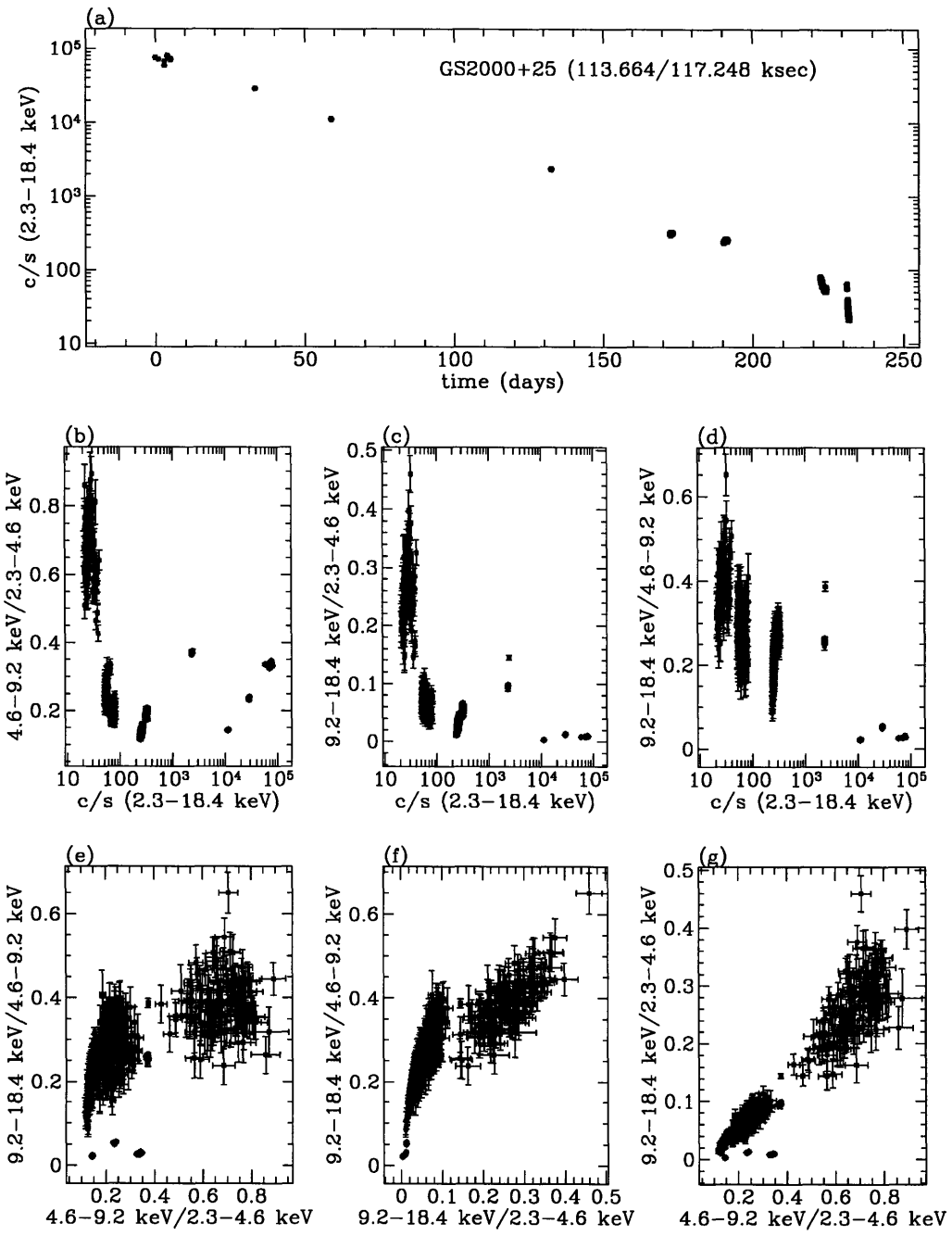

Figure 4-6: **LC/CCDs/HIDs of GS 2000+25**

Each point represents 128 s of data. 1 σ error bars are on each point. Data have been corrected for background, deadtime, and aspect. *(a):* 2-18 keV light curve (time=0 at 88/120 02:53:03). In the upper-right-hand corner is the amount of time in ksec of (usable data/usable data+low significance data). *(b):* HID, Intensity Range count-rate vs. Soft Ratio. *(c):* HID, Intensity Range count-rate vs. Wide Ratio. *(d):* HID, Intensity Range count-rate vs. Hard Ratio. *(e):* CCD, Hard Ratio vs. Soft Ratio. *(f):* CCD, Hard Ratio vs. Wide Ratio. *(g):* CCD, Soft Ratio vs. Wide Ratio.

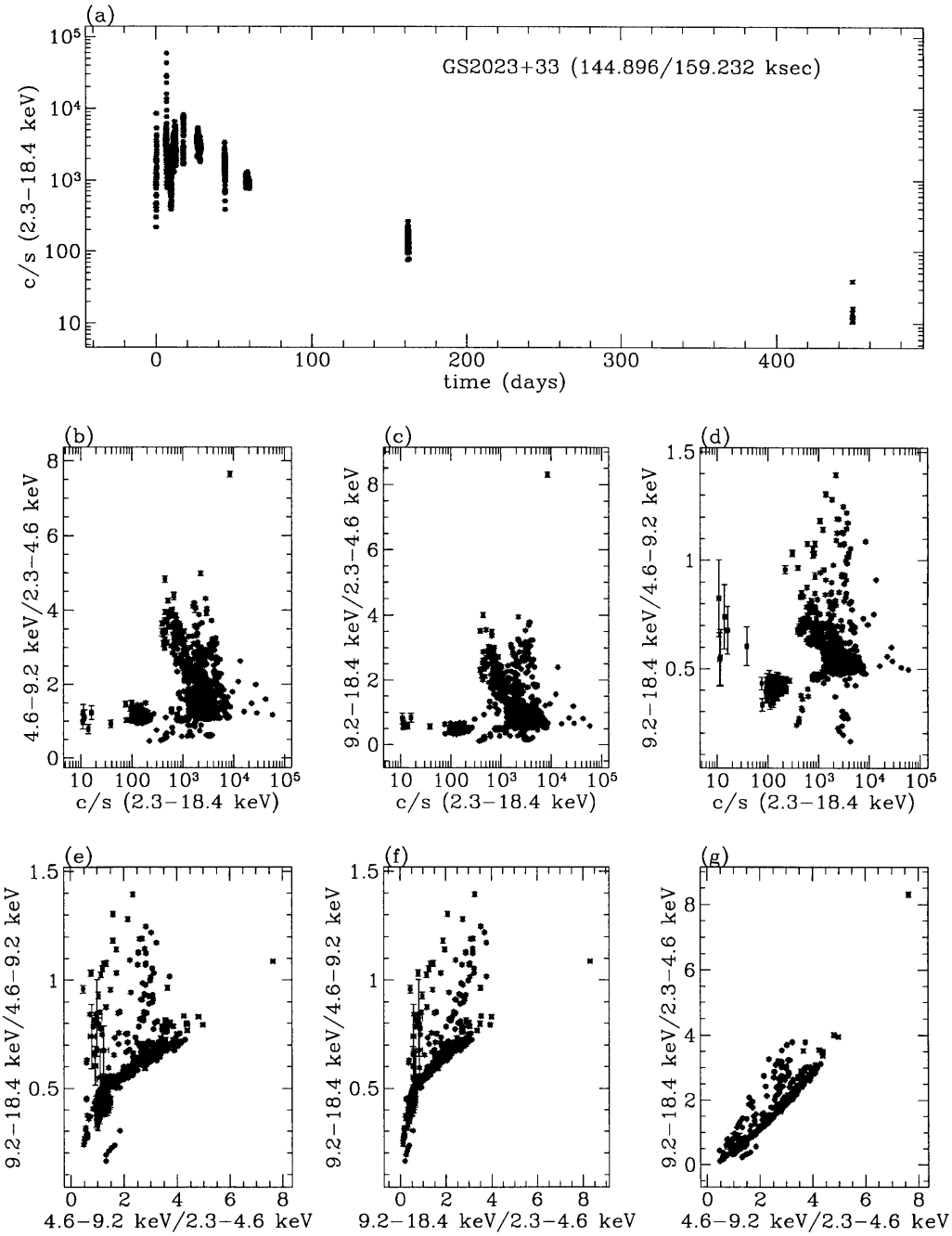

Figure 4-7: **LC/CCDs/HIDs of GS 2023+33**
Each point represents 128 s of data. 1 σ error bars are on each point. Data have been corrected for background, deadtime, and aspect. *(a):* 2-18 keV light curve (time=0 at 89/143 09:28:38). In the upper-right-hand corner is the amount of time in ksec of (usable data/usable data+low significance data). *(b):* HID, Intensity Range count-rate vs. Soft Ratio. *(c):* HID, Intensity Range count-rate vs. Wide Ratio. *(d):* HID, Intensity Range count-rate vs. Hard Ratio. *(e):* CCD, Hard Ratio vs. Soft Ratio. *(f):* CCD, Hard Ratio vs. Wide Ratio. *(g):* CCD, Soft Ratio vs. Wide Ratio.

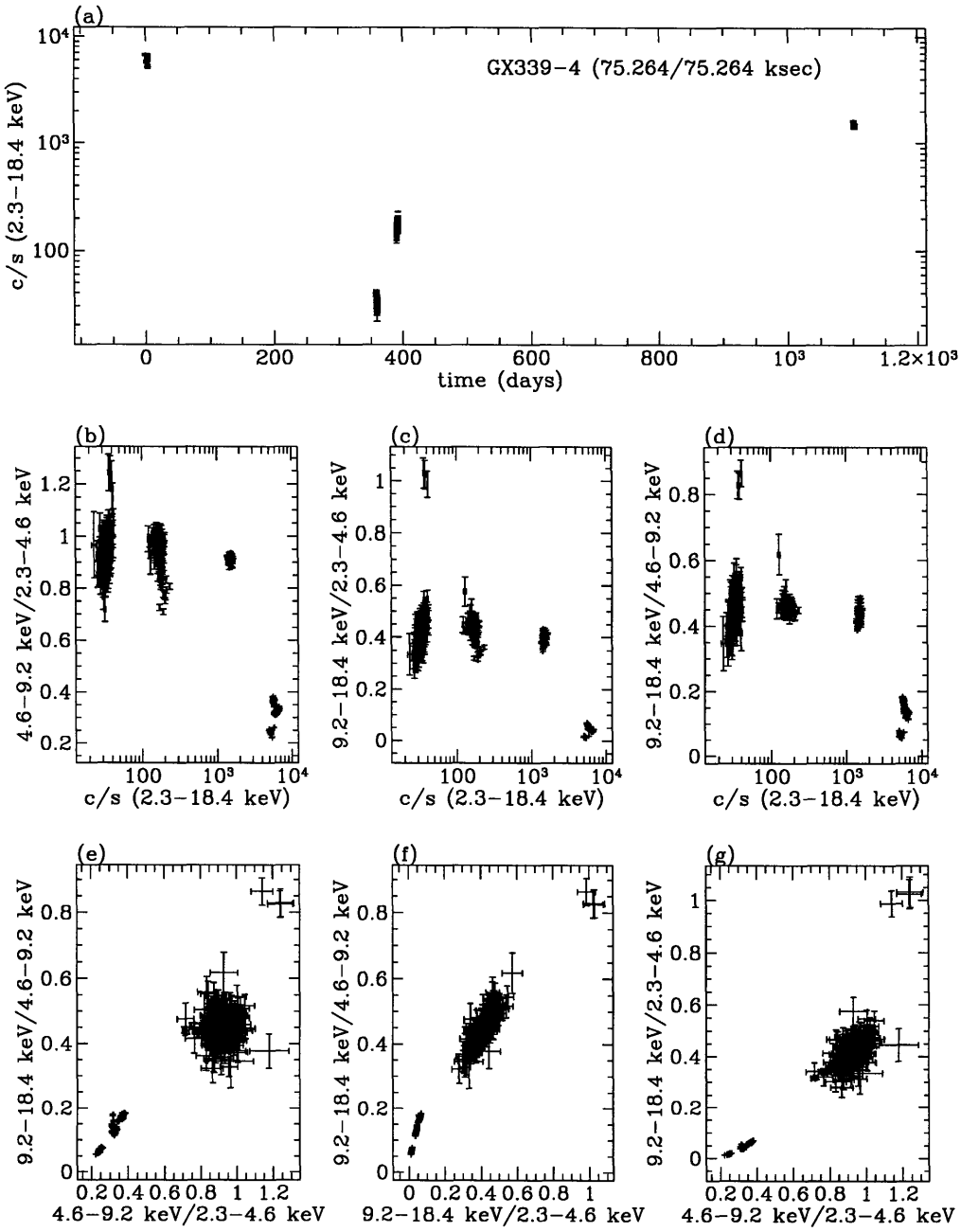

Figure 4-8: **LC/CCDs/HIDs of GX 339-4**

Each point represents 128 s of data. 1 σ error bars are on each point. Data have been corrected for background, deadtime, and aspect. *(a):* 2-18 keV light curve (time=0 at 88/247 13:36:56). In the upper-right-hand corner is the amount of time in ksec of (usable data/usable data+low significance data). *(b):* HID, Intensity Range count-rate vs. Soft Ratio. *(c):* HID, Intensity Range count-rate vs. Wide Ratio. *(d):* HID, Intensity Range count-rate vs. Hard Ratio. *(e):* CCD, Hard Ratio vs. Soft Ratio. *(f):* CCD, Hard Ratio vs. Wide Ratio. *(g):* CCD, Soft Ratio vs. Wide Ratio.

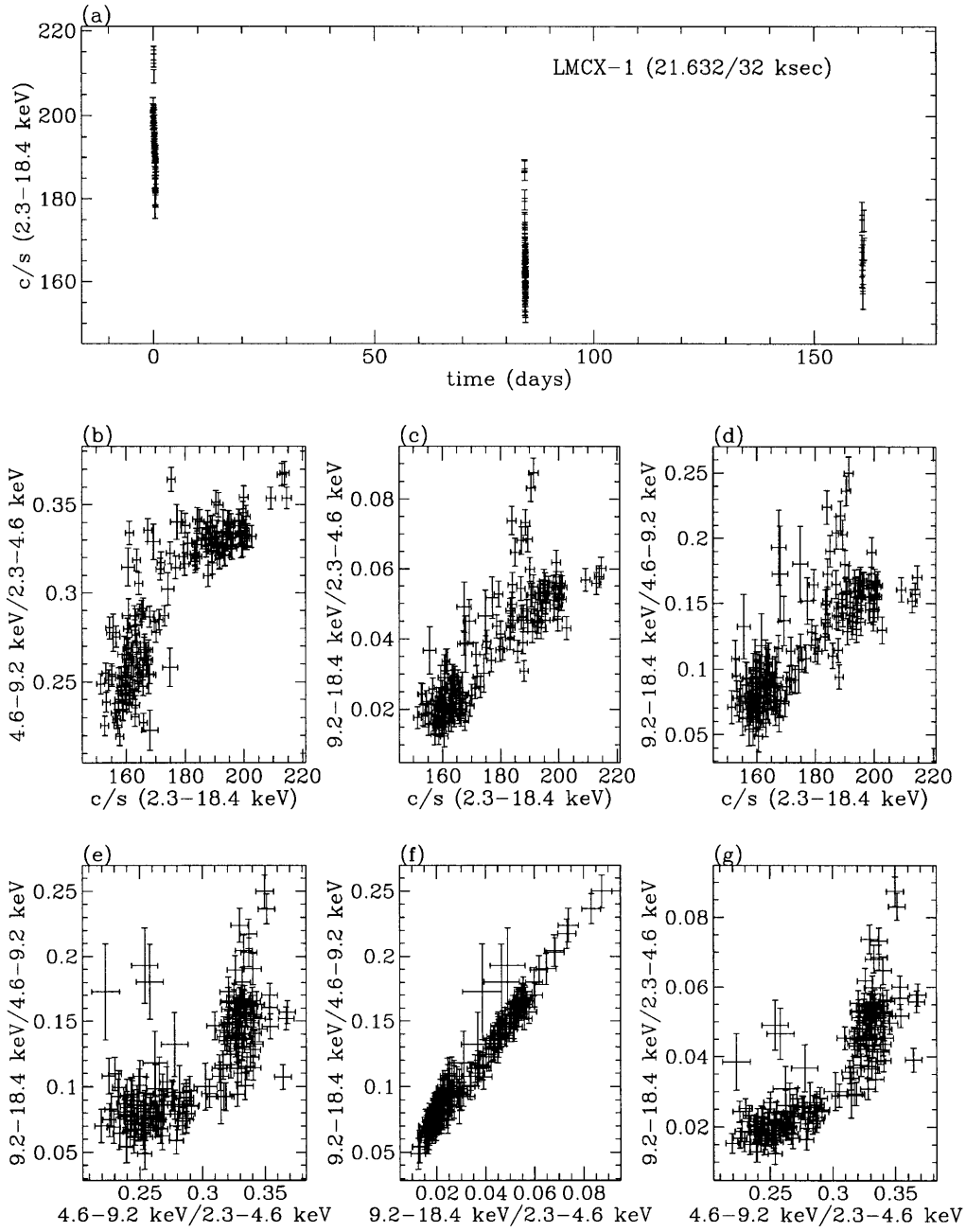

Figure 4-9: **LC/CCDs/HIDs of LMC X-1**

Each point represents 128 s of data. 1 σ error bars are on each point. Data have been corrected for background, deadtime, and aspect. *(a):* 2-18 keV light curve (time=0 at 87/112 22:55:43). In the upper-right-hand corner is the amount of time in ksec of (usable data/usable data+low significance data). *(b):* HID, Intensity Range count-rate vs. Soft Ratio. *(c):* HID, Intensity Range count-rate vs. Wide Ratio. *(d):* HID, Intensity Range count-rate vs. Hard Ratio. *(e):* CCD, Hard Ratio vs. Soft Ratio. *(f):* CCD, Hard Ratio vs. Wide Ratio. *(g):* CCD, Soft Ratio vs. Wide Ratio.

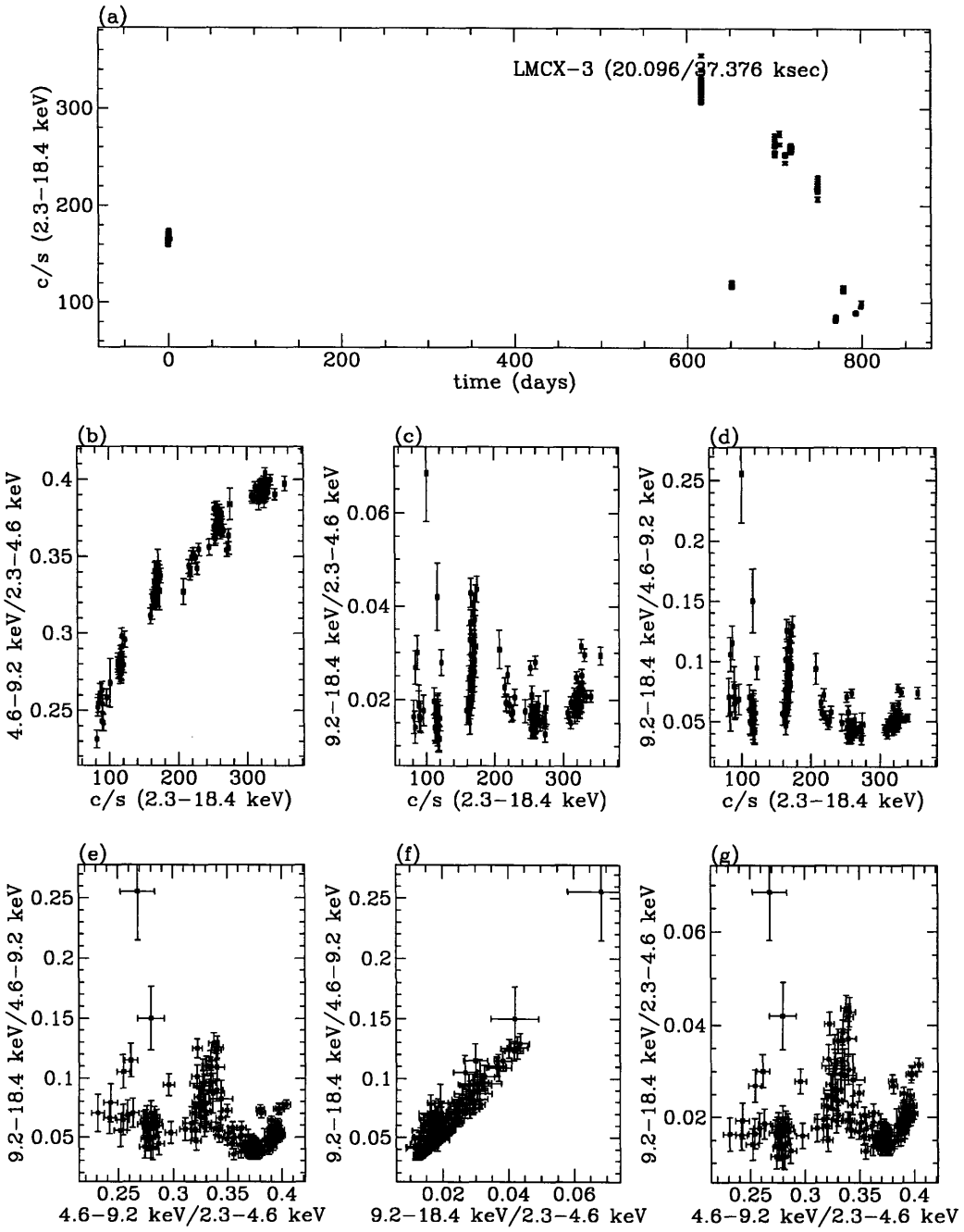

Figure 4-10: **LC/CCDs/HIDs of LMC X-3**

Each point represents 128 s of data. 1 σ error bars are on each point. Data have been corrected for background, deadtime, and aspect. *(a):* 2-18 keV light curve (time=0 at 88/008 07:49:33). In the upper-right-hand corner is the amount of time in ksec of (usable data/usable data+low significance data). *(b):* HID, Intensity Range count-rate vs. Soft Ratio. *(c):* HID, Intensity Range count-rate vs. Wide Ratio. *(d):* HID, Intensity Range count-rate vs. Hard Ratio. *(e):* CCD, Hard Ratio vs. Soft Ratio. *(f):* CCD, Hard Ratio vs. Wide Ratio. *(g):* CCD, Soft Ratio vs. Wide Ratio.

4.3.3 Hardness Ratios as a Function of Time

In this section, we present the hardness ratios (Soft Ratio, Wide Ratio, and, Hard Ratio) as a function of time in each of the sources.

We use the same data as that presented in the previous section. In panel *a* of each figure, we also show the 2.3–18.4 keV count-rate; panel *b* are the Soft Ratio vs. time; panel *c* are the Wide Ratio vs. time; and panel *d* are the Hard Ratio vs. time. The time axis covers all observations of each source – thus, the evolution during a single observation cannot usuallly be divined from these figures. Rather, these figures show, perhaps more clearly, the relationships between the various hardness ratios and the Intensity Range count-rate.

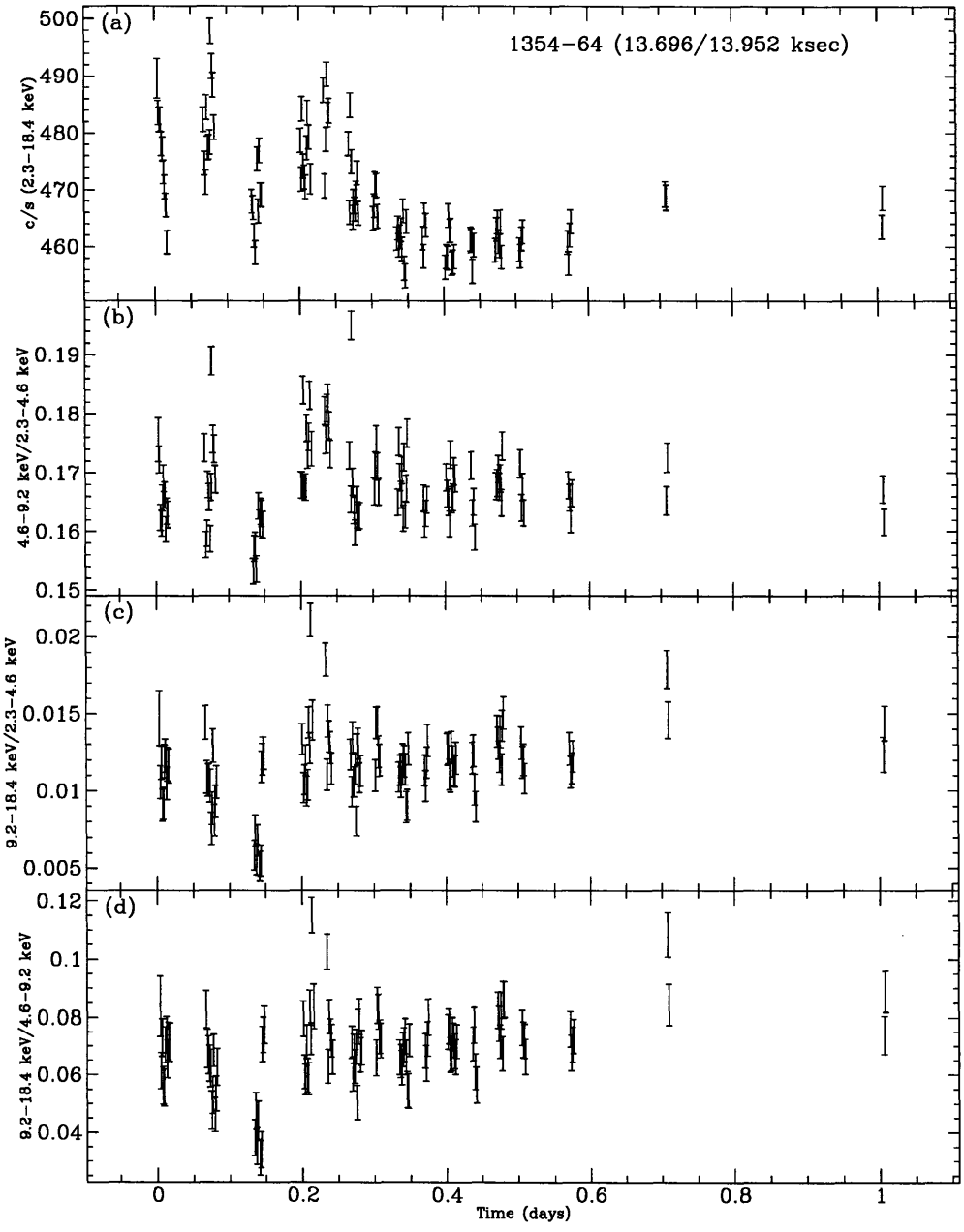

Figure 4-11: **LC and Hardness Ratios vs. Time of 1354-64**
Each point represents 128 s of data. 1 σ error bars are on each point. Data have been corrected for background, deadtime, and aspect. The time is in fractional days since 87/194 02:13:12. *(a):* 2-18 keV counts/s vs time; *(b):* Soft Ratio vs time; *(c):* Wide Ratio vs. time; *(d):* Hard Ratio vs. time.

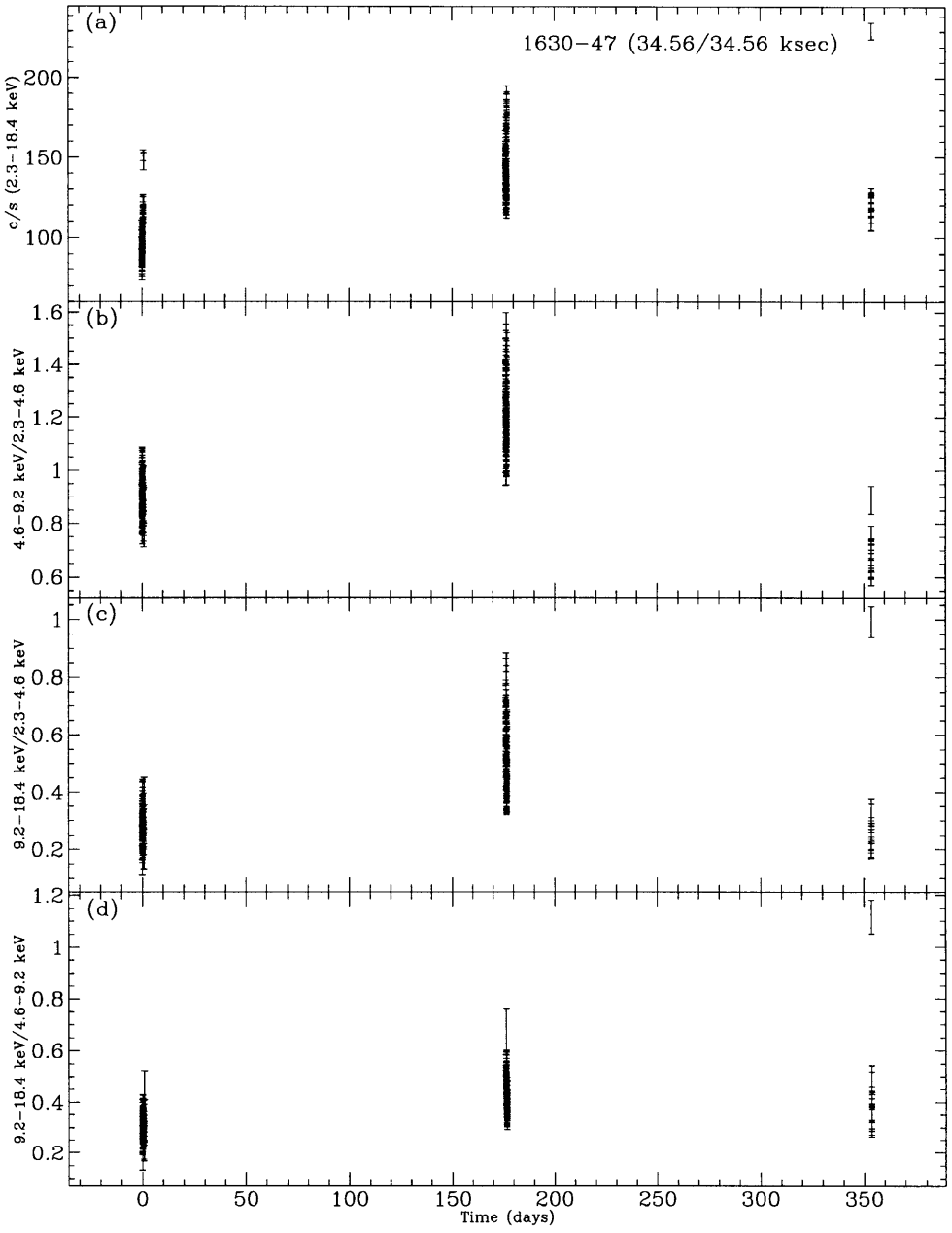

Figure 4-12: **LC and Hardness Ratios vs. Time of 1630-47**
Each point represents 128 s of data. 1 σ error bars are on each point. Data have been corrected for background, deadtime, and aspect. The time is in fractional days since 87/290 06:22:40. *(a):* 2-18 keV counts/s vs time; *(b):* Soft Ratio vs time; *(c):* Wide Ratio vs. time; *(d):* Hard Ratio vs. time.

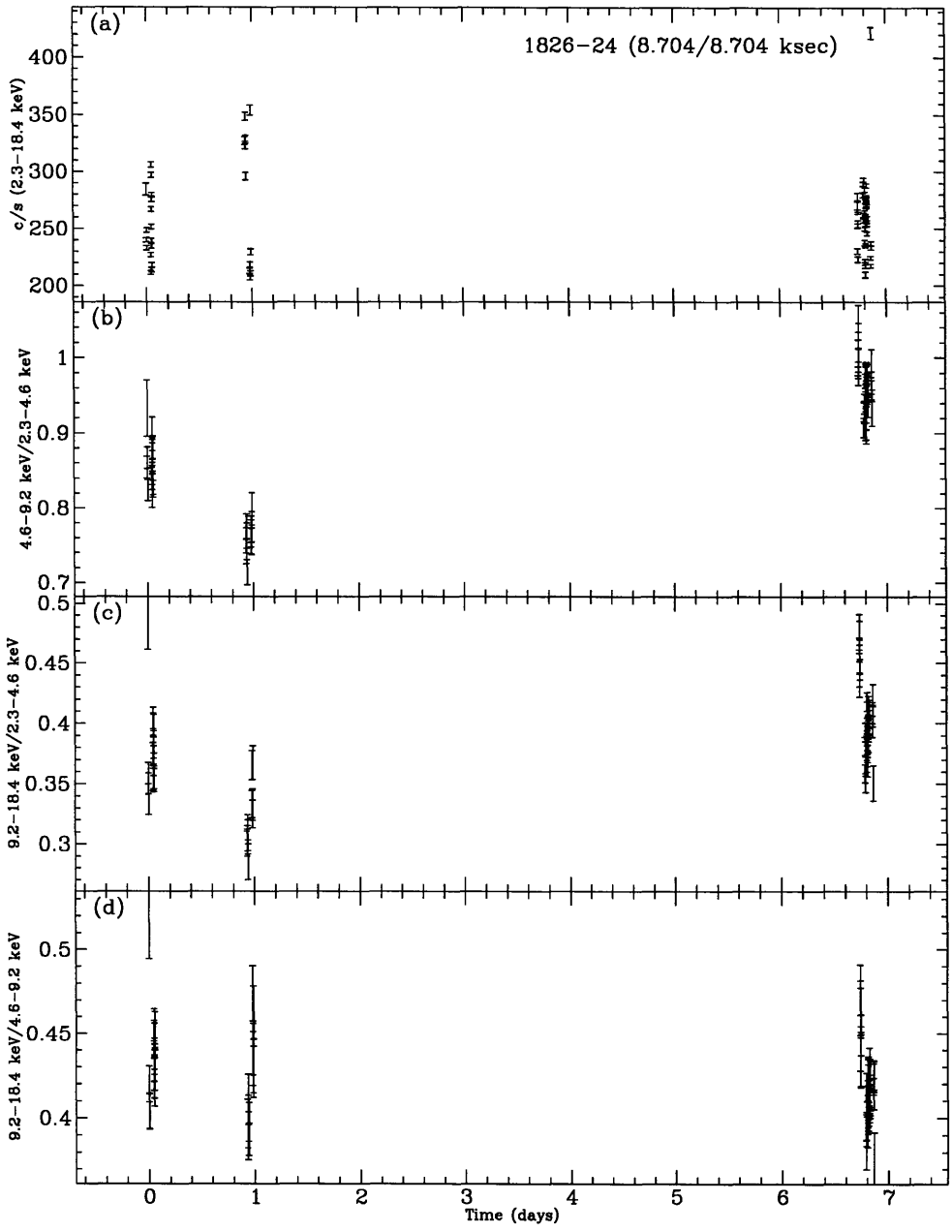

Figure 4-13: **LC and Hardness Ratios vs. Time of 1826-24**
Each point represents 128 s of data. 1 σ error bars are on each point. Data have been corrected for background, deadtime, and aspect. The time is in fractional days since 88/253 14:14:51. *(a):* 2-18 keV counts/s vs time; *(b):* Soft Ratio vs time; *(c):* Wide Ratio vs. time; *(d):* Hard Ratio vs. time.

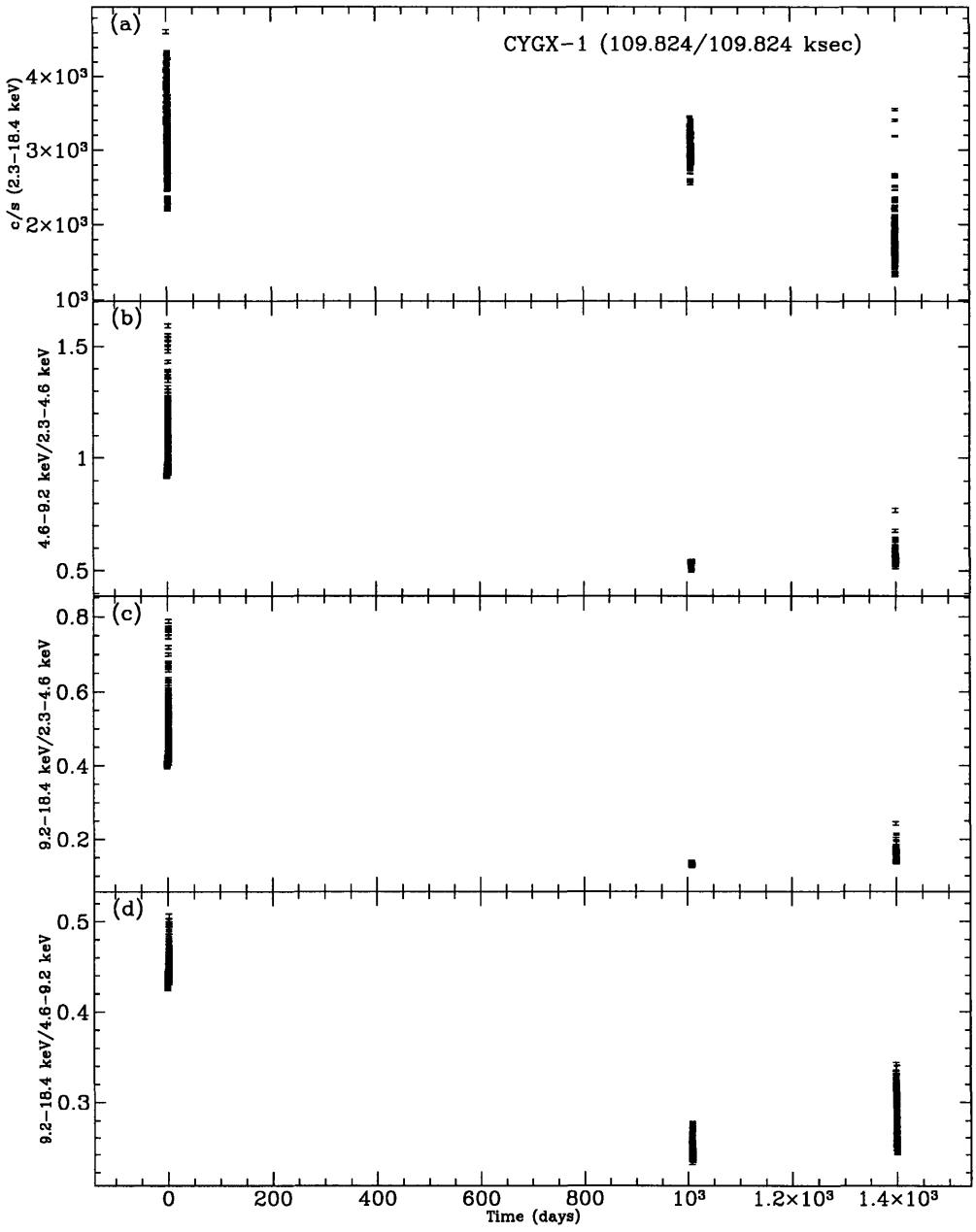

Figure 4-14: **LC and Hardness Ratios vs. Time of Cyg X-1**
Each point represents 128 s of data. 1 σ error bars are on each point. Data have been corrected for background, deadtime, and aspect. The time is in fractional days since 87/217 11:41:18. *(a):* 2-18 keV counts/s vs time; *(b):* Soft Ratio vs time; *(c):* Wide Ratio vs. time; *(d):* Hard Ratio vs. time.

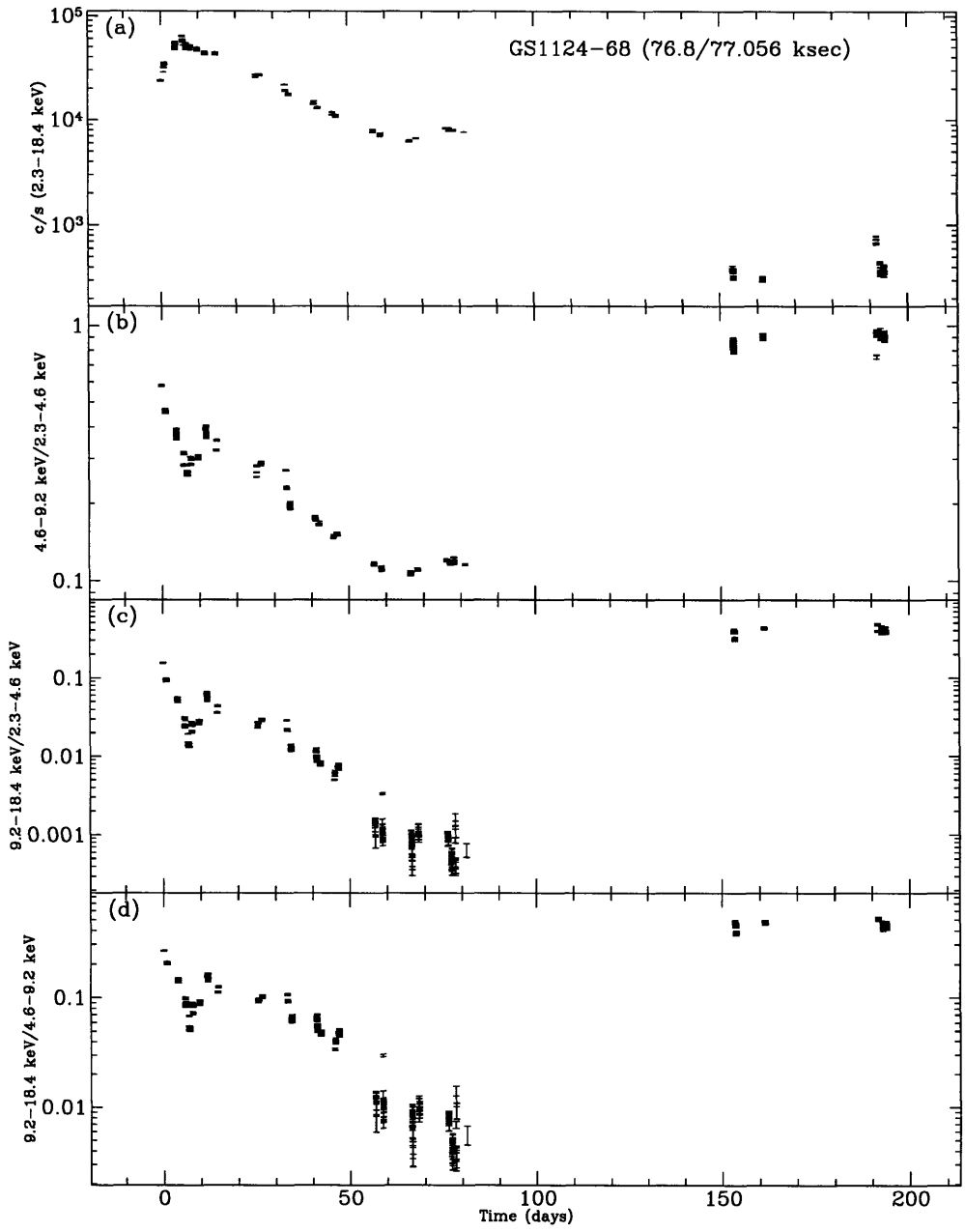

Figure 4-15: **LC and Hardness Ratios vs. Time of GS 1124-68**
Each point represents 128 s of data. 1 σ error bars are on each point. Data have been corrected for background, deadtime, and aspect. The time is in fractional days since 91/011 00:55:04. *(a):* 2-18 keV counts/s vs time; *(b):* Soft Ratio vs time; *(c):* Wide Ratio vs. time; *(d):* Hard Ratio vs. time.

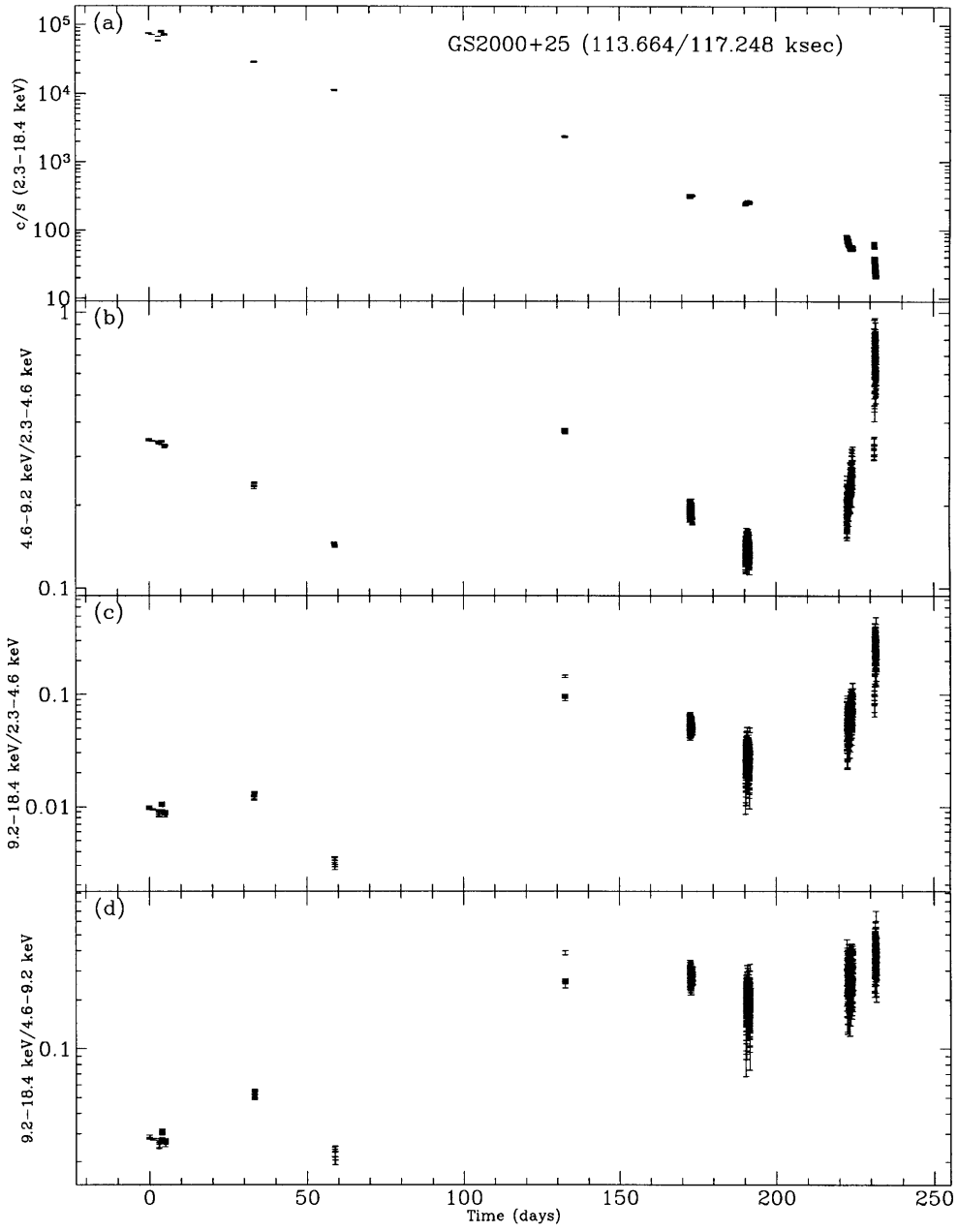

Figure 4-16: **LC and Hardness Ratios vs. Time of GS 2000+25**
Each point represents 128 s of data. 1 σ error bars are on each point. Data have been corrected for background, deadtime, and aspect. The time is in fractional days since 88/120 02:53:03. *(a):* 2-18 keV counts/s vs time; *(b):* Soft Ratio vs time; *(c):* Wide Ratio vs. time; *(d):* Hard Ratio vs. time.

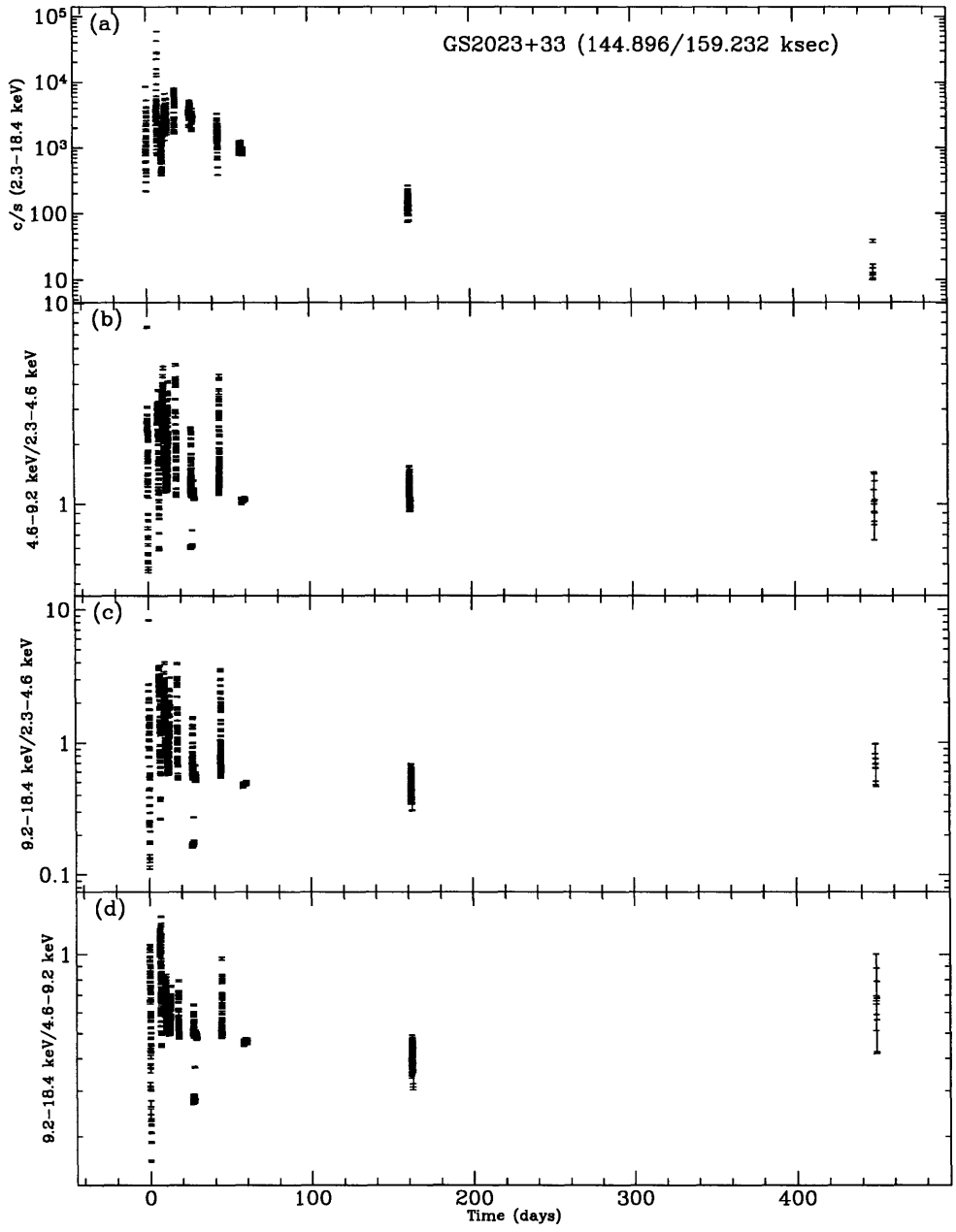

Figure 4-17: **LC and Hardness Ratios vs. Time of GS 2023+33**
Each point represents 128 s of data. 1 σ error bars are on each point. Data have been corrected for background, deadtime, and aspect. The time is in fractional days since 89/143 09:28:38. *(a):* 2-18 keV counts/s vs time; *(b):* Soft Ratio vs time; *(c):* Wide Ratio vs. time; *(d):* Hard Ratio vs. time.

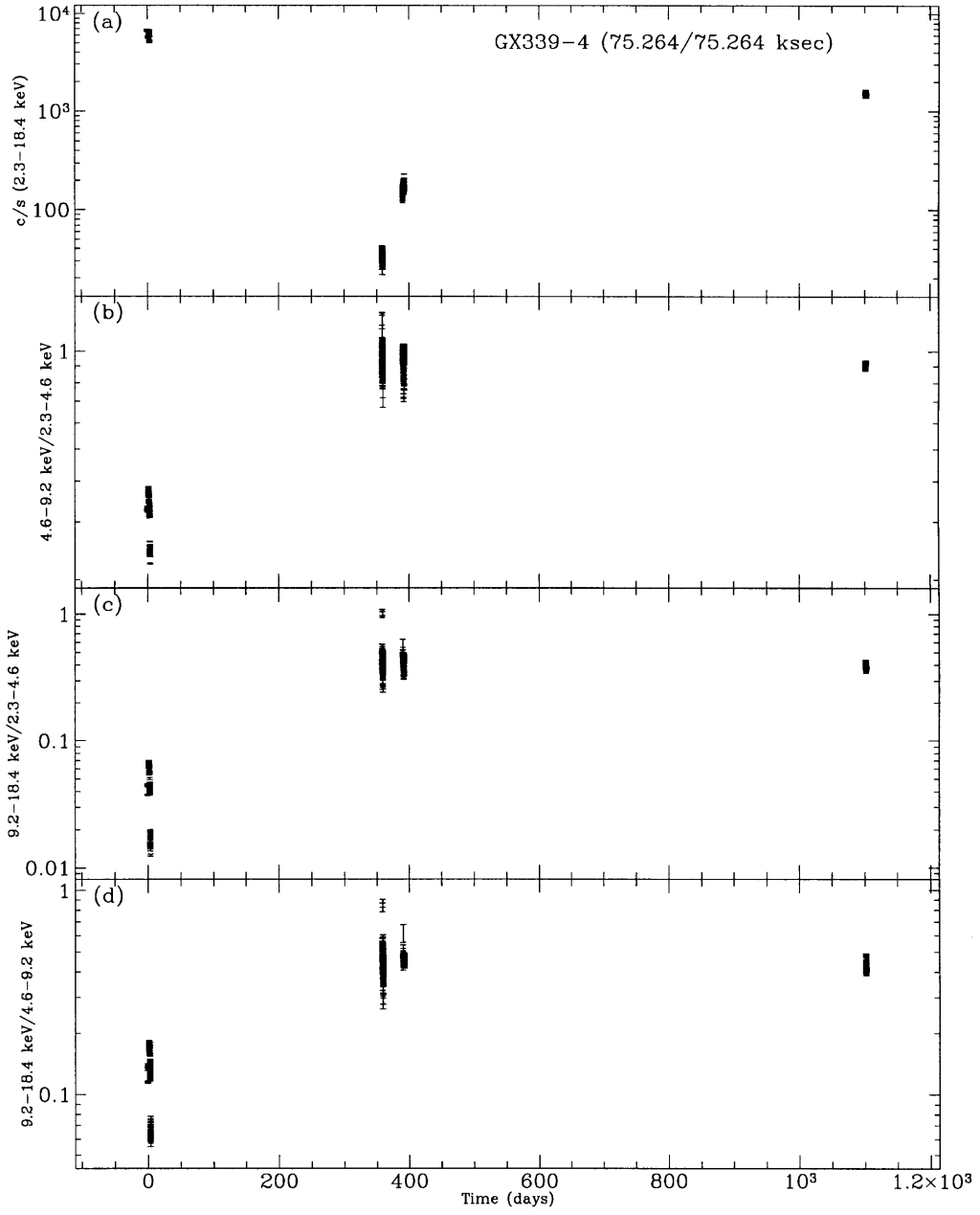

Figure 4-18: **LC and Hardness Ratios vs. Time of GX 339-4**
Each point represents 128 s of data. 1 σ error bars are on each point. Data have been corrected for background, deadtime, and aspect. The time is in fractional days since 88/247 13:36:56. *(a):* 2-18 keV counts/s vs time; *(b):* Soft Ratio vs time; *(c):* Wide Ratio vs. time; *(d):* Hard Ratio vs. time.

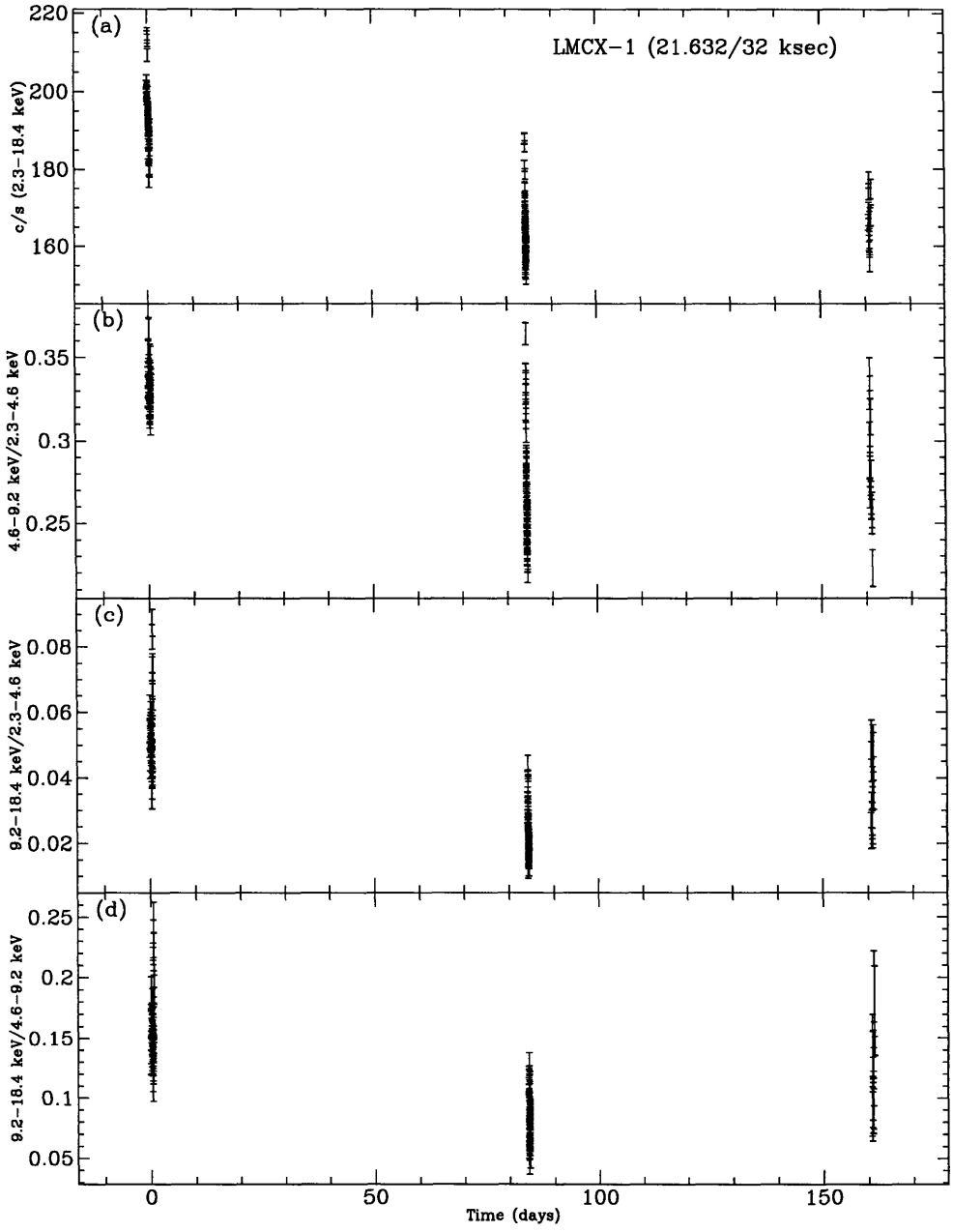

Figure 4-19: **LC and Hardness Ratios vs. Time of LMC X-1**
Each point represents 128 s of data. 1 σ error bars are on each point. Data have been corrected for background, deadtime, and aspect. The time is in fractional days since 87/112 22:55:43. *(a):* 2-18 keV counts/s vs time; *(b):* Soft Ratio vs time; *(c):* Wide Ratio vs. time; *(d):* Hard Ratio vs. time.

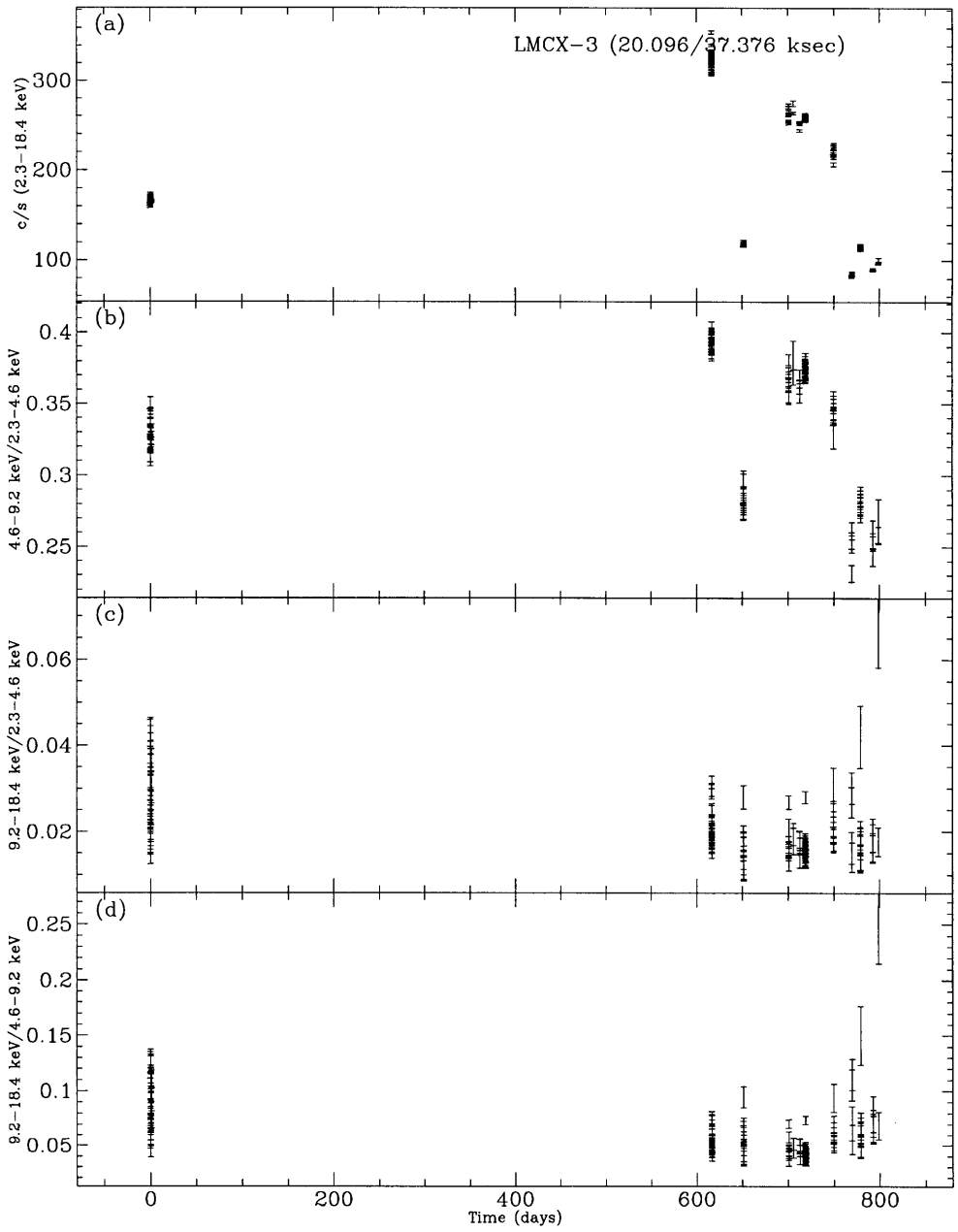

Figure 4-20: **LC and Hardness Ratios vs. Time of LMC X-3**
Each point represents 128 s of data. 1 σ error bars are on each point. Data have been corrected for background, deadtime, and aspect. The time is in fractional days since 88/008 07:49:33. *(a):* 2-18 keV counts/s vs time; *(b):* Soft Ratio vs time; *(c):* Wide Ratio vs. time; *(d):* Hard Ratio vs. time.

4.3.4 Discussion on the Individual CCDs, HIDs and LCs

Comparing the LCs, HIDs, and CCDs individually provides interesting connections among the individual sources.

The primary division between the sources is the transient novae vs. the persistent sources. The transient novae (GS 1124-68, GS 2023+33, GS 2000+25, and 1354-64) are observed to evolove through large changes in their intensity, with the exception of 1354-64, for which we analyzed only 1 day of observations (1354-64 was not observed by the LAC during its decay).

The transient with the most coverage of its outburst, GS 1124-68, shows three distinct time-phases, where the spectrum is 1) anti-correlated, 2) correlated, and 3) complexly related to the source intensity. GS 2000+25 exhibits some behavior which is consistent with this framework. We have little coverage near the beginning of its outburst, but the simultaneous spectral and intensity behavior of GS 2000+25 during the first 60 days is consistent with this kind of phase behavior over the same time-period; however, later in the outburst, the behavior is more complex, beginning relatively soft as the Intensity Range count-rate continues to decrease near day=130 at 2000 c/s, until the count-rate drops below 100 c/s, and the spectrum becomes hard. Finally, of these three sources GS 2023+33 is aberrant. The Intensity Range fluctuates wildly early in its outburst (300–60,000 c/s within single observational periods earlier than t=20 days). At the same time, its spectrum is varying wildly as well, flaring into extremely hard states – the hardest observed from any of the sources in the present study.

In all the sources, when one searches for global patterns within the CCDs and HIDs, there is one combination of parameters where the most simplified behavior is seen: the CCD, comparing Hard Ratio vs. Wide Ratio. Typically, these two parameters, for each source taken individually, are positively correlated, even when more complex behavior is evident in the CCDs comparing the Hard Ratio vs. Soft Ratio and the Wide Ratio vs Soft Ratio (see, for instance, Fig. 4-1 of 1354-64, and 4-10 of LMC X-3). The correlation, however, is not absolute, linear, or universal. For example, Cyg X-1 (Fig. 4-4) shows a change in the correlation of the Hard Ratio and

Wide Ratio between its hard and soft spectral states. GS 2023+33 shows a positive correlation which changes in slope near Wide Ratio=0.5, and shows radical increases in hardness during t=0–8-days (see Fig. 4-21) which do not exhibit this correlation.

It is interesting that, in the individual sources, the Hard Ratio and Wide Ratio appear to vary together, but this is perhaps not entirely unexpected. It has been previously shown that BHCs have at least two spectral components – the so-called ultra-soft component, which typically dominates below 5 keV, and the power-law component, which typically dominates above 10 keV. Thus, the Wide Ratio(9.2–18.4 keV/2.3–4.6 keV) is likely to be a good measure of which component dominates the spectrum: if the ultra-soft component is much stronger, the source is relatively soft, and the Wide Ratio will have low values; if the power-law component is much stronger, then the spectrum should be hard, and Wide Ratio will have high values.

If this were the only interpretation, then there should be a single locus of points in each CCD, showing unique relations between each color pair. This can be seen in the following argument.

Assume the ultra-soft component intensity and power-law components intensity of each source to be arbitrary functions of energy only – that there are no internal variables (such as temperature, power-law slope or any such intrinsic value), and that their normalizations are functions of time. The integrated counts over a time interval (δt) in a particular band is then:

$$\text{Counts} = \int_0^{\delta t} \int_{\nu_1}^{\nu_2} [A(t)\, f_{\text{us}}(\nu) + B(t)\, f_{\text{pl}}(\nu)]\epsilon(\nu)\, d\nu\, dt \tag{4.1}$$

where $f_{\text{us}}(\nu)$ is the energy dependent ultra-soft component, $f_{\text{pl}}(\nu)$ is the energy dependent power-law component, $A(t)$ and $B(t)$ are the time-dependent normalizations of the ultra-soft and power-law components (respectively), ν_1 and ν_2 are the energy boundaries of the channel, and $\epsilon(\nu)$ is the energy-dependent response function of the detector. From this, we find the general equation for a color:

$$\text{Color} = \frac{R_{\text{us,high}} + \frac{<B>_{\delta t}}{<A>_{\delta t}} R_{\text{pl,high}}}{R_{\text{us,low}} + \frac{<B>_{\delta t}}{<A>_{\delta t}} R_{\text{pl,high}}} \tag{4.2}$$

$$\begin{aligned}
R_{\text{us,high}} &= \int_{\nu_3}^{\nu_4} f_{\text{us}}(\nu)\epsilon(\nu)\, d\nu \\
R_{\text{pl,high}} &= \int_{\nu_3}^{\nu_4} f_{\text{pl}}(\nu)\epsilon(\nu)\, d\nu \\
R_{\text{us,low}} &= \int_{\nu_1}^{\nu_2} f_{\text{us}}(\nu)\epsilon(\nu)\, d\nu \\
R_{\text{pl,low}} &= \int_{\nu_1}^{\nu_2} f_{\text{pl}}(\nu)\epsilon(\nu)\, d\nu \\
< A >_{\delta t} &= \int_0^{\delta t} A(t)\, dt \\
< B >_{\delta t} &= \int_0^{\delta t} B(t)\, dt
\end{aligned} \tag{4.3}$$

where typically the energy channel boundaries are $\nu_1 < \nu_2 \leq \nu_3 < \nu_4$. The several values of R, the convolution of the respective spectral component function and the detector response, are *constants*, and the only variable values are the time-averaged normalizations. Perhaps more transparent is the single-parameter color-function:

$$\text{Color}(X) = \frac{R_{\text{us,high}} + X\, R_{\text{pl,high}}}{R_{\text{us,low}} + X\, R_{\text{pl,high}}} \tag{4.4}$$

$$X = \frac{< B >_{\delta t}}{< A >_{\delta t}} \tag{4.5}$$

where X can (in principle) take on any value between 0 and infinity. For changing values of X, and all values of R constant, Color(X) is a unique function.

Thus, we see that for constant normalizations and intrinsic spectrum, the source colors will be the same – that is, a constant spectrum produces constant colors. If the source spectrum either evolves in the amount of *relative* normalization of its two components, or in its intrinsic spectrum, then evolution in the source colors will result.

The change in color of a source with respect to X is then:

$$\frac{d\text{Color}}{dX} = \frac{R_{\text{pl,high}} R_{\text{us,low}} - R_{\text{us,high}} R_{\text{pl,low}}}{(R_{\text{us,low}} + X\, R_{\text{pl,high}})^2} \tag{4.6}$$

which translates into the change in one color with respect to another (as on a CCD):

$$\frac{d\text{Color}_1}{d\text{Color}_2} = R_0 \left(\frac{R_1 + X\, R_2}{R_3 + X\, R_4} \right)^2 \tag{4.7}$$

where R_n correspond to different convolutions of the spectral response function with the intrinsic source spectra (assumed constant) which are thus constants. When examining a CCD of a source which evolves only by changes in the relative normalizations of two components, one should see near one end of the CCD (when one component dominates) a linear track with a constant slope determined by the detector properties, which eventually slowly bends into a line of (most likely) another slope, also determined by the detector properties.

In investigating two different colors, if one of the colors is the same, then the other color should also be the same for a constant spectrum source – that is, the CCD must show a one-to-one correspondence between the colors. If the CCD does not show one-to-one correspondence, then it must be that the source is evolving in spectral parameters – a non-one-to-one correspondence in the CCD cannot be mimicked by variation in the normalization of two constant spectral components, as a variation in the ratio $< B > / < A >$ produces a change in all colors.

Therefore, when we observe in a CCD a range of color values at a constant color for one (or, between several) sources, we immediately know that this is due to intrinsic spectral variation. Likewise, when we see apparent one-to-one correspondence between colors in a CCD, we know that the evolution along this one-to-one correspondence is likely due primarily to changes in normalization of the two spectral components. When it is changes in the normalization which are dominant, then the measured colors of the source are limited by the values of the constants:

$$\frac{R_{\text{us,high}}}{R_{\text{us,low}}} \leq \text{Color} \leq \frac{R_{\text{pl,high}}}{R_{\text{pl,low}}} \tag{4.8}$$

4.3.5 Spectral Behavior of GS 2023+33 and Peak Count-rate

In this section, we describe the spectral behavior of GS 2023+33 near its peak intensity, focusing on deviations from locus behavior. For this section, time will be in units of days since 89/143 09:28:38 (UT).

In Fig. 4-21, we show the first 15 days of the intensity history of GS 2023+33, along with that of the Wide Ratio, and the CCD of Wide Ratio vs. Hard Ratio for the first 15 days and, separately, thereafter. The time-periods we discuss are not necessarily contiguous in the data-set. The panels referred to are those in Fig. 4-21, unless otherwise noted.

Period A: Time=0.0-0.15d; Red points. The Intensity varies by a factor of 10 and the spectrum also varies on 128s timescales. The spectral behavior is entirely non-locus.

Period B: Time=0.15-0.3d; Green points. Between Time=0.15-0.20, the intensity varies by a factor of two, and the spectrum also varies, but remains on the locus. Between Time=0.2-0.3, the intensity varies by a factor of 10, while spectrum varies considerably, away from the locus.

Period C: Time=0.45-0.5d; Magenta points. The intensity varies by a factor of five; the spectrum also varies, but falls along a single branch in the Wide Ratio vs. Hard Ratio CCD (panel c), which does not coincide with the locus.

Period D: Time=6.0-6.8d; Cyan points Both the intensity and the spectrum are variable during this period. The spectral behavior is branch-like which at first is close to locus behavior, but the spectrum quickly becomes harder and lies above the locus in the CCD, then softens back toward the locus.

Period E: Time=6.8-7.4d; Yellow points. The Intensity varies by a factor of 100; the spectrum also varies wildly – not along the locus, not along a branch, but like a scatter-plot, with the spectrum harder than that at the locus.

Period F: Time 9.0-13.0; Blue points. The Intensity varies by a factor of 10, and the spectrum also changes dramatically. However, the spectrum at all times lies

upon the spectral locus.

After T=15.0 d; The Intensity history after 15.0 d is shown in Fig. 4-17a. The Intensity continually drops off exponentially. During this entire period, the spectrum varies dramatically, spanning the entire flat-part of the locus ($0.5 \lesssim$Wide Ratio $\lesssim 4.0$).

We see here that, during the first 7.0 d of the nova outburst, the spectrum largely occupies the non-locus area of the CCD; after this period, however, the source spectrum was found to remain on the source locus, even while varying in Wide Ratio by a factor of 8.

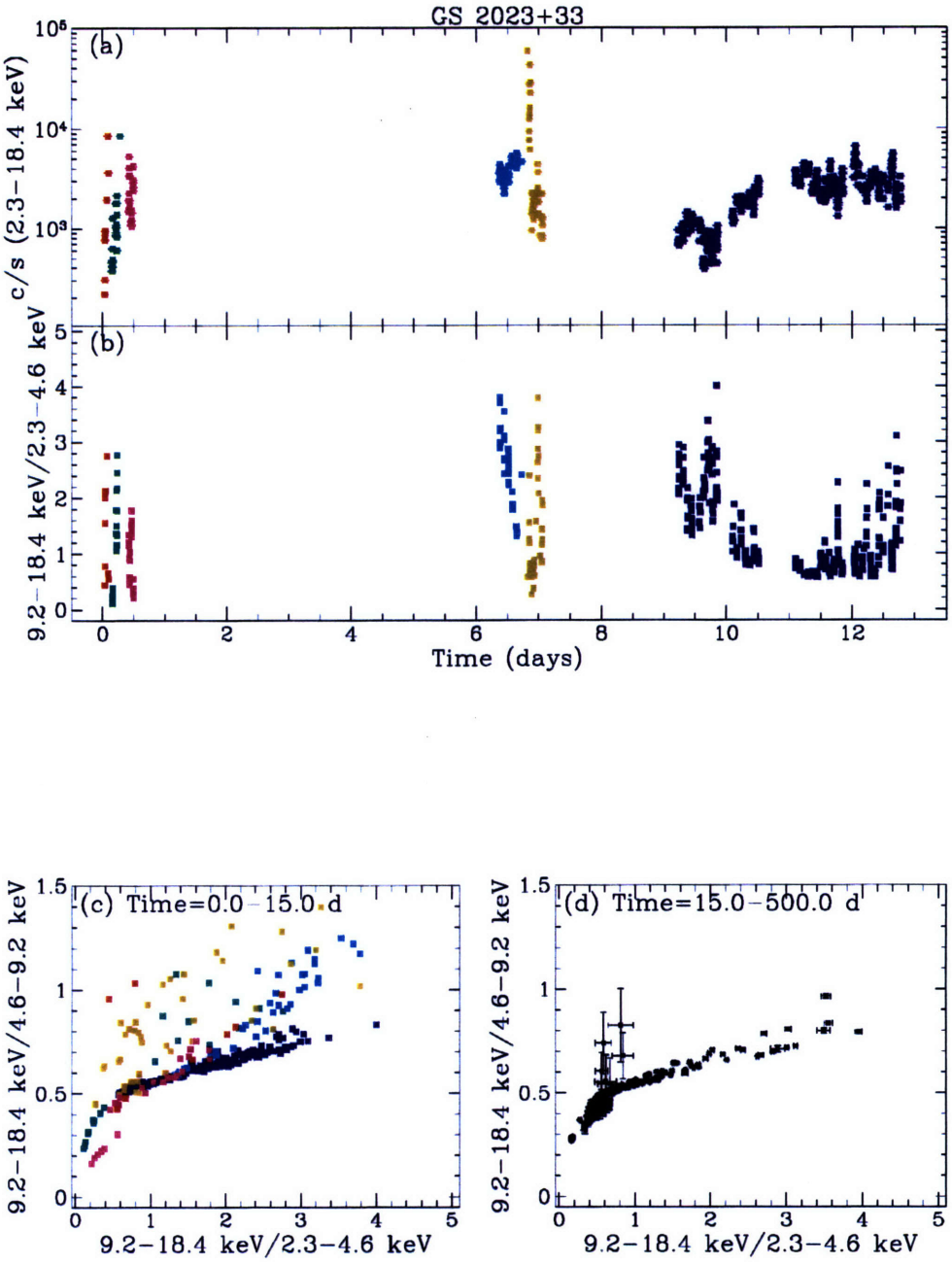

Figure 4-21: **Spectral Behavior at Peak Count-rate of GS 2023+33 (color plot)** The intensity and spectral behavior of GS 2023+33 at its peak count-rate (during the first 15 days of outburst). Error-bars on all points, except where shown, are the size of the point or smaller. The different colors are used to separate the points more clearly in time. *(a)* 2.3-18.4 keV count-rate vs. time (in days since 89/143 09:28:38); *(b)*:Wide Ratio vs time (in days since 89/143 09:28:38); *(c)* CCD of Wide Ratio vs. Hard Ratio for the period between 89/143 09:28:38 and 15.0 days later; *(d)* CCD of Wide Ratio vs. Hard Ratio for the period between time=15.0-450.0

4.4 Composite CCD

We have combined the CCDs of the individual sources in the previous section into single CCDs, for inter-comparison, and a search for similarities and patterns, which may provide clues for global phenomenon, or provide useful observational phenomenology.

In Fig. 4-22 we show the composite CCDs of seven BHCs (GS 2023+33, 1826-24, LMC X-3, LMC X-1, Cyg X-1, 1354-64, and GS 1124-68; other sources are examined in Fig. 4-23). Each source is represented by a different color, as indicated in the color legend. Error-bars are not included. Often points overlap in these plots, so some are obscured by points of other colors.

What is perhaps most noticeable in these figures is how the different sources occupy a thin locus on each CCD, in particular of the CCD showing the Hard Ratio vs. Wide Ratio (panel *b*). The most obvious exception to this is the strong spectral variability observed in GS 2023+33, which makes it at times very hard.

In Fig. 4-22a, we see the composite CCD of Hard Ratio vs. Soft Ratio. The locus is well defined, but with a finite width, and with deviations from a one-to-one correspondence by all the sources. Cyg X-1 in its spectrally hard state (1.0<Soft Ratio< 1.5), traces a thin line, which lies neatly on the broader range traced by GS 2023+33. Both these sources are overlapped at the soft end (near Soft Ratio=1) by GS 1124-68 and 1826-24. GS 1124-68 extends into the softer range, (again, overlapping with Cyg X-1 near Soft Ratio=0.6), to where it overlaps with the more variable sources LMC X-1, 1354-64, and LMC X-3.

Fig. 4-22b is the composite CCD of Hard Ratio vs. Wide Ratio for these sources. Again, the sources seem to trace a single locus across the available parameter space. The same observations hold for panel *c*, which shows the Wide Ratio vs. Soft Ratio CCD.

A closer look at the Hard Ratio vs. Wide Ratio CCD (panel *d*), zooming in on the box in panel *b*, shows that the correspondence in the spectrally soft region is close. The sources lie tightly together.

In Fig. 4-23, we present the composite CCDs of five sources (GS 1124-68 and

GS 2023+33 – both included also in Fig. 4-22, given here to gauge correspondence with the three new sources – GX 339-4, GS 2000+25, and 1630-47). Each color corresponds to a different source. The three sources GX 339-4, GS 2000+25, and 1630-47 show much more spectral variability than those in the previous figure (4-22). GS 2000+25 and 1630-47 both are displaced on average from the locus defined by GS 1124-68 and GS 2023+33 in all three CCDs. GS 2000+25 also shows much intrinsic spectral variability relative to that seen in other sources – this is particularly apparent in panel *d*, which is a zoom-in on the box in the CCD of Hard Ratio vs. Wide Ratio (panel *b*). Here, GS 2000+25 lies somewhat above a thin line occupied by both GS 1124-68 and GX 339-4.

In Fig. 4-24, we show the complete composite CCD (Wide Ratio vs. Hard Ratio) of all the spectral data for all sources; to show the full range of all the data, and more precisely show source-to-source differences, we use log-log space. Each point represents 128 s of contiguous data. The data from each source are shown in one color, although some colors were used for more than one source's data. We overlayed on this figure an arbitrary spectral-labeling scheme, making use of the letters A–J, and which is described below (and is listed in Table 4.2).

In log-log color space, we can see the differences between sources which were less apparent in linear-color space. In all, the Wide Ratio of the ten BHCs (1354-64, 1826-24, 1630-47, LMC X-1, LMC X-3, GS 2000+25, GS 2023+33, GS 1124-68, Cyg X-1, and GX 339-4) spans a factor of ~10,000. A factor of 100 of this is provided by the spectral extremes reached by GS 2023+33 (and the spectrally hard end) and GS 1124-68 (at the spectrally soft end). In the range (Wide Ratio~0.015), the several sources span values of the Hard Ratio by a factor of $\times 5$ ($0.03 <$ Hard Ratio< 0.015). Individual sources largely follow single tracks in Hard Ratio vs. Wide Ratio space, which appear to be almost parallel, with some notable exceptions (GS 2000+23, GS 2000+25). This is the kind of behavior expected as discussed in Sec. 4.3.4, when there are two spectral components which vary only in their normalizations. The displacements of the several tracks of different sources must indicate spectral differences between the sources.

The data are often crowded, with one source's points obscuring those of another. For example, Cyg X-1 has data which are obscured by 1630-47; data from 1826-24 are entirely obscured by those of GX 339-4; much of the LMC X-1 data are obscured by the data of GX 339-4 and GS 1124-68; and some GS 1124-68 data are covered by Cyg X-1 and GS 2000+25 (near Wide Ratio=0.4). We separated the Wide Ratio by source in Fig. 4-25, so that the range of Wide Ratio for each source may be plainly seen.

Super-imposed on this figure are the demarcations which are used in spectral selection, as short-hand for defining the particular spectral state for the fast-timing analysis in Ch. 5, based on the value of Wide Ratio. These demarcations were selected to be of equal width in log-space, and labeled alphabetically (A, B, C, ...) beginning at a value of Wide Ratio=0.0001. Specifically, the ranges of Wide Ratio have been labeled as indicated in Table 4.2. This permits a short-hand definition of the spectral state of the source at any particular time or any particular observation. A single letter (A, B, C) indicates that the source spectrum has a Wide Ratio in the range indicated by that label, while multiple letters (AB, BCD, EFGHI) indicate that the source during some particular time spans more than one range. We sometimes sub-divide single labels, arbitrarily numbering the sub-states (*e.g.* F1, F2, F3.....).

Table 4.2: Definition of Wide Ratio Spectral Range Labels

Label	Lower Bound (Wide Ratio)	Upper Bound (Wide Ratio)
A	0.0001	0.00032
B	0.00032	0.001
C	0.001	0.0032
D	0.0032	0.01
E	0.01	0.032
F	0.032	0.1
G	0.1	0.32
H	0.32	1.0
I	1.0	3.2
J	3.2	10.0

4.5 Summary and Conclusions

We have analyzed the CCDs and HIDs of the ten BHC sources in this study (1354-64, 1826-24, 1630-47, LMC X-1, LMC X-3, GS 2000+25, GS 2023+33, GS 1124-68, Cyg X-1, and GX 339-4). Taken together, we find that the spectral evolution of these sources on timescales longer than 128s, for individual sources, largely follows the behavior expected from sources with two spectral components which vary primarily in their relative normalization.

The color Wide Ratio(= 9.2–18.4 keV/2.3–4.6 keV) provides a parameter space over which the sources presently analyzed span four orders of magnitude – during their various spectral states, between the sources, a factor of 10,000 in Wide Ratio is covered. In the CCD showing Wide Ratio vs. Hard Ratio(=9.2–18.4 keV/4.9–9.2 keV), the tracks which these sources follow are narrow, often resolved, sometimes parallel and sometimes overlapping.

There are two interesting exceptions to this: GS 2023+33 showed strong spectral variability during its first 8 days, settling down to follow the expected locus during observations taken over the next ~400 days.

Thus, we find that the color Wide Ratio= 9.2–18.4 keV/2.3–4.6 keV provides a large amount of spectral parameter space, which we have divided for investigation into the sources' timing properties as a function of spectrum, in the next chapter.

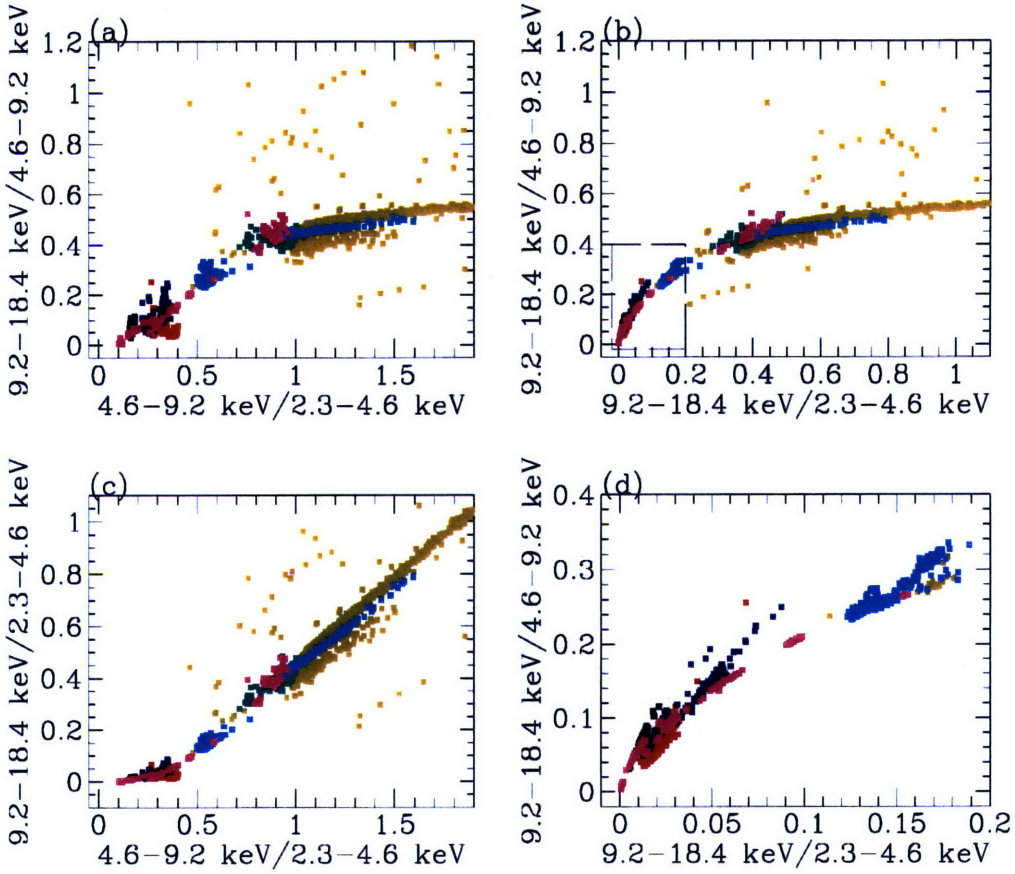

GS 1124−68
1354−64
CYG X−1
LMC X−1
LMC X−3
1826−24
GS 2023−33

Figure 4-22: **Color composite CCDs for 7 BHCs: GS 2023+33, 1826-24, LMC X-3, LMC X-1, Cyg X-1, 1354-64, and GS 1124-68**. Each color represents a different source (color legend above). Points which over-lap in position will be obscured, so not all data is visible. Each point represents 128s of contiguous data, corrected for background, dead time, and aspect. The limits are set such that not all data from GS 2023+33 are shown, Error bars are not displayed. All data in this figure are displayed (with error bars) in the individual CCD figures in this Chapter. *(a):* Hard Ratio vs. Soft Ratio. *(b):* Hard Ratio vs. Wide Ratio. *(c):* Wide Ratio vs. Soft Ratio. *(d):* Hard Ratio vs. Wide Ratio (as in panel *(b)*, zoomed in on the box)

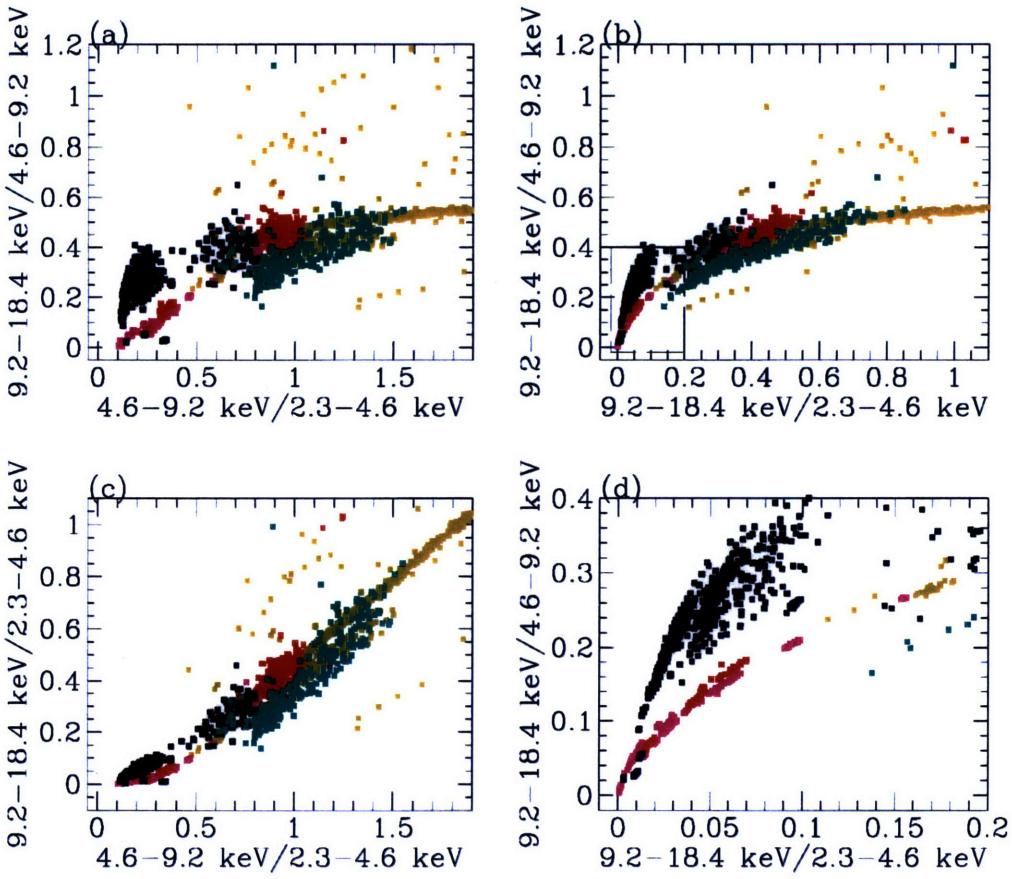

1630−47
GS 2000+23
GX 339−4
GS 1124−68
GS 2023−33

Figure 4-23: **Color Composite CCDs for 5 BHCs: GS2023+33, GS 1124-68, GX 339-4, GS 2000+25, and 1630-47**. Each color represents a different source (color legend above). Points which over-lap in position will be obscured, so not all data are visible. Each point represents 128s of contiguous data, corrected for background, dead time, and aspect. The limits are set such that not all data from GS 2023+33 are shown, Error bars are not displayed. All data in this figure are displayed (with error bars) in the individual CCD figures in this Chapter. *(a):* Hard Ratio vs. Soft Ratio. *(b):* Hard Ratio vs. Wide Ratio. *(c):* Wide Ratio vs. Soft Ratio. *(d):* Hard Ratio vs. Wide Ratio (as in panel *(b)*, zoomed in on the box)

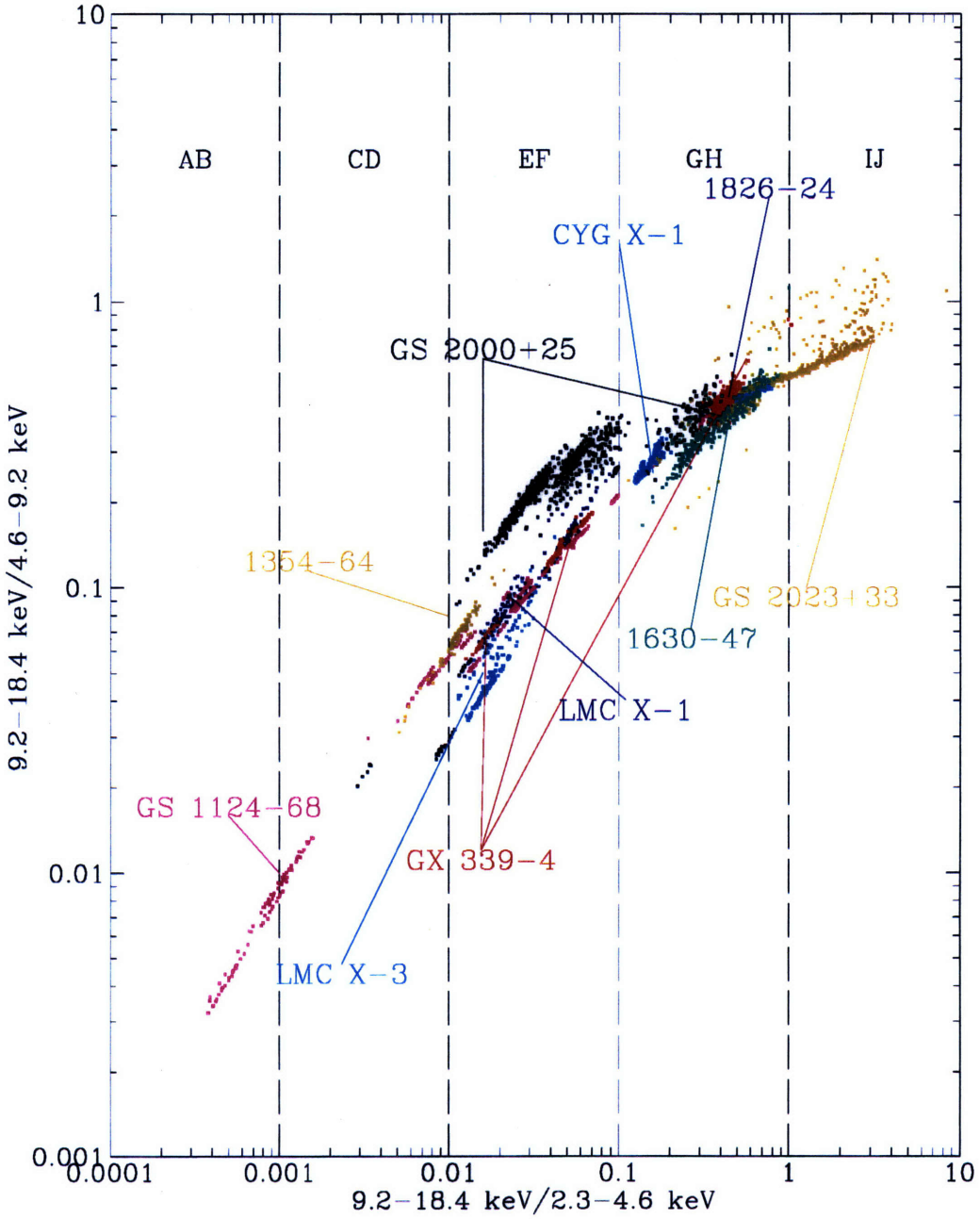

Figure 4-24: **Composite Wide Ratio vs. Hard Ratio of All Sources (color plot)** The composite CCD, showing Wide Ratio vs. Hard Ratio. Each point represents 128s of contiguous data. Each source is represented by a single color, although some colors are used for more than one source (*e.g.* yellow is used to represent both 1354-64 and GS 2023+33). Due to crowding, some points cover others, obscuring data from individual sources (for instance, 1826-24 is entirely obscured by GX 339-4).

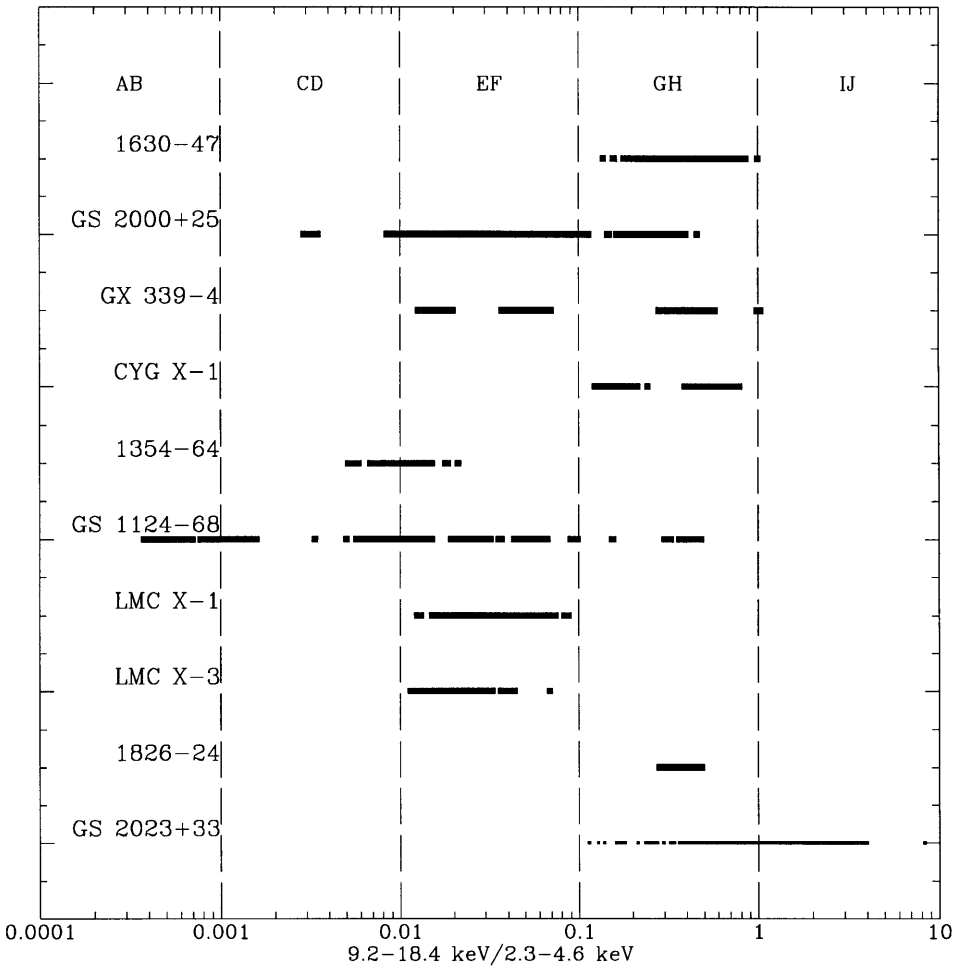

Figure 4-25: **Wide Ratio Range of Each Source** The Wide Ratio range, separated by source. These are the same data as plotted in Fig. 4-24.

Chapter 5

Power Density Spectra

The production of Power Density Spectra (PDS) is described, and the PDS are presented for each of the BHCs in the present study. The PDS are fit with parameterized models; the parameters and strength of the source variability are presented.

The PDS are produced from data separated by spectral state.

In Table 5.1, we show the data which are available to us for the timing study, separated by source and time resolution. The selection of this data is described in Sec 3.2. In all, 853 ksec are available for the fast-timing analysis; of this, 305.1 ksec have time resolution of or better than 0.06250 sec.

Table 5.1: BHC Data for Timing Analysis, by source

Source	0.00781 (ksec)	0.06250 (ksec)	0.5000 (ksec)	>0.5 (ksec)	Total (ksec)
1354-64	0.3	6.6	29.0	0.0	35.9
1630-47	0.0	7.3	11.1	17.6	36.0
1826-24	5.6	2.7	0.3	0.0	8.7
Cyg X-1	25.2	4.2	1.9	55.8	87.0
GS 1124-68	54.6	57.9	268.4	0.0	380.8
GS 2000+25	30.7	9.4	27.1	71.2	138.3
GS 2023+33	4.7	37.9	3.5	0.0	46.1
GX 339-4	15.2	23.0	15.2	18.9	72.4
LMC X-3	14.0	5.7	14.9	0.0	34.6
LMC X-1	0.0	0.0	12.7	0.8	13.5
Total	150.3	154.7	384.1	164.3	853.3

5.1 PDS Production

We have chosen to investigate the timing properties of these sources using the PDS – a representation of the data which is informationally equivalent to the raw-count-rates (except for the suppression of phase information), but has the advantage of displaying in a clear way the strength of source variability on any particular timescale which is informationally permissible by the observation. These timescales are defined by the time resolution of the data, and the total length of the observation. The highest frequency about which information can be unambiguously derived from an observation (called the Nyquist frequency, $\nu_{\rm Nyquist}$) with time-resolution of δt is:

$$\nu_{\rm Nyquist} = \frac{1}{2\,\delta t} \tag{5.1}$$

The lowest frequency about which information can be unambiguously derived is set by the observation length. Thus, if there are a total of N contiguous time bins of δt duration, the frequency resolution is:

$$\nu_{\rm res} = \frac{1}{N\,\delta t} \tag{5.2}$$

The details of our PDS production, including mathematical definitions, normalization, and computation of correction factors for dead time and background, are included in App. A. We repeat the pertinent details here.

Throughout this work, except where noted, we normalize the power in our PDS as rms^2/Hz(rms is the fractional rms variability); the amount of variability between various energy ranges, and different sources, can be directly compared by eye – greater variability results in greater power.

When producing PDS, there are, at times, intensity "spikes" which occur in the data, which are typically not due to source variability, but instead to a variety of background sources (these are described in Sec. 3.3). We systematically excluded these spikes from our analysis. When a single time bin is found, in which the number of counts is 20 σ (calculated using the intrinsic scatter of the data used for that

particular Fast Fourier Transform – or, FFT) greater than the mean number of counts, that value was replaced by a value randomly selected from a set of bins in the data used for that FFT. Such events, even if real, are in excess of the continuum variability properties of the source, and thus their exclusion has no effect on the source variability continuum measurements which are our primary focus.

In principle, it is most desirable to produce PDS which span as much frequency space as possible to provide physically interesting measurements or upper-limits. However, as the observations we investigate were planned by a number of different observers with different observational goals in mind, our raw-data set has a variety of time-resolutions, spanning from 7.8msec to 16.0 sec. Also, the particular observing conditions at the time of observations (such as the sun-angle, magnetic rigidity, recent passes through the South Atlantic Anomaly), as well as the occurrence of background events, typically restrict contiguous observations to less than 30 minutes, and often much less. Therefore, we use Composite PDS (described below) which combine high, medium, and low time resolution data into a single PDS to obtain a single PDS spanning a wide frequency range.

The data of the high, medium and low frequency range parts of the single PDS are not necessarily taken at the same time. In addition, there may be more data available in one frequency range than in others. Thus, this type of PDS is subject to systematic uncertainties due to real noise-property variations (*i.e.* change in noise properties) within a single selection criteria. For example, if the source variability is not a function of spectrum at all, then changes in the source PDS may occur between the different observation periods while the spectrum has not changed, possibly resulting in PDS which are non-continuous at the boundaries where the Composite PDS are joined. For many sources, we produced a second type of PDS ("T" -type, described below) which makes use of moderate time-resolution (0.0625s), long observation period data (512s), to produce PDS which spans across the frequency boundaries where the different PDS are joined in the Composite PDS. We compare the Composite PDS to a "T"-type PDS produced with the same spectral selection, which permits us to exclude peculiar-shaped PDS as being due to source variation

within the selection criteria.

5.1.1 Composite PDS

To make efficient use of all available data, each observation available was used to produce any (or all) of three possible types of FFTs, which we define here:

- **Low Frequency FFT**: Data is binned to 16.0 s, and a total duration of 1024 s, using 64 bins of data. The resulting frequency range is 0.0009765–0.03125 Hz.
- **Medium Frequency FFT**: Data is binned to 0.0625 s, and a total duration of 64 s, using 1024 bins of data. The resulting frequency range is 0.015625–8 Hz.
- **High Frequency FFT**: Data is binned to 7.8125 msec, with a total duration of 8 s, using 1024 bins of data. The resulting frequency range is 0.125–64 Hz.

Observational time-resolution was set at the time of observation; data can be re-binned to decrease time resolution (increase the bin-size), but not to increase time-resolution. Thus, a single observation with a duration of 1500 s and a time resolution of 7.8 msec is used to produce 187 High-Frequency FFTs, 23 Medium-Frequency FFTs and 1 Low-Frequency FFT.

Using raw data selected from that listed in Table 5.1 and in App. B.1, we produced FFTs as described in App. A, using data (separately) from the Low Energy Range (=2.3–4.6 keV), Medium Energy Range (=4.6–9.2 keV) , High Energy Range (=9.2–18.4 keV) and Intensity Range (=2.3–18.4 keV). This produces a library of Low-, Medium-, and High-Frequency FFTs from which we draw to produce PDS, based on the selection criteria we might apply for any given analysis (typically, based on the Wide Ratio).

To produce the Composite PDS, individual FFTs are selected based on their Wide Ratio (=9.2-18.4 keV/2.3-4.6 keV) – or other property – , measured during the time period covered by the FFT. Each individual FFT is made into a single PDS, with its dead-time corrected Poisson Level subtracted, and the remaining power multiplied

by the (correctly normalized) background and dead time %rms correction factors. These corrections remove from the PDS dependencies on source intensity, non-source counts, detector response, and the act of measurement, to produce a PDS which is a measurement only of source-related variability. Finally, all the resulting PDS are averaged together into a single PDS. The uncertainty in the power at each frequency is taken from the scatter in the power at that frequency. Thus, the uncertainty in the power contains any (non-biased) systematic uncertainty in the Poisson-subtraction, dead time and background %rms correction factors.

These PDS are logarithmically rebinned, and overlapping frequency ranges are dropped in the PDS which represents the lesser integrated time. For example: with 50 Medium-Frequency FFTs and 200 High Frequency FFTs, the Medium-Frequency FFTs represent 64 s $\times$ 50 = 3200 s of data, while the High-Frequency FFTs represent 8 s $\times$ 200 = 1600 s of data. Therefore, all the data <8 Hz would be dropped in the High-Frequency PDS, and then the two PDS are merged together (simply, taking the Medium-Frequency PDS and the High-Frequency PDS and placing them into the same file).

We therefore end up with a PDS, Poisson-level subtracted, normalized as $\mathrm{rms}^2/\mathrm{Hz}$, corrected for dead time and background to recover the source %rms, and binned on a logarithmic scale. We often employ different logarithmic binning factors, depending on the significance of the power and the details of the PDS. The final frequency range is 0.00097–64 Hz.

5.1.2 "T"-TYPE PDS

For comparison with the Composite-type PDS, whenever possible we produced T(otal)-type FFTs, to be used in producing T-type PDS. To produce these, data must have been contiguous for longer than 512 sec, with a time resolution of 62.5ms or higher. When such data were available, a single FFT, with Nyquist frequency of 8 Hz and frequency resolution of 0.0019531 Hz was produced from the four energy ranges (Low Energy Range, Medium Energy Range, High Energy Range, Intensity Range). Thus, the T-type PDS spans frequency ranges covered by the Low- , Medium- or High- Fre-

quency PDS. The purpose of producing these T-type PDS is purely for comparison between a single PDS spanning 0.002–8.0 Hz frequency range with the Composite PDS (which was spliced together from PDS covering different frequency ranges), to confirm the shape of the Composite PDS using a single contiguous PDS. We do not use these exclusive of the Composite PDS, because there are typically only a few observations with the necessary time resolution and observation length for any given source. When possible, we correct the resulting PDS (normalized to rms^2/Hz) directly for background and dead time.

5.2 Parameterized Fits to the PDS

The PDS by themselves contain all information regarding the variability properties of the source on the timescales covered by the FFTs (except for the phases, which have been suppressed). In principle, all source variability can be dependent on a number of independent variables, some of which may be directly measurable – such as accretion rate, source spectrum, binary orbital phase, or bolometric luminosity – and others which are not directly measurable ("hidden variables").

To understand the ensemble of variability properties represented in the PDS of a particular source, one may compare the PDS in complete detail among themselves as a function of the measurable variables of interest. The advantage of this approach over others is that all variability information is exactly preserved, and the most detailed comparison is possible. In most cases, however, the PDS permit simple parameterizations which allow the most prominent of their features to be represented by a small set of numbers, which describe the intrinsic shape of the PDS, and its normalization (the %rms variability). The advantage of this method is the reduction of the most prominent of the features into a few simple values, which may be inter-compared with those obtained from other sources and observations by other workers, and which can provide simple, quantifiable, phenomenological guidelines for theorists to calculate the compliance of their models with the observations. Also, using maximum-likelihood techniques to fit models to the data permits estimation of

uncertainties, which facilitates comparison of these parameters.

In practice, the models which may be adopted to fit the PDS may not be ideal, or even formally acceptable according to statistical tests. Discrepancies may be systematic – for example, due to the skew of a quasi-Lorentzian peak which is not accounted for in the model – or they may be due to excursions from simply parameterizable continuum behavior in the PDS – that is, deviations from the model which are non-biased, like random scatter, but significant according to the error analysis applied. There exists no *a priori* reason that such systematic and noisy PDS should not exist. Thus, while it is desirable to fit the models as closely to the data as possible, there can be a trade-off between the accuracy of the model and the number of parameters of the model. There are appropriate statistical tests to find the formal acceptability of the addition of parameters to the model (Bevington 1969). This is useful for the discovery and description of previously un-examined variability features in the PDS.

In the present work, we desire simple parameterizations which can adequately describe PDS from all 10 sources. When feasible, we avoid the introduction of new parameters, apart from switching to a more reasonable model from among those we list in Sec. 5.2.2.

5.2.1 The Procedure Used to Find the Best Fit PDS Model

After producing the PDS (described above), the data are often rebinned, either logarithmically, with equal number of bins per decade in frequency, or linearly, with equal number of bins per frequency. Errors are propagated during rebinning as Gaussian random errors (a useful assumption if the change in the underlying spectrum is small over the width of the bin). The power is attributed during rebinning to the mean frequency of the bin, with the bin-size treated as being small relative to the uncertainty in the power.

After the production of the rebinned PDS, we apply an implementation of the Levenberg-Marquardt method, based on the discussion in Press (1995), and coded into a program in traditional (non-ANSI) *C* which is called *BFIT*. The Levenberg-

Marquardt method is an algorithm which minimizes the χ^2 figure of merit:

$$\chi^2 = \sum_{i=0}^{N} \left(\frac{y_i - y(\mathbf{a}, x_i)}{\sigma_i} \right)^2 \tag{5.3}$$

where x_i is the independent variable, y_i and σ_i are the measured value and its uncertainty, and $y(\mathbf{a}, x_i)$ is the model, dependent on the independent variable x_i and the set of n parameters $\mathbf{a}$. The goal of the algorithm is to efficiently find the set of parameters $\mathbf{a}$ which produces the smallest value of χ^2 – that is, the model which most closely matches the data – which is then the "best-fit" model. The figure of merit usually quoted (as we do here) is the reduced chi-squared:

$$\chi^2_\nu = \frac{\chi^2}{N - n} \tag{5.4}$$

which is the χ^2 value divided by the number of degrees of freedom ν (dof), which is simply the difference between the number of data points and the number of free parameters in the model (Bevington 1969). If one has two data-points, and a model with two parameters (like a straight line), then the model is completely determined (that is, two points determine a line, exactly), and there are zero degrees of freedom. The use of the fitting procedure is to find the parameter values which best fit all the data, when the model is over-determined.

The formally acceptable value of χ^2_ν depends on the number of dof, but in all cases, χ^2_ν is expected to be close to 1.0 (how close depends on the number of dof). Higher values of χ^2_ν indicate a model which does not fit the data well, and therefore either the model is formally unacceptable, or the uncertainty in the data has been underestimated. Smaller values of χ^2_ν indicate that the uncertainty has been over-estimated. In practice, we often find that the χ^2_ν values are formally not acceptable. However, we usually do not attempt to modify the models to account for discrepancies, preferring instead to retain the generality of a few (perhaps over-) simplified models, which allow inter-comparison of their derived parameters, on the assumption that the systematic uncertainty is small ($\lesssim$10%).

Once the best-fit parameters have been found, it remains to determine the

confidence region of the parameters. We use the single-parameter 68.3% confidence region throughout the present work. This is found by determining the n-dimensional χ^2 function for all parameters, and projecting the surface of the χ^2 contour which is 1.0 larger than the best-fit χ^2 onto the n axes of the parameters. The intersection of this projection with each axis is the 68.3 % confidence region for that parameter (Avni 1976). Thus, for every model fit to the data, we quote the best-fit model parameters, their 68.3% formal statistical confidence region, the χ^2_ν and the number of degrees of freedom. For measurements of upper-limits, we quote 3σ upper-limit values.

5.2.2 The PDS Models Used to Fit to the Data

We use a number of models to fit to the PDS data, most of which have become widely used in describing PDS of X-ray binaries. The models are given in detail in Sec. A.4. We describe them here briefly.

Poisson-noise, which occurs in the process of measuring X-ray counts, is always in the data, and is unrelated to the source variability properties. The exact value of the Poisson level is analytically calculable in principle. In practice, instrumental effects (specifically, detector dead time – the amount of time the detector is "off" while the photon is being processed electronically) modify the value of this constant. Even this is calculable, for small fractions of dead time; however, at very large count-rates where the dead time becomes significant, the simplified assumptions break down. In such situations, the Poisson level shows a significant constant power as a function of frequency. The magnitude of these constants are typically 0.3-1.0 %rms (0.001–64 Hz), when they are seen. Their possible covariance with other model parameters, which depends on the significance of the data, results in larger uncertainties (but more accurately derived best-fit values) in the parameters of the other models.

The model shapes we used to fit to the real source variability are all continuous functions of frequency, and include:

- Power-Law, P$\propto \nu^{-\alpha_1}$

- Flat-Top Single-Power-Law, a constant power below some frequency ν_1 breaking to a Power-Law with slope α_1 above this frequency.

- Double Power-Law, represented by one power-law slope (α_1) below a critical frequency ν_1 and different, typically steeper power-law slope α_2. If we find α_1 $\lesssim$0.3 (that is, if the first power-law is very flat), then we call this model "Flat-Top Single-Power-Law" instead of a "Double-Power-Law". This is a definition of convenience, having no theoretical or observational impetus.

- Flat-Top Double-Power-Law, a constant power below some frequency ν_1 breaking to a Power-Law with slope α_1 above this frequency, breaking again to a (typically steeper) Power-Law α_2 above frequency ν_2, with $\nu_1 < \nu_2$.

- Double Flat-Top Single-Power-Law, a model in which the power is constant below some frequency ν_1, breaking to a power-law of slope α_1, which evens out into a constant value again at some higher frequency $\nu_2(> \nu_1)$, and then breaks again into a power-law of the same slope (α_1) at some higher frequency ν_3.

- Flat-Top Power-Law Exponential, a model in which the power is constant below some frequency ν_1, and continuous with the product of a power-law and an exponential function above this frequency.

In fitting models to the data, we employ one of the above models, which we call the continuum model, or Broad-Band (BB) model, and, when necessary or desirable, we add a model to account for quasi-periodic oscillations:

- Lorentzian, used to model quasi-periodic oscillations, which has a centroid frequency ν_c and Full-Width at Half-Maximum (FWHM; Γ).

- Harmonics, sometimes added to account for the appearance of Harmonics and sub-Harmonics to the QPO; the frequencies and FWHM values of these Harmonics are constrained to be 0.25, 0.5, 2.0 and 4.0 that of the Fundamental.

Using only these models (a BB plus QPO model), we fit the shapes of the PDS.

In addition to the model shapes, there is a parameter which we wish to extract from each fitting, and that is the model normalization. The model normalization is simply related to the total amount of %rms variability in that particular model; in practice, the parameter we fit for is the %rms variability of that model directly, rather than the simple normalization (in rms^2/Hz). We therefore extract from the normalization of the BB and QPO the %rms variability and its uncertainty in each of these features in any given PDS.

When fitting to the BB power, it is desirable to inter-compare the %rms variability of the various models of the individual sources between various states and energy ranges. For this reason, it is necessary to adopt a standard frequency range within which the %rms is integrated, which will be used in all fits .

In principle, we could integrate the %rms of the BB models between 0 and ∞ Hz; however, some models within the actual frequency range of the PDS may mathematically diverge, resulting in an infinite %rms with an infinite uncertainty. In addition, extrapolating the best-fit model beyond the frequency range of the observational PDS produces a quantifiable systematic uncertainty in the measured %rms. For example, extrapolating a Power-Law model with slope -1 from the observed 0.01–64 Hz to 0.001 Hz, when in fact the true model is flat-topped (that is, constant) below 0.01 Hz, produces a %rms value which is 7% too high. While it is not desirable to extrapolate models beyond the frequency range for which one actually has data, it is preferable to complete inability to inter-compare observations. If one wishes to find the %rms variability in some frequency range other than 0.001-64 Hz, one may use the model parameters we tabulate to calculate them.

Therefore, we adopt the 0.001-64 Hz frequency range for the integration range of our models, and all %rms values of BB models which we quote will be integrated between 0.001 and 64 Hz. These frequencies correspond to the minimum of the Low-Frequency FFTs and the maximum of the High-Frequency FFTs.

The %rms strength of the Lorentzians and Harmonics are integrated between $-\infty$ and ∞.

5.3 Note on Spectral State Shorthand

Throughout this chapter, we refer to spectral "states", typically as indicated by the contemporaneous Wide Ratio value as defined in the spectral study in Ch. 4. As short-hand, we use letters, which indicate a range of possible Wide Ratio values, each half a decade wide in logarithmic space, as defined in Sec. 4.4 (A, B, C, D...), increasing in sequence with increasingly hard spectrum (see Table 4.2 for their exact correspondence to Wide Ratio values). The width of these ranges was arbitrarily chosen, with the idea that the source behavior not vary measurably within a single range. This is not always the case, and there are instances in this chapter when we further subdivide the data based on the spectral values into "sub-states" (*e.g.* F1, F2, ...). In short, we have no reason to believe at the outset that the width of the Wide Ratio ranges should optimally correspond to the spectral change accompanying changes in variability properties. They are retained for convenience in referencing the timing analysis to a simultaneous spectral indicator.

5.4 Energy Dependency of the PDS for the Ten Sources

We present the PDS of all 10 sources (1354-64, 1826-24, 1630-47, LMC X-1, LMC X-3, GS 2000+25, GS 2023+33, GS 1124-68, Cyg X-1, and GX 339-4) in the four energy ranges defined in the previous chapter (Low Energy Range=2.3–4.6 keV, Medium Energy Range=4.6–9.2 keV, High Energy Range=9.2–18.4 keV, and Intensity Range=2.3–18.4 keV). For each PDS, we indicate the mean source spectrum by the Wide Ratio(=High Energy Range/Medium Energy Range). Finally, we fit the PDS with BB and QPO models to determine the parameterization of the PDS and the %rms variability in each spectral state.

5.4.1 1354-64

Of the measured 128 s values of the Wide Ratio for 1354-64 measured in Ch. 4, 80% were in the range 0.0088–0.0144 (D-type source).

Much of the high time-resolution data were taken during periods for which the background subtraction of the corrected data were inadequate (and the data were excluded). We therefore produced PDS of all the available raw data taken together. We have excluded data during those periods which we found were affected by magnetospheric electrons (see Sec. 3.4). It may be cautiously assumed that, during the 1-day period our 1354-64 data comes from, the source spectrum did not change dramatically (*i.e.*, the Wide Ratio did not increase by $> \times 10$). We base this assumption on the observation that on short timescales ($\lesssim$1000 s) and on long timescales ($\sim$1 day) we do not see evidence of spectral variability in this source of the order $\gtrsim 10\times$ in Wide Ratio (cf. Fig. 4-11). We will interpret the Composite PDS with the possibility in mind that this assumption is not true.

In Fig. 5-1, we show the Composite PDS for the four energy ranges for 1354-64, using all available data, uncorrected either for background or dead time. For these PDS, the Low-frequency power is an average of 18 FFTs, the Medium-frequency is 99 FFTs, and the High-frequency is 35 FFTs. The PDS indicates very little detectable power in all energy ranges. The detectable power appears consistent with a Power-Law model for the BB noise.

In Table 5.2, we show the parameters of the best fit Power-Law to the PDS in Fig. 5-1. The %rms values are not corrected for background or dead time; however, we include an approximate background correction factor in the table. These were found using the average corrected count-rates and observing aspect (0.96 $\pm$0.02) integrated over the two-day observation. The dead-time correction ($<$1 – 3 % for the energy ranges and count-rates considered) can be neglected. For each of the PDS, we produced fits allowing the power-law slope to vary, and holding the power-law slope fixed (at 1.15; from the best fit of the Intensity Range data). For the 2.3–4.6 keV energy range, we also fit the data only in the 0.00097–0.03125 Hz range, and found that the fit parameters were consistent with the full PDS.

The best-fit Power-Law models indicate the PDS is consistent with a Single-Power-Law in the 0.001-64 Hz frequency range and all energy ranges, with no evidence for energy dependency in the model-shape parameters. There is dependency on the model normalization – the %rms values; the %rms of the Power-Law increases, with increasing energy, from 0.94±0.08% in the Low Energy Range, 3.6±0.3% in the Medium Energy Range, to 7.7±3.0% in the High Energy Range (including the systematic uncertainty in the background correction factor). The 2.3-18.4 keV %rms variability is small, at 1.26±0.09 %.

Table 5.2: Parameters for Best-Fit Power-Law to 1354-64 Composite PDS of All Available Data

Energy Range (keV)	Power Law Slope (α)	%rms[a] (0.001-64 Hz)	χ^2_ν (dof)	Background Correction Factor
2.3–4.6	0.77 ±0.15	$2.2^{+1}_{-0.7}$	1.09 (28)	0.99 ±0.05
	(1.15)	0.95 ±0.06	1.22 (29)	0.99 ±0.05
4.6–9.2	1.33 ±0.14	$2.5^{+0.3}_{-0.2}$	1.48 (28)	1.24 ±0.05
	(1.15)	2.9 ±0.2	1.48 (29)	1.24 ±0.05
9.2–18.4	(1.15)	1.7 ±0.5	1.26 (29)	4.5 ±1.1
2.3-18.4	1.13 ±0.11	$1.2^{+0.3}_{-0.2}$	1.68 (28)	1.05 ±0.05
	(1.15)	1.2 ±0.07	1.63 (29)	1.05 ±0.05

[a] Uncorrected for background and dead time
[b] Fits applied to values in the 0.00097 – 0.03125 Hz range
Fits are to 0.00097 – 64 Hz, except as noted
Values in parenthesis are fixed
Dead time correction is <1–3% for all energy ranges

In Fig. 5-2 we show the T-type PDS of 1354-64, produced from an average of 4 FFTs.

The best fit Power-Law function parameters of the T-type PDS are given in Table 5.3. The %rms values in this table are uncorrected for background and dead time. An approximate background correction factor for each energy range was calculated and included separately in the table. The frequency range of the %rms values are 0.001–64 Hz, although the fits made use of the data in the 0.0019531–8 Hz range.

The T-type PDS show that 1354-64 is quiet, with %rms values across all energy ranges of roughly <1–3 %, or upper-limits consistent with this value. This is consistent with the amount of variability found in the Composite PDS. During this observational period 1354-64 was in the D-E spectral states (see Sec. 4.4 for a description of the spectral-state shorthand); for these PDS no simultaneous corrected data were produced. But, the mean (uncorrected) count-rates during these observations were Low Energy Range= 377 ±1 c/s; High Energy Range= 20.0 ±0.1 c/s, which produces a Wide Ratio$\lesssim$0.03 (E-state).

Table 5.3: Parameters for Best-Fit Power-Law to 1354-64 T-type PDS

Energy Range (keV)	Power Law Slope (α_1)	%rms[a] (0.001-64 Hz)	χ^2_ν (dof)	Background Correction Factor
2.3–4.6	(0.75)	1.4 ±0.3	1.2 (7)	0.99 ±0.05
4.6–9.2	(0.75)	$1.7^{+0.8}_{-0.4}$	0.5 (7)	1.24 ±0.05
9.2–18.4	(0.75)	<7.2	0.7 (7)	4.5 ±1.1
2.3-18.4	0.76±0.13	1.8 ±0.6	1.07 (6)	1.05 ±0.05
	(0.75)	1.8 ±0.2	0.91 (7)	1.05 ±0.05

[a] Uncorrected for background and dead time
Values in parenthesis are fixed
Dead time correction is <1–3% for all energy ranges
All upper limits are 3 σ
Fits applied to values in the 0.00195 – 8 Hz range

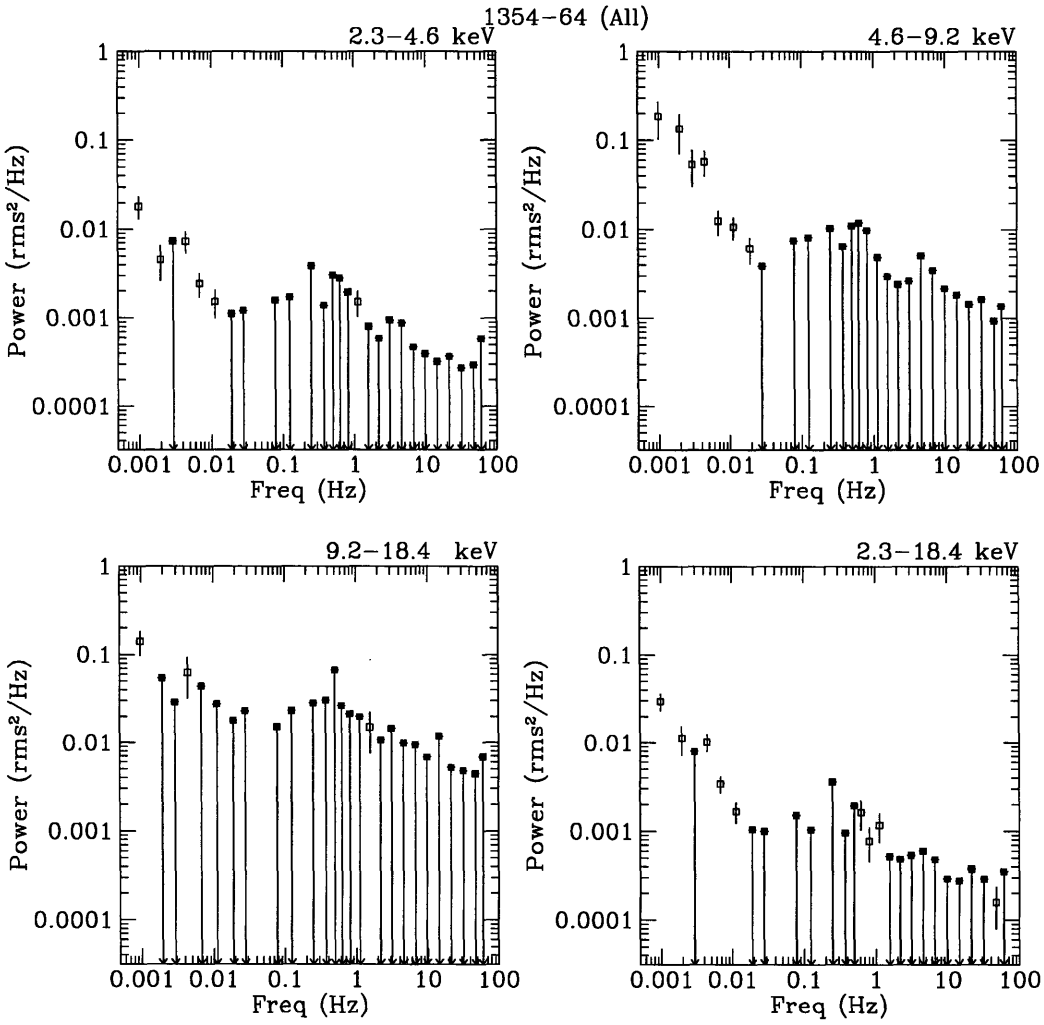

Figure 5-1: **Composite PDS of 1354-64. All data.** The Poisson-level subtracted Composite PDS 1354-64, uncorrected for background and dead time, in the Low Energy Range, Medium Energy Range, High Energy Range and Intensity Range. No spectral selection was applied – all available data were used. Upper-limits are 2 σ. Very little power is evident.

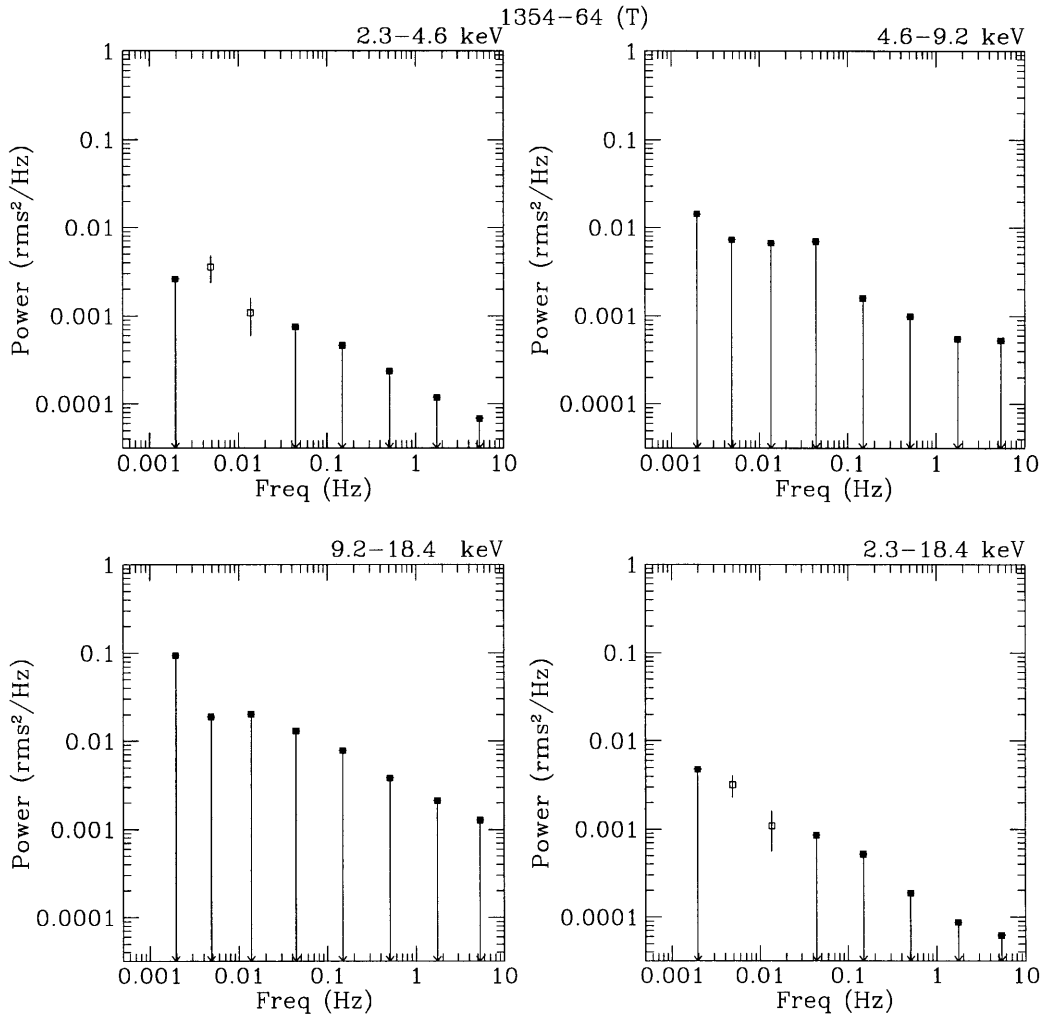

Figure 5-2: **T-type PDS of 1354-64**. The Poisson-level subtracted PDS of T-type FFTs from 1354-64, uncorrected for background and dead time, in the Low Energy Range, Medium Energy Range, High Energy Range and Intensity Range. Each PDS is composed of 4 FFTs, rebinned logarithmically, and not corrected for dead time or background. Upper-limits are 2 σ. Very little power is evident.

5.4.2 1630-47

Of the measured 128 s values of the Wide Ratio for 1630-47 measured in Ch. 4, 80% were in the range 0.23–0.65 (GH-type source). Most of the timing data for 1630-47 were obtained while the source was in the H-state. We therefore produced PDS in the G-state (Low-Frequency only) and H-state, as well as combining all data with no spectral selection, on the assumption that the spectral evolution during the 1-day long observation epoch was small. We also produced T-type PDS.

In Fig. 5-3, we show the Composite PDS for data selected by spectrum to be in the G-state. The Low-frequency PDS is an average of 10 FFTs. There were no Medium- or High-frequency FFTs. These PDS are normalized to rms^2/Hz, Poisson-level subtracted, and corrected for deadtime and background. There is little detectable power in these PDS, which appear to be consistent with a single Power-Law model.

In Fig. 5-4, we show the Composite PDS for data selected by spectrum to be in the H-state. The Low-frequency PDS is an average of 9 FFTs, and the Medium-frequency PDS is an average of 96 FFTs. There were no High-frequency FFTs. These PDS are normalized to rms^2/Hz, Poisson-level subtracted, and corrected for deadtime and background. There is little detectable power in these PDS, which appear to be consistent with a single Power-Law model.

In Fig. 5-5, we show the Composite PDS for all the available uncorrected data. The Low-frequency PDS are an average of 19 FFTs, while the Medium-frequency PDS are an average of 104 FFTs. There were no High-frequency PDS. These PDS are normalized to rms^2/Hz, but not corrected for deadtime (which is small, <1-3 %) or background. There is little detectable power in these PDS, which appear to be consistent with a single Power-Law model.

In Fig. 5-6, we show the T-type PDS for all the available uncorrected data. These PDS are normalized to rms^2/Hz, and corrected for deadtime and background. There is very little detectable power in these PDS, which appear to be consistent with a single Power-Law model. The T-type PDS are consistent with the Composite PDS.

Power-Law models were fit to the Composite PDS (G and H spectral states, and the PDS composed of all available data) and the T-type PDS. The best-fit model parameters values, along with the %rms background correction factors for the "All"-type Composite PDS, are shown in Table 5.4. The deadtime correction factor for the "All"-type Composite PDS is estimated to be <1–3%.

The best fit models indicate that all PDS are consistent with a single Power-Law, with a slope of $\sim 1.45 \pm 0.13$, which we find from averaging the G- and H- state Intensity Range best fit values. The results of the G- and H- state fits show the PDS to be identical in these two spectral ranges. The %rms variability in the G-state increases with increasing energy, from (in the G-state) <2.5% (3 σupper-limit), to 4.4 ± 0.6%, to 15.3 ± 2 % between the Low, Medium, and High energy ranges. These values are consistent with those we find in the T-type and "All" data PDS.

Table 5.4: Parameters for Best-Fit Power-Law to 1630-47 Composite PDS

Spectral Selection	Energy Range (keV)	Power Law Slope (α_1)	%rms (0.001-64 Hz)	χ^2_ν (dof)	Background %rms Correction[d]
All[ac]	2.3–4.6	$1.4^{+1.0}_{-0.48}$	< 4.0	0.47 (10)	1.7 ±0.7
(Composite)		(1.70)	$0.87^{+0.17}_{-0.26}$	0.44 (11)	1.7 ±0.7
	4.6–9.2	2.25 ±0.3	2.7±0.2	1.57 (10)	1.85 ±0.8
	9.2–18.4	1.78 ±0.2	4.5±0.4	1.05 (10)	2.8 ±2.2
	2.3–18.4	1.68 ±0.3	2.2±0.14	1.59 (10)	1.9 ±0.6
All[e]	2.3–4.6	(1.20)	<4.5	1.46 (12)	–
(T-type)	4.6–9.2	(1.20)	7.2±0.6	1.25 (11)	–
	9.2–18.4	$0.99^{+0.18}_{-0.13}$	13.5^{+4}_{-3}	3.04 (11)	–
	2.3–18.4	1.24 ±0.15	$6.9^{+0.9}_{-0.6}$	1.2 (11)	–
G[b]	2.3–4.6	(2.23)	<2.5	0.6 (6)	–
	4.6–9.2	2.1 ±0.3	4.4±0.6	1.3 (5)	–
	9.2–18.4	1.9 ±0.3	15.3±2	0.77 (5)	–
	2.3–18.4	2.2 ±0.3	4.1±0.6	0.29 (5)	–
H[c]	2.3–4.6	(1.26)	<3.3	0.83 (11)	–
	4.6–9.2	(1.26)	$4.8^{+1.3}_{-0.8}$	2.22 (11)	–
	9.2–18.4	1.36±0.3	$10.3^{+2.1}_{-1.4}$	1.32 (11)	–
	2.3–18.4	1.26±0.15	5.0±0.6	1.74 (10)	–

[a] Uncorrected for background (above) and deadtime (< 1-3%)
[b] Fits applied to values in the 0.00097 – 0.03125 Hz range
[c] Fits applied to values in the 0.00097 – 8.0 Hz range
[d] Included only when %rms has not already been corrected
[e] Fits applied to values in the 0.00195 – 8.0 Hz range
Values in parenthesis are fixed
Upper-limits are 3 σ

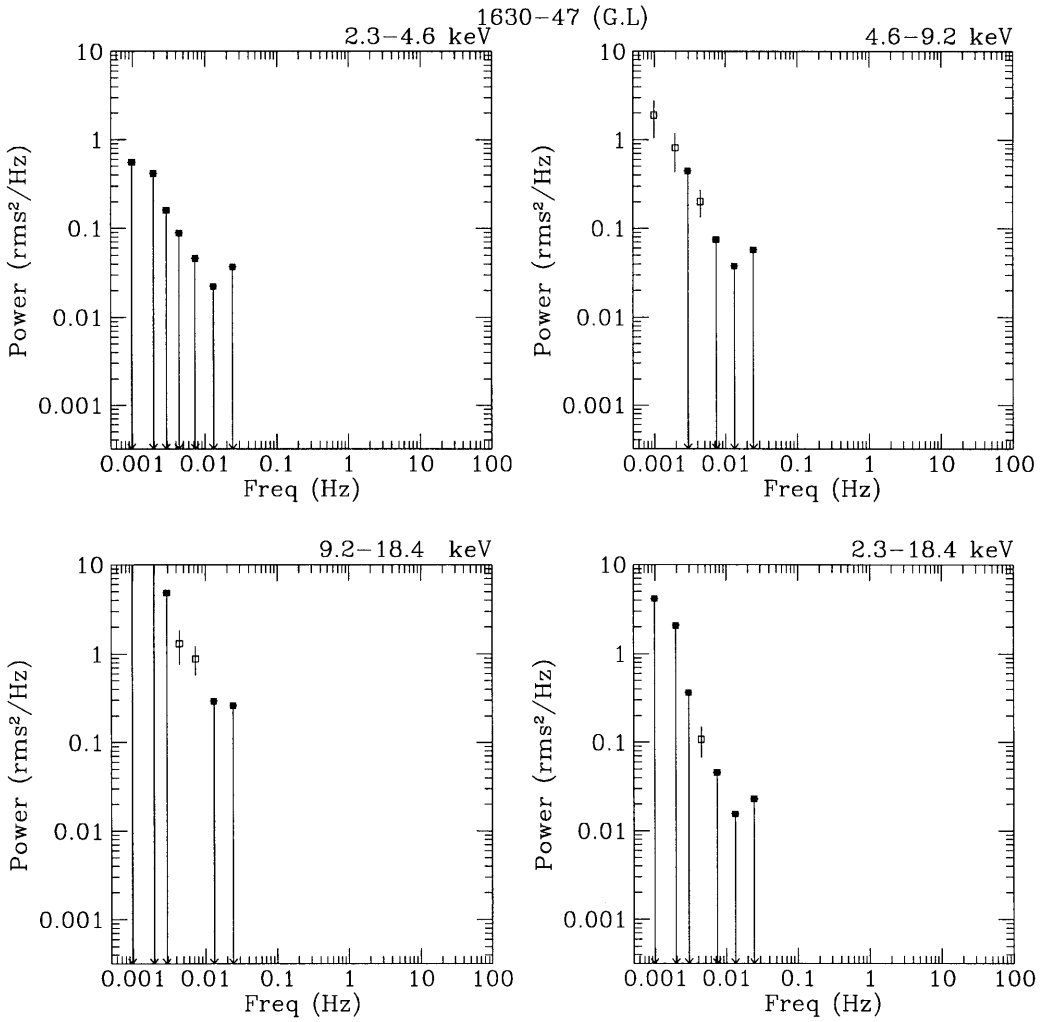

Figure 5-3: **1630-47 PDS, G-state Data.** Composite PDS 1630-47, corrected for both background and deadtime, in the Low Energy Range, Medium Energy Range, High Energy Range and Intensity Range, using data selected spectrally to be in the G-state. Upper-limits are 2 σ. Very little power is evident.

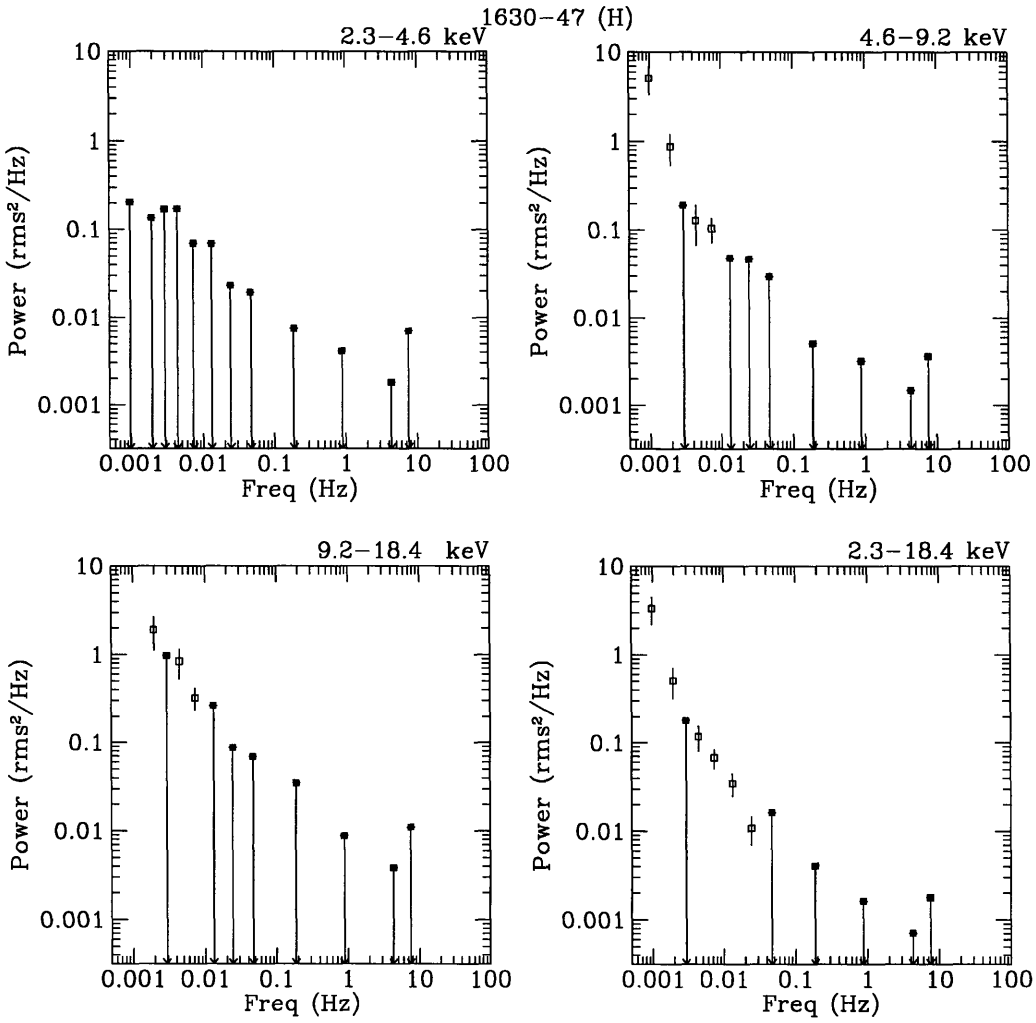

Figure 5-4: **1630-47 PDS, H-state Data.** Composite PDS 1630-47, corrected for both background and deadtime, in the Low Energy Range, Medium Energy Range, High Energy Range and Intensity Range, using data selected spectrally to be in the H-state. Upper-limits are 2 σ. Very little power is evident.

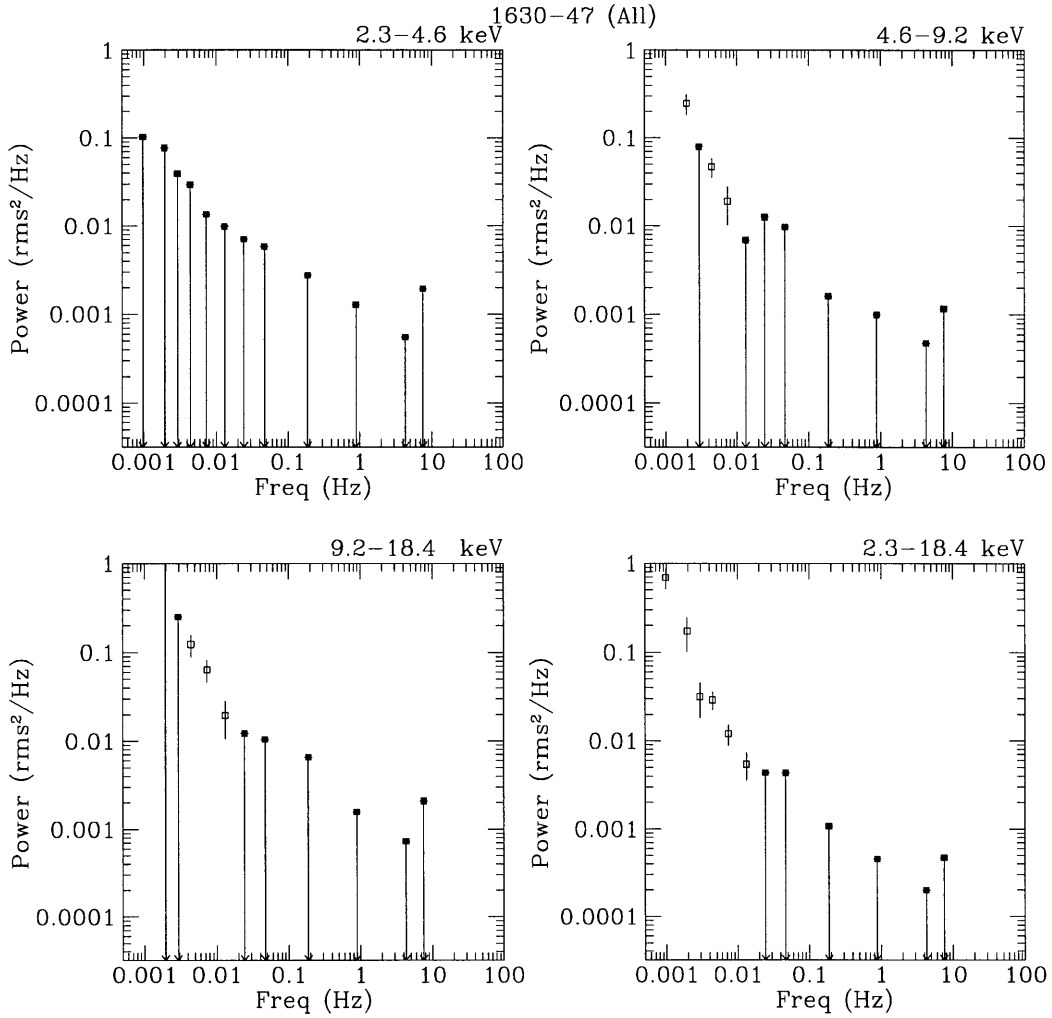

Figure 5-5: **1630-47 PDS, All Data.** Composite PDS 1630-47, uncorrected for background and deadtime, in the Low Energy Range, Medium Energy Range, High Energy Range and Intensity Range, using all available raw data (no selection based on spectrum). Upper-limits are 2 σ. Very little power is evident.

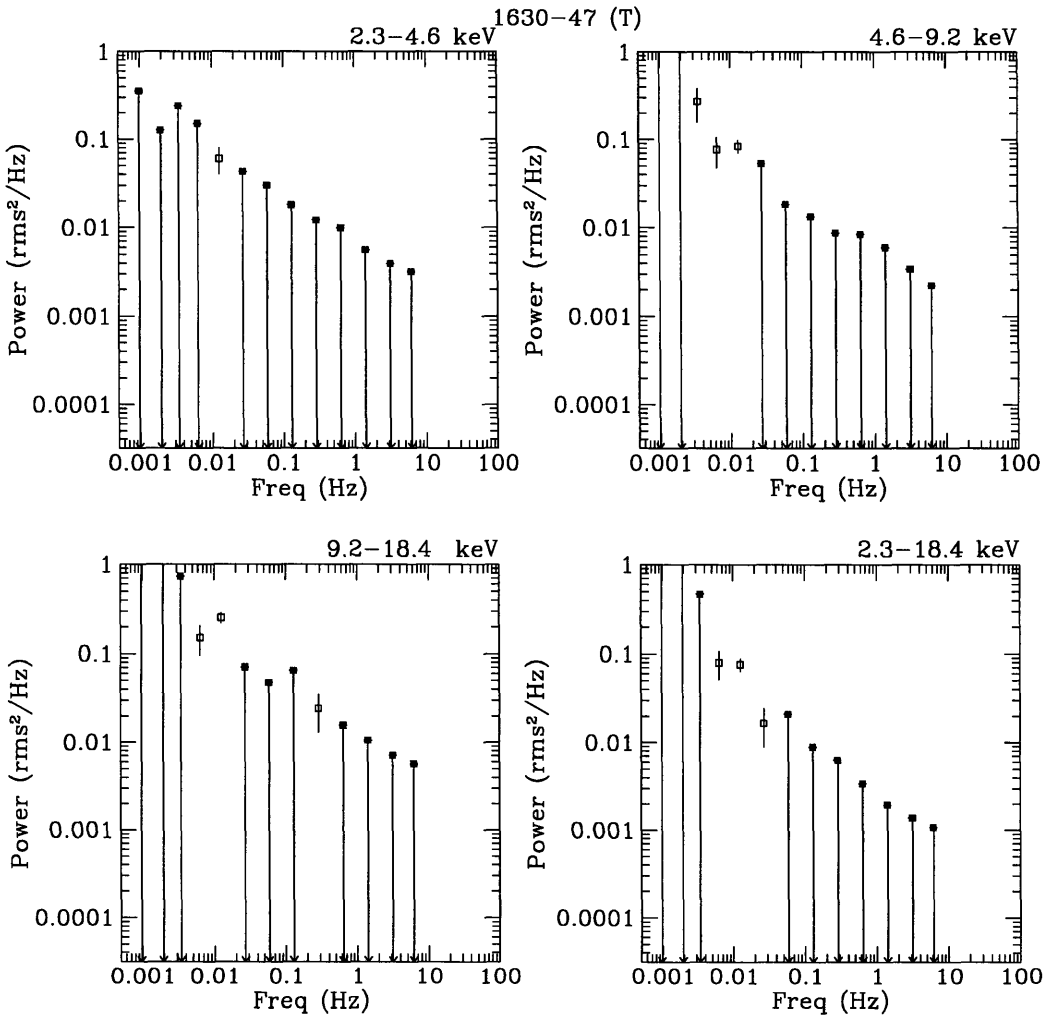

Figure 5-6: **1630-47 PDS, T-type** . T-type PDS 1630-47, corrected for background and deadtime, in the Low Energy Range, Medium Energy Range, High Energy Range and Intensity Range. These PDS are an average of 3 FFTs. Upper-limits are 2 σ.

5.4.3 1826-24

Of the measured 128 s values of the Wide Ratio for 1826-24 measured in Ch. 4, 80% were in the range 0.33–0.44 (H-type source). We produced Composite PDS of the combined G and H spectral state data and H-state data alone, as well as T-type PDS.

In Fig. 5-7, we show the Composite PDS for data selected by spectrum, to be in the GH-state. There is only one Low-frequency FFT, so it was not used in these fits. The Medium-frequency PDS is an average of 97 FFTs, and the High-frequency PDS is an average of 487 FFTs. These PDS are normalized to rms^2/Hz, and corrected for deadtime and background. The power is significant and strong over almost the full frequency range in all energy ranges. It follows a simple power-law, with no strong deviations.

In Fig. 5-8, we show the T-type PDS made from all available data. The PDS are an average of 9 FFTs. These PDS are normalized to rms^2/Hz, but not corrected for deadtime or background. These PDS have constant power at frequencies 0.002–0.02, which could not be seen in the Composite GH-state PDS, which does not cover this frequency range. At higher frequencies, the PDS decreases as a power-law, consistent with the form found from the Composite GH-state PDS.

Flat-Top-Power-law functions were fit to the Composite and T-type PDS; the resulting parameters are shown in Table 5.5. For the GH-state PDS, the break-frequency parameter was frozen at a value lower than the lowest frequency in the GH-state Composite PDS, found from the T-type PDS (see Table 5.5).

The best-fit of the GH data shows that the source variability is consistent with a single power-law, however, the T-type PDS shows a Flat-Top component below $\sim 0.014 \pm 0.002$ Hz. The %rms variability is strong, and energy dependent, increasing from 27.3 ± 0.4 %, to 33.9 ± 0.4 %, to 37.7 ± 0.1 % across the Low-, Medium-, and High Energy Ranges while in the GH state (values from the T-type PDS are consistent with these, after correction for background and deadtime effects).

Table 5.5: Parameters for Best-Fit Flat-Top Power-Law to 1826-24 PDS

Spectral Selection	Energy Range (keV)	ν_1 (Hz)	(α_1)	%rms (0.001-64 Hz)	χ^2_ν (dof)	Background Corr. Factor
All[a]	2.3–4.6	$0.0135\ ^{+0.0013}_{-0.0017}$	0.95 ±0.02 [c]	23.0 ±0.4	1.12 (36)	1.16 ±0.15
(T-type)	4.6–9.2	$0.0142\ ^{+0.0017}_{-0.0012}$	1.02 ±0.02 [c]	26.8 ±0.4	1.33 (36)	1.25 ±0.17
	9.2–18.4	0.0153 ±0.0016	1.06 ±0.03 [c]	23.7 ±0.7	1.08 (36)	1.57 ±0.22
	2.3–18.4	$0.0139\ ^{+0.0017}_{-0.0011}$	1.01 ±0.01 [c]	24.4 ±0.3	1.10 (36)	1.26 ±0.16
GH[b]	2.3–4.6	(0.0144)	0.97 ±0.02	27.3 ±0.4	1.39 (22)	–
	4.6–9.2	(0.0144)	1.04 ±0.01	33.9 ±0.4	1.30 (22)	–
	9.2–18.4	(0.0144)	1.03 ±0.03	37.7 ±0.1	1.25 (22)	–
	2.3–18.4	(0.0144)	1.04 ±0.01	31.3 ±0.3	1.35 (22)	–

[a] Fits applied to values in the 0.00195 – 8.0 Hz range
[b] Fits applied to values in the 0.0156 – 64 Hz range
[c] Uncorrected for background (see above) and deadtime (<1–3%)
Values in parenthesis are fixed

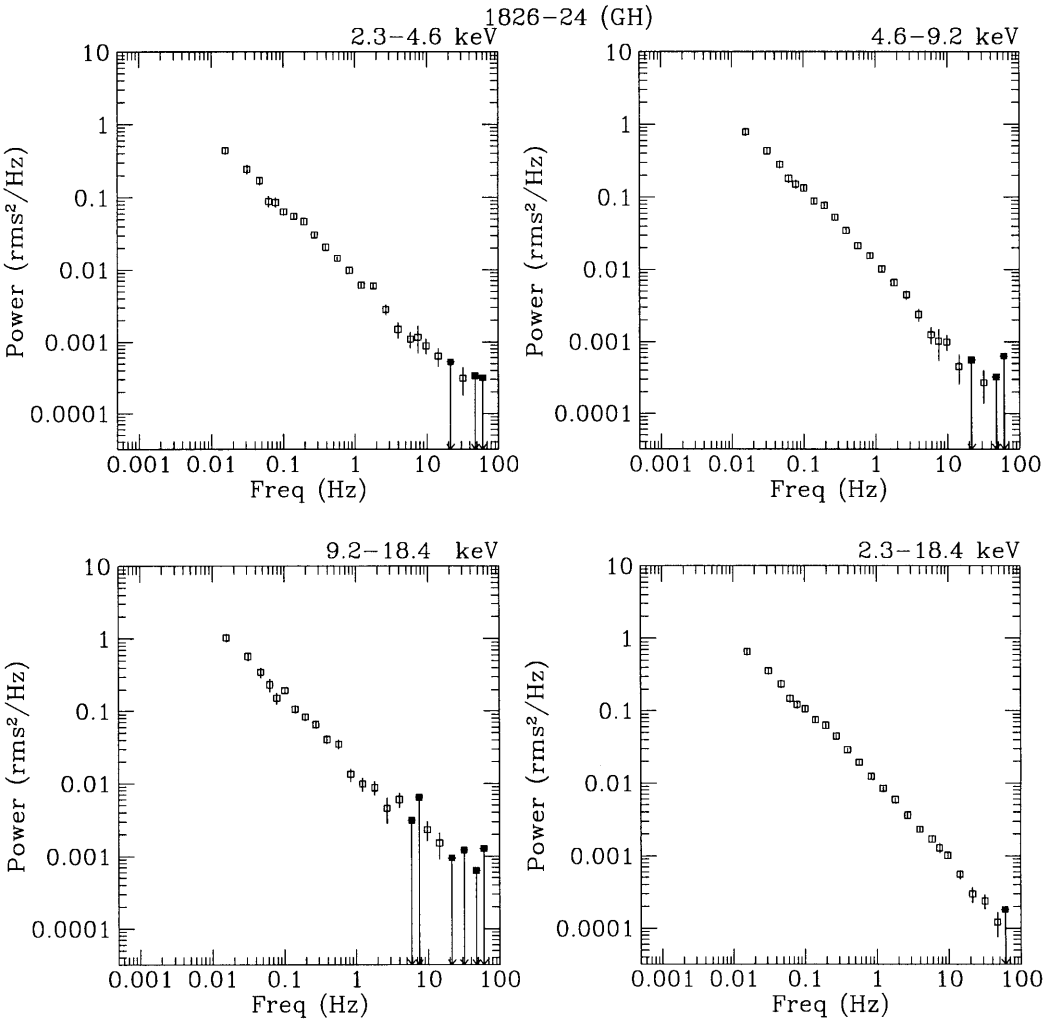

Figure 5-7: **1826-24 PDS, GH-state Data**. Composite PDS for 1826-24, corrected for both background and deadtime, in the Low Energy Range, Medium Energy Range, High Energy Range, Intensity Range energy ranges, using data selected spectrally to be in the GH-states. Upper-limits are 2 σ.

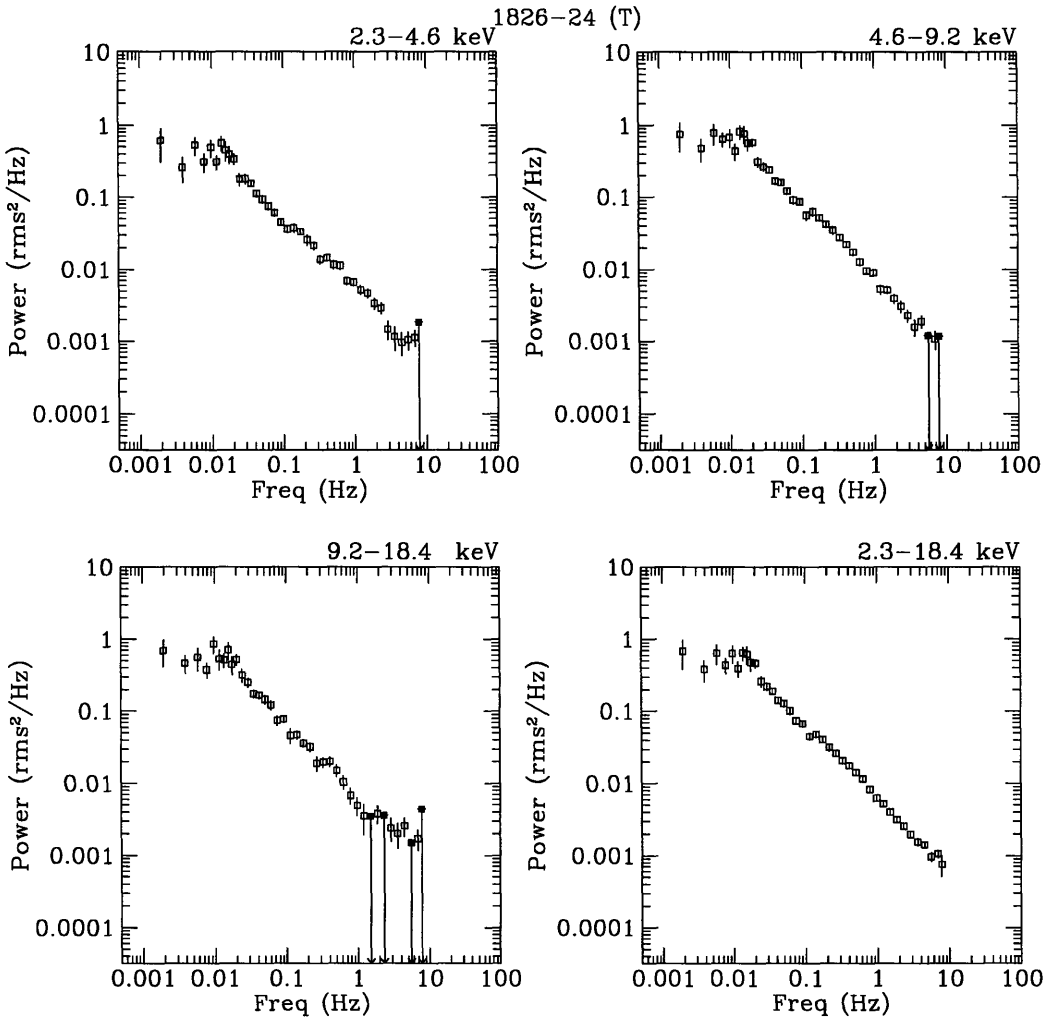

Figure 5-8: **1826-24 PDS, All Data. T-type.** T-type PDS for 1826-24, not corrected for background or deadtime, in the Low Energy Range, Medium Energy Range, High Energy Range, Intensity Range energy ranges, using all available data. Upper-limits are 2 σ.

5.4.4 Cyg X-1

Of the measured 128 s values of the Wide Ratio for Cyg X-1 measured in Ch. 4, 80% were in the range 0.13–0.51 (GH-type source).

We investigated differences in the PDS of Cyg X-1 due to the different spectral states. The data for Cyg X-1 when it is in the G-state have values of Wide Ratio which are largely in one of two ranges: 0.12–0.15 and 0.16–0.18. These in turn correspond largely to two different observation epochs (90/129–131 and 91/156–157, respectively). We therefore sub-divided these data into two spectral groups: Wide Ratio=0.1–0.15 (G1), and 0.15–0.32 (G2). We also produced PDS of H-state data (Wide Ratio=0.32–1.0) which, again, largely corresponds to a third observational epoch (87/217-220). We also produced T-type PDS. We divided the T-type PDS on the basis of time (i.e., into the three different observational epochs, which themselves correspond to specific ranges of Wide Ratio) into three parts: T1 (Wide Ratio=0.32–1.0), T2 (0.1–0.15) and T3 (0.15–0.32). Thus, the T-type PDS T1 corresponds to the Composite PDS of H-state data; T2 to G1; and T3 to G2.

We show the Composite PDS of the G1-state data in Fig. 5-9. The Low-Frequency PDS are an average of 8 FFTs, Medium-Frequency PDS of 244 FFTs, and High-Frequency PDS of 2074 FFTs. The power in this state is both strong and significant. The PDS in all energy ranges are flat-topped at low frequencies, breaking to a power-law near 0.1 Hz, with a significant deviation from power-law near 1 Hz, and rolling off at high frequencies ($\gtrsim$10 Hz). This QPO deviation is more convincingly shown in Fig. 5-11, where the PDS is given in νP (rms^2) normalization.

In Fig. 5-10, we show the Composite PDS of the G2-state (Wide Ratio=0.15–0.32) data. No Low-Frequency FFTs were used; 114 Medium-frequency FFTs and 927 High-frequency were averaged into single PDS. In the areas in which the frequency space over-lapped, we discarded the Medium-frequency data. The power has been corrected for dead-time and background. The shape of the PDS is similar but not identical to that seen in the G1-state PDS: the Power breaks from a constant at a lower frequency ($\sim$0.05, compared to $\sim$0.1 Hz), and the QPO near 1 Hz is no longer evident, although there is still complexity in the power-law, which we can better

characterize with model fits.

In Fig. 5-11, we show the PDS of the G1 and G2-states together, renormalized as νP (see Sec. A.3). For all three different energy ranges, and the summed energy range, the PDS of the Wide Ratio=0.1–0.15 data (whose points are connected to guide the eye) and the Wide Ratio=0.15–0.32 data (points are not connected) are identical above 10 Hz.

Below 10 Hz, the PDS are inconsistent with being the same, and appear to be complex functions of frequency. Most evident is the presence of a QPO peak near 1 Hz in the PDS of the softer data, which is not present in the spectrally harder data. Also, the %rms of the harder data is equal or greater than the softer data in the frequency range 0.001– $\sim$7 Hz. Below 0.1 Hz, the power decreases in the softer data for decreasing frequency, diminishing by $> \times 10$, while for harder data it remains constant to within a factor of 2.

Beginning at low frequencies, the harder spectrum %rms is greater than the softer PDS %rms; it increases below 0.1 Hz, then (as seen in the energy ranges 2.3–4.6, 4.6–9.2, and 2.3–18.4) decreases until $\sim$1 Hz where it is constant or slightly increases until $\sim$3 Hz, above which it follows a single power-law.

The %rms value seems to "dip" near the QPO frequency of 1 Hz as if, in inverse of QPO, the power were *supressed* at that frequency relative to nearby frequencies. The statistical significance of such a feature is difficult to calculate *a posteriori*, and in a region of frequency space where the behavior is complex. We fit to 4.6–9.2 keV PDS, in the frequency range 0.125–3.6 (selected by eye, thus most likely giving the most significant fit), a power-law and a Lorentzian. The power-law was permitted to vary in magnitude and slope, while the FWHM and centroid frequency of the Lorentzian were held fixed at the best-fit value of the T-type PDS in the 2.3–18.4 keV range (see Table 5.8). The best fit %rms value of the "dip" was -5.9 $^{+0.7}_{-0.6}$ %, which χ^2_ν= 1.4 (19 DOF). Without the Lorentizian, the best fit power-law mode had χ^2_ν=2.29 (20 DOF). The formal probability of producing a change in χ^2_ν of this much or greater is $\sim$0.2%.

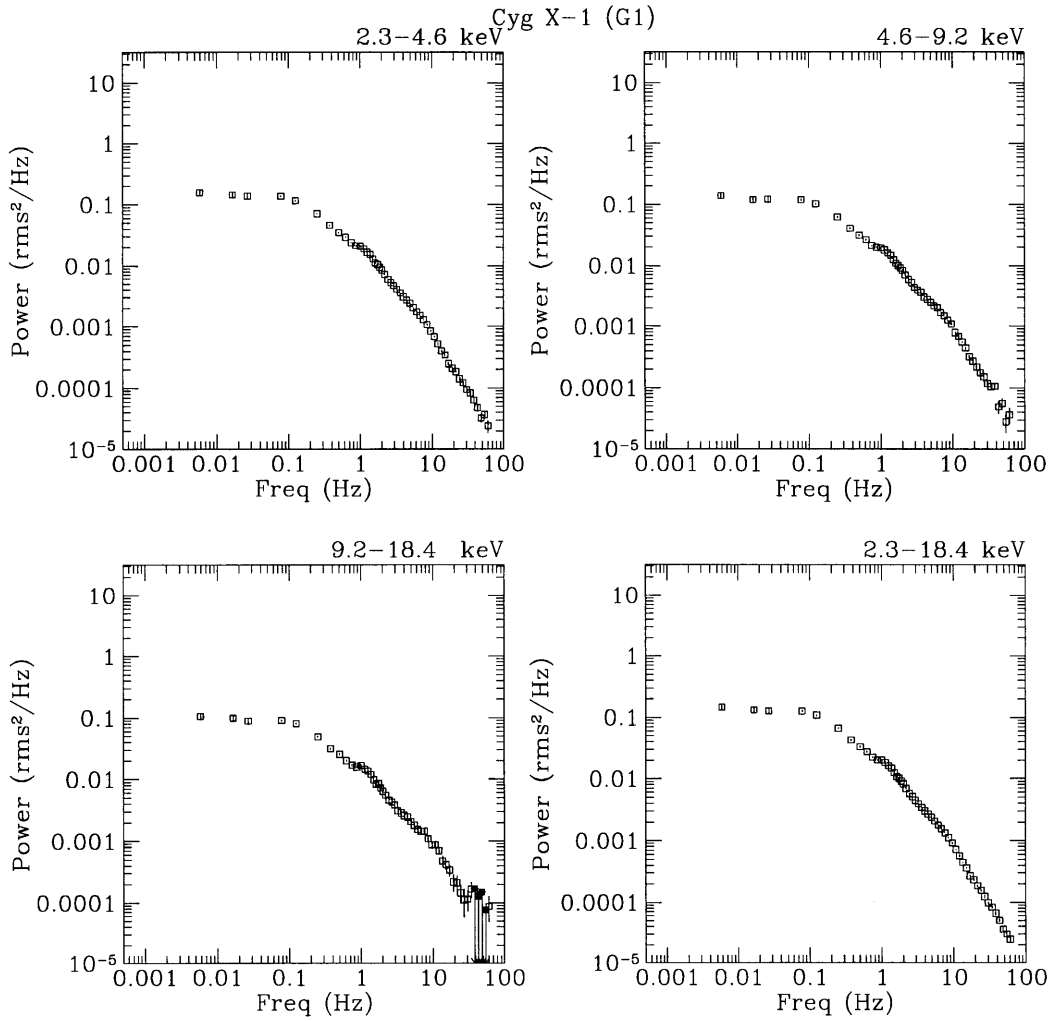

Figure 5-9: **Cyg X-1 Composite PDS G1 (Wide Ratio=0.1–0.15)**. The Composite PDS in the three energy ranges and the sum energy range (indicated in each panel). Corrections for background and deadtime have been applied. Upper-limits are 2σ.

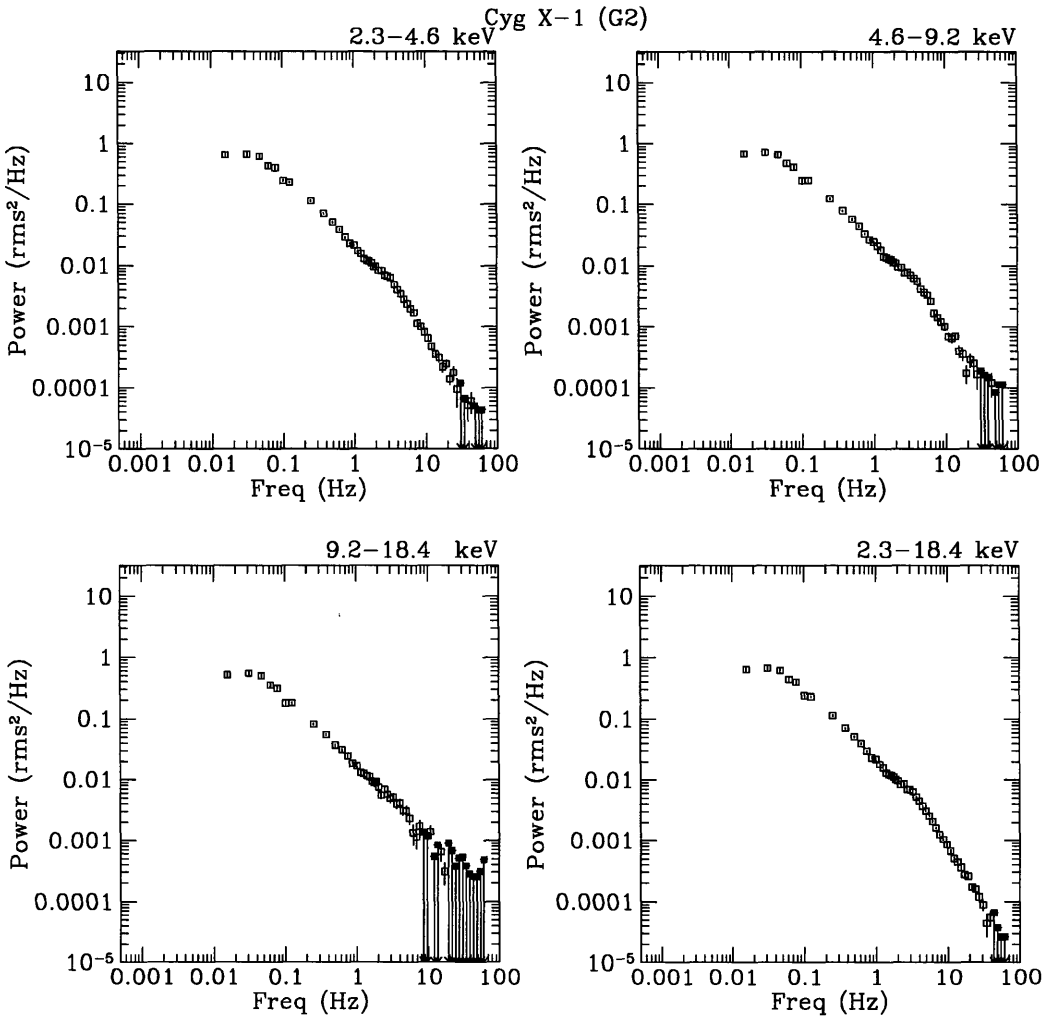

Figure 5-10: **Cyg X-1 Composite PDS G2 (Wide Ratio=0.15–0.32)**. The Composite PDS in the three energy ranges and the sum energy range (indicated in each panel). Upper-limits are 2σ.

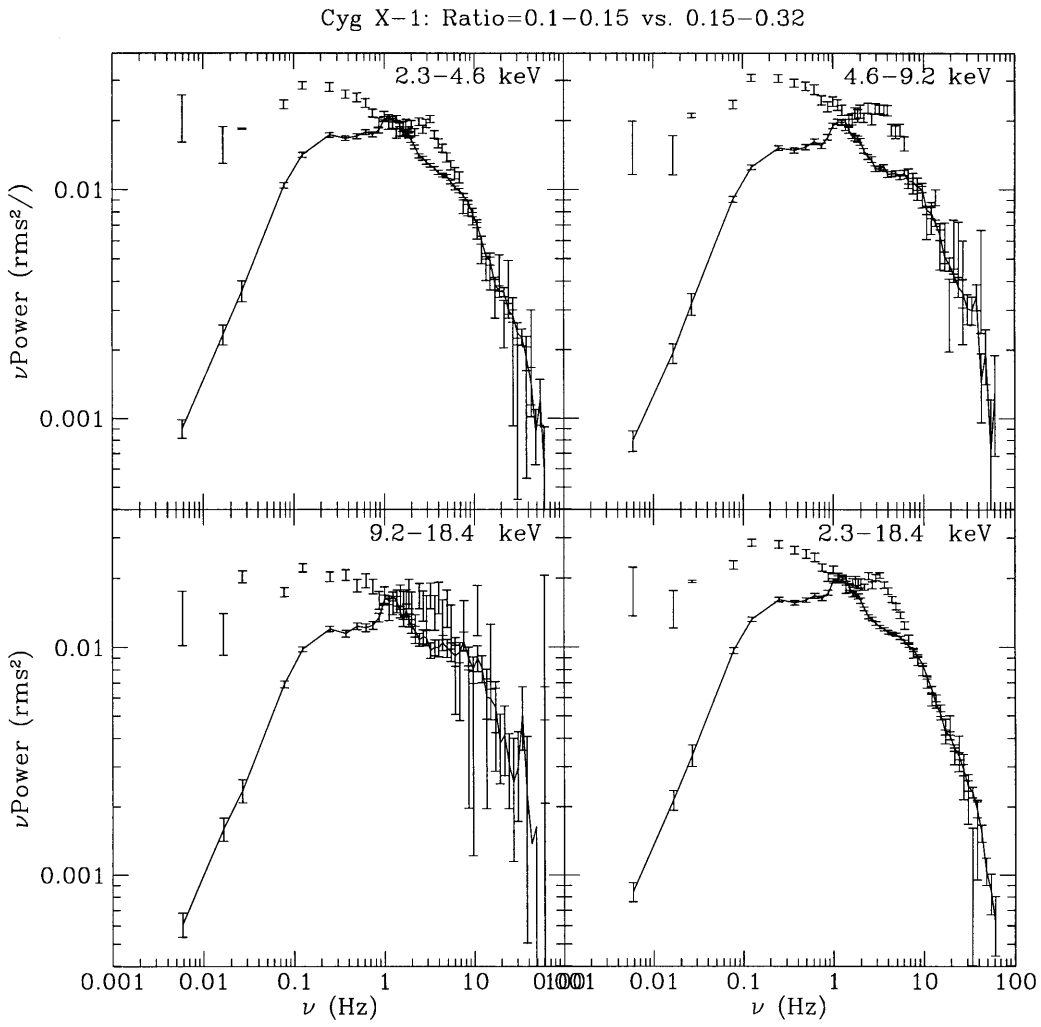

Figure 5-11: **Cyg X-1 Composite PDS, G1 and G2.** 8 PDS of Cyg X-1, in 4 energy ranges (indicated in each panel). There are two PDS for each energy range: one from data taken when the source Wide Ratio is in the range 0.1–0.15 (G1, from Fig. 5-9; connected by a line to guide the eye), and one from data taken when the source Wide Ratio is in the range 0.15–0.32 (G2, from Fig. 5-10; unconnected points). The 1σ error bars are included. The spectrally soft PDS shows a QPO feature near 1 Hz, while the harder PDS does not have this feature. The PDS show roughly equal %rms values above 10 Hz, and %rms values which are not equal below 10 Hz.

In Fig. 5-12, we show the Composite PDS of the H-state (Wide Ratio=0.32–1.0) data. No Low-Frequency or High-Frequency FFTs were used; 59 Medium-frequency FFTs were averaged to produce these PDS. The power has been corrected for dead-time and background. The power is strong and significant over all energy ranges, beginning with a constant flat-top at low frequencies, breaking to a power-law near 0.1 Hz, with no noticeable, systematic deviations above this.

In Fig. 5-13, we show the T-type PDS made from (T1) data when the source was in the Wide Ratio=0.32–1.0 spectral state. The PDS are an average of 3 FFTs, and are corrected for deadtime and background. The PDS is consistent with that found from the Composite PDS of the H-state data. More detailed comparison is performed with the model fits in this section.

In Fig. 5-14, we show the T-type PDS made from (T2) data when the source was in the Wide Ratio=0.1–0.15 spectral state. The PDS are an average of 8 FFTs, and are corrected for deadtime and background. The PDS is consistent with that found from the Composite PDS of the G1-state data. More detailed comparison is performed with the model fits in this section.

In Fig. 5-15, we show the T-type PDS made from (T3) data when the source was in the Wide Ratio=0.15–0.32 spectral state. The PDS are an average of 8 FFTs, and are corrected for deadtime and background. The PDS is consistent with that found from the Composite PDS of the G2-state data. More detailed comparison is performed with the model fits in this section.

In Tables 5.6 & 5.7 we give the best-fit parameters for a Flat-Top-Double-Power-Law model to the Composite PDS in the 3 separate plus summed energy ranges for the spectral states Wide Ratio=0.1-0.15 (G1); 0.15–0.32(G2); and 0.32-1.0 (H). The PDS fit with these models are shown in Figs. 5-9, 5-10, & 5-12, respectively.

We attempted to fit the G1 (Wide Ratio=0.1–0.15) PDS with a Flat-Top-Power-Law-Exponential-Decay model and also the Flat-Top-Single-Power-Law model, both with a Lorentzian included near 1 Hz to account for the QPO. We found the fits to be considerably worse than the Flat-Top-Double-Power-Law Model, with typical χ^2_ν=5.0–20.0 (including the Lorentizian model for QPO). A Zero-Centered Lorentzian,

in which the centroid frequency is held fixed, while the FWHM and %rms are permitted to vary, was also tried, and found to be inadequate, with $\chi^2_\nu \sim 40$. We therefore used only the Flat-Top-Double-Power-Law model (with additional QPO component) for Cyg X-1.

In Fig. 5-16, we show the residuals of the best-fit Flat-Top-Double-Power-Law model, not including a Lorentzian near 1 Hz. There is a clear significant excess near 1 Hz in the PDS of the 2.3–4.6 keV, 4.6–9.2 keV, and 2.3–18.4 keV energy ranges. Flat-Top-Double-Power-Law models which do not include Lorentzians have χ^2_ν of 13-18 in these PDS (compared with 1.56-1.93 with the QPO component; see Table 5.6).

The %rms variability in the G1, G2 and H states is high, in the 28-40 % range. In the H-state the variability is largely color-less, showing little or no dependency on the energy range. In the G1 and G2 states, the energy dependency of the %rms variability is non-monotonic, remaining constant or increasing betwen the Low Energy Range and Medium Energy Range then decreasing in the High Energy Range.

The power-law slopes in the G1 and G2 states are measureably steeper than in the H-state (compare $\alpha_1 \sim 1.15 \pm 0.01$ to 1.05 ± 0.2; and $\alpha_2 \sim 1.95 \pm 0.03$ to 1.52 ± 0.02). The two different break frequencies do not appear to be related: ν_2 decreases with increasing hardness (from 7.8, to 4.5, to 1.35 Hz) while ν_2 first decreases then increases (from 0.15, to 0.05, to 0.08 Hz in states G1, G2 and H).

We fit the QPO in the G1-state with a Lorentzian model which produced a centroid frequency of $\sim 1.11 \pm 0.03$ Hz, and a FWHM of 1.17 ± 0.07 Hz in the Intensity Range PDS. The QPO exhibits energy dependence in its FWHM, which decreases with increasing energy from 1.30 ± 0.09, to 1.04 ± 0.08, to 0.80 ± 0.1 Hz between the Low, Medium, and High Energy Ranges. Similarly, the %rms variability decreases with increasing energy range from 11.7 ± 0.5 in the Low Energy Range to 8.2 ± 0.6 in the High Energy Range.

We also fit a Lorentzian to the G2-state PDS. In the Intensity Range a peak was found at 3.14 Hz, with FWHM 0.7 ± 0.3 Hz. The %rms value is $3.5^{+0.3}_{-0.4}$ %. These values were fixed for the Low Energy Range, Medium Energy Range, and High Energy Range PDS, in which the %rms was consistent with being colorless.

Table 5.6: Broad-Band Parameters for Best-Fit Flat-Top-Double-Power-Law Cyg X-1 Composite PDS

Spectral Range (Wide Ratio)	Fit ID[d]	Energy Range (keV)	ν_1 (Hz)	ν_2 (Hz)	(α_1)	(α_2)	%rms (0.001-64 Hz)	χ^2_ν (dof)
G1[a]	1	2.3–4.6	0.153±0.004	7.2 ±0.2	1.167 ±0.007	1.90 ±0.02	28.5±0.2	1.61 (48)
(0.1–0.15)	2	4.6–9.2	0.148 ±0.004	$8.4^{+0.6}_{-0.3}$	1.096 ±0.007	$1.88^{+0.07}_{-0.04}$	28.3 ±0.2	1.41 (48)
	3	9.2–18.4	0.147 ±0.005	$9.3^{+2.3}_{-1.3}$	1.06 ±0.02	$1.88^{+0.4}_{-0.2}$	25.7±0.2	0.85 (48)
	4	2.3–18.4	0.152±0.004	7.8±0.1	1.140±0.006	1.93±0.02	28.1±0.2	1.73 (48)
(QPO suppressed)	5	2.3–4.6	0.181 ±0.003	5.0 ±0.1	1.169 ±0.005	1.81 ±0.01	30.59±0.09	15.7 (51)
	6	4.6–9.2	0.177 ±0.003	7.2 ±0.2	1.119 ±0.005	1.85 ±0.03	29.90±0.09	13.7 (51)
	7	9.2–18.4	0.107 ±0.005	$1.27^{+0.08}_{-0.04}$	0.81 ±0.02	1.36 ±0.02	27.0 ±0.2	1.84 (51)
	8	2.3–18.4	0.187 ±0.003	7.0 ±0.1	1.181 ±0.004	1.92 ±0.01	30.00 ±0.08	18.3 (51)
G2[b]	9	2.3–4.6	0.052±0.003	4.3 ±0.3	1.16 ±0.01	1.99±0.05	39.1±0.3	1.61 (47)
(0.15–0.32)	10	4.6–9.2	0.050±0.003	$4.6^{+0.3}_{-0.5}$	1.13 ±0.01	$1.92^{+0.07}_{-0.09}$	41.5 ±0.3	2.01 (47)
	11	9.2–18.4	$0.045^{+0.004}_{-0.003}$	$4.8^{+0.6}_{-0.8}$	1.10±0.02	$2.1^{+0.3}_{-0.2}$	35.2±0.4	1.49 (47)
	12	2.3–18.4	0.051±0.003	$4.5^{+0.3}_{-0.1}$	1.15 ±0.01	1.95±0.03	39.4±0.3	1.40 (47)
H[c]	13	2.3–4.6	$0.080^{+0.006}_{-0.005}$	1.5 ±0.1	1.08±0.02	1.59±0.03	30.8 ±0.3	1.79 (79)
(0.32–1.0)	14	4.6–9.2	$0.080^{+0.006}_{-0.005}$	$1.3^{+0.1}_{-0.2}$	1.03±0.02	1.49±0.02	30.0 ±0.2	1.39 (79)
	15	9.2–18.4	0.078±0.006	$1.1^{+0.2}_{-0.1}$	0.98 ±0.03	1.34±0.04	30.1 ±0.3	1.45 (79)
	16	2.3–18.4	$0.079^{+0.006}_{-0.004}$	$1.35^{+0.09}_{-0.07}$	1.04±0.02	1.52±0.02	30.2 ±0.2	1.60 (79)

[a] Fits applied to values in the 0.001 – 64 Hz range
[b] Fits applied to values in the 0.0156 – 64 Hz range
[c] Fits applied to values in the 0.0156 – 8 Hz range
[d] For reference with Table 5.7

Best-fit models were found from the T-type data. As with the Composite data, we used only Flat-Top-Double-Power-Law models, in addition to a QPO Lorentzian. The best-fit Parameters are shown in Table 5.8. Some of the parameters derived from the best-fit models appear inconsistent with those from the corresponding Composite PDS, which we interpret as being due to the the lack of data above 8.0 Hz in the T-type PDS. For example, in the T2 PDS, the second break frequnency ν_2 is significantly lower than that found in the G1 PDS (1.6 Hz vs. 7.8 Hz) certainly because there is no data above 8.0 Hz to constrain the break, and therefore the model finds a break near the QPO frequency. This, in turn affects the total %rms (which is moderately lower), and the best fit model parameters of the QPO, which are themselves more complexly related to energy than in G1.

In the fits to the T3 PDS, the derived BB parameters are consistent with those found in the G2 PDS. The QPO parameters are somewhat different, however, largely due to the fitting. Using the Intensity Range PDS, if the QPO frequency is pertmitted to wander, the fit becomes unstable, and no QPO peak is found. If the QPO peak is fixed to ν_c=3.14 Hz and FWHM=0.72 Hz, the χ^2_ν value is high >2.50.

Table 5.7: QPO Parameters for Best-Fit Flat-Top-Double-Power-Law Cyg X-1 Composite PDS

Spectral Range (Wide Ratio)	Fit ID[d]	Energy Range (keV)	ν_c (Hz)	FWHM (Hz)	%rms
G1[a]	1	2.3–4.6	1.07±0.04	1.30±0.09	11.7±0.5
(0.1–0.15)	2	4.6–9.2	1.15 ±0.03	1.04 ±0.08	10.1±0.4
	3	9.2–18.4	1.14±0.03	0.8 ±0.1	8.2 ±0.6
	4	2.3–18.4	1.11 ±0.03	1.17 ±0.07	10.8 ±0.4
	5	2.3–4.6	–	–	–
	6	4.6–9.2	–	–	–
	7	9.2–18.4	–	–	–
	8	2.3–18.4	–	–	–
G2[b]	9	2.3–4.6	(3.14)	(0.72)	$3.5^{+0.3}_{-0.4}$
(0.15–0.32)	10	4.6–9.2	(3.14)	(0.72)	$3.3^{+0.5}_{-0.6}$
	11	9.2–18.4	(3.14)	(0.72)	<6.0
	12	2.3–18.4	$3.14^{+0.09}_{-0.07}$	0.7±0.3	$3.5^{+0.3}_{-0.4}$
H[c]	13	2.3–4.6	–	–	–
(0.32–1.0)	14	4.6–9.2	–	–	–
	15	9.2–18.4	–	–	–
	16	2.3–18.4	–	–	–

[a] Fits applied to values in the 0.001 – 64 Hz range
[b] Fits applied to values in the 0.0156 – 64 Hz range
[c] Fits applied to values in the 0.0156 – 8 Hz range
[d] For reference with Table 5.6
Values in parenthesis are fixed
Upper-limits are 3 σ

If we fix the QPO peak to 1.15 Hz and FWHM=0.79 Hz (as was found in the softer T2 data), the χ^2_ν values are lower (1.07–1.85); the %rms values of the QPO, however, are significantly negative, at approximately -4.1 ±0.7 %. It seems plain that the T3 PDS is more complex than the simple BB model.

The fits to the T1 data, the best-fit parameters are consistent with those found in the Composite H PDS, except for the first break frequency (ν_1) which is measured to be higher (~0.11 ±0.01, compared to 0.078±0.006), and the %rms variabilities are ~1.5% lower (28.7±0.3 % vs. 30.2 ±0.3 %), across all energy ranges. We attribute this difference to (small) source variability within the Wide Ratio=0.32–1.0 range.

Table 5.8: Broad-Band Parameters for Best-Fit Flat-Top-Double-Power-Law Cyg X-1 T-type PDS

Observational Epoch (Wide Ratio)	Fit ID[a]	Energy Range (keV)	ν_1 (Hz)	ν_2 (Hz)	(α_1)	(α_2)	%rms (0.001-64 Hz)	χ^2_ν (dof)
T2 (0.1–0.15)	1	2.3–4.6	0.120 ±0.005	1.6 ±0.1	0.99 ±0.04	1.58 ±0.03	25.8 ±0.2	1.39 (31)
	2	4.6–9.2	0.123 ±0.005	$1.1^{+0.5}_{-0.2}$	1.02 ±0.04	1.28±0.06	24.5 ±0.2	1.53 (31)
	3	9.2–18.4	0.132 ±0.006	1.9±0.2	1.00±0.04	1.41±0.08	22.5 ±0.3	1.35 (31)
	4	2.3–18.4	0.124 ±0.005	1.6±0.2	1.03 ±0.04	1.46 ±0.03	25.0 ±0.2	1.38 (31)
T3 (0.15–0.32)	5	2.3–4.6	0.050 ±0.003	3.5 ±0.1	1.15 ±0.01	2.3±0.1	34.2 ±0.3	1.70 (34)
	6	4.6–9.2	0.049 ±0.003	3.4±0.2	1.12 ±0.01	2.1±0.1	34.6 ±0.3	1.56 (34)
	7	9.2–18.4	0.049 ±0.003	(3.6)	1.13±0.02	$2.4^{+0.4}_{-0.5}$	31.1 ±0.5	1.30 (34)
	8	2.3–18.4	0.049 ±0.003	3.6±0.1	1.14 ±0.01	2.21 ±0.07	34.0 ±0.3	1.62 (34)
T1 (0.32–1)	9	2.3–4.6	0.131 ±0.007	$3.3^{+0.9}_{-0.4}$	1.22±0.02	1.83±0.12	28.5±0.3	1.07 (33)
	10	4.6–9.2	0.11 ±0.01	1.3±0.2	1.00±0.07	1.54±0.06	28.5±0.3	1.85 (33)
	11	9.2–18.4	0.11 ±0.01	$0.73^{+0.7}_{-0.2}$	$1.04^{+0.09}_{-0.06}$	$1.25^{+0.14}_{-0.02}$	27.6±0.3	1.02 (33)
	12	2.3–18.4	0.11 ±0.01	1.3 ±0.1	0.98 ±0.07	1.56 ±0.04	28.7±0.3	1.20 (33)

[a] For reference with Table 5.9
Values in parenthesis are fixed
Upper-limits are 3 σ
Fits applied to values in the 0.0156 – 8.0 Hz range

Table 5.9: QPO Parameters for Best-Fit Flat-Top-Double-Power-Law Cyg X-1 T-type PDS

Observational Epoch (Wide Ratio)	Fit ID[a]	Energy Range (keV)	ν_c (Hz)	FWHM (Hz)	%rms
T2 (0.1–0.15)	1	2.3–4.6	1.14 ±0.04	0.6 ±0.2	5.3 ±1
	2	4.6–9.2	1.21±0.06	1.0 ±0.1	8.0 ±1
	3	9.2–18.4	(1.15)	(0.79)	7.0 ±0.5
	4	2.3–18.4	1.15 ±0.04	$0.79^{+0.2}_{-0.1}$	6.8 ±1
T3 (0.15–0.32)	5	2.3–4.6	(1.15)	(0.79)	$-4.3^{+0.9}_{-0.7}$
	6	4.6–9.2	(1.15)	(0.79)	$-4.2^{+1.2}_{-0.9}$
	7	9.2–18.4	(1.15)	(0.79)	<15
	8	2.3–18.4	(1.15)	(0.79)	−4.1±0.7
T1 (0.32–1)	9	2.3–4.6	(1.15)	(0.79)	5.6±1.0
	10	4.6–9.2	(1.15)	(0.79)	<17.7
	11	9.2–18.4	(1.15)	(0.79)	<7.3
	12	2.3–18.4	(1.15)	(0.79)	<15.6

[a] For reference with Table 5.8
Values in parenthesis are fixed
Upper-limits are 3 σ
Fits applied to values in the 0.0156 – 8.0 Hz range

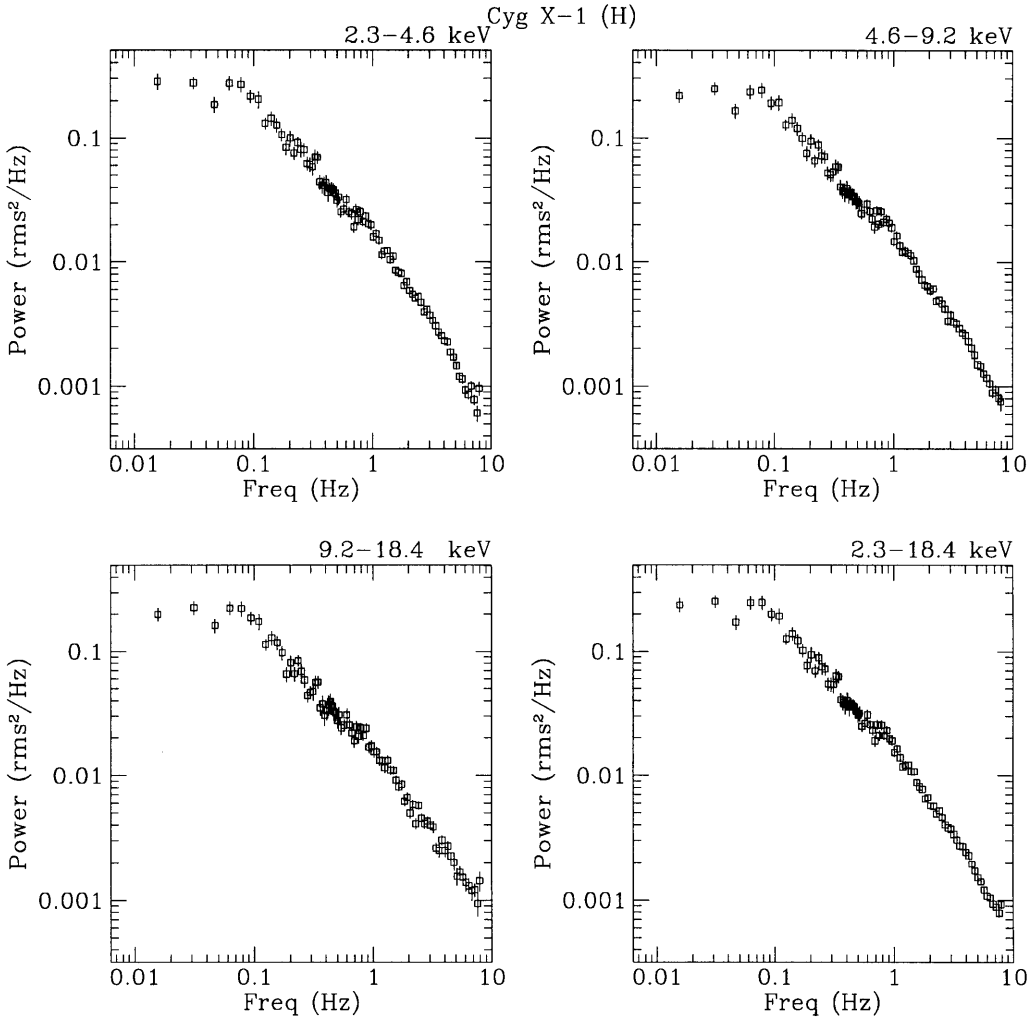

Figure 5-12: **Cyg X-1 Composite PDS Wide Ratio=0.32–1.0.** The Composite PDS in the three energy ranges and the sum energy range (indicated in each panel). Upper-limits are 2σ.

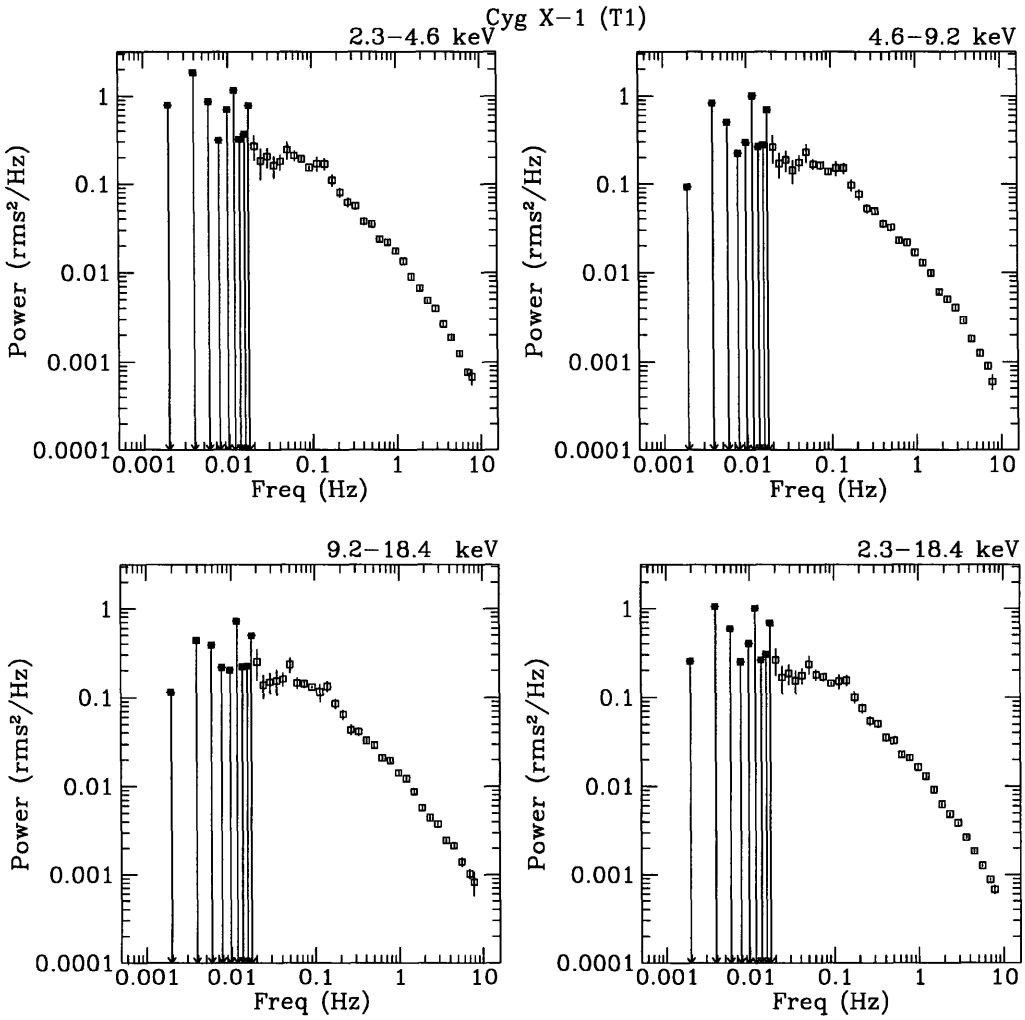

Figure 5-13: **Cyg X-1 T-type PDS, Wide Ratio=0.32-1.0.** PDS in three energy ranges, plus the summed energy range (indicated in each panel). Data are corrected for background and deadtime. Upper-limits are 2σ.

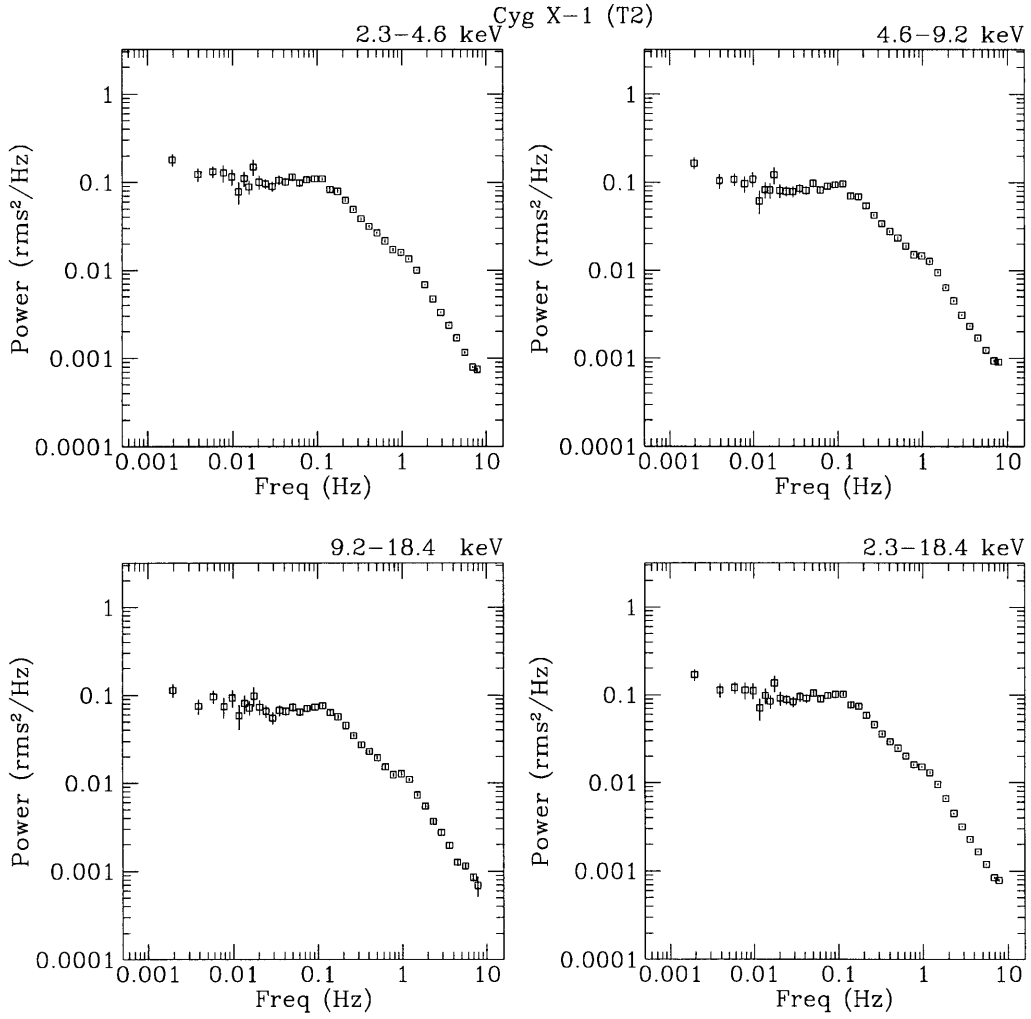

Figure 5-14: **Cyg X-1 T-type PDS, Wide Ratio=0.10–0.15**. PDS in three energy ranges, plus the summed energy range (indicated in each panel). Data are corrected for background and deadtime. Upper-limits are 2σ.

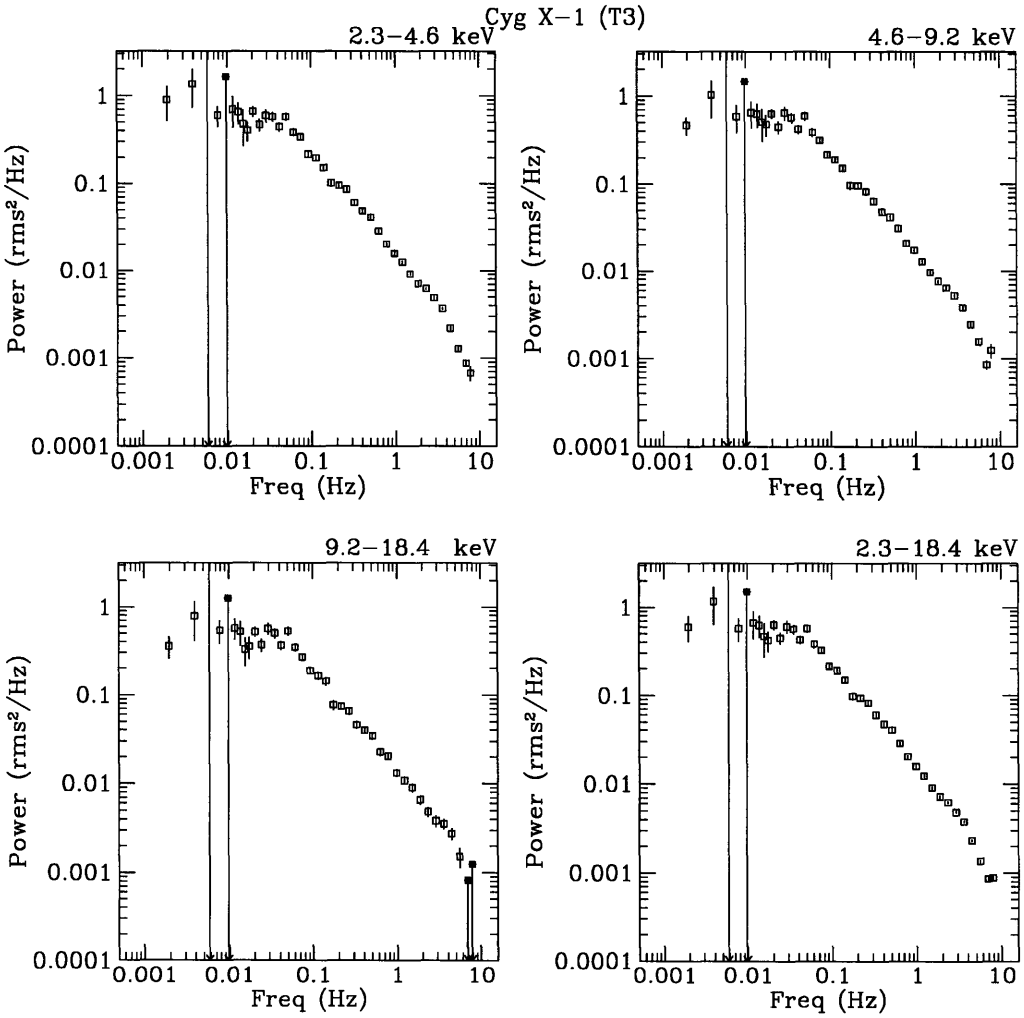

Figure 5-15: **Cyg X-1 T-type PDS, Wide Ratio=0.32–1.0.** PDS in three energy ranges, plus the summed energy range (indicated in each panel). Data are corrected for background and deadtime. Upper-limits aare 2 σ.

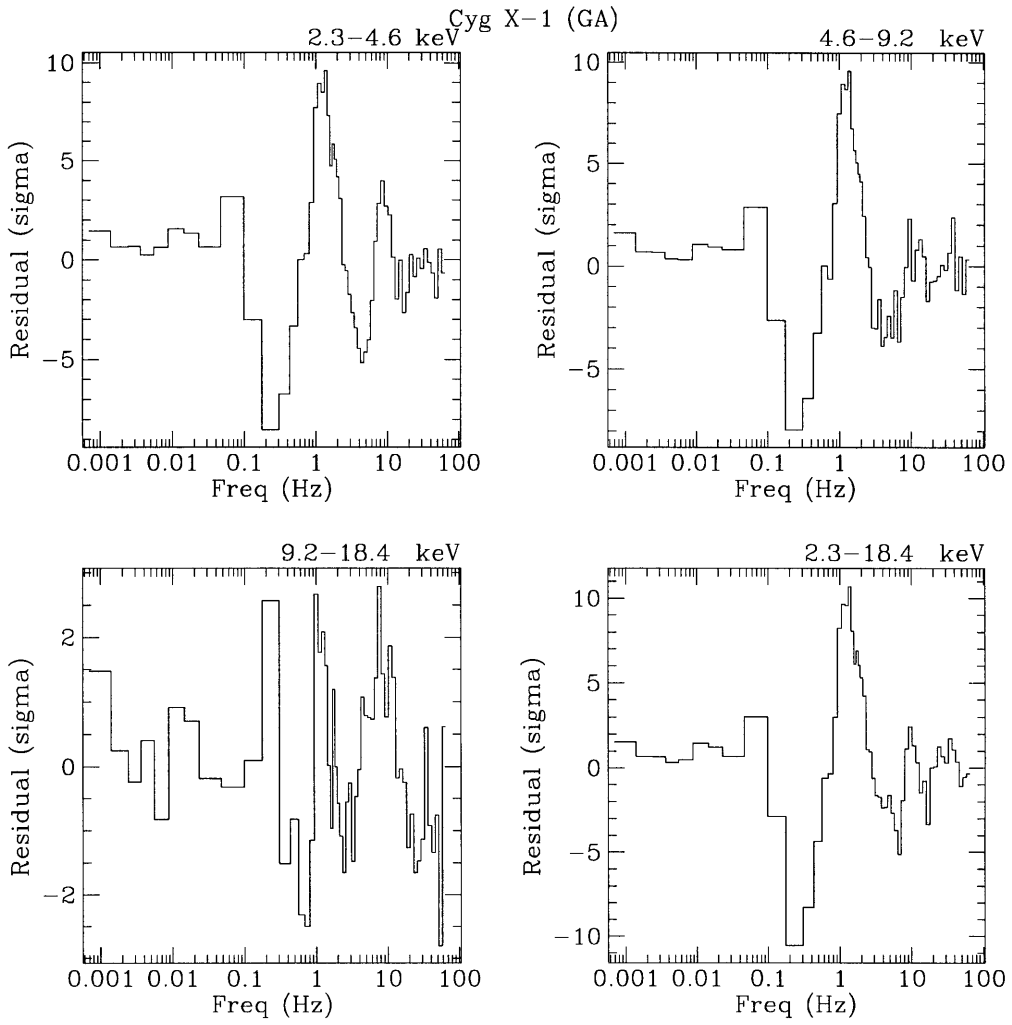

Figure 5-16: **Cyg X-1 Composite PDS Wide Ratio=0.1–0.15**. Residuals (in σ) of the best-fit Flat-Top-Double-Power-Law model, with no Lorentzian included, subtracted from the data, for the PDS shown in Fig. 5-9. There is a clear significant excess near 1 Hz in the PDS of the 2.3-4.6 keV, 4.6–9.2 keV, and 2.3–18.4 keV energy ranges. The seeming excess near 10 Hz in some of the PDS disappears when a Lorentzian near 1 Hz is included in the model.

5.4.5 LMC X-1

Of the measured 128 s values of the Wide Ratio for LMC X-1 measured in Ch. 4, 80% were in the range 0.018–0.055 (EF-type source). All of the available raw data were taken when the source spectrum was in the E-state. We have excluded data during those periods which we found were affected by magnetospheric electrons (see Sec. 3.4). There is no data in our sample with the necessary time-resolution to produce T-type PDS.

In Fig. 5-17, we show the Composite PDS of LMC X-1 in the E-state ($0.01 <$ Wide Ratio < 0.032) which is an average of 16 Low-Frequency FFTs; no Medium- or High-Frequency FFTs were available.

Most interesting about this PDS is the correlation between %rms and the energy range of the PDS. Also notable in these PDS is the complex shape of the PDS, which does not lend itself to simple parameterization.

In Table 5.10, we show the parameters of a best-fit power-law model to this data. The fits are fair to poor; without a more obviously representative model, however, we rely upon the results of the power-law model.

In the Intensity Range, the PDS slope is constrained to 1.08 $\pm$0.1, with the appearance of a flat-top near 0.0027 Hz. These parameters were not well constrained in the other PDS, and so they were held fixed, to extract the values of the %rms in each energy range. The %rms variability increases significantly with increasing energy, from 5, to 12, to 35% across our three energy ranges, for our assumed best-fit model. It must be noted that during one of the observational epochs, variability in the High Energy Range may have been contributed by precipitating electron events (see Sec 3.3). However, we have not seen evidence of significant variability being added to the Medium Energy Range by the electron events, and therefore we believe that the positive correlation between the %rms and energy is real.

The best-fit Power-Law model applied to the Intensity Range data produces a χ^2_ν of 4.59 (6 dof); the Flat-Top model was therefore preferred.

Table 5.10: Parameters for Best-Fit Flat-Top-Power-Law to LMC X-1 Composite PDS

Spectral Range (Wide Ratio)	Energy Range (keV)	ν_1 (Hz)	Power Law Slope (α)	%rms (0.001-64 Hz)	χ^2_ν (dof)
E	2.3–4.6	(0.0027)	(1.08)	5.2±0.2	3.3 (7)
(0.01–0.032)	4.6–9.2	(0.0027)	(1.08)	12.0±0.3	2.4 (7)
	9.2–18.4	(0.0027)	(1.08)	35 ±2	3.5 (7)
	2.3–18.4	$0.0027\ ^{+0.0008}_{-0.0005}$	1.08±0.1	6.5 ±0.7	1.5 (5)

Fits applied to values in the 0.00097 – 0.03125 Hz range
Values in parenthesis are fixed

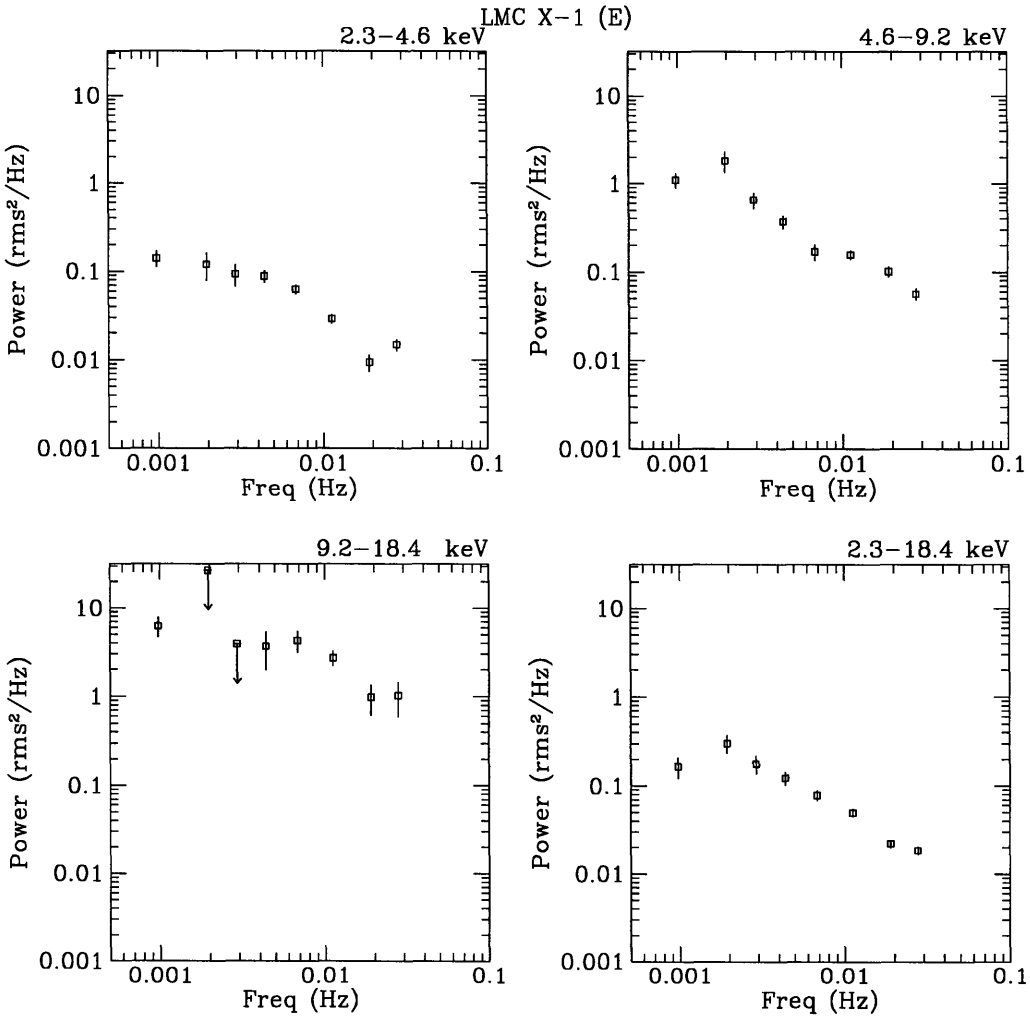

Figure 5-17: **LMC X-1 Composite PDS.** The Composite PDS of LMC X-1 in the three energy ranges and the sum energy range (indicated in each panel). Corrections for background and deadtime have been applied. Upper-limits are 2 σ.

5.4.6 LMC X-3

Of the measured 128 s values of the Wide Ratio for LMC X-3 measured in Ch. 4, 80% were in the range 0.014–0.031 (E-type source). All of the available raw data were taken when the source spectrum was in the E-state.

The Composite PDS from LMC X-3 is shown in Fig. 5-18. The Low-Frequency range is an average of 10 FFTs, the Medium-Frequency range is 96 FFTs, and the High Frequency range is 103 FFTs. The vast majority of the LMC X-3 data is in the E-state, leaving only 8 High Frequency FFTs and 1 Medium Frequency FFT while the source was in the F-state.

The T-type PDS for LMC X-3 is shown in Fig. 5-19. The PDS shown is an average of 29 FFTs. No correction for background or dead time has been applied to the PDS (normalized as rms^2/Hz). Very little significant power is in evidence.

We fit the Composite PDS of LMC X-3 with a power-law model, the best fit parameters listed in Table 5.11. The power-law slopes are not well constrained by the PDS (α_1=1.7±0.3 in the Intensity Range). The %rms variability is consistent with strong energy dependence, with 1.4±0.2% in the Low Energy Range increasing to 19^{+4}_{-5} % in the High Energy Range, increasing with increasing energy.

The best-fit model parameters for a power-law fit to the T-type PDS of LMC X-3 are given in Table 5.11. No correction was made to the data for background or dead time. We estimated a background correction factor for each energy range, which is listed in the table. We estimate the dead time correction to be at the level of $\lesssim$1–3%. We find the best fit model parameters are consistent with those found from the E-type PDS. The (highly uncertain) power-law slopes and the %rms values (after applying the background correction factor listed in the table) are consistent with those found in the E-type PDS, showing an increase in source %rms variability with increasing energy, from 1.4±0.3%, to $14.6^{+8.7}_{-2.2}$ (statistical)±5.7 (systematic) %.

Table 5.11: Parameters for Best-Fit Power-Law to LMC X-3 Composite PDS

Spectral Range (Wide Ratio)	Energy Range (keV)	Power Law Slope (α_1)	%rms (0.001-64 Hz)	χ^2_ν (dof)	Background Cor Factor
E[a]	2.3–4.6	1.6 ±0.2	1.4±0.2	1.33 (28)	–
(0.01–0.032)	4.6–9.2	$1.3^{+0.2}_{-0.3}$	<6	2.13 (28)	–
	4.6–9.2	(1.67)	<6	2.11 (29)	–
	9.2–18.4	$2.1^{+0.7}_{-0.5}$	19^{+4}_{-5}	1.09 (28)	–
	2.3–18.4	1.7 ±0.3	1.3±0.1	1.26 (28)	–
All[bc]	2.3–4.6	$1.6^{+0.5}_{-0.4}$	$1.3^{+0.3}_{-0.2}$	0.25 (6)	1.13 ±0.05
(T-type)	4.6–9.2	$1.8^{+0.8}_{-0.5}$	$1.4^{+0.4}_{-0.3}$	1.15 (6)	1.56 ±0.32
	9.2–18.4	$1.3^{+0.6}_{-0.4}$	$2.7^{+1.6}_{-0.8}$	0.95 (6)	5.42 ±2.10
	2.3–18.4	$1.8^{+0.4}_{-0.3}$	1.2±0.1	0.37 (6)	1.31 ±0.14

[a] Fits applied to values in the 0.00097 – 64 Hz range

[b] Fits applied to values in the 0.001952 – 8 Hz range

[c] %rms values are uncorrected for background (see above) and dead time (<1–3%)

Upper-limits are 3 σ

Values in parenthesis are fixed

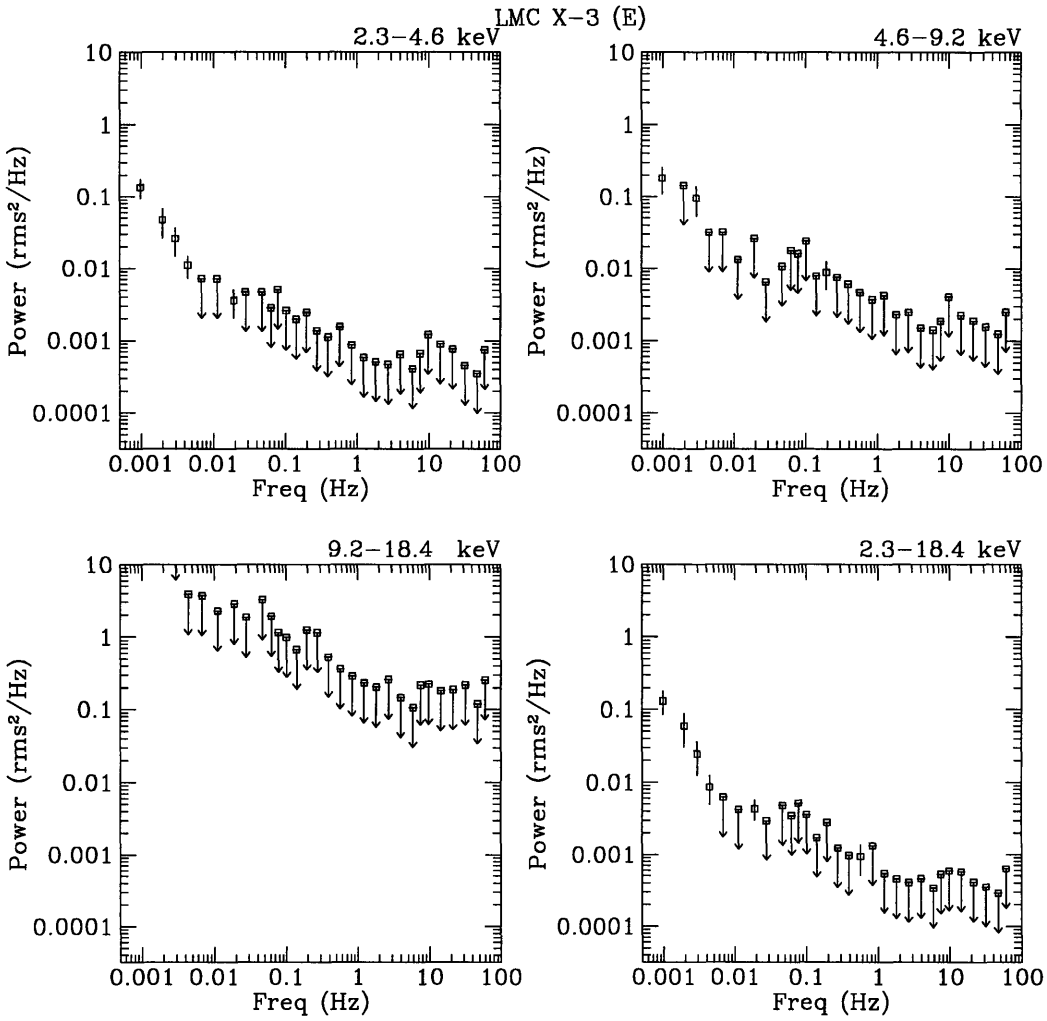

Figure 5-18: **LMC X-3 E-state Composite PDS.** The Composite PDS of LMC X-3 in the three energy ranges and the sum energy range (indicated in each panel). Corrections for background and dead time have been applied. Upper-limits are 2σ.

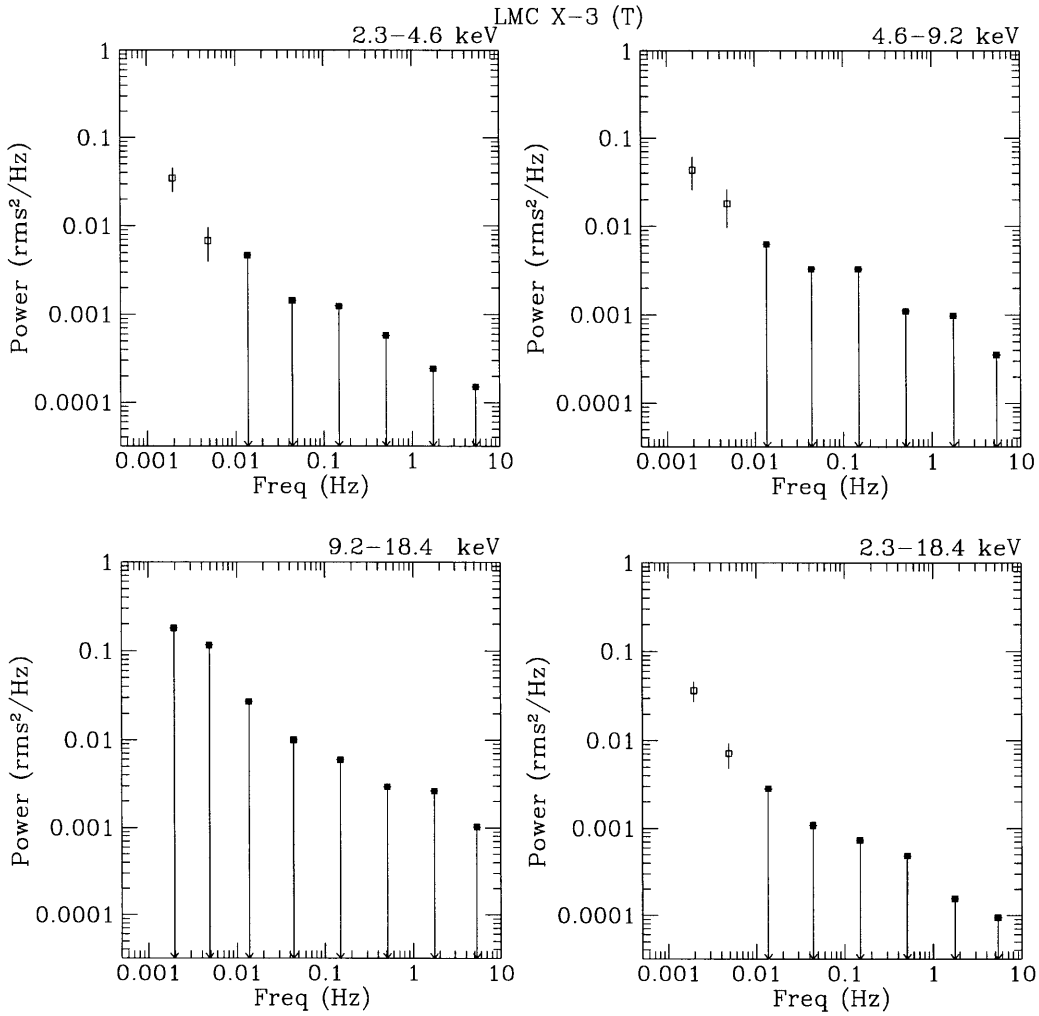

Figure 5-19: **LMC X-3 T-type PDS**. The T-type PDS of LMC X-1 in the three energy ranges and the sum energy range (indicated in each panel). Corrections for background and dead time have *not* been applied.

5.4.7 GS 1124-68

Of the measured 128 s values of the Wide Ratio for GS 1124-68 measured in Ch. 4, 80% were in the range 0.00098–0.38 (BCDEFGH-type source). Of all the sources in the present study, GS 1124-68 shows the most spectral diversity during the observations. We divided the data for Composite PDS into the spectral groups: ABCD, E, F1 (Wide Ratio=0.032–0.050), F2 (Wide Ratio=0.05–0.1), and GH. We produced T-type PDS for each of these spectral ranges, for comparison with the Composite PDS.

In Fig. 5-20, we show the PDS of GS 1124-68 in the three energy bands, plus the intensity band, while the source occupied the spectral states A, B, C and D (Wide Ratio=0.0001–0.01). The PDS is an average of 8 Low-Frequency FFTs, 315 Medium-Frequency FFTs, and 2266 High-Frequency FFTs. The data have been corrected for dead time and background.

In Fig. 5-21, we show the PDS of GS 1124-68 in the three energy bands, plus the intensity band, while the source occupied the spectral state E (Wide Ratio=0.01–0.032). The PDS is an average of 16 Low-Frequency FFTs, 487 Medium-Frequency FFTs, and 1203 High-Frequency FFTs. The data have been corrected for dead time and background.

In Fig. 5-22, we show the PDS of GS 1124-68 in the three energy bands, plus the intensity band, while the source occupied the spectral state F1 (Wide Ratio=0.032–0.05). The PDS is an average of 3 Low-Frequency FFTs, 169 Medium-Frequency FFTs, and 870 High-Frequency FFTs. The data have been corrected for dead time and background.

In Fig. 5-23, we show the PDS of GS 1124-68 in the three energy bands, plus the intensity band, while the source occupied the spectral state F2 (Wide Ratio=0.05–0.1). The PDS is an average of 1 Low-Frequency FFTs, 83 Medium-Frequency FFTs, and 535 High-Frequency FFTs. The data have been corrected for dead time and background.

In Fig. 5-24, we show the PDS of GS 1124-68 in the three energy bands, plus the intensity band, while the source occupied the spectral state F2 (Wide Ratio=0.1-1.0). The PDS is an average of 2 Low-Frequency FFTs, 83 Medium-Frequency

FFTs, and 524 High-Frequency FFTs. The data have been corrected for dead time and background.

In Fig. 5-25, we show the T-type PDS of GS 1124-68 in the three energy bands, plus the intensity band, while the source occupied the spectral states ABCD (Wide Ratio=0.0001–0.01). The PDS are averaged from 30 FFTs. The data have been corrected for dead time and background.

In Fig. 5-26, we show the T-type PDS of GS 1124-68 in the three energy bands, plus the intensity band, while the source occupied the spectral states ABCD (Wide Ratio=0.01–0.032). The PDS are averaged from 41 FFTs. The data have been corrected for dead time and background.

In Fig. 5-27, we show the T-type PDS of GS 1124-68 in the three energy bands, plus the intensity band, while the source occupied the spectral states F (Wide Ratio=0.032–0.1). The PDS are averaged from 18 FFTs. The data have been corrected for dead time and background.

In Fig. 5-28, we show the T-type PDS of GS 1124-68 in the three energy bands, plus the intensity band, while the source occupied the spectral states GH (Wide Ratio=0.1–1.0). The PDS are averaged from 7 FFTs. The data have been corrected for dead time and background.

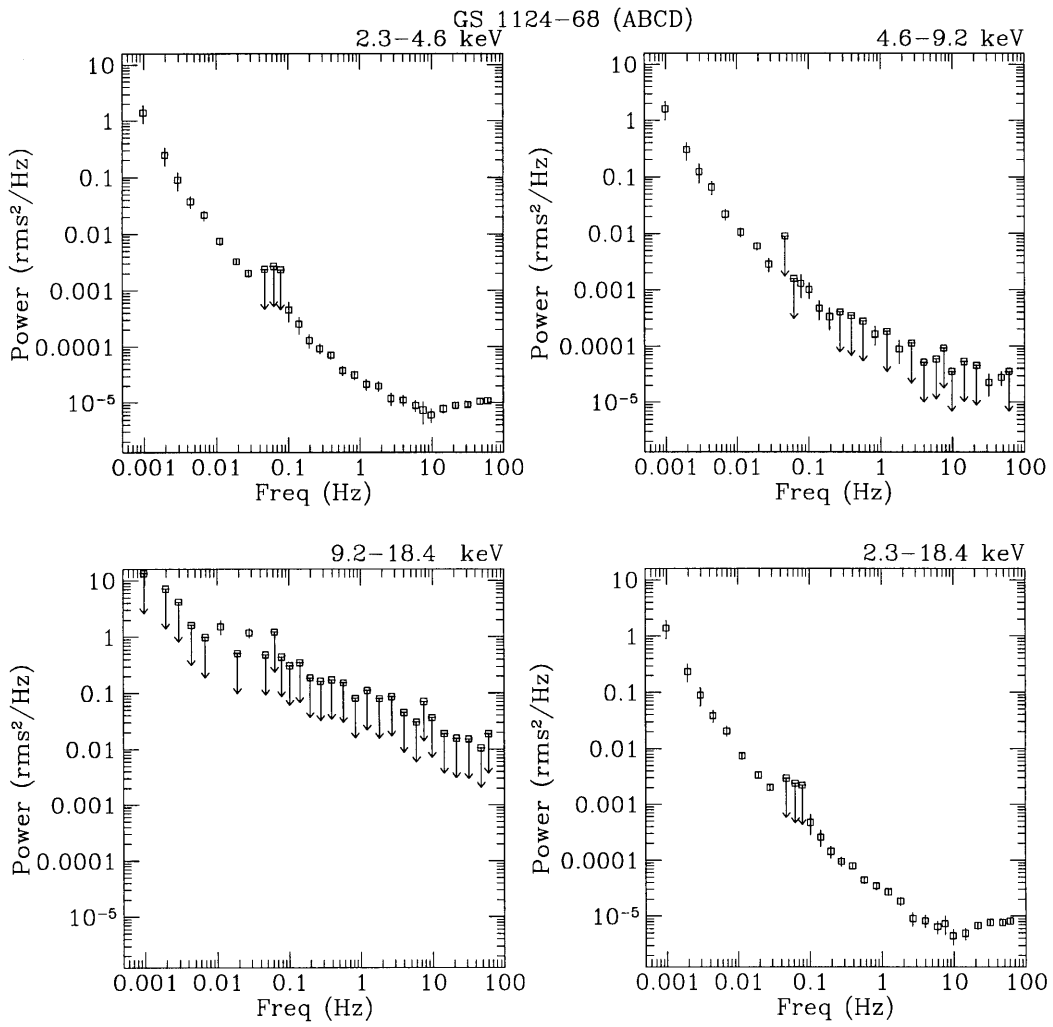

Figure 5-20: **Energy Dependence of PDS in GS 1124-68, ABCD spectral states.** The PDS of GS 1124-68 in the three energy ranges, while the source is in the spectral states A, B, C and D. Corrections to the %rms for background and dead time have been applied.

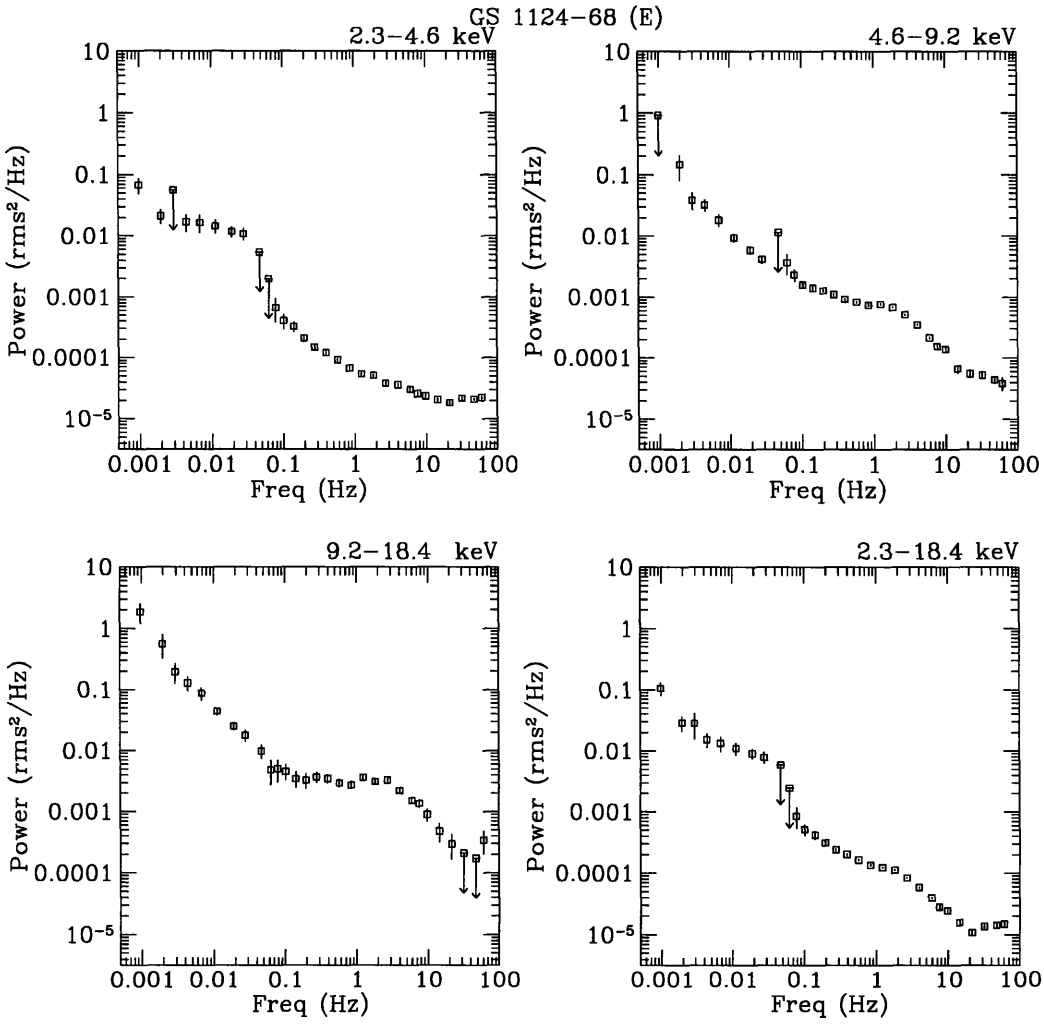

Figure 5-21: **Energy Dependence of PDS in GS 1124-68, E spectral states.** The PDS of GS 1124-68 in the three energy ranges, while the source is in the spectral state E. Corrections to the %rms for background and dead time have been applied.

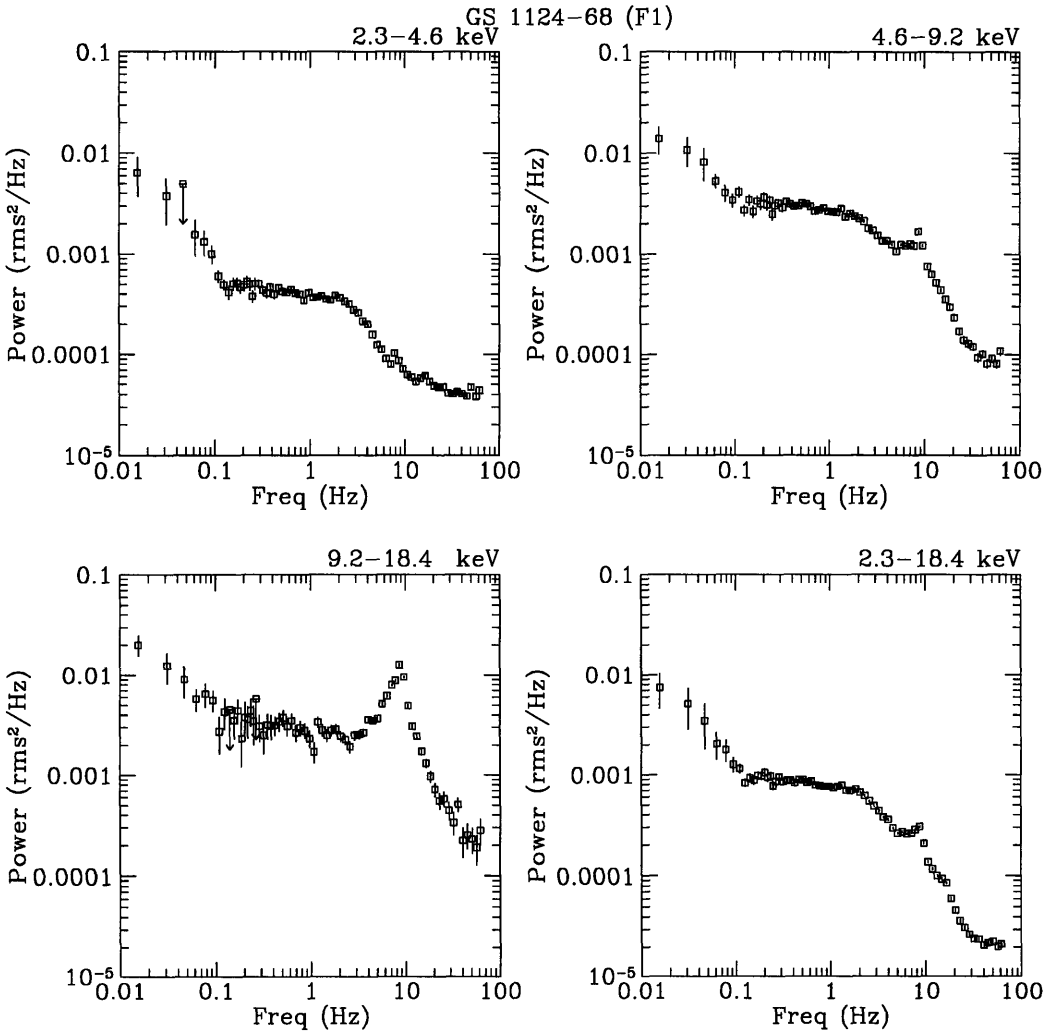

Figure 5-22: **Energy Dependence of PDS in GS 1124-68, F1 spectral states.** The PDS of GS 1124-68 in the three energy ranges, while the source is in the spectral state F1. Corrections to the %rms for background and dead time have been applied.

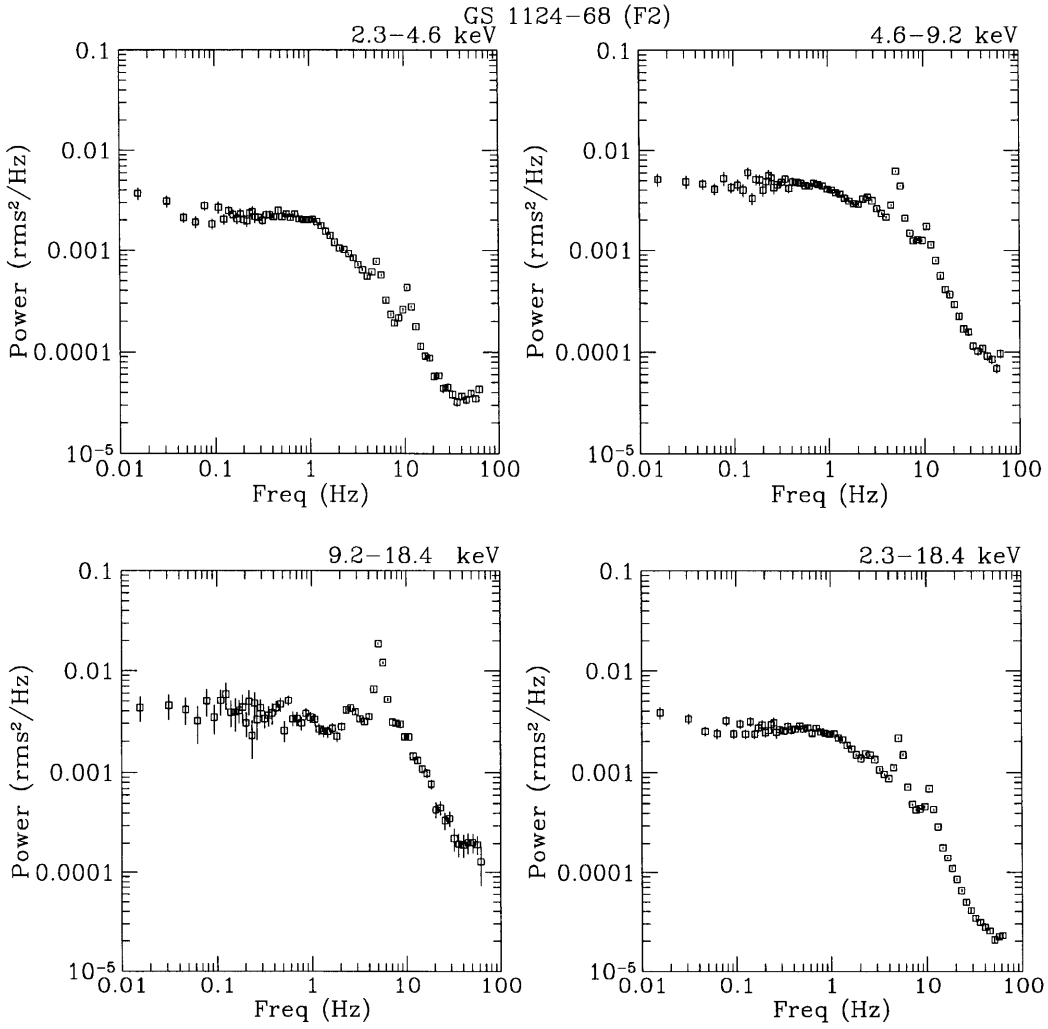

Figure 5-23: **Energy Dependence of PDS in GS 1124-68, F2 spectral states.** The PDS of GS 1124-68 in the three energy ranges, while the source is in the spectral state F2. Corrections to the %rms for background and dead time have been applied.

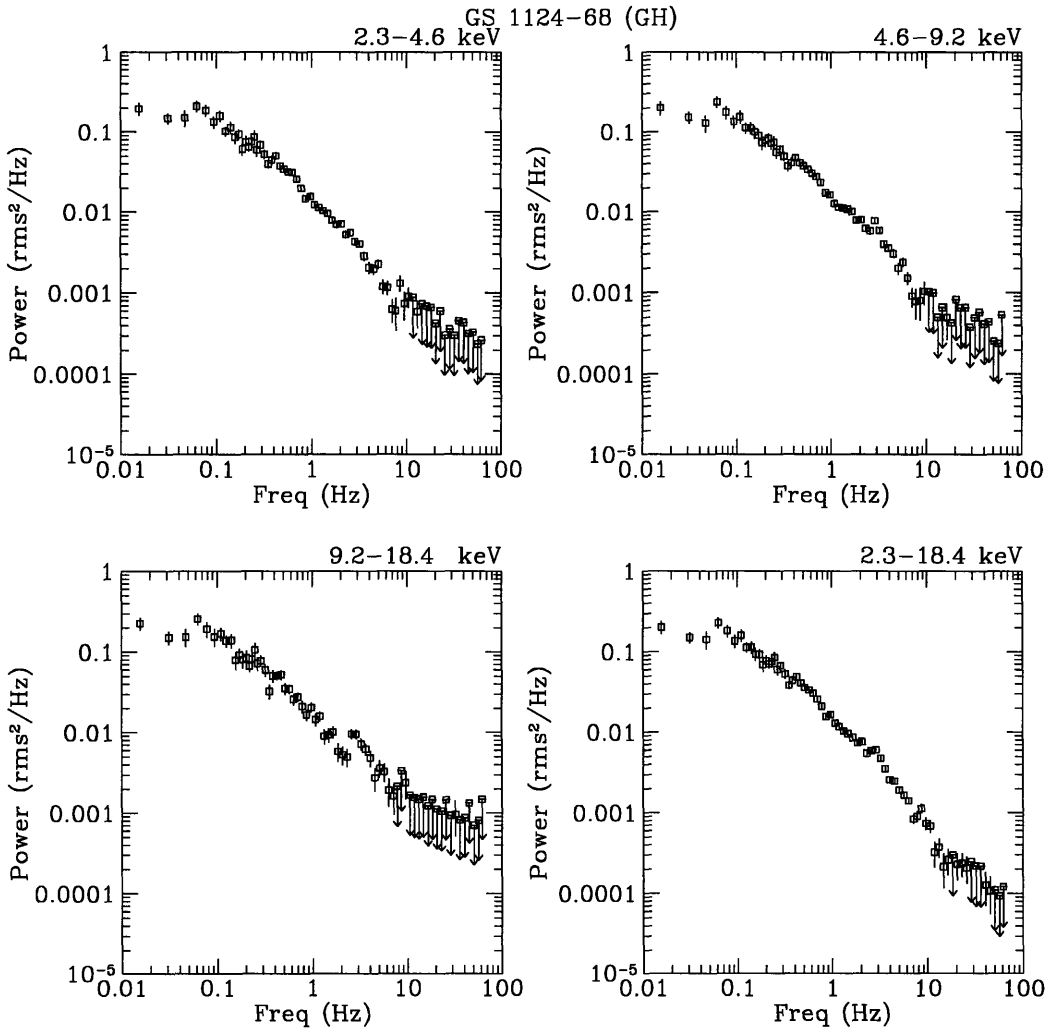

Figure 5-24: **Energy Dependence of PDS in GS 1124-68, GH spectral states.** The PDS of GS 1124-68 in the three energy ranges, while the source is in the spectral state GH. Corrections to the %rms for background and dead time have been applied.

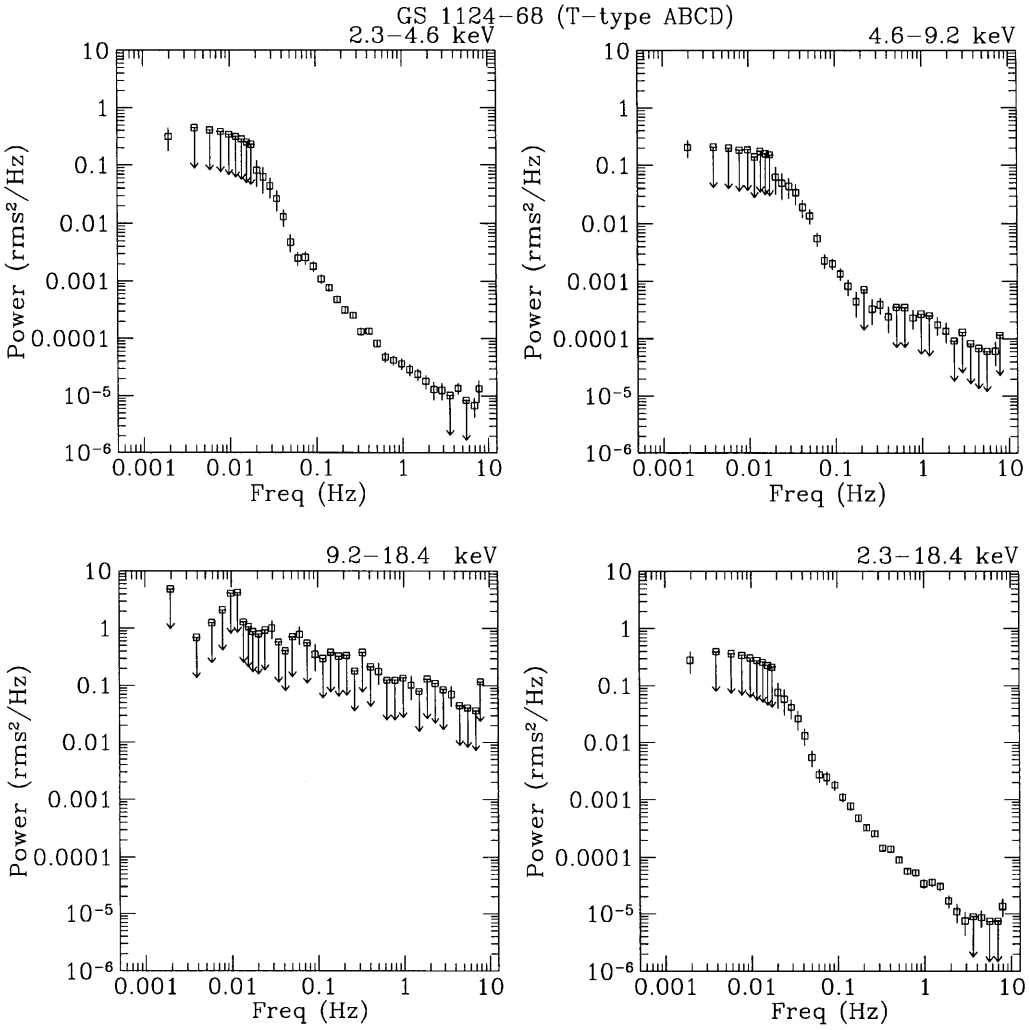

Figure 5-25: **Energy Dependence of PDS in GS 1124-68, T-type, ABCD spectral states**. The T-type PDS of GS 1124-68 in the three energy ranges, while the source is in the spectral states ABCD. Corrections to the %rms for background and dead time have been applied.

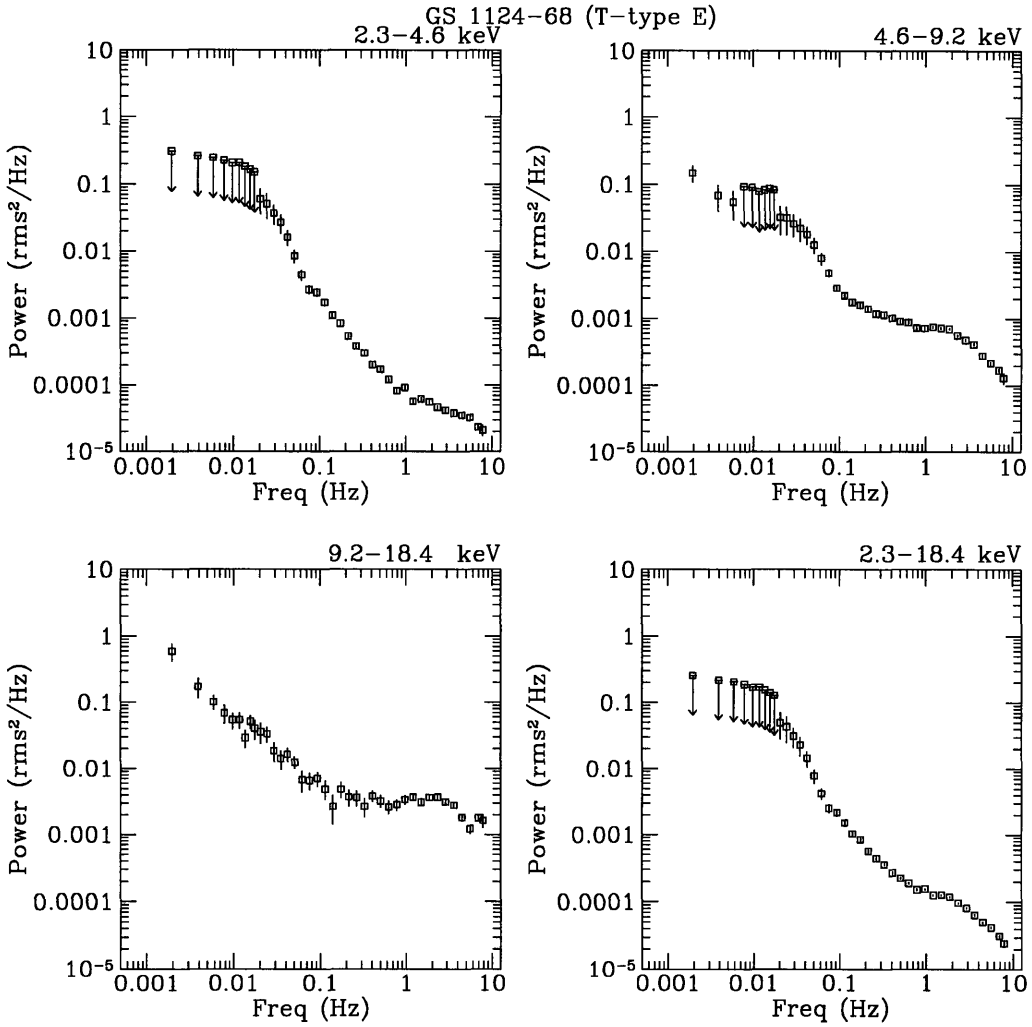

Figure 5-26: **Energy Dependence of PDS in GS 1124-68, T-type, E spectral states.** The T-type PDS of GS 1124-68 in the three energy ranges, while the source is in the spectral states E. Corrections to the %rms for background and dead time have been applied.

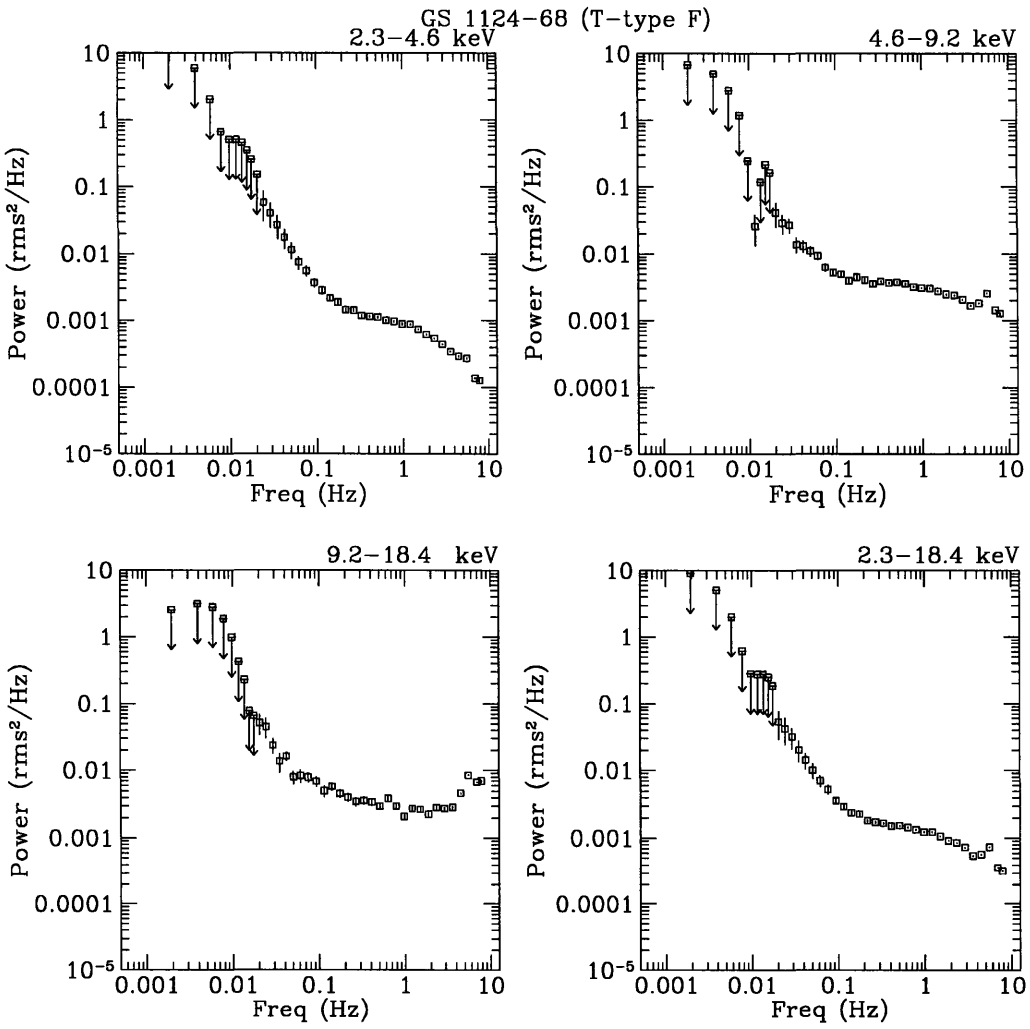

Figure 5-27: **Energy Dependence of PDS in GS 1124-68, T-type, F spectral states.** The T-type PDS of GS 1124-68 in the three energy ranges, while the source is in the spectral states F. Corrections to the %rms for background and dead time have been applied.

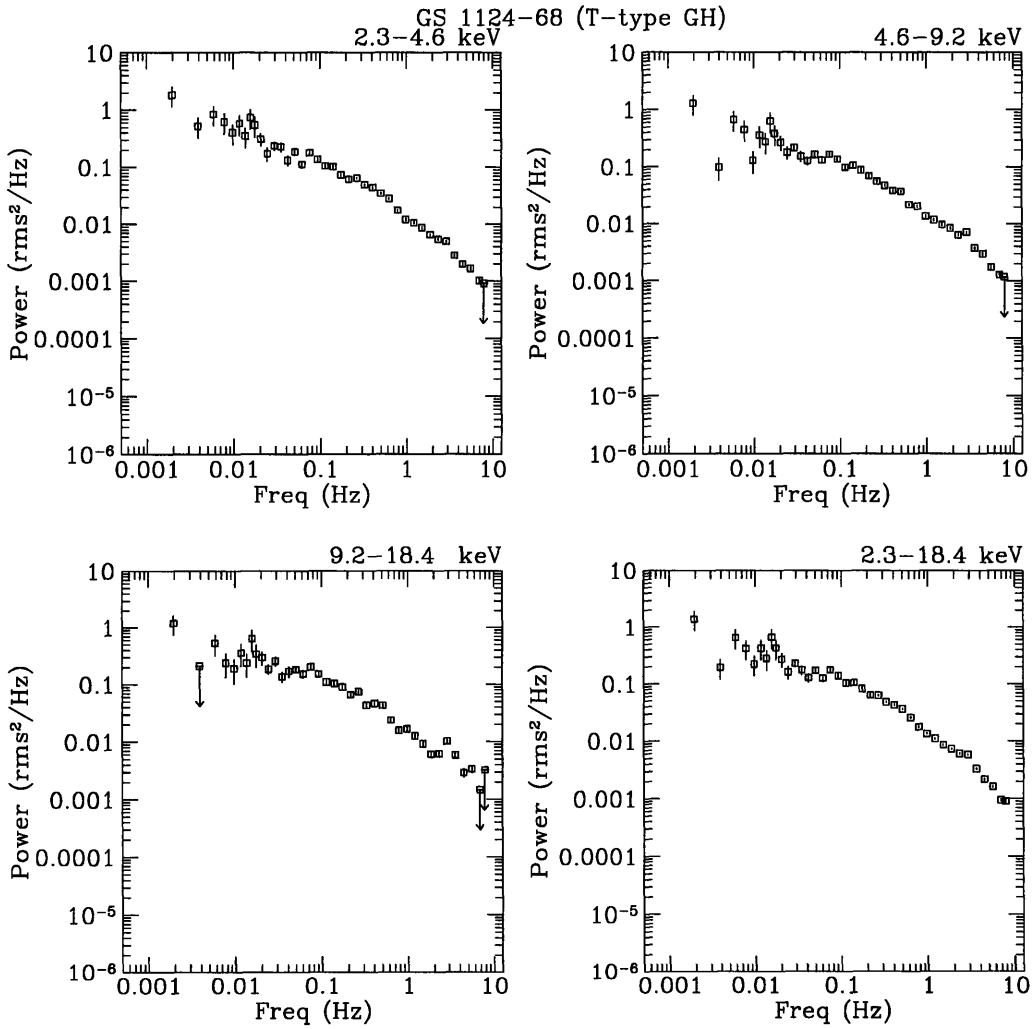

Figure 5-28: **Energy Dependence of PDS in GS 1124-68, T-type, GH spectral states.** The T-type PDS of GS 1124-68 in the three energy ranges and the Intensity Range, while the source is in the spectral states GH. Corrections to the %rms for background and dead time have been applied.

In comparing the Composite PDS with the T-type PDS, a number of discrepancies are evident. In the PDS covering the ABCD spectral range, the Composite PDS shows a power-law dependency, down to ~0.001 Hz; in the T-type PDS, the PDS shows evidence of flattening at frequencies below 0.01 Hz. In the Composite PDS of the E-state data, we see that the shapes of the PDS are energy dependent; the Low Energy Range PDS is flat below ~0.1 Hz, while the Medium Energy Range and High Energy Range PDS both rise in a power-law. Above 0.1 Hz in the Low Energy Range the PDS follows a power-law (flattening to a constant, due to the very high dead time during these observations, outside the regime where the Poisson-level can be accurately calculated).

It is apparent that the spectral-binning used to produce the PDS are too coarse, and finer binning is necessary. To achieve this, we note that in Ch. 4, the time-evolved Wide Ratio value shows little evolution over single observational epochs. We thus adopted the method of producing PDS over single observational epochs, and comparing the properties of the PDS as a function of the averaged Wide Ratio, which we perform in Sec. 5.4.7.

PDS of QPO, by Spectral State

In Fig. 5-29, we show the 20 PDS (all High-Frequency), re-binned linearly to focus on the 1-15 Hz range, with the power on the same scale to show the relative importance of various features in distinct spectral states, and at different energies. These data are the same as that used in Figs. 5-20 – 5-24 in the High-Frequency range. The BB and QPO power typically increase with increasing energy, as is most evident in panels F1 and F2.

In Fig. 5-30, we show the 20 PDS (all High-Frequency), re-binned linearly to focus on the 1-15 Hz range, with the power scaled arbitrarily (normalized to rms^2/Hz)to allow the important features of each individual PDS to be visible. These data are the same as that used in Figs. 5-20 – 5-24 in the High-Frequency range, and in Fig. 5-29. The magnitude of the QPO increases relative to the BB power, demonstrating that the QPO is spectrally harder than the BB variability.

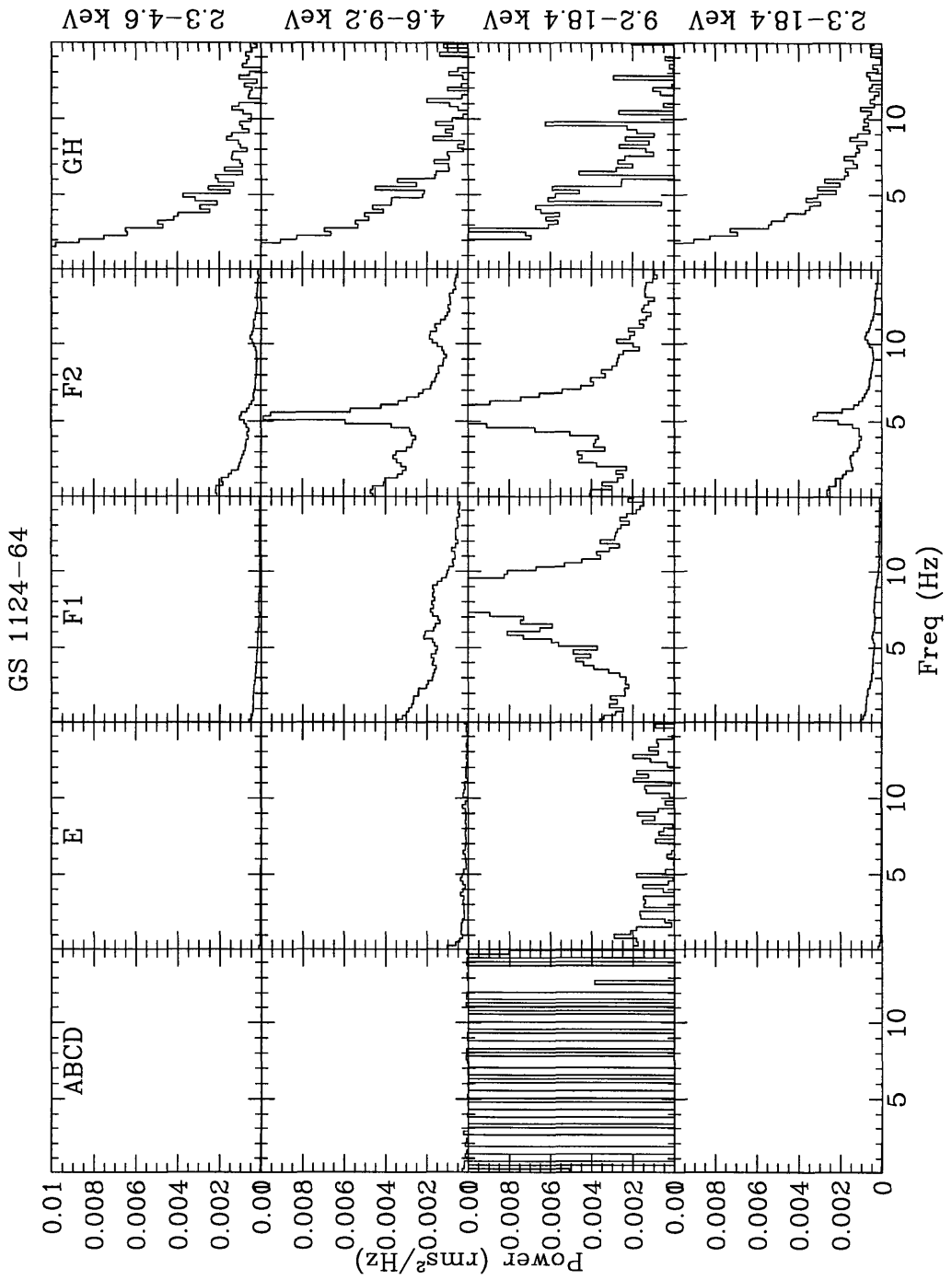

Figure 5-29: **Energy and Spectral Dependence of PDS for GS 1124-68.** 20 PDS for GS 1124-68, in the spectral states ABCD, E, F1, F2, and GH (marked at the top of each column), each in the three energy ranges and intensity range (marked by row). The Power is in rms^2/Hz; all PDS are set to the same scale, so that the relative power in each energy range and each spectral state can be directly compared.

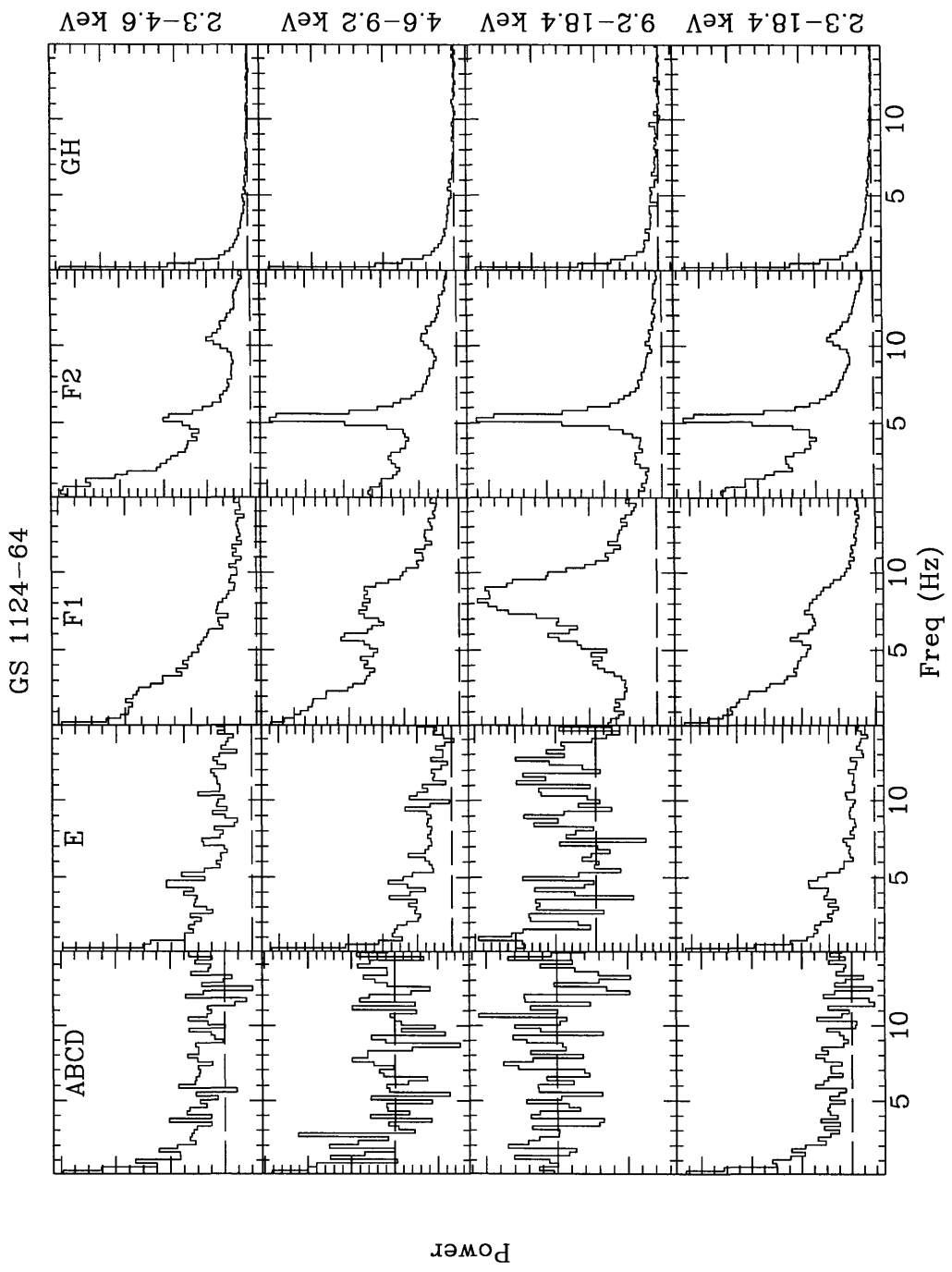

Figure 5-30: **Energy and Spectral Dependence of PDS for GS 1124-68.** 20 PDS for GS 1124-68, in the spectral states ABCD, E, F1, F2, and GH (marked at the top of each column), each in the three energy ranges and intensity range (marked by row). The Power is scaled arbitrarily, to show the extremes of each individual PDS. The dashed horizontal line is at zero power.

PDS OF GS 1124-68 DIVIDED BY DAY AND SPECTRUM

The separation of PDS by observational epoch with simultaneous description of source spectrum by CCD and HID has been investigated (Takizawa et al. 1996), although the energy dependent characteristics of the PDS were not investigated. Also, the strength of the BB component was not investigated. We focus on the dependencies of all the PDS components, as a function of Wide Ratio.

The QPO properties in the summed 1.2–18.4 keV range shown by GS 1124-68 have been examined in detail (Takizawa et al. 1996, hereafter, T96). We here re-examine these properties, using the Wide Ratio spectral indicator, and in our three energy ranges, as well as the Intensity Range. To ease comparison, we adopted the same time-periods used by T96, and the same labels for these time periods (by number 1-15), with two exceptions: 1) we did not distinguish between observation 5L and 5H (where "L" stands for periods within the trough of a flip-flop , while "H" stands for the elevated count-rate periods around the flip-flop) – they are joined under the single header "5"; also, we split observation 11 into 11a and 11b. The limit times for the data used here are listed in Table 5.12, along with the frequency range of the resultant PDS, and the mean Wide Ratio for each observation period. The uncertainty listed in the Wide Ratio is the 1σ spread.

In Fig. 5-31, we show light-curves in the Low Energy Range, Medium Energy Range, and High Energy Range, and the Wide Ratio as a function of time for the first 40 days of the GS 1124-68 outburst, which was the period during which QPO was observed. With the exception of observations 5& 11, the numbering of the points follows T96 , and indicates single observation periods, the data for which was averaged together for the present analysis.

In Fig. 5-32 we show the CCD of the average Wide Ratio vs. Hard Ratio of the 19 observational epochs currently considered. This figure can be directly compared with the CCD of all sources (Fig. 4-24). The position of each observation on the CCD is indicated by the observation number, and the spread of the Wide Ratio and Hard Ratio values are typically of the size of the observation number or smaller, with the exception of observation #18, where the spread is ~twice the value of Wide Ratio

Table 5.12: Division of GS 1124-68 Data

Observation ID	Start Time (UT)	End Time (UT)	PDS Freq Range	<Wide Ratio>
1	91/011 00:51	01:17	0.0156–8.0 Hz	0.155 ±0.004
2	91/011 19:37	20:42	0.0156–8.0	0.097 ±0.006
3	91/011 20:49	91/012 00:05	0.0156–64.0	0.092 ±0.003
4 (not used)	–	–	–	–
5	91/014 19:48	23:25	0.0156–8.0	0.054 ±0.004
6	91/016 18:46	23:27	0.0156–8.0	0.026 ±0.005
7	91/017 18:05	21:57	0.0156–8.0	0.014 ±0.001
8	91/018 17:30	21:27	0.0156–8.0	0.024 ±0.003
9	91/020 15:17	17:15	0.0156–8.0	0.027 ±0.001
10	91/022 17:18	20:09	0.0156–64.0	0.058 ±0.004
11a	91/025 12:48	13:10	0.0156–64.0	0.036 ±0.001
11b	91/025 13:46	13:56	0.0156–64.0	0.044 ±0.001
12	91/036 10:34	11:07	0.0156–64.0	0.027 ±0.002
13	91/037 10:05	12:13	0.0156–64.0	0.029 ±0.001
14	91/044 05:04	08:38	0.0156–8.0	0.024 ±0.004
15	91/045 06:11	08:10	0.0156–64.0	0.013 ±0.001
16	91/051 23:29	91/053 04:32	0.0156–64.0	0.0093 ±0.0017
17	91/056 20:56	91/058 00:19	0.0156–64.0	0.0068 ±0.0007
18	91/067 14:28	91/109 20:13	0.0156–64.0	0.0009 ±0.0007
19	91/137 03:12	91/204 21:04	0.0156–64.0	0.3995 ±0.1578

and Hard Ratio of its location. As the numbers follow chronological order, we can follow the source along its track over the range of its observational period. Beginning with observation 1, the Wide Ratio decreases monotonically through observation 7 (Wide Ratio$\sim$0.015), where it increases through observation 10, decreasing to 11a, increasing to 11b, and then again decreasing through to the observational epoch 18, finally hardening in the final observational epoch 19 (indeed, epochs 18 and 19 were separated on the basis of this hardening).

We show the complete Composite PDS used for fitting in Figs. 5-33, 5-34, 5-35, & 5-36. Each column corresponds to a different observational epoch (labeled at the top of each column), while each row corresponds to a different energy range of data from which the PDS are taken (labeled to the far right of each row). All power has been corrected for background and dead time; however, as we found previously,

the high count-rates during some of these observations make the dead time corrected Poisson level approximation inadequately accurate, resulting in additional constant components which are apparent at high-frequencies (where the source variability is low).

As found previously (T96), QPO is detected during observations 1, 2, 3, 5, 10, 11b, and 15. As we show in Fig. 5-46, the QPO during observation 11 appears only in the second half. In Fig. 5-37, we show the PDS with the detected QPO, in the three energy ranges. The QPO %rms increases with increasing energy, for each observation (except observation 15, where the S/N is too low in the High Energy Range to demonstrate this).

In Fig. 5-38, we show the best fit QPO centroid frequency of the fundamental (first harmonic) as a function of the intensity in the Low Energy Range, Medium Energy Range, High Energy Range, and of the Wide Ratio. Each point is marked with its corresponding observation number. The upper-limits in the figure connote intensity or Wide Ratio values where no QPO was found. In the Low Energy Range- and Medium Energy Range (panels a and b), the centroid frequency is a complex function of intensity. In the High Energy Range (panel c), during observations 1-3 and 5, the centroid frequency increases from 3.0, to 5.0, to 7.0 Hz, while the 9.2–18.4 keV intensity is roughly constant ($\sim$1900-2100 c/s). In observations 6-9, the intensity is lower, and no QPO is observed. In observation 10, the 9.2-18.4 keV intensity is back up to 1780 $\pm$100 c/s, and the QPO has re-appeared at 8.0 Hz. In observation 11, the intensity dropped to $\sim$1400 c/s, and the QPO centroid frequency also decreased to 6 Hz. In observations 12-14, the intensity was again lower, but no QPO was detected. In observation 15, at a count-rate of $\sim$140 c/s, QPO with a centroid frequency of $\sim$4.5 Hz was detected.

In Table 5.13, we list the centroid frequency, FWHM, and %rms of the fundamental QPO in each PDS in which QPO was identified by T96. In addition, we find (weak) QPO in Observation # 8 and 11a. The fundamental was identified for each observation as that QPO peak with the greatest %rms in the 9.2–18.4 keV range, or, if none are identified, in the 4.6–9.2 keV range.

For each fit, we adopted one of several possible broad-band models to account for the continuum power: Power-Law, Double Power-Law, Flat-Top with Double-Power-Law, or Double-Flat-Top with Double Power-Law. The model employed for a given observation period was typically that which best fit the PDS of 2.3–18.4 keV; parameters of these models were then adjusted or fixed to describe the PDS of the three energy ranges. There are several instances where the model parameters are unconstrained; the parameters which determine the frequency dependence (but not the % rms) were then fixed to either the value obtained in the 2.3–18.4 keV PDS or from the PDS of an adjacent energy range.

The QPO was fit as a series of harmonics, with frequencies and FWHM values which are factors of 0.25, 0.5, 1.0, 2.0, and 4.0 of those of the fundamental (which was chosen as that frequency with the highest detectable %rms variability in the highest possible energy range). Thus, the centroid frequency and the FWHM quoted can be dependent upon the harmonic QPO. Typically, only the sub-Harmonic at 0.5 ν_c and the second Harmonic at 2 ν_c were invoked (permitting the best-fit value of the %rms in each to be determined), as the 0.25 ν_c Harmonic could have significant covariance with the broad-band power, and $4\nu_c$ was often above the Nyquist frequency (the highest frequency of the PDS). For a few, however, three or four harmonics were found to produce significant %rms values.

In general, the fits were good to poor, with χ^2_ν of 1-3. Of these, the worst was the 2.3–18.4 keV PDS of Observation 3, with χ^2_ν= 7.52 (68 dof). A closer-look at this PDS shows that the detailed shape of the QPO is highly inconsistent with simple Harmonic Lorentzians; when the FWHM of the 0.25, 0.5, and 2.0 ν_c harmonics are permitted to vary, the χ^2_ν decreases to 3.38 (65 dof).

In all cases, the %rms of the fundamental increases with increasing energy range.

We present some general results of the detailed PDS best-fits in Fig. 5-39. In panels *a*, *b* and *c*, points from the same observation period are labeled by their ID, and connected by lines. In panel *a*, we show the %rms as a function of energy for the broad-band PDS component (*e.g.* Single-Power Law, Flat-Top Double Power-

Law) for those observations in which QPO was identified. Generally, the broad-band power increases between the Low Energy Range and Medium Energy Range, and then *decreases or remains constant* (with the exception of observation 3) between the Medium Energy Range and High Energy Range. In panel *b* we see that for those observations where there was no QPO identified, the broad-band %rms increases continuously from the Low Energy Range through the High Energy Range.

In panel *c*, we show that the %rms of the QPO itself increases as a function of energy. On average, the %rms of the QPO increases with increasing energy. The QPO %rms variability has been investigated previously, and it was found that the %rms variability as a function of energy flattens out in the 10-20 keV energy range (Dotani 1992).

In panel *d*, we show the mean broad-band %rms for all observations when QPO is present (solid line) and when QPO is absent (broken line) as a function of energy. In the Low Energy Range and Medium Energy Range the broad-band power is considerably larger when QPO is present than when QPO is absent (compare 9.8±0.1 and 18.3±0.5 %rms with 2.8±0.05 and 10.0±0.2 %rms). However, in the High Energy Range, the variability is comparable (15.4±0.8 %rms with QPO, 17.1±0.4 %rms without).

There are at least two ways one could physically interpret this. First, the mechanism or realization of QPO at high energies (in the High Energy Range) may act as a "source" for broad-band variability at lower energies (in the Low Energy Range and Medium Energy Range); thus, the presence of QPO activates broad-band variability at lower energies. This interpretation predicts that stronger QPO at high energies should cause stronger broad-band variability at lower energies. Second, the QPO itself may act as a resonant "sink" of variability in the High Energy Range; for instance, if we think of the variability (both broad-band and QPO) as indicating geometric variability of an accretion disk (that is, "shaking"), and the photon energy as a monotonic indicator of the location of the variability, then we might expect some correlation between the resonant frequency and photon energy.

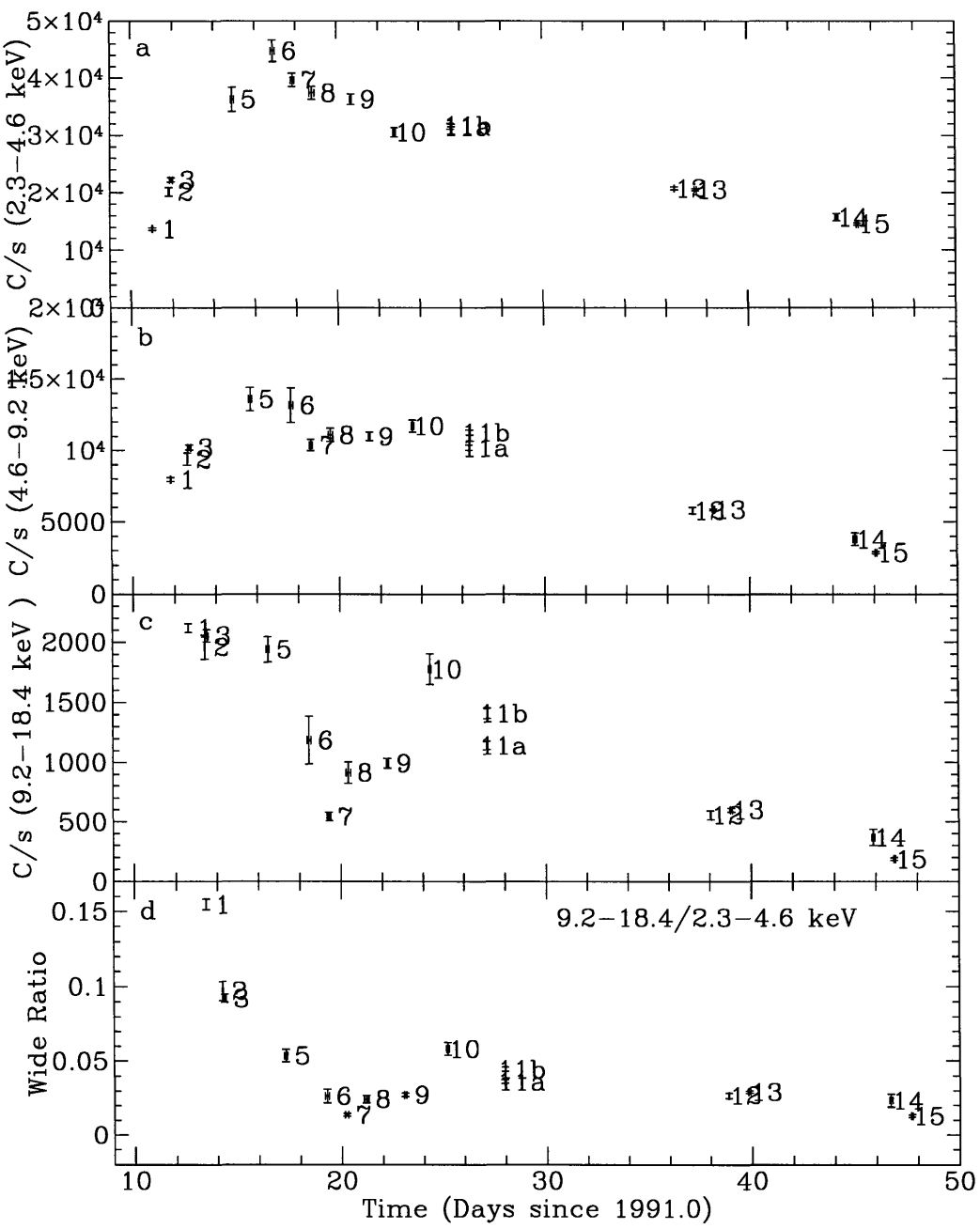

Figure 5-31: **40-day LC's and Wide Ratio vs. Time for GS 1124-68.** Lightcurves and hardness ratio for first 40 days of GS 1124-68 outburst. **(a)** 2.3–4.6 keV lightcurve; **(b)** 4.6–9.2 keV lightcurve; **(c)** 9.2–18.4 keV lightcurve; **(d)** Wide Ratio vs. time. All count-rates are corrected for aspect, background, and dead time. The numbering follows T96.

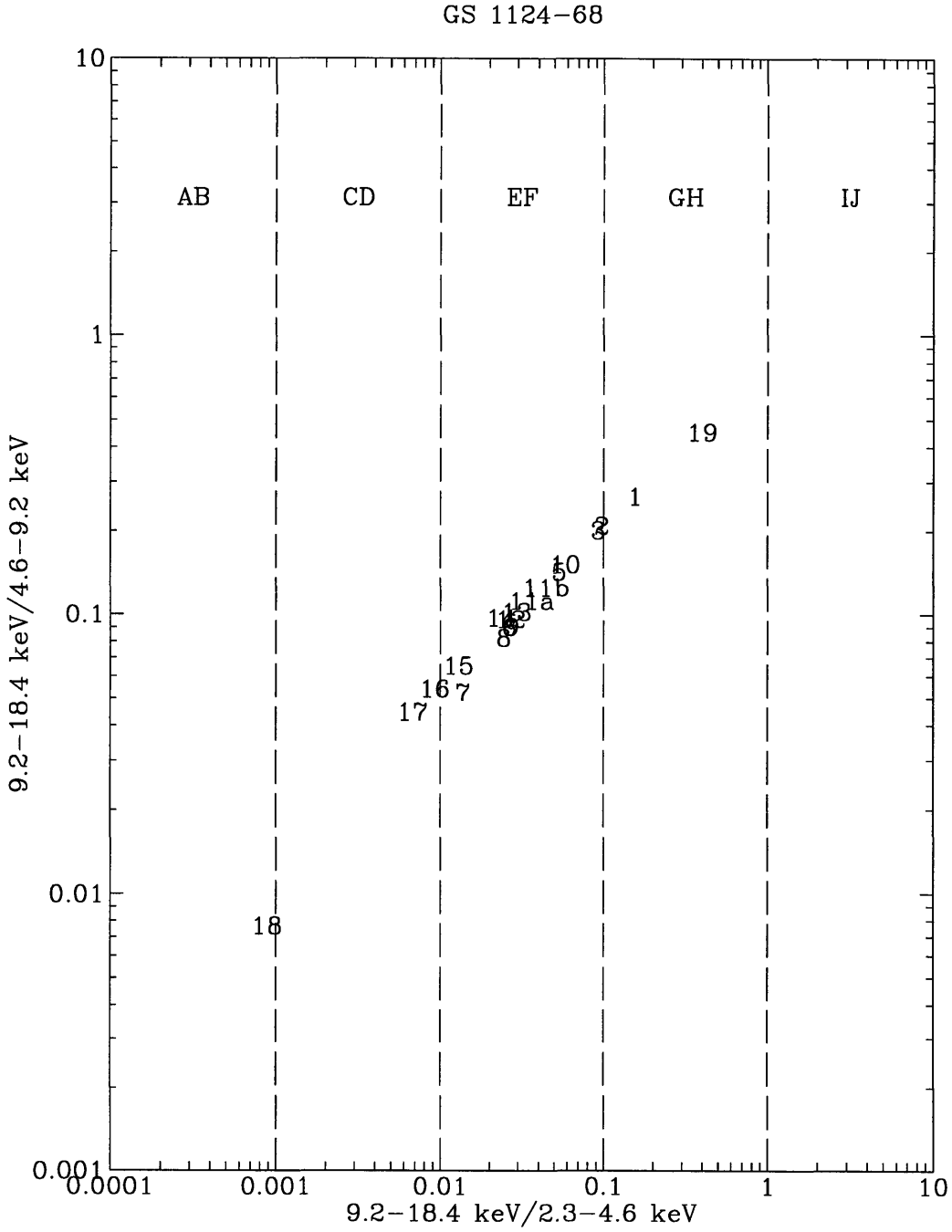

Figure 5-32: **Wide Ratio vs. Hard Ratio CCD for 19 Observation periods, GS 1124-68.** The spread of each point is typically the size of the number marking each point, except for #18, where it is ∼2× the Wide Ratio and Hard Ratio values of the point. The number (1-15) follows T96 with 16-19 added (as indicted in Table 5.12). This figure may be directly compared to Fig. 4-24

.

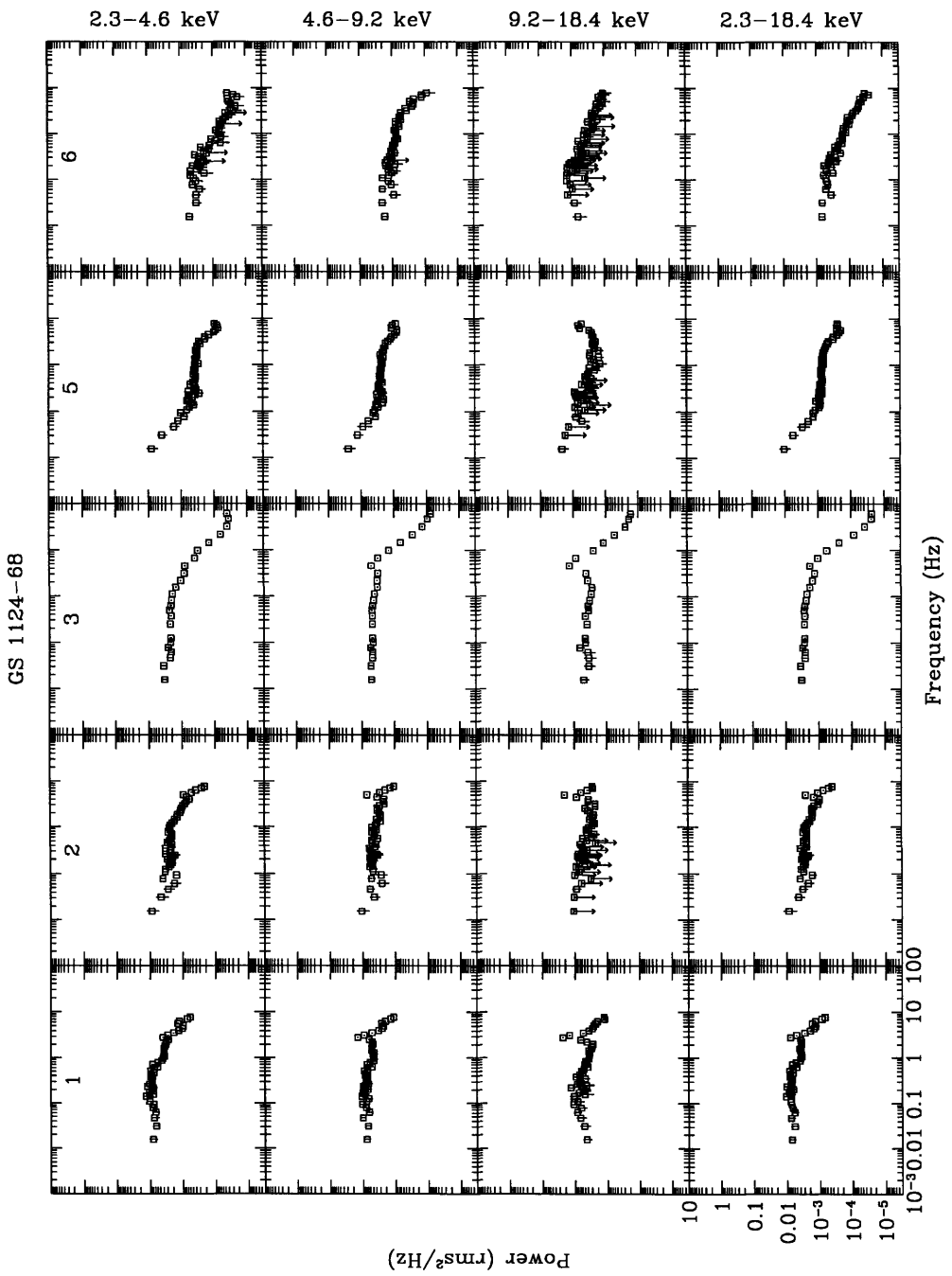

Figure 5-33: **Composite PDS of Periods 1–6, GS 1124-68.** Observation period is indicated at the top of each column, following numbering of Table 5.12. The energy-range of the PDS are constant in each row, and are labeled on the far right. Data have been corrected for dead time and background. Upper-limits are 2σ. The scale for all panels is marked on the lower-left hand panel.

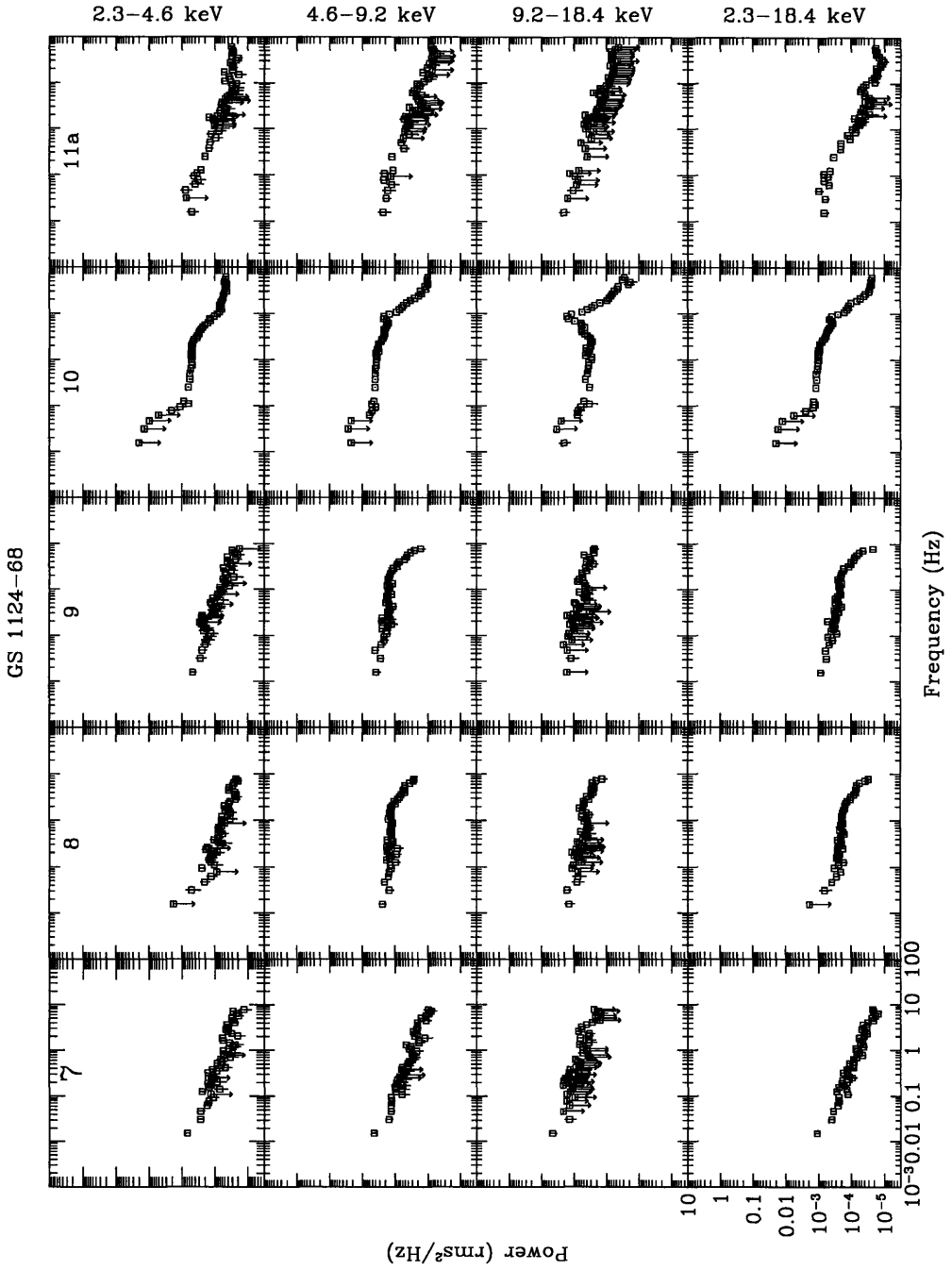

Figure 5-34: **Composite PDS of Periods 7–11a, GS 1124-68** Observation period is indicated at the top of each column, following numbering of Table 5.12. The energy-range of the PDS are constant in each row, and are labeled on the far right. Data have been corrected for dead time and background. Upper-limits are 2σ. The scale for all panels is marked on the lower-left hand panel.

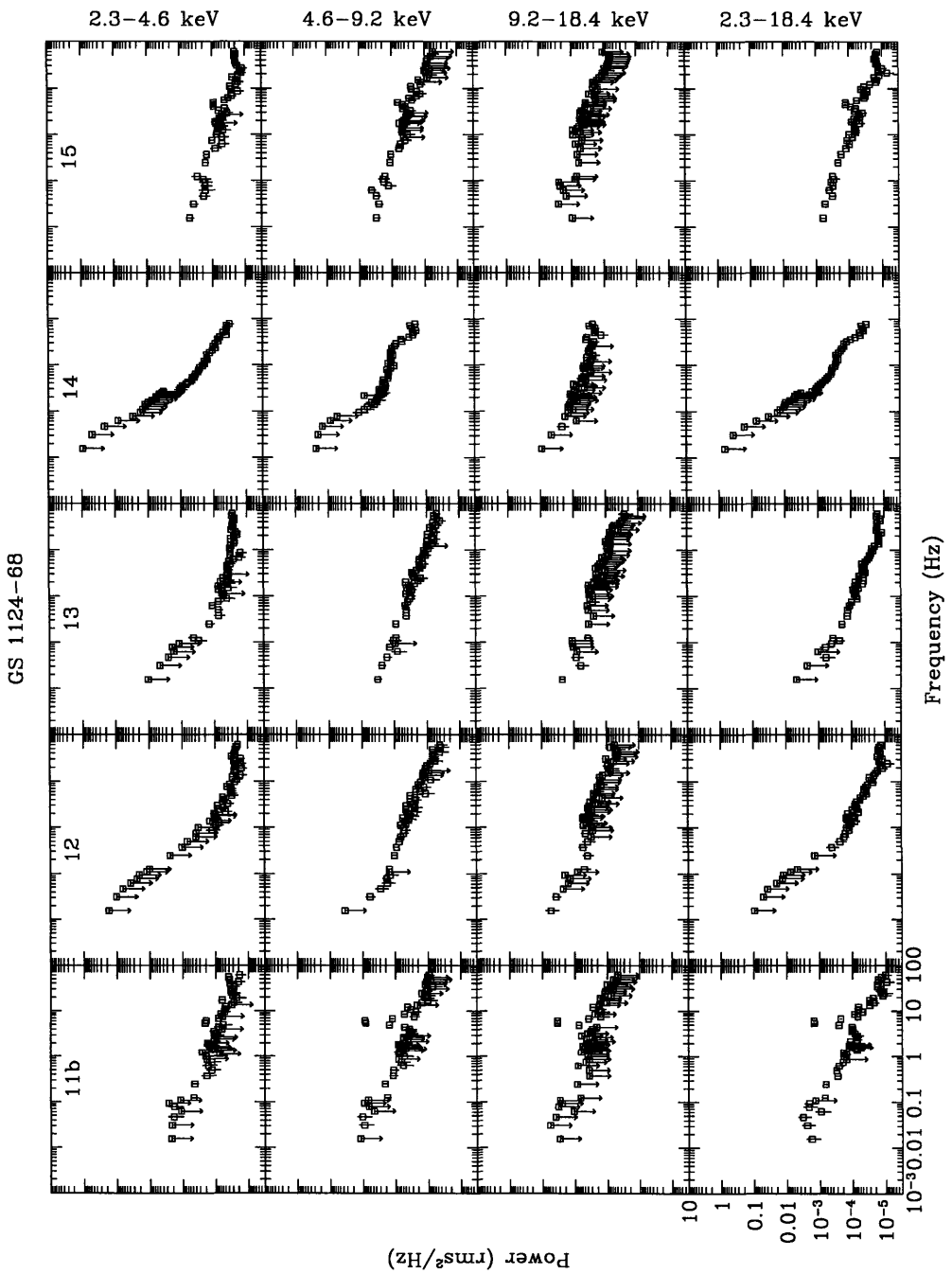

Figure 5-35: **Composite PDS of Periods 11b-15, GS 1124-68** Observation period is indicated at the top of each column, following numbering of Table 5.12. The energy-range of the PDS are constant in each row, and are labeled on the far right. Data have been corrected for dead time and background. Upper-limits are 2σ. The scale for all panels is marked on the lower-left hand panel.

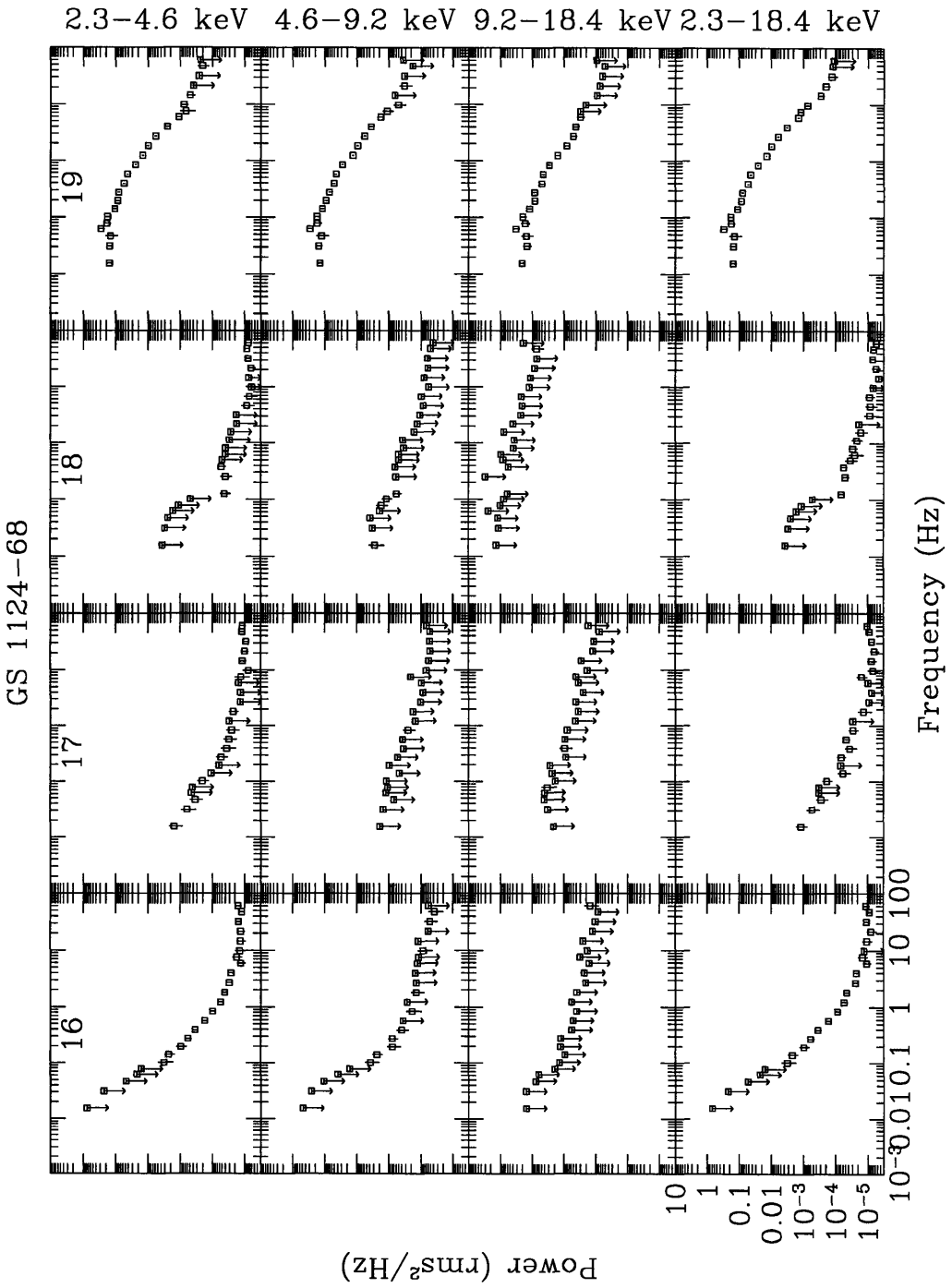

Figure 5-36: **Composite PDS of Periods 16-19, GS 1124-68** Observation period is indicated at the top of each column, following numbering of Table 5.12. The energy-range of the PDS are constant in each row, and are labeled on the far right. Data have been corrected for dead time and background. Upper-limits are 2σ. The scale for all panels is marked on the lower-left hand panel.

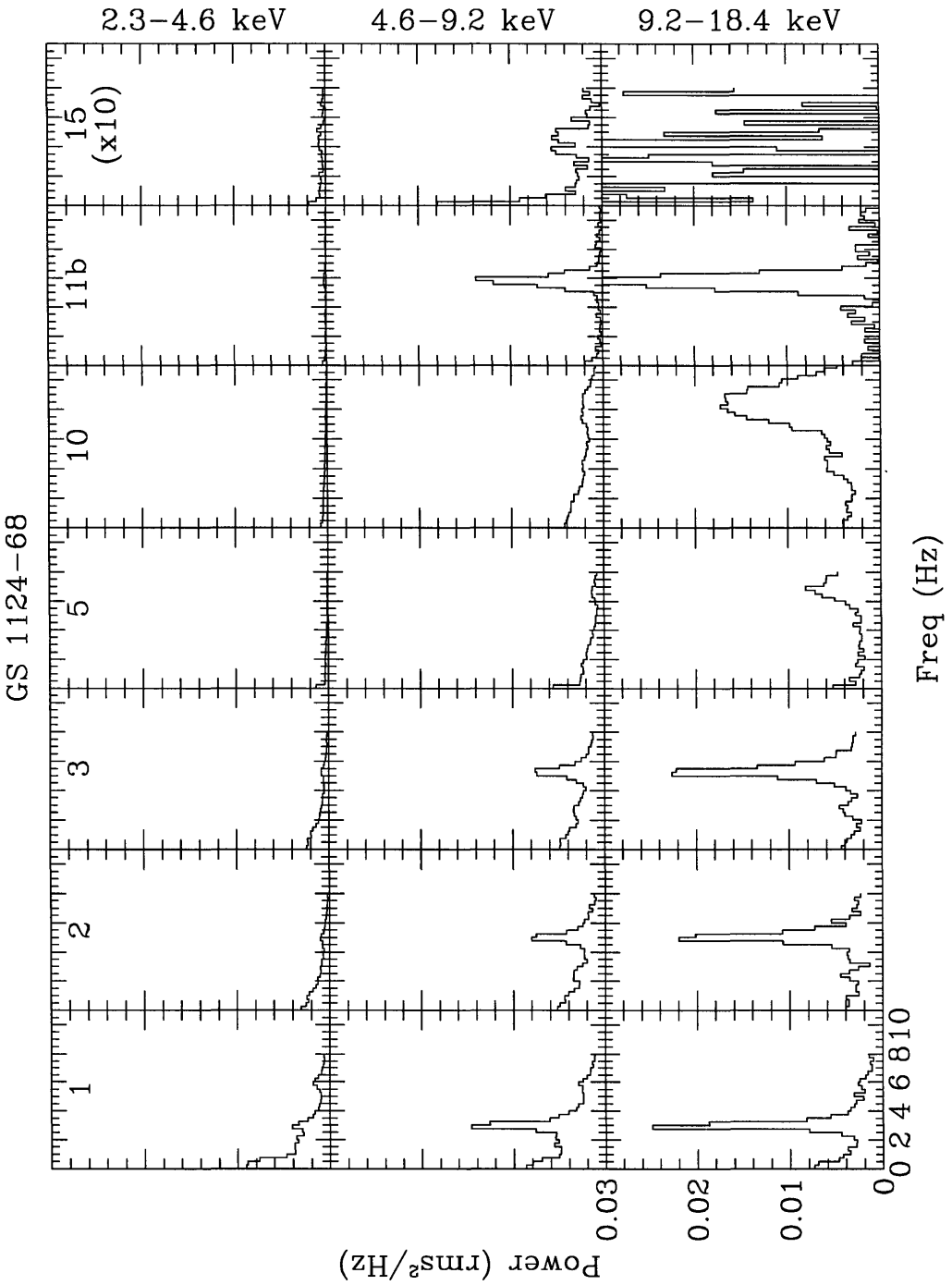

Figure 5-37: **PDS in Three Energy Ranges for 7 Different GS 1124-68 Observations.** The PDS for 7 observations (1,2,3,5,10,11b, and 15, at the top of each column) in the three energy ranges (marked on the right of each row). Power is normalized as rms^2/Hz (corrected for background and dead time), and the scale in each panel is identical to the marked panel on the bottom left, except for those of column 7 (observation 15) which have been expanded by a factor of 10. In each PDS, it is clear that the QPO power increases with increasing energy.

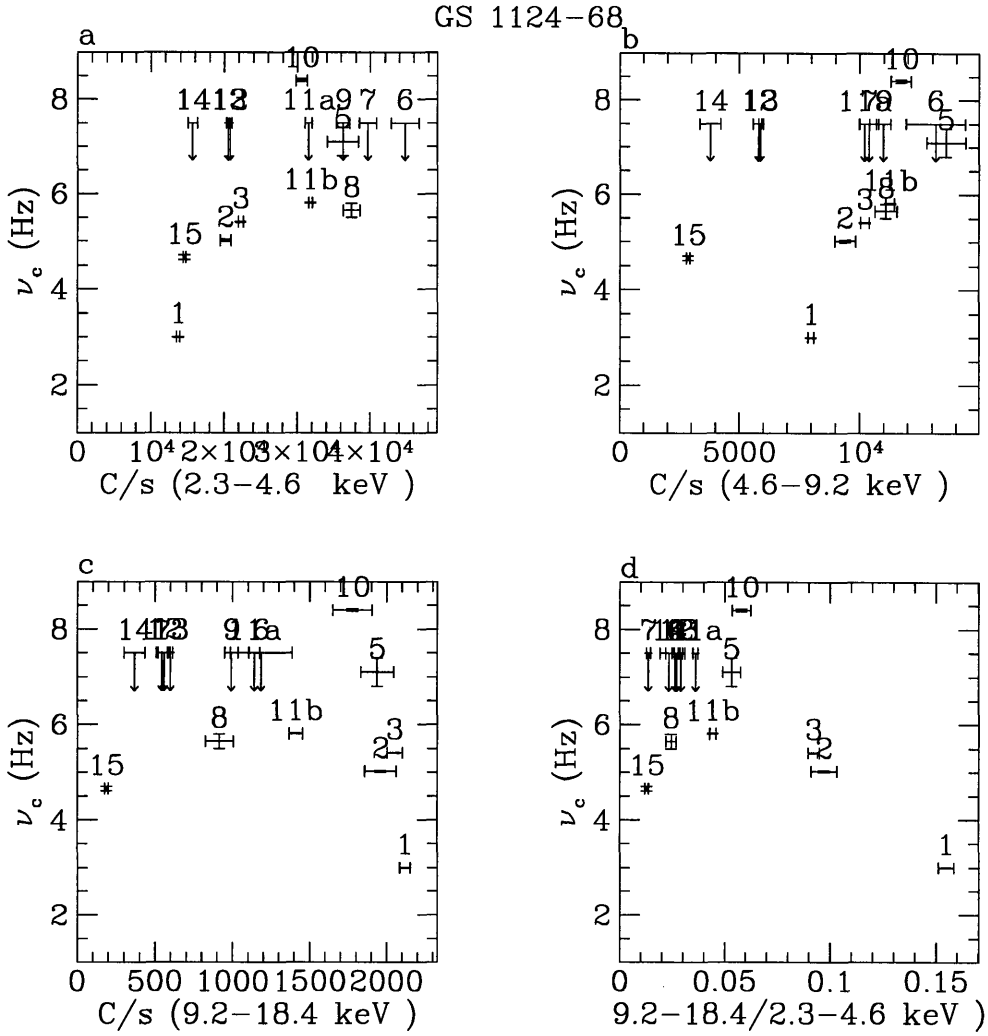

Figure 5-38: **Centroid Frequency vs. Intensity, GS 1124-68.** Best fit QPO centroid frequency vs. Intensity in the Low Energy Range, Medium Energy Range, and High Energy Range (panels a, b, and c, respectively). Panel d is the Best fit QPO centroid frequency vs. Wide Ratio. The upper-limits mark the intensity and hardness values at which no detectable QPO was found. Each point is marked 1-3, 5-15, corresponding to a single observation period. In the High Energy Range, where the QPO is strongest, the ν_c takes on a range of values while the 9.2–18.4 keV intensity is constant.

Table 5.13: GS 1124-68 QPO Fundamental Parameters

Observation ID	Energy Range (keV)	ν_c (Hz)	FWHM (Hz)	% rms	χ^2_ν (dof)
1	2.3–4.6	3.004±0.008	0.37±0.1	2.4 ±0.1	1.61 (39)
	4.6–9.2	2.98 ±0.01	0.36±0.05	4.9 ±0.2	1.24 (39)
	9.2–18.4	3.004±0.008	0.29±0.05	7.0 ±0.1	2.46 (39)
	2.3–18.4	2.98±0.001	0.50±0.06	4.0 ±0.1	1.24 (39)
2	2.3–4.6	5.02±0.05	1.02±0.2	1.6 ±0.2	1.20 (41)
	4.6–9.2	5.08±0.02	1.04±0.05	4.8±0.1	3.34 (44)
		5.07±0.02	0.80±0.04	4.8±0.1	1.99 (43)
	9.2–18.4	5.04±0.02	0.87±0.04	9.0 ±0.1	3.21 (44)
		5.02±0.02	0.69±0.04	7.9±0.2	1.99 (43)
	2.3–18.4	5.03±0.02	0.83±0.05	2.86±0.08	1.80 (41)
3	2.3–4.6	5.33±0.02	0.97±0.06	1.74±0.05	1.33 (500)
	4.6–9.2	5.325±0.008	0.69±0.03	5.4 ±0.1	1.34 (500)
	9.2–18.4	5.33±0.009	0.74±0.03	10.6±0.1	1.32 (509)
	2.3–18.4	5.329±0.007	0.82±0.03	3.19±0.05	1.80 (501)
5	2.3–4.6	(7.38)	(2.46)	<0.80	1.56 (43)
	4.6–9.2	6.82±0.09	$1.7^{+0.4}_{-0.6}$	2.4±0.4	1.64 (41)
	9.2–18.4	(7.38)	(2.46)	9.2±0.2	1.97 (46)
	2.3–18.4	7.4±0.1	2.45±0.3	1.3 ±0.14	2.29 (41)
8*	2.3–4.6	(5.65)	(2.2)	0.9±0.07	1.65 (47)
	4.6–9.2	(5.65)	(2.2)	2.7±0.1	1.95 (47)
	9.2–18.4	(5.65)	(2.2)	8.8±0.6	2.00 (47)
	2.3–18.4	5.65±0.15	$2.2^{+0.9}_{-0.6}$	1.0±0.04	0.99 (42)
10	2.3–4.6	(7.72)	(3.7)	0.7±0.1	1.64 (46)
	4.6–9.2	8.11 ±0.05	3.9 ±0.2	6.0 ±0.3	1.68 (44)
	9.2–18.4	8.43 ±0.03	3.27±0.08	16.4±0.2	1.73 (45)
	2.3–18.4	7.72 ±0.04	3.7 ±0.1	2.55 ±0.06	2.27 (44)
11a	2.3–4.6	(7.5)	(2.11)	<0.36	1.27 (52)
	4.6–9.2	(7.5)	(2.11)	1.4±0.2	1.75 (50)
	9.2–18.4	(7.5)	(2.11)	<5.1	0.76 (52)
	2.3–18.4	7.8±0.3	2.11±0.6	0.56±0.07	2.55 (52)
11b	2.3–4.6	(5.82)	(0.35)	1.10±0.08	1.47 (48)
	4.6–9.2	5.816±0.009	0.33±0.08	$8.0^{+0.8}_{-0.4}$	1.06 (46)
	9.2–18.4	5.81±0.01	0.36 ±0.15	15.7^{+3}_{-1}	0.72 (47)
	2.3–18.4	5.813±0.008	0.36±0.07	3.2±0.3	1.36 (46)
15	2.3–4.6	4.5 ±0.1	$1.3^{+0.3}_{-0.2}$	0.67±0.05	1.20 (46)
	4.6–9.2	4.83±0.09	$1.1^{+0.3}_{-0.2}$	1.6±0.2	1.22 (39)
	9.2–18.4	(4.68)	(1.14)	<4.8	1.58 (51)
	2.3–18.4	4.68±0.04	0.96 ±0.14	0.75±0.04	1.36 (39)

Frequency ranges used to fit and Wide Ratio are in Table 5.12
Values in parenthesis are fixed
Upper-limits are 3 σ

Table 5.14: GS 1124-68 PDS Broad-Band Parameters: Part 1/3

Obs. ID	Energy Range (keV)	Model	% rms	ν_1	ν_2	ν_3	α_1	χ^2_ν (dof)
1	2.3–4.6	DFTPL	15.4±0.3	0.55±0.02	1.00±0.05	$1.80^{+0.12}_{-0.07}$	1.38 ±0.05	1.61 (39)
	4.6–9.2	DFTPL	19.2 ±0.3	0.53 ±0.03	$0.75^{+0.08}_{-0.03}$	3.1 ±0.1	1.60 ±0.09	1.24 (39)
	9.2–18.4	DFTPL	16.6±0.3	(0.53)	(0.74)	(3.10)	(1.60)	2.46 (43)
	2.3–18.4	DFTPL	16.2±0.3	0.54±0.02	0.99±0.06	1.9 ±0.1	1.20 ±0.05	1.25 (39)
5	2.3–4.6	DFTPL	5.7±0.2	(0.001)	0.15±0.01	2.18 ±0.08	1.49±0.09	1.56 (43)
	4.6–9.2	DFTPL	13.6 ±0.7	(0.001)	0.13±0.02	1.77 ±0.06	1.14 ±0.1	1.65 (41)
	9.2–18.4	DFTPL	12.4±0.4	(0.001)	(0.13)	(1.98)	(1.38)	1.97 (46)
	2.3–18.4	DFTPL	7.43±0.09	(0.001)	0.132 ±0.009	1.98 ±0.05	1.38 ±0.08	2.29 (41)

Values in parenthesis are fixed
Model: DFTPL = Double Flat-Top Power-Law

Table 5.15: GS 1124-68 PDS Broad-Band Parameters: Part 2/3

Obs. ID	Energy Range (keV)	Model	% rms	ν_1	ν_2	α_1	α_2	χ^2_ν (dof)
2	2.3–4.6	FTPL	9.9±0.4	1.10 ±0.04	–	1.22±0.06	–	1.55 (42)
	4.6–9.2	FTPL	16.2±0.2	(1.00)	–	(0.93)	–	3.34 (44)
		FTPL	20.9±0.6	(1.00)	–	0.65 ±0.03	–	1.99 (43)
	9.2–18.4	FTPL	13.8±0.4	(1.00)	–	(0.93)	–	3.90 (44)
		FTPL	36.0 ±3	(1.00)	–	0.1 ±0.06	–	1.99 (43)
	2.3–18.4	FTPL	12.6±0.2	1.00±0.05	–	0.93±0.03	–	1.88 (42)
3	2.3–4.6	FTDPL	8.8±0.1	0.77±0.04	3.4±0.2	0.76±0.04	1.71±0.06	1.34 (507)
	4.6–9.2	FTDPL	17.9±0.2	0.62±0.07	6.6±0.2	0.40±0.03	1.73±0.05	1.33 (507)
	9.2–18.4	FTDPL	21.9±0.3	(0.125)	8.0±0.3	0.06±0.02	1.74±0.07	1.32 (509)
	2.3–18.4	FTDPL	11.3±0.1	0.78±0.04	$6.5^{+0.2}_{-0.1}$	0.70±0.02	1.71±0.02	1.80 (501)
6*	2.3–4.6	FTDPL	2.1±0.1	0.124±0.03	(2.47)	0.71±0.05	(1.43)	1.84 (46)
	4.6–9.2	FTDPL	$9.9^{+1.3}_{-0.7}$	0.10±0.06	$2.5^{+0.3}_{-0.2}$	0.27±0.04	1.4±0.2	0.82 (44)
	9.2–18.4	FTDPL	12.1±0.5	(0.10)	(2.47)	(0.27)	(1.43)	1.48 (48)
	2.3–18.4	FTDPL	3.00±0.03	0.11±0.02	(2.47)	0.51±0.03	(1.43)	1.57 (46)
7*	2.3–4.6	PL	2.24±0.09	–	–	(0.57)	–	1.68 (47)
	4.6–9.2	PL	$5.5^{+1.1}_{-0.8}$	–	–	0.61 ±0.08	–	1.12 (46)
	9.2–18.4	PL	29 ±2	–	–	0.32 ±0.05	–	1.44 (46)
	2.3–18.4	PL	2.6 ±0.1	–	–	0.57±0.04	–	1.94 (46)
8*	2.3–4.6	DPL	1.72±0.05	(2.18)	–	(0.162)	(1.45)	1.65 (47)
	4.6–9.2	DPL	8.54±0.07	(2.18)	–	(0.162)	(1.45)	1.95 (44)
	9.2–18.4	DPL	15.7±0.4	(2.18)	–	(0.162)	(1.45)	1.99 (47)
	2.3–18.4	DPL	3.2±0.2	2.18 ±0.08	–	0.16±0.02	$1.45^{+0.2}_{-0.1}$	0.99 (42)
		DPL	3.2±0.2	2.18 ±0.08	–	0.16±0.02	$1.45^{+0.2}_{-0.1}$	0.99 (42)
9*	2.3–4.6	DPL	2.05±0.06	(2.41)	–	(0.20)	(1.39)	1.82 (48)
	4.6–9.2	DPL	9.5±0.2	2.48±0.2	–	(0.12)	1.57 ±0.09	1.03 (45)
	9.2–18.4	DPL	17.9±0.4	(2.41)	–	(0.20)	(1.39)	3.88 (47)
	2.3–18.4	DPL	6.3±0.2	2.4±0.1	–	0.20±0.02	1.39 ±0.07	1.55 (45)
10	2.3–4.6	DPL	4.9±0.2	2.38±0.09	–	0.14 ±0.03	1.7 ±0.12	1.60 (46)
	4.6–9.2	DPL	$23.8^{+2}_{-0.5}$	$1.98^{+0.12}_{-0.06}$	–	$0.14^{+0.3}_{-0.2}$	$1.59^{+0.4}_{-0.1}$	1.68 (44)
	9.2–18.4	DPL	18.0±0.6	$1.43^{+0.6}_{-0.3}$	–	0.26±0.07	0.60±0.05	1.73 (45)
	2.3–18.4	DPL	6.4±0.2	2.14±0.04	–	0.15±0.02	1.84 ±0.1	2.27 (44)
11a	2.3–4.6	PL	2.5±0.3	–	–	0.66±0.06	–	1.27 (50)
	4.6–9.2	PL	5.1±0.5	–	–	0.67±0.06	–	1.76 (50)
	9.2–18.4	PL	8.1±1.0	–	–	(0.74)	–	0.78 (50)
	2.3–18.4	PL	2.6±0.1	–	–	0.74±0.03	–	2.55 (48)
11b	2.3–4.6	PL	$2.7^{+0.4}_{-0.3}$	–	–	0.78±0.2	–	1.47 (48)
	4.6–9.2	PL	6.6 ±0.8	–	–	0.74 ±0.07	–	1.06 (46)
	9.2–18.4	PL	$6.8^{+1.2}_{-1.5}$	–	–	(0.82)	–	0.71 (47)
	2.3–18.4	PL	3.6±0.2	–	–	0.78 ±0.05	–	1.36 (39)
12*	2.3–4.6	PL	3.0±0.2	–	–	(0.84)	–	0.82 (52)
	4.6–9.2	PL	5.6±0.2	–	–	(0.84)	–	1.80 (52)
	9.2–18.4	PL	10.5±0.7	–	–	(0.84)	–	1.63 (52)
	2.3–18.4	PL	3.8±0.1	–	–	0.84±0.06	–	1.21 (51)
13*	2.3–4.6	PL	2.0±0.3	–	–	1.1±0.1	–	0.95 (51)
	4.6–9.2	PL	7.4±0.2	–	–	0.50±0.02	–	0.85 (52)
	9.2–18.4	PL	11.1±0.3	–	–	0.63±0.06	–	1.21 (51)
	2.3–18.4	PL	2.9±0.1	–	–	0.70±0.04	–	1.40 (51)
14*	2.3–4.6	PL	5.1 ±0.2	–	–	0.98 ±0.04	–	0.74 (48)
		DPL	3.6±0.05	(2.53)	–	(0.69)	(1.63)	1.56(48)
	4.6–9.2	DPL	8.5 ±0.3	$2.4^{+0.2}_{-0.1}$	–	0.37±0.05	$1.5^{+0.2}_{-0.1}$	1.54 (45)
	9.2–18.4	PL	24.7±0.8	–	–	(0.40)	–	1.97 (48)
		DPL	10.5±0.5	(2.53)	–	(0.69)	(1.63)	4.76 (48)
	2.3–18.4	PL	6.2±0.2	–	–	1.02±0.02	–	3.3 (47)
		DPL	4.3±0.2	$2.5^{+0.4}_{-0.2}$	–	$0.69^{+0.09}_{-0.05}$	$1.6^{+0.2}_{-0.1}$	1.55 (45)
15	2.3–4.6	PL	2.3 ±0.3	–	–	0.60±0.06	–	1.20 (46)
	4.6–9.2	PL	7.9±0.8	–	–	0.55±0.05	–	1.35 (46)
	9.2–18.4	PL	7.8±0.2	–	–	(0.61)	–	1.58 (51)
	2.3–18.4	PL	3.0±0.2	–	–	0.61±0.03	–	1.74 (46)

* Observations with no QPO reported by T96
Upper-limits are 3 σ
Values in parenthesis are fixed
Models: PL==Power Law; DPL == Double Power Law; FTPL== Flat-Top Power-Law;
FTDPL == Flat-Top Double Power Law; DFTPL= Double Flat-Top Power-Law

Table 5.16: GS 1124-68 PDS Broad-Band Parameters: Part 3/3

Obs. ID	Energy Range (keV)	Model	% rms	ν_1	ν_2	α_1	α_2	χ^2_ν (dof)
16	2.3–4.6	PL	10.0±0.4	–	–	(1.67)	–	0.41 (22)
	4.6–9.2	PL	10.7±0.8	–	–	(1.67)	–	0.66 (22)
	9.2–18.4	PL	<17.4	–	–	(1.67)	–	0.99 (22)
	2.3–18.4	PL	10.1±0.3	–	–	1.67±0.1	–	0.73 (21)
17	2.3–4.6	PL	<3.3	–	–	(1.21)	–	0.89 (22)
	4.6–9.2	PL	<1.7	–	–	(1.21)	–	1.10 (22)
	9.2–18.4	PL	<9.6	–	–	(1.21)	–	1.28 (22)
	2.3–18.4	PL	1.1±0.1	–	–	1.21±0.1	–	1.65 (21)
18	2.3–4.6	PL	0.89±0.1	–	–	(0.88)	–	1.18 (22)
	4.6–9.2	PL	3.0±0.3	–	–	(0.88)	–	0.94 (22)
	9.2–18.4	PL	<73	–	–	(0.88)	–	1.65 (22)
	2.3–18.4	PL	1.1±0.1	–	–	0.88±0.1	–	1.37 (21)
19	2.3–4.6	FTDPL	31.8±0.3	(0.09)	(0.65)	(0.73)	(1.42)	1.56 (23)
	4.6–9.2	FTDPL	32.4±0.5	(0.09)	(0.65)	(0.73)	(1.42)	1.37 (23)
	9.2–18.4	FTDPL	32.7±0.6	(0.09)	(0.65)	(0.73)	(1.42)	1.00 (23)
	2.3–18.4	FTDPL	32.3±0.4	0.09±0.02	0.65±0.06	0.73±0.06	1.42±0.02	3.32 (19)

Upper-limits are 3 σ
Values in parenthesis are fixed
Models: PL==Power Law; DPL == Double Power Law; FTPL== Flat-Top Power-Law;
FTDPL == Flat-Top Double Power Law; DFTPL= Double Flat-Top Power-Law

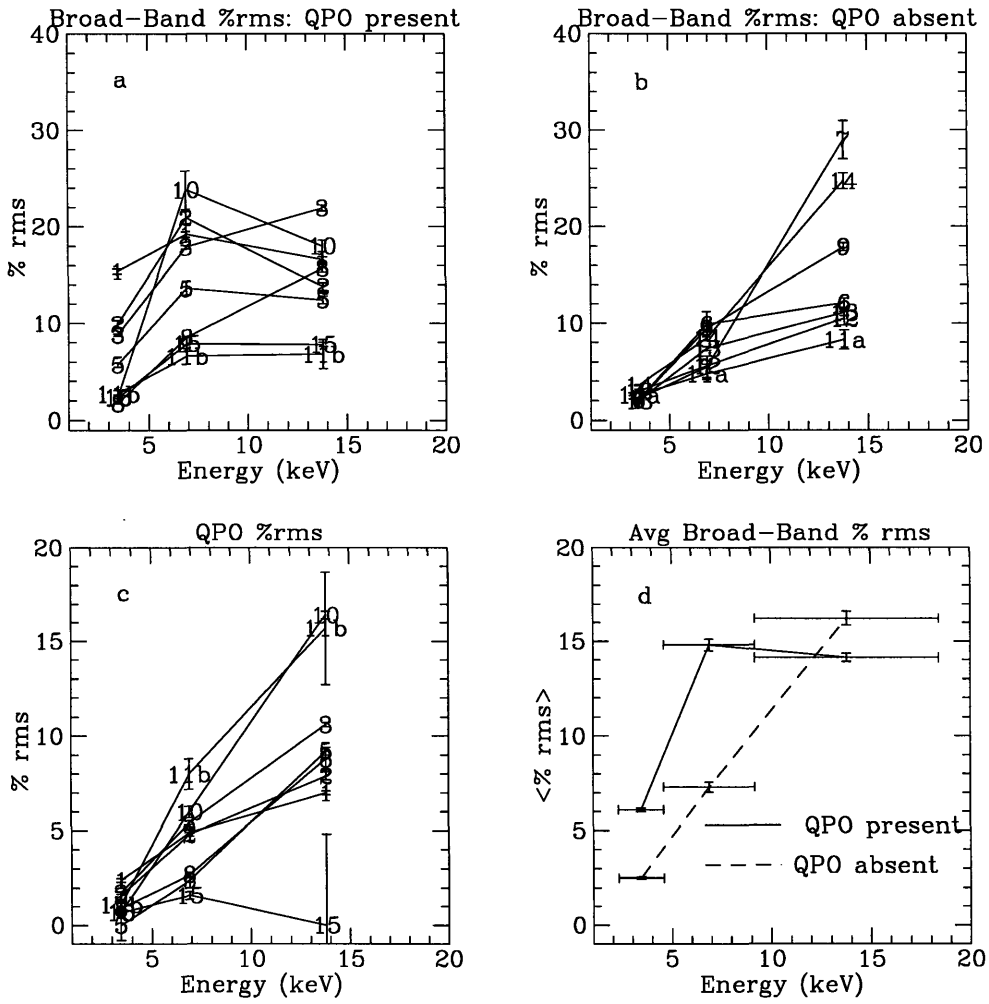

Figure 5-39: **QPO and Broad-Band %rms vs. Energy, GS 1124-68.** Points are marked with corresponding Observation IDs, using only observations #1–15. *(a)*: The broad-band %rms variability as a function of energy during observations when QPO is present. *(b)*: The broad-band %rms variability as a function of energy during observations when QPO is absent. *(c)*: %rms variability of the fundamental QPO feature as a function of energy. *(d)*: The averaged broad-band %rms variability as a function of energy when QPO is present (solid line) and absent (broken line).

QPO Centroid Frequency vs. Energy

We investigated the QPO centroid frequency as a function of energy for observations 1, 2, 3, and 10, where the QPO are relatively strong, and we have high-significance data. FFTs were produced in the energy ranges beginning at 2.3, 4.6, 6.9, 9.2, 11.5, 14.8 and 16.1 keV which were 2.3 keV wide. These FFTs had a Nyquist frequency of 8.0 Hz (for observations 1, 2, and 3) or 16.0 (for observation 10), and were 1024 bins long each. There were a total of 23, 23, 62, and 164 FFTs each for observations 1, 2, 3 and 10, respectively. These FFTs were averaged into a single PDS, which was then rebinned to a frequency resolution of 0.125 Hz and cropped to the frequency range 1-5 Hz (Obs 1 and 2), 4-8 Hz (Obs 3), or 1-16 Hz (Obs 10). The resulting PDS were then fit with either a Flat-Top Single Power-law plus a Lorentzian, or a Single Power Law plus Lorentzian model for the power as a function of frequency.

The best-fit values of the centroid frequency for each observation and frequency range (where a significant best-fit value could be determined) are shown in Fig. 5-40. The centroid frequencies show no dependence on energy. The centroid frequency as a function of energy for each observation was fit with a line, producing best-fit slopes consistent with zero, with 1-σ values on the slopes of 0.0014, 0.012, 0.0042, and 0.0018 Hz/keV for observations 1, 2, 3 and 10, respectively.

Energy Dependency of the VHS QPO of GS 1124-68

In a manner identical to that done for the VHS of GX 339-4 (see Fig. 5-51 in Sec. 5.4.8), we divided the data by spectrum and produced PDS of each spectral limit (see Fig. 5-41). The evolution of the shape of the PDS with Wide Ratio is similar, but not identical, to that observed from GX 339-4. In the spectral states marked "F4" and "F3" (Wide Ratio=0.060–0.075 and 0.050–0.060, respectively) the PDS is Flat-Top-Power-Law with QPO (as in GX 339-4). The "F2" state is, as in GX 339-4, also a single power-law (however, GX 339-4 has an additional flat component near 3 Hz). Finally, in state "F1" while GX 339-4 has a power-law slope down to $\sim$0.02 Hz (perhaps flattening below), GS 1124-68 shows a clear flattened component below $\sim$0.1 Hz. Thus, while there are differences between the two sources, the PDS show

extremely similar behavior between GX 339-4 and GS 1124-68 in their VHS.

In Fig. 5-42, we show the PDS from High-Frequency PDS of the F-state data only, for the Low Energy Range, Medium Energy Range, and High Energy Range (corrected for background and dead time). The data are binned linearly, to show in greater detail the QPO peaks near 6 and 8 Hz. There is very strong energy dependence in the QPO, with the %rms variability increasing greatly with increasing energy. The energy dependency is similar to that seen for the VHS QPO of GX 339-4 (see Fig. 5-53).

In Fig. 5-43, we show nine PDS (each arbitrarily normalized) in nine different energy ranges, as obtained from data taken 11 Jan 1991 (observations 1, 2, & 3). The strength of the QPO peak near 5 Hz grows relative to the power below 1 Hz with increasing energy. The QPO peak is detectable all the way up to the 18.4–23.0 keV range in these data. The QPO peak is visible at all energies between 2.3 and 23.0 keV.

In Fig. 5-44, we show the PDS in nine energy ranges for data obtained on 22 Jan 1991 (Observation 10). The QPO is not evident in the 2.3–4.6 keV energy range, increasing in relative importance to the power below 1 Hz with increasing energy, visible up to the 16.1–18.4 keV range.

In Fig. 5-45, we show the PDS in nine energy ranges for data obtained on 25 Jan 1991 (Observation 11b). Unlike the previous two QPO figures, there is very little power below 1 Hz with which to compare the QPO power. The QPO increases in relative importance to the power below 1 Hz with increasing energy, visible up to the 16.1–18.4 keV range.

These figures (5-42, 5-43, 5-44, 5-45) illustrate that the QPO in GS 1124-68 has varying energy dependencies in relation to that of the continuum power.

In Fig. 5-46 we show the light curves in the Low Energy Range, Medium Energy Range and High Energy Range on Jan 25 1991 (observations 11a and b). During the first 20 minutes (observation 11a), the count-rates in these ranges decrease, while the Wide Ratio remains constant near 0.037. In the left column, we show the High-Frequency PDS in the three separate energy ranges taken during this period – no QPO

is evident. After a break in the observation, the source is observed again (observation 11b), and the count-rate has increased over the last measurement in all three energy ranges, and the source spectrum has hardened, to Wide Ratio=0.045. In the right column, we show the PDS in the three separate energy ranges – the Medium Energy Range and High Energy Range show strong QPO which was not present previously.

This is as has been demonstrated to occur also in GS 1124-68 data on Jan 14 1991 by T96, in which it can be seen in troughs of "flip-flops" that low-frequency-noise dominates with no QPO in evidence, while at the peaks of "flip-flops" QPO near 6 Hz is strong. The "flip-flop" transitions occur on $\sim$1 sec timescales.

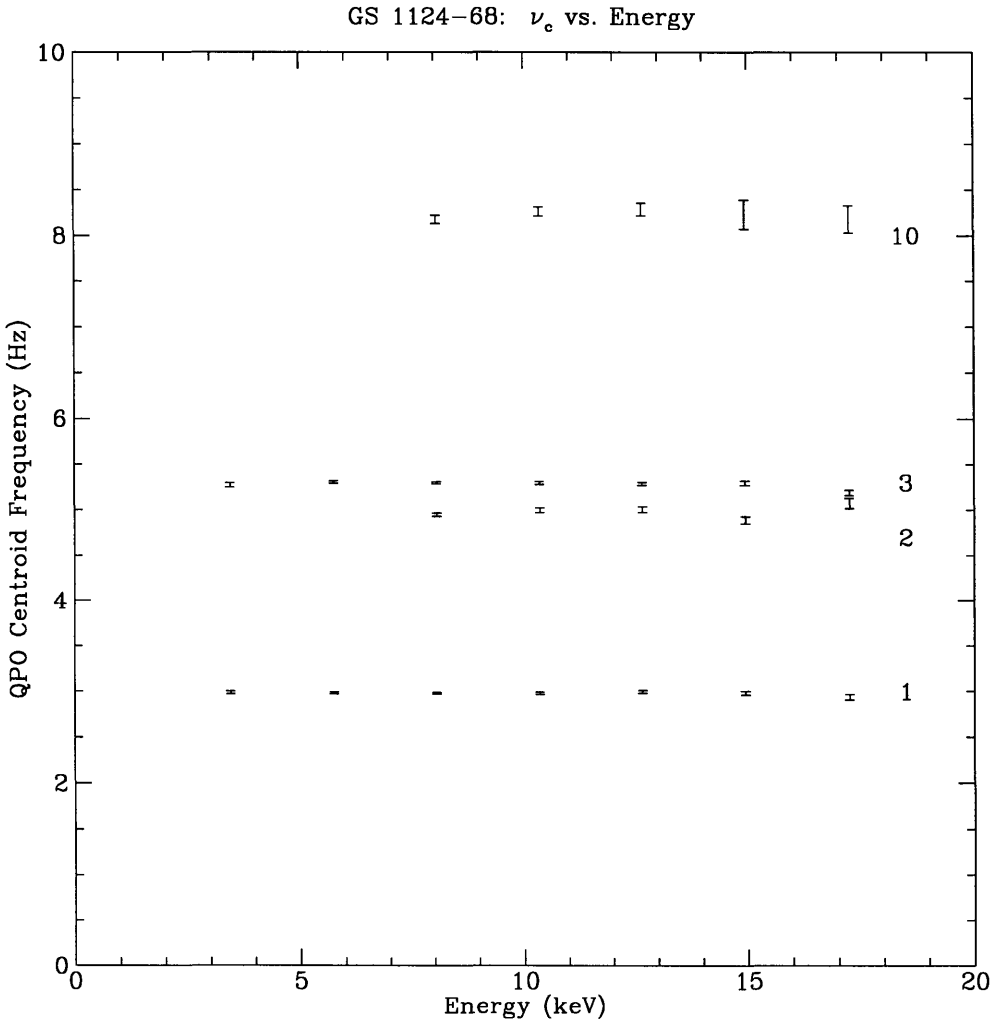

Figure 5-40: **QPO Centroid Frequency vs. Energy, GS 1124-68**. The QPO centroid frequency as a function of energy for observations 1, 2, 3, and 10. The ν_c is constant as a function of energy. The observation number is noted next to each set of values.

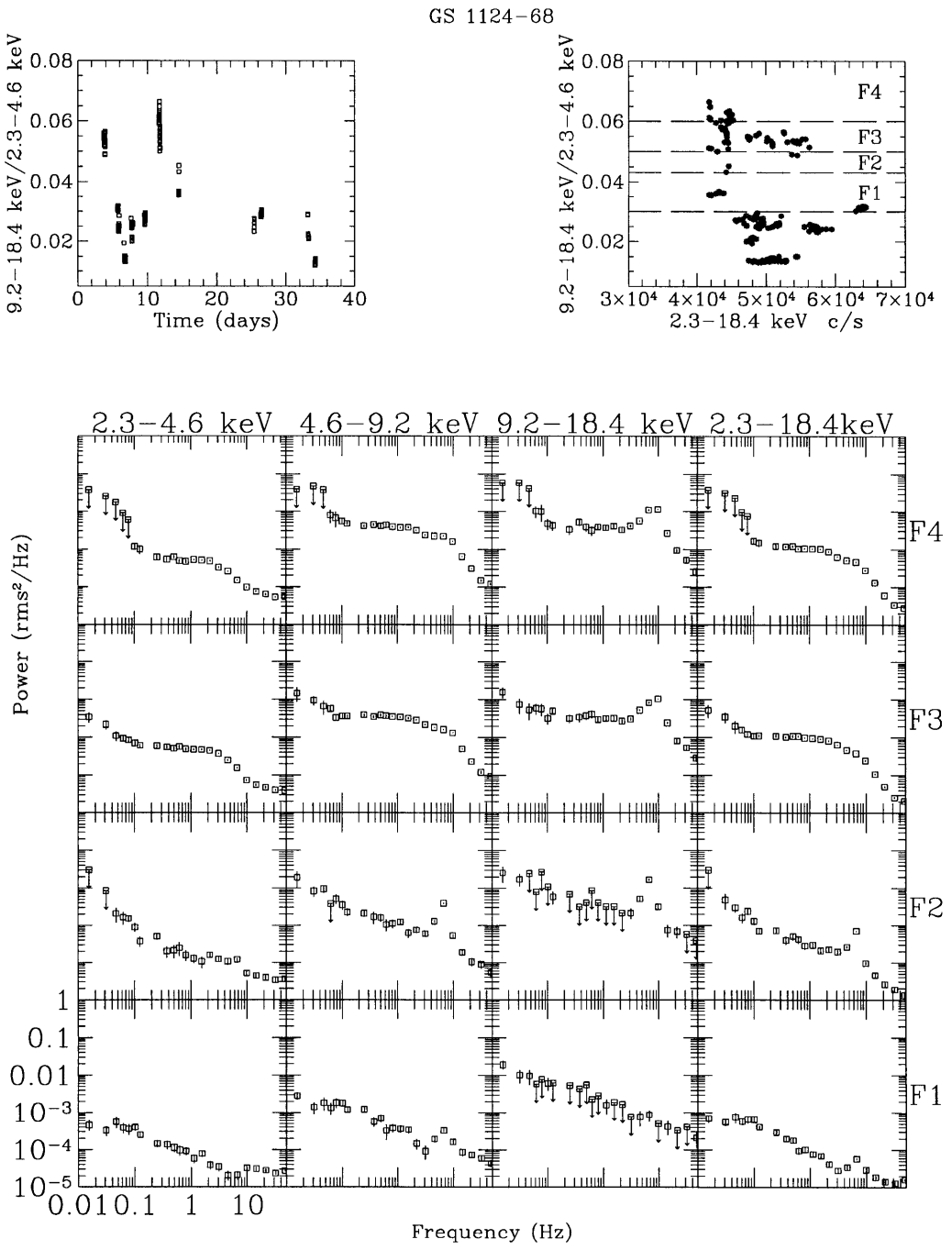

Figure 5-41: **Detailed HID and PDS of GS 1124-68 with QPO** *Upper left-hand panel* is the Wide Ratio vs. time, during the period in which QPO was observed from GS 1124-68 (first 40-days of outburst, since Jan 11 1991). *Upper right-hand panel* is the HID, Intensity Range count-rate vs. Wide Ratio during all GS 1124-68 observations. The panel has been divided by Wide Ratio value, and each region is labeled. *Bottom Panels*: The PDS in three energy ranges plus the intensity range (labeled by column). Upper-limits are 2σ. The data were divided by spectral hardness (each row is labeled, and corresponds to a label in the HID above). The BB PDS characteristics evolve – as the spectrum softens, the BB PDS changes from a flat-top-power-law with break frequency near ~3 Hz (F4, F3) to a single power-law (F2) and again to Flat-Top-Power-Law, now with a break frequency of 0.1 Hz (F1); the QPO remains throughout. This Figure may be directly compared to that of GX 339-4 (Fig. 5-51)

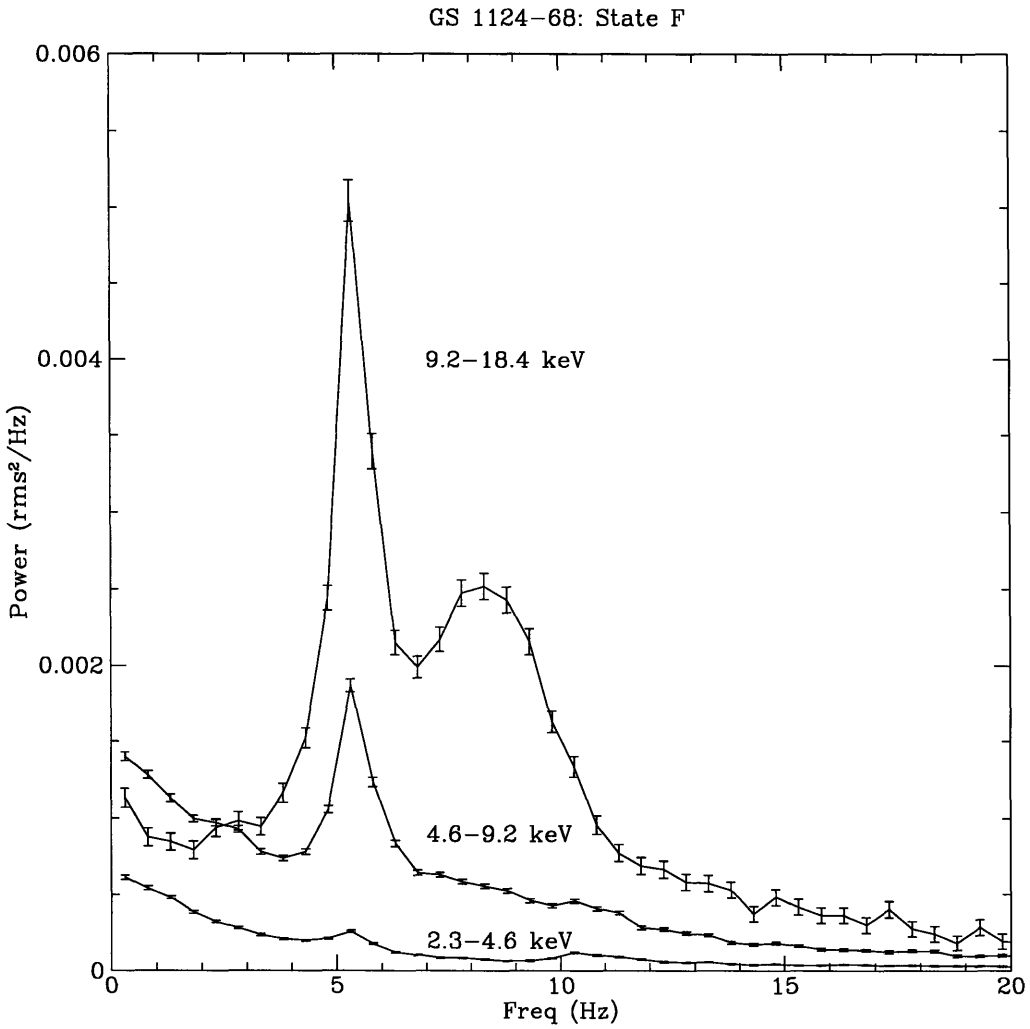

Figure 5-42: **Energy Dependence of QPO in GS 1124-68.** The PDS of GS 1124-68 in the three energy ranges, while the source is in state "F". Corrections to the %rms for background and dead time have been applied. There is clearly strong energy dependence, with the QPO %rms increasing with increasing energy, as has also been found by Belloni et al. (1996) and T96

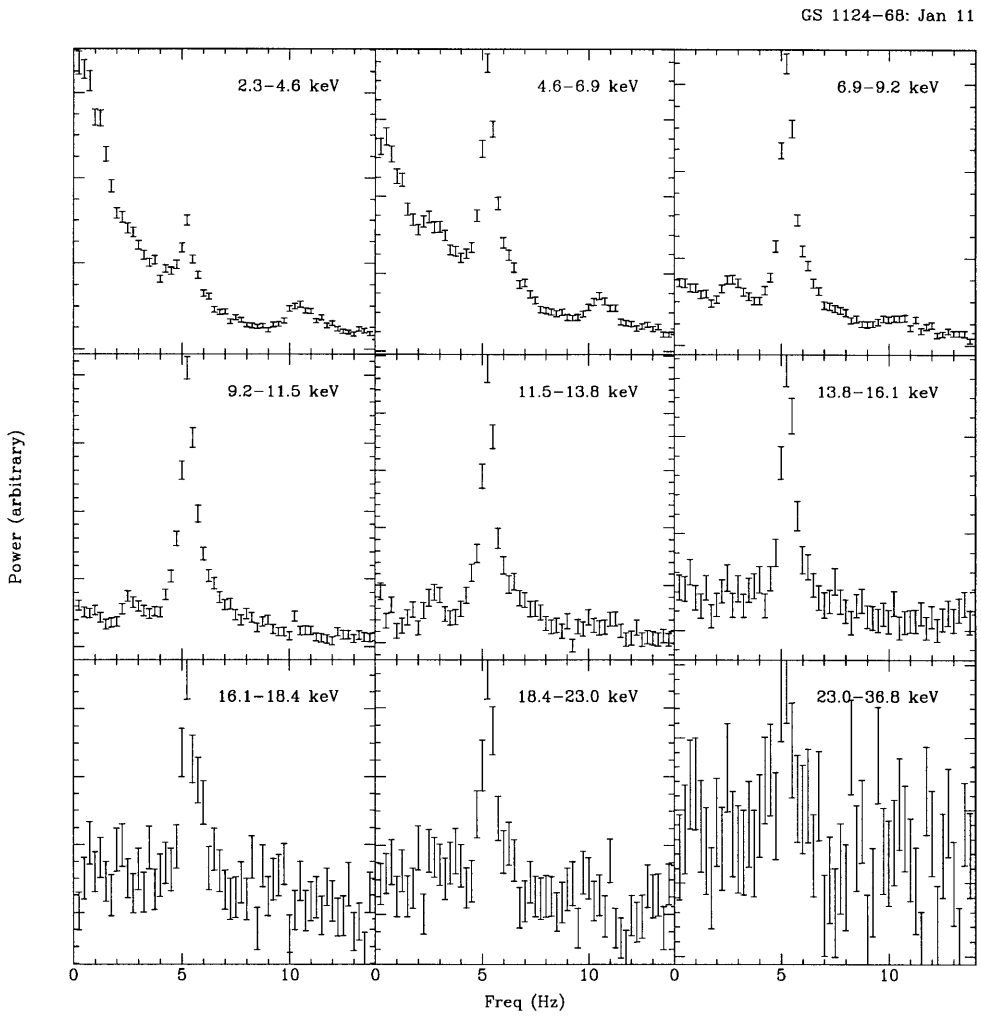

Figure 5-43: **Energy Dependent PDS F-state QPO in GS 1124-68, Jan 11.** Nine PDS of GS 1124-68, separated by energy-range of the data. The normalization of each PDS is arbitrary, and thus cannot be inter-compared to find the strength of the same features at different energies (for this, see 5-42). The data used in this plot were taken between 91/011 20:54 UT and 91/012 02:00 UT. Each PDS is an average of 1185 individual transforms, each taken of 4 s of data with a Nyquist frequency of 16 Hz.

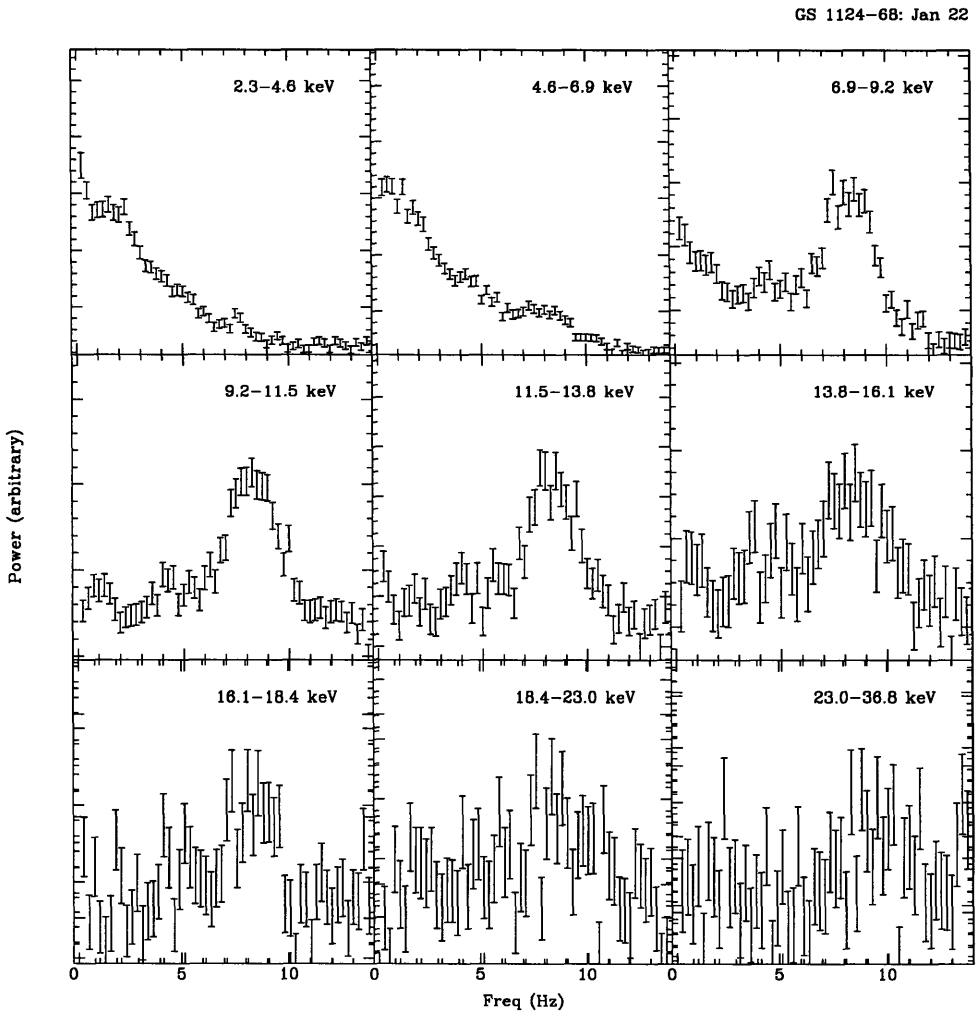

Figure 5-44: **Energy Dependent PDS F-state QPO in GS 1124-68, Jan 22.** Nine PDS of GS 1124-68, separated by energy-range of the data. The normalization of each PDS is arbitrary, and thus cannot be inter-compared to find the strength of the same features at different energies (for this, see 5-42). The data used in this plot were taken between 91/022 17:19–20:10 UT. Each PDS is an average of 1329 individual transforms, each taken of 4 s of data with a Nyquist frequency of 16 Hz.

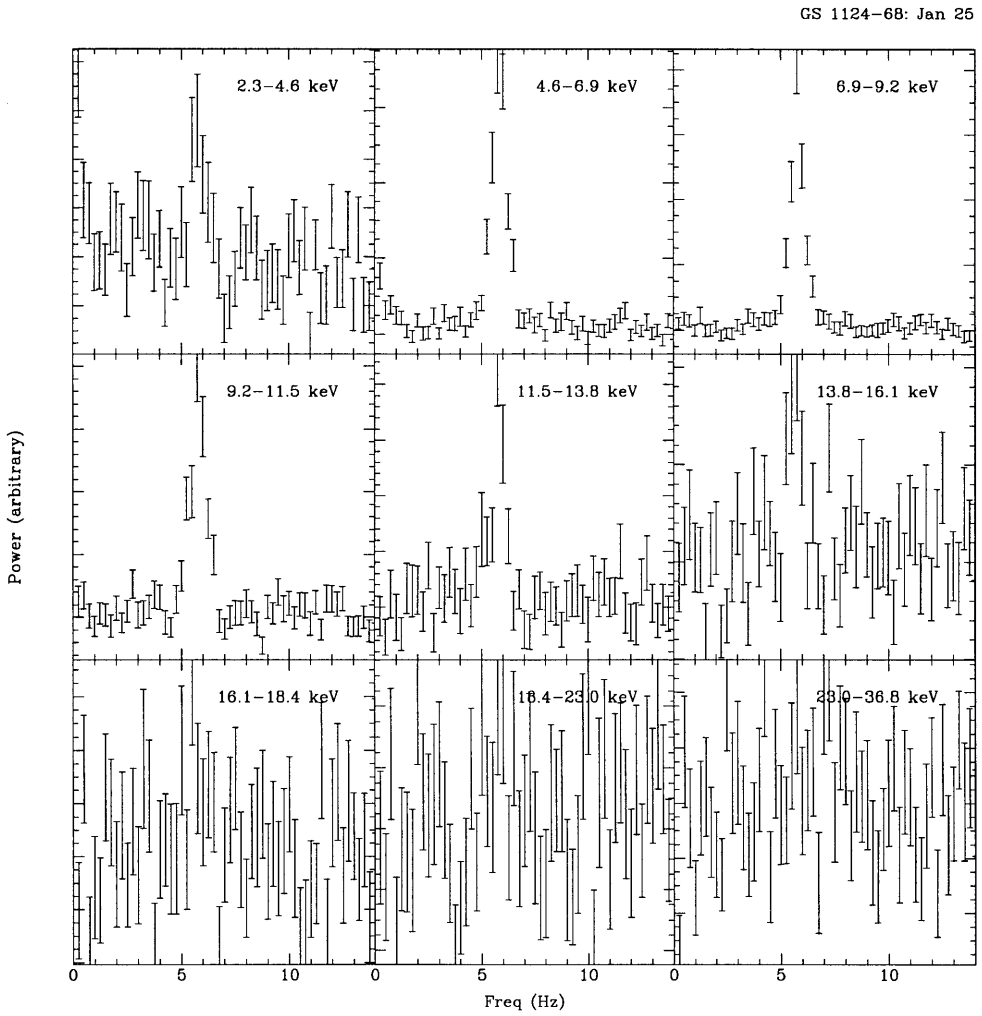

Figure 5-45: **Energy Dependent PDS F-state QPO in GS 1124-68, Jan 25.** Nine PDS of GS 1124-68, separated by energy-range of the data. The normalization of each PDS is arbitrary, and thus cannot be inter-compared to find the strength of the same features at different energies (for this, see 5-42). The data used in this plot were taken 91/025 between 13:46–13:54 UT. Each PDS is an average of 112 individual transforms, each taken of 4 s of data with a Nyquist frequency of 16 Hz.

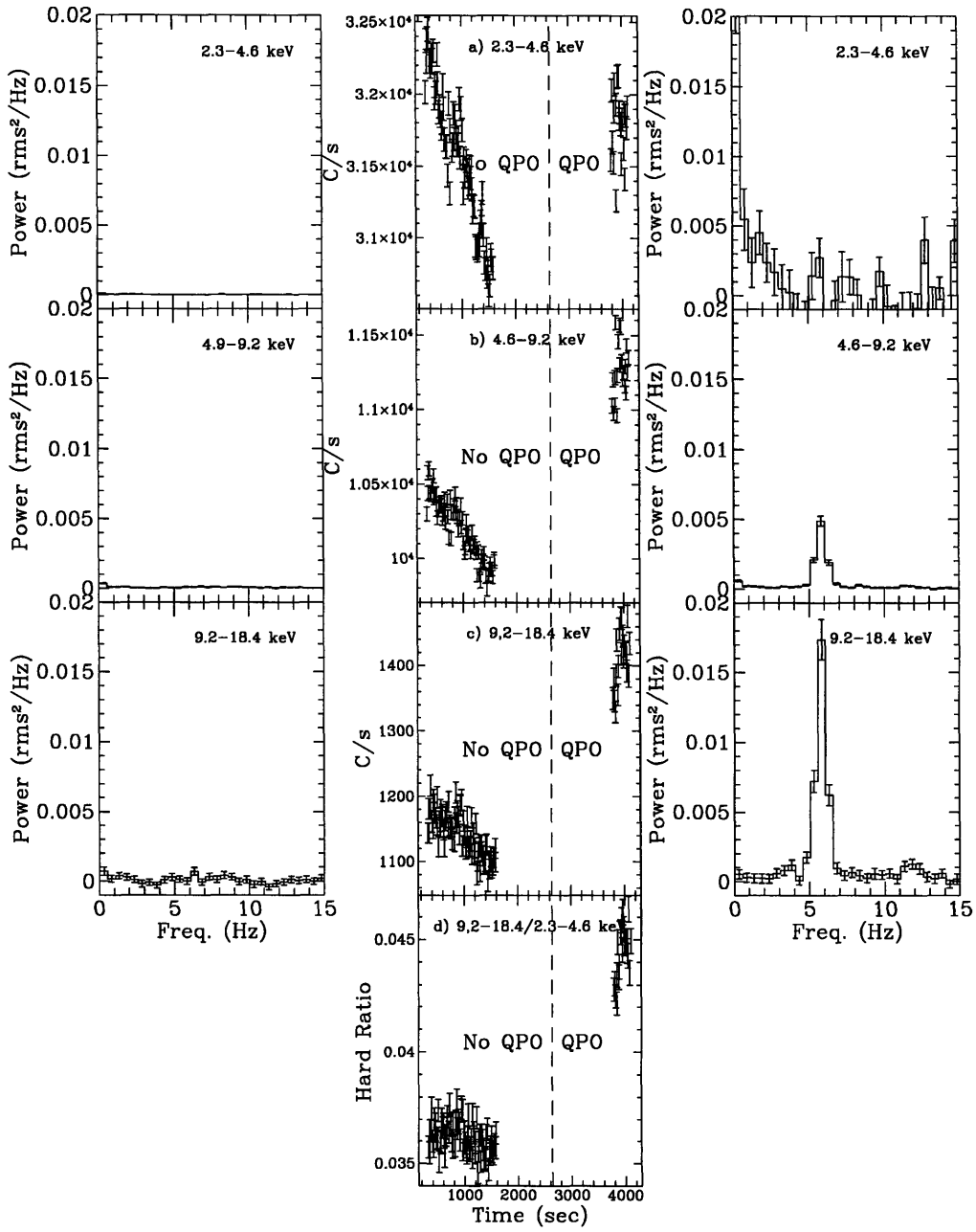

Figure 5-46: **The Onset of QPO Jan 25 1991, GS 1124-68.** The onset of QPO, coincident with the spectral hardening of GS 1124-68. Panels a-c show the count rate during the period Jan 25 1991 12:48-13:56 UT, in three different energy ranges (as marked). The broken line separates the data into two regions, where no QPO was detected and where QPO was detected. On either side of panels a-c are corresponding PDS across the energy range indicated; on the right are PDS taken during the time when no QPO was present, and on the left are PDS taken when QPO was present. Panel d (bottom middle) shows the hard ratio 9.2-18.4 keV/2.3-4.6 keV as a function of time. The appearance of QPO was coincident with the spectral hardening of GS 1124-68, as well as an increase in intensity, during the unobserved period of 13:10-13:46 UT.

5.4.8 GX 339-4

Of the measured 128 s values of the Wide Ratio for GX 339-4 measured in Ch. 5, 80% were in the range Wide Ratio=0.044–0.56 (FGH-type source). There were no data obtained in which the source had Wide Ratio intermediate to F and H (G-state). There is a small amount of data in which the source was softer (E-state), but only enough to produce 2 High-Frequency FFTs. Therefore, we focus on F and H states. We subdivided the F-state data into F1 and F2 states (F1 is Wide Ratio=0.032-0.05; F2 is Wide Ratio=0.05–0.1).

We produced Composite PDS for data in the F1 and F2 states from GX 339-4. The F1 PDS is an average of 2 Low-Frequency FFTs, 107 Medium-Frequency FFTs, and 867 High-Frequency FFTs. The F2 PDS is an average of 2 Low-Frequency FFTs, 79 Medium-Frequency FFTs, and 670 High-Frequency FFTs. The Composite PDS are shown together in Fig. 5-47.

The spectrally harder and slightly higher intensity F2 data has measurably stronger (in %rms) continuum noise properties in the Low Energy Range, Medium Energy Range, and Intensity Range, while having similar or less strong noise in the High Energy Range. The character of the continuum noise properties between the F1 and F2 states are markedly different.

We compare the Low Energy Range, Medium Energy Range, and Intensity Range PDS. From low-frequency to high-frequency, the F1 noise begins either flat or moderately sloped, dropping in the 0.1–1.0 Hz region where it again flattens out; near 2 Hz, the frequency dependence of the power becomes again into a power-law, which is interrupted near 8 Hz with a strong QPO Lorentzian, then continuing on to the frequency limit of the PDS (64 Hz). Note that, in the PDS of the Low Energy Range data, there is an F1 point almost completely obscured by an F2 point near 8 Hz. The F2 noise begins completely flat at low frequencies, slowly rolling over to decreasing power with frequency near 1 Hz, meeting a "kink" in the PDS near 2 Hz, with a moderate Lorentzian near 8 Hz, above which the PDS drops off as a power-law.

We attempted several models to fit the F1 and F2 data separately. We fit the 2.3-18.4 keV PDS of the F1 state initially, as these provide the highest significance

data, and thus permit more precise fitting of the models; in addition, the F1 state has a broad component near 2 Hz which the applied best-fit model must account for.

The models Flat-Top-Single-Power-Law, Flat-Top-Double-Power-Law, Flat-Top-Power-Law-Decaying-Exponential, were all tried, in conjunction with a single Lorentzian, were fit to the 2.3-18.4 keV PDS. None fit acceptably, with typical χ^2_ν~13-90, the discrepancy caused largely by the broad feature near 2 Hz. This broad feature was more successfully accounted for by the addition of a second Lorentzian component – the parameters of which indicate that the lower-frequency component is not a sub-harmonic of the more evident QPO feature at 6 Hz (compare 6.0 ±0.02 to 1.91 ±0.05 Hz); however, the fit χ^2_ν were poor – 2.5 (82 dof). Changing the model to a Double Flat-Top Single-Power-Law Model provided a worse fit (χ^2_ν= 3.3 for 83 dof), and so that model was also discarded. Flat-Top-Single-Power-Law model with a primary QPO peak at 6 Hz with sub-harmonics at half and quarter frequencies also failed (χ^2_ν= 5.0 with 82 dof) in the absence of an additional broad component near 2 Hz.

Thus, we adopted a Flat-Top Single-Power-Law model, with a QPO near 6 Hz with harmonic components, and an additional broad Lorentzian near 2 Hz. The major discrepancies between the data and the model came from the QPO frequencies in the range of 4-8 Hz, where it is evident that the 6 Hz component has a finite and measurable skew, which we did not take into account in our modeling (see Fig. 5-48). The results of these fits are shown in Tables 5.17,5.18, & 5.19.

In the High Energy Range PDS, comparison between the PDS is made more difficult by the sensitivity limits. Much of the data in the 0.5-5 Hz region are upper-limits to power. However, below 0.5 Hz, we see that the F1 power roughly follows a power-law, with greater %rms variability then the F2 power, which is flat in that frequency region. Unlike in the other energy ranges, the strengths of the QPO peaks are more comparable. We show this in greater detail in the Fig. 5-49. The F1 state, across all energy ranges, shows stronger QPO; for the F2 state, the QPO power is less than or comparable to the continuum power in the Low Energy Range and Medium Energy Range but for the High Energy Range the QPO power dominates over the continuum near 6 Hz.

Table 5.17: BB Parameters for Best-Fit Flat-Top Power-Law to GX 339-4 F-state Composite PDS

Wide Ratio	Energy Range (keV)	Flat-Top Power-Law ν_1 (Hz)	(α)	%rms (0.001-64 Hz)	χ^2_ν (dof)
0.032–0.05	2.3–4.6	0.071±0.009	1.08 ±0.04	5.0 ±0.2	1.17 (82)
(F1)	4.6–9.2	0.076±0.01	$1.3^{+0.1}_{-0.08}$	8.4 ±0.3	2.31 (82)
	9.2–18.4	0.098±0.03	1.8±0.3	11 ±1	1.13 (84)
	2.3–18.4	$0.088^{+0.08}_{-0.07}$	1.20±0.03	5.4±0.1	2.51 (82)
0.05–0.1	2.3–4.6	1.21±0.03	1.57 ±0.04	8.7±0.1	1.30 (83)
(F2)	4.6–9.2	1.20 ±0.03	1.63 ±0.07	12.9 ±0.3	1.35 (83)
	9.2–18.4	1.2±0.2	$1.1^{+0.2}_{-0.1}$	$11.4^{+1.0}_{-1.3}$	0.94 (83)
	2.3–18.4	1.23 ±0.03	1.68±0.04	9.4±0.1	1.38 (83)

Values in parenthesis are fixed
Upper-limits are 3 σ

We produced a Composite PDS for GX 339-4 in the H-state. These data were also used to produce the PDS for states labeled S2-4 in Fig. 5-52; here, we have combined all that data, selected by Wide Ratio=0.32–1.0, into a single average PDS, which is shown in Fig. 5-50. The PDS is an average of 34 Low-Frequency FFTs, 313 Medium Frequency FFTs, and 206 High Frequency FFTs.

We attempted to fit the 2.3-18.4 keV PDS with a number of models, which could then also be applied to the other, typically less constrained PDS. A pure exponential failed to fit both the low-frequency flat component and the longer tail at higher frequencies (with a χ^2_ν=13.9). A simple flat-top-power-law function also fails to account for the decrease in power at higher-frequencies, which is sharper than can be accounted for in a single power-law (χ^2_ν=5.5). A Flat-Top-Double-Power-Law model produced a better fit (χ^2_ν=2.38); however, the fit was not stable, as the higher break-frequency/power-law slope are strongly covariant, and not well constrained above 10 Hz, where the data significance is low. We settled on using a Flat-Top-Power-Law-Exponential function, which provided moderately acceptable fits.

We provide the results of the best-fit Flat-Top-Power-Law-Exponential function to the GX 339-4 H-state Composite PDS in Table 5.20. The %rms variability in

Table 5.18: QPO Parameters for Best-Fit Flat-Top Power-Law to GX 339-4 F1 & F2 -states Composite PDS

Wide Ratio	Energy Range (keV)	ν_c (Hz)	FWHM (Hz)	%rms
0.032–0.05	2.3–4.6	1.86±0.06	1.2±0.2	2.1 ±0.2
(F1)	4.6–9.2	1.79±0.07	1.2±0.2	4.1 ±0.5
	9.2–18.4	(1.76)	(1.40)	<7.6
	2.3–18.4	1.76 ±0.06	1.40±0.2	2.9 ±0.2
0.05–0.1	2.3–4.6	(1.76)	(1.40)	<2.6
(F2)	4.6–9.2	(1.76)	(1.40)	<10
	9.2–18.4	(1.76)	(1.40)	<5.8
	2.3–18.4	(1.76)	(1.40)	<3.9

Values in parenthesis are fixed
Upper-limits are 3 σ

Table 5.19: Parameters for Best-Fit Harmonic QPO GX 339-4 F1 & F2 -states Composite PDS

Wide Ratio	Energy Range (keV)	ν_c (Hz)	FWHM (Hz)	$\%rms_{1/4}$	$\%rms_{1/2}$	$\%rms_1$	$\%rms_2$	$\%rms_4$
0.032–0.05	2.3–4.6	5.95 ±0.04	0.84±0.07	–	<0.57	1.54±0.05	<0.99	–
(F1)	4.6–9.2	6.00 ±0.02	0.93±0.04	<2.1	0.6±0.2	5.37±0.09	1.5±0.02	<1.5
	9.2–18.4	5.99±0.03	1.06±0.09	<2.5	< 1.8	10.1±0.3	$3.7^{+0.7}_{-0.8}$	<4.1
	2.3–18.4	6.00±0.02	0.86±0.04	<0.3	0.38±0.08	2.67±0.04	0.6±0.1	<0.61
0.05–0.1	2.3–4.6	6.1 ±0.1	$4.4^{+0.6}_{-0.5}$	2.6±0.4	2.2±0.2	2.2 ±0.2	<1.9	<1.8
(F2)	4.6–9.2	6.52±0.05	2.8±0.2	1.8±0.4	3.1 ±0.2	6.0 ±0.2	2.8±0.3	<4.2
	9.2–18.4	6.63±0.07	2.3 ±0.2	<6	2.5 ±0.5	9.7±0.4	4.3 ±0.9	$3.3^{+0.5}_{-0.8}$
	2.3–18.4	6.33±0.05	3.1±0.2	1.8±0.2	2.1 ±0.09	3.31 ±0.08	1.6±0.1	<1.8

Upper-limits are 3 σ

the Low Energy Range, Medium Energy Range, and Intensity Range was found to be 42-47 %, while that in the High Energy Range was considerably lower at 33 ±1%.

Table 5.20: Parameters for Best-Fit Flat-Top-Power-Law-Decaying-Exponential to GX 339-4 State H Composite PDS

Energy Range (keV)	Break Freq. (Hz)	Power Law Slope (α)	Exponential Freq (Hz)	%rms[a] (0.001-64 Hz)	χ^2_ν (dof)
2.3–4.6	0.035±0.003	0.88 ±0.03	$6.2^{+1.7}_{-1.3}$	43.8±0.8	1.71 (37)
4.6–9.2	0.036±0.003	0.86 ±0.035	$4.2^{+1.3}_{-1.0}$	47.3±1	1.67 (37)
9.2–18.4	0.026±0.003	1.04±0.04	$12.4^{+18}_{-6.5}$	34 ±1	1.03 (37)
2.3–18.4	0.036±0.002	0.93 ±0.02	$6.8^{+1.0}_{-0.8}$	42.2±0.5	1.84 (37)

Values in parenthesis are fixed

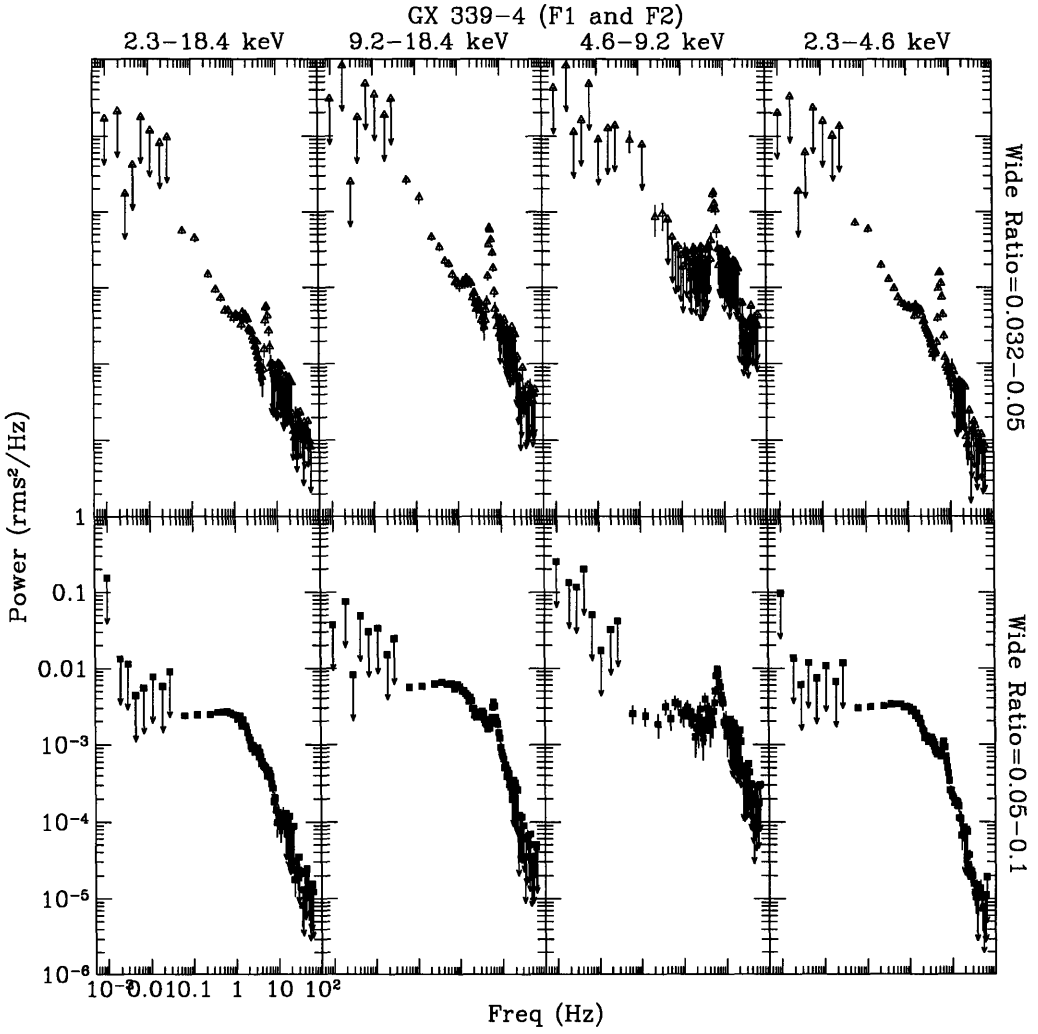

Figure 5-47: **GX 339-4 Composite PDS for F1 and F2 States.** The PDS of GX 339-4 in the three energy ranges, while the source is in state F1 (Wide Ratio=0.032–0.05; open triangles) and F2 (Wide Ratio=0.05–0.1; solid squares). Corrections to the %rms for background and dead time have been applied. Error bars are 1 σ and upper limits are 2σ. The spectrally softer F1 state shows a larger QPO component (in %rms) relative to the noise properties in the vicinity of 6 Hz then the spectrally harder F2 state in the Low Energy Range, Medium Energy Range and Intensity Range; the components are more comparable in the High Energy Range.

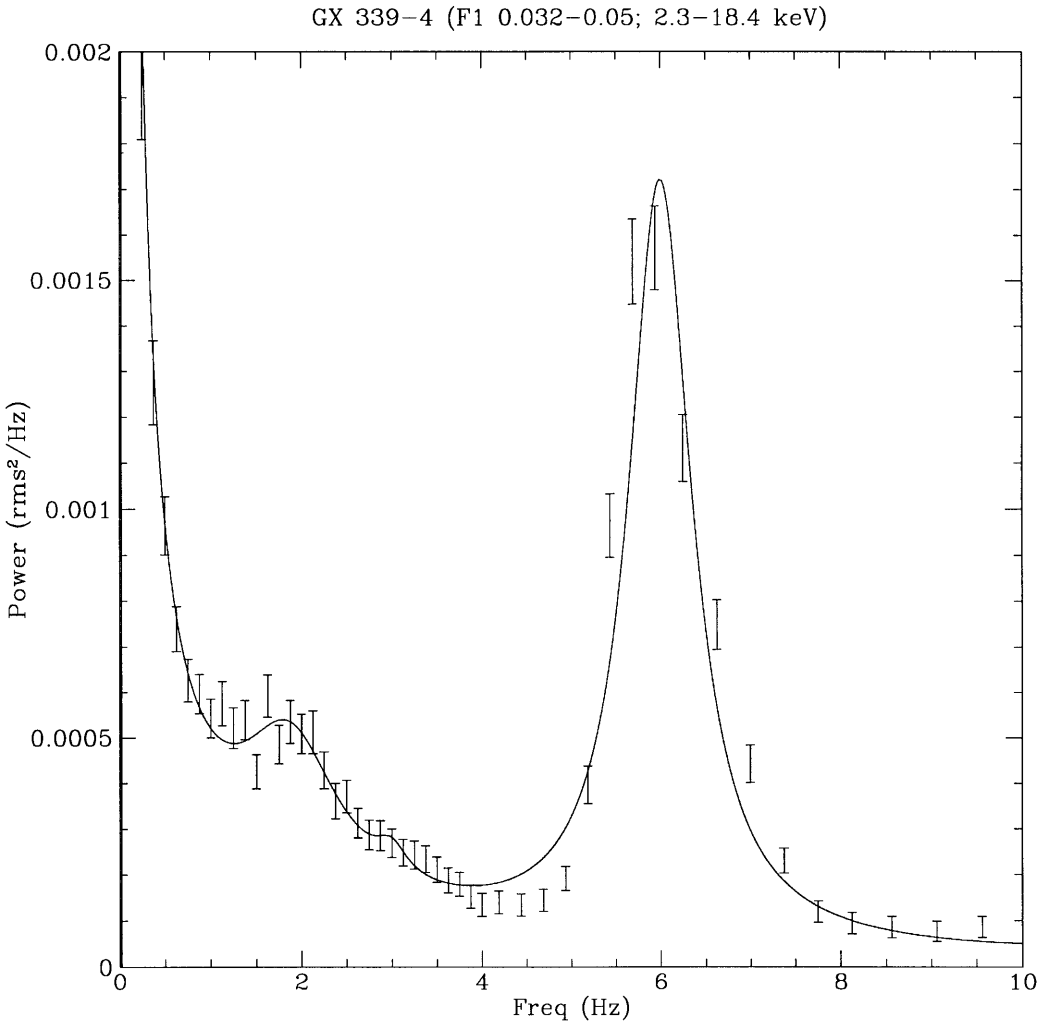

Figure 5-48: **GX 339-4 F1 state – QPO and Best-Fit model.** The F1 (Wide Ratio=0.032–0.05) PDS in the 2.3–18.4 keV energy range, with the best-fit model (Flat-Top Single-Power-Law, QPO at 6 Hz with harmonics, and additional broad Lorentzian near 2 Hz). The data indicate a large skew in the 6 Hz QPO, which is not accounted for in the model.

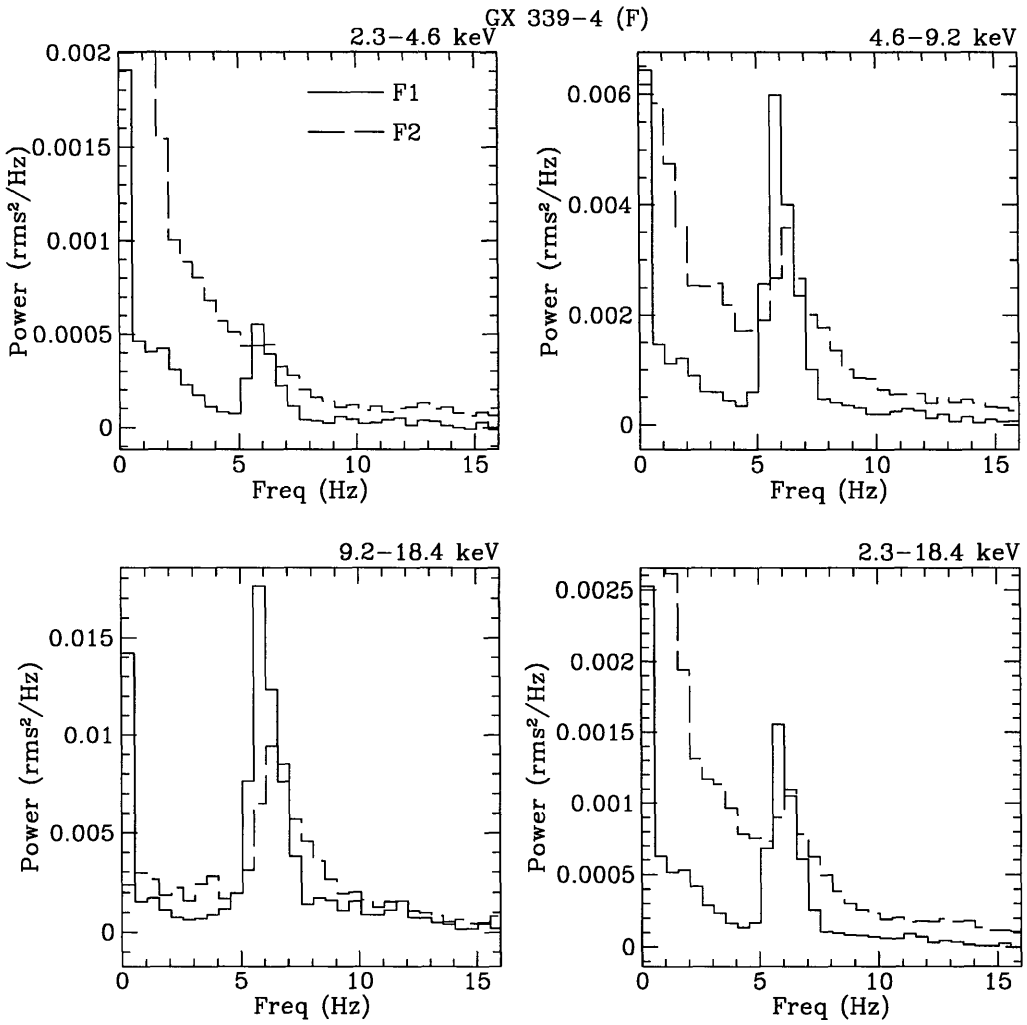

Figure 5-49: **GX 339-4 F1 and F2 States; Energy-Dependent PDS of QPO.** Comparison of the High-Frequency Energy-dependent PDS of states F1 (Wide Ratio=0.032–0.05) and F2 (Wide Ratio=0.05–0.1). In all energy ranges, the QPO during F1-state dominates over the continuum noise near 6 Hz, while in the F2 state, the QPO is comparable or less than the continuum noise in the Low Energy Range and Medium Energy Range, and dominant in the High Energy Range. In the Low Energy Range and Medium Energy Range, the F2 state has stronger continuum noise than the F1 state; in the High Energy Range, the continuum noise properties are more comparable, although the deviate in the lowest (0.125 Hz) bin.

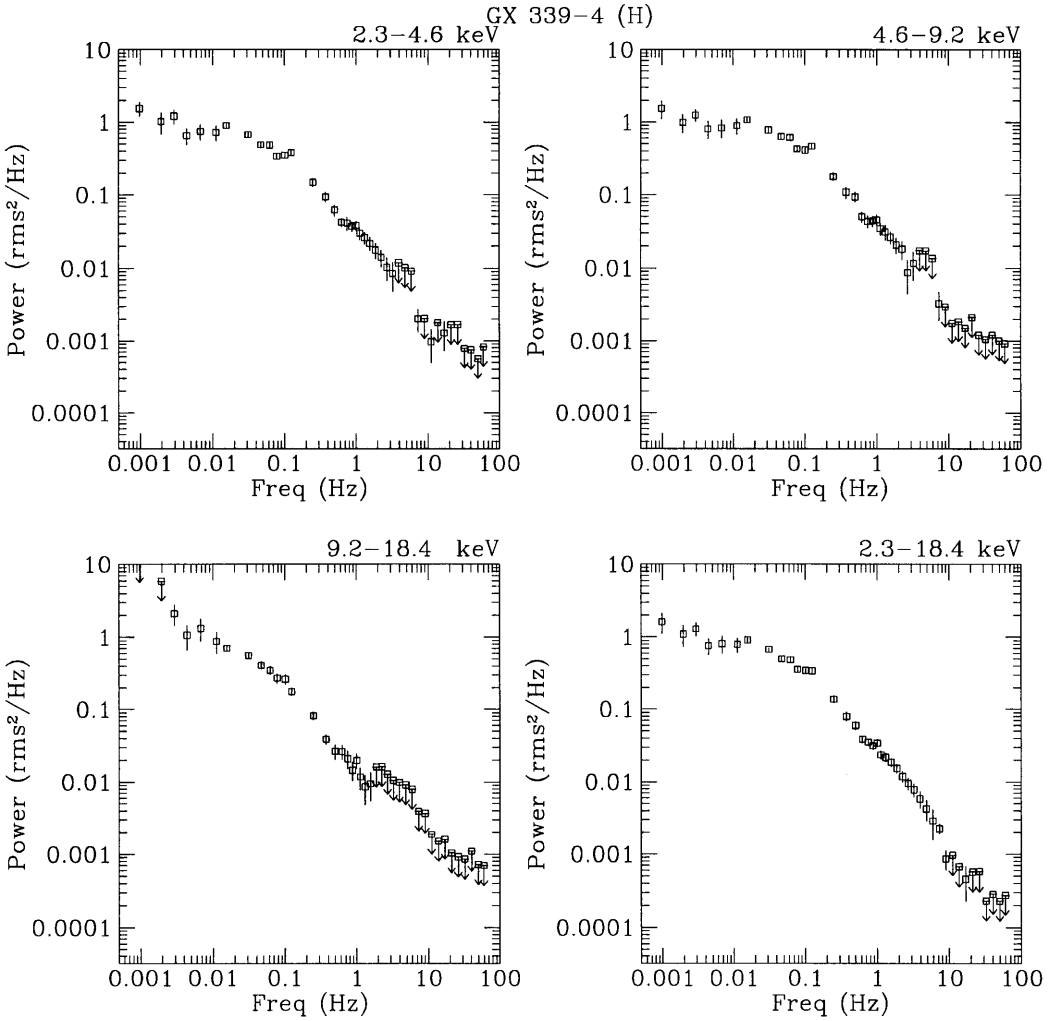

Figure 5-50: **GX 339-4 Composite PDS of H-state data** The Composite PDS of GX 339-4 in the three energy ranges, while the source is in H state. Corrections to the %rms for background and dead time have been applied.

The Very High State of GX 339-4

We closely examined the data obtained in the September 1988 observations of GX 339-4, divided by source spectrum. In Fig. 5-51, we show the Wide Ratio as a function of time during these observations. The source spectrum (measured by Wide Ratio) hardens between t=0 and 2 days; over the next two days, the source spectrum globally softens, while exhibiting short-term reversals – variously hardening and softening. For example, near time=3 days, the Wide Ratio increases, then decreases, then increases again.

We divided the data by spectrum, and labeled the spectral regions (F1-4; all in the F-state) on the hardness-intensity diagram (HID) in the upper-right panel of Fig. 5-51. There are at least three separate tracks in the HID – a nearly constant count-rate track (near I=5800 c/s 2.3–18.4 keV, crossing the regions labeled "F3" and "F4"), a nearly constant Wide Ratio track (near Wide Ratio=0.045 – labeled as "F2"), and a steeply sloped track (the Wide Ratio region labeled "F1"). These tracks correspond to those found in Fig. 5 of Miyamoto et al. (1991) and Fig. 5.28 of Ebisawa (1991).

We used the Medium-Frequency and High-Frequency FFTs in each spectral region to produce Composite PDS, in the three energy ranges (Low Energy Range, Medium Energy Range, and High Energy Range) and the full Intensity Range. We also show these PDS in Fig 5-51, in the bottom 16 panels. The scale of all PDS is given in the bottom left panel. Each column is headed with the energy range of the data used for those PDS, and each row is labeled according to spectrum, corresponding to the divisions in the HID at the top of the figure.

Discussing the 2.3–18.4 keV PDS, as the spectrum decreases in hardness, the nature of the PDS changes dramatically, from a flat-top-power-law (states F4 and F3), to a state which has a power-law below $\sim$1 Hz, which flattens into a flat-top, breaking again to a power-law above $\sim$2 Hz (state F2), to a pure power-law state, with some evidence of flattening below 0.03 Hz, which was neglected in our fits (state F1).

The strength of QPO increases with increasing energy, independent of the

spectral state.

We fit the Composite PDS produced from the F1-4 data of GX 339-4. We used different functions for the different PDS, identifying by eye the type of model to be used. The models used were Single-Power-Law (for F1), Double-Flat-Top-Single-Power-Law (for F2, with the the low-frequency flat-top ν_1 frozen to below 0.01 Hz), and Flat-Top-Single-Power-Law (states F3 and F4). For all these, we also fit Harmonic QPO, allowing the %rms normalization in the first two harmonics and sub-harmonics to vary. Typically, the High Energy Range PDS did not constrain the models well; for these PDS, we froze the BB model parameters (except the %rms) at their best fit values found from the Intensity Range PDS.

In Table 5.21, we list the QPO and BB %rms values found from these fits. The χ^2_ν were typically poor (1.3-3.6 for $\sim$75 dof).

The BB-noise is considerably weaker in the (F1) spectrally soft state (Wide Ratio=0.03–0.043), when the PDS is power-law-shaped than when it is flat-top-power-law shaped (compare 3.9–6.3% for all energy ranges in the Power-Law state with 8-20% in the Flat-Top-Power-Law state). Without exception, the broad-band (BB) %rms variability increases from the Low Energy Range to the Medium Energy Range and then is either constant, or decreases between the Medium Energy Range and the High Energy Range. Also without exception, the %rms of the QPO Fundamental increases with increasing energy. This behavior is identical to that seen from GS 1124-68 when Very-High State (VHS) QPO is observed from it, and thus may be a general characteristic of VHS QPO.

The strength of the QPO does not show monotonic dependence on the spectral hardness of GX 339-4. The QPO strength is greatest in the state with the BB model Double-Flat-Top-Single-Power-Law, and is less in the states where the BB model is either Power-Law or Flat-Top-Power-Law. Looking at the PDS, one might be misled to believe that the %rms of the QPO in the Low Energy Range PDS increases with increasing spectral hardness; our model fits do not bear this out. One is apparently misled by the relative strength of the BB power, which accounts for a dominant portion of the %rms at the QPO frequency when the spectrum is hard, but

considerably less when the spectrum is soft. While we do see dependence between the QPO %rms in the Low Energy Range it is not monotonic, nor pronounced, with the %rms values in the range of 1.1–2.9%.

Table 5.21: %rms of QPO and BB in GX 339-4

Wide Ratio	Energy Range (keV)	QPO %rms	BB %rms (0.001-64 Hz)	χ^2_ν (dof)
0.030–0.043	2.3–4.6	1.79±0.04	3.89±0.09	1.36 (139)
(F1)	4.6–9.2	5.97±0.08	6.3±0.2	1.87 (139)
	9.2–18.4	10.5±0.2	5.6±0.5	1.36 (140)
	2.3–18.4	2.89±0.04	4.45±0.07	2.42 (139)
0.043–0.050	2.3–4.6	$2.29^{+0.3}_{-0.08}$	13.5±0.8	2.25 (46)
(F2)	4.6–9.2	8.7±0.1	23.3±1.5	2.60 (46)
	9.2–18.4	17.4±0.4	24.3 ±2	1.58 (49)
	2.3–18.4	4.24±0.06	15.4±0.7	4.28 (46)
0.050–0.060	2.3–4.6	1.1±0.2	8.4±0.2	1.13 (48)
(F3)	4.6–9.2	5.7±0.1	13.0±0.2	1.43 (47)
	9.2–18.4	11.5±0.4	8.9±0.7	1.05 (48)
	2.3–18.4	2.7 ±0.1	9.5±0.1	1.39 (46)
0.060–0.075	2.3–4.6	1.85±0.06	8.8±0.1	2.73 (47)
(F4)	4.6–9.2	5.9±0.1	13.2±0.3	2.12 (45)
	9.2–18.4	9.3±0.2	8.0±0.4	2.30 (47)
	2.3–18.4	3.24±0.05	9.6±0.1	2.71 (45)

Fits applied to values in the 0.125 – 64 Hz range

In Table 5.22, we show the best-fit model parameters for the models fit to the Composite F1-4 PDS. The PDS for F1-4 were averages of 316, 551, 212, and 458 FFTs, respectively. The χ^2_ν for these models are listed in Table 5.21. The break-frequency, at which flat-top models become power-laws, is inversely proportionally to spectral hardness, going from 1.80±0.07, to 1.33±0.04, to 1.20±0.02, while changing from the F2–F3–F4 states. The Power-Law slope in the F2-F4 (Flat-Top) states is considerably steeper than that in the F1 (simple Power-Law) state (1.6–1.7 vs. 1.08±0.03 in the Intensity Range).

The QPO FWHM and centroid frequency exhibit some dependency (again, non-monotonic) on spectral hardness. In the Intensity Range the FWHM goes from 0.5, to 1.0, to 3.6, and back down to 2.3 as the spectrum hardens between states F1–4.

The centroid frequency goes from 5.8, to 6.3, to 7.4, to 6.3 as the spectrum hardens between states F1–4. In all states, no energy dependence on the QPO parameters is seen.

Table 5.22: GX 339-4 Very High State 2.3–18.4 keV PDS Broad-Band Parameters

			Broad-Band				QPO	
Wide Ratio	Model	Energy Range (keV)	ν_1 (Hz)	ν_2 (Hz)	ν_3 (Hz)	α_1	FWHM (Hz)	ν_c (Hz)
0.030–0.043	PL	2.3–4.6	–	–	–	0.91±0.02	0.53±0.03	5.80±0.02
(F1)		4.6–9.2	–	–	–	1.00±0.03	0.53±0.02	5.80±0.01
		9.2–18.4	–	–	–	(1.00)	0.55±0.03	5.78±0.01
		2.3–18.4	–	–	–	0.97±0.02	0.47±0.02	5.80±0.01
0.043–0.050	DFTPL	2.3–4.6	(0.001)	0.56±0.03	1.72±0.07	1.51±0.04	$0.59^{+0.2}_{-0.3}$	6.40±0.04
(F2)		4.6–9.2	(0.001)	0.79±0.08	1.73±0.08	1.43±0.04	1.07±0.06	6.37±0.02
		9.2–18.4	(0.001)	(0.59)	(1.79)	(1.66)	1.4±0.1	6.42±0.04
		2.3–18.4	(0.001)	0.57±0.02	1.69±0.05	1.51±0.03	0.95±0.05	6.36±0.02
0.050–0.060	FTPL	2.3–4.6	$1.35^{+0.1}_{-0.05}$	–	–	1.57±0.05	(3.58)	(6.9)
(F3)		4.6–9.2	(1.33)	–	–	(1.58)	3.17±0.2	7.08±0.07
		9.2–18.4	(1.33)	–	–	(1.58)	3.55±0.3	7.38±0.09
		2.3–18.4	1.33 ±0.04	–	–	1.57±0.03	3.40±0.3	6.9 ±0.1
0.060–0.075	FTPL	2.3–4.6	1.20±0.03	–	–	1.64±0.04	(2.27)	(6.27)
(F4)		4.6–9.2	$1.11^{+0.07}_{-0.03}$	–	–	1.53±0.05	2.35±0.1	6.38±0.03
		9.2–18.4	(1.20)	–	–	(1.70)	1.80 ±0.1	6.39±0.04
		2.3–18.4	1.21 ±0.02	–	–	1.71±0.04	2.37±0.09	6.27±0.03

Fits applied to values in the 0.0156 – 64 Hz range
Values in parenthesis are fixed
Models: PL==Power Law; DPL == Double Power Law; FTPL== Flat-Top Power-Law;
FTDPL == Flat-Top Double Power Law; DFTPL= Double Flat-Top Power-Law

Comparison of PDS of Different Intensities, Same Spectrum, GX 339-4

With GX 339-4, we are presented with the observational opportunity to compare the PDS of the source when it is in the same spectral state, as indicated by the Wide Ratio, but at a wide range of intensities. In Fig. 4-8c it can be seen that on three separate occasions, the source was in an identical range of Wide Ratio (roughly, 0.35–0.5), even while the source intensity varied by a factor of ~50 (from 30–1500 c/s in the Intensity Range). We reproduce Fig. 4-8c below in Fig. 5-52. We have marked off the Wide Ratio=0.35–0.5 range, and labeled 4 separate Intensity–Wide Ratio states (S1–4). State S1 (open triangles) is the high intensity state (2.3–18.4 count-rate ~5-7 $\times$ 10^3 c/s), previously identified as the source in "Very High State" (Miyamoto et al. 1991)

States S2 (solid squares), S3 (open squares), and S4 (solid triangles) fall within the Wide Ratio=0.35–0.5 range, but the intensities of these states were roughly 30, 150, and 1500 c/s. GX 339-4 was in these separate Intensity Range–Wide Ratio states

on different days (see Fig. 4-8a).

We selected data when the source was in its separate S1-S4 state, and produced FFTs in the three energy ranges, plus the Intensity Range; these were combined into Composite PDS. The number of FFTs averaged into each are given in Table 5.23. The results are shown in Fig. 5-52.

The PDS for the states S2, S3, & S4 which have the same Wide Ratio but different intensities, are similar in %rms across 4 orders of magnitude in frequency space (0.00097–8 Hz), in spite of the large variation in intensity. The state S1, (the "Very High State") deviates strongly from the states S2–4, with lower %rms (by $\sim\times$ 10) in the frequency range 0.0097–8 Hz. Near 8 Hz, the %rms values of the S1 data do approach those of spectrally harder S2–S4 states.

Table 5.23: Parameters for Best-Fit Power-Law to GX 339-4 T-type PDS

State Label	Intensity 2.3–18.4 keV c/s	Wide Ratio (approx.)	# Low-Freq FFTs	# Medium Freq FFTs	# High Freq FFTs
S1	$(5\text{–}7)\times10^3$	0.01–0.07	4	186	1537
S2	25-40	0.35–0.5	10	58	0
S3	120-200	0.35–0.5	8	62	0
S4	1500-1800	0.35–0.5	0	16	0

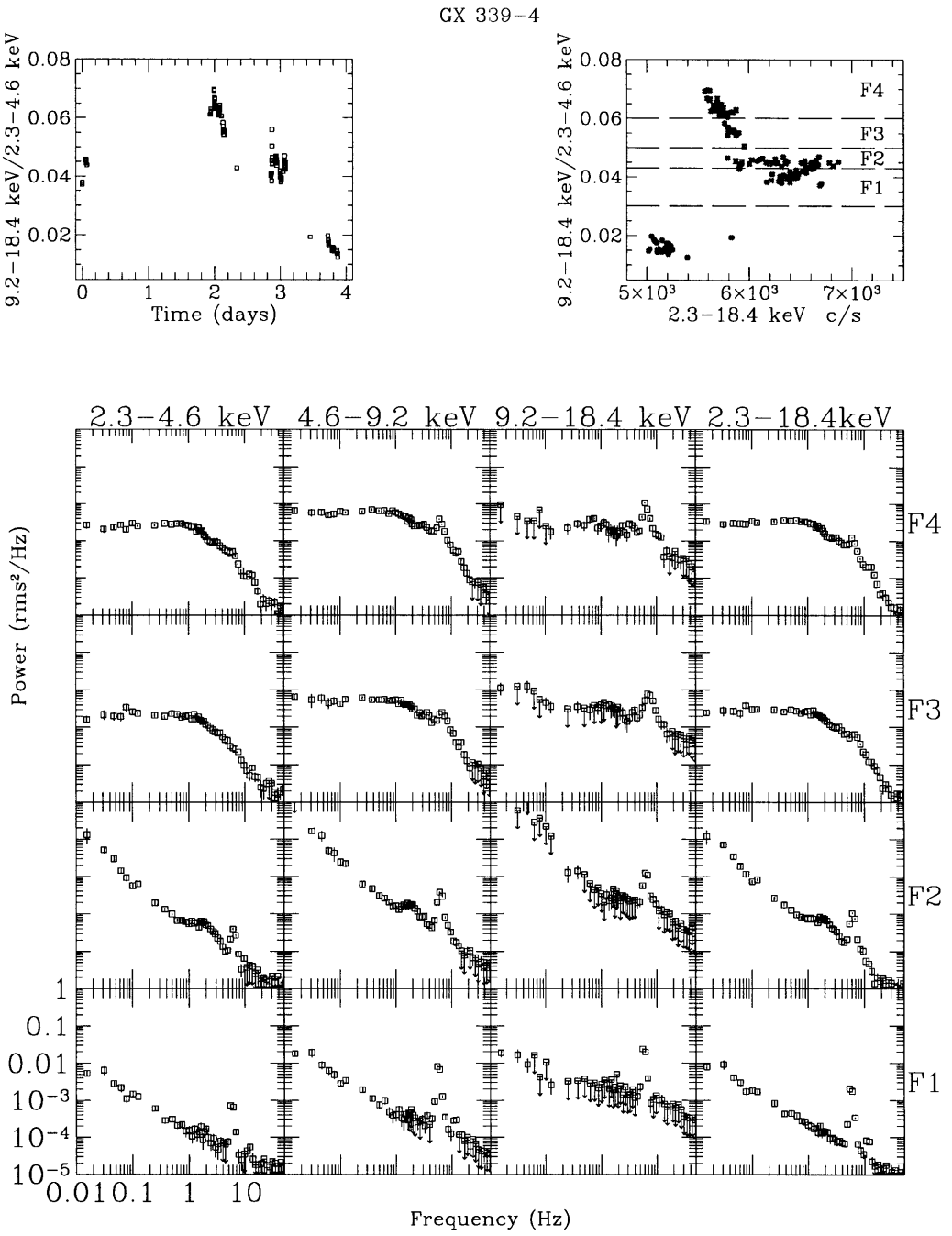

Figure 5-51: **Detailed HID and PDS of GX 339-4 with QPO** *Upper left-hand panel* is the Wide Ratio vs. time, during the period in which QPO was observed from GX 339-4 (Sept 1988; time=0 is 88/247 13:37 UT). *Upper right-hand panel* is the HID, Intensity Range count-rate vs. Wide Ratio during the Sept 1988 observation. The panel has been divided by Wide Ratio value, and each region is labeled. *Bottom Panels*: The PDS in three energy ranges plus the intensity range (labeled by column) of the Sept 1988 observations. Upper-limits are 2σ. The data was divided by spectral hardness (each row is labeled, and corresponds to a label in the HID above). The BB PDS characteristics evolve – as the spectrum softens, the BB PDS changes from a flat-top-power-law to a pure power-law, while the QPO remains throughout. This Figure may be directly compared to that of GS 1124-68 (Fig. 5-41).

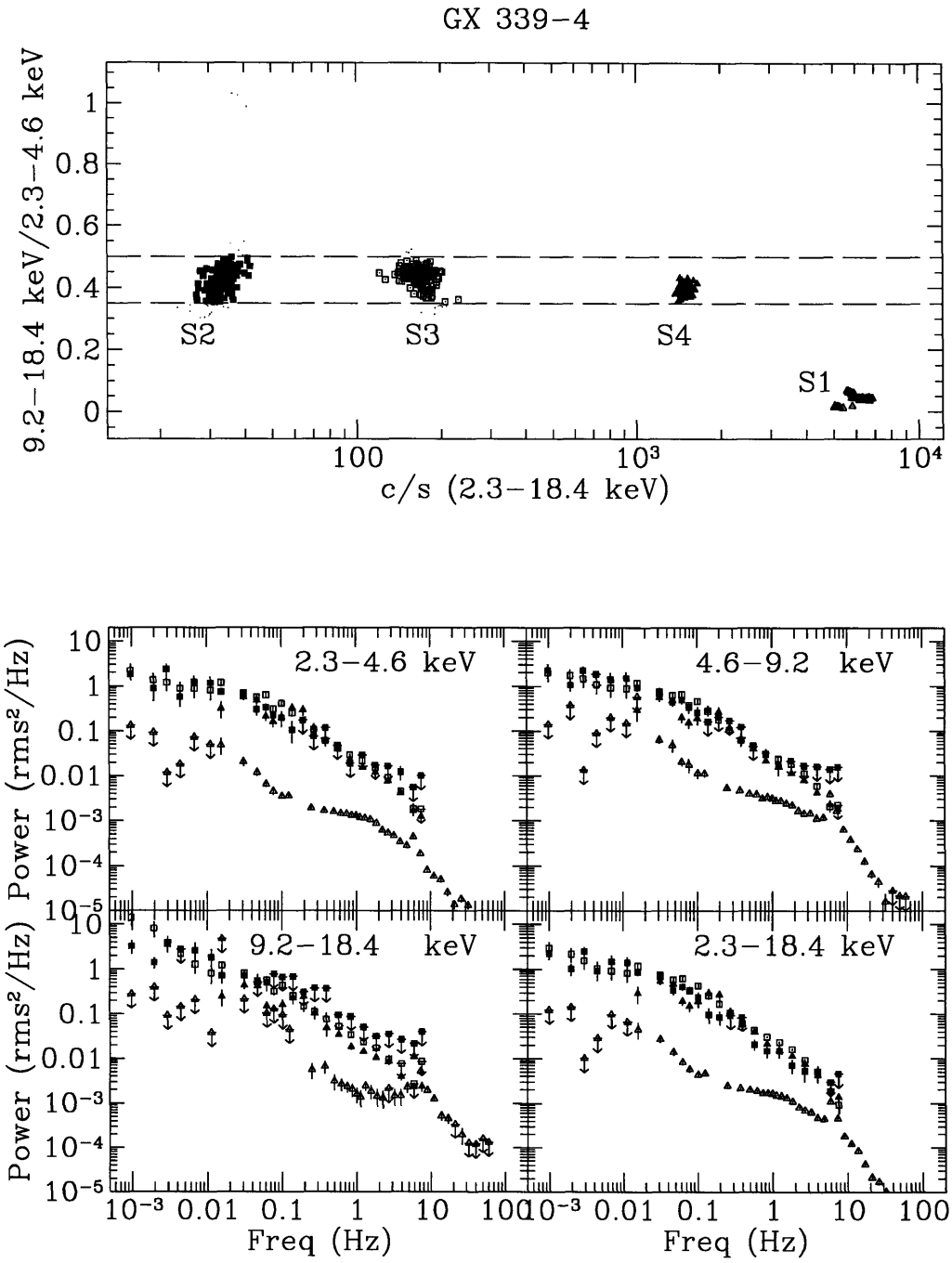

Figure 5-52: **GX 339-4 Intensity Dependence of PDS.** Comparison of PDS of GX 339-4 at different intensities and Wide Ratio. *Top Panel:* HID 2.3-18.4 keV Intensity (c/s) vs. Wide Ratio for GX 339-4, showing only data selected for the present analysis (compare with Fig. 4-8c); data are marked for reference, with the symbols in the the HID corresponding to those in the PDS in the bottom panels: S1 (open triangles), S2 (solid squares), S3 (open squares) S4 (solid triangles). The vertical lines at Wide Ratio=0.35 and 0.5 mark the range used to select S2, S3, and S4. *Bottom Panels:* PDS in three energy ranges, plus the sum energy range. Symbols correspond to the state occupied by the source, indicated in the HID. Error bars are 1 σ, and upper-limits (indicated by arrows pointed down) are 2 σ. States S2, S3, and S4 have similar PDS across all energy ranges, in spite of large variation in intensity.

Energy Dependence of the VHS QPO in GX 339-4

In Fig. 5-53, we show the PDS from High-Frequency PDS of the F-state data only, for the Low Energy Range, Medium Energy Range, and High Energy Range (corrected for background and deadtime). The data are binned linearly, to show in greater detail the QPO peak near 6 Hz. There is very strong energy dependence in the QPO, with the %rms variability increasing greatly with increasing energy. The energy dependency is similar to that seen for the VHS QPO of GS 1124-68 (see Fig. 5-42).

In Fig. 5-54, we show the PDS in nine energy ranges for data obtained 88/247–250. The energy range used to produce each PDS is labeled in the upper-right of each panel. This figure shows the prominence of the QPO in GX 339-4 relative to power at low frequencies, as a function of energy. The power-scale is arbitrary. The QPO near 6 Hz increases in strength with increasing energy, relative to the power below 1 Hz. This is similar to behavior seen in GS 1124-683 VHS QPO.

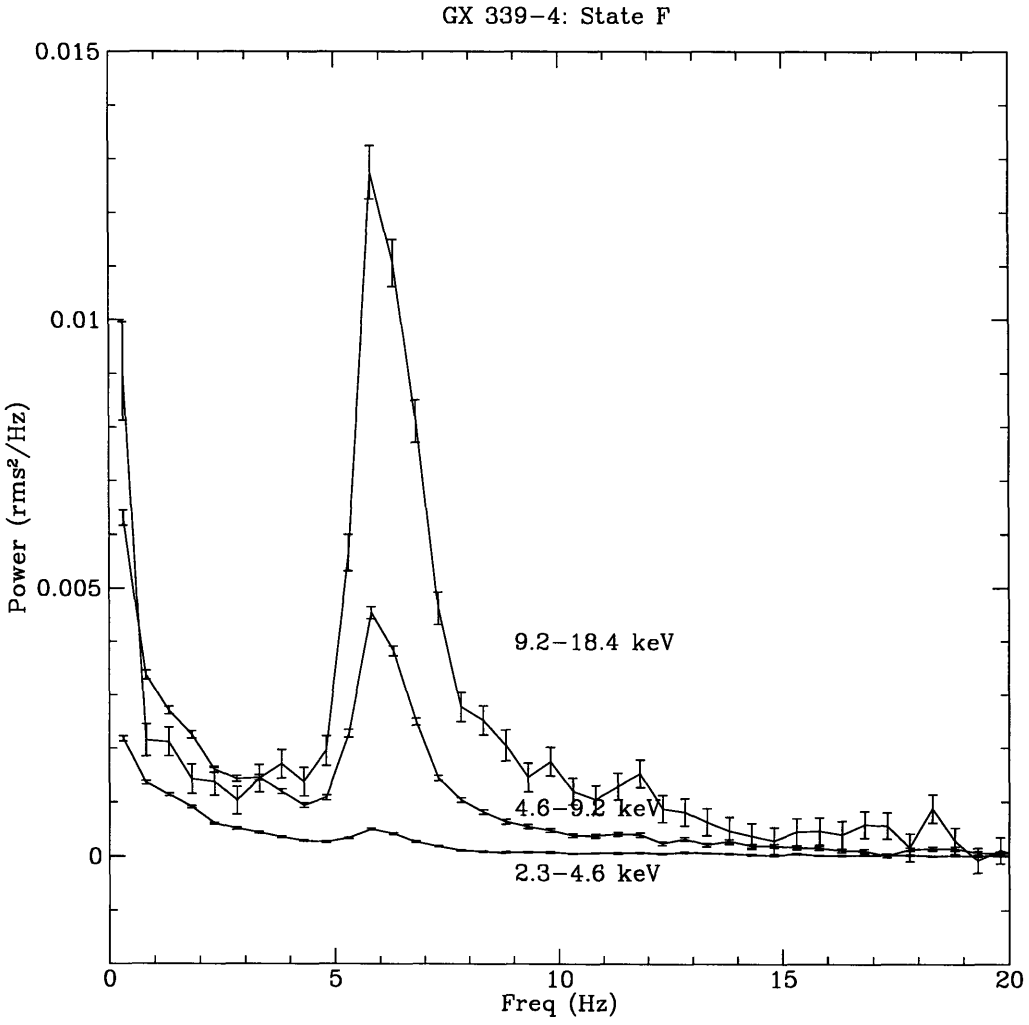

Figure 5-53: **Energy Dependence of QPO in GX 339-4.** The Composite PDS of GX 339-4 in the three energy ranges, while the source is in state "F". Data have been Poisson subtracted, and corrections to the %rms for background and dead time have been applied. This figure may be directly compared to Fig. 5-42 of GS 1124-68.

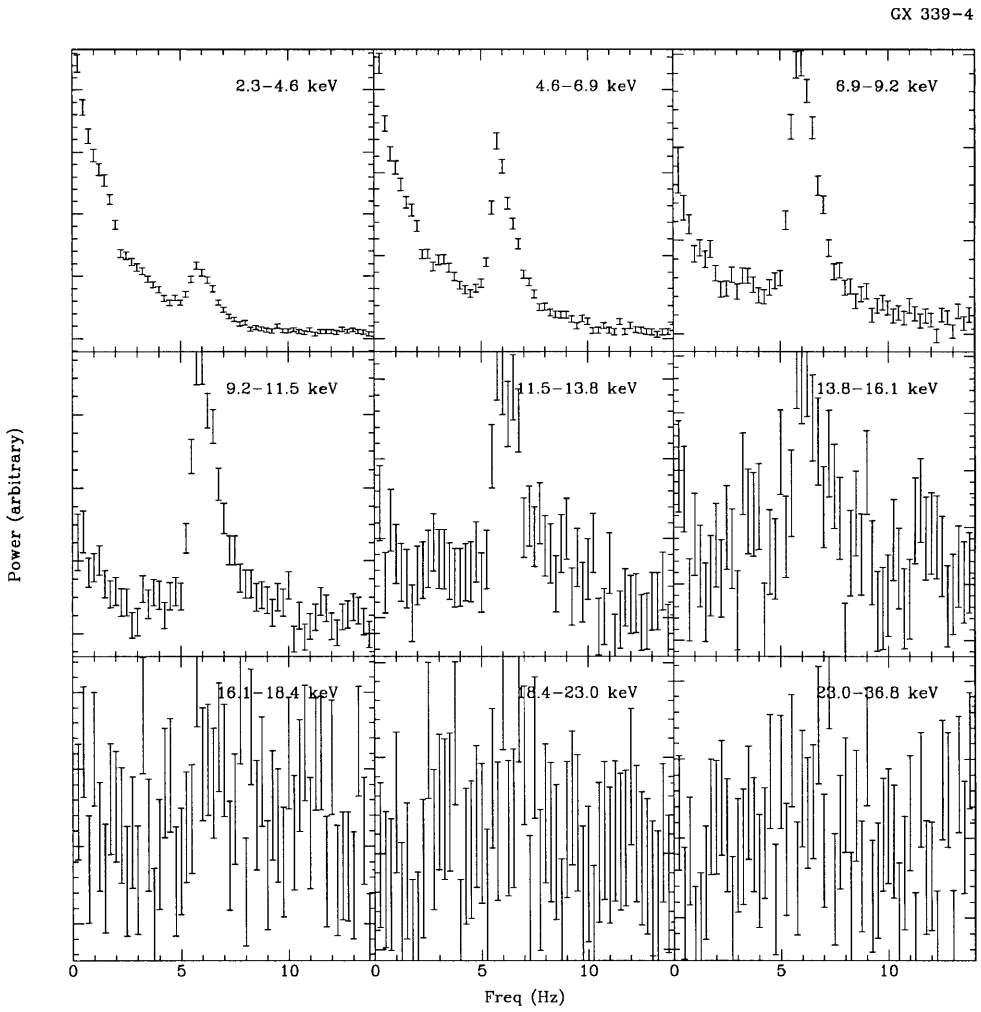

Figure 5-54: **Energy Dependent PDS of F-state GX 339-4** Nine PDS of GX 339-4, separated by energy-range of the data. The normalization of each PDS is arbitrary, and thus cannot be inter-compared to find the strength of the same features at different energies (for this, see 5-53). The data used in this plot were taken 88/247, 249, and 250. Each PDS is an average of 3097 individual transforms, each taken of 4 s of data with a Nyquist frequency of 16 Hz. The LFN (at 0.25-2 Hz) is detectable in the energy range 2.3-13.8 keV. The 6 Hz QPO is detectable in the energy range 2.3-16.1 keV, and is weak compared to the LFN in the 2.3-4.6 keV range, but becomes stronger relative to the LFN as the energy increases. By eye, we compare this Figure to Fig. 5-44.

5.4.9 GS 2000+25

Of the measured 128 s values of the Wide Ratio for GS 2000+25 measured in Ch. 4, 80% were in the range 0.021–0.23 (EFG-type source).

We produced a Composite PDS for GS 2000+25 in the D-state. The PDS is an average 15 Medium Frequency FFTs, and 36 High Frequency FFTs; there were no Low-Frequency FFTs. As there is little detectable power evident in this PDS, we fit a power-law model to the PDS; parameters for the best fit model are listed in Table 5.24.

We produced a Composite PDS for GS 2000+25 in the E-state. The PDS is an average 12 Low Frequency FFTs, 66 Medium Frequency FFTs, and 277 High Frequency FFTs. As there is little detectable power evident in this PDS, we fit a power-law model to the PDS; parameters for the best fit model are listed in Table 5.24.

We produced a Composite PDS for GS 2000+25 in the F-state. The PDS is an average of 25 Low Frequency FFTs, 193 Medium Frequency FFTs, and 947 High Frequency FFTs. As there is little detectable power evident in this PDS, we fit a power-law model to the PDS; parameters for the best fit model are listed in Table 5.24.

We produced a Composite PDS for GS 2000+25 in the GH-state. The PDS is an average of 7 Low Frequency FFTs, no Medium Frequency FFTs, and 28 High Frequency FFTs. As there is little detectable power evident in this PDS, we fit a power-law model to the PDS; parameters for the best fit model are listed in Table 5.24.

In an individual check of PDS of individual observation periods, a period of significant power was found, on day 252 of 1988 (Sept 8), between 15:45 and 17:24 UT. During this period, the source was in a spectral state with Wide Ratio=0.09–0.1. We show the PDS, from an average of 44 Medium-Frequency FFTs, in Fig. 5-59. We fit the data with a Flat-Top-Power-Law function with an additional Lorentzian component to account for QPO near 2 Hz. We find that the QPO component is required by the data in the Low Energy Range (compared χ^2_ν= 3.4 (29 dof) without the QPO component to 0.7 (26 dof) with the QPO component. This is the first detection of QPO from GS 2000+25. Based on the source spectrum and Flat-Top-

Single-Power-Law nature of the PDS and comparing this to the Wide Ratio and timing behavior of other sources in this study, we determine that GS 2000+25 was in the Low-State when the QPO was detected.

We further subdivided the PDS by energy; in Fig. 5-60, we show the PDS (with arbitrary normalization) in nine energy ranges. We fit the Flat-Top-Single-Power-Law plus QPO model to the Low Energy Range, Medium Energy Range, and High Energy Range PDS made from data taken during the period when the LS QPO was observed. The best-fit model parameters are listed in Table 5.26. The centroid frequency (Intensity Range PDS) is 2.63±0.06, FWHM is 1.7±0.2, and the %rms is consistent with being independent of energy,

GS 2000+25, Separated by Observation Period

Because we find high upper-limits to the %rms variability in the GS 2000+25 data divided by the coarse spectral bins, there is good reason to believe that better measurements can be obtained by using finer spectral binning. We split the data by observation epoch, which has been guided by the time-evolved spectral variability seen in Fig. 4-16.

Selecting observational epochs so that the Wide Ratio does not vary greatly, we divided the data into 8 epochs as listed in Table 5.27, along with the frequency range of the resulting Composite PDS, and the mean Wide Ratio (and 1σ standard deviation of measured 128s averaged values during this epoch). Observation epoch 3 had no combined timing and spectral data, and thus we did not produce PDS from this period.

We show the Composite PDS of data taken during the 7 observational epochs (1-2, 4-8) from GS 2000+25 in Figs. 5-61 & 5-62. The best-fit model parameters are listed in Table 5.28. Observations 1 & 2 have power-law PDS (with a constant component, due to systematic uncertainty in the subtracted Poisson level caused by high count-rate), when the Wide Ratio is in the range 0.01–0.0125 (E-state). During observation 4, the spectrum is harder (Wide Ratio=0.096 ±0.005; F-state), and the timing properties produce a flat-top PDS at $\nu < 2.5$ Hz, dropping to a power-

law above this ($\alpha_1 \sim 1.3$), with a Lorentzian near the break-frequency (discussed in Sec. 5.4.9 – we do not discuss the Lorentzian further here). In observation periods 5–7, the sensitivities of the PDS are not sufficient to find a model by eye. We fit these data with power-law models – freezing the power-law slope to $\alpha_1=1.0$ when the fits were unstable (had completely unconstrained power-law slopes).

In observation 8, the spectral hardness was the greatest observed from this source of these eight epochs, (Wide Ratio=0.4; H-state). However, the time-resolution of the data was only sufficient to produce Low-Frequency PDS, in which significant power was found. We modelled this PDS as a power-law with slope frozen at $\alpha_1=1$; the fit values are only moderatly shallower, but with no significant improvement in the poor χ^2_ν values obtained with the slope frozen at 1.0.

For all PDS, the BB %rms variability is measured to be or is consistent with increasing %rms variability with increasing energy, with the notable exception of observation epoch when QPO was detected (# 4). This statement is also true for the sources Cyg X-1, GS 1124-68, and GX 339-4. It may be that this is a generic trait of variability in BHC sources exhibiting QPO.

Observation #5 has a Wide Ratio range which is roughly consistent with that observed from GS 1124-68 and GX 339-4 while they exhibit VHS QPO. After finding the best-fit models in the Intensity Range we added a Lorentzian, with ν_c=4, 5, and separately 6 Hz, with FWHM=1.0 Hz, to obtain 3σ upper-limits of the %rms variability of such component, which were 7.2%, 4.8%, and 7.5% (respectively). In the High Energy Range the corresponding 3σ upper-limits were 29%, 26%, and 30%. As these limits are greater than the measured strength of VHS QPO in GX 339-4 and GS 1124-68, we thus cannot exclude the presence of VHS QPO in this observation.

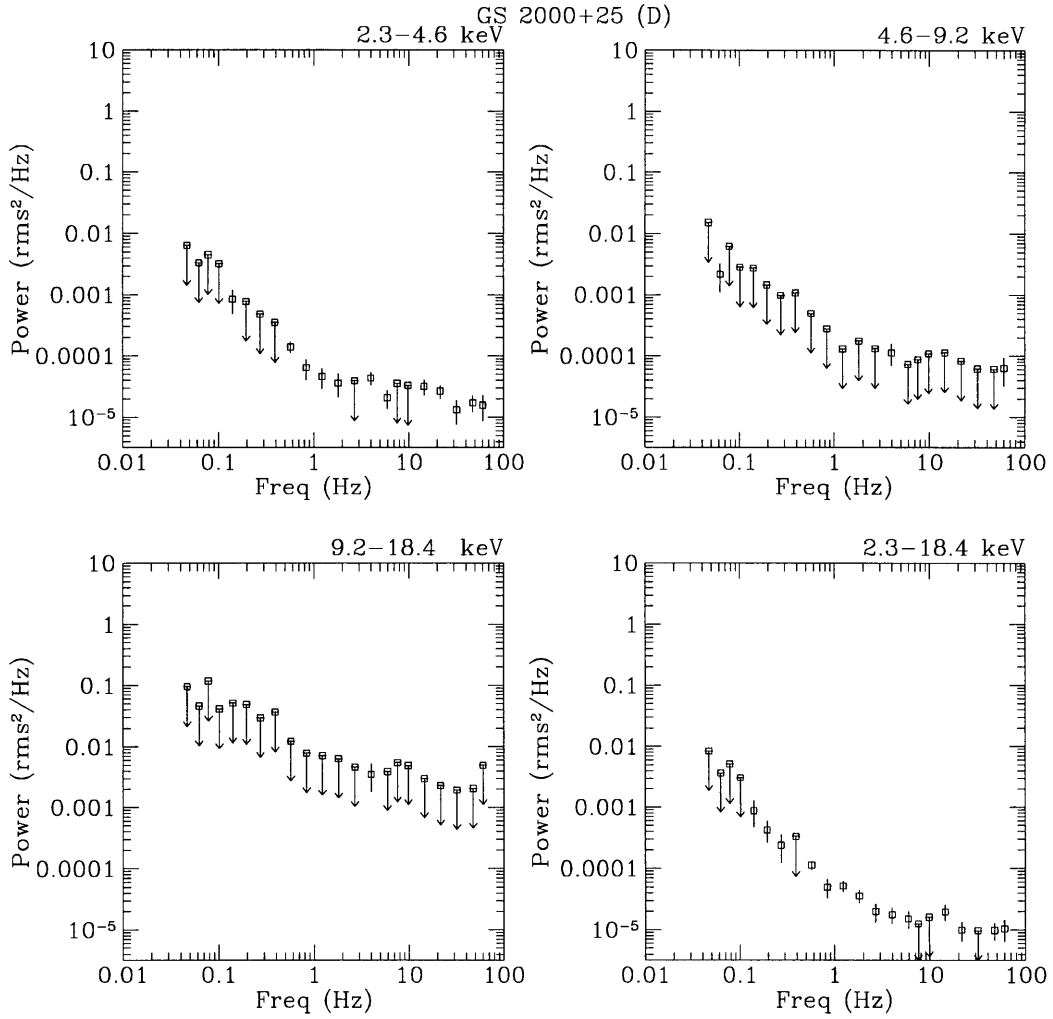

Figure 5-55: **GS 2000+25 Composite PDS in D-spectral state.** The Composite PDS in the three energy ranges and the sum energy range (indicated in each panel). Corrections for background and deadtime have been applied.

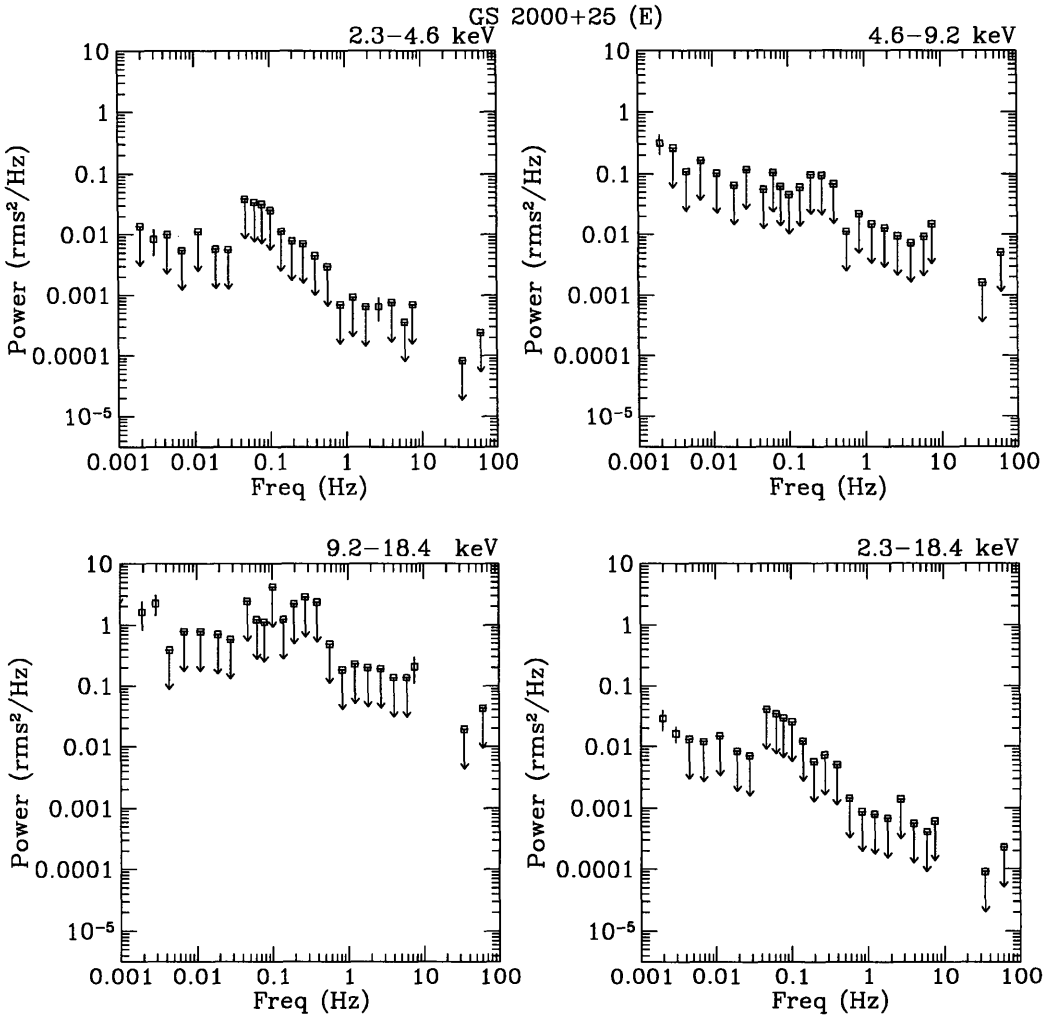

Figure 5-56: **GS 2000+25 Composite PDS in E-spectral state.** The Composite PDS in the three energy ranges and the sum energy range (indicated in each panel). Corrections for background and deadtime have been applied. Upper-limits are 2σ.

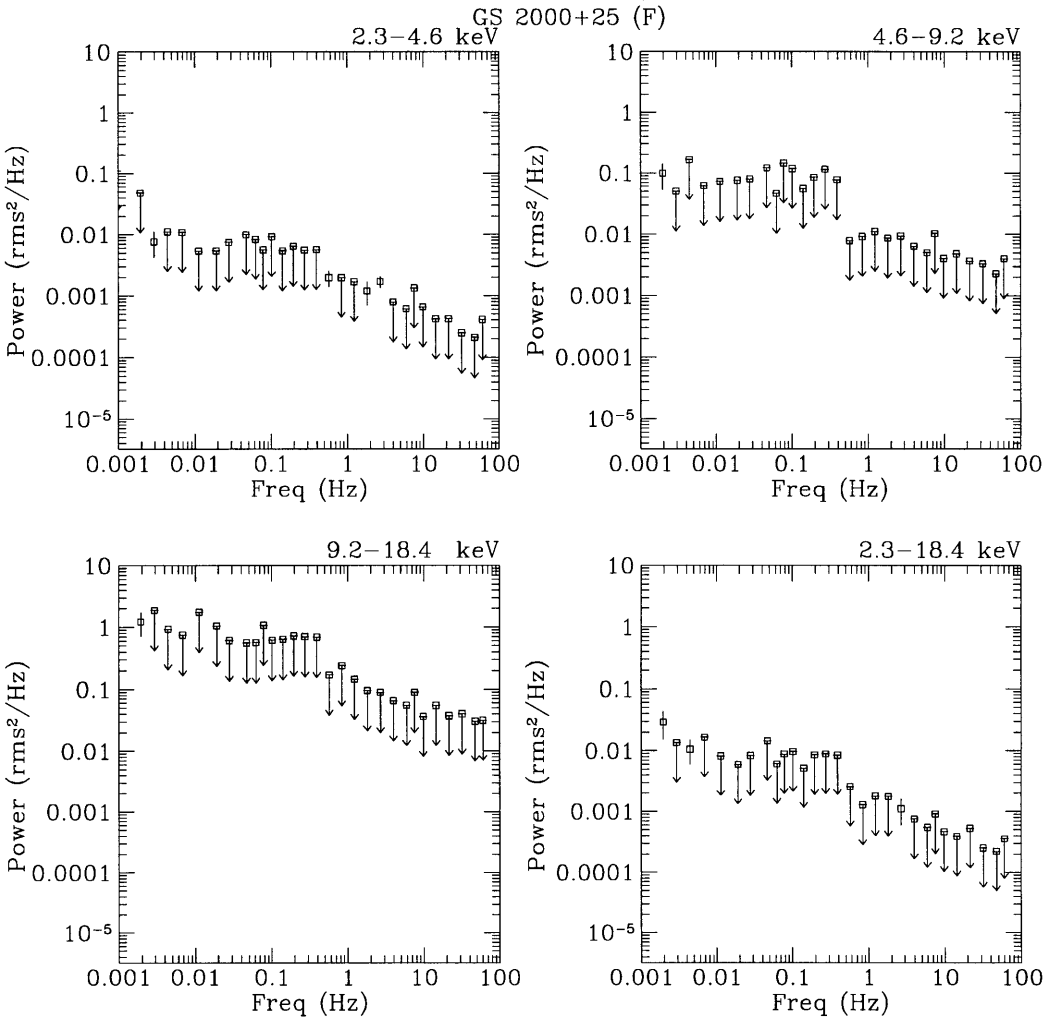

Figure 5-57: **GS 2000+25 Composite PDS in F-spectral state.** The Composite PDS in the three energy ranges and the sum energy range (indicated in each panel). Corrections for background and deadtime have been applied. Upper-limits are 2σ.

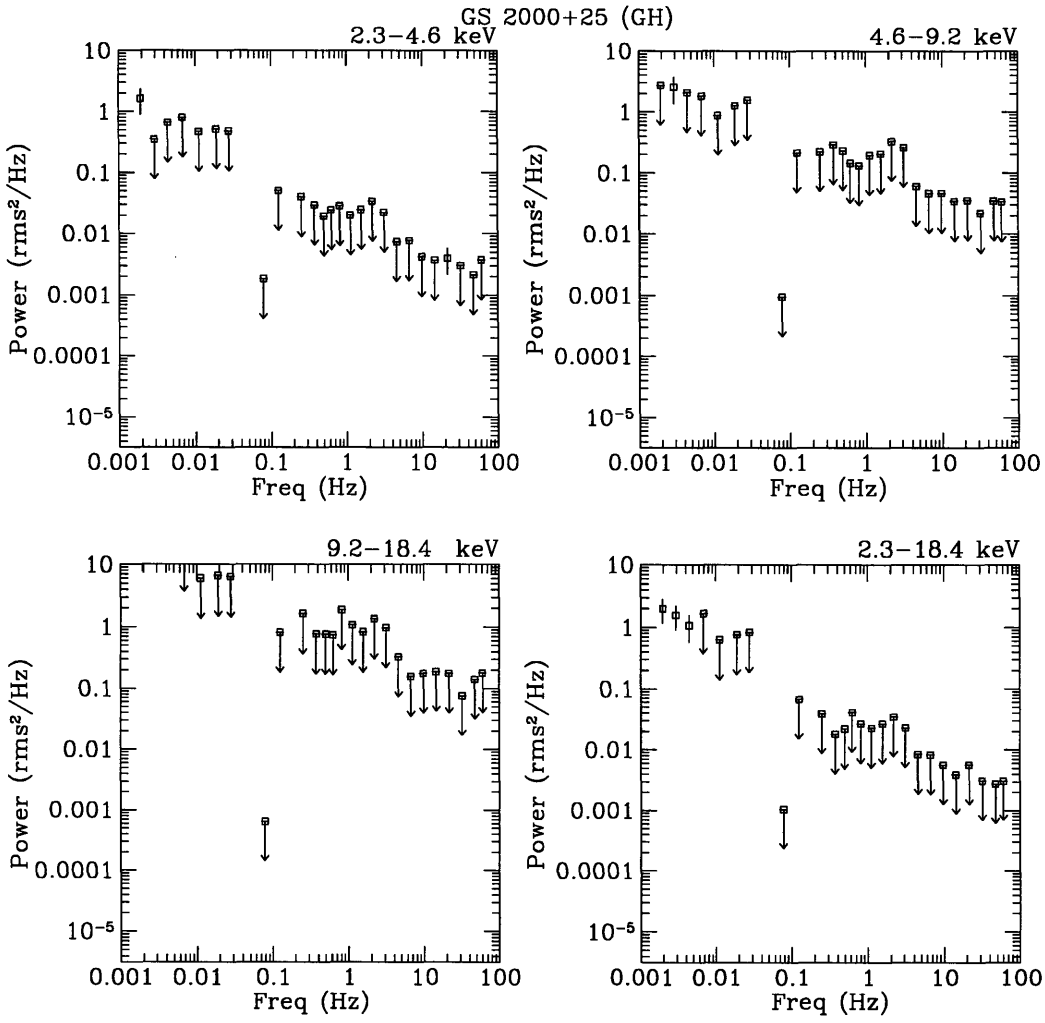

Figure 5-58: **GS 2000+25 Composite PDS in GH-spectral state.** The Composite PDS in the three energy ranges and the sum energy range (indicated in each panel). Corrections for background and deadtime have been applied. Upper-limits are 2σ.

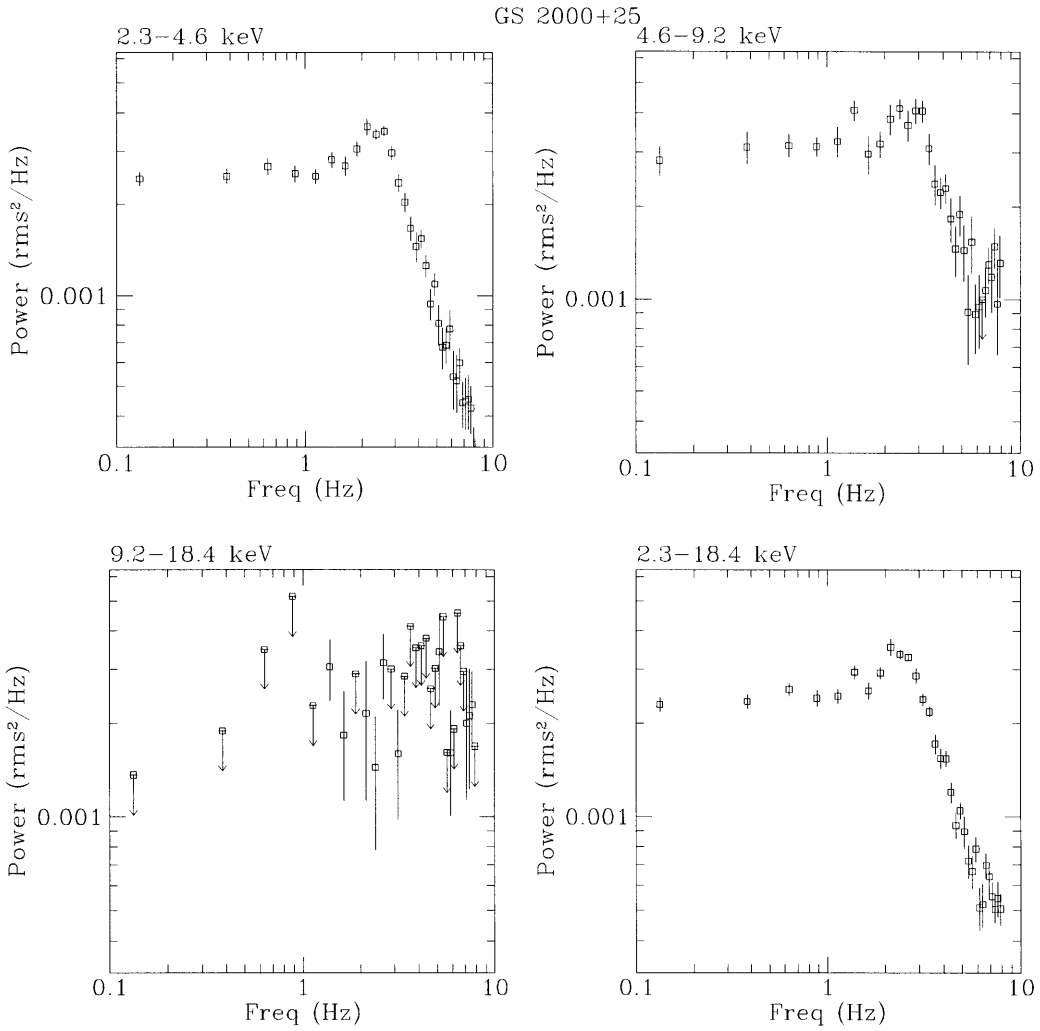

Figure 5-59: **GS 2000+25 PDS of State with QPO.** The PDS in the three energy ranges and the sum energy range (indicated in each panel). Corrections for background and deadtime have been applied to the Power. Upper-limits are 2σ.

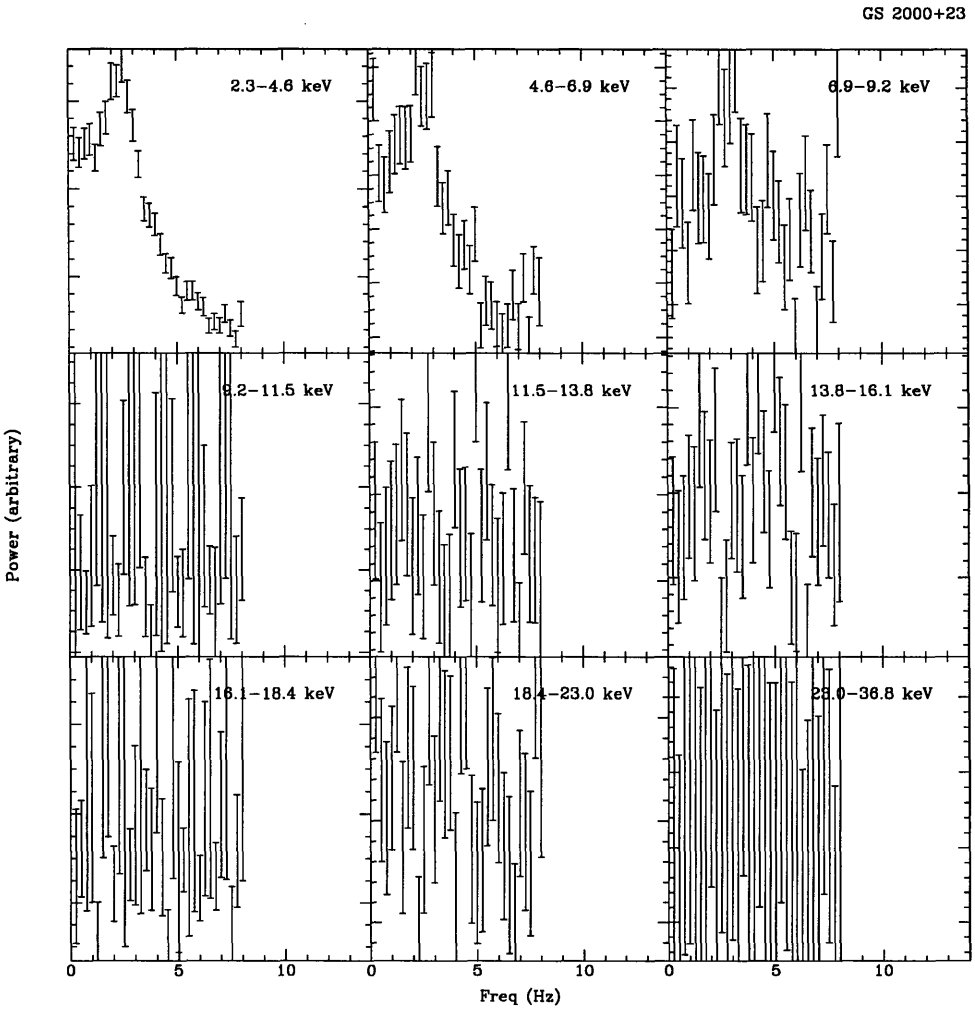

Figure 5-60: **GS 2000+25 Nine-Energy Range PDS of state QPO.** The PDS in nine energy ranges of GS 2000+25, (labeled in each figure). The power-scale in each individual panel is arbitrary.

Table 5.24: Parameters for Best-Fit Power-Law to GS 2000+25 Composite PDS

Wide Ratio	Energy Range (keV)	Power Law Slope (α)	%rms[b] (0.001-64 Hz)	χ^2_ν (dof)
0.0032–0.01[b]	2.3–4.6	$0.92^{+0.25}_{-0.13}$	$3.9^{+0.4}_{-0.7}$	1.67 (5)
(D)		(1.00)	3.7 ±0.3	1.4 (6)
	4.6–9.2	$1.4^{+1.7}_{-0.57}$	<11	1.81 (5)
		(1.00)	4.8 ±0.5	1.54 (6)
	9.2–18.4	(1.00)	<25.8	0.48 (6)
	2.3–18.4	$1.1^{+0.2}_{-0.1}$	$3.5^{+0.4}_{-0.5}$	1.55 (5)
0.01–0.032[a]	2.3–4.6	$1.18^{+0.7}_{-0.5}$	<7.9	1.07 (13)
(E)		(1.00)	1.3 ±0.2	0.63 (14)
	4.6–9.2	1.06 ±0.3	<22.8	0.77 (13)
		(1.00)	5.8 ±0.8	0.72 (15)
	9.2–18.4	$2.2^{+0.6}_{-0.4}$	<4.0	0.48 (13)
		(1.00)	11.7±0.3	1.37 (14)
	2.3–18.4	1.1±0.2	<6.1	0.91 (13)
		(1.00)	2.1±0.2	0.85 (14)
0.032–0.1[a]	2.3–4.6	1.7 ±0.5	<2.3	0.60 (13)
(F)		(1.00)	1.6 ±0.3	0.67 (14)
	4.6–9.2	3.00 ±0.06	<0.3	1.12 (13)
		(1.00)	<4.9	1.46 (14)
	9.2–18.4	$1.4^{+0.5}_{-0.3}$	<27.8	0.65 (28)
		(1.00)	15.7 ±2	0.69 (29)
	2.3–18.4	1.5±0.4	<3.1	0.58 (13)
		(1.00)	1.9±0.2	0.66 (14)
0.1–0.32[b]	2.3–4.6	$1.9^{+1.1}_{-0.7}$	<16.5	0.90 (24)
(GH)		(1.00)	9.5±2	0.92 (25)
	4.6–9.2	$1.1\ ^{+0.4}_{-0.3}$	<59	0.81 (24)
		(1.00)	20±3	0.79 (25)
	9.2–18.4	$1.0^{+0.2}_{-0.1}$	<150	0.72 (24)
		(1.00)	62±6	0.70 (25)
	2.3–18.4	$1.18^{+0.2}_{-0.1}$	<24	0.77 (24)
		(1.00)	20±2	0.90 (25)

a Fits applied to values in the 0.00097 – 64 Hz range
b Fits applied to values in the 0.00156 – 64 Hz range
Values in parenthesis are fixed
Upper-limits are 3 σ

Table 5.25: Parameters for Best-Fit Flat-Top Power-Law + Lorentzian to GS 2000+25 for Composite PDS]

Wide Ratio	Energy Range (keV)	Flat-Top Power-Law[a] %rms (0.001-64 Hz)	QPO[b] %rms	χ^2_ν (dof)
0.0032–0.01	2.3–4.6	<3.9	-1.3±0.2	3.38 (20)
(D)	4.6–9.2	3.7±0.7	<4.8	1.45 (20)
	9.2–18.4	<40	<17.5	1.45 (20)
	2.3–18.4	<7.3	<0.45	3.11 (20)
0.01–0.032	2.3–4.6	<12	<5.9	0.92 (24)
(E)	4.6–9.2	<48	<26	1.47 (24)
	9.2–18.4	<180	<60	1.27 (24)
	2.3–18.4	<12	<6	3.11 (24)
0.032–0.1	2.3–4.6	9.7±2	$4.8^{+1.2}_{-1.6}$	0.88 (28)
(F)	4.6–9.2	<25.5	<10.2	1.80 (28)
	9.2–18.4	<175	<129	1.18 (28)
	2.3–18.4	$4.7^{+3.3}_{-1.3}$	<8.9	1.21 (28)
0.1–0.32	2.3–4.6	<63	<57	0.88 (28)
(GH)	4.6–9.2	<120	<121	1.23 (24)
	9.2–18.4	<320	<250	1.42 (24)
	2.3–18.4	<57	<66	1.97 (24)

[a] Flat-Top Power-Law has ν_1=2.23 and α_1=1.28 (both fixed)
[b] QPO has ν_c=2.63 and FWHM=1.69 (both fixed)
Upper-limits are 3 σ

Table 5.26: Parameters for Best-Fit Flat-Top Power-Law + Lorentzian to GS 2000+25 when QPO is present

Energy Range (keV)	Flat-Top Power-Law ν_1 (Hz)	(α_1)	%rms (0.001-64 Hz)	QPO ν_c (Hz)	FWHM (Hz)	%rms	χ^2_ν (dof)
2.3–4.6	2.88 ±0.05	2.05 ±0.07	12.6 ±0.1	–	–	–	3.40 (29)
	2.80 ±0.2	1.8 ±0.2	$11.9^{+0.2}_{-0.5}$	$2.41^{+0.15}_{-0.09}$	$1.3^{+0.6}_{-0.3}$	$4.9^{+1.3}_{-0.7}$	0.79(26)
4.6–9.2	2.9 ±0.3	1.3 ±0.2	16.2±0.9	(2.63)	(1.68)	5.6 ±0.7	1.52 (28)
9.2–18.4	(2.23)	(1.28)	9.7 ±1.4	(2.63)	(1.68)	$5.4^{+1.3}_{-1.7}$	1.91 (30)
2.3–18.4	$2.2^{+0.3}_{-0.1}$	$1.3^{+0.2}_{-0.1}$	12.5 ±0.3	2.63±0.06	1.7±0.2	6.3±0.5	1.39 (26)

Fit is of single observation period with Wide Ratio=0.09-0.1
Values in parenthesis are fixed
Fits applied to values in the 0.125 – 8.0 Hz range

Table 5.27: Division of GS 2000+25 Data

Observation ID	Start Time (UT)	End Time (UT)	PDS Freq Range	<Wide Ratio> (1σ)
1	88/120 02:53	88/130 00:24	0.0156–64	0.0096 (0.0014)
2	88/153 09:46	88/153 13:14	0.0156–8.0	0.0125 (0.00081)
3	88/178 22:28	88/179 00:12	–	–
4	88/252 15:45	88/252 17:24	0.0156–8.0	0.0961 (0.0049)
5	88/292 15:38	88/293 14:00	0.00097–64.0	0.0543 (0.0076)
6	88/310 09:36	88/311 19:13	0.00097–64.0	0.0348 (0.0059)
7	88/342 14:41	88/344 13:07	0.0156–64.0	0.123 (0.025)
8	88/351 09:32	88/352 01:03	0.00097–0.0312	0.40 (0.15)

Table 5.28: GS 2000+25 PDS Broad-Band Parameters

Obs. ID (Wide Ratio[a])	Energy Range (keV)	Model	% rms	ν_1	α_1	χ^2_ν (dof)	Freq. Range (Hz)
1	2.3–4.6	PL	$5.1^{+1.2}_{-0.9}$	–	1.59±0.11	0.86 (21)	0.0156–64
(0.0096 ±0.0014)	4.6–9.2	PL	$4.4^{+1.3}_{-0.7}$	–	1.34 ±0.18	1.19 (21)	
	9.2–18.4	PL	$9.8^{+1.9}_{-2.6}$	–	(1.38)	0.55 (21)	
	2.3–18.4	PL	3.9±0.6	–	1.38 ±0.08	1.35 (21)	
2	2.3–4.6	PL	$8.1^{+2.2}_{-1.6}$	–	1.4±0.1	2.11 (15)	0.0156–8.0
(0.01250 ±0.0008)	4.6–9.2	PL	23.9±5.7	–	1.9 ±0.1	1.82 (15)	
	9.2–18.4	PL	14 ±3	–	1.35±0.25	1.57 (15)	
	2.3–18.4	PL	13±3	–	1.58 ±0.09	2.55 (15)	
4[b]	2.3–4.6	FTPL	11.6±0.2	$2.5^{+0.1}_{-0.2}$	1.6±0.1	0.73 (45)	0.0156–8.0
(0.0961±0.0049)	4.6–9.2	FTPL	16.0±0.8	2.9±0.2	1.3±0.2	1.42 (45)	
	9.2–18.4	FTPL	8.8±1.8	(2.23)	(1.28)	1.47 (45)	
	2.3–18.4	FTPL	12.2 ±0.4	$2.23^{+0.3}_{-0.2}$	$1.28^{+0.16}_{-0.12}$	0.99 (43)	
5	2.3–4.6	PL	0.4±0.1	–	(1.81)	4.96 (29)	0.00097–64.0
(0.0543±0.0076)	4.6–9.2	PL	1.4±0.2	–	(1.81)	1.37 (30)	
	9.2–18.4	PL	4.0±0.7	–	2.5±0.5	0.89 (28)	
	2.3–18.4	PL	0.7±0.1	–	$1.81^{+0.35}_{-0.27}$	1.92 (28)	
6	2.3–4.6	PL	<3.0	–	1.0±0.2	1.09 (28)	0.00097–64.0
(0.0348±0.0059)	4.6–9.2	PL	$3.6^{+1.4}_{-0.8}$	–	1.2±0.2	1.72 (28)	
	9.2–18.4	PL	$7.5^{+0.7}_{-0.3}$	–	$2.0^{+0.3}_{-0.2}$	2.52 (28)	
	2.3–18.4	PL	$1.5^{+0.3}_{-0.2}$	–	1.2±0.1	1.07 (28)	
7	2.3–4.6	PL	<7.8	–	(1.00)	1.32 (23)	0.0156–64.0
(0.123±0.025)	4.6–9.2	PL	<23.6	–	(1.00)	1.62 (23)	
	9.2–18.4	PL	<87	–	(1.00)	0.63 (23)	
	2.3–18.4	PL	<6.6	–	(1.00)	1.00 (23)	
8	2.3–4.6	PL	13±1.2	–	(1.00)	2.06 (7)	0.00097–0.0312
(0.40±0.15)	4.6–9.2	PL	23±1.7	–	(1.00)	1.71 (7)	
	9.2–18.4	PL	63±4	–	(1.00)	2.42 (7)	
	2.3–18.4	PL	23±1.3	–	(1.00)	3.11 (7)	

[a] Mean value ±1 σ

[b] Lorentzian included in Fit – see previous section

Values in parenthesis are fixed

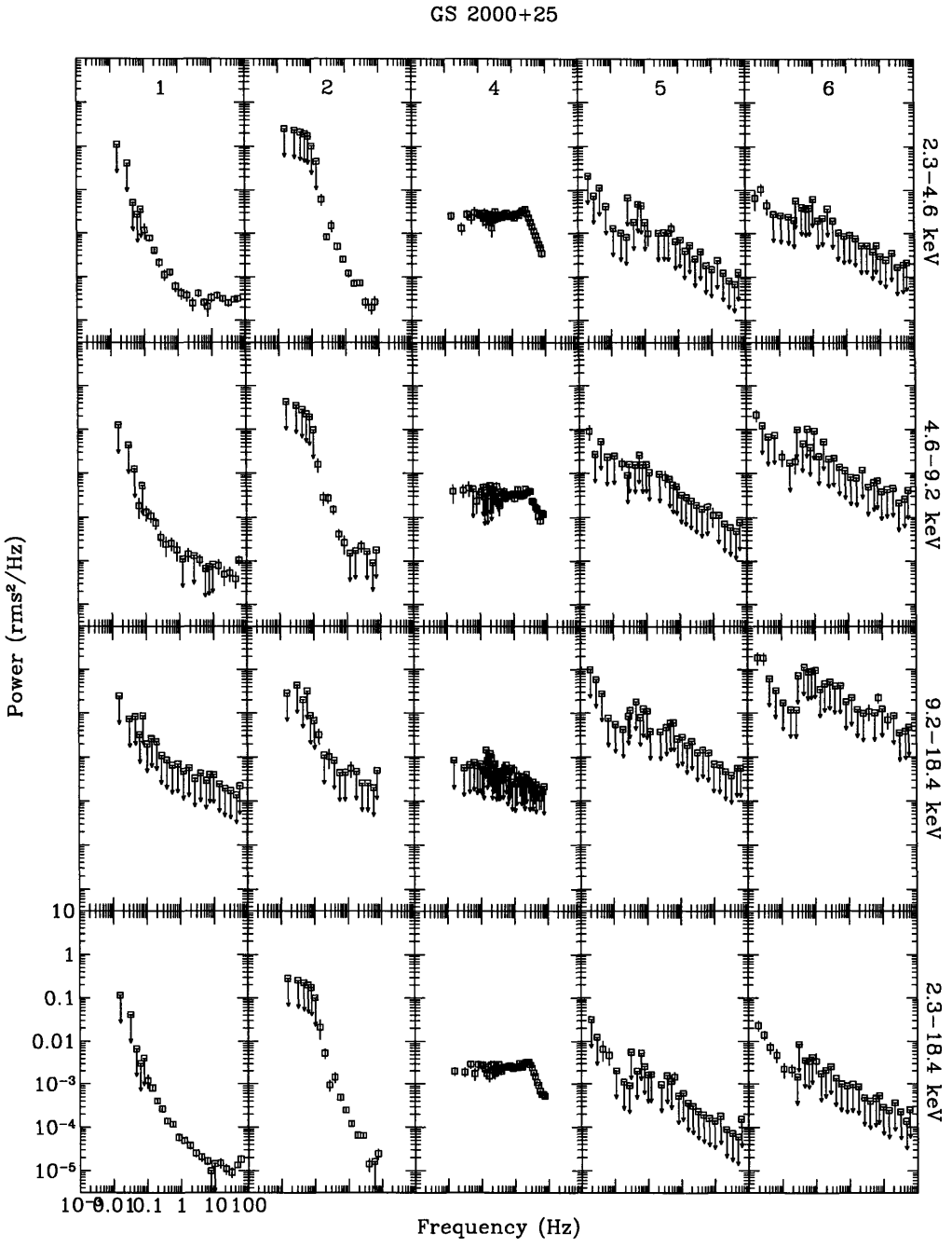

Figure 5-61: **GS 2000+25 Composite PDS, Observations #1–6.** The Composite PDS in the three energy ranges and the sum energy range (indicated in each panel), during the observational epochs listed in Table 5.27. Each column is composed of PDS from a single observational epoch (indicated at the top of the top panel), and each row is composed of PDS from a single energy range (indicated to the far right). Corrections for background and deadtime have been applied. Upper-limits are 2σ.

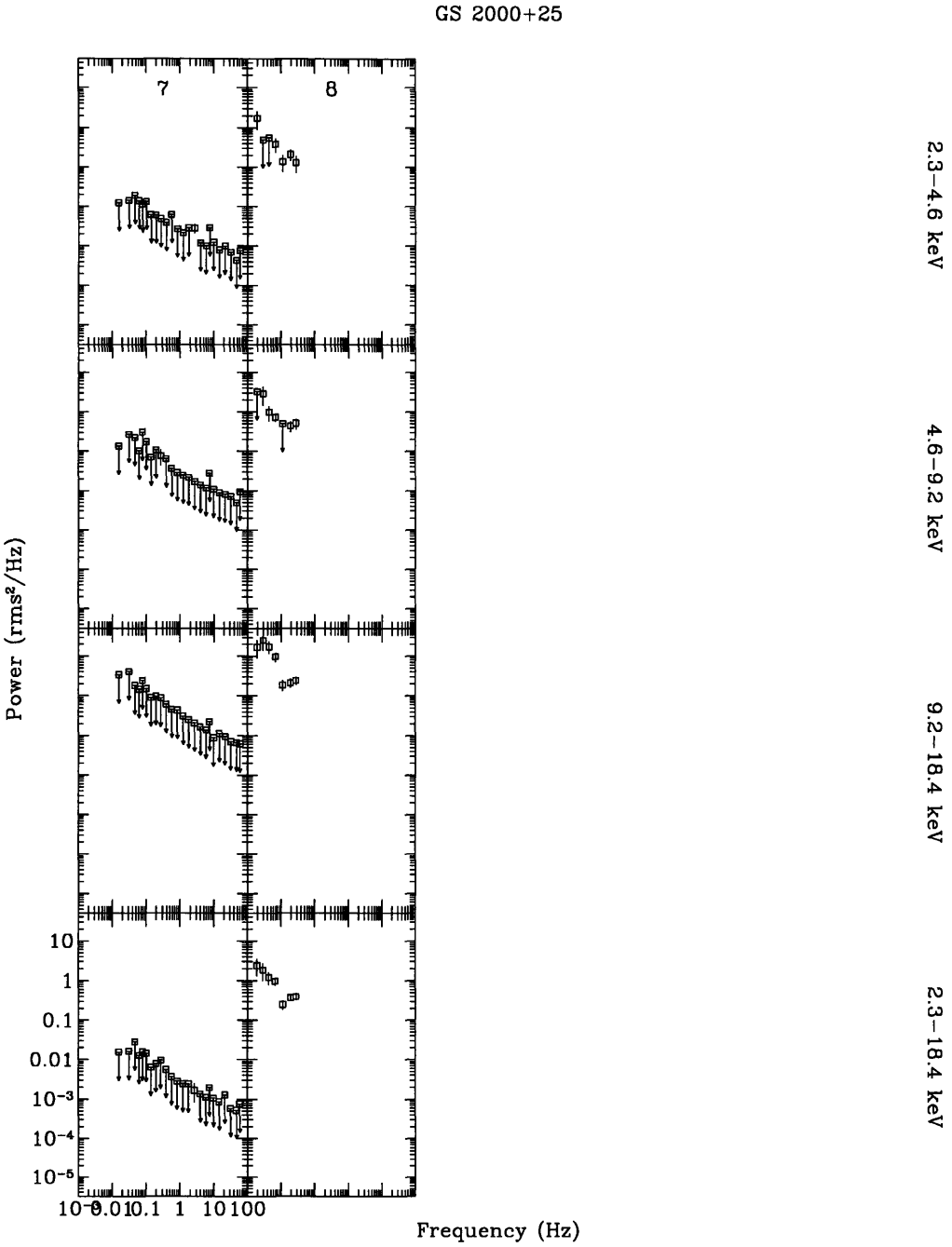

Figure 5-62: **GS 2000+25 Composite PDS, Observations #7–8.** The Composite PDS in the three energy ranges and the sum energy range (indicated in each panel), during the observational epochs listed in Table 5.27. Each column is composed of PDS from a single observational epoch (indicated at the top of the top panel), and each row is composed of PDS from a single energy range (indicated to the far right). Corrections for background and deadtime have been applied. Upper-limits are 2σ.

5.4.10 GS 2023+33

Of the measured 128 s values of the Wide Ratio for GS 2023+33 measured in Ch. 4, 80% were in the range 0.38–2.05 (HI-type source). Of all the sources in the present sample, GS 2023+33 is, on average, the spectrally hardest.

In Fig. 5-63, we show the Composite PDS for GS 2023+33 in the G-state (Wide Ratio=0.1–0.32), for the three energy ranges, plus the summed intensity range. The PDS are composed of an average of 2 Medium-Frequency FFTs, and 8 High-Frequency FFTs. There were no Low-Frequency FFTs. The %rms variability in these PDS are low, with very little detectable power. We fit the data with a single power-law, and (based on results from this source in the H-spectral state) a Flat-Top Double Power-Law model with several fixed parameters.

The results for the best-fit Single Power Law model are shown in Table 5.29. The strength of variability in this state shows strong energy dependence; in the Low Energy Range, the %rms is $< 4.3\%$ (3σ upper-limit) while in the High Energy Range, it is $17\pm3\%$.

The results for the best-fit Flat-Top Double Power-Law model are shown in Table 5.30. The data were not sufficiently constraining to determine all the individual parameters of this model simultaneously, for any of the energy ranges. We therefore fixed all the the parameter values, except the %rms value. As with the single-Power-law model, we find the %rms value to be strongly energy dependent, being $<3.9\%$ (3σ upper-limit) in the Low Energy Range, and being $15.4^{+1.6}_{-2.5}$ in the High Energy Range, assuming the model parameters which have been fixed.

In Fig. 5-64, we show the Composite PDS for GS 2023+33 in the H-state (Wide Ratio=0.32–1.0), for the three energy ranges, plus the summed intensity range. The PDS are composed of an average of 9 Low-Frequency FFTs, 352 Medium-Frequency FFTs, and 82 High-Frequency FFTs. The power is strong and significant, showing a flat-top with a double-power-law at higher frequencies. We used a Flat-Top Double Power-Law to fit these PDS. The best-fit parameters are given in Table 5.30.

In Fig. 5-65, we show the Composite PDS for GS 2023+33 in the I-state (Wide Ratio=1.0–3.2), for the three energy ranges, plus the summed intensity range. The

Table 5.29: GS 2023+33 Best-Fit Single-Power-Law Parameters, G-state

Wide Ratio	Energy Range (keV)	Power Law Slope (α)	%rms (0.001-64 Hz)	χ^2_ν (dof)
0.1–0.32	2.3–4.6	(1.00)	<4.3	0.69 (21)
(G)	4.6–9.2	(1.00)	<14.6	0.80 (21)
	9.2–18.4	(1.00)	18^{+2}_{-3}	0.98 (21)
	9.2–18.4	1.2±0.2	22^{+8}_{-5}	0.97 (20)
	2.3–18.4	(1.00)	$5.9^{+1.1}_{-1.6}$	0.78 (21)
	2.3–18.4	$1.67\ ^{+0.4}_{-0.3}$	<59	0.59 (20)

Fits applied to values in the 0.0156 – 64 Hz range
Values in parenthesis are fixed
Upper-limits are 3 σ

PDS are composed of an average of 5 Low-Frequency FFTs, 228 Medium-Frequency FFTs, and 463 High-Frequency FFTs. The power in this PDS is both strong, and significant. No Flat-Top is evident, down to ν~0.001 Hz. We used a Double Power-Law to fit these PDS. The best-fit parameters are given in Table 5.30.

In Fig. 5-66, we show the Composite PDS for GS 2023+33 in the J-state (Wide Ratio=1.0–3.2), for the three energy ranges, plus the summed intensity range. The PDS are composed of an average of 9 Medium-Frequency FFTs, and 228 High-Frequency FFTs. We used a Flat-Top Double Power-Law to fit these PDS; however, the Flat-Top Frequency is not evident in the 0.0156–64 Hz frequency range. We constrained the first break frequency (where the power goes from being constant into a power-law) to be below 0.001 Hz, thus making the model effectively a Double Power-Law model. The best-fit parameters are given in Table 5.30. We find that the fit of a broken-power-law is a significant improvement over a single-power-law; for the Intensity Range PDS, the χ^2_ν drops from 3.5 (20 dof) to 1.03 (18 dof).

In Table 5.30, we show the best-fit parameters for GS 2023+33 in its various spectral states. For some PDS the data were not of sufficient quality to strongly constrain all model parameters; in these cases we held one or more of the parameters fixed with a value found in another, better determined state.

In states G and J, the frequency range covered by the PDS was 0.0156–64 Hz.

This does not cover the frequency range where the power is constant (the "flat-top") and thus we can not fit for this parameter. We adopted the assumption that in state G, the power becomes constant at the value found in state H (0.013 Hz) while in state J, the power does not become constant until below 0.001 Hz (if at all). For $\alpha_1 = 1$, $\alpha_2 = 2$, and Break Frequency 2 = 2.5 Hz, converting from a model with constant power below 0.013 Hz to one with a power-law all the way down to 0.001 Hz increases the %rms value by a factor of $\times 1.11$ (thus, 7 $\pm$1.0% becomes 7.77$\pm$1.11%).

Table 5.30: Parameters for Best-Fit Flat-Top-Double-Power-Law GS 2023+33 Composite PDS

Spectral Range (Wide Ratio)	Energy Range (keV)	ν_1 (Hz)	ν_2 (Hz)	(α_1)	(α_2)	%rms (0.001-64 Hz)	χ^2_ν (dof)
G[a]	2.3–4.6	(0.013)	(2.53)	(1.03)	(2.05)	<3.9	0.61 (21)
0.1–0.32	4.6–9.2	(0.013)	(2.53)	(1.03)	(2.05)	<12.3	0.79 (21)
	9.2–18.4	(0.013)	(2.53)	(1.03)	(2.05)	$15.4^{+1.9}_{-2.5}$	0.93 (21)
	2.3–18.4	(0.013)	(2.53)	(1.03)	(2.05)	$5.2^{+0.9}_{-1.2}$	0.72 (21)
H[b]	2.3–4.6	0.012 ±0.002	2.41 ±0.08	1.06 ±0.02	2.07 ±0.06	33.2 ±0.6	1.18 (25)
0.32–1.0	4.6–9.2	0.013 ±0.002	$2.63^{+0.7}_{-0.09}$	1.04 ±0.02	2.15 ±0.07	31.7 ±0.5	1.26 (25)
	9.2–18.4	0.011 ±0.002	2.57 ±0.1	1.01 ±0.02	1.94 ±0.06	31.8 ±0.5	1.17 (25)
	2.3–18.4	0.013 ±0.002	2.53 ±0.07	1.03 ±0.01	2.05 ±0.04	31.7 ±0.5	1.56 (25)
I[b]	2.3–4.6	(0.001)	$2.71^{+0.7}_{-0.2}$	1.07 ±0.02	$2.04^{+0.6}_{-0.2}$	$35.6^{+1.1}_{-1.1}$	1.05 (26)
1.0–3.2	4.6–9.2	(0.001)	2.43 ±0.1	1.01 ±0.02	1.93 ±0.07	35.2 ±0.7	0.833 (26)
	9.2–18.4	(0.001)	2.38 ±0.15	0.99 ±0.01	1.87 ±0.09	34.6 ±0.6	1.22 (26)
	2.3–18.4	(0.001)	2.38 ±0.1	1.02 ±0.01	1.88 ±0.05	35.0 ±0.6	1.47 (26)
J [a]	2.3–4.6	(0.013)	(2.69)	1.11±0.13	$1.93^{+3.5}_{-0.9}$	21.5 ±1.9	0.75 (19)
3.2–10.0	4.6–9.2	(0.013)	$3.0^{+0.6}_{-0.4}$	1.09±0.06	$2.3^{+0.6}_{-0.4}$	31.4 ±1.9	1.01 (18)
	9.2–18.4	(0.013)	2.4 ±0.5	1.04±0.06	$2.00^{+0.4}_{-0.3}$	31.8 ±1.8	0.83 (18)
	2.3–18.4	(0.013)	$2.7^{+0.3}_{-0.1}$	1.06 ±0.06	$2.15^{+0.22}_{-0.15}$	29.5±2.0	1.03 (18)

[a] Fits applied to values in the 0.0156 – 64 Hz range
[b] Fits applied to values in the 0.00097 – 64 Hz range
Values in parenthesis are fixed
Upper-limits are 3 σ

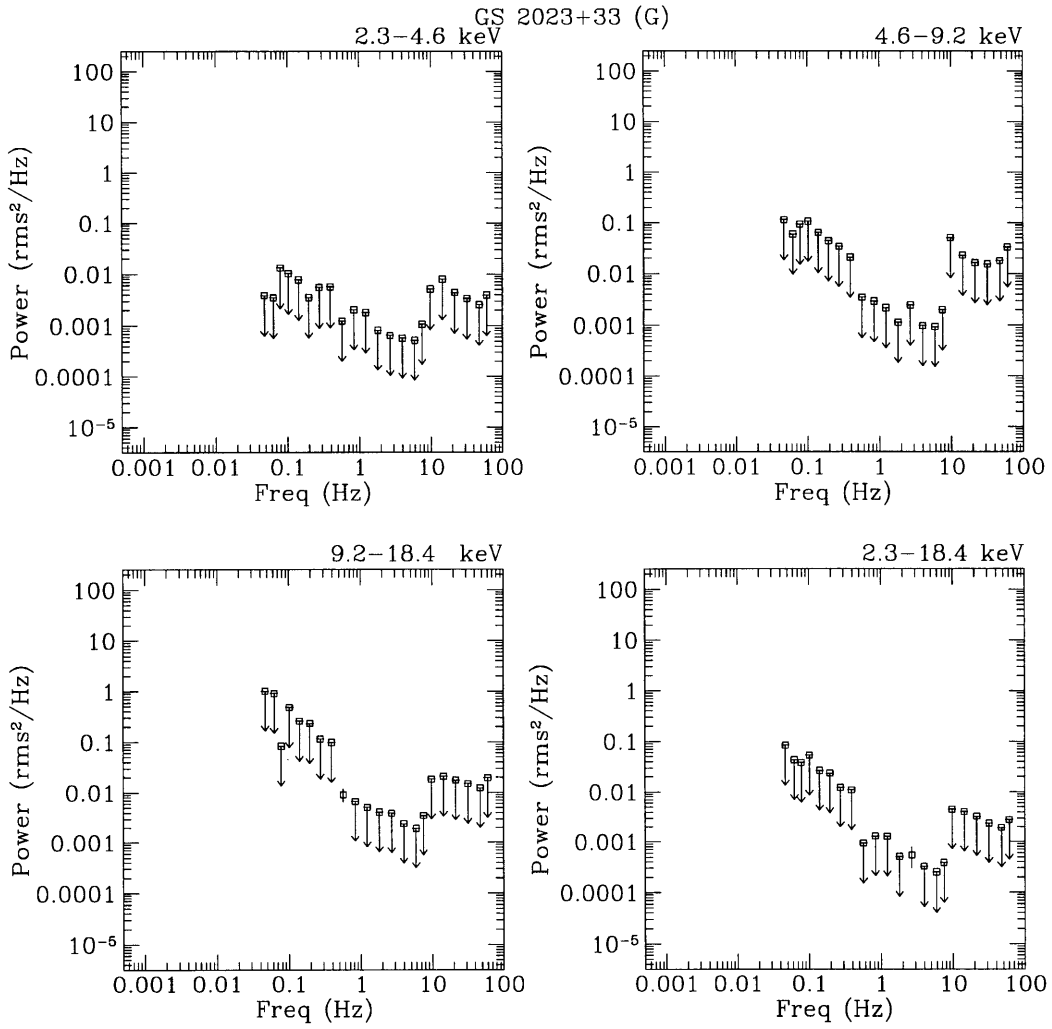

Figure 5-63: **GS 2023+33 Composite PDS in the G-state.** Composite PDS for GS 2023+33 in the Low Energy Range, Medium Energy Range, High Energy Range, Intensity Range energy ranges, using data selected spectrally to be in the G-state (Wide Ratio=0.1–0.32). Upper-limits are 2 σ.

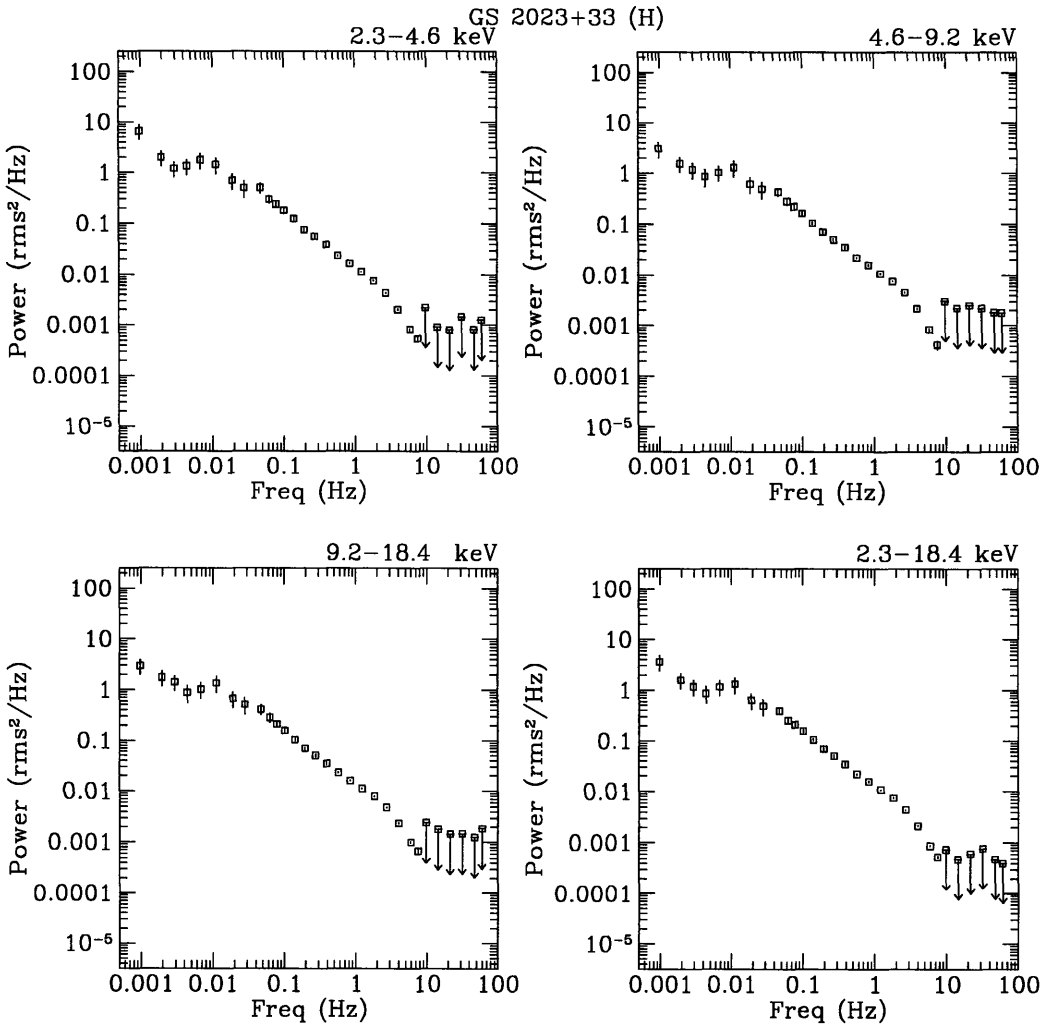

Figure 5-64: **GS 2023+33 Composite PDS in the H-state.** Composite PDS for GS 2023+33, corrected for both background and deadtime, in the Low Energy Range, Medium Energy Range, High Energy Range, Intensity Range energy ranges, using data selected spectrally to be in the H-state (Wide Ratio=0.32–1.0). Upper-limits are 2 σ.

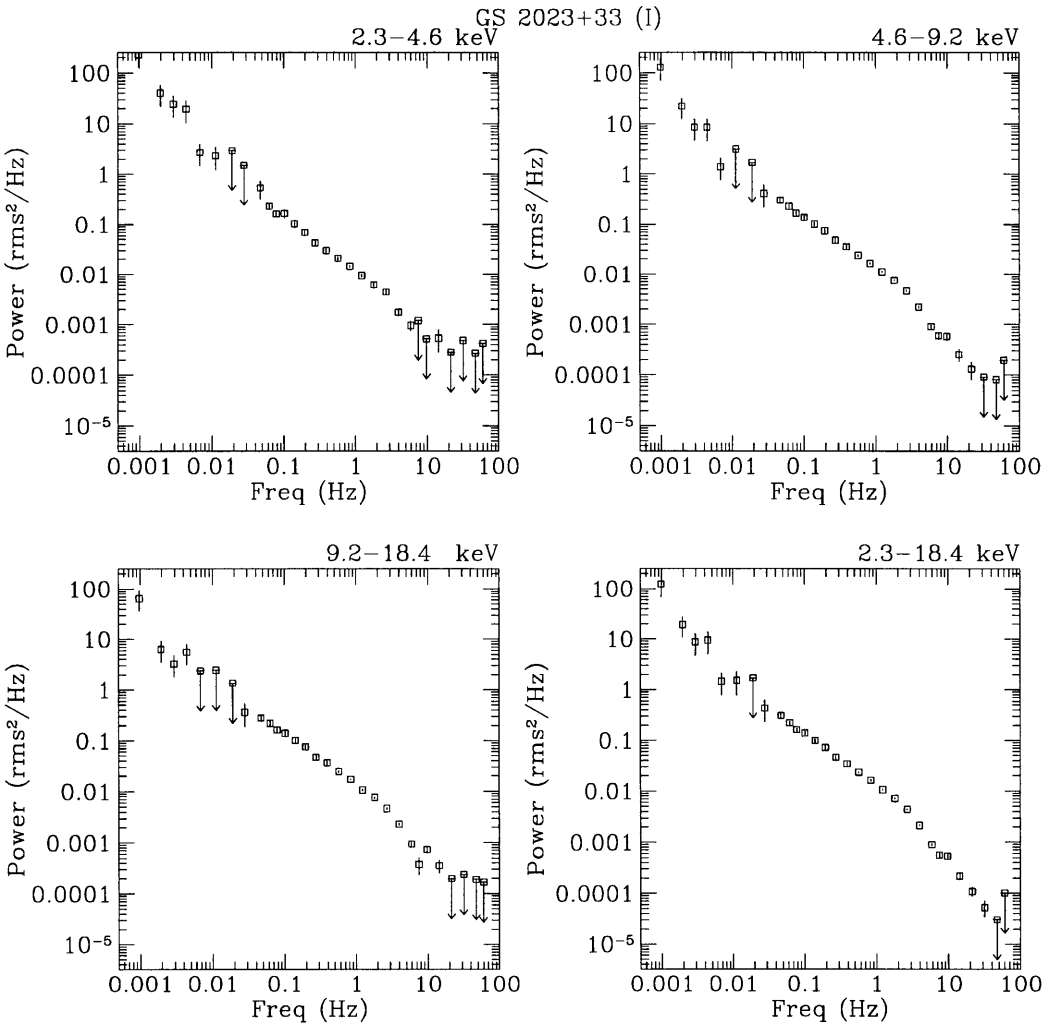

Figure 5-65: **GS 2023+33 Composite PDS in the I-state.** Composite PDS for GS 2023+33, corrected for both background and deadtime, in the Low Energy Range, Medium Energy Range, High Energy Range, Intensity Range energy ranges, using data selected spectrally to be in the I-state (Wide Ratio=1.0-3.2). Upper-limits are 2 σ.

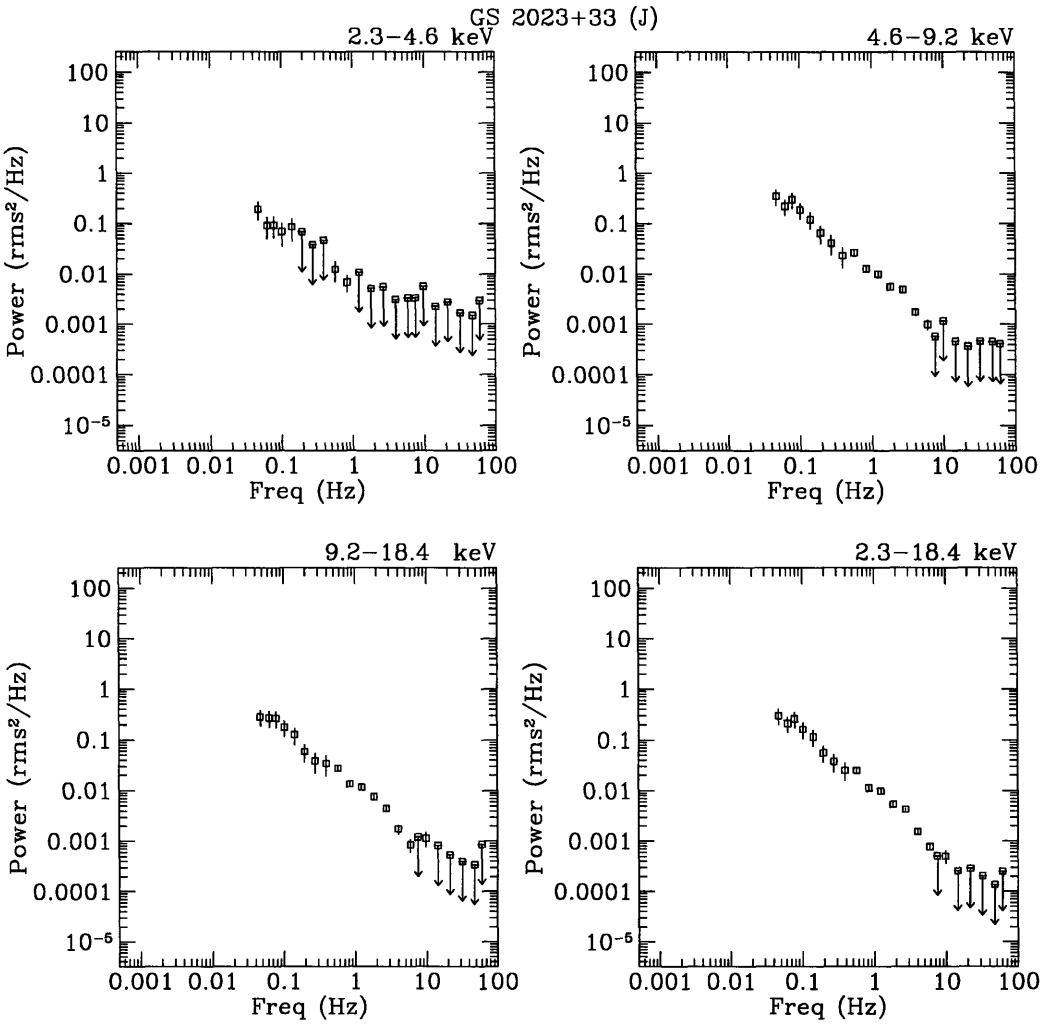

Figure 5-66: **GS 2023+33 Composite PDS in the J-state.** Composite PDS for GS 2023+33, corrected for both background and deadtime, in the Low Energy Range, Medium Energy Range, High Energy Range, Intensity Range energy ranges, using data selected spectrally to be in the J-state (Wide Ratio=1.0-3.2). Upper-limits are 2 σ.

Chapter 6

Black Hole Candidates: Discussion

6.1 General Definition of "High State", "Low State", and "Very High State"

Through the joint analyses of the fast-timing and spectral behavior of the 10 black hole candidates (BHCs) in the present study (1354-64, 1826-24, 1630-47, LMC X-1, LMC X-3, GS 2000+25, GS 2023+33, GS 1124-68, Cyg X-1, and GX 339-4) we have established for the first time a quantitative description for specifying the source state. In this chapter, we summarize the joint timing and spectral results, describe the means of specifying source state, discuss the behaviors of sources observed by *Ginga* within this phenomenological description, and point out aberrations to these behaviors within the present data-set.

First, we describe the behaviors which we use as loose indicators of source state (cf. Tanaka & Lewin 1995; Van der Klis 1995), and which we use to compare to the observed behavior and produce more quantitative definitions.

- Low State (LS): Spectrally hard; PDS has some frequency below which the power is extremely flat as a function of frequency ($P \propto \nu^{-\alpha_1}, \alpha_1 \lesssim 0.3$).
- High State (HS): Spectrally soft: PDS is consistent with a simple power-law.
- Very High State (VHS): Spectrum is unspecified; PDS is unspecified, except for

the presence of strong QPO.

On the basis of these indicators, we identify sources to be in these states.

6.2 Timing Properties vs. Wide Ratio

In Fig. 6-1, we illustrate the dependence of the PDS models and %rms variability on the source spectrum (indicated by the Wide Ratio, the count rate ratio in the energy channels 9.2–18.4 keV/2.3–4.6 keV). For each source, we show the 128 s average values of the Wide Ratio. In each Wide Ratio range the source spectrum was observed to occupy, we place a description of the best-fit model of the contemporaneous PDS, including the %rms variability in the three energy ranges (Low Energy Range=2.3–4.6 keV, Medium Energy Range=4.6–9.2 keV , and High Energy Range=9.2–18.4 keV) and the total Intensity Range (=2.3–18.4 keV), and their 1σ uncertainties. These are listed on five lines for each source: the top line contains the model acronym (see caption), line 2 is the Low Energy Range %rms variability, line 3 the Medium Energy Range %rms variability, line 4 the High Energy Range %rms variability, and line 5 the Intensity Range %rms variability. Models which were uncertain in form, due to a limited frequency range of the PDS or too low-significance of the power, are written in parenthesis. Models which included QPO are indicated. Only a few models for GS 1124-68 are shown, and the timing properties are less simply related to the source spectrum than is shown in this figure; however, the models noted represent the general trend observed from GS 1124-68 as a function of spectrum.

In the spectrally soft range (Wide Ratio$\sim$0.0003–0.03, A-E states), the PDS are consistent with being exclusively power-law in form (so-called "High State"). These PDS show significant energy dependence in the strength of variability, either increasing in strength with increasing energy, or peaking in strength in the Middle Energy Range and then decreasing in the High Energy Range. The typical %rms variability (0.001-64 Hz; 2.3–18.4 keV) is in the range <1–15%.

Between Wide Ratio=0.03–0.1, the PDS of GX 339-4 and GS 1124-68 exhibit a transition between power-law and flat-top-power-law models, and strong 3-10 Hz

QPO (5-15% rms; 2.3–18.4 keV) indicative of the VHS is present. The ratio of the strength of the QPO in the High Energy Rangeto that of the Low Energy Rangeis $4-10\times$ higher than the ratio of the BB power in the same energy ranges. The QPO, therefore, is measurably spectrally harder than the BB variability.

The strength of the QPO is energy dependent, as is the broad-band variability; the QPO, however, is spectrally much harder than the broad-band variability, with typically 4-10$\times$ stronger variability in the 9.2-18.4 keV energy range than the 2.3–4.6 keV energy range when compared with the broad-band variability (see Sec. 6.8).

At Wide Ratio$\geq$ 0.1, the PDS of all sources, except 1630-47, are almost exclusively Flat-Top, indicative of the Low State. At values of Wide Ratio$\gtrsim$0.2, the %rms variability shows no strong energy dependence, and is roughly 30-40%rms.

6.3 Determining State-Behavior by Spectrum

In Fig. 6-2, we show the Wide Ratio vs. Hard Ratio CCD, with the 128 s average colors. We have drawn ellipses around the areas which largely correspond to the behavior which has been described as "Low State", "High State" and "Very High State" (see Tanaka & Lewin 1995 and Van der Klis 1995 for discussions). These are not error-ellipses, but merely illustrate where the corresponding behavior is found in most of the sources in the present study. There are several notable exceptions to the expected behavior within these regions, which are discussed separately below.

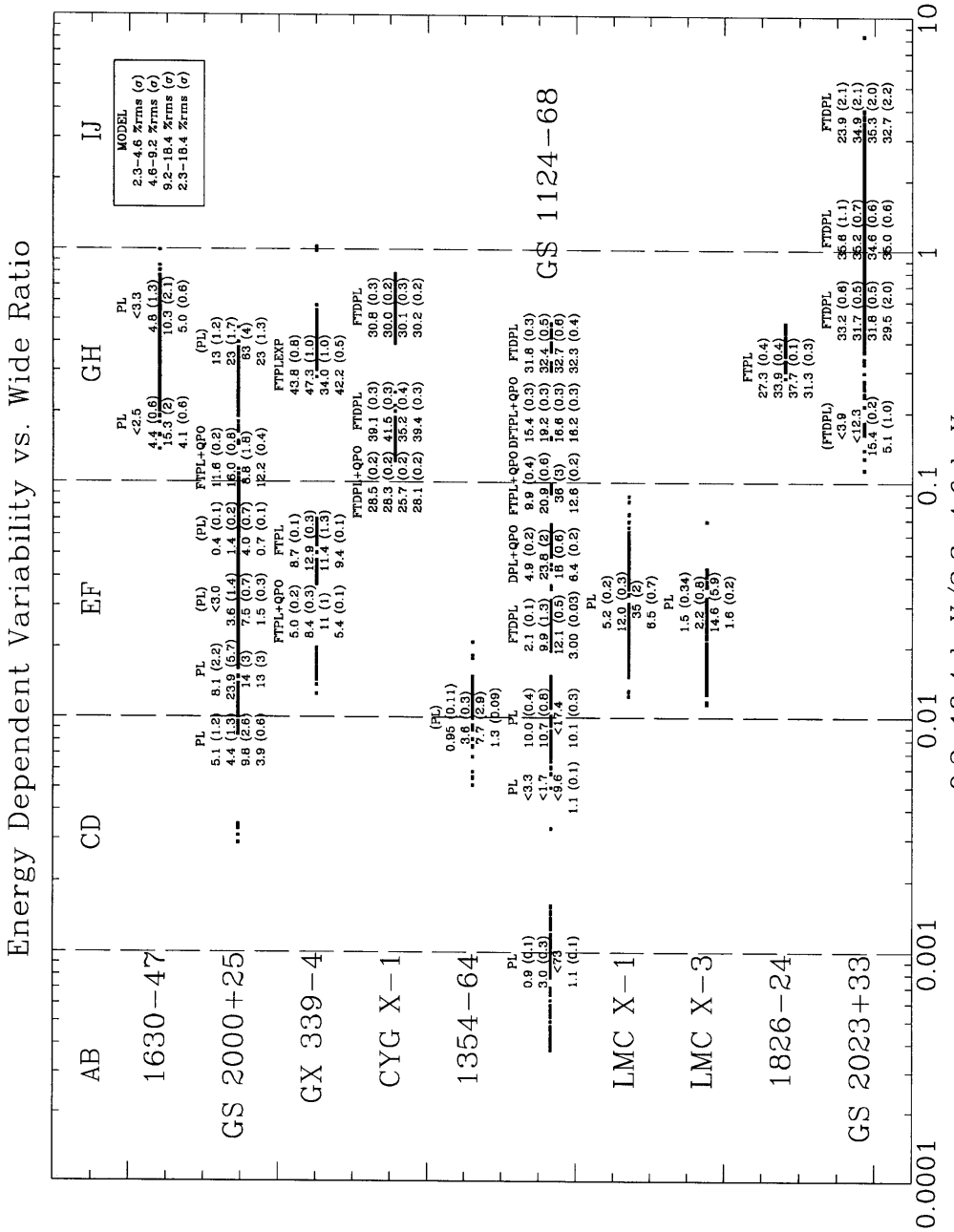

Figure 6-1: **Energy Dependent Variability vs. Wide Ratio**. Illustration of the energy dependent variability for each BHC as a function of Wide Ratio. The square points to the side of the source name are the 128 s average Wide Ratiovalues. At approximately the corresponding Wide Ratio, we list the PDS model used and the %rms variability with its uncertainty in parenthesis (see Key in upper-right corner). Models: PL=Power-Law; FTPL= Flat-Top Power-Law; FTPLEXP= Flat-Top-Power-Law-Exponential; FTDPL= Flat-Top Double-Power-Law; DPL= Double-Power-Law; DFTPL= Double-Flat-Top-Power-Law; QPO=quasi-periodic oscillation. Upper-limits to %rms variability are 3σ.

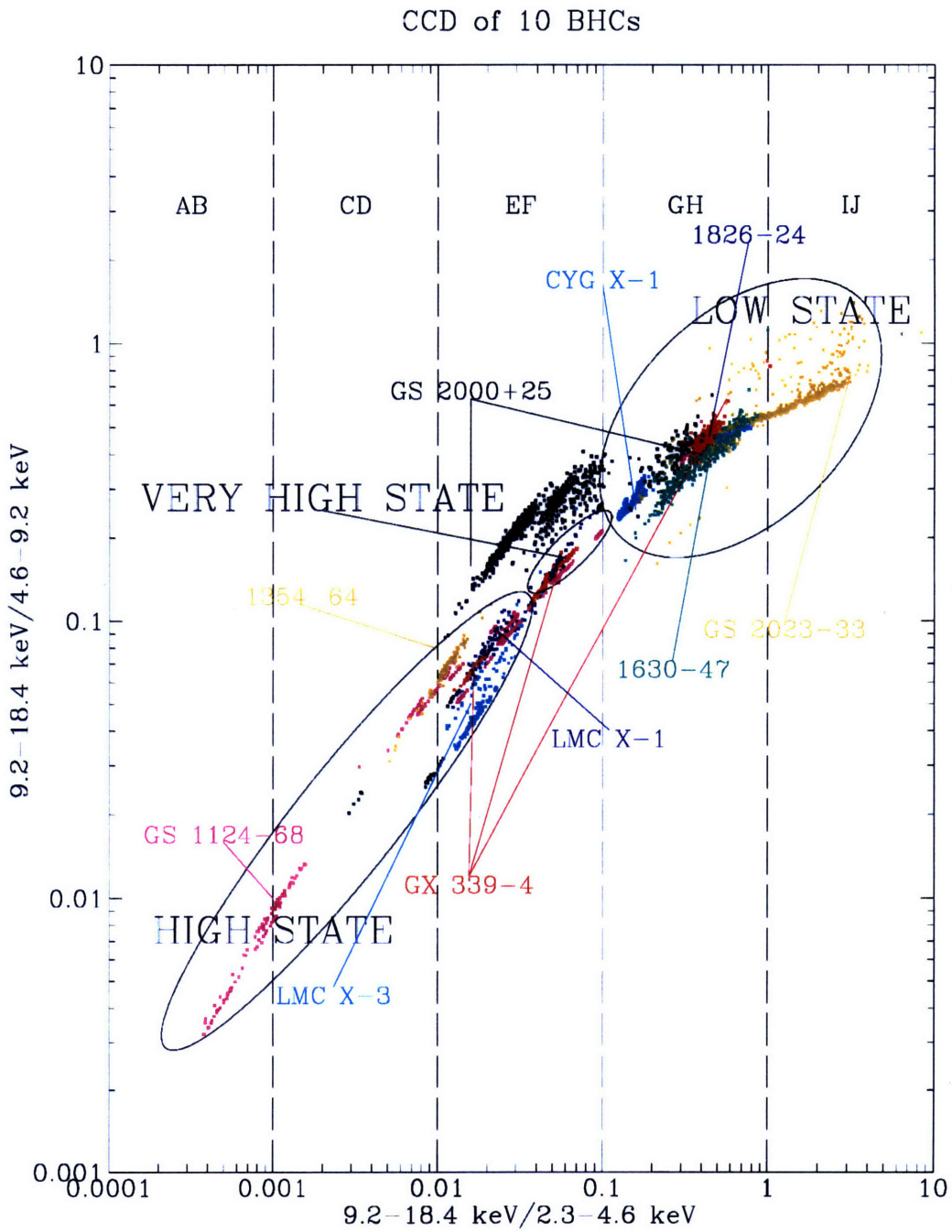

Figure 6-2: **States of BHCs on CCD, (Color Image).**

6.4 Quantitative Description of State-Paradigm Behavior

Based on the correlated timing and spectral properties of these sources, we provide a general, quantitative description of the state-behavior. There are exceptions to this behavior among the sources in the present study.

In the **High State**, the source spectrum is soft, with Wide Ratio $\lesssim$0.032. The timing properties result in a PDS consistent with Single Power-Law in the 0.001–64 Hz Frequency range in the Intensity Range (=2.3–18.3 keV), with slope α_1 ~1.0-2.0, and a %rms variability in the 0.001-64 Hz frequency range of <1–15 %rms. The %rms variability shows significant energy dependence. In some sources, the %rms variability increases from <1–5 %rms in the Low Energy Range (=2.3–4.6 keV) to 8–15% in the High Energy Range; in others, the variability is higher in the Medium Energy Range than in the Low Energy Range , but lower in the High Energy Range than in the Medium Energy Range.

In the **Low State**, the source spectrum is hard, with Wide Ratio $\gtrsim$0.1. The timing properties produce a PDS which, over some frequency range, is almost constant (consistent with a power-law of slope $\alpha_1 \lesssim 0.3$) – the so-called "flat-top". The flat-top range is below some frequency ν_1, where we observe ν_1 to be $0.01 \leq \nu_1 \leq 2.6$ Hz. The Low State timing properties may include QPO (so-called "LS QPO"), which has energy dependence similar to that of the continuum variability, and which may be differentiated from VHS QPO on this basis. The LS %rms variability is typically colorless and strong (~30-40% rms).

In the **Very High State**, the Wide Ratio is between that of the the High and Low States ($0.032 \leq$Wide Ratio≤ 0.1). The characteristic timing property is the presence of QPO (in the frequency range of 3.0–10.0 Hz for GS 1124-68 and GX 339-4), whose frequency depends on source hardness, and whose strength increases more sharply with energy than the continuum variability strength. Thus, the QPO spectrum is quite distinct from that of the continuum variability (it is also distinct from the Low-State QPO; see Sec. 6.8). The continuum timing properties can be like that

of the High State (simple Power-Law) or the Low State (Flat-Top Power-Law or Flat-Top-Double-Power-Law). The transition between the two is observed to occur near Wide Ratio$\sim$0.055 ($\pm$0.01, approximately).

6.4.1 Aberrant Behavior within the State Paradigm

There exist several exceptions to the source behavior description of the "state" paradigm, observed with *Ginga*. We discuss these here.

1630-47 was observed spectrally in the GH-state (Wide Ratio=0.1–1.0; cf. Table 4.2), which we have identified as "Low-State". However, its timing behavior was consistent with "High-State" behavior (pure Power-Law PDS; energy dependent %rms variability).

GS 2000+25, in the Wide Ratio range of 0.02—0.1, has a higher than expected Hard Ratio. In particular, in the Wide Ratio range of 0.04–0.1, where Very High State Behavior is expected, we see no evidence for QPO in the PDS, although the limits on QPO of strength similar to that found in GX 339-4 can not exclude its presence in GS 2000+25. At Wide Ratio=0.1, we observe, as expected, Low-State timing behavior – a Flat-Top Power-Law PDS (with Low-State QPO) in GS 2000+25. Perhaps interestingly, at its spectrally hardest, GS 2000+25 still exhibits strong energy dependence in its %rms variability; the quality of the data is insufficient to extract useful model parameters, but using the same model (Power Law with slope 1) for all energy ranges, the %rms variability is strongly energy dependent (increasing from 13 $\pm$1.2%, to 23 $\pm$1.7% to 63 $\pm$4% between the Low Energy Range, Medium Energy Range, and High Energy Range data, respectively.

GS 1124-68 does not strictly behave according to the Low-State – Very High State – High State description given here. The exceptions to this description include:

1. the presence of VHS QPO during observation 1 (see Sec 5.4.7), when the Wide Ratio$\sim$0.15 (within the Low-State);

2. the presence of QPO during observation 15, when Wide Ratio=0.013, within the High-State;

3. the presence of QPO in observation 15, and its absence in observation 7, when both have Wide Ratio$\sim$0.013;

4. observation 16 shows strong ($\sim$10% rms), energy independent variability, consistent with a single- Power-Law of slope $\alpha_1 = 1.67 \pm 0.1$, when Wide Ratio=0.009 (High State), and the variability is expected to be energy-dependent and weaker;

5. Low-State timing behavior (that is, the presence of a flat-top) is observed at spectral hardnesses ($0.02 \leq$ Wide Ratio ≤ 0.03) in the range where VHS or HS behavior is expected (see Observations #6, 8, & 9). In this same spectral range during other observations (see Observations 12, 13, and 14), distinct High-State timing behavior is observed. This has been referred to as the "hysteresis" in the source by Miyamoto et al. (1995).

It remains to be seen what the meaning of these aberrant behaviors is. The source 1630-47 is included in the class of BHCs based on its spectral and timing properties. The fact that its timing properties are inconsistent with those of BHCs with measured mass functions in the same spectral state does not support this classification. GS 1124-68 and GS 2000+25 are classified as BHCs as the masses of their compact objects are > 3.0 $M_\odot$. Therefore, the aberrant behaviors observed from these sources expand the types of behavior expected from BHCs, as they cannot be excluded as BHCs.

6.4.2 Energy Dependence of PDS Parameters

In the present analysis there is one instance where energy dependence on PDS parameters (apart from the %rms variability) is indicated: Obsevations #2, 3, 6, and 14 of GS 1124-68, when the power-law slope (α_1) becomes significantly flatter with increasing energy range. This may be due to combined HS–LS behavior, in which at low frequencies the HS power-law variability dominates, and at high frequencies, the energy dependent Flat-Top-Power-Law increases in strength with increasing energy range, producing apparently flatter PDS power-law dependency on frequency at higher energies.

6.5 Low-State QPO

We report for the first time the detection of QPO in the Low-States of Cyg X-1 (ν_c=1.1 Hz, FWHM=1.2 Hz) and GS 2000+25 (ν_c=2.6 Hz, FWHM=1.7 Hz). We compare the properties of LS QPO to those of VHS QPO below (in Sec. 6.8).

In Fig. 6-3 we show the energy dependence of the LS QPO in Cyg X-1 and GS 2000+25. The LS QPO is either slightly anti-correlated with energy (as seen in Cyg X-1) or constant (as seen in GS 2000+25).

Low-State QPO has also been detected previously in GX-339-4 (Grebenev et al. 1991) with the ART-P spectrometer, with a centroid frequency of 0.8 Hz, FWHM of 0.15 Hz, and a %rms variability of of 7.0±0.8% in the 3-25 keV energy range. When the LS QPO was detected from GX 339-4, the spectrum was pure-power-law, with a photon slope of 1.733±0.004. This places GX 339-4 at a somewhat different (Wide Ratio, Hard Ratio) vector than either Cyg X-1 or GS 2000+25 (near 0.32, 0.4; see Fig. 6-7).

In Cyg X-1, the LS QPO produces excess power at the ν_c=1.1 Hz when the Wide Ratiois in the range 0.1–0.15. This frequency increases to 3.14 Hz for the Wide Ratiorange of 0.15–0.32 (see Table 5.7). An alternative interpretation of the PDS is that, while the QPO produces excess power while Wide Ratio=0.1–0.15, it produces a *deficit* of power (of strength ∼-4.1 ±0.7 %) when Wide Ratio=0.15–0.32 (see Table 5.9). If the correct interpretation is the former one, then it is useful to note that the %rms variability dependence on energy remains the same as that of the BB variability. If the alternative interpretation is correct, then it is useful to note that the deficit of variability is also relatively color-less, and that a deficit of variability supports the interpretation that the LS QPO is produced by the same physical mechanism as the BB variability. We are cautious about forwarding the alternative interpretation, as the PDS model fits are no better (or worse) than the fits with LS QPO at higher frequency; we mention it only as an interesting possibility to be kept in mind during future analyses.

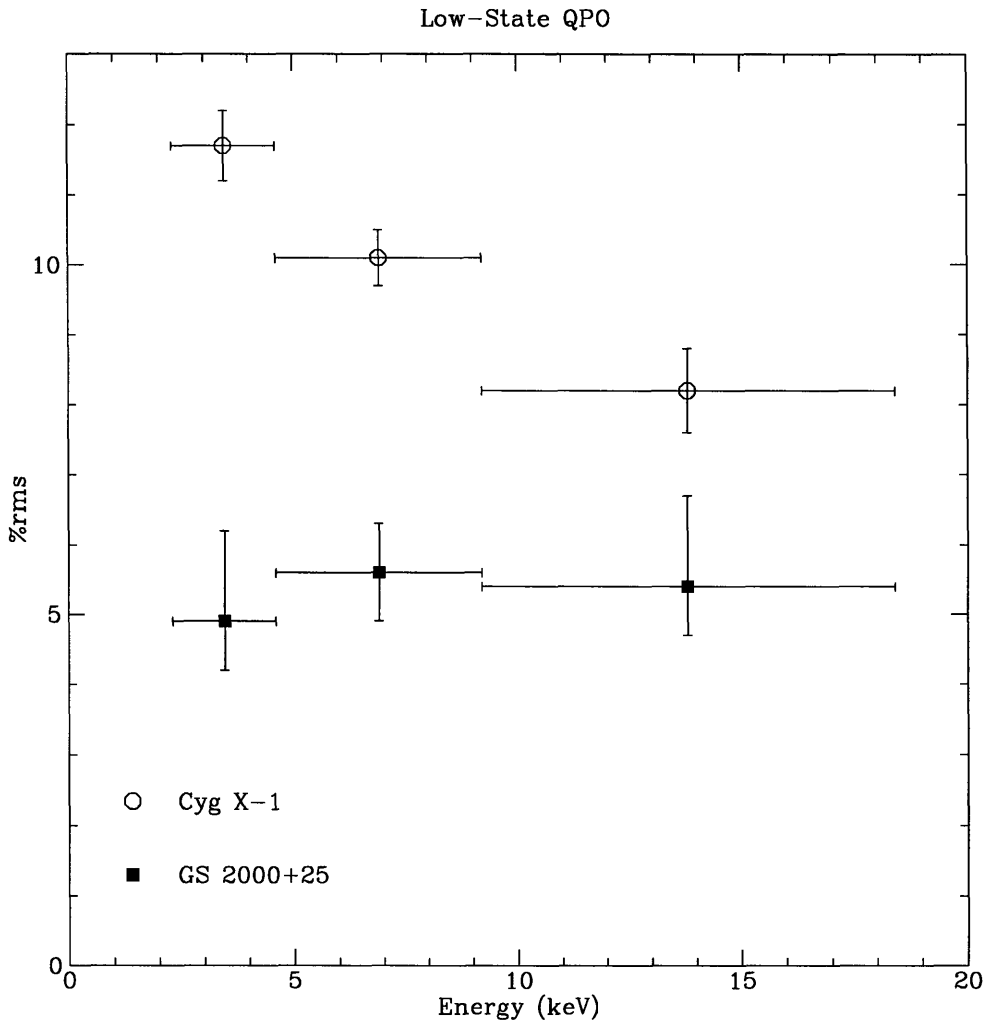

Figure 6-3: **%rms of Low-State QPO vs. Energy Range, Cyg X-1 and GS 2000+25.** Cyg X-1 (open circles) and GS 2000+25 (solid squares) Error bars on the %rms are 1σ, while on energy they represent the energy range of the PDS. Low-State QPO %rms variability is either slightly reddish (as in Cyg X-1), or colorless (as in GS 2000+25).

6.6 Very High State QPO

In Fig. 6-4, we show the behavior of the VHS QPO in GX 339-4 and GS 1124-68 as a function of spectral hardness. Each point is marked with an observation ID from Table 5.12 (for GS 1124-68) as described in Sec. 5.4.8 (for GX 339-4, the markers F1–4 indicate data taken from four different spectral ranges where GX 339-4 exhibited VHS QPO).

In both sources, the centroid frequency is dependent on spectral hardness. The centroid frequency is greatest near Wide Ratio=0.055 ($\pm$0.01 approximately), and decreases as the source becomes spectrally harder and as the source becomes spectrally softer. The same is true for the FWHM of the QPO – it is greatest at Wide Ratio=0.055, and smaller as the source is spectrally harder or softer.

In Fig. 6-5, we show the %rms variability as a function of energy range of the PDS for several PDS components in GS 1124-68 and GX 339-4. In both GS 1124-68 and GX 339-4 (panels a and d), the VHS QPO %rms increases with increasing energy. The BB power (panels b and e), however, increases with increasing energy from the Low Energy Range to the Medium Energy Range; it then remains constant or decreases between the Medium Energy Range and High Energy Range.

In GS 1124-68, when there is no QPO observed (panel c), the BB power increases with increasing energy across all three energy ranges. To produce this panel, we used observations 6, 7, 9, 12, and 14, in which VHS QPO were not observed, but the source spectrum was similar to during times when VHS QPO were observed. No such similar data exist for GX 339-4.

Taken together, these results indicate that: the energy spectrum of the VHS QPO is spectrally harder than that of the underlying BB variability; and, nonetheless, the strength of the underlying BB variability (in GS 1124-68) depends on the presence or absence of QPO. One might interpret this to mean that, while the physical process producing the VHS QPO is separable from that of the BB variability, there is nonetheless interaction between the two processes which affects the spectrum of the BB variability.

We note that, while there is no simultaneous spectral data for the six hour observation period during which 0.08 Hz QPO were found in LMC X-1 (Ebisawa et al. 1989), in the 13-hrs following this period, the Wide Ratio was in the range 0.033-0.087 (Fig. 6-2) which is very close to the VHS tracks of GS 1124-68 and GX 339-4. Although High-Frequency PDS were produced, no 3-10 Hz QPO were reported.

The VHS occurs in GS 1124-68 and GX 339-4 not at a spectral extreme, but (spectrally) between the Low State and High State. In both sources, the timing properties have been observed to evolve while VHS QPO is observed, such that the BB timing properties have the character of LS variability or HS variability. It seems natural to interpret the VHS as a transition stage between the Low State and the High State. Therefore, any source which undergoes a transition from the Low State to the High state should exhibit Very High State behavior in the interim. Of the ten sources in the present study, only Cyg X-1 remains as a source known to change states, but from which Very High State behavior has not yet been observed. However, observations with the X-ray satellite *R*XTE of a Low –High state transition of Cyg X-1 in 1996, found a "bump" in the PDS near 9 Hz, which is being investigated as possibly QPO of the type observed from GS 1124-68 and GX 39-4 (W. Cui, private communication).

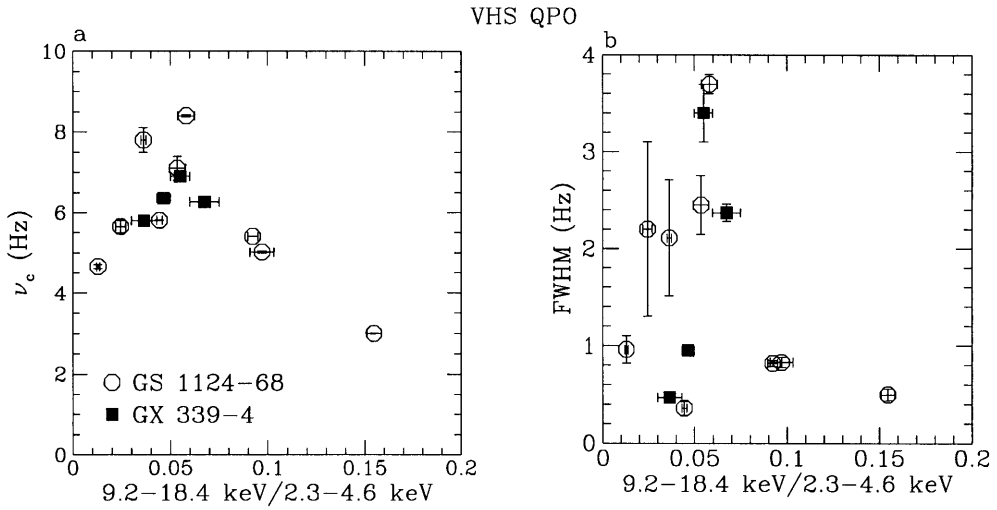

Figure 6-4: ν_c **and FWHM vs. Wide Ratio VHS QPO of GX 339-4 and GS 1124-68**. *Panel a*: Centroid frequency of the fundamental QPO in the VHS, as a function of Wide Ratio for GS 1124-68 (open circles) and GX 339-4 (solid squares). Centroid frequency is maximum near Wide Ratio=0.055, and decreases away from this. *Panel b*. The FWHM of the fundamental vs. Wide Ratio. The QPO width is greatest near Wide Ratio=0.055, and is lower at values below and above this. 1σerror bars are included on all points.

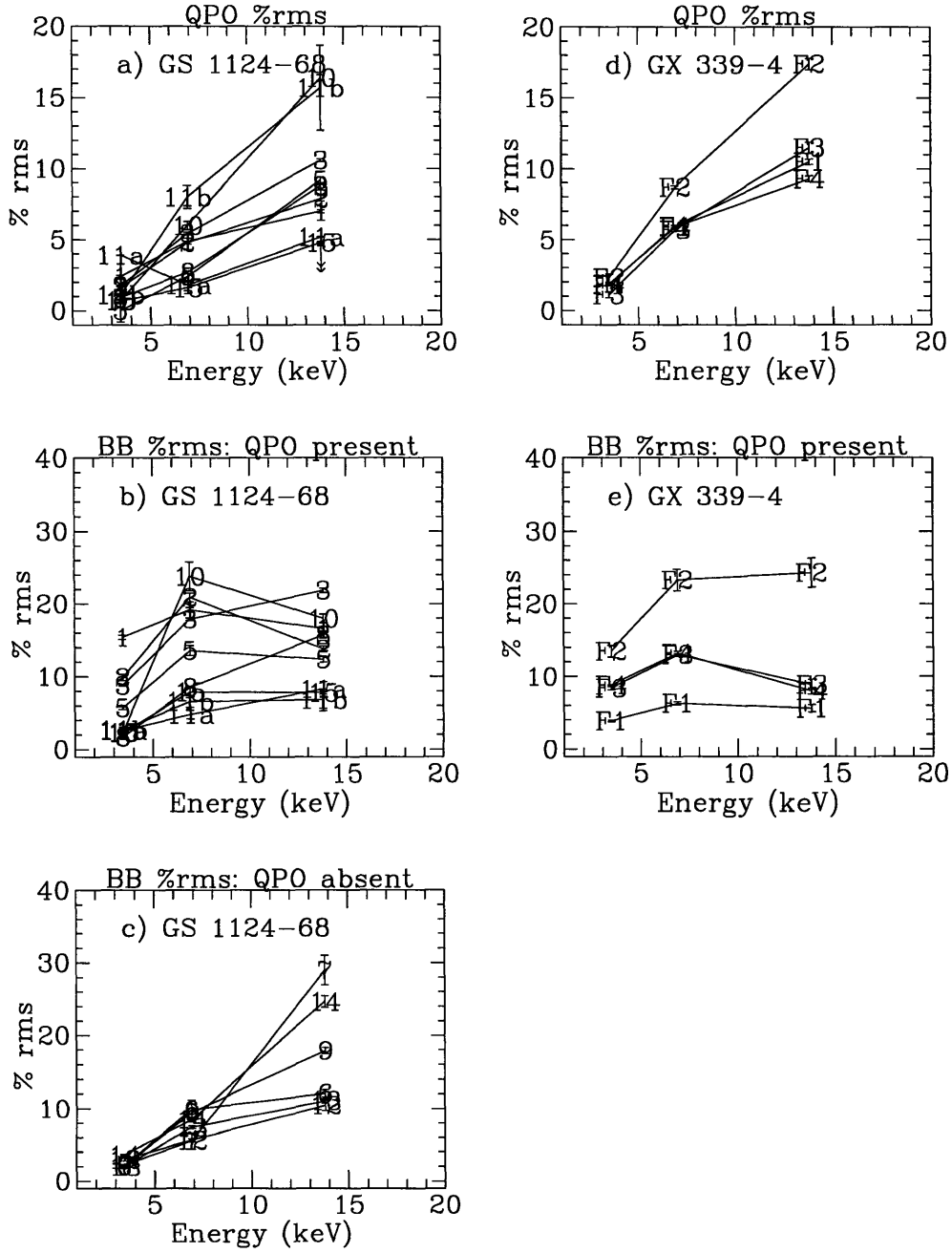

Figure 6-5: **QPO and BB %rms, Very High State QPO of GS 1124-68 & GX 339-4**. The %rms variability in the QPO and BB components when QPO is present or absent, in GS 1124-68 and GX 339-4. Upper-limits are 3-sigma. Points for GS 1124-68 are marked with observation IDs from Table 5.12; points from GX 339-4 are marked with spectral indicator IDs taken from Fig. 5-51 *(a)*: QPO %rms vs. Energy range from GS 1124-68. *(b)*: BB %rms (when QPO is present) vs. Energy range from GS 1124-68. *(c)*: BB %rms (when QPO is absent) vs. Energy range from GS 1124-68. *(d)*: QPO %rms vs. Energy range from GX 339-4. *(e)*: BB %rms (when QPO is present) vs. Energy range from GX 339-4.

6.7 The Very High State as Transition Between the Low State and High State

We argue that the Very High State (VHS) is a transition state between Low State and High State.

We have observed that, spectrally, the VHS is in between the Low-State and the High State (see Fig. 6-2). We have also seen that the VHS QPO frequency first increases with decreasing Wide Ratio until Wide Ratio=0.055 ($\pm$0.01, approximately), and then decreases as Wide Ratio decreases (see Fig. 6-4). The FWHM of VHS QPO is at its maximum observed value (in both GX 339-4 and GS 1124-68) near Wide Ratio=0.055.

In Fig. 6-6, we show the PDS of GS 1124-68 and GX 339-4 in the VHS (that is, when 3-10 Hz QPO is present); the Wide Ratio is indicated in the upper-right corner of each panel. In both GS 1124-68 and GX 339-4, we see that as the Wide Ratio decreases, the PDS changes from a Flat-Top Power-Law (that is, Low-State PDS) to a Single Power-Law (High-State PDS), and that this change occurs near Wide Ratio=0.055, which is also where the dependence between VHS QPO ν_c and the Wide Ratio changes from a correlation to an anti-correlation (see Fig. 6-4). This indicates that the VHS QPO is related to the continuum variability behavior, and that its properties are affected by the change in state of the BHC, between the Low State and the High State.

In light of the change of both the continuum variability behavior from Low-State-type to High-State-type and the dependence of the QPO centroid frequency on the Wide Ratio from a correlation to an anti-correlation near Wide Ratio=0.055, it seems reasonable to conclude that the changes in the continuum variability properties and VHS QPO properties are related.

It is not surprising that there exists a region of spectral parameter space, intermediate to the Low-State and High-State, where the source undergoes the observable changes between the two states – it is obvious that such a region should exist. We have determined that this region occurs in the Very High State.

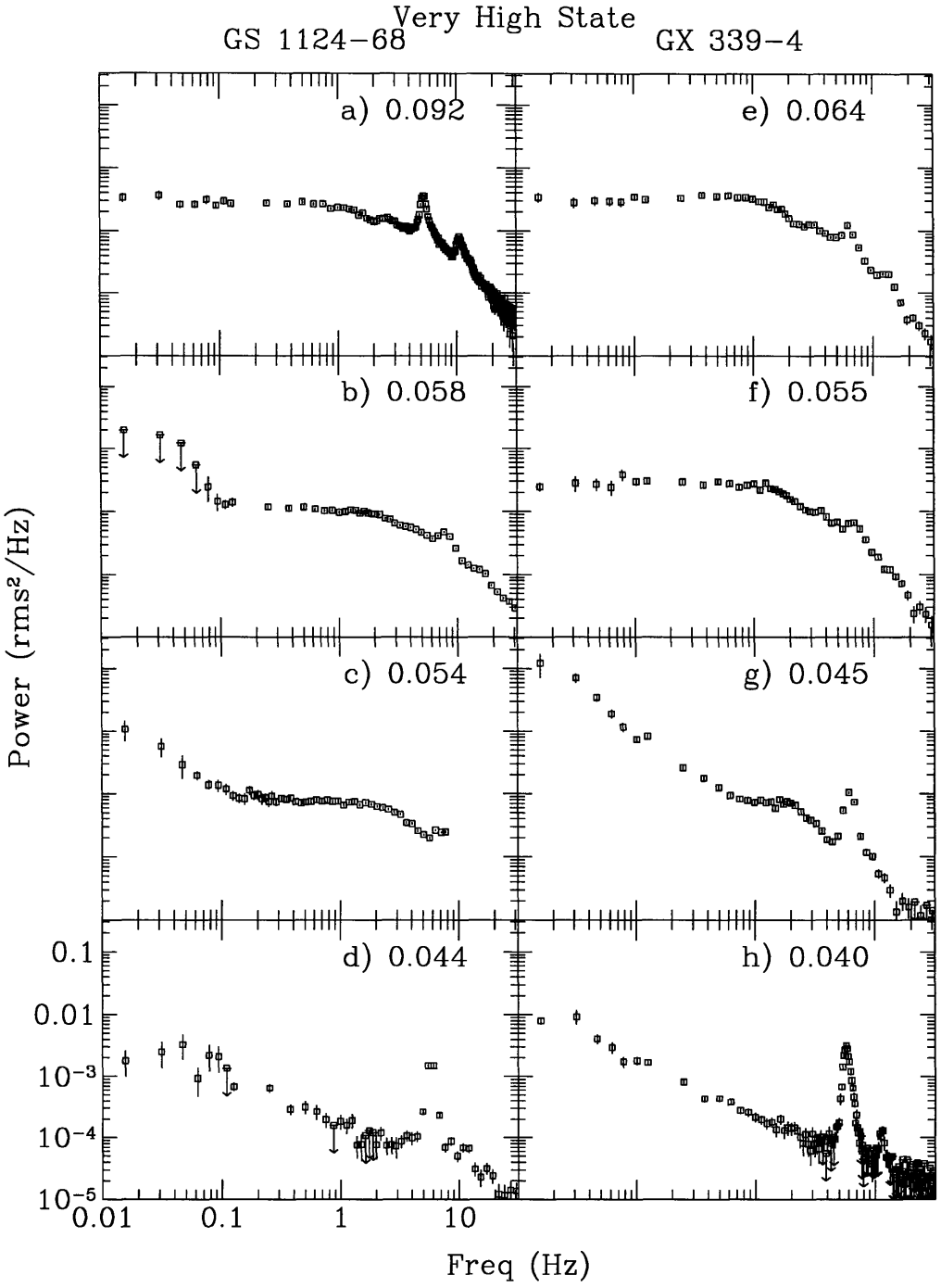

Figure 6-6: **Very High State PDS vs. Wide Ratio of GS 1124-68 & GX 339-4** . The energy range of the PDS is 2.3–18.4 keV. Each panel is marked with the mean Wide Ratio (the spread in each is ~0.001–0.004). The PDS in the left column are from GS 1124-68, and those in the right column from GX 339-4. Upper-limits are 2σ. We list below the observation number (for GS 1124-68, from Table 5.12) or source state (for GX 339-4, from Fig. 5-51). **a**: Obs. 3; **b**: Obs. 10; **c**: Obs. 15 **d**: Obs. 11b; **e**: F4; **f**: F3; **g**: F2; **h**: F1.

6.8 Comparison Betweeen the Very-High State QPO and Low-State QPO

We describe the similarities and differences between what we call Very High State (VHS) QPO and Low State (LS) QPO.

In Fig. 6-7, we show the positions on the Composite CCD (see Fig. 6-2) of the sources GS 1124-68 and GX 339-4 when they exhibit Very High State QPO, and GX 339-4, Cyg X-1 and GS 2000+25 when they exhibit Low State QPO (we show a more detailed figure of this data in Fig. 6-8, with GX 339-4 in the LS excluded). We show only a few points for each source, selected to show the range of spectral behavior exhibited by these sources in the VHS. The VHS QPO does not occur at the spectral extreme, when the sources are spectrally softest; instead, VHS QPO occurs when the Wide Ratio is intermediate to the Wide Ratio observed in the LS and HS regions. Most of the VHS QPO in both GS 1124-68 and GX 339-4 occur when Wide Ratio=(0.04–0.07), and also when these sources lie on the same Wide Ratio vs. Hard Ratio track, with Hard Ratio=(0.12–0.18).

The VHS QPO is present only in this intermediate (to HS and LS) range of Wide Ratio values. Some sources (1354-64 and LMC X-3, as well as GS 1124-68) are at times spectrally softer, when no VHS QPO is observed. Other sources (GX 339-4, GS 1124-68, Cyg X-1, GS 2000+25, GS 2023+33, 1630-47, and 1826-24) are at times spectrally harder, when no VHS QPO is observed. GS 2000+25 was observed to have Wide Ratio values in the appropriate range, but with measurably higher Hard Ratio and no VHS QPO was observed. LMC X-1 at times has the correct spectrum (overlapping in Wide Ratio and Hard Ratio with GS 1124-68 and GX 339-4 when VHS QPO is observed from these two sources), but QPO have been reported (Ebisawa 1991).

We fit the track along which the VHS QPO was found in GS 1124-68 and GX 339-4. The relationship between the Wide Ratio and Hard Ratio is:

$$\mathrm{HardRatio} = 0.201 \times \left(\frac{\mathrm{WideRatio}}{0.1}\right)^{0.564} \tag{6.1}$$

with a systematic uncertainty in the resulting Hard Ratio of ~10%. It should be noted that the LS QPO of Cyg X-1 occurs while Cyg X-1 lies along this track; this is not surprising as many of the source spectra evolve along this track.

To compare the relative strength of the VHS and LS QPO in the sources Cyg X-1, GS 2000+25, GX 339-4, and GS 1124-68, we define the variability ratio:

$$R_{QPO,BB} = \frac{\%\mathrm{rms}_{\mathrm{QPO}}(9.2-18.4\mathrm{keV})}{\%\mathrm{rms}_{\mathrm{QPO}}(2.3-4.6\mathrm{keV})} \div \frac{\%\mathrm{rms}_{\mathrm{BB}}(9.2-18.4\mathrm{keV})}{\%\mathrm{rms}_{\mathrm{BB}}(2.3-4.6\mathrm{keV})} \qquad (6.2)$$

which is a ratio of two ratios, each being the ratio of the High Energy Range %rms variability to the Low Energy Range %rms variability, in the QPO and (separately) the broad-band components. Values of the variability ratio which are consistent with 1.0 mean the QPO and BB components have the same energy spectrum; values which are greater than 1.0 mean the QPO is spectrally harder than the BB component.

In Table 6.1, we give the variability ratio for the four sources in which we find QPO, from the PDS when the source is in the spectral state where QPO was detected in the Low Energy Range and High Energy Range PDS. For GS 2000+25 and Cyg X-1, the QPO is the same or slightly softer than the spectrum of the BB variability. The variability ratio of GX 339-4, on the other hand, is different; significantly higher values of $R_{QPO,BB}$ indicate the VHS QPO is spectrally harder than the BB variability. The same is often true for GS 1124-68: the VHS QPO is spectrally harder during observations 1, 3, 5, 10, and 11b. During observations 2, 8, and 15, however, the QPO spectrum is consistent with the spectrum of the BB variability.

The similarity between the energy dependence of %rms variability in the LS QPO and the simultaneously observed continuum variability argues for a common mechanism, which is not the case for VHS QPO.

We are unable to characterize the LS QPO of GX 339-4 reported previously (Grebenev et al. 1991), as no information on the energy dependence of the variability is available.

Table 6.1: %rms Variability Ratio of QPO Sources

Source	Note	Table Ref.	$R_{QPO,BB}$
Cyg X-1	G1	5.7	0.77 ±0.07
GS 2000+25		5.26	1.35±0.52
GX 339-4	F1	5.21	4.07 ±0.4
	F2		4.2 ±0.7
	F3		9.9 ±2.0
	F4		5.5 ±0.36
GS 1124-68	Obs # 1	5.13, 5.14, 5.15	2.7 ±0.14
	2		1.4 ±0.2
	3		2.45 ±0.09
	5		>4.4
	8		1.07 ±0.11
	10		6.4 ±1.0
	11b		5.7 ±1.9
	15		1.14 ±0.5

Lower-limit is 3σ .

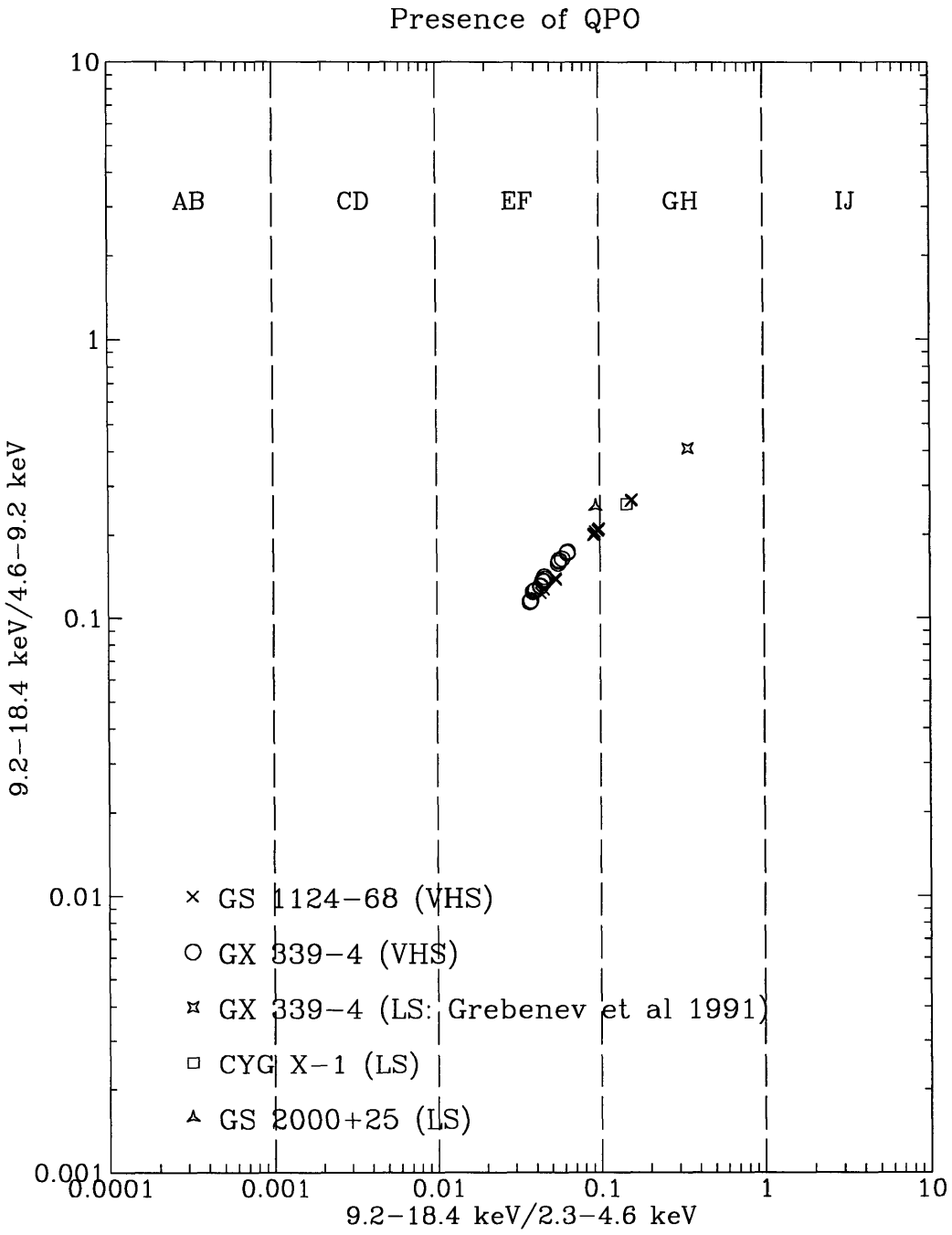

Figure 6-7: **Very High State and Low State QPO, Located on the Wide Ratio vs. Hard Ratio CCD.** The position on the Wide Ratio vs. Hard Ratio CCD, when QPO is observed from GS 1124-68 (Very High State), GX 339-4 (Very High State and Low State), Cyg X-1 (Low State), and GS 2000+25 (Low State). For clarity, only a few representative points for each source is shown (all points are shown in Fig. 6-8). This figure may be directly compared with the full composite CCD in Fig. 4-24.

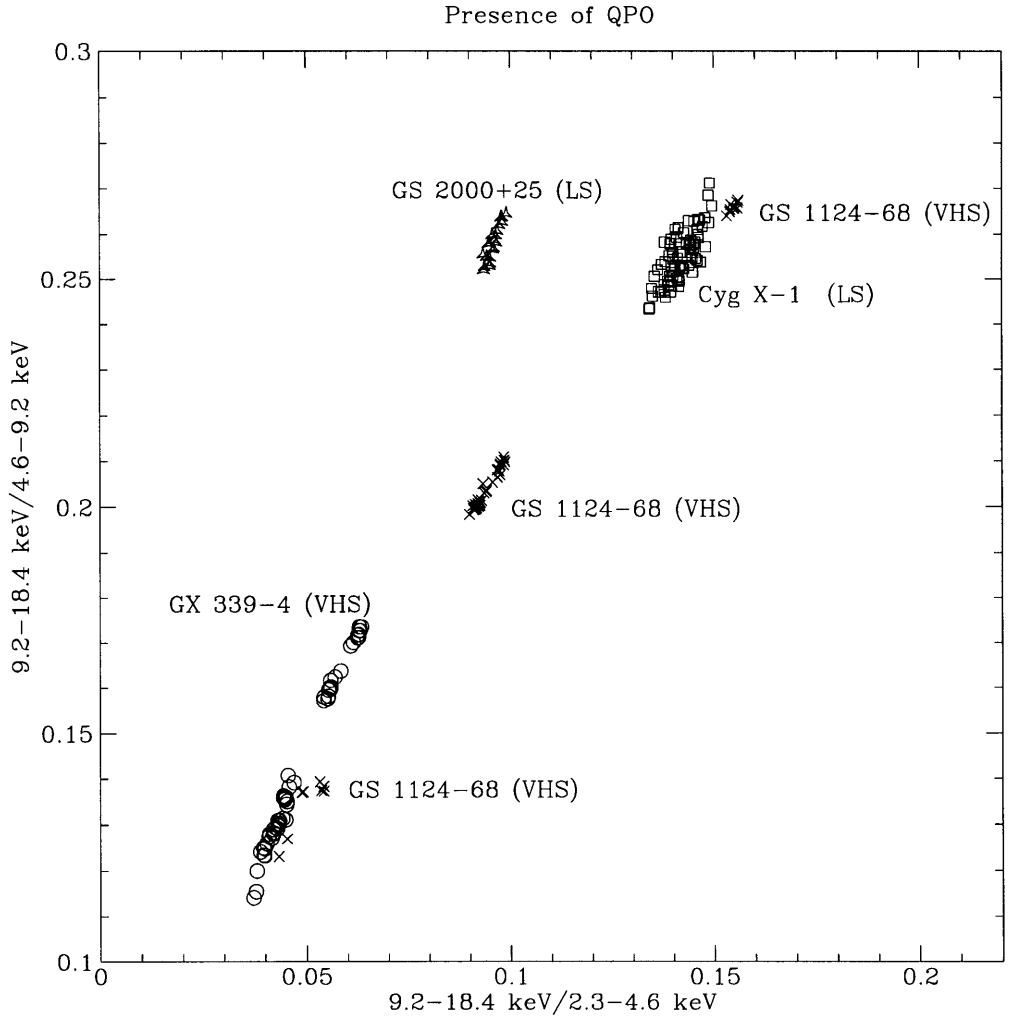

Figure 6-8: **Very High State and Low State QPO, Located on the Wide Ratio vs. Hard Ratio CCD, detail**. This is a detail of Fig. 6-7, focusing on the QPO.

Part II

Gamma Ray Bursts

Chapter 7

Gamma Ray Bursts

7.1 Current Observational Situation

The history and observational status of Gamma-Ray Bursts (GRBs) has been reviewed by Fishman & Meegan (1995). We describe the more important properties of GRBs, according to the current observations.

Until 1991, the GRB distance scale was completely unknown. The prevailing opinion was that the sources were likely to be from nearby neutron stars in the galactic disk, a mere ~few parsec away. After the launch of BATSE (see Sec. 7.2), two observational results came to light which drastically altered our perception of the sources (Meegan et al. 1992): 1) the GRB distribution was consistent with being spatially limited in extent in Euclidean space (that is, we could see past where the burst rate per unit volume begins to decrease) and 2) the sources are isotropically distributed across the sky (that is, they are consistent with coming from random directions).

Following this, two locations for GRBs became the focus of observational investigation. The first is in an extended galactic halo (cf. Hakkila et al. 1994; Hakkila et al. 1995). The halo is limited in the size of its core radius from below by the lack of surplus bursts toward the Galactic Center (for example, if the core radius were $<$ 8 kpc, our 8 kpc distance from the Galactic Center would insure that we would see more GRBs toward the GC than away from the GC). The halo is limited in the size

of its core radius from above by the lack of surplus bursts toward M31, on the assumption that the M31 GRB halo would be identical to that of the Galaxy, requiring that a larger halo place M31 GRBs closer to us, making more of them detectable. The second focus for distance-scale observational investigations has been cosmological distances, where the source population may be either non-evolving or evolving (Dermer 1992; Piran 1992; Mao & Paczynski 1992; Fenimore et al. 1993; Lubin & Wijers 1993; Wickramasinghe et al. 1993; Cohen & Piran 1995; Rutledge et al. 1995; Horack et al. 1995; Caditz 1995). These investigations have typically found the peak-flux distribution to be consistent with a non-evolving parent population, with the faintest GRBs observed by BATSE coming from a red-shift of $(1+z)\sim 2$.

No convincing counterparts in any wave band, either persistent or transient, have been identified with GRBs, individually or statistically (Fishman & Meegan 1995, and references therein).

7.2 The Burst and Transient Source Experiment

In this thesis all data which are discussed pertaining to GRBs were obtained with the Burst and Transient Source Experiment (BATSE; Fishman & et al. 1989; Fishman et al. 1992 and references therein) on the *Compton* Gamma-Ray Observatory (*C*GRO; Kniffen 1989). We repeat the salient details here.

BATSE (see Fig. 7-1) is composed of eight detector modules, each containing a Large Area Detector (LAD) optimized for sensitivity and directional response and a Spectroscopy Detector (SD) optimized for energy spectral resolution and coverage; we are interested mostly in results from the LADs. The eight LADs contain $\sim$2000 cm^2 NaI detectors, which are arranged so that the eight faces are separately parallel to the eight sides of a regular octahedron, covering 4π ster of the sky. The nominal energy range of the LADs is 25-2000 keV, divided into four channels (25-50 keV; 50-100 keV; 100-300 keV; and >300 keV). These detector modules are mounted on the corners of the *C*GRO satellite (Fig. 7-2), such that the angular response of the ensemble of modules is as an octahedran. This provides full sky (4π ster) coverage

by these detectors.

The primary scientific goal of this instrument is the detection and characterization of GRBs. Normally, the instrument is in a mode of operation in which count-rates in all 8 detectors are monitored until an event which meets the "burst trigger" criteria is observed. The burst trigger criteria are a 5.5σ increase in count-rate separately in two energy channels (#2–3, 50–300 keV), on one or more of three timescales – 64ms, 256ms, 1024ms – in two or more detectors, when compared to the average count-rates over the previous 17 seconds. Following a burst "trigger", the time-resolution of the data acquisition increases to as high as μ-second (for certain data-modes) for a period of $\sim$300-900 seconds.

BATSE may have as many as several triggers a day, although some of these may be due to background events. These are removed from the GRB data-stream by identification through a number of indicators. For example, events due to the SAA are identified by the space-craft location above the earth, and by the count-rate-history during this period. Particle-bombardments can illuminate oppositely facing detectors (GRBs do not), and so bursts which are observed in oppositely facing detectors can be excluded. Solar flares are localized to come from the direction of the sun, and are spectrally softer than GRB. Cyg X-1 is sometimes bright enough to trigger by appearing over the limb of the earth during orbit; these events are identified by coming from near the earth limb, in the direction of Cyg X-1. These events, and others like them, are discarded, and the remaining events are GRBs. The detection rate of GRBs with BATSE is roughly 1/day.

Three cumulative catalogs – referred to as the 1B, 2B, and 3B catalogs – have been published with high-level data-products of these GRBs (Fishman et al. 1994; Meegan & et al. 1994; Meegan et al. 1996). More detailed, low-level data-products (raw count-rates in different energy ranges) are available electronically or on CD-ROM. The analyses we apply here deal with the high-level data-products provided in the catalogs, and also compiled high-level products (count rates, durations) produced by other investigators.

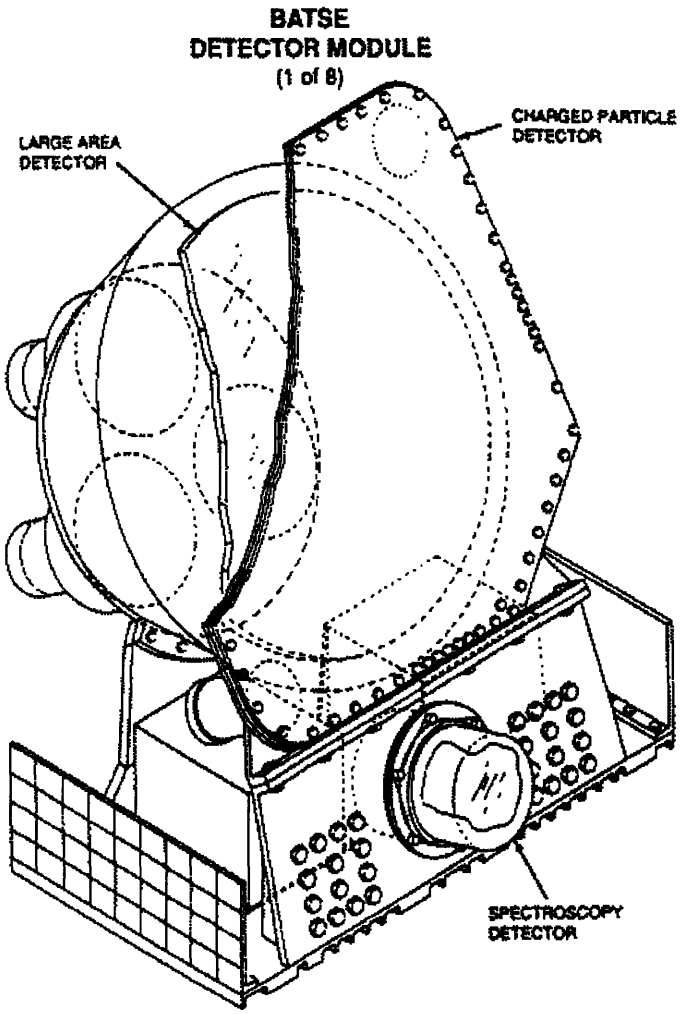

Figure 7-1: **The BATSE Instrument Module.** A BATSE Instrument module, showing a schematic of a LAD and SD. Eight identical modules are mounted on *C*GRO(Fig. 7-2) , providing full-sky coverage.

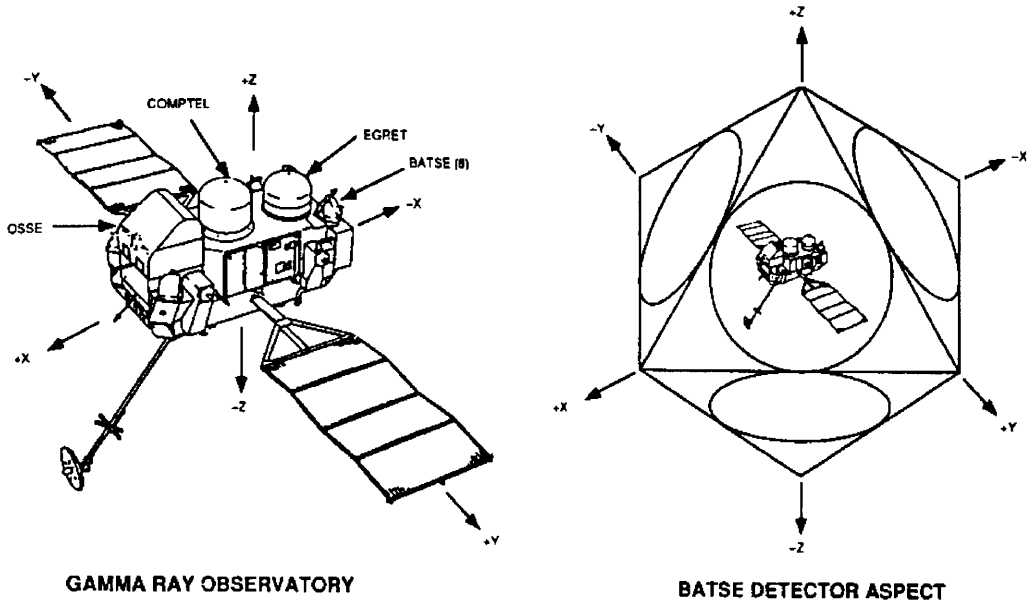

Figure 7-2: **The** *Compton* **Gamma Ray Observatory**. The eight BATSE modules (Fig. 7-1) are mounted on the corners of the observatory, providing an octahedran-like angular-response.

Chapter 8

Durations: In Search of The Clock

The interest in Gamma-ray Burst (GRB) durations rose from conflict between the two major proposals for the location of GRBs: either in other galaxies as distant as $(1+z)$=2.0 or higher (see Ch. 9), or within our own galaxy. If GRBs originate at high red-shift, then cosmological effects should affect the observable properties of GRBs; for example, the observed GRB duration (or, mean duration of the GRB duration distribution) should increase by a factor of $(1+z)$; or, spectral line emission or other spectral indicator should decrease by a factor of $(1+z)$ (see Mallozzi et al. 1995 for analysis of this spectral effect). Thus, one can compare, in principle, the burst duration or spectral indicator between the very brightest (and therefore close) and very dim (and therefore distant) GRBs and see this difference in burst properties.

Naturally, time-dilation cannot be the cause of differences in the duration distributions of bright and faint bursts in a galactic population. However, a positive correlation between burst luminosity and duration, such as is expected from relativistic bulk motion which may be associated with GRBs (Brainerd 1994), will produce a peak-flux – duration correlation as well. The effects of relativistic bulk motion may be active in a cosmological population as well and therefore may contribute to observed differences in the duration distributions between bright and faint bursts in either a cosmological or galactic scenario.

8.1 The Duration Focus

The root of all questions regarding gamma-ray bursts remains: what is it that causes them to occur? With *a priori* knowledge of what causes gamma-ray bursts to occur, one could in principle derive all their characteristics. With no knowledge of what makes them occur, one must take the opposite approach: define their phenomenology, and (hopefully) their parent population will make itself obvious.

There are many astrophysical transient events which have been observed, particularly in high-energy astrophysics. Examples of these are: black hole X-ray transients, Soft Gamma-ray Repeaters, and X-ray bursts. Almost without exception, these phenomena have characteristic temporal structure which greatly aid in the identification of their class. Black hole X-ray transients, observable in the 1-50 keV range (and, often, up to MeV, in the optical and radio as well) have rise-times of a few days, and decay exponentially on a timescale of 40-days (see Tanaka & Lewin 1995 for review). Soft-gamma-ray repeaters, with a few notable exceptions, are simply short (milli-second) spikes, typically with little discernible structure (Kouveliotou 1995). Type I X-ray bursts, produced by a thermonuclear flash on the surface of a neutron star, typically have short rise-times ($\lesssim$ 1 s) and decay exponentially on a timescale of a few-10s of seconds (Lewin et al. 1993). Type II X-ray bursts, which have only been observed from two neutron star low-mass X-ray binaries (The Rapid Burster, and GRO J1744-28), and have different temporal profiles between them; the Rapid Burster has a characteristic 4-humped profile (for bursts which are $\lesssim$30 s) or are roughly flat-topped (for bursts $\gtrsim$30 s), while GRO J1744-28 burst profiles are roughly triangular (Lewin et al. 1993; Kouveliotou et al. 1996).

Each of the phenomena has a characteristic timescale involved, which permits easy definition of the time-scale of the event, typically to within a few percent, which can be compared to that of other events of similar type. This is not true of GRBs.

GRBs do not have simple intensity profiles – "simple", in the sense of being easily defined by a single (or even a few) functions or descriptions; they can be extremely variable, increasing and decreasing in intensity many times during the

process of the burst; or they can be smooth, rising slowly and tailing off slowly, with no discernible structure. Some GRBs exhibit "pre-cursors" (Koshut et al. 1995), up to several 10s of seconds before the main burst emission. Merely identifying burst duration by eye requires full light-curve coverage of at least ~100s of seconds, as emission can stop entirely for 10-10^2 of seconds, and then begin again.

In Figure 8-1 we show intensity profiles in the 50-300 keV range of several GRBs detected by BATSE. The diversity of GRB intensity profiles is considerable.

This diversity of burst profiles makes the definition of characteristic time-scales difficult. Because the bursts lack any sort of universal structure, workers in the field turn to the integrated emission itself as a means to pull out a burst time-scale (Kouveliotou et al. 1993; Koshut 1995). The burst time-scales which are in common use to describe GRBs observed by BATSE are the amount of time elapsed (T_N) during the detection of N% of the total burst flux (in some energy passband), where typical values for N are 50 and 90. The integration is taken over the central portion of the burst, that is, T_{50} is the amount of time elapsed between the detection of 25% and 75% of the burst counts fluence, and T_{90} is the amount of time elapsed between the detection of 5% and 95% of the burst counts fluence.

This permits the comparison of duration properties among the bursts detected. At the very least, these time-scales proffer the information that photons from the burst were detected across this time-scale in the energy pass-band of the detector. The usefulness of such a definition has been in the assumption that the measured time-scale is somehow related to a physical timescale for a process which is related to the emission (for example, the duration of thermonuclear-flash (type I) X-ray bursts is related to the cooling time-scale of the neutron star surface). Seeing the broad diversity of GRB intensity profiles, it seems unlikely that a more useful GRB time-scale can be devised, which can describe the entire class of sources.

In Figure 8-2, we show the distribution of burst durations measured by BATSE, as they have been given in the third BATSE (3B) catalog (Meegan et al. 1996); the procedure and systematics associated with these measurements have been described (Koshut 1995). Here, the burst durations have been binned logarithmically. As has

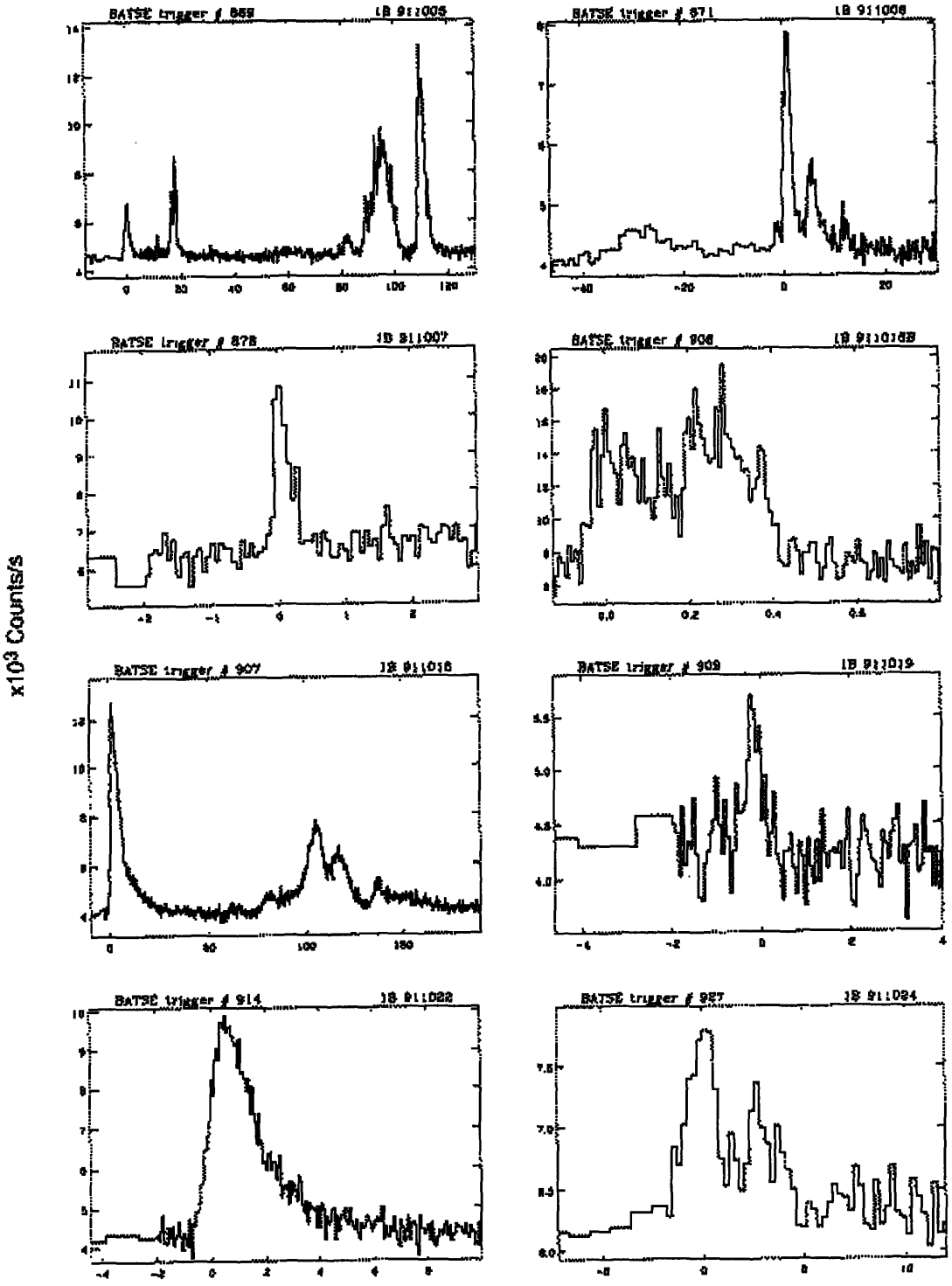

Figure 8-1: **Examples of GRB intensity profiles.** This is a more or less standard page from the 1B BATSE Burst catalog of light-curves (Fishman et al. 1994). Note the diversity of intensity profiles. The x-axis is time in seconds, and the y-axis is 1000 counts/sec.

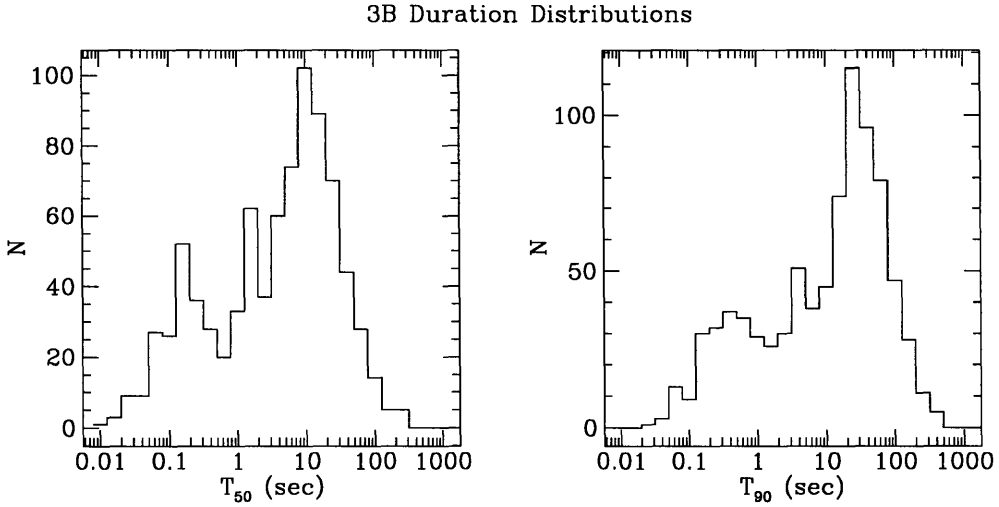

Figure 8-2: **GRB Durations – 3B catalog**. Data taken from Meegan et al. (1996). Left panel shows the distribution of the T_{50} durations, and the right panel shows the distribution of the T_{90} durations, of 834 GRBs taken from the 1122 bursts in the 3B catalog, when both values were measured.

been pointed out previously (Kouveliotou et al. 1993), the distribution is log-normal and bimodal, with modes at ~0.5s and 30s, and a minima at roughly 2.0s; thus, GRBs are often divided up for analysis into separate groups of "long" GRBs (duration $\gtrsim$2.0) sec) and "short" GRBs (duration $\lesssim$2.0 sec). It has been shown that the shorter GRBs are also spectrally harder than the long GRBs (Kouveliotou et al. 1993; Lestrade et al. 1993).

8.1.1 Previous Duration-Based Analyses

There has been an effort to use durations of GRBs as the standard clock, by which cosmological time-dilation may be observed. The approach has been to rely on the statistical properties of the duration distribution, because the durations of individual GRBs vary dramatically, making burst-to-burst comparisons impossible. The diversity of GRB intensity profiles is a source of considerable systematic uncertainty, as is the expected brightness bias (that is, brighter bursts provide more counts producing more accurate durations). Examine the duration distribution shown in Fig. 8-2. The expected effect of cosmological time-dilation is small for the peak-flux range of GRBs observed by BATSE – $\lesssim$2.0 (see Sec. 8.1.1), much smaller than the range of durations covered by the observed duration distribution of GRBs.

Soon after the availability of the BATSE data, a signature consistent with time-dilation of a factor ~2 (no quoted confidence) was reported (Norris et al. 1994). These analyses made use of wavelet-filtering and S/N equalizing algorithms, to equalize the S/N between observed GRBs, to remove brightness bias. It was pointed out that the reported effect could also be produced by a finite-width luminosity function (Band 1994), and that a cosmological distribution was not required by the data. Other analyses (Mitrofanov et al. 1994) found no evidence for a time-dilation between "weak" and "strong" GRBs (using 60 bursts from 1B BATSE data, based on the $V/V_{\max}$ value of each burst). Further analyses using more bursts, again using wavelet-filtering and S/N equalization (Norris et al. 1995), found that the ratio of centroids of the duration distributions in three (non-independent) energy ranges (> 25 keV, 50–320 keV, and 115–320 keV) for both T_{90} and T_{50} measures were in the range of

2.0–2.4, with ~10% uncertainty.

Magnitude of Expected Duration–Peak-Flux Correlation

If we are to look for the effects of time-dilation, it is useful to review the expected magnitude of the effect. In Fig. 8-3, we plot the red-shift of GRBs as a function of peak-flux, assuming a non-evolving GRB source population with standard-candle peak flux and power-law photon spectrum of $\alpha = 2.0$, for sources with a peak-flux (measured on a 256ms timescale) of 0.5 phot $cm^{-2}sec^{-1}$ originating from $(1+z)$=1.8 and $(1+z)$=3.0 (cf. Ch. 9). These red shifts are the limits of the 90% confidence region derived from the shape of the peak-flux distribution. We have approximately marked the peak-flux region corresponding to the "Bright" and "Dim+Dimmest" peak-counts range used by Norris et al. (1995). Comparing the mean $(1+z)$ values for the "Bright" and "Dim+Dimmest" bursts, we expect the relative amount of duration stretching, from:

$$= \frac{< 1 + z_{\rm brt} >}{< 1 + z_{\rm dim} >} \tag{8.1}$$

to be between 1.3 – 1.9 (90% confidence) depending on the actual maximum red shift of the observed BATSE bursts. The dependencies are such that, if GRB intensity profiles provided standard clocks to within ~10%, one could easily pick out the peak-flux/duration dependency.

For comparison, if the source population has a luminosity–duration correlation due to relativistic bulk motion, the results of Brainerd (1994) predict the expected increase in mean duration between bursts in the slope=$-3/2$ part of the peak-flux distribution curve (that is, the bright end) and bursts which are ×10-50 fainter to be in the range ~1.7–3.0 (from their Fig.1), depending on the intrinsic spectrum.

We have seen GRBs' intensity profiles are complex and non-universal. Further, it has been demonstrated that differences in the duration distributions between bright and faint bursts need not be due solely to the effects of time-dilation, but may also be due to intrinsic population characteristics which cause correlations between

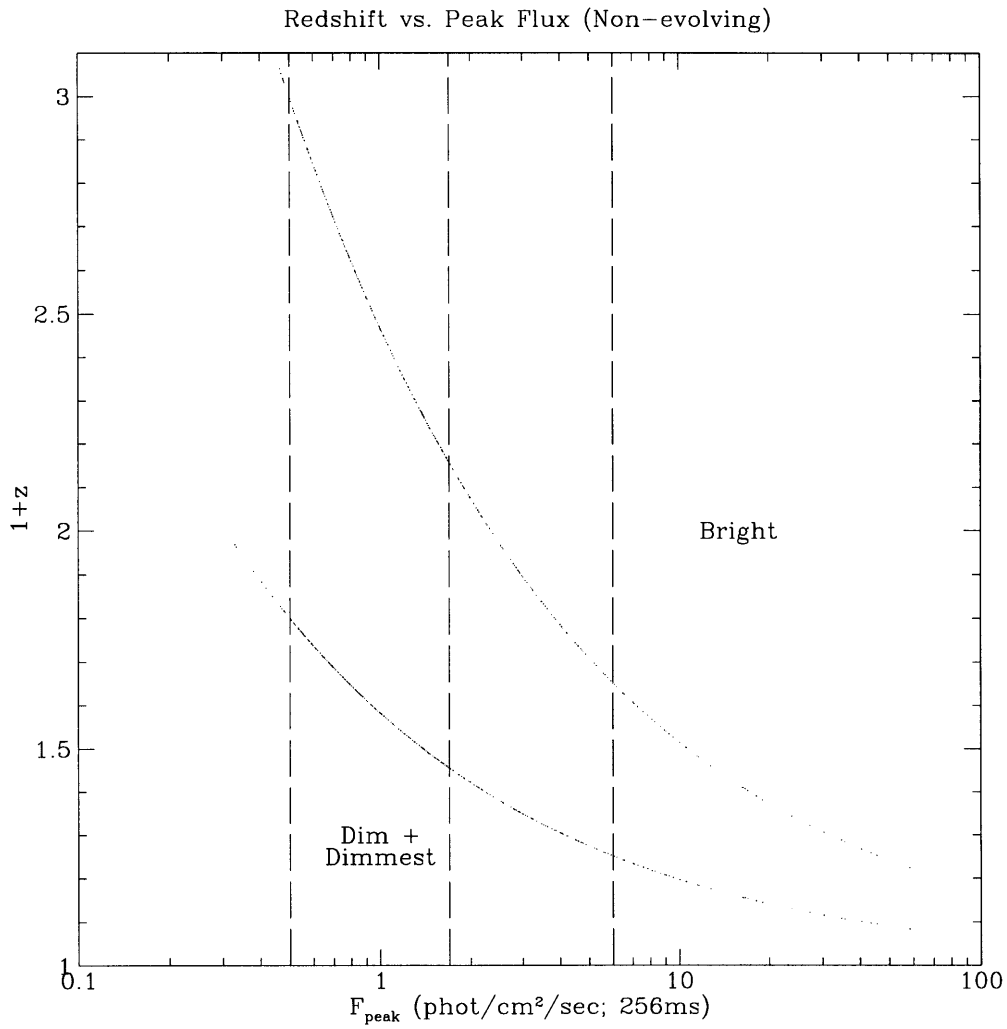

Figure 8-3: $(1+z)$ **vs. Peak Flux, Non-Evolving Standard Candle Population** . The 3B BATSE Peak Flux (256ms timescale) vs. expected red shift, for ~900 GRBs in the 3B catalog, assuming GRB sources at 0.5 photcm^{-2}sec^{-1} at red shift of 1.8 (bottom points) or 3.0 (top points) (cf. Ch. 9) in a non-evolving population.

the duration and luminosity. Thus, the motivation for analyzing duration distributions of GRBs has presently changed; it is done no longer to distinguish between a cosmological population and a Euclidean one, but to characterize the source population itself. This may not forever be the case: if the source of GRBs does not come to light, as more and more GRBs are observed by BATSE and other instruments, it may become possible to distinguish between the effect of cosmological time-dilation on burst durations and the effect of luminosity-correlated durations.

8.1.2 Analyses in this Chapter

Our analyses are as follows. In Sec. 8.2, we examine burst durations found by Norris et al. (1994; 1995), probing for systematic effects, and comparing their "bright" bursts duration distribution with that of their fainter bursts. We similarly investigate duration distributions of data drawn from the 3B Catalog. In Sec. 8.3, we apply non-parametric tests to search for correlations between peak flux and burst durations in the 3B BATSE catalog durations, and in Norris et al. durations. In Sec. 8.4, we describe a method to find the most-likely red-shift of an individual GRB (assuming a cosmological distribution), in data-sets where peak-flux – duration correlations are found, and we apply this method to the 3B BATSE catalog durations. In Sec. 8.5, we describe a method for extracting the correlation between luminosity and duration (in an assumed Euclidean distribution) in data-sets where peak-flux – duration correlations are found, and we apply this method to the 3B data set. In Sec. 8.6, we describe how to identify the signature of luminosity correlated observational parameters, and a means to extract zero-th order information about the intrinsic luminosity function from such observations.

8.2 Fitting the Log-Normal Duration Distribution To Burst Duration Data

In this section, we examine the duration distributions produced and studied previously (Norris et al. 1994; Norris et al. 1995) and compare them to samples drawn from the 3B Catalog duration data. To do so, we use least χ^2 fits to duration distributions, and compare the log-centroid durations and the log-widths of these distributions.

Durations measured from the raw lightcurve data were kindly provided by J. Norris and R. Nemiroff (private communication). This data also included: the BATSE burst catalog number, the peak counts in LAD channels 1-4 (>25 keV) in a 256ms time bin, and 11 measures of each burst duration.

The procedure of measuring durations used by Norris et al. has been described (Norris et al. 1994; Norris et al. 1995). We repeat the salient details. The time profiles were examined visually, yielding coarse duration estimates. The background count-rate is fit, using a quadratic model (and, for bursts longer than 131 sec, a fourth or fifth order model). The background subtracted count-rates are combined with randomly generated Poisson noise, to equalize the signal-to-noise of all bursts to the same level – that of the faintest burst. Each resulting profile was then passed through a high-pass filter using a wavelet transform, removing wavelet coefficients which represent less than 1σ point-to-point fluctuation (that is, structure which is not significantly distinct from temporal structure on slightly different timescales). These are then passed through a low-pass filter, which also removes wavelets of the same amplitude range, but measured against the ambient background level (that is, structure which is not significantly different from the background). Finally, a "trigger" level of constant significance is applied to the resulting light-curve, on timescales separated by a factor of two between 512ms and 32s, to determine lower and upper limits on t_0 and t_{100} (the times when 0% and 100% of the total burst detected fluence have been detected). The resulting time profiles are then integrated between these times to produce t_5, t_{25}, t_{75}, and t_{95}, from which $T_{90}(=t_{95} - t_5)$ and $T_{50}(=t_{75}-t_{25})$ are found. This procedure was followed for 11 different realizations of random noise, producing the 11 measurements

of T_{90} and T_{50} for each burst detected by BATSE.

8.2.1 Log-Normal Distribution Fits to Norris' Data

From the 11 duration measures of the GRB durations (from the 11 different noise realizations and passes through the duration measuring algorithm), we use the median value (that is, the sixth largest value) for our analyses.

In Fig. 8-4, we compare the measurements made by Norris from the raw BATSE data to the measures in the 3B catalog (Meegan et al. 1996). We started with the 444 GRBs with measured T_{50} from Norris' results, excluding GRBs which had a dispersion $\sigma_{T_{50,90}}$ in the duration measure $> 20\%$ of the median value:

$$\sigma_{T_{50,90}} = \sqrt{< T_{50,90}^2 > - < T_{50,90} >^2} \tag{8.2}$$

and for which durations are measured to be longer than 1.5 s.

In Fig. 8-4a, we show the ratio of the Norris T_{50} duration to the 3B T_{50} duration, as a function of burst peak flux. For some bursts, there is disagreement on the duration by $\gtrsim \times 2$. In Fig. 8-4b, we show the three burst peak-counts (on 256ms timescale) ranges used by Norris et al. ("Bright", "Dim" and "Dimmest"), as a function of the 3B peak flux on the 256ms time-scale. The peak-counts rate used by Norris is well-correlated with the 3B peak-flux values; however, the correlation is $\sim$30% wide, which is larger than the uncertainty in the 3B peak-flux values in most of this peak flux range. We include, in panels *c* and *d*, the duration ratio (as in panel *a*) but as a function of 3B duration (panel *c*)and Norris' duration (panel *d*). We can see in panel *c*, that there are about five long 3B bursts which Norris' finds to be a factor $\gtrsim$3 shorter, and there are about 8 short 3B bursts which Norris' finds to be a factor $\gtrsim$2 longer. There is no strong trend (*i.e.* one in which the fainter Norris bursts would be a factor of 2 longer than the 3B bursts) between the Norris' duration measures and the 3B duration measures.

First, we attempt to reproduce the results of (Norris et al. 1995) using their data, and applying identical selections. We used only bursts with BATSE burst

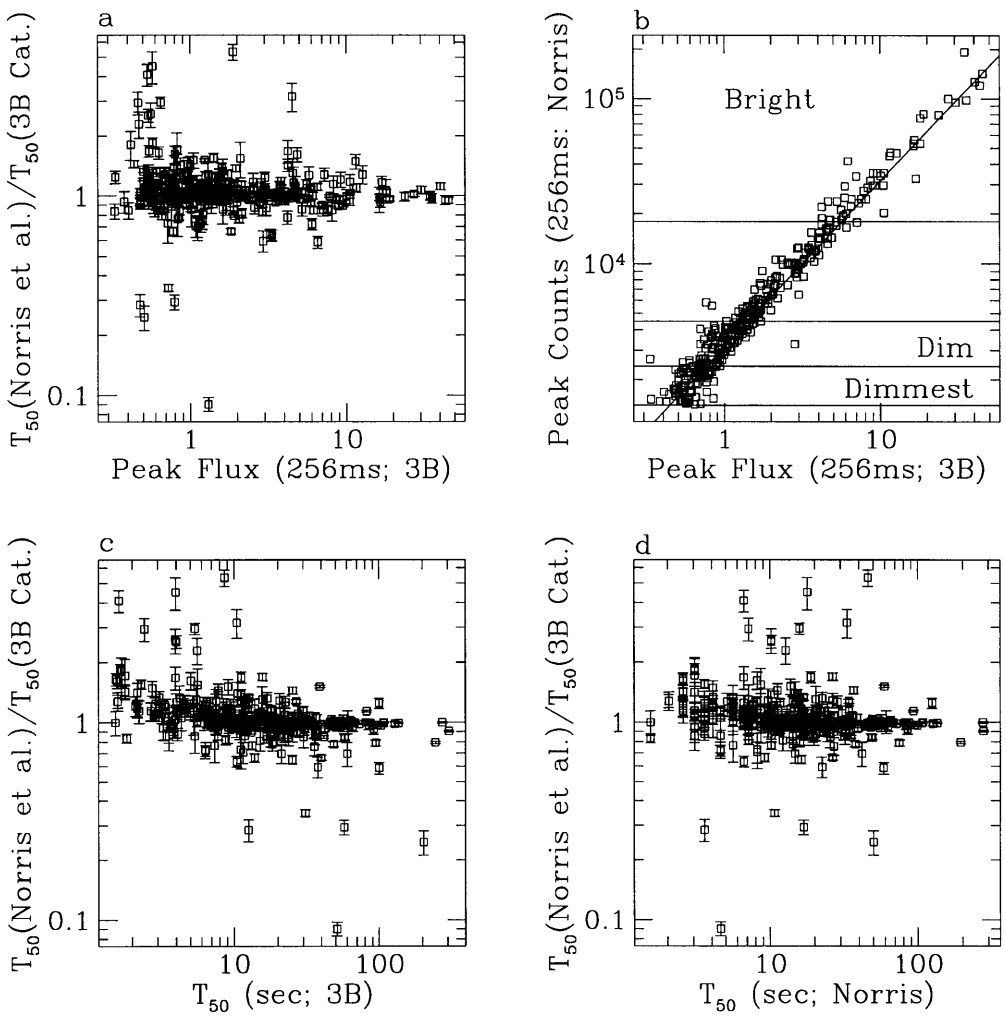

Figure 8-4: **Comparison of Norris et al. Peak Counts and T_{50} with 3B Peak Flux and T_{50}** *Panel a*: Ratio of the Norris measured T_{50} to that of the 3B Catalog (Duration Ratio), as a function of the 3B Peak Flux (256ms timescale; P_{256}). *Panel b*: Norris Peak Counts vs. 3B P_{256}. The two correspond linearly, but the scatter is larger than the reported 3B uncertainty. *Panel c*: The Duration Ratio vs. the 3B T_{50}. There are about 10 bursts which are discrepant by $\gtrsim \times 3$; Norris' analysis measures these bursts closer to the mean duration. *Panel d*: The Duration Ratio vs. the Norris et al. T_{50}.

number < 2538 (i.e. which would have been included in the 2B, but not the 3B BATSE catalog), and used only bursts with median durations > 1.5 s (that is, T_{90}>1.5 s or T_{50}> 1.5 s). This we call the "Norris 2B" sample. The durations were binned logarithmically in 5 bins/decade. Bins with no bursts in them were excluded from the fit, and the uncertainty in the number of bursts in each bin was taken to be $\sqrt{N}$. The resulting histogram was fit using a χ^2 minimization technique to a log-normal distribution:

$$p_{\rm lognorm}(T_{\rm N}, \log(T_c), \log(\sigma_T)) \propto exp^{-0.5\left(\frac{\log(T_c)-\log(T_{\rm N})}{\log(\sigma_T)}\right)^2} \tag{8.3}$$

where $\log(T_c)$ is the (base 10) logarithm of the centroid duration of the distribution (in units log[sec]), and $\log(\sigma_T)$ is the (base 10) logarithm of the width of the distribution (in units log[sec]). If the two distributions are identical, except for a relative shift of a factor of 2.00, as reported, we expect that the differences between the log-centroid and log-widths should be consistent with log(2)=0.30. The differences (and upper-limits) we discuss are always the "Dim+Dimmest" value (either log-centroid or log-width) minus the "Bright" value. All fits are performed in log-space, as we apply normal-statistics, and the log-normal distribution will only be normal in log-space.

In Table 8.1, we show the results of these fits, which are the logarithmic centroid duration ($\log[T_c]$), the logarithmic σ ($\log[\sigma_T]$), and their uncertainties, which we take to be normal. Reduced χ^2 values were acceptable (in the range of 0.4-2 for 10 d.o.f). The difference between the $\log(T_c)$ of the "Bright" and "Dim+Dimmest" samples in the T_{90} (T_{50}) distributions is 0.24 $\pm$0.08 (0.37 $\pm$0.1 – 1σ uncertainties). Both differences are significant at $\gtrsim 3\sigma$. The $\log(\sigma_T)$ widths of the T_{90}(T_{50}) distribution are consistent with one another, with 3σ upper-limits in their difference of <0.28 (<0.28).

We then perform the analysis again using all bursts (not limited to the 2B catalog bursts), again with median durations >1.5s. This we call the "Norris 3B" sample. The results are shown in Table 8.1. The difference between the $\log(T_c)$ of the "Bright" and "Dim+Dimmest" samples in the T_{90} (T_{50}) distributions is 0.32 $\pm$0.08

(0.26 $\pm$0.12 – 1σ uncertainties); the T_{90} difference is 4σ significant, while the T_{50} value is < 3σ. The log(σ_T) widths of the T_{90}(T_{50}) distribution from the "Norris 3B" samples are, again, consistent with one another, to <0.23 ($\lesssim$0.40; 3σ upper-limits).

We selected out those bursts which had high systematic uncertainties in the duration measurements provided by Norris. This was done by calculating the spread in the 11 duration measurements provided for each burst as Eq. 8.2. We then excluded those bursts with $\sigma_{T_{50,90}}/T_{50,90}$ >0.2 (i.e. more than 20% fractional uncertainty; chosen arbitrarily). This is the "Norris 3B + Precision" sample.

In Fig. 8-5 we show the measured peak counts (on 256ms timescale) vs median T_{90} duration for the "bright" and "dim+dimmest" groups of GRBs. In this figure, the points with the 4-pointed stars have values of $\sigma_{T_{90}}/T_{90}$ >0.2. As can be seen in the figure, these bursts preferentially have lower values of T_{90}. Also, there is a disparity between the number of bright bursts (26 of 75) and the number of dim+dimmest bursts (15 of 243) which are excluded on this basis.

The results of fits to the "Norris 3B + Precision" duration distributions are shown in Table 8.1. The centroid and widths of the T_{50} and T_{90} distributions are everywhere consistent, with the 3σ upper-limit to the log-centroid of <0.15 and to the log-width of <0.16 for the T_{90} distribution and of <0.31 and <0.37 (respectively) for the T_{50} distribution.

While the fact that a selection based on the measurement precision results in the disappearance of the reported duration distribution differences, this does not necessitate that the reported effect be due to this systematic. A possible explanation is the magnitude of the systematic uncertainty, if the affected data are not excluded entirely from the analysis, is not great enough to alter the result.

To investigate the impact of the wide dispersion of durations in the shorter bursts, we used all eleven of the measured durations for each burst. Burst durations >1.5 s were used only. These were binned to five bins per decade, each assigned a weight of 1/11, and uncertainty in the number was $\sqrt{1/11}$. We call this the "Norris 3B + All Measures" sample. We then fit to the resultant distributions as above.

The results of the fits to the "Norris 3B + All Measures" sample are shown

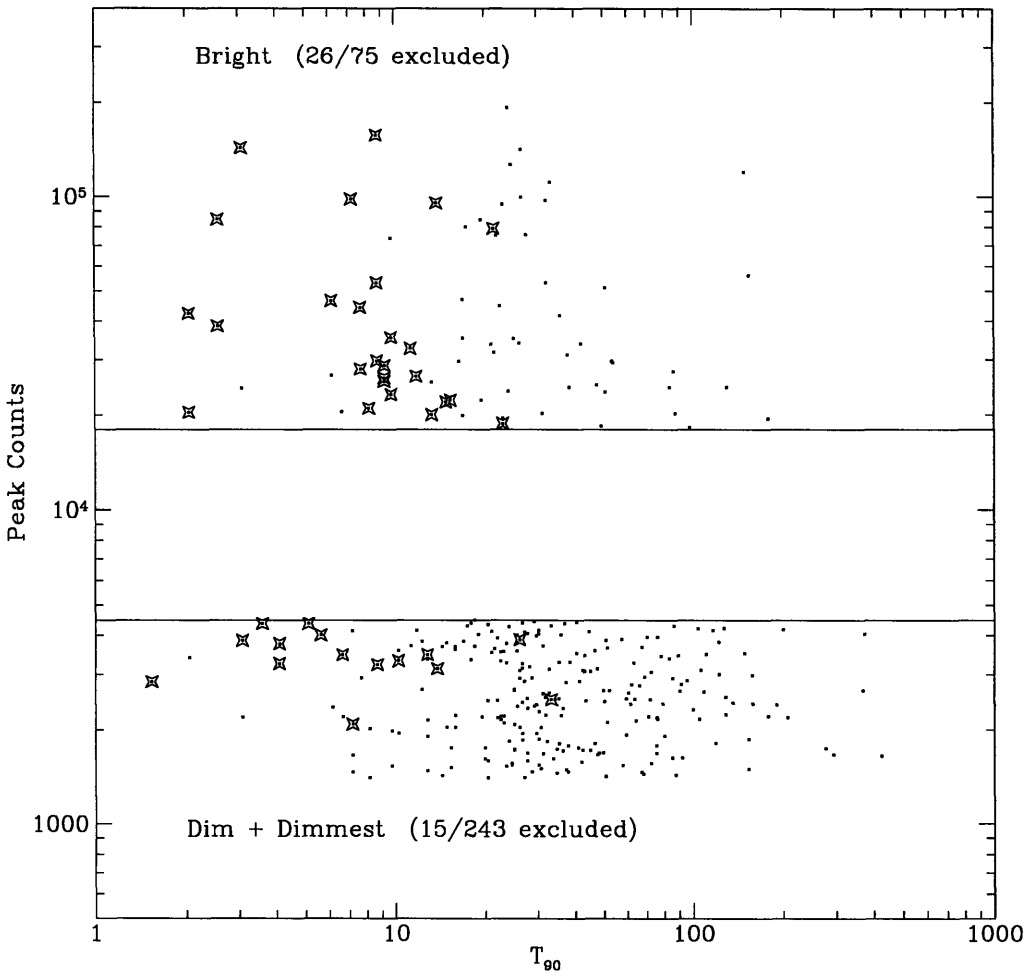

Figure 8-5: **Norris et al. data – T_{90} vs Peak Counts.** Data provided by Norris et al. Each point gives the peak counts (in 256ms) vs the median value of T_{90} found by Norris et al, for the bursts which fit in their "bright" and "dim + dimmest" groups (based on peak counts, see text). The points which also have 4-pointed stars on them have dispersions in the 11 duration measures > 20% (arbitrarily chosen); 26 of the 75 bright bursts have this high dispersion, while only 15/243 of the dim+dimmest bursts do. In both cases, it is the shorter bursts which have higher relative dispersions.

in Table 8.1. The difference between log-centroids of "Bright" and "Dim+Dimmest" sample T_{90} (T_{50}) distribution is 0.21 $\pm$0.06 (0.27$\pm$0.06); the width of the distributions are consistent with being the same, with 3σ upper-limits of <0.17 (<0.28).

Finally, we performed a similar fitting on bursts from the BATSE 3B catalog. These were divided into Bright and Dimmest groups on the basis of peak-flux on a 1024ms times-scale, of 3.0–50 (Bright) and 0.3–0.9 (Dimmest) phot cm^{-2} sec^{-1}. These ranges roughly (but not exactly) correspond to the "Bright" and "Dim+Dimmest" ranges of Norris et al. (cf. Fig. 8-4). The χ^2_ν of the T_{90} measures were high (3.2 and 2.4, 10 dof) while those of the T_{50} distributions were more acceptable (1.1 and 1.8, 10 dof). There is no measurable difference between the Bright and Dimmest burst duration distributions in these samples, with 3σ upper limits on the differences between log[T_c (s)] and log[σ_T (s)] of <0.25 – 0.28, corresponding to a factor of 1.8–1.9 in linear (sec) space.

Joint Fitting of Duration Distributions

Separately, we found the best fit model for two log-normal Gaussian distributions simultaneously for the "Bright" and "Dim+Dimmest" bursts (cf. Eq. 8.3):

$$p_{\rm joint}(T_{\rm N}) = p_{\rm lognorm}(T_{\rm N}, \log(T_c), \log(\sigma_T)) + p_{\rm lognorm}(T_{\rm N}, \log(T_c) + MT_c, \log(\sigma_T) + M\sigma_T) \tag{8.4}$$

where $\log(T_c)$ and $\log(\sigma_T)$ are the log-centroid and log-width of "Bright" distribution; MT_c is the difference between the log-centroid of the "Bright" distribution and that of the "Dim+Dimmest" distribution; and $M\sigma_T$ is the difference between the log-width of the "Bright" distribution to produce that of the "Dim+Dimmest" distribution. If the "'Dim+Dimmest" burst distribution is the "Bright" distribution stretched by a factor of two, then both $M\sigma_T$ and MT_c should be 0.3. We performed these fits for the "Norris 3B" sample, the "Norris 3B + Precision" sample, and the 3B sample of bursts.

The results of these fits, plus comparable values drawn from Norris et al. (1995,

Table 1) are given in Table. 8.2. The results of our fits to the Norris T_{90} data show that the centroids of the Bright and Dim+Dimmest distributions are different, at approximately 3-4σ significance, consistent with the values (but with larger uncertainties) found by Norris et al. . The widths of the distributions, however, are not as different as the centroids; we find that the width of the T_{90} distribution does not change between the "Bright" and "Dim+Dimmest" bursts, with a 3σ upper-limit $M\sigma_T \lesssim 0.11 - 0.14$. This is consistent with the results of Norris et al. (1995). The results of the T_{90} distributions are consistent with those of the T_{50} distributions.

The 3B Catalog sample indicates no difference between the duration distributions of the Bright and Dimmest bursts (see Table 8.1 for flux ranges). This result is discrepant from the Norris et al. result by 5σ (T_{90}) and 2.3σ (T_{50}). The χ^2_ν of the T_{90} fit, however, is unacceptably high, indicating the log-normal distribution model is unacceptable and the derived parameters in doubt.

We also fit these distributions with the requirement that $MT_c = M\sigma_T$, as expected for a red-shifted distribution. We find for these joint-fit values that the additive logarithmic factors are consistent with zero, with 3σ upper-limits of 0.204, 0.19, 0.25, 0.27 (for Norris' data) and 0.09, 0.156 (for 3B Catalog data); these translate into 3σ upper-limits in the linear factor difference between Bright GRBs and Dim (or "Dim+Dimmest") GRBs of $\sim$1.23–1.86.

8.2.2 Discussion and Conclusion

We examined the GRB distributions of T_{90} and T_{50} found from the BATSE raw data by Norris et al. (1994; 1995). We find that the "Bright" and "Dim+Dimmest" GRBs have distinct log-normal centroids at a barely significant level (3σ); the centroid of the "Bright" burst group is larger by a factor between 1.8–2.5 (T_{90}) or 1.7–3.5 (T_{50}; 1σ confidence ranges) than the "Dim+Dimmest" group; naturally, the centroids of the T_{90} and T_{50} distributions are not independent of each other. These are discrepant from the difference between the centroid values found from the 3B Catalog data 0.65–0.97 (1σ confidence).

The widths of each of these distributions are independent of the centroids;

we find that the width of the "Bright" burst distribution, is larger by a factor of between 0.7–1.02 (T_{90}) and 0.53–1.07 (T_{50}; 1σ confidence) compared to that of the "Dim+Dimmest" bursts.

We compare these results to those of Norris et al. (1995). Norris et al. finds that the amount of time-dilation in the centroids of the distribution is consistent with $\sim$2.2$\pm$10% (approximate; cf. their Table 2). This is within our 1σ confidence range for the distribution centroids alone. The amount of time-dilation in the widths of their distributions are $<$1.8 (3σ upper-limit). This is consistent with our limit of $<$1.8 (3σ upper-limit). Thus, we agree on the amount of time-dilation in both the centroids and widths.

If differences between duration distributions of "Bright" and "Dim+Dimmest" bursts are due to cosmological effects (red-shifting of the durations), then the factor increase in the width of the distributions should be approximately that of the centroid. Therefore, we should expect that a model which requires the factor increase in the distribution centroid to equal that of the width would provide a more reliable and significant measurement of the amount of time-dilation due to cosmological effects than a model which allows the factor increase in the centroid to vary independently of that of the width. We conclude that joint fitting for these values restricts the factor increase of the centroid and width between the "Bright" and "Dim+Dimmest" duration distributions to be limited to 0.98–1.60 (T_{90}) and 0.93–1.78 (T_{50}; 99.73% confidence) by Norris' data, and to 0.62–1.23 (T_{90}) and 0.79–1.45 (T_{50}) by the 3B Catalog data.

On the basis of the joint distribution fitting, we conclude that the amount of duration-distribution difference in these burst samples is consistent with no difference at all, with 99.73% limits of 0.62–1.78. These results are consistent with those found previously with this data-set (Norris et al. 1994; Norris et al. 1995).

We must comment on the difference between the present conclusions, that the effects of cosmological time dilation are limited to a relative shift in the duration distributions of 0.62-1.78 (99.73% confidence) and those of Norris et al. (1995), that the difference is significant at a factor of $\sim$2.0 ($\pm$10%). The discrepancy appears

to be rooted in our inclusion of the log-width of the duration distribution. Norris et al. (1995) do not include with equal weighting the log-width of the distribution. We do not see how the duration distribution width and centroid can escape being equally effected by cosmological time dilation. Had we relied on centroid measurements alone, our conclusions would be consistent with those of Norris (although with larger uncertainties).

Table 8.1: Moments of Gamma-Ray Burst Duration Distributions

Moments of Duration Distribution: Norris 2B

Brightness Group	Peak Intensity (Kcts/sec) Min	Max	T_{90} N (bursts)	$\log[T_c\ (s)]$	$\log[\sigma_T\ (s)]$	T_{50} N (bursts)	$\log[T_c\ (s)]$	$\log[\sigma_T\ (s)]$
Bright	18	256	54	1.32 ± 0.07	0.45 ± 0.09	51	0.80 ± 0.09	$0.49\ ^{+0.09}_{-0.11}$
Dim	2.4	4.5	102	1.59 ± 0.04	0.37 ± 0.03	102	1.14 ± 0.05	0.43a ± 0.04
Dimmest	1.4	2.4	73	1.54 ± 0.05	0.37 ± 0.05	73	1.20 ± 0.05	0.41 ± 0.05
Dim + Dimmest	1.4	4.5	175	1.56 ± 0.03	0.39 ± 0.03	175	1.17 ± 0.04	0.43 ± 0.03

Moments of Duration Distribution: Norris 3B

Brightness Group	Peak Intensity (Kcts/sec) Min	Max	T_{90} N (bursts)	$\log[T_c\ (s)]$	$\log[\sigma_T\ (s)]$	T_{50} N (bursts)	$\log[T_c\ (s)]$	$\log[\sigma_T\ (s)]$
Bright	18	256	75	1.21 ± 0.07	0.47 ± 0.07	71	$0.80\ ^{+0.09}_{-0.11}$	$0.49\ ^{+0.12}_{-0.09}$
Dim	2.4	4.5	141	1.55 ± 0.04	0.39 ± 0.03	140	1.03 ± 0.06	0.48 ± 0.05
Dimmest	1.4	2.4	102	1.49 ± 0.04	0.40 ± 0.05	101	1.09 ± 0.06	0.50 ± 0.07
Dim + Dimmest	1.4	4.5	243	1.53 ± 0.03	$0.40\ ^{+0.02}_{-0.03}$	241	1.06 ± 0.04	0.48 ± 0.04

Moments of Duration Distribution: Norris 3B + Precision

Brightness Group	Peak Intensity (Kcts/sec) Min	Max	T_{90} N (bursts)	$\log[T_c\ (s)]$	$\log[\sigma_T\ (s)]$	T_{50} N (bursts)	$\log[T_c\ (s)]$	$\log[\sigma_T\ (s)]$
Bright	18	256	49	1.49 ± 0.04	0.25 ± 0.05	57	$0.90\ ^{+0.08}_{-0.10}$	0.50 ± 0.12
Dim	2.4	4.5	127	1.60 ± 0.03	0.35 ± 0.03	125	1.12 ± 0.04	0.42 ± 0.04
Dimmest	1.4	2.4	101	1.49 ± 0.04	0.39 ± 0.05	99	1.10 ± 0.06	0.49 ± 0.07
Dim + Dimmest	1.4	4.5	228	1.57 ± 0.03	0.36 ± 0.02	224	1.12 ± 0.03	0.44 ± 0.03

Moments of Duration Distribution: Norris 3B + All Measures

Brightness Group	Peak Intensity (Kcts/sec) Min	Max	T_{90} N (measures)	$\log[T_c\ (s)]$	$\log[\sigma_T\ (s)]$	T_{50} N (measures)	$\log[T_c\ (s)]$	$\log[\sigma_T\ (s)]$
Bright	18	256	73.3	1.33 ± 0.04	$0.41\ ^{+0.03}_{-0.04}$	68.9	0.82 ± 0.06	0.49 ± 0.06
Dim	2.4	4.5	140.4	1.56 ± 0.04	0.38 ± 0.03	135.2	$1.09\ ^{+0.05}_{-0.06}$	$0.46\ ^{+0.06}_{-0.04}$
Dimmest	1.4	2.4	101.8	$1.51^{+0.03}_{-0.04}$	0.38 ± 0.04	98.3	$1.09\ ^{+0.05}_{-0.07}$	0.47 ± 0.08
Dim + Dimmest	1.4	4.5	242.2	1.54 ± 0.04	0.40 ± 0.04	233.6	$1.09\ ^{+0.05}_{-0.06}$	0.45 ± 0.07

Moments of Duration Distribution: 3B Catalog bursts

Brightness Group	Peak Intensity (phot $cm^{-2}sec^{-1}$;1024ms) Min	Max	T_{90} N (bursts)	$\log[T_c\ (s)]$	$\log[\sigma_T\ (s)]$	T_{50} N (bursts)	$\log[T_c\ (s)]$	$\log[\sigma_T\ (s)]$
Bright	3.0	40.0	109	1.45 ± 0.06	0.55 ± 0.08	77	0.95 ± 0.08	0.51 ± 0.08
Dimmest	0.3	0.9	304	1.35 ± 0.06	0.58 ± 0.05	235	1.00 ± 0.05	0.52 ± 0.05

Table 8.2: Multiplication Factor Between "Bright" and "Dim+Dimmest" Centroids and Widths

Sample	T_{90} $MT_c \pm 1\sigma$	$M\sigma_T \pm 1\sigma$	χ^2_ν	T_{50} $MT_c \pm 1\sigma$	$M\sigma_T \pm 1\sigma$	χ^2_ν
Norris et al. 1995[a] (Method 1)	0.32 ± 0.03	0.11 ± 0.04	–	0.35 ± 0.03	0.14 ± 0.04	–
Norris et al. 1995[a] (Method 2)	0.36 ± 0.04	0.03 ± 0.04	–	0.37 ± 0.04	0.09 ± 0.04	–
"Norris 3B"	$0.32\ ^{+0.08}_{-0.07}$	$-0.07^{+0.06}_{-0.07}$	1.14 (19)	$0.35\ ^{+0.22}_{-0.12}$	$-0.09^{+0.12}_{-0.18}$	0.95 (17)
"Norris 3B + All Measures"	0.21 ± 0.06	-0.01 ± 0.05	0.79 (21)	$0.31^{+0.11}_{-0.10}$	$-0.08\ ^{+0.10}_{-0.11}$	0.79 (17)
3B Catalog	$-0.09^{+0.07}_{-0.08}$	$0.04^{+0.1}_{-0.08}$	2.8 (21)	$0.06^{+0.12}_{-0.09}$	$0.01^{+0.09}_{-0.12}$	1.5 (21)

Sample	T_{90} $(MT_c = M\sigma_T) \pm 3\sigma$	χ^2_ν	T_{50} $(MT_c = M\sigma_T) \pm 3\sigma$	χ^2_ν
"Norris 3B"	$0.11\ ^{+0.094}_{-0.12}$	1.75 (20)	$0.12^{+0.13}_{-0.15}$	1.22 (18)
"Norris 3B + All Measures"	$0.09\ ^{+0.10}_{-0.097}$	1.07 (22)	0.12 ± 0.15	1.03 (18)
3B Catalog	$-0.03\ ^{+0.12}_{-0.18}$	2.7 (22)	$0.04\ ^{+0.12}_{-0.14}$	1.4 (22)

[a] From Norris et al. 1995; Table 1

All values are log(sec); 0.3 corresponds to ×2 duration stretching

8.3 The Correlation Between Gamma-Ray Burst Duration and Peak Flux

8.3.1 Summary

Using non-parametric tests, we examine data in the 3B BATSE catalog for correlations between burst duration (T_{50}, T_{90}) and peak flux (P_{64}, P_{256}, P_{1024}). Using the Spearman and Kendall rank-correlation tests, we find no evidence for peak-flux – duration correlation in the present samples, drawn from the BATSE 3B Catalog. We find some evidence for such a correlation using duration measures provided by Norris et al. (1994; 1995), but find this disappears when bursts with fractionally large systematic uncertainties (>20%) in their duration measurement are excluded. Comparing duration distributions of bright and faint bursts from the 3B catalog and (separately) Norris' data using the KS test, we find that the factor difference between the centroids and widths is limited (3 σ) to $\lesssim$1.6-2.8, depending on the combination of duration and flux measure used and selection criteria.

8.3.2 Introduction

The basis of this work has appeared previously (Rutledge et al. 1996b), and has been expanded upon here.

Interest in the relationship between burst duration and peak flux of cosmic Gamma Ray Bursts (GRBs) has grown. Investigations were first motivated by cosmological-origin models, which predict a correlation due to time-dilation. Correlation between peak flux and duration may also be due to an intrinsic relationship between burst luminosity and duration (Brainerd 1994).

A dependence between the co-moving photon energy and the burst duration may also produce a measurable effect in a cosmological scenario. If the dependence of duration on photon energy is $t \propto E^{-1}$, then the effect of time-dilation on the observed duration will be exactly cancelled; if the exponent is < -1 then burst durations will be *anti*-correlated with peak flux; if the exponent is > -1, the burst durations will

be correlated with peak flux. Fenimore et al. (1995) report that the pulse-width of GRBs as a function of energy is consistent with a power-law dependence of between 0.37-0.42.

Using the Spearman and Kendall non-parametric tests (Press et al. 1995), we search for correlations between the duration measures (T_{50}, T_{90}) and peak flux measures (P_{64}, P_{256}, P_{1024}) in the BATSE 3B catalog.

8.3.3 Data Selection

We use data from the BATSE 3B catalog (Meegan et al. 1996). We draw samples comparing both the duration measures (T_{50}, T_{90}; Kouveliotou et al. 1993; Koshut 1995) with all three peak flux measures (P_{64}, P_{256}, P_{1024}), producing six different data samples. In addition, we apply three data-selection criteria (see Table 8.3), which results in a total of 18 different (but not independent) data samples.

Table 8.3: The GRB Data Selection Criteria

Ref.	Relative Uncertainty	Duration Cutoff
$T_N > 4\times$	<0.2	$T_N > 4\times$ Peak Flux Integration Time
$T_N > 1.5$ s	<0.2	$T_N > 1.5$ s
No Relative Uncertainty	None	$T_N > 1.5$ s

In the "$T_N > 4\times$" sample, data for each of the six pairs of (duration, peak flux) were drawn, requiring that the quoted relative uncertainty in both the peak flux and duration measures of a burst is less than 20% (arbitrarily chosen), and that the value of the duration measure T_{50} for each burst be at least four times the integration time scale of the peak flux measure for that sample.

In the "$T_N > 1.5$ s" sample, data were drawn, requiring that the quoted relative uncertainty in both the peak flux and duration measures of a burst is less than 20%, and that the value of the duration measure T_N for each burst be greater than 1.5 s.

In the "No Relative Uncertainty" sample, data were drawn requiring only that the value of the duration measure T_N for each burst be greater than 1.5 s.

8.3.4 Spearman and Kendall's Tau Correlation

We applied the Spearman rank-order correlation test, and the similar Kendall's Tau test (Press et al. 1995). The Spearman Tau test ranks the durations and peak fluxes in ascending order, and finds if there is any tendency for lower-ranked durations to be associated with higher (or lower) ranked peak fluxes. The Kendall test is more loose than this, in that it checks (peak flux, duration) pairs against each other; the relative ordering of the peak fluxes (which one is greater) is compared against that of the durations, and it is found if there is a significant tendency that if one pair has a greater value of peak-flux that it will also have a greater (or lessor) value of duration.

To gauge the sensitivity of these tests to intrinsic duration distribution stretching, we used the data samples above to mimic the amount of duration stretching due to a cosmological sample, assuming sources of peak flux=0.5 phot $cm^{-2}sec^{-1}$ (measured on the timescale used for that sample) originate at a red shift of 2.0 (*cf.* Ch. 9), with an Ω_0=1.0 cosmology and assuming a simple photon power-law spectrum of slope α=2.0. Based on these assumptions we produced a sample of $t_{\rm stretch}$ durations from the observed $t_{\rm dur}$ durations:

$$\sqrt{1+z(F_2)} = \frac{1}{2} + \sqrt{\frac{1}{4} + (1 + z(F_1) - \sqrt{1+z(F_1)})\sqrt{\frac{F_2}{F_1}}} \tag{8.5}$$

$$t_{\rm stretch} = t_{\rm dur}\left(\frac{1}{2} + \sqrt{\frac{1}{4} + (2-\sqrt{2})\sqrt{\frac{0.5{\rm phot\,cm^{-2}\,sec^{-1}}}{F_{\rm peak}}}}\right)^2 \tag{8.6}$$

where $t_{\rm dur}$ is either T_{50} or T_{90} (whichever was used for that sample), resulting in a "hand-inserted" red shift factor. This is a different means of inserting a mimicked red shift in the sample than employed previously (Rutledge et al. 1996b). The resulting samples were also subjected to the Spearman and Kendall's Tau tests.

In Table 8.4, we show the resulting probability of the data samples being produced from a randomly distributed population, from the Spearman and Kendall's Tau correlation tests (indicated by $t_{\rm dur}$).

There is no indication of correlation between peak flux and duration in any of the observed 3B samples. These tests usually find convincing correlations between peak fluxes and durations in the t_{stretch} samples, except for the "No Relative Uncertainty" samples – in which it may be the case the greater fractional uncertainty of the data diminishes the ability of the test to detect the hand-inserted correlation.

Table 8.4: % significance from Spearman / Kendall tests

	$T_N > 4\times$									
		T_{50}					T_{90}			
	N	Spearman		Kendall		N	Spearman		Kendall	
	(bursts)	t_{dur}	t_{stretch}	t_{dur}	t_{stretch}	(bursts)	t_{dur}	t_{stretch}	t_{dur}	t_{stretch}
P_{64}	352	3	0.06	3	0.06	340	6	0.1	6	0.1
P_{256}	471	7	$5 \cdot 10^{-3}$	7	$4 \cdot 10^{-3}$	452	44	0.1	43	0.1
P_{1024}	488	4	$2 \cdot 10^{-5}$	4	$2 \cdot 10^{-5}$	488	69	0.07	69	0.07
	$T_N > 1.5$ sec									
		T_{50}					T_{90}			
	N	Spearman		Kendall		N	Spearman		Kendall	
		t_{dur}	t_{stretch}	t_{dur}	t_{stretch}		t_{dur}	t_{stretch}	t_{dur}	t_{stretch}
P_{64}	304	0.4	$1 \cdot 10^{-3}$	0.4	$1 \cdot 10^{-3}$	293	9	0.07	8	0.05
P_{256}	457	3	$2 \cdot 10^{-3}$	14	$1 \cdot 10^{-3}$	435	39	0.08	37	0.06
P_{1024}	526	17	$6 \cdot 10^{-3}$	17	$5 \cdot 10^{-3}$	526	34	4	34	3
	No Relative Uncertainty									
		T_{50}					T_{90}			
	N	Spearman		Kendall		Spearman		Kendall		
		t_{dur}	t_{stretch}	t_{dur}	t_{stretch}	t_{dur}	t_{stretch}	t_{dur}	t_{stretch}	
P_{64}	597	90	0.6	91	0.6	7	26	8	24	
P_{256}	597	78	0.8	76	0.8	2	37	2	35	
P_{1024}	597	39	4	39	4	0.1	90	0.2	86	

8.3.5 Dropping the High-Flux bursts

The correlation of peak flux with duration should be undetectable in the range where the peak fluxes in the $-3/2$ part of the integrated peak flux distribution (see Sec. 8.5).

As this is the case, we took only bursts with peak fluxes below the $-3/2$ part of the integrated peak flux distribution, identified by eye as occurring approximately at 10.0, 6.0, and 3.0 phot $cm^{-2}sec^{-1}$ in the P_{64}, P_{256}, and P_{1024} measures (see Fig 8-6). We then re-performed the above analysis for the resulting burst samples.

Table 8.5: % significance from Spearman/Kendall Tests; Low Flux Bursts Only

$t_N > 4\times P$ Integration time										
		T_{50}					T_{90}			
	N	Spearman		Kendall		N	Spearman		Kendall	
	(bursts)	t_{dur}	$t_{stretch}$	t_{dur}	$t_{stretch}$	(bursts)	t_{dur}	$t_{stretch}$	t_{dur}	$t_{stretch}$
P_{64}	303	27	4	26	4	290	19	2	18	2
P_{256}	401	87	8	88	8	380	85	13	84	13
P_{1024}	390	78	2	77	1	390	35	14	34	14
$T_N > 1.5$ sec										
		T_{50}					T_{90}			
	N	Spearman		Kendall		N	Spearman		Kendall	
	(bursts)	t_{dur}	$t_{stretch}$	t_{dur}	$t_{stretch}$	(bursts)	t_{dur}	$t_{stretch}$	t_{dur}	$t_{stretch}$
P_{64}	260	23	2	21	2	251	29	3	27	2
P_{256}	387	84	6	84	6	365	79	13	78	13
P_{1024}	419	48	17	49	17	419	5	76	5	75
No Relative Uncertainty										
		T_{50}					T_{90}			
	N	Spearman		Kendall		Spearman		Kendall		
	(bursts)	t_{dur}	$t_{stretch}$	t_{dur}	$t_{stretch}$	t_{dur}	$t_{stretch}$	t_{dur}	$t_{stretch}$	
P_{64}	553	22	28	22	28	2	86	2	84	
P_{256}	525	2	83	3	84	0.1	53	0.1	55	
P_{1024}	489	0.8	74	0.8	75	$7\cdot10^{-3}$	75	$7\cdot10^{-3}$	14	

The resulting probabilities of generating the observed correlation with a random distribution, as found by the Spearman and Kendall tests are shown in Table 8.5.

Except for one case, there is no significant correlation present in the 3B data between T_{50} or T_{90} with any of the three peak flux measures (P_{64}, P_{256}, P_{1024}). The data-sets in which the red-shift was inserted by hand (as above) do not show any correlation between peak-flux and duration either, indicating that, without the high-flux bursts, the scatter in GRB durations is too great to permit a correlation of the magnitude expected to be measured by these tests.

The data which do appear to show a correlation is the sample of (P_{1024}, T_{90}) selected using the "No Relative Uncertainty" criteria. We considered the possibil-

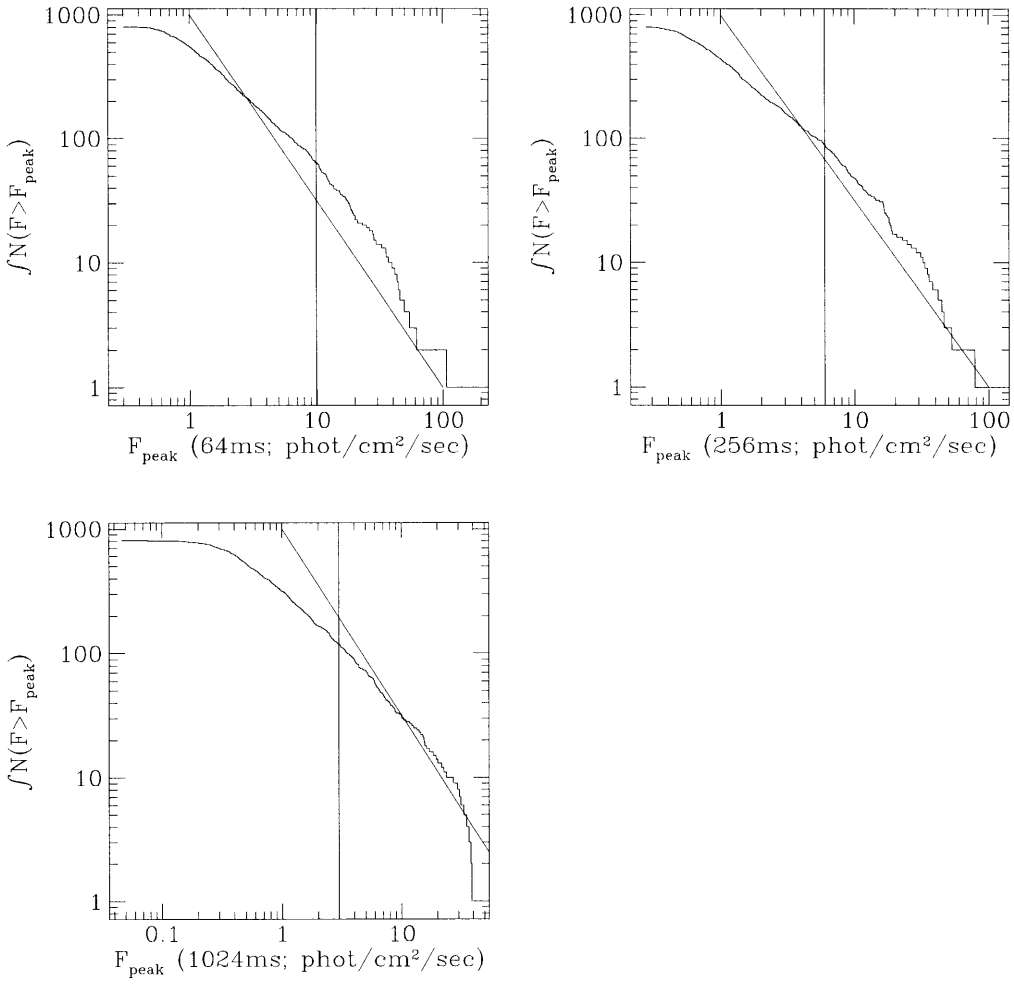

Figure 8-6: **3B Peak Flux Distributions**. These are the observed peak flux distributions of BATSE GRBs in the 3B catalog. The three panels show the measured peak flux distribution P_{64}, P_{256}, and P_{1024}. No corrections or data selection criteria have been applied. Each panel contains a power-law of slope -3/2, arbitrarily normalized, for comparison. Each panel also contains a vertical line where the cut-off was made, by eye, to select bursts which are not in the -3/2 power-law slope part of the distribution.

ity that this correlation is due only to the inclusion of lower-precision duration/flux measurements. This sample has 7 (of the 489) bursts with peak fluxes lower than the lowest peak flux in the "T_N> 1.5 sec" sample. If these seven are removed from the sample, the probability of correlation increases only slightly from 0.007 to 0.01 %, compared to 5% for the "T_N> 1.5 s" sample, which covers the same peak-flux range, but has 15% fewer bursts (419 compared to 482). As they cover identical peak flux ranges, and differ in the number of bursts by only 15%, we conservatively conclude that the reason the "No Relative Uncertainty" sample shows a more significant correlation than the "T_N> 1.5 s" sample is not the larger sample size, but the inclusion of bursts with higher relative uncertainties in their duration and peak-flux measures.

8.3.6 Spearman and Kendall's Tau Test on Norris' Data

We applied the Spearman and Kendall's Tau test on Norris' duration and peak counts data. We sought the probability that the observed data set was produced by populations with no correlation between the peak counts and T_{50} or T_{90} durations. We applied the tests to the T_{90} and T_{50} measures, for all available data ("Norris 3B"; see Sec. 8.2) and for duration measures with dispersion <20% ("3B + Precision"). The results are listed in Table 8.6. When all data are included, there are significant correlations between the peak counts and duration (probabilities 0.002–0.03%). In the "3B + Precision" data-set, there is no significant correlation between peak counts and duration (18-45%).

Table 8.6: Results of Spearman and Kendall's Tests on Norris' data

	T_N> 1.5 s					
		T_{50}			T_{90}	
	N (bursts)	Spearman t_{dur}	Kendall t_{dur}	N (bursts)	Spearman t_{dur}	Kendall t_{dur}
Norris 3B	497	0.02	0.03	498	$2 \cdot 10^{-3}$	$2 \cdot 10^{-3}$
Norris 3B + Precision	428	18	18	421	71	45

8.3.7 Duration Distribution Comparisons Using the Kolmogorov–Smirnov Test

We investigated the amount of relative "shift" between the duration distributions of the brightest bursts and the faintest bursts permitted by each of these data-sets. This was done in the following manner (similar to that used by Norris et al. 1995).

For each of the samples used ("T_N> 1.5 s", "$T_N > 4\times$", "No Relative Uncertainty", and "Norris 3B"), two separate distributions were produced, of the 10% highest and, separately, the 40% lowest peak flux values, using the fluxes of all detected bursts.

The durations of the "10% highest" group were multiplied by a constant factor (the "Relative Shift") and the resulting distribution compared with the duration distribution of the "40% lowest" group using the Kolmogorov–Smirnov (KS) test (Press et al. 1995), producing the probability of the two distributions being drawn from the same population as a function of "Relative Shift".

This method does not, strictly speaking, exactly produce the confidence region of the time-dilation factor, because the relative time-dilation factor varies from burst to burst. The present analysis approximately produces the average time-dilation factor between the two burst ensembles, accurate in the limit that the two separate distributions sample a small amount of red-shift space compared to the amount of relative time-dilation between them. As the bright distribution was selected to cover the -3/2 part of the distribution, no significant difference in the durations of bursts due to time-dilation should occur. The faint bursts peak fluxes range by up to a factor of 2, which produces a difference in red-shift of ~ 1.26 (assuming the faintest bursts to be at a red-shift of 2; *cf.* Fig. 8-3). The mean fluxes of the two distributions are separated by a factor of $\gtrsim 10$.

The results of these comparisons are shown in Figures 8-7, 8-8, 8-9, 8-10. The integration time of the peak flux, as well as the duration measure relevant to that data set, is noted in the upper-right of each panel. A horizontal line is drawn at the level where the "Relative Shift" is excluded at the 99.73% level.

For all samples 3B Catalog tested, the KS probabilities at a Relative Shift of 1.0 are >65%, indicating that the distributions are indistinguishable. The limits on the amount of Relative Shift each data sample can tolerate is dependent upon the selection criteria and the peak-flux and duration measures used. The 3σ upper-limits to the amount of Relative Shift are 1.6–2.8, depending on the combination of duration and peak flux measured used, and the data selection criteria.

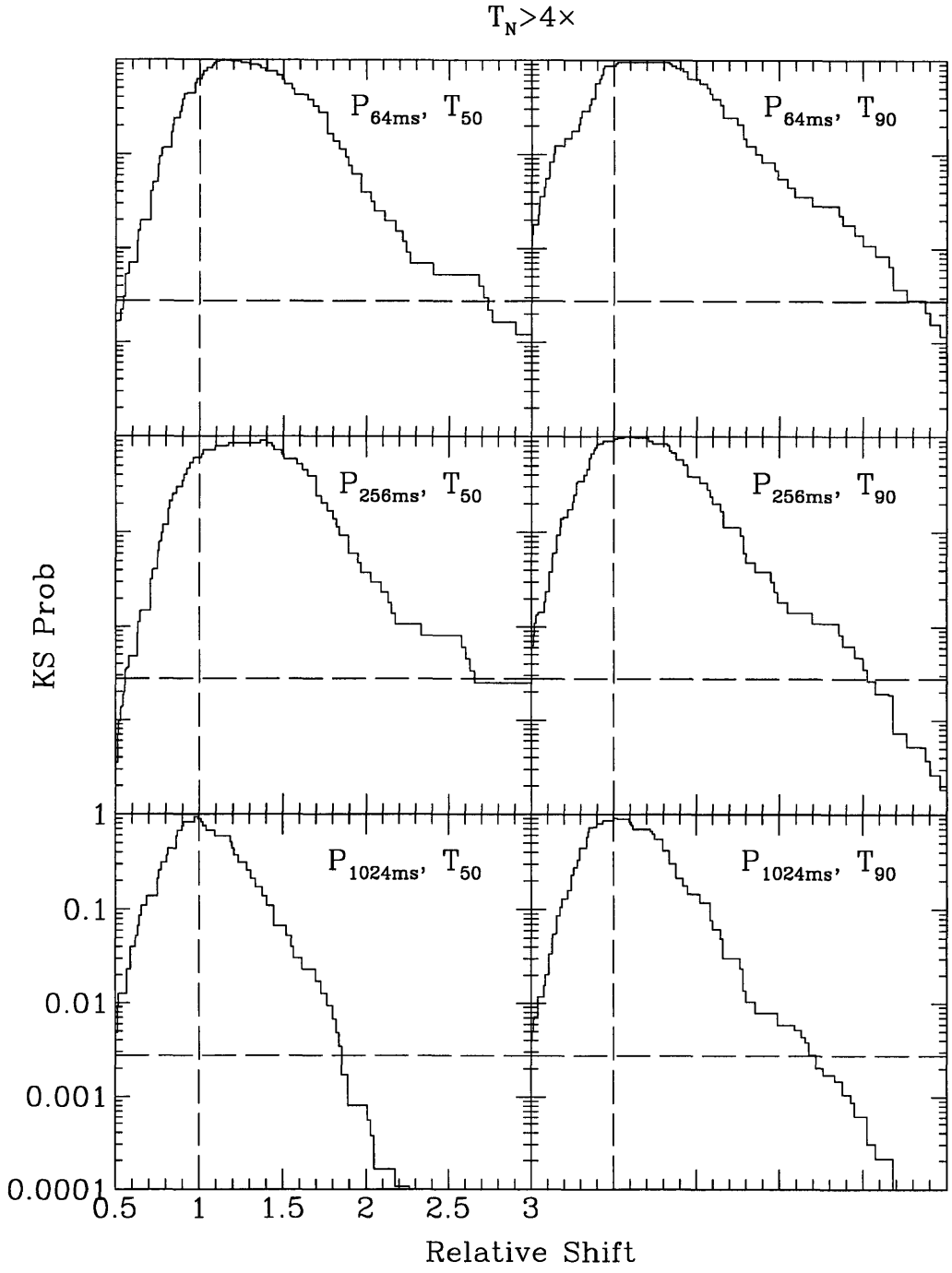

Figure 8-7: **Relative-Shift KS Distributions, "T_N> 4×" sample** The horizontal line marks the boundary where the KS probability of the amount of "Relative-Shift" between the two distributions is 0.0027%. The vertical line marks the point of no "Relative-Shift" (where the durations of one sample were multiplied by 1).

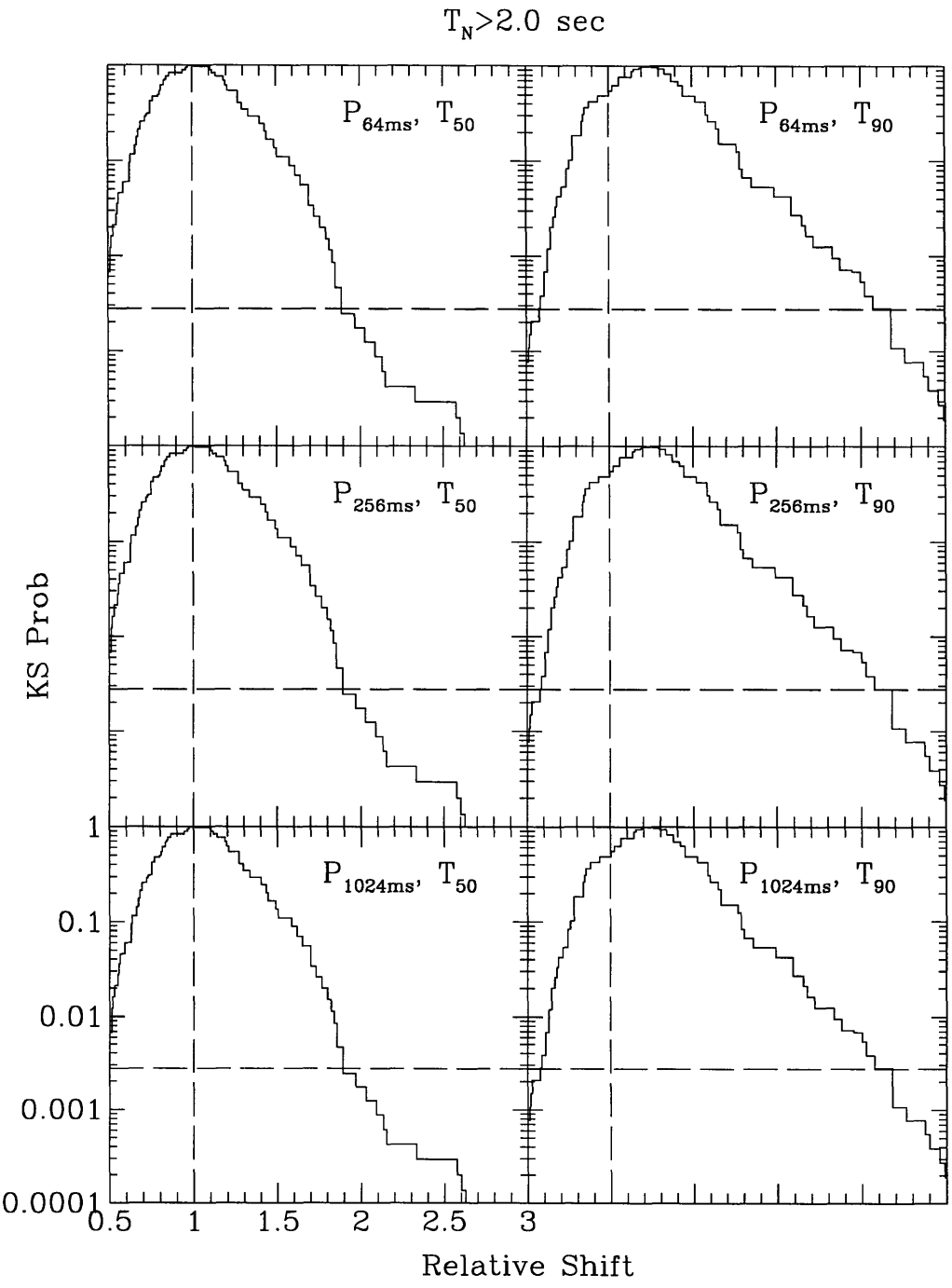

Figure 8-8: **Relative-Shift KS Distributions, "T_N> 1.5 sec" sample** The horizontal line marks the boundary where the KS probability of the amount of "Relative-Shift" between the two distributions is 0.0027%. The vertical line marks the point of no "Relative-Shift" (where the durations of one sample were multiplied by 1).

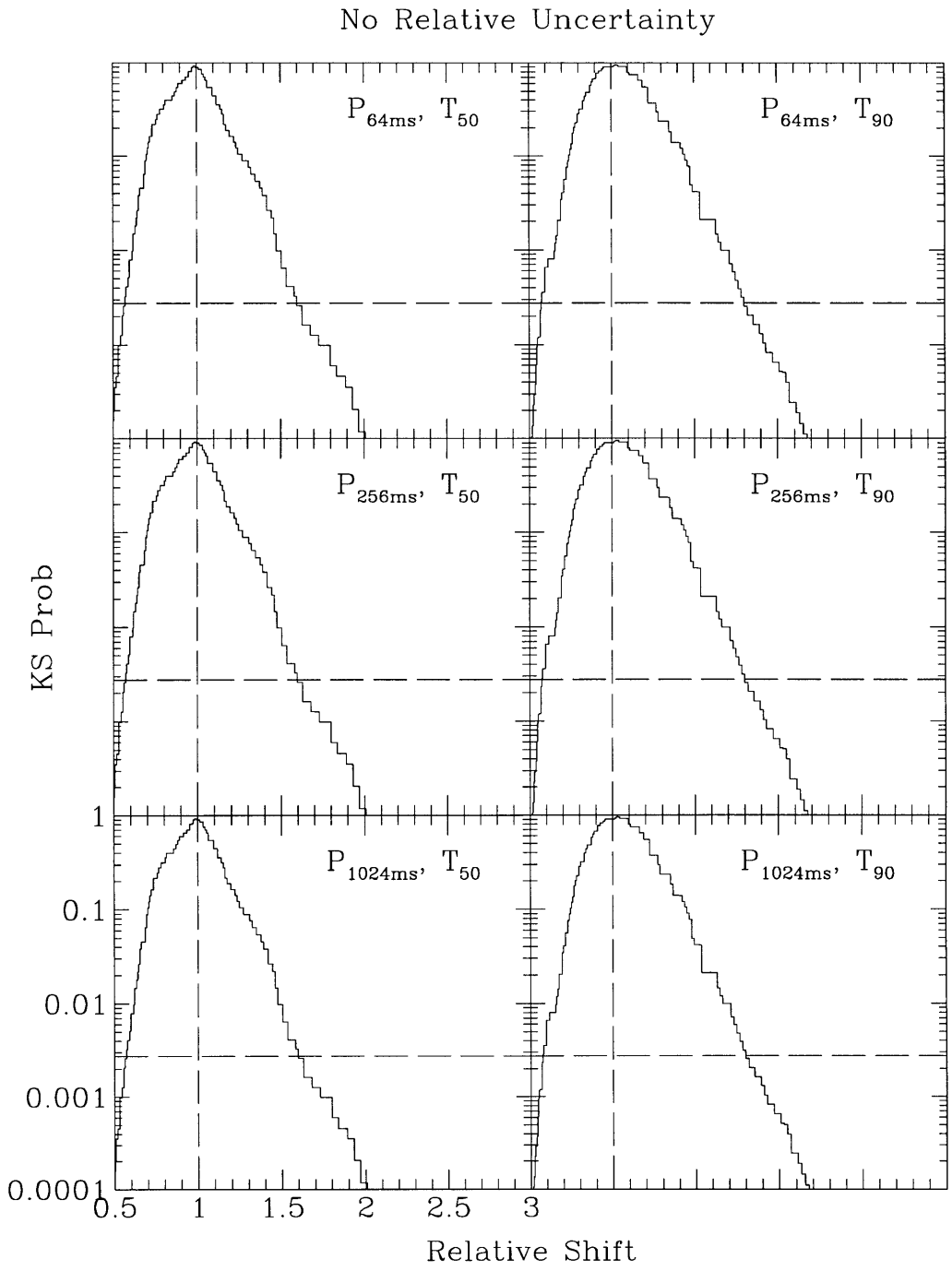

Figure 8-9: **Relative-Shift KS Distributions, "No Relative Uncertainty"** The KS distributions of data selected for the "No Relative Uncertainty" sample. The horizontal line marks the boundary where the KS probability of the amount of "Relative-Shift" between the two distributions is 0.0027%. The vertical line marks the point of no "Relative-Shift" (where the durations of one sample were multiplied by 1).

We also examined the amount of Relative Shift permitted by the duration distributions of "Bright" and "Dim+Dimmest" produced by Norris et al. (1995). We used the data samples "Norris 3B", which is comprised of all bursts with durations >1.5 sec, and "Norris 3B + Precision" which has the additional constraint that the dispersion in the 11 measured durations for any particular burst be <20% of the median duration.

The results are shown in Fig. 8-10. The "Norris 3B" distributions constrain the amount of Relative Shift between the "Bright" and "Dim+Dimmest" samples to 1.1–2.7 (T_{50}) and 1.1–2.7 (T_{90}; 99.73% confidence). The "Norris 3B + Precision" data sample constrains the amount of relative shift to 1.0–2.5 (T_{50}) and 0.9–1.6 (T_{90}; 99.73% confidence).

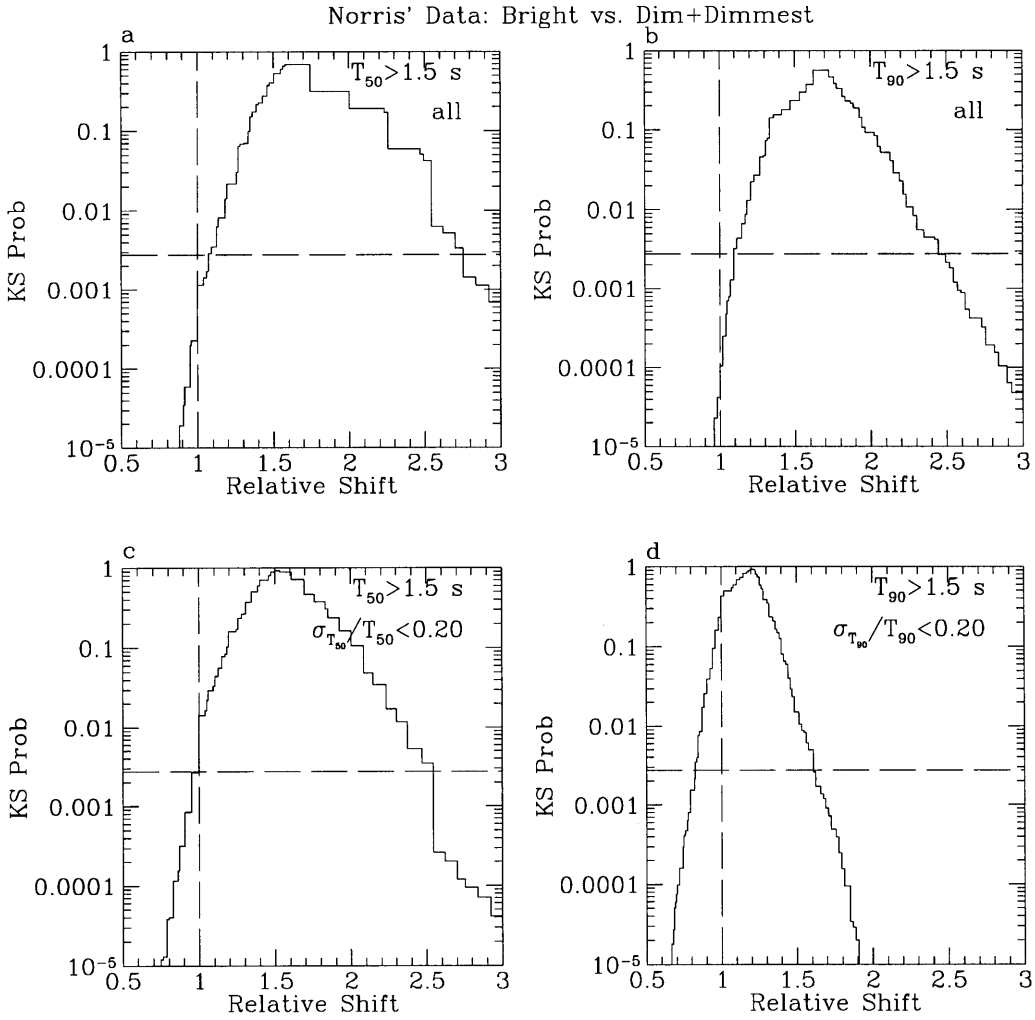

Figure 8-10: **Relative-Shift KS Distributions, "Norris 3B"** The KS distributions of data selected for the "Norris 3B" sample. The horizontal line marks the boundary where the KS probability of the amount of "Relative-Shift" between the two distributions is 0.0027%. The vertical line marks the point of no "Relative-Shift" (where the durations of one sample were multiplied by 1).

8.3.8 Discussion and Conclusions

Non-parametric analyses of the correlation between the durations and peak fluxes of bursts in the 3B catalog have been presented. There is no demonstrated correlation between either the duration measure T_{50} or T_{90} with any of the peak flux measures (P_{64}, P_{256}, P_{1024}) in any of the data samples drawn from the BATSE 3B catalog.

Koshut et al. (1995) found that the application of the methods which produce the values of T_{50} and T_{90} in the 3B catalog has some systematic dependencies on burst intensity. The systematic effect can decrease the measured duration of fast-rise-exponential-decay (FRED) burst profiles by $\sim 25\%$ relative to the bright bursts; this may be a significant effect in diminishing an increase in burst duration in fainter bursts relative to brighter bursts, such as the factor of ~ 2 difference reported in mean duration in other work (Norris et al. 1994; Davis et al. 1994; Norris et al. 1995). The FRED bursts, with their exponential decline, represent a case where this effect should be the extremely pronounced. Bursts which are highly variable will be substantially less affected.

There also may be a propensity for "wings" or other out-laying intensity structure, such as precursors, to be detected in bursts which have greater fluxes, which has the effect of producing systematically longer durations in bright bursts than in faint bursts, or in producing large dispersions in different noise realizations of such bright bursts.

Using the durations found by Norris et al. (1995) from BATSE raw data, we find a significant correlation between burst durations (both T_{50} and T_{90}) and peak count-rates (on a 256ms timescale). However, when we exclude bursts from the sample in which the 11 duration measures had a dispersion of >20% of the median value (decreasing the sample size 15%, from ~500 to ~420) the significant correlation disappears.

In the work by Norris, the duration measures used were not taken directly from the available BATSE catalogs, but were re-measured using wavelet transform and filtering techniques to isolate the burst envelopes from variations in background, and to separate the individual peaks from the burst profile. Additionally, the separation

of bursts by intensity is done by burst peak counts, whereas the present work uses peak flux (which is peak counts, corrected for aspect and energy response).

Wijers & Paczyński (1994) selected GRBs T_{50}>3.0 s and, using the values of T_{50} and P_{64}, found that the difference between the mean duration of these the top 10% and the faintest 10-20% (that is, the 10% of bursts which ranked in the 10-20% range) was $\log(T_{50}) = 0.34 \pm 0.11$. The two distributions compared each had 19 bursts in them. We attempted to reproduce this result, to compare it with results in the 2B catalog, but found we were unable. Using only bursts with $T_{50}>$ 3.0 sec, and measured P_{64}, we found a total of 252 bursts in the 2B catalog. We produced distributions of the brightest 10% and the second faintest 10% (10%-20%). We found the difference between the means of the $\log(T_{50})$ distributions to be 0.0 ± 0.13. In the 3B catalog, the same analysis produces a difference of 0.02 ± 0.13.

Examining the results of the KS distributions, the present results supersede those previously reported (Rutledge et al. 1996b), which were produced with a KS test which contained a programming error, the result of which was substantially more stringent 3σupper-limits had been produced. The present results derived from the 3B Catalog data show that the brightest 10% and faintest 40% of the BATSE bursts (using any of the three catalog peak-flux measures) have duration distributions which are consistent with one another, and which weakly constrain the amount of "Relative Shift" between the two distributions to $\lesssim$1.6–2.8 (depending on the combination of peak-flux measure and duration measure used).

In comparing the "Bright" and "Dim+Dimmest" duration distributions from Norris' data using the KS test, we limit the amount of "Relative Shift" to be between 1.0–2.5 (T_{90}) and 0.9–1.6 (T_{50}; 99.73% confidence range).

We find no evidence for correlation between any of the three peak flux measures (P_{64}, P_{256}, P_{1024}) with either of the two duration measures (T_{50}, T_{90}) in the 3B catalog. While the duration measures found by Norris et al. (Norris et al. 1995) do produce a correlation with the peak-count-rate (256ms time-scale), this correlation disappears when bursts with fractionally large systematic uncertainties in the measured durations (>20%) are excluded from the samples (~15% of the total sample),

which does not support the conclusion that the correlation in this sample is intrinsic in the observations. The amount of "relative shifting" between the brightest 10% of GRBs and the faintest 40% is only weakly constrained to $\lesssim$1.6–2.8 (3σ limit), consistent with, but with much larger uncertainty, results found by previous analyses (Norris et al. 1994; Davis et al. 1994; Norris et al. 1995; Wijers & Paczynski 1994).

The present analysis is not sensitive to non-monotonic variations in the duration distribution as a function of peak flux.

8.4 The Luminosity vs. Red Shift Relation

8.4.1 Summary

We describe a means to investigate the constraints on gamma-ray burst (GRB) flux – red shift relationship in the cosmological scenario. Using the burst duration as a standard duration, and the burst peak flux as a standard candle, the absolute values of the red shifts of any two bursts can be determined. Using multiple pairings of bursts, a statistical distribution of the red shift of any individual burst can be produced, the properties of which are determined solely by the properties of the intrinsic duration distribution and luminosity distribution. We apply the method to bursts in the 3B BATSE catalog, and find the non-physical result of the brightest bursts having medians near (1+z)=1.0, and 1+z *decreasing* with decreasing burst flux. This non-physical result is due to the broad log-normal distribution of the observed duration distribution, which substantially affects the statistics of the $(1 + z)$ distribution.

8.4.2 Introduction

A leading paradigm for the spatial distribution of GRBs places the progenitors at significant red shifts. As the progenitor population has not been identified, there exists no *a priori* information on the expected intrinsic characteristics (*i.e.* intrinsic duration distribution, luminosity function, time-dependent spectrum). It cannot even be ruled out that GRBs have more than one parent population.

Most previous work has sought to find the *relative* amount of the duration differences between bursts of different peak intensities, to measure the time-dilation expected from a cosmological origin. Duration measures, such as T_{50} and T_{90}, are used in spite of large observed dispersion, because there exist few time-scale measurements available to all GRBs which might otherwise be used. One such measurement is the peak in the νF_ν photon energy spectrum (Mallozzi et al. 1995).

There does exist a method to find the *absolute* red shifts of GRBs. This has been applied recently to burst ensembles, to check for consistency between reported

relative amounts of time-dilation in GRBs and the observed different peak fluxes (Horack et al. 1996).

Here we describe how to use this method applied to individual bursts, to find a most likely *absolute* red shift for that particular burst.

8.4.3 METHOD

If one has two GRBs which are known *a priori* to have identical co-moving durations and peak luminosities, one may use the values of these properties to find their *absolute* red shift of origin.

To simplify this analysis we make the following assumptions: 1) GRBs durations are not a function of the co-moving energy, which is not necessarily the case (Fenimore et al. 1995); 2) the GRB duration distribution does not evolve with red shift; 3) the GRB luminosity function does not evolve with red shift; 4) Ω_0= 1; 5) the GRB spectrum can be represented as a power-law.

To simplify discussion, consider (first) two GRBs of identical duration, of identical peak flux, at two different red shifts. The ratio of their observed durations will be:

$$r = \frac{t_1}{t_2} = \frac{(1+z_1)}{(1+z_2)} \frac{(1+z_1)^\tau}{(1+z_2)^\tau} \tag{8.7}$$

where we've included an extra power of $(1+z)^\tau$ to account for differences in burst duration due to co-moving energy. If $\tau = -1$ then r=1 and no cosmological time-dilation effect would be observed. We will assume throughout a value $\tau = 0$.

The ratio of the burst peak fluxes will be:

$$\chi = \frac{P_2}{P_1} = \left(\frac{1+z_1}{1+z_2}\right)^\alpha \left(\frac{1-\frac{1}{\sqrt{1+z_1}}}{1-\frac{1}{\sqrt{1+z_2}}}\right)^2 \tag{8.8}$$

where we have assumed a simple power-law photon spectrum with slope α (cf Ch. 9). Inverting these two equations for the red shifts gives:

$$1+z_1 = \left(\frac{\frac{\sqrt{\chi}}{r^{(\alpha-1)/2}} - 1}{\frac{\sqrt{\chi}}{r^{\alpha/2}} - 1}\right)^2 \tag{8.9}$$

$$1 + z_2 = \left(\frac{\frac{\sqrt{\chi}}{r^{\alpha/2}} - \frac{1}{\sqrt{r}}}{\frac{\sqrt{\chi}}{r^{\alpha/2}} - 1} \right)^2 \tag{8.10}$$

These two equations are exactly solvable, given the ratio of durations r and peak fluxes χ.

Now, we take a sample of N bursts, and number them i=1, N. For each burst in turn, beginning at j=1, we calculate $(1 + z_{j,i})$, using bursts with odd values of $j - i$ for $i < j$ and for even values of $i - j$ for $i > j$. This way, we compare each burst with the maximum range of peak flux values, and each resulting calculation of $(1 + z_{j,i})$ is statistically independent of all other values of $(1 + z_{j,i})$ produced; specifically, the value of $(1 + z_{j,i})$ is used for the distribution of burst j, but the value of $(1 + z_{i,j})$ is not used for burst i.

If all GRBs follow the above assumptions, we can expect a mode at the most-likely value of $(1 + z)$; the statistics of the distribution of $(1 + z)$ will be dependent on the GRB luminosity function, duration distribution function, and the accuracy of the measurements of both.

Although we find no evidence for time-dilation (see Sec. 8.3), we demonstrate this test on BATSE 3B Catalog data in the following section.

8.4.4 Data Selection

We use data from the BATSE 3B catalog (Meegan et al. 1996). We use bursts with values of T_{90} and P_{1024} listed with relative accuracy of better than 20%, with all values of T_{90}>1.5 seconds and values of P_{1024}>0.5 phot $cm^{-2}sec^{-1}$. This gives us a sample of 424 bursts.

Applying Spearman rank-order correlation between the duration and peak fluxes gives the probability of producing the observed correlation in this sample as 55% from a randomly generated sample.

8.4.5 RESULTS

We produced $(1+z)$ values for the 424 bursts in the present data-set. We separated the 424 bursts into 6 groups, based on their peak flux values (on 1024ms time scales). Five of these groups had 80 bursts, the sixth (also, the highest flux group) contained 24 bursts. The $(1+z)$ values for all bursts in each of the six peak-flux divisions were concatenated into six $(1+z)$ distributions; these are shown in the Fig. 8-11. (panel *a* corresponds to the lowest peak fluxes, panel *f* to the highest peak fluxes). The broken line in each panel is drawn at the median value of the distribution.

Inter-comparing the distributions of different peak flux ranges, there is clear difference in the qualitative shapes of the distributions, and in the median of the distributions, which increases with increasing peak-flux range from a non-physical value of $\sim$0.3 to 0.9.

To aid in interpreting these results, we compared the observed distributions with three simulated distributions.

1. First, we used a boot-strap method to produce simulated distributions. For each observed burst (with values of peak flux and duration), we drew, with replacement, from the observed peak-flux distribution and duration distribution, to produce 10,000 $(1+z)$ values. Thus, the resulting distribution was produced with the assumption that there exists no correlation between the duration and peak fluxes of bursts. These 10,000 values for each of the $\sim$80 bursts in each distribution, were used to produce a simulated distribution, which is included in the Fig. 8-11 with the results; the simulated distributions are not visually discernible from the observed distributions – one must inspect the figure closely to see that there are two distributions in each panel. The changes in the $(1+z)$ distriutions therefore appear to be due only to the different peak-flux values of each group.

2. We simulated a data-set of bursts which has the observed peak-flux distribution (that is, using the 424 observed peak fluxes in the sample of interest) and a log-normal duration distribution, with a centroid value of $\log(T_c)$=1.17 and a log-width of 0.01 (considerably narrower than the observed value of $\sim$0.4; cf. Sec. 8.3), assuming a non-evolving standard-candle-luminosity cosmological scenario with the

faintest burst in the present data-set coming from $(1+z)$= 2.0, and a power-law photon spectral slope of 2.0 (cf. Ch. 9). This simulated data-set was analyzed in the same manner as the observed data-set (described above), and produced highly peaked (half-width of ~20%) medians at $(1+z)$ values >1, which decrease with increasing peak flux range, as expected, from $(1+z)$~2.0 to ~1.2. Visual inspection easily discerns the simulated distribution from the observed distributions (compare Fig. 8-11 with Fig. 8-12).

3. We simulated a data-set of bursts which have the observed peak flux distribution in a non-evolving standard-candle cosmological scenario (assuming the faintest burst in the present data-set coming from $(1+z)$=2.0, and power-law photon spectral slope of 2.0), but with a co-moving log-normal duration distribution of width $\sigma = 0.5$ and mean $\log(T_{90})$=1.17. For each peak-flux value, a random co-moving duration was generated and increased by a factor of $(1+z)$ to produce the expected observed duration. The simulated data-set was analyzed as the observed data-set (described above), producing six $(1+z)$ distributions. The simulated $(1+z)$ distributions were qualitatively similar to the observed distributions (see Fig. 8-13).

8.4.6 Discussion and Conclusions

There is a strong difference between $(1+z)$ distributions of the simulated data-sets, depending on whether a delta-function duration distribution or a log-normal duration distribution is assumed. In the former, the $(1+z)$ distributions are highly peaked with median values >1, which decrease with increasing peak-flux to $(1+z)$~1.0 for the brightest bursts; the median values in these cases are accurate estimates of the most-likely red-shifts of bursts which make up the distribution. In the latter, the $(1+z)$ distributions show the complex behavior seen in the observed data, with median values of $(1+z)$ <1, which increase with increasing peak-flux to $(1+z)$~1.0 for the brightest bursts; the median $(1+z)$ values are un-physical, and are poor estimators of the most-likely redshifts of the bursts which make up the distribution.

The qualitative behavior of the observed $(1+z)$ distributions as a function of peak-flux range is *not* due to a correlation between peak-flux and duration, as

the behavior is also found in data-sets simulated with identical duration and peak-flux distributions, where there is no (i.e. random) correlation between peak-flux and duration.

We have shown a method which can, in principle, produce the peak-flux – absolute red shift relationship of GRBs in a cosmological scenario. We have found that the $(1+z)$ distributions of bursts found with this method are qualitatively similar to simulated data-sets where there is no intrinsic relationship between burst duration (drawn from a log-normal distribution) and peak-flux, as well as to simulated data-sets where there is the expected correlation between peak-flux and duration, when the duration distribution is broad.

We find that the medians for most of the bursts' $(1 + z)$ distributions in the present sample occur at the non-physical values of $(1+z) < 1$; the value of the median increases with decreasing peak flux, until for the brightest bursts $(1 + z) \sim 1$ – having the opposite sense from what is expected from the simple model above. Based on comparison with our simulated data-sets, this is due to the broad dispersion in the observed log-normal duration distribution. We conclude that this technique is not capable of extracting most-likely $(1 + z)$ values for individual GRBs in its present form; perhaps with further refinement, involving more quantitative statistical comparisons with boot-strapped distributions, most-likely $(1 + z)$ values be can extracted for ensembles and individual bursts.

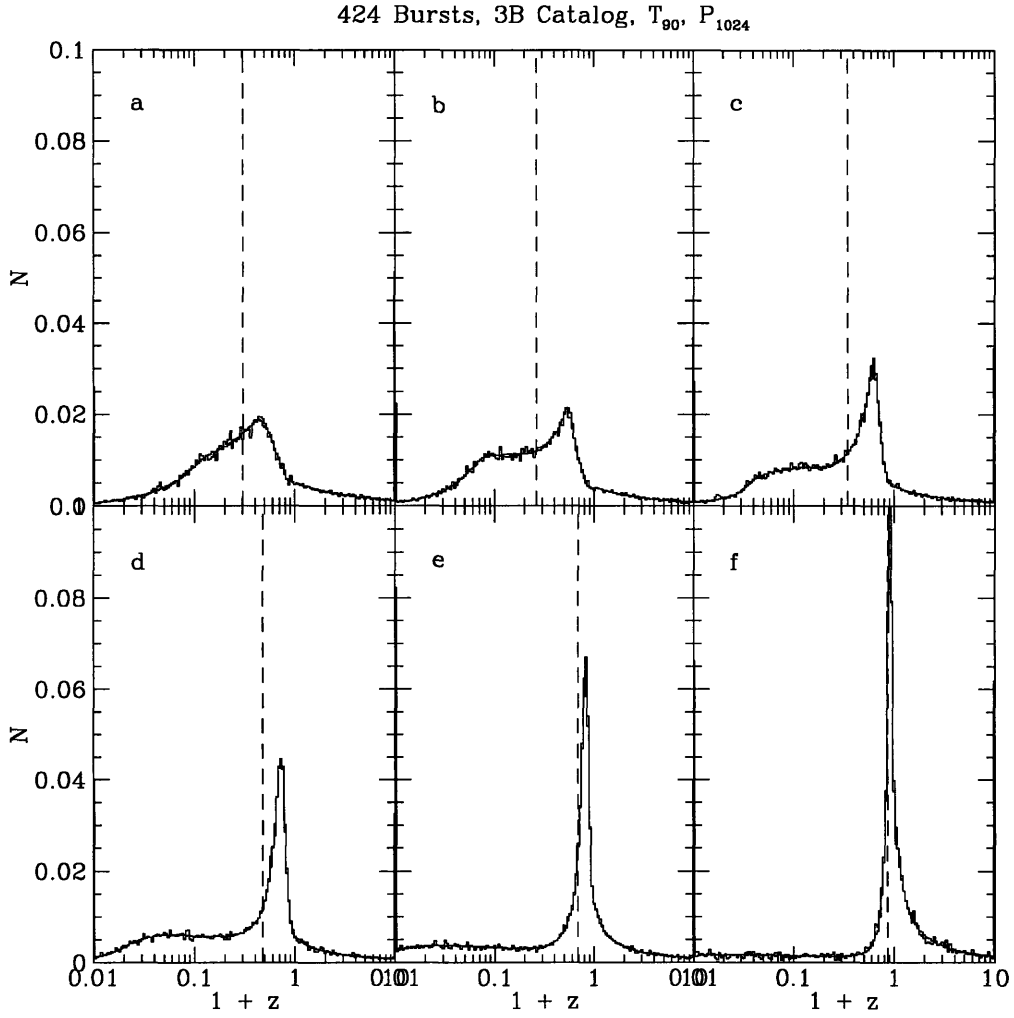

Figure 8-11: $(1 + z)$ **Distributions** The $(1 + z)$ distributions of 6 groups of $\sim$ 80 bursts, sorted by peak-flux, in order of increasing peak-flux range; the distribution in panel *a* represents GRBs from the lowest 80 peak-flux values, and panel *f* represents the highest 24 peak-flux values. The vertical broken line is at the median value of the observed distribution in each panel. Also, the distribution of $(1 + z)$produced from a boot-strapped simulation of GRBs with no correlation between duration and peak-flux is shown. The simulated and real data-sets are qualitatively similar, as to be indiscernible.

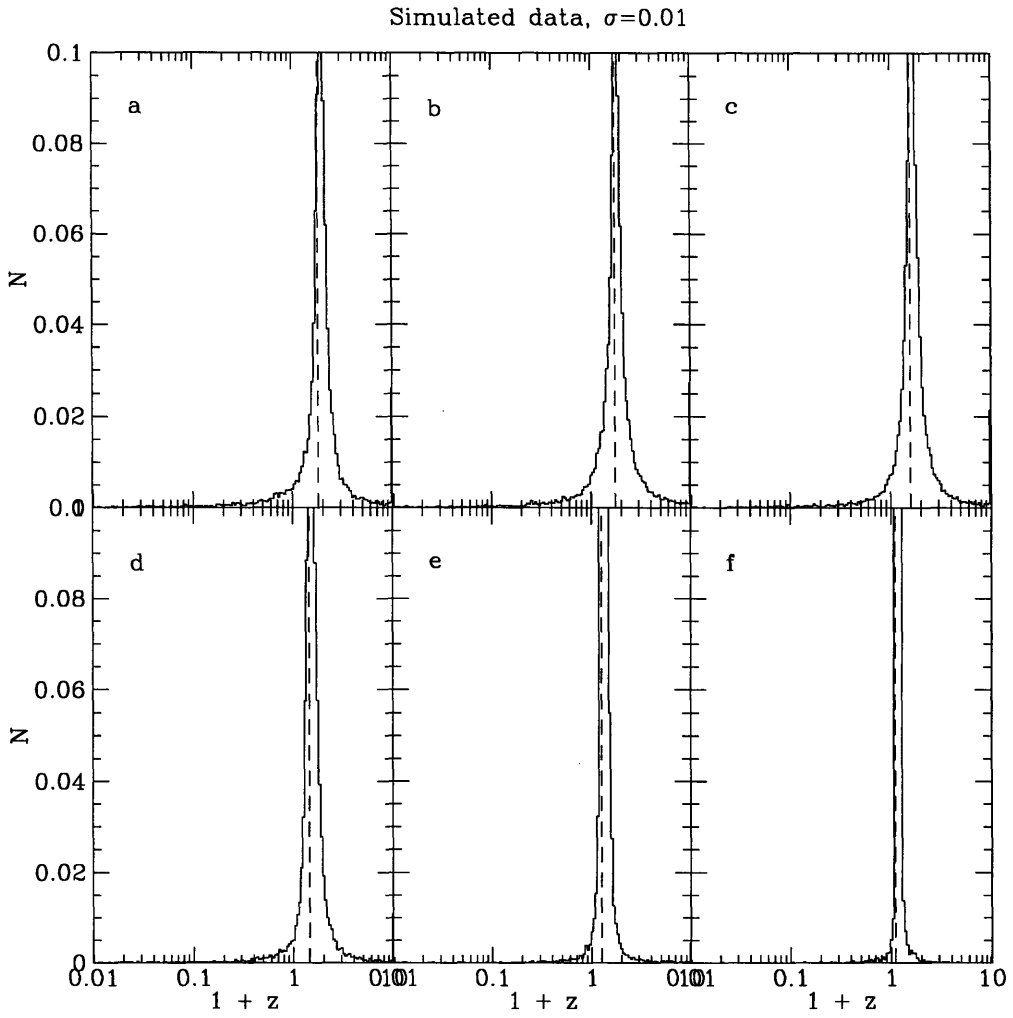

Figure 8-12: **Simulated $(1+z)$ distribution, σ=0.01** This is the resulting $(1+z)$ distribution, for six peak-flux ranges (increasing from panel *a* through *f*), using the observed peak flux distribution, and a simulated duration distribution, with log-width of 0.01 (compare with ~0.4 observed). Thus the duration distribution at any peak flux value is only 2% wide, while the mean duration decreases by ~40% between the brightest and faintest bursts. The median $(1+z)$ values follow the expected $(1+z)$ values for bursts in each peak-flux range.

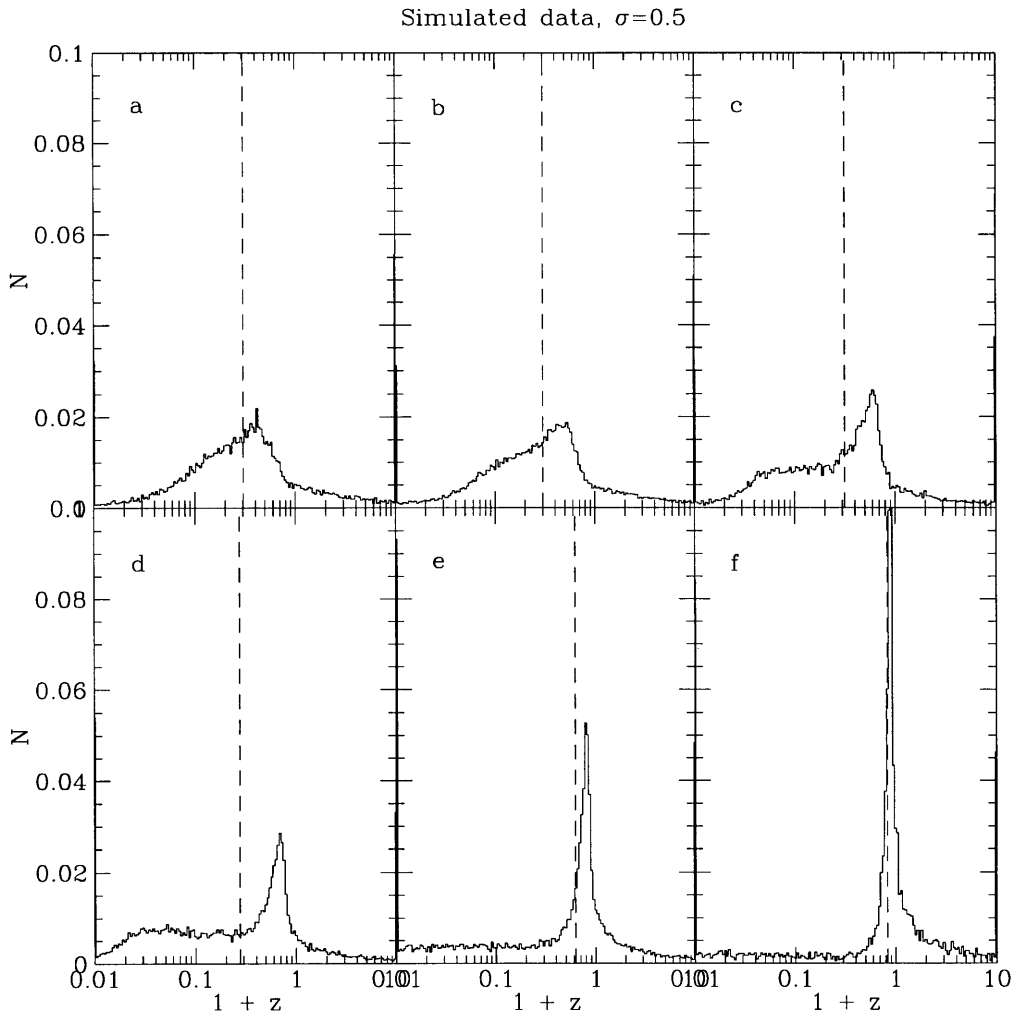

Figure 8-13: **Simulated** $(1+z)$ **distribution,** σ**=0.5** This is the resulting $(1+z)$ distribution, for six peak-flux ranges (increasing from panel *a* through *f*), using the observed peak flux distribution, and a simulated duration distribution, with log-width of 0.5 (compare with ~0.4 observed). Thus the duration distribution at any peak flux value is about 1000% wide, while the mean duration decreases by ~40% between the brightest and faintest bursts. The $(1+z)$ distributions are qualitatively similar to both the observed distribution and the distributions in which there is no correlation between burst duration and peak flux (see Fig. 8-11)

8.5 Constraints on the Gamma-ray Burst Luminosity-Duration Relationship in the Galactic Scenario

8.5.1 Summary

We present a method to investigate constraints on the luminosity-duration relationship in the context of galactic models. The observed duration distribution cannot be explained by a one-to-one correspondence between luminosity and duration; a distribution of durations as a function of luminosity is required.

This work has appeared previously (Rutledge et al. 1996a).

8.5.2 Introduction

Several authors have reported a correlation between cosmic GRB duration and peak-fluxes (Norris et al. 1994; Norris et al. 1995; Davis et al. 1994; Wijers & Paczynski 1994). These have often been interpreted as being due to cosmological red shift effects; however, blast-wave models or relativistic beaming predict a luminosity-correlated duration which may also be responsible for all or part of this effect (Brainerd 1994). As such, it is useful to develop a formalism to investigate the possible contributions of luminosity-duration correlations to the observed effects.

First, we describe a simple way to understand how peak-flux (F_p) correlated durations can result from duration correlated luminosities in a Euclidean scenario. We assume a frequency density distribution n(r) (see Fig. 8-14a), which can be considered constant out to some radius r_b, and a single population of GRB sources, comprised of a fraction (f) with intrinsic luminosity L_1 and duration t_1 and the remaining fraction (1-f) with intrinsic luminosity L_2 and duration t_2. We take $L_1 < L_2$.

The parameters of the observed duration distribution must remain constant as a function of F_p for $F_p > F_b$, as the proportion of sources of different luminosities (and therefore, different durations) remains the same. Only at $F_p < F_b$ will the duration

distribution change, as fewer high luminosity bursts are observed relative to low-luminosity bursts ("missing bursts", Fig. 8-14b). The value of F_b can be identified by analysis of the peak-flux distribution. At peak-fluxes below F_b, the properties of the duration distribution become dominated by the low-luminosity bursts, as their number grows out of proportion to the high-luminosity bursts. Thus, if low-luminosity bursts are on average *longer* in duration, then the peak-flux distribution of faint bursts will be dominated by low-luminosity, *longer* bursts.

In a like fashion, if burst duration (or any observational property) is correlated to the intrinsic luminosity, one should observe evidence for deviation from homogeneity in the integrated number vs. peak flux distribution at different F_p values; the sub-sample with higher intrinsic luminosity will show evidence for deviation from homogeneity at a higher F_p value. Thus, if low-luminosity bursts have longer durations, the peak-flux distribution of long-duration bursts will deviate from homogeneity at a lower peak-flux value than that of short-duration bursts (which are therefore of higher luminosity).

In the next section, we describe a simple model for burst distribution in Euclidean space, with an intrinsic one-to-one correlation between duration and luminosity.

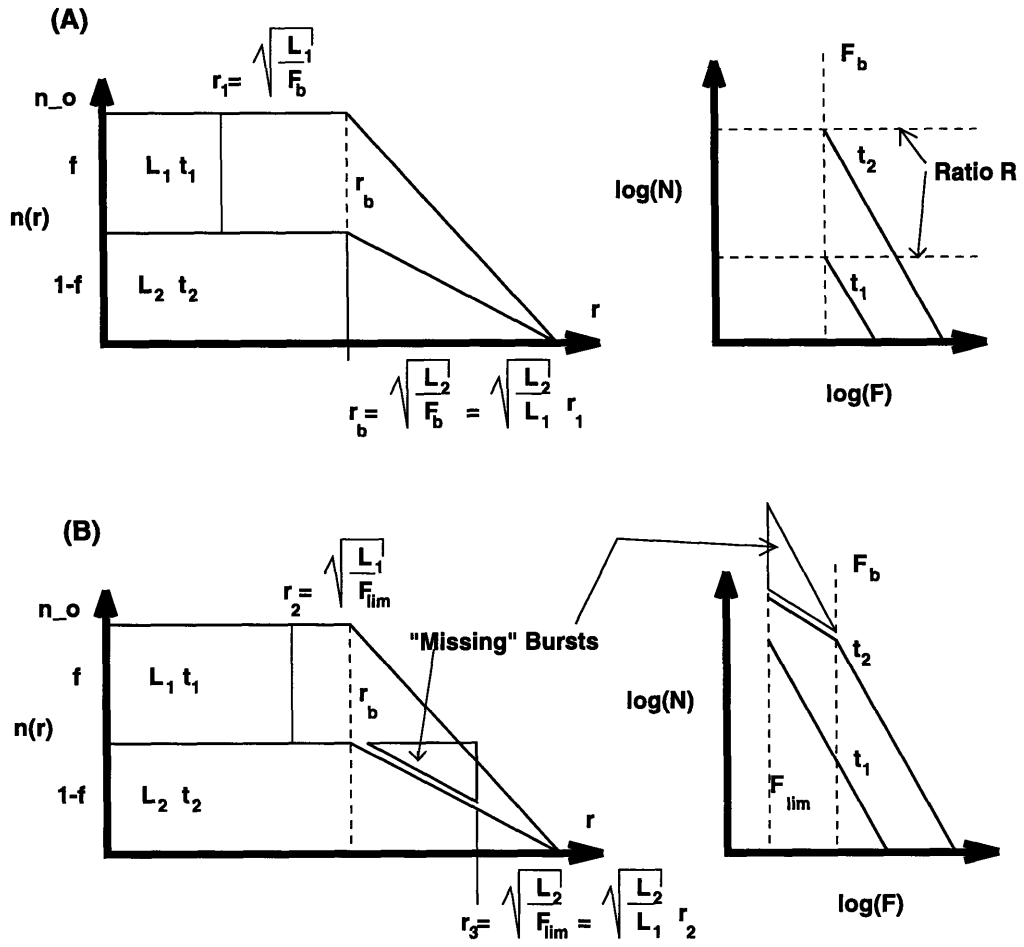

Figure 8-14: **Producing Luminosity Correlated GRB Durations – Schematic** When sampling a homogenous distribution (panel *a*), the mean value of properties correlated with luminosity remain constant as a function of peak-flux, as the relative proportion of bursts with each luminosity remains constant. When the peak-flux is low enough to sample the non-homogenous distribution (panel *b*), the high-luminosity bursts go "missing" – the relative proportion of high-luminosity bursts decreases, and the mean value of properties correlated with luminosity become dominated by low-luminosity bursts. This can *only* occur when non-homogeneity has been observed in the population – that is, when the peak-flux distribution deviates from the -3/2 power-law expeected from a homogenous population in a Euclidean geometry.

8.5.3 Model and Analysis

We assume a power-law intrinsic luminosity distribution:

$$\phi(L) = AL^{-\beta} \quad 1 < L < \chi \tag{8.11}$$

where A, β, and χ are constants. A is a normalization constant; β is the assumed power law slope of the luminosity function; and χ is the observed full width of the power-law luminosity function.

We assume a power-law relationship between the burst time-scale ($t_{\rm dur}$) and the burst intrinsic luminosity:

$$t_{\rm dur}(L) = t_0 L^{-\lambda} \tag{8.12}$$

where t_0 and λ are constant. We assume a GRB frequency density distribution:

$$n(r) \propto \frac{1}{1+r^{\alpha}} \quad , r < r_{\rm tidal} \tag{8.13}$$

$$= \quad 0 \quad , r > r_{\rm tidal} \tag{8.14}$$

where $r_{\rm tidal}$ is the radius at which objects which are gravitationally bound to the Galaxy are tidally stripped by M31.

We define $r_{\rm max}$:

$$r_{\rm max} = \sqrt{\frac{\chi}{F_{\rm lim}}} \tag{8.15}$$

where χ is the observed full width of the luminosity function and $F_{\rm lim}$ is the minimum observable flux. Thus, a burst of luminosity χ at a distance $r_{\rm max}$ will produce a measured peak flux $F_p = F_{\rm lim}$.

To apply this model in analyses, we assume a frequency density distribution function (α), an intrinsic luminosity function power-law (β) and a width to the luminosity function (χ). The observational parameter we test against is the integrated number distribution as a function of duration, $N(T > T')$:

$$N(T > T') = \int_1^{\chi} \int_0^{\left(\frac{L}{\chi}\right)^{1/2} r_{\rm max}} \frac{r^2}{1+r^{\alpha}} \, {\rm d}r \; \phi(L) \; {\rm d}L \tag{8.16}$$

where the overall constant has been dropped. If we rewrite this using Eq. 8.12:

$$N(T > T') = \int_{\frac{T'}{T_{\min}}\chi^{-\lambda}}^{1} \int_0^{\left(\frac{T^{-1/\lambda}}{\chi}\right)^{1/2} r_{\max}} \frac{r^2}{1+r^\alpha}\, \mathrm{d}r\; T^{1-\frac{1}{\lambda}(1+\beta)} \mathrm{d}T \qquad (8.17)$$

where, again. we drop the overall constant of normalization. Due to the one-to-one nature of the assumed duration-luminosity relationship (Eq. 8.12), there is a unique relationship between the duration – luminosity parameter (λ), the observed minimum and maximum burst durations, and the assumed luminosity function width (χ):

$$\lambda = \frac{\ln(t_{\mathrm{dur,max}}/t_{\mathrm{dur,min}})}{\ln(\chi)} \qquad (8.18)$$

Then, we assume values for $r_{\max}$, r_{tidal}, χ, β, α, measure the value of λ from the data sample, produce the theoretical integrated duration distribution (Eq. 8.17) and compare it using a KS test to the observed distribution.

We have done this for the following range of values (cf. Hakkila et al. 1994; Hakkila et al. 1995): ($\alpha = 2.0$; $2 \leq r_{\mathrm{tidal}} \leq 20, \delta r_{\mathrm{tidal}} = 20\%$; $3 \leq r_{\max} \leq 100, \delta r_{\max} = 20\%$; $2 \leq \chi \leq 100, \delta\chi = 25\%$; $-3 \leq \beta \leq 3, \delta\beta = 0.25$), where the values indicated by "δ" indicate the increment between parameter values which were tested. For all combinations of these parameters, no acceptable distributions (KS probability > 0.001) were found when compared to our 3B Catalog data-set of (T_{50}, P_{1024}) values (see Sec. 8.2.1). This is as expected, as our non-parametric tests searching for correlation between peak-flux and duration found no evidence of correlation.

8.6 Comment on the Spectral Hardness/Spatial Distribution Correlation

Kouveliotou (Kouveliotou 1996) shows preliminary evidence that, when the GRB populations are divided into three spectral hardness groups (hard, mid, and soft), the hard and soft bursts have different peak-flux distributions – specifically, that the number-peak-flux distribution of spectrally hard bursts departs from a -3/2 power-

law at a higher peak flux than the spectrally soft GRBs. Here, we comment on the possible significance of this observational result.

For reasons we discuss above (in the context of burst durations, but the discussion holds if we substitute burst spectral hardness), the fact that the integrated-number vs. peak-flux distribution of the hard bursts "rolls over" at a higher peak-flux than the soft-bursts can be interpreted, if we assume all GRBs come from a single population, as meaning that hard bursts have higher intrinsic luminosity than the soft bursts. Using a power-law luminosity function (Eq. 8.11) and estimating the luminosities of the hard bursts and soft bursts as at single luminosities ($L_{\rm hard}$, $L_{\rm soft}$), then if soft bursts make up a fraction f of the total population and hard bursts make up the remaining $1-f$ (Fig. 8-14), we find the ratio:

$$\frac{f}{1-f} = \left(\frac{L_{\rm hard}}{L_{\rm soft}}\right)^{\beta} \tag{8.19}$$

From Fig. 8-14, we define R as the ratio of hard bursts observed with $F > F_b$ to soft bursts observed with $F > F_b$, which can be measured directly to observational accuracy, and is equivalent to:

$$\mathrm{R} = \frac{(1-f)\; n_0 \; \frac{L_{\rm hard}}{L_{\rm soft}}^{3/2} r_1^3}{f\; n_0\; r_1^3} \tag{8.20}$$

Combining Eqns. 8.19 & 8.20 produces an equation for the power-law luminosity slope:

$$\beta = \frac{3}{2} - \frac{\ln(\mathrm{R})}{\frac{\mathrm{L_{hard}}}{\mathrm{L_{soft}}}} \tag{8.21}$$

If the value at which the peak flux distribution of hard bursts deviates from homogeneity is observable, while that of the soft bursts is not, then the a lower limit may be placed on the ratio of luminosities (i.e., the width of the luminosity function):

$$\frac{L_{\rm hard}}{L_{\rm soft}} \geq \frac{F_{\rm b,hard}}{F_{\rm lim}} \tag{8.22}$$

Thus, with an observed value of R, and a lower limit on $L_{\rm hard}/L_{\rm soft}$, the value of

the slope of the luminosity function β (Eq. 8.21) can be determined to observational certainty – with both upper and lower limits.

Also, one can find a lower limit on the ratio of the frequency density of hard bursts to that of soft bursts:

$$\frac{f}{1-f} = R\left(\frac{L_{\rm hard}}{L_{\rm soft}}\right)^{\frac{3}{2}} \tag{8.23}$$

while an upper limit on the width of the luminosity function (which has been found using other methods – *e.g.*Hakkila et al. 1995) permits an upper-limit to be placed on this value.

Importantly, definitive demonstration of different peak flux distributions of bursts separated by spectral hardness can be interpreted as evidence for the correlation between spectral hardness and burst luminosity, and thus for a finite width luminosity function.

8.7 Summary and Conclusions

We have applied a number of tests to examine burst duration distributions as a function of peak flux. We described a means for extracting information about the observed GRB luminosity function.

8.7.1 Fitting the Log-Normal Duration Distribution To Burst Duration Data

We examined the best-fit log-normal duration distributions to the "Bright" and "Dim+Dimmest" GRBs from the Norris et al. (1994; 1995) data. If we interpret any differences in the "Bright" and "Dim+Dimmest" GRB duration distributions as being due only to cosmological time-dilation, then we expect time-dilation to affect the distribution centroids and widths equally. When we jointly search for this common factor, we find that the multiplicative factor difference between the "Bright" and "Dim+Dimmest" GRB duration distributions is limited to between 0.98–1.60

(for T_{90}) and 0.93–1.78 (for T_{50}; 99.73% confidence limits) – consistent with no time-dilation in these distributions.

If, on the other hand, we examine the distribution widths separately from the distribution centroids, we find the time-dilation factor for the centroids to be 1.8–2.5 (T_{90}) or 1.7–3.7 (T_{50}; 1σ confidence ranges), while the widths show time-dilation factors of 0.7–0.97 (T_{90}) and 0.53-1.07 (T_{50}; 1σ confidence). These are consistent with the analysis by Norris et al. (1995), however Norris produces more stringent limits (*e.g.* a centroid time-dilation factor of 2.09 $\pm$0.14 and a width time-dilation factor of 1.32 $\pm$0.13) which are distinct from each other at the >4 σ level, and consistent with our results. We conclude that, based on the Norris et al. (Norris et al. 1995) results, the peak-flux correlated differences in the duration distributions cannot be due exclusively to time-dilation – some other process must be working, perhaps those described by (Brainerd 1994). However, we find from our analysis that pure time-dilation cannot be excluded, and the time-dilation factors constrained to the limits listed above.

8.7.2 Non-Parametric Tests

We applied non-parametric tests to search for correlations in the observed peak-flux – duration relation of GRBs, using values from the 3B catalog. The advantage of Spearman and Kendall's rank-correlation tests are that they are very sensitive to monotonic correlations in the data of any form, at the expense of being able to place observational limits on physically interesting parameters. We compared both duration measures in the 3B catalog (T_{50}, T_{90}) to each of all three peak-flux measures (P_{64}, P_{256}, P_{1024}).

No correlations between any of the three peak-flux measures and either of the two duration measures from the 3B Catalog were found. When we inserted a red-shift of the expected magnitude "by hand" into the data-set, correlations are found (probability of random occurrence <0.0005) between all three peak-flux measures (P_{64}, P_{256}, P_{1024}) and T_{50} in data-sets which require durations and peak-flux measures to have $<20\%$ measurement uncertainty; less convincing correlations (prob $\lesssim 0.001$)

are found for most (but not all) of the combinations of peak-flux and T_{90} duration with "hand-inserted" redshifts. We find that by excluding the bursts in the $-3/2$ part of the peak-flux distribution where no correlation between peak-flux and duration is expected, the rank-correlation tests loose their sensitivity to the red-shift inserted "by hand", and no correlation is found between either of the two duration measures and any of the three peak-flux measures.

In the durations and peak-counts data measured by Norris et al. (Norris et al. 1995), we find a significant correlation when all data is included. This correlation disappears when durations with systematic uncertainties in the duration fractionally measure >20% (arbitrarily chosen, leaving 428 of 497 GRB duration–peak counts pairs remaining) are excluded from analyses.

We also compared the duration distributions of the brightest 10% and faintest 40% for the three different flux measures in the 3B Catalog (P_{64}, P_{256}, P_{1024}) using the KS-test. We conclude that the amount of "relative-shift" between the two distributions is limited to $\lesssim$1.8–2.5 (3σ, depending on the combination of flux measure and duration measure).

The KS test was also applied to the duration – peak counts data provided by Norris et al. (Norris et al. 1995). Using the KS test and bursts >1.5 sec, we find that the "Dim+Dimmest" burst distribution is consistent with the "Bright" burst distribution stretched by a relative factor of $\sim$1.1–2.7 (T_{50}) or 1.1–2.5 (T_{90}; 99.73% confidence). If the additional constraint of <20% dispersion (relative to the median value) in the 11 burst measures is applied (excluding 15% of the sample), the 99.73% confidence ranges become 1.0–2.5 (T_{50}) and 0.9–1.6 (T_{90}).

We conclude that we do not see observational evidence for time-dilation or evidence of correlation between peak-flux and duration in either the 3B catalog or Norris' data set.

8.7.3 $(1+z)$ Distributions

We described a method which, in principle, could provide the GRB peak–flux vs. *absolute* $(1+z)$ relationship, by finding the most-probable $(1+z)$ value for each

particular burst. In practice, we find that the very large width of the log-normal distribution of GRBs causes the distribution to produce median $(1 + z)$ values in the un-physical range <1.0; the median $(1 + z)$ values are low for low-peak flux bursts ($(1 + z)$ ~0.3) and increase with increasing peak-flux, towards $(1 + z)$ =1.0. It is perhaps possible that a more refined statistical approach than applied here can somehow extract most likely $(1 + z)$values from the distributions which are physically reasonable.

8.7.4 Luminosity – Duration Correlation in a Galactic Scenario

We described a very simple model to jointly produce the observed GRB peak-flux distribution and the duration distribution, assuming a halo-model for the GRB parent population, and a one-to-one single power-law relationship between the burst luminosity and duration. We applied this model to 3B Catalog data, using a grid of reasonable model parameters values, and found that no combination of parameters could simultaneously re-produce both the peak-flux distribution and duration distribution.

8.7.5 Spectral-Hardness Correlated with GRB Luminosity?

We commented on the recent finding by Kouveliotou (1996), that the peak-flux distribution of spectrally hard GRBs rolls over and significantly lower values of peak flux than spectrally soft GRBs. If confirmed, this may imply that the spectral hardness is positively correlated with burst luminosity. We described a means to extract zero-th order approximations to the observational luminosity power-law slope, and the relative numbers of spectrally "hard" and "soft" bursts in the GRB population.

Chapter 9

Gamma-ray Burst Peak Flux Distributions

9.1 The Cosmological Distribution

9.1.1 Introduction

More than 20 years after their discovery (Klebesadel et al. 1973), gamma ray bursts (GRBs) continue to be elusive about their origin or, possibly, origins.

A number of workers report results which are consistent with the cosmological hypothesis, using data obtained by the Burst and Transient Source Experiment (BATSE) on the *Compton* Gamma Ray Observatory (CGRO) (Fishman & et al. 1989).

A small subset of 'simple' single-peaked GRBs observed by BATSE showed that bursts with the lowest peak fluxes had longer rise times than GRBs with the highest peak fluxes (Kouveliotou et al. 1993; Kouveliotou & et al. 1994).

Dermer (1992) found that a cosmological model with no source evolution and a q_0=1/2 Friedmann cosmology could reproduce the differential $< V/V_{\rm max} >$ distribution from 126 BATSE GRBs. It was also found that the observed $< V/V_{\rm max} >$ could accommodate moderate frequency density (that is, the number of bursts per unit time per unit volume) evolution, with $(1+z)^p$, for $p = -2$, 0, and 2.

Piran (1992) found the BATSE-observed $< V/V_{\rm max} >$ statistic (see, *e.g.*, Schmidt, Higdon, & Heuter 1988) and number distribution $N(V/V_{\rm max})$ are consistent with two flat-space cosmological models, one with a zero cosmological constant and mass density $\Omega_{\rm M}$=1, and a second with $\Omega_{\rm M}$=0.1 and a non-zero cosmological constant (Λ), with the faintest GRBs coming from $z_{\rm max}\sim$1. It was also found that the $< V/V_{\rm max} >$distribution could accommodate some frequency density evolution, with $(1+z)^p$, for $p = -3$ to 3/2.

Mao & Paczyński (1992, hereafter MP), assuming no evolution in the burst rate (a constant frequency density), and an Ω_0=1, $\Lambda = 0$ universe, found that BATSE GRBs with assumed photon number spectral indices in the range 0.5–1.5 (somewhat flatter than actually observed by BATSE) would match the $< V/V_{\rm max} >$ value from the first $\sim$ 150 GRBs observed by BATSE (Meegan et al. 1992) if the faintest GRBs originated from $z_{\rm max}$=1.1-2.6.

Lestrade et al. (1993), following a suggestion by Paczyński (1992), used 20 GRBs observed by the PHEBUS instrument on board GRANAT with durations < 1.5 s. They showed that stronger bursts (in peak counts above background in a 1/4 sec time bin) had a significantly shorter average duration than weaker bursts. Using a Kolmogorov-Smirnov (KS) test, a 97% probability that the stronger GRBs were drawn from a different duration population than the weaker GRBs in this sample was found.

Wickramasinghe et al. (1993) fit the log N – log $F_{\rm peak}$ curve of 118 BATSE GRBs with a model of GRBs of cosmological origin, assuming a constant number of burst sources per co-moving volume – a different assumption than that made by MP – which does not take into account the effect of time-dilation on the burst rate. It was found that GRBs at the completeness flux limit could originate at $z_{\rm max}$=0.4-1.7, depending on the assumed source spectrum (photon number spectral slope in the range of 1.5-2.5; softer spectrum produced higher $z_{\rm max}$ values).

Davis et al. (1995), using an analysis of pulse-width distributions from 135 BATSE GRB lightcurves found that dim GRBs have pulse-widths that are a factor of$\sim$ 2 greater than that of bright bursts, consistent with the dimmest GRBs coming

from a z$\sim$1.

Tamblyn & Melia (1993) found that, assuming a "standard" energy-spectral break at 300 keV, the average value of ratio of the flux detection limit to the peak burst flux to the 3/2 power ($< (F_{min}/F_{max})^{3/2} >$) as a function of the observed full-sky burst rate for several different GRB instruments (*i.e.* PVO, SMM, KONUS, APEX, SIGNE, and BATSE) is consistent with a non-evolving cosmological population.

Fenimore et al. (1993), using a composite intensity distribution of BATSE and Pioneer Venus Orbiter (PVO) experiments, fit a homogeneous model of standard candle sources, with the faintest BATSE bursts coming from $z \sim 0.80$; using model-derived distances to the brightest sources within the error boxes of 8 bright GRBs, they found that host galaxies must be fainter than an absolute magnitude of -18.

Lamb, Graziani & Smith (1993) found that bursts which are "smooth" on short ($\sim$64 ms) timescales have peak counts integrated on a 1024 msec timescale (B) which indicate "smooth" bursts are both faint (*i.e.* low number of counts) and bright (*i.e.* high number of counts), while bursts which are "variable" on short timescales are faint only. The "smooth" and "variable" classification is based on a parameter V, the ratio of the peak counts in a 64 msec time bin to the peak counts in a 1024 msec time bin ($C^{64}_{\rm max}/C^{1024}_{\rm max}$), measured by the second most brightly illuminated Large Area Detector of BATSE. There is a known systematic correlation of V with burst duration (Rutledge & Lewin 1993); the minimum V value is a function of duration $t_{\rm dur}$, the result of which is that all GRBs of $t_{\rm dur} \lesssim 400$ msec are included in the "variable" class. These short GRBs make up $\sim 2/3$ of the "variable" class.

It might thus appear that the conclusion of LGS requires that short GRBs be faint, while long GRBs be both bright and faint, in apparent contradiction to the conclusions of Lestrade et al. (1993). However, since the durations of these short, "variable" bursts are less than the sampling period, B represents a measure of counts-fluence, rather than a sampled instantaneous peak flux. Thus, one should not conclude that the results of LGS are in contradiction to those of Lestrade et al. (1993) – specifically, that shorter GRBs have higher peak fluxes than longer GRBs, consistent with the time dilation effect predicted by Paczyński(1992)

Norris et al. (1994), using three tests to compare the time-scales of 131 bright and dim GRBs observed by BATSE of duration greater than 1.5 s, finds temporal, intensity, and fluence scaling effects consistent with a cosmological time dilation, with results consistent with the dimmest GRBs coming from a z$\sim$1.

Wijers & Paczyński (1994) analyzed the time dilations of bright and faint samples of bursts, and found the relative duration distribution widths were the same. They concluded that the effect is more convincingly explained by a cosmological origin than by a distribution intrinsic to the source population.

A cosmological source of GRBs is not necessarily the sole explanation of the results of these analyses. It cannot be ruled out that the results are consistent with the intrinsic characteristics of a population located in an extended galactic halo (or, corona). Hakkila et al. (1994; 1995) have produced a detailed study of the constraints on galactic populations from BATSE observations.

Here, we use the cosmological model for GRBs suggested by MP, except we adjust Ω_0 and $z_{\rm max}$ to find log N – log $F_{\rm peak}$ distributions consistent with BATSE observations, for a range of assumed energy spectra, in order to set limits on the acceptable parameter space for non-evolving cosmological models, and for cosmological models with evolving frequency density and luminosity. We calculate the number of GRBs which would be required to differentiate between values of Ω_0 of 0.1 and 1, and also between values of 0.1 and 0.5, depending on the sensitivity of the detector as indicated by $z_{\rm max}$. Finally we calculate the amount of integration time required to distinguish between these two values of Ω_0.

9.1.2 Previous Work

The present analysis has appeared previously (Rutledge et al. 1995); other analyses have used peak-flux distribution parameters, rather than the distribution itself, for investigating frequency density evolution with the 2B catalog data (Horack et al. 1995) or zero-evolution using the 1B catalog data (Piran 1992; Mao & Paczynski 1992; Lubin & Wijers 1993). Some analyses have used raw count-rates which can differ from the corresponding flux values by a factor of 2.7 for BATSE because they are not

aspect corrected, introducing a potentially large systematic (Dermer 1992; Cohen & Piran 1995). Other analyses have mis-formulated the problem, making their analysis one of positive frequency density evolution, rather than zero-evolution as claimed (Wickramasinghe et al. 1993; Caditz 1995). Finally, Fenimore et al. (1993) used the detailed differential peak-flux distribution of 1B catalog data and Pioneer Venus Orbiter data to find the faintest observed GRBs in a non-evolutionary scenario come from a red shift of z= 0.80 $\pm$ 0.05.

9.2 Analysis

Throughout this paper, we assume a cosmological constant Λ=0, and a universe dominated by non-relativistic matter, which sets $\Omega_0 = 2q_0$, and spherical symmetry of radiation (no beaming). The effects of beaming on GRB observations have been considered elsewhere (Mao & Yi 1994).

We also make extensive use of the Kolmogorov-Smirnov test for comparing an observed distribution with a model distribution (*cf.* Press et al. 1988, p. 491). This test results in a probability that, given the model distribution, another observed distribution as disparate or more disparate could be drawn from the source population. Thus, a KS probability of 1% implies that only 1% of the data sets of the same size as the observed data set would be as or more disparate from the model as the observed data set. Subsequently, when we say "90% confidence limits", we mean the boundary around those models with KS probabilities of >10%.

9.2.1 Number- Peak Flux Distribution

This discussion follows closely the model described by MP; we have assumed their "simplest" model, with no adjustable parameters, except we adjust one of the parameters (Ω_0).

THE ASSUMED SPECTRUM

We here discuss our choice of the assumed GRB spectrum, as this effects our results quantitatively, although not qualitatively, and warrants clarification.

We first assume that all GRBs have identical peak luminosities (*i.e.* are standard candles), with (first) identical power law photon number spectra:

$$\frac{dI_\nu}{d\nu} = C_z \nu^{-\alpha} \tag{9.1}$$

$$C_z = C_0(1+z)^l \tag{9.2}$$

where I_ν is in the units photons $\sec^{-1}$, and C_z is a z-dependent peak luminosity normalization, which accounts for the peak luminosity evolution with red shift. We chose to represent the evolution by power-law for its simplicity, unmotivated by any theoretical expectation that it should actually follow a power-law form.

The exponent α has been found to be largely in the range of 1.5–2.5 (Schaefer et al. 1994) for 30 GRBs selected from among 260 GRBs in the first BATSE catalog (Meegan & et al. 1994). We are motivated to use a simple power-law spectrum, as a simple power-law spectrum (of α=2.0) was assumed in producing the observed peak photon flux values in the BATSE 1B catalog. Schaefer et al. (1994) found that single power-law spectra adequately describe the observed GRB spectra for the majority of bursts. Using data from Table 5 Schaefer et al. (1994) we produced the number histogram (Fig. 9-1) of the 30 measured α, for fits over all "valid energy ranges". The majority of these GRBs have α between 1.5 and 2.5. In fits over energy ranges < 500 keV, the resultant values of α tend to be harder.

The single power-law energy spectrum is an over-simplification of the true GRB energy spectrum. Band et al. (1993) found that GRB energy spectra are well described at low energies by a power-law with an exponential cutoff, and at high energies by a simple (steeper) power-law, of the form:

$$\frac{dI_\nu}{d\nu} = C_z \nu^{-\alpha_b} \exp^{-\nu/\nu_b} \quad \nu < \nu_b(\alpha_b - \beta) \tag{9.3}$$

$$= C_z \nu_b^{-\alpha_b} \exp^{-1} \nu^{-\beta} \quad \nu > \nu_b(\alpha_b - \beta) \tag{9.4}$$

where C_z is as in Eq. 9.2 (here, we use α_b to differentiate between this power law and the single power-law parameter α). In Fig. 9-2a, we show the fit spectral models for the $\sim$ 55 bursts produced by Band et al. (1993) (their Table 4), normalized at 50.0 keV, over the energy range 50-5000 keV. As Band et al. concluded, there is no "universal" spectrum, and this complicates interpretation of analyses which rely on a single assumed "universal" spectrum, such as has been performed by Tamblyn and Melia (1993). However, a spectrum which largely follows the behavior of the burst spectra, has the values α_b=1.0, $\beta = 2.5$, and $h\nu_b = 300$ keV (hereafter, the complex spectrum). Further, the majority of these spectral models are steeper than a single power-law $\alpha = 1.0$, but more shallow than a single power-law $\alpha = 2.5$. We show these three models in Fig. 9-2b; the complex spectrum lies at all times between the single power-law spectra $\alpha = 1.0$ and 2.5.

Our approach here is to perform the analyses separately for two single-power law spectral slopes (α=1.0, and 2.5) and for the above-defined complex spectrum. Thus, the acceptable parameter space of cosmological models will be conservatively defined by the acceptable parameter space spanned by models for each of the assumed energy spectra. Our use of single power-law spectra will be justified by the qualitatively similar behavior between model parameter space using the complex spectra and that using single power-law spectra.

Procedure for Single Power-law Spectra

We assume the burst detectors are sensitive only to photons within a fixed frequency range ($\nu_1 \leq \nu \leq \nu_2$). For a source with a single power-law photon spectrum, located at red shift z, the part of the spectrum which is shifted into the detector bandwidth is:

$$I(z) = \int_{\nu_1(1+z)}^{\nu_2(1+z)} \frac{dI_\nu}{d\nu} d\nu = I_z(1+z)^{-\alpha+1} \tag{9.5}$$

$$I_z = (1+z)^l \int_{\nu_1}^{\nu_2} C_0 \nu^{-\alpha} d\nu \tag{9.6}$$

$$I_z = I_0(1+z)^l \tag{9.7}$$

Thus, $I(z)$ is the peak luminosity (photons $\sec^{-1}$) measured at red shift z which will be in the detector bandwidth at z=0. I_z includes the term $(1+z)^l$, which we use to make an accounting of evolution in the peak luminosities of GRBs as a function of red shift, and I_0 is a constant. This form of evolution is here adopted as a convenience, and is not motivated either by observations of evolving populations (*e.g.* radio galaxies, faint blue galaxies) by theoretical predictions. This limits the usefulness of the conclusions to describe only those models which can be accommodated by power-law evolution over the range of red shifts the model implies GRBs are observed by BATSE.

To find the measured luminosity, we must correct for time dilation, by dividing I(z) by an additional red shift factor (1+z). The number of photons measured at red shift z=0 will be equal to the photon luminosity at z=0, multiplied by the ratio (f) of the solid angle subtended by the detector (of area A) to the total solid angle (4π ster) (Weinberg 1972, p. 421):

$$f = \frac{A}{4\pi R_0^2 r_z^2} \tag{9.8}$$

This measured flux (in phot cm^{-2} $\sec^{-1}$) is:

$$F(z) = \frac{I_0}{4\pi} \frac{(1+z)^{-\alpha+l}}{R_0^2 r_z^2} \tag{9.9}$$

where I_z is in photons $\sec^{-1}$ and r_z, the co-ordinate distance, is (from Weinberg 1972, p. 485):

$$r_z = \frac{z q_0 + (q_0 - 1)(\sqrt{2q_0 z + 1} - 1)}{H_0 R_0 q_0^2 (1+z)} \tag{9.10}$$

where q_0 is the deceleration parameter, H_0 is the Hubble parameter at the current epoch, R_0 is the expansion parameter at the current epoch.

We find the total number of GRBs observable out to a red shift z' during an observation period of Δt at the present epoch:

$$N_b(z') = \int_0^{z'} \frac{\Delta t}{1+z} 4\pi n_z r_z^2 \frac{dr_z}{dz} \frac{dz}{\sqrt{1-kr^2}} \tag{9.11}$$

where $k = -1$, 0, or 1 for an open, critical, and closed universe, and n_z is the number of GRBs per co-moving volume per co-moving time (frequency density) as a function

of red shift z, accounting for evolution, which we take simply to be of a power-law form:

$$n_z = n_0(1+z)^p \tag{9.12}$$

with n_0 a constant. When p=0, the model is one of no evolution; when p>0, then we have "positive" evolution – an increasing co-moving burst rate with increasing red shift – and when p<0 we have "negative" evolution – a decreasing co-moving burst rate with increasing red shift. Eq. 9.11 can be rewritten as:

$$N_b(z') = \Delta t \frac{4\pi n_0}{q_0^4 (R_0 H_0)^3} \int_0^{z'} \frac{(1+z)^{p-4} \left(z q_0 + (q_0 - 1)[\sqrt{1+2q_0 z} - 1]\right)^2}{\sqrt{1+2q_0 z}}\, dz \tag{9.13}$$

Using these assumptions, we perform the following analysis. We define a sample of M GRB peak fluxes, taken from the second BATSE catalog (Meegan & et al. 1994), from bursts which have a peak flux measured on the 1024 msec time scale greater than 0.3 photons $cm^{-2}sec^{-1}$in the 100-300 keV band, the peak flux to which the trigger efficiency is confidently known (C. Meegan, private communication). We find 394 bursts which meet these criteria.

We sort the peak fluxes in increasing order and produce an observational integrated number – peak flux curve. We correct the observational number – peak flux curve for the BATSE trigger efficiency table, given in the second catalog. We use an analytic approximation to the trigger efficiency of the form:

$$\text{efficiency} = A - B \exp^{\frac{C - F_{\text{peak}}}{D}} \tag{9.14}$$

$$\begin{aligned} A &= 0.9989 \\ B &= 0.003933 \\ C &= 0.6496 \\ D &= 0.0748 \end{aligned}$$

and F_{peak} is the peak flux measured by BATSE. This equation is accurate to better than 1.2%, which is sufficient accuracy for the burst sample sizes considered here.

We assume a value for $\Omega_0(=2q_0)$, which sets the functional dependence of r_z on z (Eqn. 9.10). We then:

1. assume a value for $z_{\max}$, the red shift from which the burst with lowest observed peak flux was emitted ($F(z_{\max})$), and numerically integrate Eqn. 9.11 to find $N_b(z_{\max})$;

2. set $N_b(z_{\max})$=M (here, 394). This sets the value n_0 as a function of assumed $z_{\max}$ and q_0, with knowledge of H_0.

Then, for each burst, ordered in increasing peak flux, we do the following:

1. from Eqn. 9.9, we find the ratio of burst peak flux to the minimum peak flux of a detected GRB to be:

$$\frac{F(z)}{F(z_{\max})} = \left(\frac{r_{z_{\max}}}{r_z}\right)^2 \left(\frac{1+z}{1+z_{\max}}\right)^{-\alpha+l} \tag{9.15}$$

   This sets the value z at which the burst flux $F(z)$ was measured. The ratio of r_z with $r_{z_{\max}}$ is independent of n_0, H_0 and R_0 – thus, dependent only on z, α, and l.

2. Using z in Eqn. 9.11, we find $N_b(z'(F))$, which permits us to produce a theoretical log N – log F_{peak} distribution, for an assumed $z_{\max}$, α, and Ω_0, l, and p.

After producing a theoretical log N – log F_{peak} distribution as we describe, we compare this to the observed distribution, using a single distribution KS test, to find the probability that the observed distribution was produced by the model distribution.

This was done for 2 values of α (1.0 and 2.5), and for $0.1 \leq z_{\max} \leq 955$ at points separated by $\Delta \log(z_{\max})=0.041$, and for $10^{-2} \leq \Omega_0 \leq 2$, separated by $\Delta \log(\Omega_0)=0.041$.

The calculation was performed for the case of no frequency density or peak luminosity evolution (p=0, l=0), and separately for frequency density evolution (in-

teger values of p between -4 and 4, inclusive) and peak luminosity evolution (integer values of l between -4 and 4, inclusive).

Procedure for Complex Spectrum

The procedure to fit the log N – log F_{peak} curve for the assumed complex spectrum is similar to that followed above, differing only in detail. The single power-law spectrum is responsible for the simple analyticity of Eqn. 9.15, the ratio of the peak fluxes of standard candle bursts at different red shifts. The complex spectrum requires that the ratio be found numerically. A further systematic complication is that, as the origin of the spectral "break" is not well understood, exactly at what co-moving energy the spectral break should be placed is not obvious, although the observational limit that the vast majority of the spectral breaks have $E_b < 400$ keV (Band et al. 1993) provides an important guide. We have made the choice to set the co-moving breaking energy for each simulation so that the observed breaking energy is at the top of the passband of the 2B catalog peak fluxes (300 keV) for a burst at the *implied* lowest redshift z_{min} (that is, for the brightest burst). Thus, for a model with z_{max} which requires a certain z_{min}, then the assumed spectrum has E_b=300(1+z_{min}) keV (found iteratively) and therefore for all fainter bursts the E_b (observed at earth) will lie between 300 – 300(1+z_{min})/(1+z_{max}) keV, as breaking energy is held constant. We discuss the implications of this choice further in Sec. 9.4.

As in Eq. 9.9, the measured flux for the complex spectrum burst is:

$$F(z) = \frac{\int_{\nu_1(1+z)}^{\nu_2(1+z)} \frac{dI_\nu}{d\nu} d\nu}{4\pi R_0^2 r_z^2} \tag{9.16}$$

where the differential photon spectrum is given in Eqns. 9.3-9.4, and the values α_b=1.0 and β=2.5 are adopted. Thus, the ratio of burst peak flux to the minimum peak flux of a detected GRB is (replacing Eq. 9.15):

$$\frac{F(z)}{F(z_{max})} = \left(\frac{r_{z_{max}}}{r_z}\right)^2 \left(\frac{\int_{\nu_1(1+z)}^{\nu_2(1+z)} \frac{dI_\nu}{d\nu} d\nu}{\int_{\nu_1(1+z_{max})}^{\nu_2(1+z_{max})} \frac{dI_\nu}{d\nu} d\nu} \right) \tag{9.17}$$

The value of $E_{\rm b}$ ($=h\nu_b$; Eq. 9.3 & 9.4) is found by iteratively $\mathrm{F}(z_{\rm min})/\mathrm{F}(z_{\rm max})$ (=ratio of the highest to lowest observed GRB peak flux) until $E_{\rm b}/(1+z_{\rm min}) = 300$ keV. The integral is evaluated with the limits $h\nu_1 = 50$keV and $h\nu_2 = 300$ keV (the pass-band in which the peak flux is measured in the 2B catalog).

Once the value of $E_{\rm b}$ is set, the analysis proceeds using Eq. 9.17 to find the value z at which the burst flux $F(z)$ was measured.

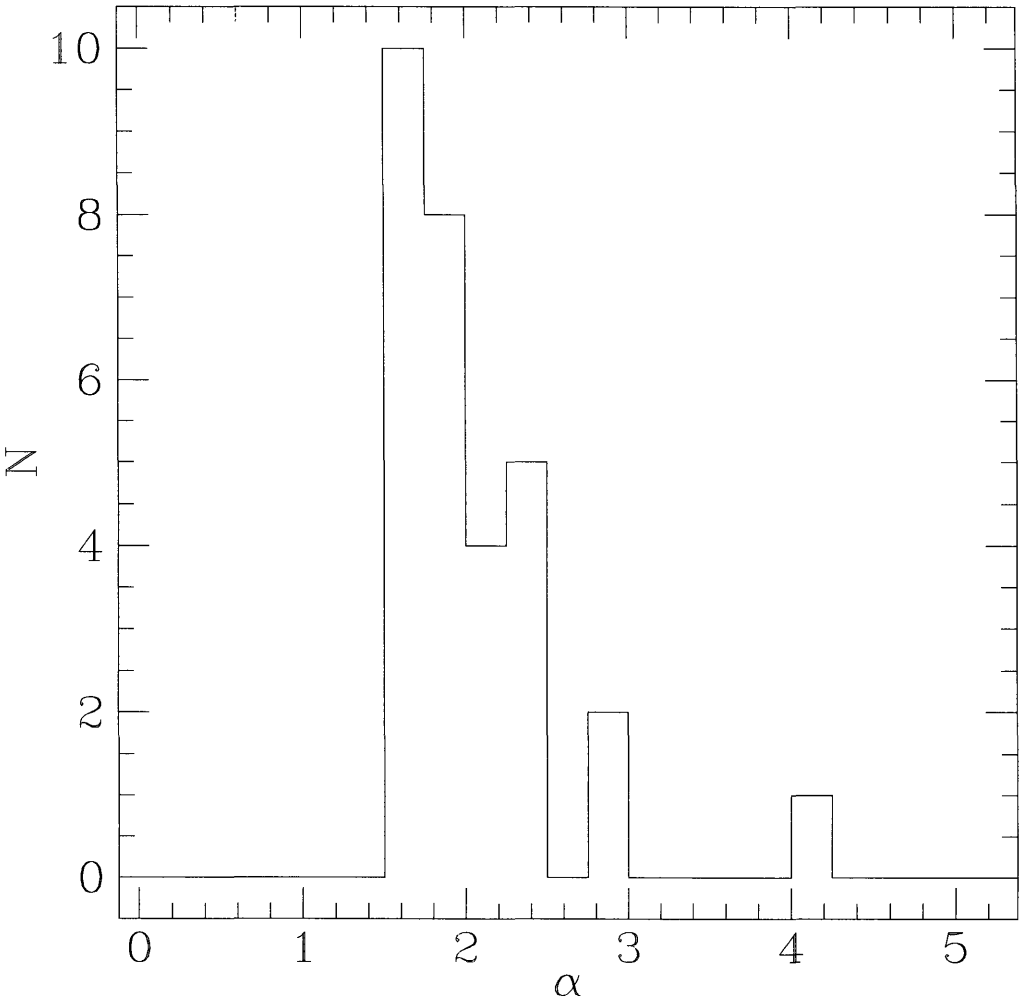

Figure 9-1: **Number vs. Photon Number Power Law Slope** α; for 30 GRBs. Data was taken from Schaefer et al. (1994); bursts were selected for this sample which had peak photon fluxes greater than 4 photons cm^{-2} sec^{-1} on the 64 msec timescale – however, some "interesting" bursts were also included.

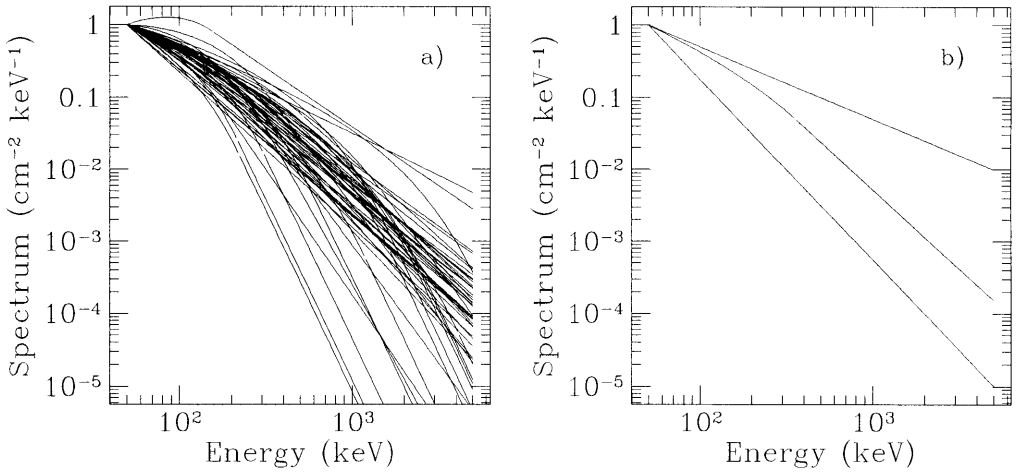

Figure 9-2: **Band Spectral Parameterization of 55 BATSE Bursts** (a) The spectral models fit by Band et al. (1993) to 55 GRBs, normalized at 50 keV. We show these models for the energy range 50-5000 keV, although the BATSE GRB spectra largely span 20-2000 keV, to show the extrapolated behavior of the spectra at higher energies. (b) Single power-law spectra with α=1.0, and 2.5, and the complex spectrum (see text), normalized at 50 keV. These spectra define the limiting and average behavior of the observed spectra found by Band et al. (1993)

9.2.2 Observational Confrontation with Cosmological Model

An essential parameter to this model is Ω_0. Using the zero-evolution and "standard candle" luminosity assumptions, we estimate how many GRBs are required to differ between parameter values of Ω_0 with a KS probability of 1%, assuming a detector which is sensitive to GRBs out to a red shift $z_{\max}$. Our motivation for doing so is that this parameter is the least constrained by the present analysis of those in the considered model. A calculation of how many GRBs are required to constrain the parameter, based on these very (and probably, overly) simple assumptions, would set an upper limit to the number of GRBs required for the intrinsic characteristics of the source population (*e.g.* luminosity function, frequency density evolution, luminosity evolution) to manifest themselves.

We wish to estimate the number of GRBs (N) required to discern between two values of Ω_0, assuming standard candle GRBs of constant number per co-moving time per co-moving volume. To do this, we assume a $z_{\max}$, the red shift at which the standard candle GRBs produce a flux at the completion limit.

We produce log N – log F_{peak} distributions for Ω_0=1.0 and Ω_0=0.1, assuming a constant number of bursts per co-moving time per co-moving volume, sampled at 200 points separated by a constant amount of co-moving time-volume. The normalized distributions are the cumulative probability distributions, and are not a function of the number of detected bursts. We compare the two distributions using a single distribution KS test.

For those cases when the number of required GRBs was less than the sampling of the cumulative probability distribution, the process was repeated, with the cumulative probability distributions sampled, instead of with 200 GRBs, with N GRBs found in the first iteration.

We perform the same analysis to estimate the number of GRBs required to discern between values of Ω_0=0.5 and Ω_0=0.1.

9.3 Results

9.3.1 Number – Peak Flux Distribution: No Evolution

The results of fitting the peak photon count rate number distributions to model populations with no evolution (p=0, l=0) are shown in Fig. 9-3. Each panel indicates the spectrum assumed ("complex" or single power-law α=1.0, 2.5). The lines are constant KS probability (1%, 10% and 33%) that the modeled number-peak flux distribution produces a distribution as or more disparate than the observed distribution.

The most probable values of $z_{\max}$, evaluated at (Ω_0=1) are ~1–2.2 (depending on the assumed spectrum). For all spectra considered, the 90% confidence limits on $z_{\max}$ are 0.8-3.0 (at Ω_0=1) and are largely insensitive to the assumed value of Ω_0. As these confidence ranges assume the source population to be entirely of a single spectral type, the confidence range is systematically overestimated.

As expected, the behavior of the complex spectral model as a function of (Ω_0, $z_{\max}$) is qualitatively similar to that of the single power-law spectra models, and the resulting acceptable parameter space is between that of the α = 1.0 and 2.5 models. We therefore proceed with confidence that the behavior of the two single power-law models will place conservative limits on the behavior of the complex spectrum model. It is desirable to do so only because of the computational demands of the complex spectral model.

Each of the comparisons of theoretical curves with the observed curves results in a value of the constant n_0. This value is the necessary normalization to obtain the number of observed GRBs M during the observation period out to $z_{\max}$, from Eq 9.13.

Following the procedure used by MP (Eq 13-15), we re-normalize n_0 to n_*, the number of GRBs per L^* galaxy per 10^6 years at the current epoch. In Fig. 9-3, the lines marked "10", "1.0", and "0.1" indicate n_* in units of GRB per L^* galaxy per 10^6 yr. For all spectra considered, the value of n_* is conservatively in the range 0.3-5.0 per L^* galaxy per 10^6 yr at Ω_0=1 (99% confidence), consistent with values found by other investigators (Dermer 1992; MP; Wickramasinghe et al. 1993).

For high $z_{\max}$, one might reasonably expect that there is evolution in the

luminosity density of galaxies. The re-normalization (to n_*) we adopted here is thus pertinent only for red shifts where such evolution can be neglected. To change the values back to burst rate per co-moving volume at the present epoch, one multiplies by the galaxy luminosity density we used (from (Efstathiou et al. 1988)):

$$n_0 = n_* \times \phi^* \Gamma(2+\alpha_g) \tag{9.18}$$

$$\phi^* \Gamma(2+\alpha_g) \sim 1.67 \times 10^{-2} L^* h_{100}^3 \mathrm{Mpc}^{-3} \tag{9.19}$$

As this re-normalization is multiplication by a constant, the *relative* burst frequency densities do not change; thus n_* may be used to compare frequency densities beyond red shifts where evolution becomes important, with the assumption that at such red shifts the burst frequency densities are unrelated to galaxy evolution.

9.3.2 Observational Confrontation with Cosmological Model

As is evident in Fig. 9-3, the Number distributions are largely insensitive to the value of Ω_0, for the 394 GRBs in this sample.

In Fig. 9-4a & b, we show the number of GRBs which would be required to discern between Ω_0=1 and 0.1, & Ω_0=0.5 and 0.1, from the number-peak flux distribution, using data which is complete for standard candle GRBs out to a red shift of z_{max}.

The points are the results of the calculation at a few values of z_{max}, assuming different spectra (α=1.0 or 2.5); the lines between the points are there to "guide the eye", and also identify the spectral slope assumed for the calculation. The solid line is α=1. and the dashed line is α=2.5.

The most likely z_{max} for BATSE GRBs calculated in the previous section was (2.2, 1.0) for α = (1.0, 2.5). For both spectra, this corresponds to $\sim$ 9,000 required for BATSE to discern between Ω_0=1 and 0.1. Similarly, approximately 20,000 GRBs are required to discern between Ω_0=0.5 and 0.1.

The uncertainties on these values are large. Permissively, if the actual z_{max} value is 3.0 (90% upper limit for α=1.0), then only $\sim$4,000 (or 10,000) GRBs are required

to discern between Ω_0=1 and 0.1 (or 0.5 and 0.1).

The number of GRBs required diminishes by 4 orders of magnitude when $z_{\rm max}$ changes from 0.5 to 10. For Ω_0=1.0, a change in depth of $z_{\rm max}$=1.0 to 10.0, requires an increase in detector sensitivity of a factor of (30, 400) for α=(1.0,2.5).

In Fig. 9-4c & d, we show the coverage (in years $\times 4\pi$ ster) required for a detector complete to burst peak fluxes out to $z_{\rm max}$ to obtain the number of GRBs required to discern between different values of Ω_0 in the log N – log $F_{\rm peak}$ distribution, assuming a constant number of GRBs per co-moving time, per co-moving volume. We normalize to 394 GRBs detected with peak flux > 0.3 phot cm^{-2} sec^{-1}on the 1024 msec integration timescale in the 2.7 $\times$ 10^8 s ster coverage of the second BATSE catalog, which introduces $\sim$5% uncertainty in the coverage.

At the minimum, BATSE (assuming 2.6 π ster coverage) would require $\gtrsim$ 6 years integration time before the parameter Ω_0 becomes reasonably constrained by the Number– peak flux distribution to permit confrontation between the cosmological models using only the distribution. The most likely required integration time is $\sim$30 years. Detectors sensitive out to $z_{\rm max}$=10 would give statistically different Number-peak flux distributions after a few weeks of full sky coverage, measuring $\lesssim$200 GRBs.

9.3.3 Number – Peak Flux Distribution: with Evolution

Frequency Density Evolution

In Figs. 9-5 - 9-7, we show the results of comparison of the observed BATSE number – peak flux distribution with distributions calculated including evolution in the frequency density of GRBs for $-4 \leq p \leq 4$. As in Fig. 9-3, the solid lines are constant KS probability (1%, 10% and 33%) that the assumed model could produce a distribution as or more disparate than that observed. The broken lines are constant n_* (see Sec. 9.3.1). In panels a, b, and h of each figure, the constant n_* lines are marked in units of GRBs per L^* galaxy per 10^6 yr and are identical to the lines in the other panels.

In the case of "negative" density evolution (p<0; panels b, d, f, and h), stronger

evolution has the effect of decreasing the implied $z_{\max}$ values. If the number density decreases with increasing $(1+z)$, lower values of $z_{\max}$ are required; as a result, higher values of n_* are required, increasing by a factor of $\sim$10 as p decreases from -1 to -4. This behavior is qualitatively the same independent of the assumed spectrum (of those considered here). The observed number – peak flux distribution is consistent with strong negative density evolution up to p=-4, but requires a lower $z_{\max}$ and a higher n_* (by $\times 10$) than a zero-evolution scenario.

In the case of "positive" density evolution (p$>$ 0; panels a, c, e, and g), stronger evolution has the effect of increasing the implied $z_{\max}$ values. For p$>$2, the models could not always be reasonably fit to the observed distribution for values of $z_{\max} <$1000, and exhibit dependency on the assumed spectrum. The $z_{\max}$ values are strongly dependent on the assumed source spectrum, with the range of acceptable $z_{\max}$ values increasing greatly for lower values of Ω_0 ($<$1).

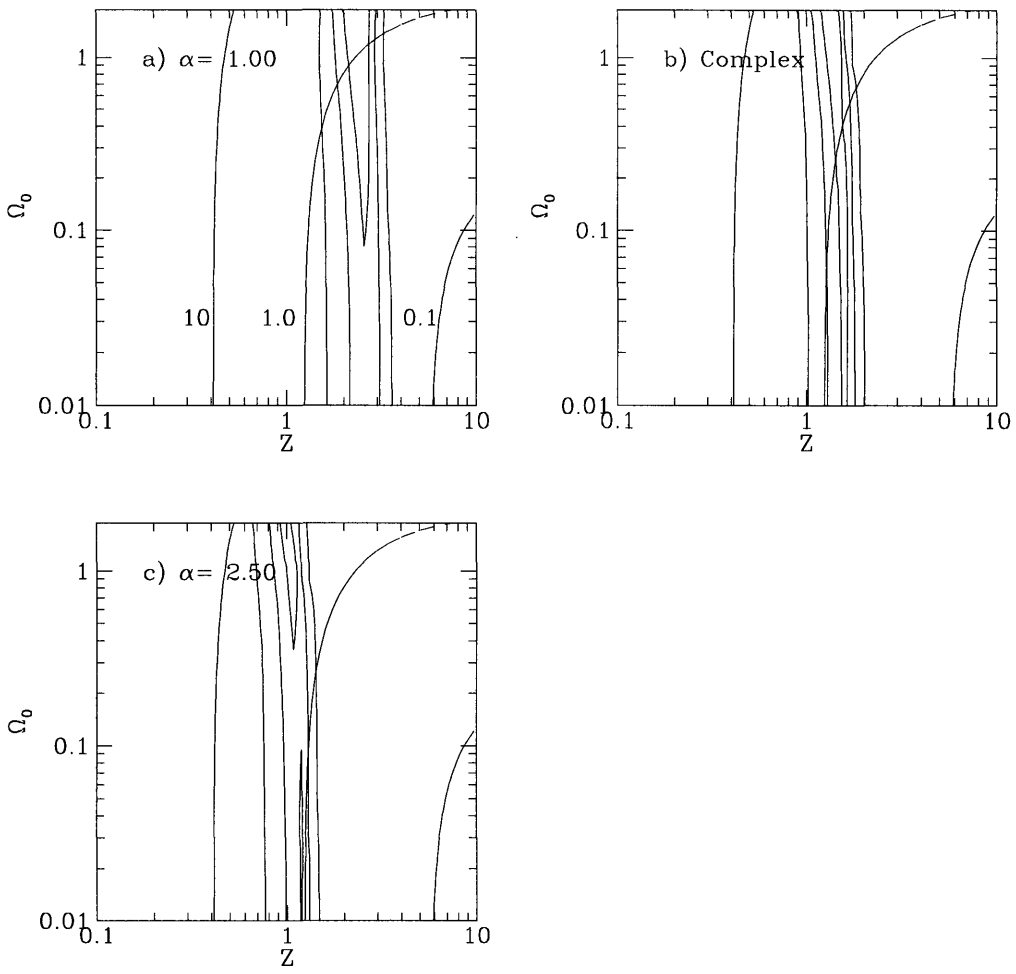

Figure 9-3: **Non-Evolving Parameters, and Gamma-ray Burst Rate per L_* galaxy** Results of comparisons of the BATSE observed number – peak flux curves with that expected from a constant number per co-moving time per co-moving volume source distribution, assuming different source photon spectra (complex, or single photon power law α=1.0, 2.5; marked in each panel), as a function of Ω_0, and the red shift of the faintest bursts observed (z_{max}). The solid lines are constant KS probability (1%, 10%, and 33%; lower KS probability lines enclose higher KS probability lines – the outer two lines are 1% and the inner two lines are 33%). The broken lines are the constant n_*, the number of bursts per L^* galaxy per 10^6 years at the current epoch, and are marked with their value.

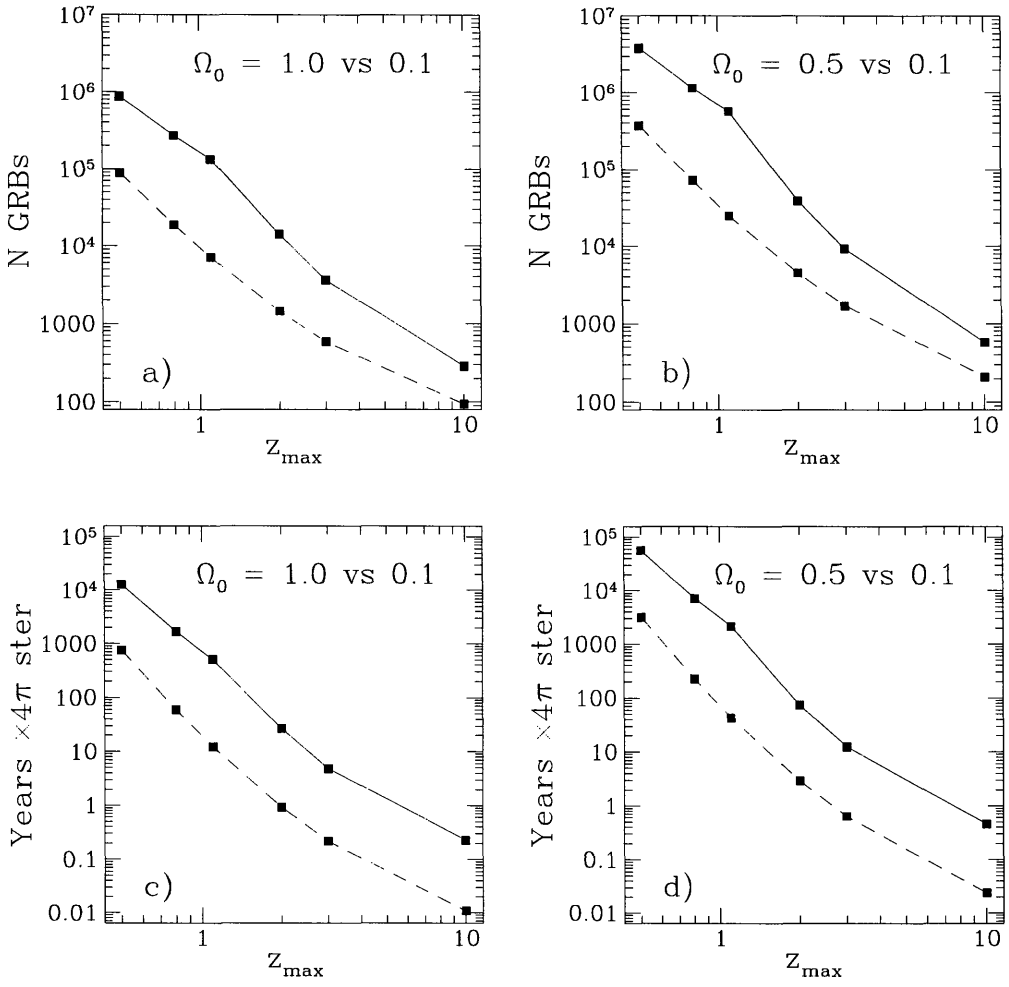

Figure 9-4: **Number of Observed GRBs Needed to Test Cosmological Models** Estimations of the required number of GRBs to differentiate (at the 99% confidence level) between two different values of Ω_0, assuming standard candle GRBs and a constant number of GRBs per co-moving time per co-moving volume, as a function of the value z_{max}, the red shift at which the standard candle GRB would produce a flux equal to the completion limit, assuming no evolution in the GRB population. Solid line is α=1.0, broken line is α=2.5. a) Number of GRBs needed to differentiate between Ω_0=1.0 and 0.1, as a function of the z_{max}. b) Number of GRBs needed to differentiate between Ω_0 = 0.5 and 0.1 as a function of z_{max} c) Coverage (in years 4 π ster) required to integrate the number of GRBs needed to differentiate between Ω_0=1.0 and 0.1. d) Coverage (in years 4 π ster) required to integrate the number of GRBs needed to differentiate between Ω_0=0.5 and 0.1.

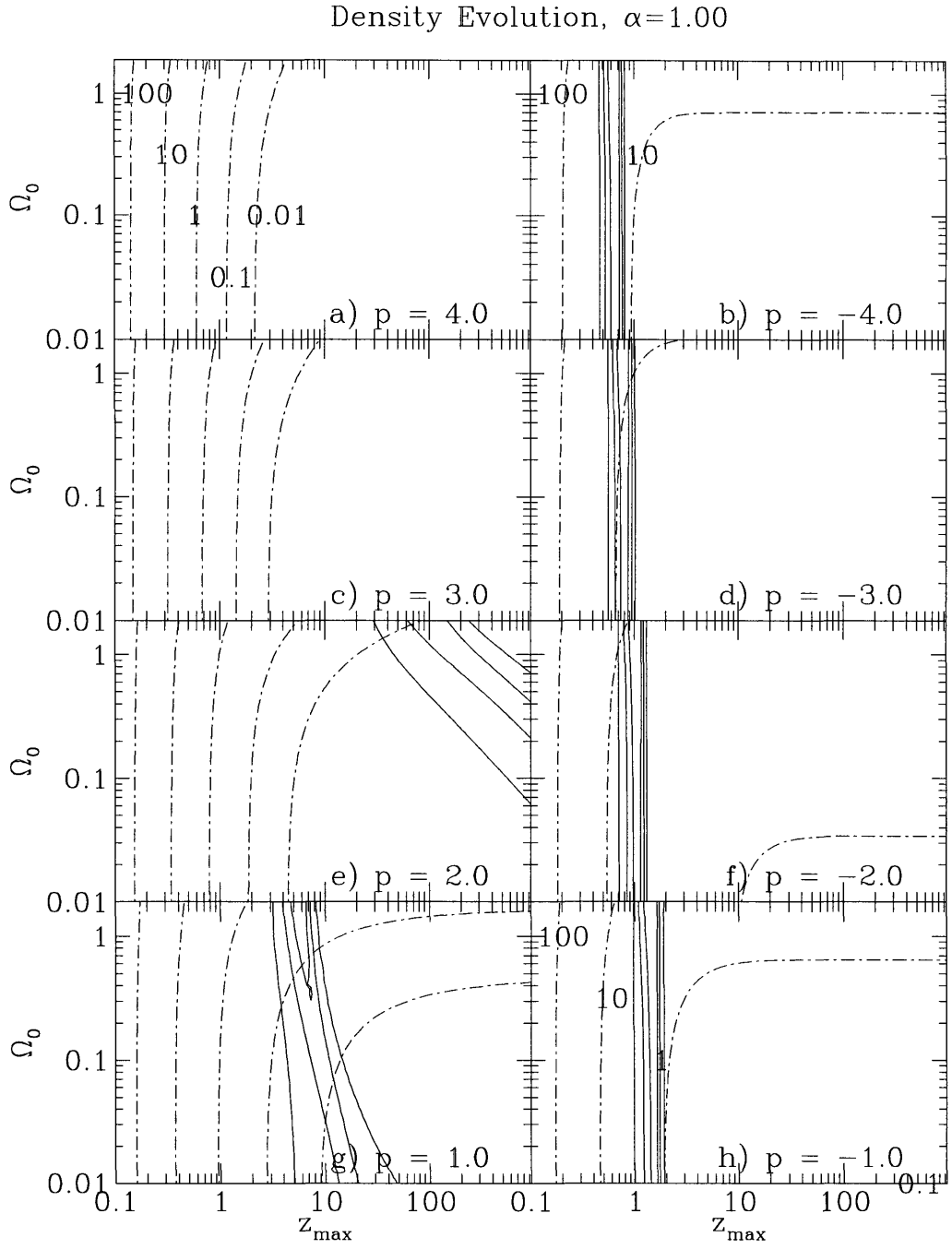

Figure 9-5: **GRB Models – Frequency-Density Evolution Parameters, Power-Law Photon Slope=1.** Results of comparisons of the BATSE observed number – peak flux curves with that expected from a parent population evolving in number per co-moving volume according to Eq. 9.12, assuming a source power law photon index slope of 1.0, as a function of Ω_0, and the red shift of the faintest bursts observed ($z_{\mathbf{max}}$). The solid lines are constant KS probability (1%, 10%, and 33%; note that lower KS probability lines enclose higher KS probability lines – the outer two lines are 1% and the inner two lines are 33%). The "wiggly"ness of the lines is due to the finite resolution of the probability calculation, and does not reflect real structure in the probability contours. The broken lines are constant in n_*, the number of bursts per L^* galaxy per 10^6 years at the current epoch, and are marked with their value.

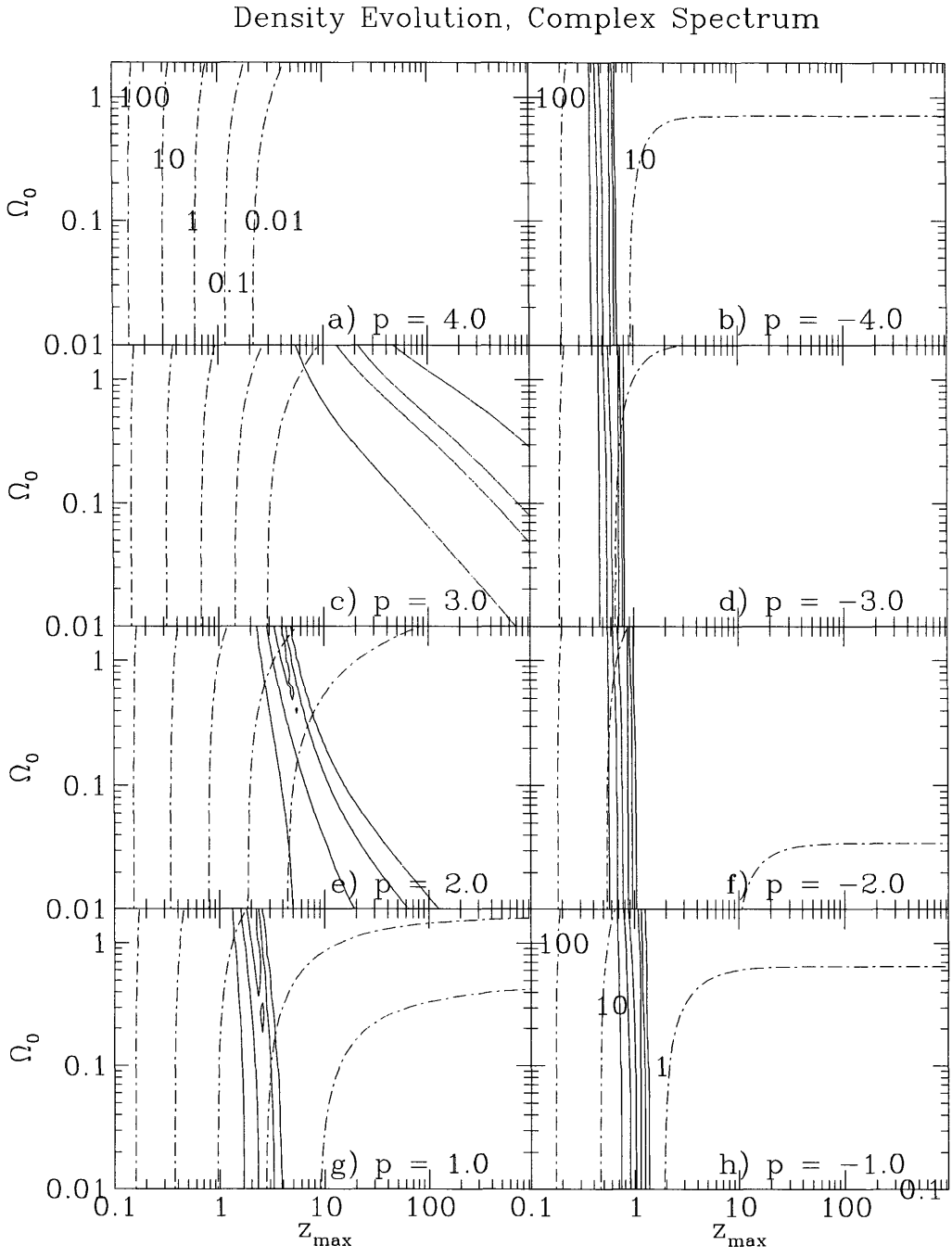

Figure 9-6: **GRB Models – Frequency-Density Evolution Parameters, Complex Photon Spectrum** This is identical to Fig.9-5, except a "complex" photon spectrum is assumed (see text).

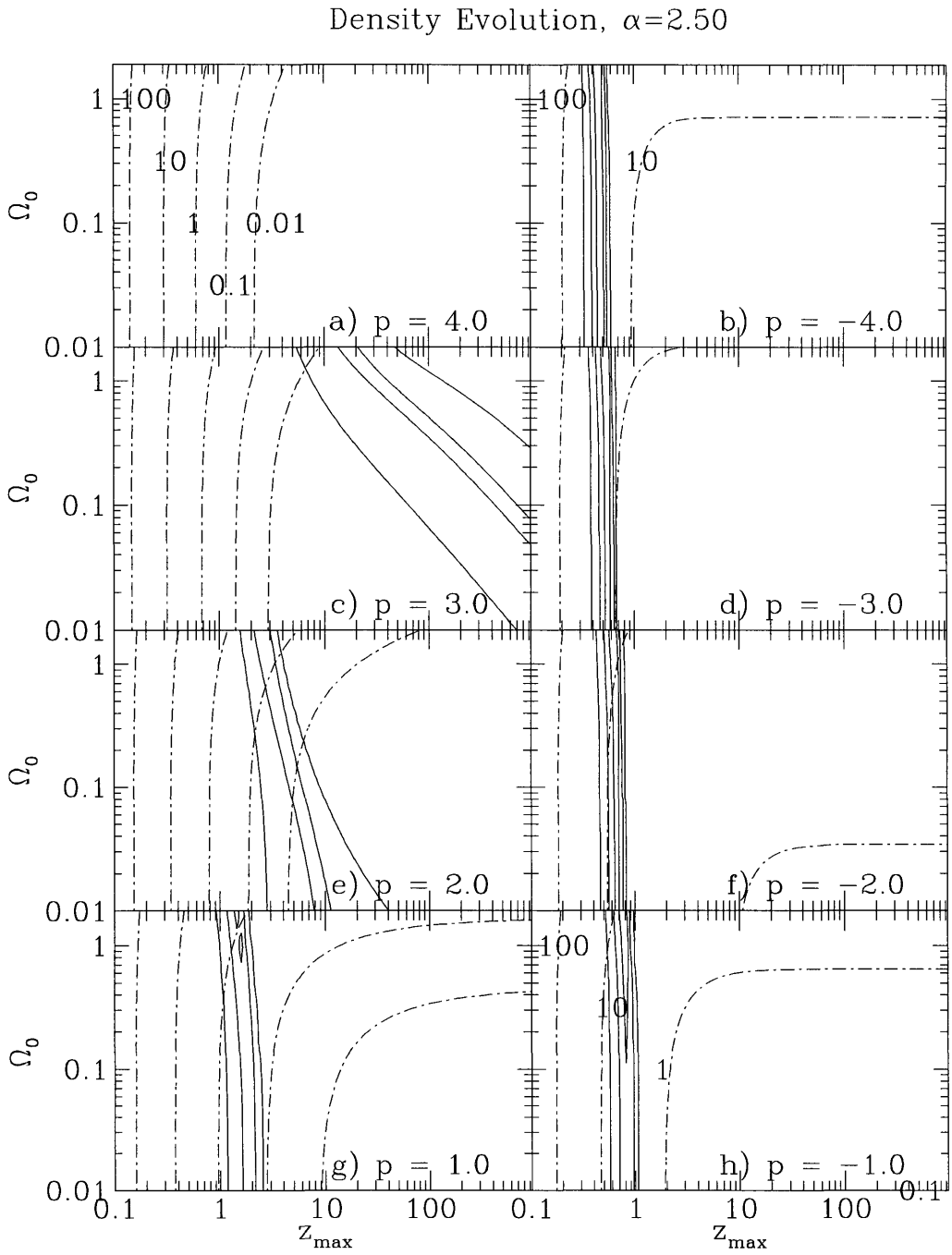

Figure 9-7: **GRB Models – Frequency Density Evolution Parameters, Power-Law Photon Slope=2.5** This is identical to Fig.9-5, except a photon power law spectral index of 2.5 is assumed.

Peak Luminosity Evolution

Figs. 9-8 - 9-10 show the results of comparison of the observed BATSE number – peak flux distribution with distributions calculated including evolution in the peak luminosity of GRBs with (1+z) according to Eq. 9.2. As in Fig. 9-3, the broken lines are constant KS probability (1%, 10% and 33%) that the observed number – peak flux distribution could have been drawn from the model distribution. The solid lines are constant n_*. In panel a of each figure, the constant n_* lines are marked in units of GRBs per L^* galaxy per 10^6 yr at the present epoch, and are identical to the lines in the other panels.

In the case of "negative" luminosity evolution (l<0; panels b, d, f, and h), stronger evolution has the effect of decreasing the implied $z_{\mathbf{max}}$ values, while increasing the n_* values. The most probable values of $z_{\mathbf{max}}$ decrease from the range of $\sim$ 1.0-2.2 (no evolution) to $\sim$ 0.3-0.7 (p=4), and the range of implied n_* increases by a factor of 10 ($\sim$ 0.3-5 to 3-50 GRBs per L^* galaxy per 10^6 yr at the present epoch).

In the case of "positive" luminosity evolution (l>0; panels a, c, e, and g), stronger evolution increases the value of $z_{\mathbf{max}}$, and also constrains the value of Ω_0 from above. Thus, for models with $l > 0$, the observed number - peak flux distribution distorts the acceptable parameter space considerably from that of zero evolution models; the acceptable parameter space becomes a strong function of both $z_{\mathbf{max}}$ and Ω_0 (see Figs 9-8g, 9-9c, and 9-10c). Acceptable parameter space is found for l as high as 3, (complex spectrum or α=2.5) (Figs. 9-9c and 9-10c).

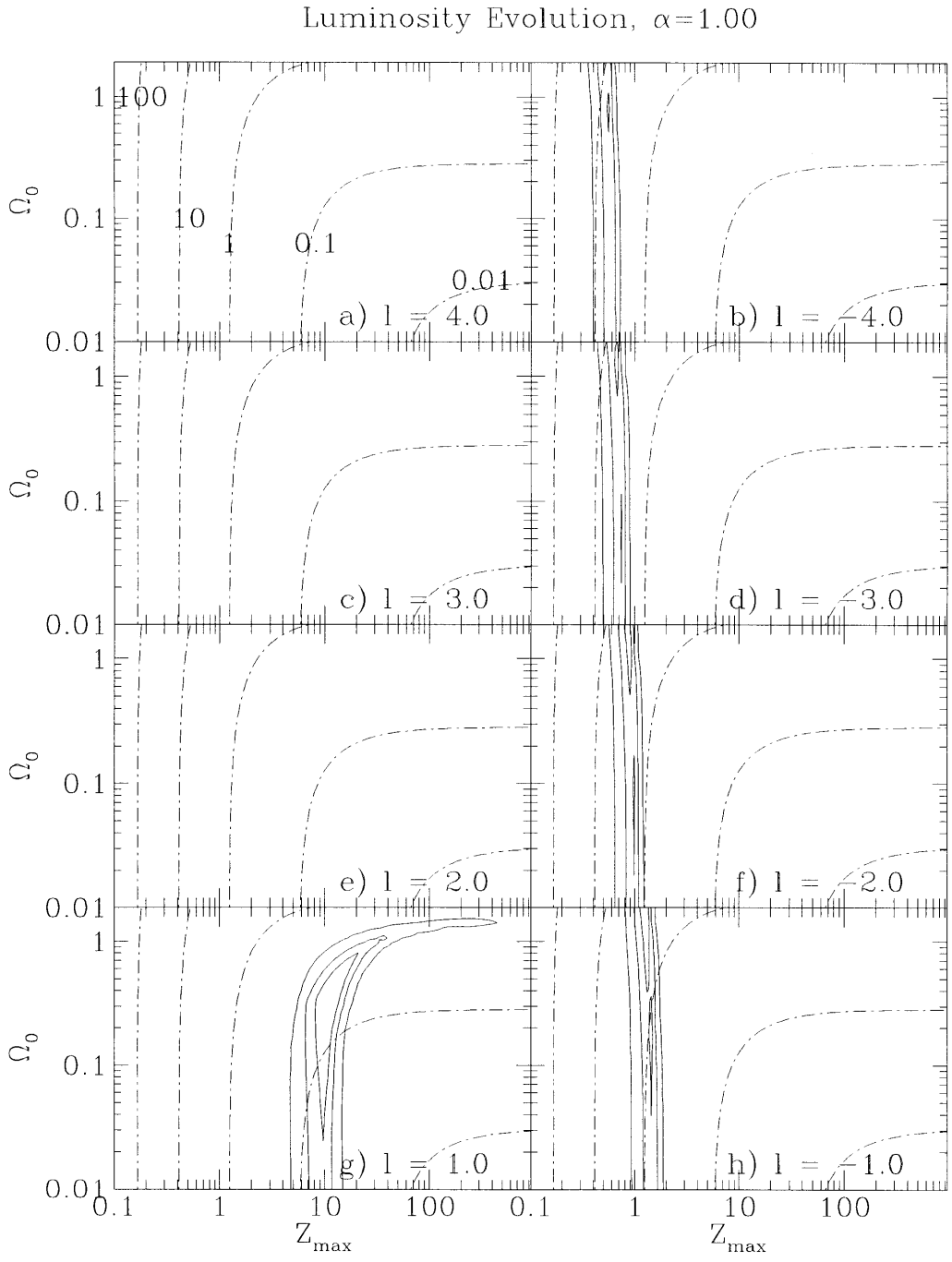

Figure 9-8: **GRB Models – Luminosity Evolution Parameters, Power-Law Photon Slope=1** Results of comparisons of the BATSE observed number – peak flux curves with that expected from a parent population evolving in peak luminosity according to Eq. 9.5, assuming a source power law photon index slope of 1.0, as a function of Ω_0, and the redshift of the faintest bursts observed ($z_{\rm max}$). The solid lines are constant KS probability (1%, 10%, and 33%) that the observed Number – peak flux distribution can be drawn from the simulated distribution. The broken lines are constant in n_*.

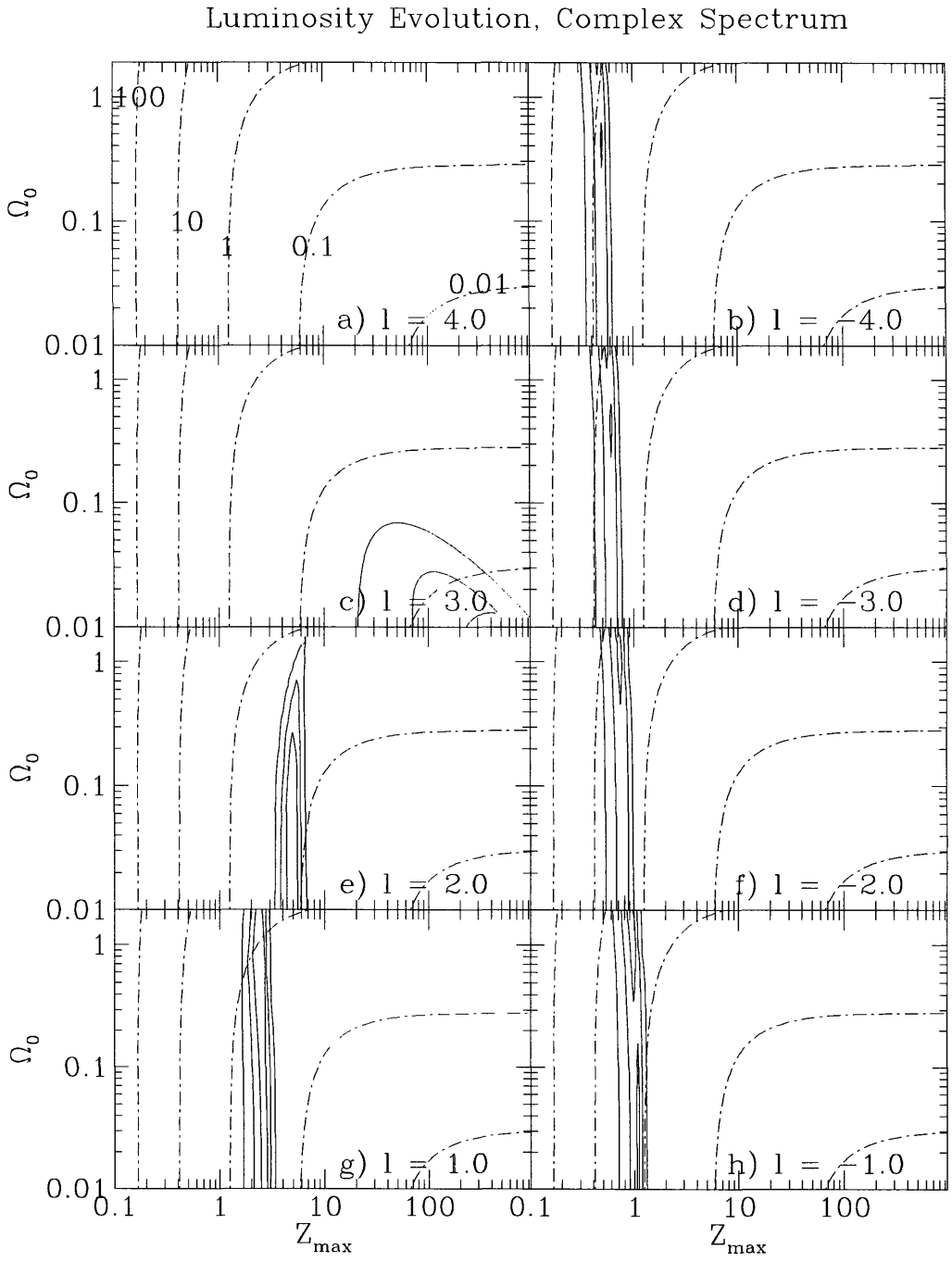

Figure 9-9: **GRB Models – Luminosity Evolution Parameters, Complex Photon Spectrum** This is identical to Fig.9-8, except a "complex" photon spectrum is assumed (see text).

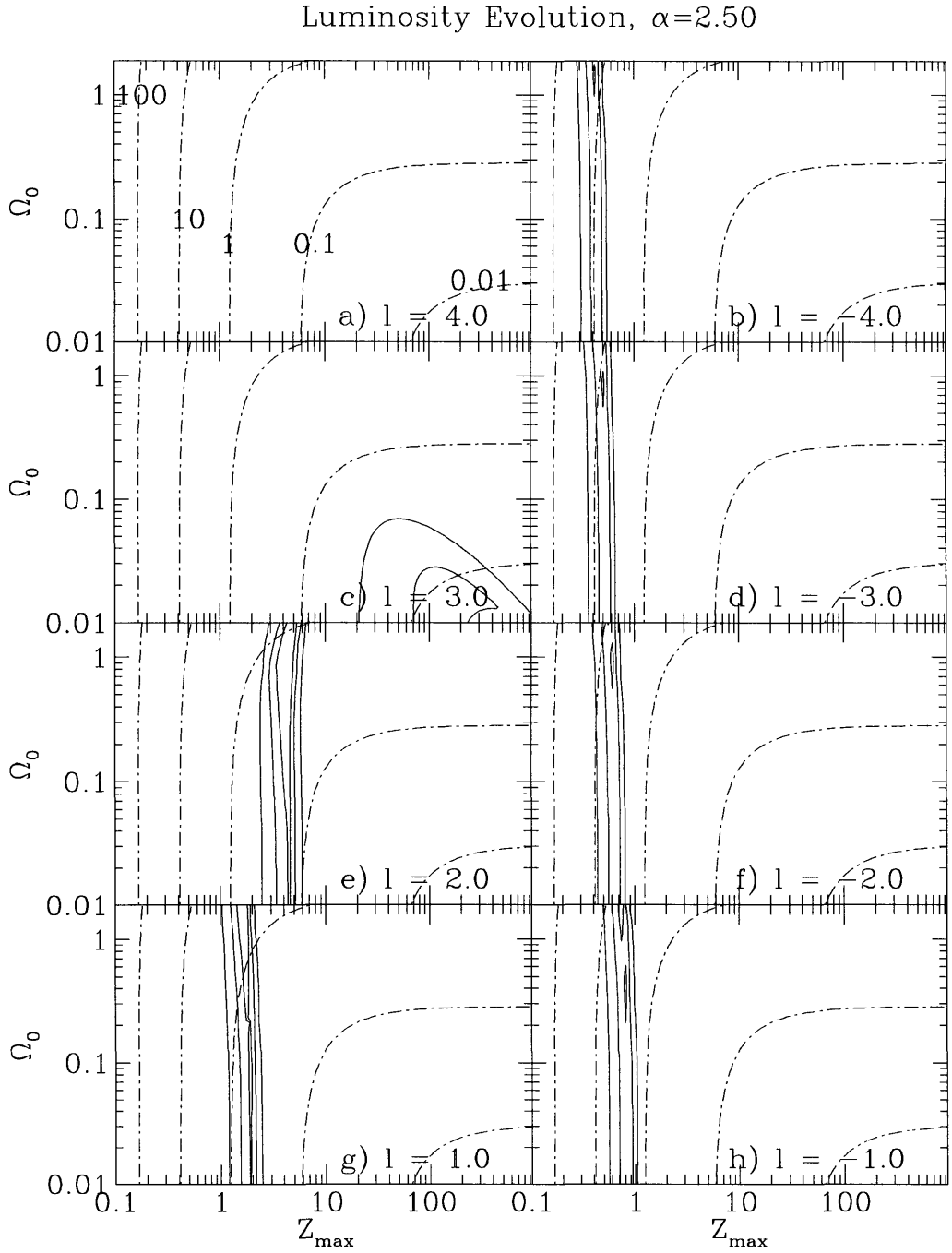

Figure 9-10: **GRB Models – Luminosity Evolution Parameters, Power-law photon slope=2.5** This is identical to Fig.9-8, except a photon power law spectral index of 2.5 is assumed.

9.3.4 Relative Time Dilation

For values of $z_{\rm max}$ and Ω_0 which produced models with KS probabilities >1%, we also found the ratio $R_{\rm rel}$:

$$R_{\rm rel} = (1 + z_{\rm max})/(1 + z_{\rm min}) \tag{9.20}$$

the ratio of the maximum redshift of GRBs in the sample to the minimum redshift of GRBs in the modeled 394 GRB sample. This ratio is the maximum amount of relative time dilation (or relative energy shift) between GRBs within the observed sample. In models with no source evolution, this ratio is very close to $(1+z_{\rm max})$. However, when strong positive frequency density evolution is present (p>1), this ratio was usually much smaller than $(1+z_{\rm max})$. This is not unexpected, as frequency density must change sharply in $(1 + z)$, requiring that the bursts be localized within a small range of redshifts. For all spectra considered, the ratio $R_{\rm rel}$ is always $\lesssim$9 (for all models with Ω_0<1 and KS probability >10%) even for $z_{\rm max}$ values in the range of 100-1000.

In Fig. 9-11, panels a, b, and c, we show the 1% KS probability contours for the models for each assumed spectrum with positive frequency density evolution which still had acceptable parameter space at $z_{\rm max}$<1000 (taken from Figs. 9-5e, 9-6c, and 9-7c). In all cases, the values of $R_{\rm rel}$ are smaller than $(1+z_{\rm max})$, indicating that all 394 observed GRBs (in these models) come from $z_{\rm min}$> 1. The very shallow spectrum $\alpha = 1.0$ requires a range of $R_{\rm rel}$ which is relatively high (30-60) while the more realistic complex spectrum, as well as the $\alpha = 2.5$ spectrum, has relatively low values of $R_{\rm rel}$ (5-8) for models which place the faintest observed BATSE bursts at $z_{\rm max}$ 100-1000.

We show similar results in Figs. 9-11d-f for the models with positive peak-luminosity evolution (taken from Figs. 9-8g, 9-9c, and 9-10c). In all cases, the value of $R_{\rm rel}$ is, at lowest, only a factor of a few lower than $z_{\rm max}$, requiring large amounts of relative time-dilation for bursts at high values of $z_{\rm max}$ (factor of 20-200 for $z_{\rm max}\sim$20-800). Models with relatively small amounts of peak luminosity evolution (l=1 - 2), place the faintest GRBs at $z_{\rm max}\sim$10 with $R_{\rm rel} \sim 10$.

9.4 Discussion and Conclusions

We have examined the observed log N – log F_{peak} distribution of 394 GRBs observed by BATSE, and, assuming a cosmological model with a constant number of bursts per comoving volume per comoving time, the distribution is consistent with the "standard candle" GRBs with peak fluxes > 0.3 phot cm^{-2} sec^{-1}originating at z_{max}=0.8-3.0 (90% confidence), with the most likely values in the range of 1.0-2.2, largely insensitive to the assumed Ω_0.

In performing this analysis we assumed that consistent model parameter space of the observed GRB sample could be bracketed by the single power-law spectral models (α=1.0 and 2.5) which, themselves, "bracket" the GRB broken power-law spectra fit by Band et al. (Band et al. 1993) (see Fig. 9-2). We find this assumption to be justified, as the dominant portion of the Band et al. (1993) spectra fall between these two single power-law spectral models, and the behavior of the complex spectrum also fell between that of the two single power-law spectral models. We presumed that the broken power-law parameter E_b is constant (that is, is measured to be $E_b/(1+z)$ from a burst at the redshift 1+z) and that a dominant number of bursts have an $E_b\sim$ 300 keV. In the worst possible case of inconsistency with this assumption – that E_b varies randomly – the behavior of the models will be bracketed by behavior of the broken power-law spectrum at its extremes, which behaves like a single power-law spectrum of $\alpha\gtrsim$1.0 or $\lesssim$2.5.

Our choice for the the value of E_b in our simulations was made to maximize the effect of the difference between the "complex" spectrum and the power-law spectrum. This was done to see if the power-law approximation models produce grossly different results from the more observationally correct "complex" spectrum. We find that the behavior of the "complex" spectrum model is within the limits of the behavior set by the two single-power-law spectrum models. This is not unexpected; if the redshifts over which the bursts span are modest in extent, then the broken power-law model behavior is dominated by the low-end of the spectrum (*i.e.* $\alpha_b = 1.0$; Eqn. 9.3), while if the bursts span over a large range of redshifts, the broken power-law model behavior

is dominated by the the high-end of the spectrum (*i.e.* $\beta = 2.5$; Eqn. 9.4).

We find that, for the zero-evolution models, strong limits may be placed on the GRB rate at at 0.3-5.0 GRBs per L^* galaxy per 10^6 yr, for $\Omega_0 \lesssim 1$. This is consistent with the values found by MP for an Ω_0=1 universe (although MP assumed flatter energy spectra than has been observed by BATSE ; α=0.5-1.5 vs 1.5-2.5) and with those found by Piran (1992) .

When this work was largely complete, similar analyses by Cohen & Piran (1995) considering non-evolving cosmological models using the 2B BATSE data base came to our attention. Our conclusions are consistent with their analyses.

We find that, for BATSE, $\gtrsim$4000 (most likely $\sim$ 9,000) GRBs are required to use log N – log F_{peak} to constrain a zero-evolution, standard-candle peak luminosity cosmological model parameter Ω_0 to between 1.0 and 0.1, and $\gtrsim$9000 to constrain Ω_0 to between 0.5 and 0.1. This requires a minimum of 6 yrs of BATSE integration; a duty cycle of 50% places this above the projected mission lifetime of BATSE.

The observed number – peak flux distribution can accommodate both peak luminosity evolution of GRBs and frequency density evolution.

The frequency density evolution, if any, can be accommodated by a power law in $(1+z)^p$ for the ranges of z_{max} and Ω_0 considered here. We find no acceptable models for p$\gtrsim$3.

If we assume the difference in timescales (by $\times$2) between bright and faint bursts found by Norris et al. (1994a) and Wijers & Paczyński (1994) is due to the relative time dilation of bursts within the sample, then we find acceptable model-parameter space which would place the faintest GRBs observed by BATSE at z as high as 1000 with maximum relative time dilation of $R_{rel} \sim 8$. As the aforementioned studies necessarily average over a substantial fraction of the brightest and faintest bursts, the relative time dilation they measure should be somewhat smaller than our parameter R_{rel} (which compares only the brightest and faintest single bursts). We find that values of R_{rel} as high as $\sim$ 10 are consistent with the measurements of the factor of two difference in timescale between bright and faint bursts.

The p=1 (frequency density evolution) model is identical to the assumed

GRB model used by Wickramasinghe (1993) (which they proposed as a non-evolving model). For Ω_0=1 in this model, we find higher values of the most probable $z_{\rm max}$ (1.7-3.0 vs. 0.5-1.7; comparing with their Fig. 2, at the completion limit). This is probably due to the fact that we use a lower flux limit (and thus, "see" to greater redshifts); when we perform the same analysis to the 99% flux limit of BATSE (the flux limit used by Wickramasinghe & Paczyński), we find $z_{\rm max}$ in the range 0.9-1.7, similar to that found by Wickramasinghe & Paczyński (1993).

We have found that the strongest positive frequency density evolution scenario (p=2) with acceptable model parameters for all spectra considered permit $z_{\rm max}$ to be as great as ~200, with values of $R_{\rm rel}$ as high as 9 for hard bursts, and in the range of 2-5 for softer bursts. When we consider that many GRBs of different spectra were averaged over by Norris et al. (1994a) and Wijers & Paczyński (1994) to obtain the timescale difference of a factor of 2 between bright and faint bursts, we estimate that the p=2 scenario cannot be excluded on this basis; averaging together harder GRBs with softer GRBs diminishes the higher values of $R_{\rm rel}$, and the averaging together of many bursts of different peak fluxes (and thus, at different redshifts) diminishes the amount of relative timescale difference within the burst sample to an level consistent with these observations.

Application of Eq. 9.9 to the p=2 scenario shows that the implied photon luminosities in the redshifted passband at the epoch of the source are a function of α, $z_{\rm max}$, and Ω_0, and can be different for different assumed spectra by several orders of magnitude or identical to within a factor of order unity, dependent on the assumed Ω_0. For example, for an assumed spectrum of α=1.5, the p=2 scenario places statistically acceptable (KS prob > 1%) populations at ($z_{\rm max}$, Ω_0) of about (10, 1.0), (60, 0.2), and (200, 0.06). For these values of ($z_{\rm max}$, Ω_0) the ratio of photon luminosity to flux is 4×10^{59}, 2×10^{62}, and 7×10^{64} (all in units of cm$^{-2}h_{80}^{-2}$. The implied source luminosity to flux ratio of non-evolving population, with a source at $z_{\rm max}$ of 1.5 for Ω_0=1 is 6×10^{57} cm$^{-2}h_{80}^{-2}$. Thus, the evolutionary scenarios require sources with much greater luminosities, by up to 7 orders of magnitude, than non-evolving scenarios.

Photons with energies as high as 10 GeV have been observed from some GRBs (Schneid et al. 1992; Kwok & et al. 1993; Dingus & et al. 1994; Sommer et al. 1994). The Cosmic Microwave Background Radiation is capable of scattering photons at such energies when they are emitted from very high redshifts (Babul et al. 1987). There is essentially a "wall" in redshift-space to photons of a given energy due to scattering by the CMBR, such that photons of energy E MeV will not be observed if they are emitted beyond a redshift $z{\sim}7400(E/1\mathrm{MeV})^{-0.484}$ (Babul et al. 1987). Thus, photons of energy 1 GeV would not be observed from a GRB if the GRB occurred at a redshift greater than $\sim$260. Photons of such energies have been detected from only a very small fraction of the observed GRBs, and these GRBs are typically among the brightest observed, which may come from redshifts a factor of $\sim$5-8 lower than the maximum redshift; for example, if z_{max}=1000, the brightest GRBs would come from redshifts 125-200, and would thus these high energy photons would not be scattered by the CMBR. Thus, the observation of some such photons is not inconsistent with BATSE seeing GRBs from redshifts as great as 1000.

The implied comoving burst rate in the strong (p=2) frequency density evolution scenario is $\times$100 higher for hard bursts (α=1.5) than for soft bursts (α=2.5). For weaker (p=1) frequency density evolution, the comoving burst rate of harder GRBs is only $\sim\times$10 greater than that of the softer GRBs. These high spectrally-dependent differences in the relative comoving burst rates are a constraint on models which contain strong GRB frequency density evolution. Further, 'standard-candle' models which contain strong frequency density evolution require that the GRBs of different spectra either have different number–peak flux relations, or that the relative burst rates conspire with the evolution rate and space-time geometry in the epoch where the majority of GRBs of a particular spectrum occur to produce identical number–peak flux distributions, independent of the intrinsic source spectrum. In Fig. 9-12, we show the cumulative distributions of the 100 spectrally hardest and 100 spectrally softest GRBs from the present sample; a 2-distribution KS test shows them to be statistically identical (KS probability 59%).

The peak luminosity evolution, if any, can be accommodated by a power law

in $(1+z)^l$. For the peak luminosity evolution models, the relative time dilation between the faintest and brightest bursts ($R_{\rm rel}$) can be as high as 200 for the models considered here, and is very roughly between $(1+z_{\rm max})/4$ and $(1+z_{\rm max})$, favoring the high value for low $z_{\rm max}$, but decreasing to the low value for high $z_{\rm max}$. With the estimate that $R_{\rm rel}$ must be $\lesssim$10 to be consistent with the observed amount of relative time dilation within the GRB sample, then the present analyses excludes luminosity evolution models which place the faintest observed GRB in the present sample at $z_{\rm max} \gtrsim 10$. If we also require, as we have in the frequency density evolution, that the luminosity evolution scenarios permit relative time dilation of at least a factor of 2, then we find that that negative luminosity evolution cannot be stronger than l= 2.

We conclude that the Number-peak flux distribution of GRBs observed by BATSE is consistent with a homogeneous, zero evolution source population, to a $z_{\rm max}$ most probably in the range 1.0-2.0 for GRBs with peak luminosities of $\sim$0.3 phot cm^{-2} sec^{-1}, and that the flattening observed in this distribution is consistent with being due only to cosmological effects. The amount of frequency density evolution of the form given by Eqn. 9.12 is constrained, with the exponent p <2. The amount of peak luminosity evolution of the form given by Eqn. 9.7 is constrained, with the exponent l < 2.

As the constraints on $z_{\rm max}$, p, and l, improve with greater numbers of GRBs, we expect similar future work with larger samples to be useful in the parameterization of the GRB source population. However, to put practical limits on GRB cosmological models, much deeper observations are required.

We wish to draw the reader's attention to the fact that in considering one evolution model (frequency density evolution or luminosity evolution), that the other evolutionary model was held to be zero, which may not be the actual observational case. Given the wide range of acceptable parameters for even this case, it is not at all clear that it is possible to jointly constrain all these different functions and values (frequency density evolution, luminosity density evolution, $z_{\rm max}$, Ω_0, n_*) with the single observational log N – log $F_{\rm peak}$ curve. We also wish to point out that, as we have assumed power-law forms of the evolution, the validity of these conclusions is

limited to actual evolution which follows power-law form.

If flattening of this distribution from the expected (from Euclidean geometry and spatial homogeneity) -3/2 power law are due only to cosmological effects, then BATSE will not integrate sufficient numbers of GRBs with peak flux > 0.3 phot $cm^{-2}sec^{-1}$to constrain Ω_0 to the range 0.1–1.0 during its projected lifetime, which would, with certainty, permit confrontation with cosmological models. However, Hakkila et al. (1994) estimates that BATSE can integrate enough GRBs in its lifetime to permit confrontation with a variety of galactic models. A mission with much fainter flux limits ($\times$ 70-400), fortuitously pointed toward M31, could permit both after integrating for a period of months.

We find that the results of the present analysis is supporting, but not compelling, evidence of a cosmological origin for GRBs and much further work is required to investigate this hypothesis.

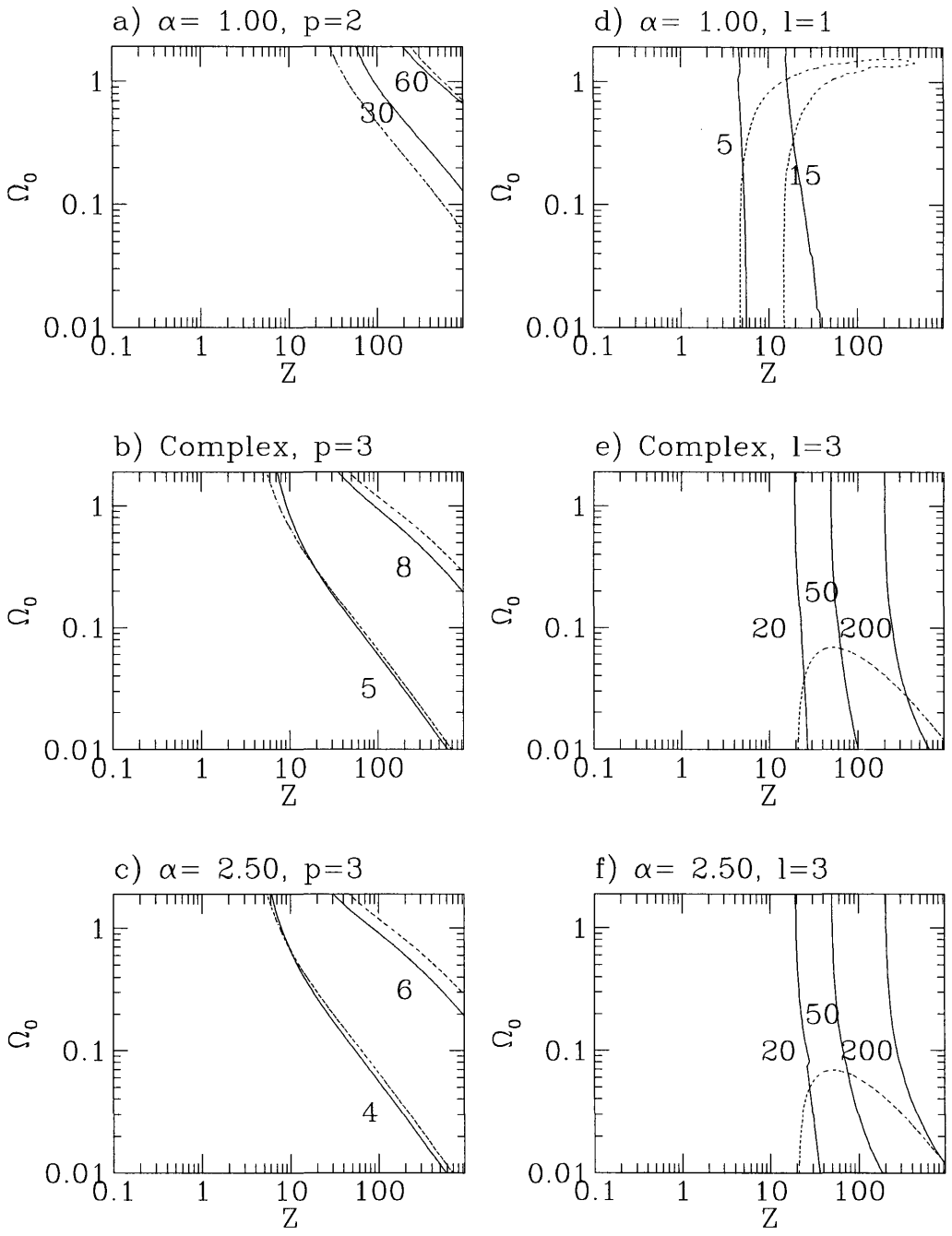

Figure 9-11: **Acceptable $R_{\rm rel}$ from GRB Models** This figure shows the range of acceptable values of $R_{\rm rel}$ for selected models with KS probabilities >1%. The broken lines are constant KS probability enclosing models at >1%. The two solid lines in each panel are marked constant $R_{\rm rel}$. The value of $R_{\rm rel}$ changes monotonically between the two solid contours. Each panel indicates the assumed spectrum and the model parameter which is different from zero(p for frequency density evolution, l for peak luminosity evolution).

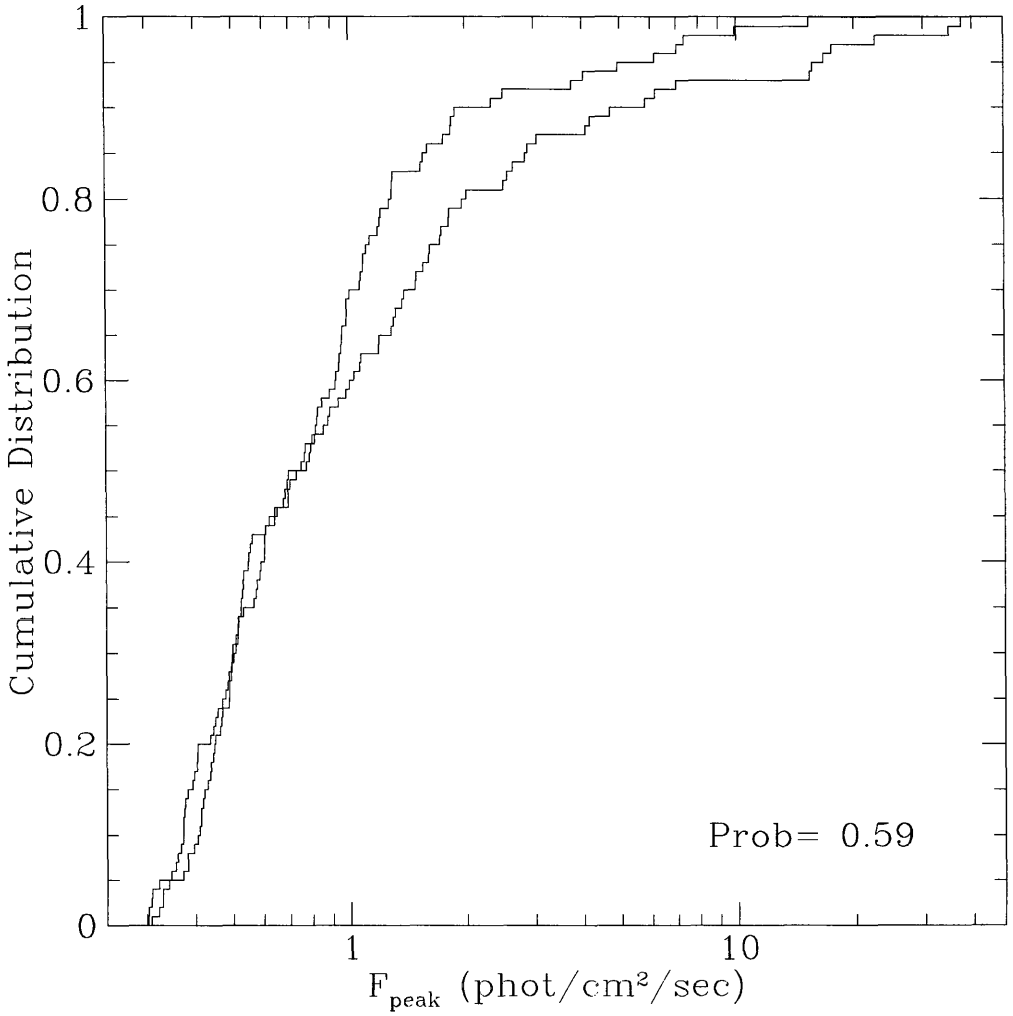

Figure 9-12: **Cumulative $F_{\rm peak}$ Distribution of Spectrally Hard and Soft Bursts** Comparison of the cumulative distribution for the 100 hardest (determined by the ratio of the 100-300 keV photon fluence to the 50-100 keV photon fluence) and 100 softest GRBs with 1024msec peak photon flux > 0.3 phot cm^{-2} sec^{-1}. They are statistically identical, with a KS probability of 0.59

Part III

Conclusions, Appendicies

Chapter 10

Summary of Conclusions from the BHC and GRB Analyses

In this chapter, we summarize the conclusions of both the black hole candidate (BHC) analyses and the gamma-ray burst GRB) analyses.

10.1 Black Hole Candidate Conclusions

- We have described a quantitative phenomenology of BHCs, based on their combined fast-timing (0.001 – 64 Hz) and spectral behavior in the 2-20 keV energy range. This phenomenology incorporates the previously identified High, Very High, and Low-states. We have not demonstrated that this behavior is unique to BHCs. However, our work will facilitate comparisons with other sources in future analyses.

- Behavior known as "High-State" occurs when the source spectrum corresponds to a hardness ratio (Wide Ratio; 9.2–18.4/2.3–4.6 keV) $\lesssim$0.03 as measured by the *Ginga* LAC. The High-State variability (*i.e.* PDS) is consistent with a single-power-law with %rms variability which increases with increasing energy between the three energy ranges 2.3–4.6 keV, 4.6–9.2 keV, and 9.2–18.4 keV. The strength of the High-State variability is typically in the 1-10% range (2.3–18.4

keV; 0.001-64 Hz).

- Behavior known as "Low-State" occurs when the source spectrum corresponds to a Wide Ratio $\gtrsim$0.1 as measured by the *Ginga* LAC. As the source spectrum approaches this value (*i.e.*, spectrally softens) the %rms variability decreases, changing from being energy independent in strength (with ~30-40% rms variability) to increasing in strength with increasing energy. This behavior was observed in several BHCs. It is significant that this behavior is also observed in GS 2023+33, which was never observed to transit out of the Low-State, as this demonstrates that the timing properties of GS 2023+33 change with changing Wide Ratio in the same manner as sources which do change from Low-State to High State.

- Behavior known as "Very-High-State" (when strong, peaked 3-10 Hz QPO is observed) occurs when 0.03 $\lesssim$ Wide Ratio $\lesssim$ 0.1. When the QPO is observed, the ratio of the broad-band (0.001-64 Hz) %rms variability in the 9.2–18.4 keV range to that in the 2.3–9.2 keV range is considerably lower than in periods when no QPO is observed. Also, the QPO is spectrally harder than the broad-band variability; the ratio of the strength of variability in the 9.2–18.4 keV band relative to that of the 2.3–4.6 keV band is typically 4-10$\times$ larger than that of the broad-band variability.

It should be noted:

- The Very High State (of GS 1124-68 and GX 339-4) is spectrally intermediate to the Low and High State, and the broad-band (0.001–64 Hz) variability properties are observed to change from those observed in the Low-State to those observed in the High-State, as the spectral hardness decreases. The Very High State QPO centroid frequency and FWHM (both absolutely and fractionally, as FWHM/ν_c) are each at their maximum observed values near Wide Ratio~0.055, and have lower values when the Wide Ratio is higher or lower. The frequency dependence of the strength of the continuum variability changes from Low-State

to High-State also near Wide Ratio$\sim$0.055. Thus, the frequency dependence of the continuum variability and the QPO centroid frequency are related.

- If the Very High State is the transition between the Low and High state as suggested here, then it should be observed in sources which are known to transit between these two states (*e.g.* Cyg X-1). This is presently under investigation (Cui et al. 1996, in progress).

- The source 1630-47 is spectrally in the Low-State (as defined here) but its variability properties were like that of the High-State. Thus, the classification of 1630-47 as a BHC is suspect.

- For a period, LMC X-1 occupied the same CCD parameter space as GX 339-4 and GS 1124-68 in their Very High States; however, the time resolution of the observation was insufficient to confirm the presence of QPO which, according the the present study, should have been present.

- We find QPO, which we call Low-State QPO, in GS 2000+25 and Cyg X-1, with frequencies $\sim$1-3 Hz, and which are broad ($\delta\nu/\nu_c \sim 0.5 - 1.0$). The LS QPO is spectrally distinct from and broader than Very High State QPO observed in other sources. The relation of the LS QPO in the sources GS 2000+25 and Cyg X-1 to that of GX 339-4 ($\nu_c = 0.8, \mathrm{FWHM} = 0.15$; Grebenev et al. 1991) is uncertain, as the energy dependence of the QPO in GX 339-4 in its Low-State is not known. The LS QPO is spectrally indistinct from the continuum variability, and may be distinguished from Very High State QPO on this basis.

10.2 Gamma-Ray Burst Conclusions

We conclude:

- Fitting log-normal models to the duration distributions of data samples drawn from the 3B Catalog (Meegan et al. 1996), we see no evidence for any distinction

between duration distributions in two different peak flux groups. The 3σ upper-limit on the factor difference between the centroid (and width) of the bright burst distribution and that of the dim burst distribution of <1.24 (T_{90}) and <1.44 (T_{50}). We estimated from a non-evolving standard-candle cosmological model that the expected factor is 1.3–1.9. Thus, our results do not exclude this scenario.

- By fitting log-normal distribution models to data samples drawn from the durations provided by J. Norris, we see that the centroids of T_{90} duration distributions drawn from "Bright" and "Dim+Dimmest" bursts are different by an additive (base-10 logarithmic) factor of $0.32^{+0.08}_{-0.07}$; the widths, however, are the same, to an additive (base-10 logarithmic) factor $-0.07^{+0.06}_{-0.07}$. We conclude that the centroids are different, while the widths are not, contrary to what is expected from a difference due exclusively to cosmological time-dilation. The quantitative results of Norris et al. (1995) are in agreement with our quantitative results, but we differ in interpretation. The results of identical analysis using T_{50} distributions are consistent with those of T_{90} distributions. When we require that the additive factors be equal, as expected if the differences are due to cosmological time dilation, the factor is limited to $0.11^{+0.094}_{-0.12}$ (99.73% confidence); thus, we find no significant difference between the two distributions. The results of the T_{50} distributions are consistent with those of the T_{90} distributions.

- Non-parametric and rank-order parametric analyses find no evidence for correlation between any of the three peak-flux measures (P_{1024}, P_{256}, P_{64}) and either of the two duration measures (T_{50}, T_{90}) in the 3B Catalog (Meegan et al. 1996). Inserting a red-shift factor of the magnitude expected from cosmological time-dilation into the data produces a significant correlation, indicating that the tests are sensitive to such correlations in these data-samples. Applying these same analyses to Norris' duration and peak-counts data, the significant correlation which we do find disappears when bursts with systematic uncertainties in du-

ration >20% of the median (∼15% of the total data sample) are excluded from analyses.

- We described a method which, in principle, could produce the peak-flux – red-shift relationship of a cosmological GRB population. We found that, in practice, the large log-normal FWHM of the duration distribution causes the median values of the red-shift distributions to drop *below* $(1 + z)$=1.0, to non-physical values. The faintest bursts produce a $(1 + z)$ distribution with median value $(1 + z)\sim 0.3$. The median $(1 + z)$ increases with increasing peak flux, and for the brightest bursts is $(1 + z)\sim 1.0$.

- We described a simplified model for jointly producing the GRB and peak-flux distributions, from a Euclidean parent population and a one-to-one luminosity–duration relationship.

- We commented on a result by Kouveliotou et al. (1996) which finds that spectrally hard GRBs have a peak-flux distribution which departs from a -3/2 power-law at higher values than the spectrally soft GRBs. This result, if confirmed, may represent the first evidence of a finite-width luminosity function for GRBs. From this, one can extract the approximate slope of the observed luminosity function, as well as the relative fraction of spectrally "hard" and "soft" bursts in the parent population.

- We investigated the consistency of the GRB peak-flux distribution with standard cosmologies, including non-evolving and evolving parent populations. The Number-peak flux distribution of GRBs observed by BATSE is consistent with a homogeneous, zero evolution source population, to a $z_{\rm max}$ most probably in the range 1.0-2.0 for GRBs with peak fluxes of ∼0.3 phot cm^{-2} sec^{-1}. The flattening at the low-flux end observed in this distribution is consistent with being due only to cosmological effects. The amount of frequency density evolution of the form $\propto (1+z)^p$ is constrained, with the exponent p <2. The amount of peak luminosity evolution of the form $\propto (1 + z)^l$ is constrained, with the exponent l

$< 2.$

Appendix A

Power Density Spectra and Their Normalization

Power Density Spectra (PDS) are used to display the amount of variability in a specific source over all timescales permitted within the information content constraints of an observation. The information content of the data excludes the possibility of quantifying variability which occurs on timescales longer than the duration (T) of the observation, or on timescales shorter than the time resolution (t_{bin}) of the observation. Such variability may, in fact, exist in a given source, but it cannot be measured from that observation.

This is typically done by representing the data, according to Fourier's theorem, as the sum of a series of sinusoidal functions.

We describe here the methods used to produce power-density spectra in this thesis.

A.1 Power Density Spectra

The generation of power density spectra in this thesis follows methods outlined by several references (Van der Klis 1989; Lewin et al. 1988; Ebisawa 1991).

During an observation, a detector will observe *counts*, which is the response of the detector to photons plus non-photonic background counts. Typically, the data

is represented by the number of counts which occurs during an elapsed time bin t_{bin}, which is the time resolution of the data. Data is accumulated in consecutive N time bins, producing as data the number of counts x_k in each time bin $k = [0, N-1]$; the total duration of such an observation is then $N\,t_{bin}$. The total number of counts is $N_{ph} = \Sigma_{k=0}^{N-1} x_k$.

One may represent this array of data x_k, with no loss of the information content of the data, as complex-valued Fourier amplitudes a_j:

$$a_j \equiv \Sigma_{k=0}^{N-1} x_k e^{2\pi i j k/N} \quad \left(j = 1,\ \frac{N}{2}\right) \tag{A.1}$$

The Fourier amplitude a_j is a complex vector. The strength of variability is related to the magnitude of this vector $|a_j|$. The word "power" is generally used to describe any value proportional to $|a_j|^2$, up to a constant of proportionality. This constant of proportionality (the normalization) may be any value at all; however, certain values, related to the mean source intensity and/or the total number of detected counts, have useful properties which aid interpretation of the PDS. Two normalizations are often used in X-ray astrophysics: the Leahy-normalization (Leahy et al. 1983, described below) and the Normalized Power Density Function (Miyamoto et al. 1994):

$$P_j = N\,t_{bin}\,2\frac{|a_j|^2}{N_{ph}^2} \tag{A.2}$$

where $N\,t_{bin}$ is the total duration of the observation (the product of number of time-bins and the time-resolution), and P_j therefore has the normalization of rms^2/Hz. The amount of power P_j which is observed is related to the strength of oscillations at a frequency $\nu_j = j/(N\,t_{bin})$, which is typically expressed in terms of the fractional root-mean-square excess (% rms) power, where by "excess" it is meant in excess of the power expected from a Poisson-distributed process. The advantage of this normalization is that a source with a constant amount of fractional variability will have the same value of P_j independent of the source intensity. Thus, one can directly compare PDS normalized this way, and immediately see differences in the variability properties.

The utility of the Leahy-normalization (Leahy et al. 1983) of PDS is that, for a Poisson dominated process, the probability of producing a value $P_{j,Leahy}$ is exactly that given by a χ^2 distribution with two degrees of freedom. A handy rule of thumb which is often used to estimate this probability is Prob $\sim e^{-P_{j,Leahy}/2}$. Thus, the *a priori* probability of producing a particular spike or broader noise feature in a PDS can be estimated on the fly. This makes the Leahy-type normalization useful in determining the significance of any particular feature (for instance, a spike due to a coherent pulsar frequency, or a broad Lorentzian due to QPO). The Leahy-normalized power is found:

$$P_{j,Leahy} = 2\frac{|a_j|^2}{N_{ph}^2} \tag{A.3}$$

The Normalized Power is related to the Leahy-normalized power by a factor equal to the mean intensity of the source during the observation:

$$P_{j,Leahy} = \frac{P_j}{N_{ph}/(N\, t_b in)} \tag{A.4}$$

Because this thesis is largely concerned with the comparative magnitudes of power, rather than the search for new features, we use almost exclusively the Normalized Power Density Spectrum (P_j).

A.2 Dead time Correction

The following was taken from a discussion by Lewin (private communication), and is partially based on information in several references (Van der Klis 1989; Dotani 1988; Mitsuda & Dotani 1989).

In data modes MPC1, 2, and 3, the detector dead time is due to analog-to-digital conversion, and is fixed to be $\tau = 206 \pm 1\mu$ sec * detector. If the incident count-rate is M_i, and the count-rate which is registered by the analog-to-digital conversion unit is M, then these count-rates are related by:

$$M = M_i(1 - \tau\, M) \tag{A.5}$$

This gives rise to the dead time correction factor (the amount by which each detected count is multiplied by to produce the number of incident counts):

$$f_{dt} = \frac{M_i}{M} = \frac{1}{1 - \tau\, M} \tag{A.6}$$

Finally, the Poisson level of a Leahy-normalized power spectrum is given by:

$$A_o(j) = 2 \times (1 - M_{c,obs}\tau)^2 \left[1 + 2\left(\frac{M_{c,obs}\tau}{1 - M_{c,obs}\tau}\right)\left(\frac{\tau}{T/N}\right)\sin^2\frac{\pi j}{N}\right] \tag{A.7}$$

where T is the total duration of the observation, N is the number of bins in the FFT, and j is the bin index, which corresponds to a frequency $\nu_j = j/T$

A.2.1 Summary of Production of Power Density Spectrum

We summarize the steps by which the Normalized Power Density Spectra in this thesis were produced.

First, using a series of raw data of N contiguous bins, a Fast-Fourier-Transform (FFT) is performed, using the *four1* implementation (Press et al. 1995). These are normalized as Normalized Power Spectral Density functions (Eq. A.2), and the dead-time corrected Poisson level, found from Eq. A.7 (divided by mean source count-rate to change its normalization from Leahy to the Normalized) is subtracted. The resulting power in each bin is corrected for detector dead-time, by multiplying the power (normalized as $\mathrm{rms}^2/\mathrm{Hz}$) by the square of the dead time correction factor f_{dt} (Eq. A.6). Finally, the correction for background is applied, by multiplying the power in each bin by the square of the ratio of the total count-rate to the background subtracted count-rate.

This results in the Normalized Power Density Spectrum, corrected for non-source background counts, detector dead time response, and Poisson counting statis-

tics.

A.3 νP Normalization

It is often illuminating to plot PDS in log Frequency-log Power space in a normalization $\nu P(\nu)$, where one multiplies the power (in units rms^2/Hz) by the frequency at which the power was observed. PDS in this normalization have the useful property that, in frequency ranges where the value of this is increasing, the %rms is divergent (integrates to $> \infty$); where the value is decreasing, the %rms is convergent. As it is physically unreasonable for the total %rms to diverge, one can see in PDS plotted in this way at what frequencies the physics of the source changes, to avoid a divergent catastrophe.

A.4 Models Used to Fit the PDS

In this section, we describe the models used in this thesis to fit to PDS.

In all cases, the models are singly dependent upon the the frequency, and are normalized with the units rms^2/Hz.

A.4.1 Lorentzian

The Lorentzian model is often employed to fit to peaked QPO power:

$$P_{\rm Lor}(\nu, A_{\rm Lor}, \Gamma, \nu_c) = \frac{A_{\rm Lor}}{\pi} \frac{(\Gamma/2)^2}{(\nu - \nu_c)^2 + (\Gamma/2)^2} \tag{A.8}$$

where ν_c is the "centroid frequency" and Γ is the Full-Width at Half-Maximum (FWHM), and $A_{\rm Lor}$ is a normalization related to the %rms variability of the feature.

A.4.2 Harmonic QPO

We at times implement a model of QPO in which several peaks are harmonically related, where the centroid frequencies and FWHM are integral powers of two of the fundamental frequency:

$$P_{\rm Har}(\nu, \Gamma, \nu_{\rm c}) = \sum_{j=-2}^{2} P_{\rm Lor}(\nu, A_{\rm Lor,j}, 2^j\Gamma, 2^j\nu_{\rm c}) \tag{A.9}$$

where Γ is the FWHM of the fundamental feature, ν_c is the centroid frequency of the fundamental feature, and $A_{\rm Lor,j}$ are five independently variable parameters which are related to the %rms variability in the individual harmonic features.

Often, using all five Lorentzian models introduces large covariances between the power of one harmonic and a broader-band feature (say, for instance, the cut-off frequency of a Flat-Top Single Power-Law Model). The covariance is manifested during the process of fitting to the best-fit model, as anomalously high (or negative) values of the %rms in the harmonic, or by causing an instability in the fitting procedure, such that the search procedure for a best-fit value loops around a local cusp. When this occurs, the harmonic is suppressed, by setting its %rms value to zero and freezing it's FWHM and centroid frequency.

A.4.3 Power Law

The Power-Law model is often used to fit to broad-band power:

$$P_{\rm pl}(\nu, A_{\rm pl}, \alpha_1) = A_{\rm pl}\ \nu^{-\alpha_1} \tag{A.10}$$

where $A_{\rm pl}$ is a constant related to the %rms variability of the feature, and α_1 is variously called the exponent or power-law slope.

A.4.4 Broken Power Law

The Broken Power Law model is employed when an anomalous decrease in power at high frequency is observed which is inconsistent with a single Power Law model:

$$P_{\rm br.pl}(\nu, \alpha_1, \alpha_2, \nu_1) \quad = A_{\rm br.pl}\nu^{-\alpha_1} \quad \nu \leq \nu_1 \tag{A.11}$$

$$= A_{\rm br.pl}\frac{\nu_1^{\alpha_2}}{\nu_1^{\alpha_1}}\nu^{-\alpha_2} \quad \nu > \nu_1$$

(A.12)

A.4.5 Flat-Top Single Power-Law

This model is a constant power below some frequency ν_1, continuous with a power-law model at frequencies higher than ν_1.

$$P_{\rm ft.pl}(\nu, A_{\rm ft.pl}, \alpha_1, \nu_1) \quad = A_{\rm ft.pl} \quad \nu \leq \nu_1 \tag{A.13}$$

$$= \frac{A_{\rm ft.pl}}{\nu_1^{-\alpha_1}}\,\nu^{-\alpha_1} \quad \nu > \nu_1$$

A.4.6 Flat-Top Broken Power-Law

This model is constant below some frequency ν_1, continuous with a power-law model with a power-law slope α_1 between the frequency ν_1 and ν_2, continuous with a power-law model with a slope α_2 at frequencies $\nu > \nu_2$.

$$P_{\rm ft.br.pl}(\nu, A_{\rm ft.br.pl}, \alpha_1, \nu_1) \quad = A_{\rm ft.br.pl} \quad \nu \leq \nu_1 \tag{A.14}$$

$$= \frac{A_{\rm ft.br.pl}}{\nu_1^{-\alpha_1}}\,\nu^{-\alpha_1} \quad \nu_1 < \nu < \nu_2$$

$$= \frac{A_{\rm ft.br.pl}\nu_2^{-\alpha_1}}{\nu_1^{-\alpha_1}\nu_2^{-\alpha_2}}\,\nu^{-\alpha_2} \quad \nu > \nu_2$$

A.4.7 Flat-Top Power-Law Exponential

This model is constant below some frequency ν_1, continuous with a power-law-exponential model above with a power-law slope α_1 between the frequency ν_1 and an exponential decay frequency of ν_e:

$$P_{\text{ft.pl.exp}}(\nu, A_{\text{ft.pl.exp}}, \alpha_1, \nu_1, \nu_e) = A_{\text{ft.pl.exp}} \quad \nu \leq \nu_1 \quad \text{(A.15)}$$
$$= \frac{A_{\text{ft.pl.exp}}}{\nu_1^{-\alpha_1} \exp^{-\nu_1/\nu_e}} \nu^{-\alpha_1} \exp -\nu/\nu_e \quad \nu > \nu_1$$

A.4.8 Double Flat-Top Single Power-Law

This model describes power density spectra which are constant below some frequency ν_1, follow a power-law with slope α_1 for $\nu_1 < \nu < \nu_2$, is again a constant value at frequencies $\nu_2 < \nu < \nu_3$, and again follows a power-law with slope α_1 for $\nu > \nu_3$:

$$P_{\text{doub.ft.pl}}(\nu, A_{\text{doub.ft.pl}}, \alpha_1, \alpha_2, \nu_1, \nu_2, \nu_3) = A_{\text{doub.ft.pl}} \quad \nu \leq \nu_1 \quad \text{(A.16)}$$
$$= \frac{A_{\text{doub.ft.pl}}}{\nu_1^{-\alpha_1}} \nu^{-\alpha_1} \quad \nu_1 < \nu \leq \nu_2$$
$$= \frac{A_{\text{doub.ft.pl}} \nu_2^{-\alpha_1}}{\nu_1^{-\alpha_1}} \quad \nu_2 < \nu \leq \nu_3$$
$$= \frac{A_{\text{doub.ft.pl}} \nu_2^{-\alpha_1}}{(\nu_1 \nu_3)^{-\alpha_1}} \nu^{-\alpha_1} \quad \nu > \nu_3$$

where $A_{\text{doub.ft.pl}}$ is a normalization factor related to the %rms variability.

A.5 Approximate Background Count Rates in the Three Energy Ranges

Using data which has and has not been corrected for background, we have found *Ginga* background count-rates in the three energy ranges, as well as an approximate FWHM of the distribution of these count-rates. These were found by taking the uncorrected and the simultaneous corrected count-rate data for all 10 sources, integrated over 128 seconds, in which the total count-rate was less than 600 c/s (and, therefore, dead time corrections are negligible at the <1–2% level). The corrected count-rate had the aspect correction removed, which results in the raw count-rate corrected only for background. This was subtracted from the observed raw count-rate, and a

histogram of the difference in each energy range was produced. These distributions were roughly Lorentzian, and were therefore fit to find the peak and the FWHM, the results of which are shown in Table A.1.

The relative variance of these background count-rates is high, and thus the background count-rates listed here are only useful in projecting rough subtraction of high count-rate data.

Table A.1: Approximate Background Count Rates and Widths of Countrate Distributions

Energy Range (keV)	Background c/s	FWHM c/s
2.3–4.6	14.1	8.0
4.6–9.2	18.5	6.3
9.2–18.4	14.7	5.1

Appendix B

Observation Times

B.1 Complete Observation List

In this section, we provide a complete observation list, sorted by source, for the 10 sources which are the subject of this thesis. The list was provided by T. Dotani (private communication).

The list is provided in Table B.1. We give the source name, start time of the observation (in year day/month hh:mm UT) and end time of the observation, and the elapsed (real) time of the observation, in minutes.

Table B.1: Complete Observation List for the 10 *Ginga* BHCs

Source	Start Time (UT)[a]	End Time (UT)[a]	Elapsed Time (minutes)
LMC X-3	87 3/5 16:59	3/5 18:37	98
	88 1/8 4:56	1/9 10:18	1762
	89 9/15 21:54	9/16 3:02	307
	89 10/20 13:40	10/20 18:11	271
	89 12/9 1:43	12/9 6:40	298
	89 12/14 4:18	12/14 5:30	72
	89 12/19 29:37	12/21 2:58	1821
	89 12/26 17:40	12/27 17:51	1451
	90 1/12 12:44	1/12 16:07	202
	90 1/28 1:23	1/28 4:36	193
	90 2/16 22:53	2/18 4:55	1802
	90 2/26 10:53	2/26 17:08	374
	90 3/12 5:57	3/12 7:36	100
	90 3/18 2:54	3/19 11:13	1938
LMC X-1	87 4/22 16:39	4/23 14:40	1320
	87 7/16 4:16	7/16 11:22	425
	87 9/30 14:58	10/1 8:15	1037
	88 10/18 31:21	10/18 14:12	51
GS 2023+33	89 5/23 9:27	5/23 21:44	737
	89 5/29 15:37	5/30 16:03	1465
	89 6/1 14:44	6/2 23:05	1941
	89 6/3 6:11	6/5 4:05	2753
	89 6/9 19:43	6/10 2:14	391
	89 6/18 17:32	6/19 17:28	1435
	89 6/20 14:08	6/21 4:07	839
	89 7/6 6:31	7/6 17:11	640
	89 7/20 0:29	7/20 7:14	405
	89 7/21 0:25	7/21 3:45	200
	89 7/21 22:40	7/22 5:23	403
	89 11/1 0:07	11/2 0:00	1432
	90 8/16 0:22	8/16 20:42	1220
GS 2000+25	88 4/26 21:09	4/26 21:57	49
	88 4/27 1:03	4/27 6:11	308
	88 4/28 2:57	4/28 9:40	402
	88 4/29 1:17	4/29 4:34	197
	88 4/30 1:42	4/30 4:53	190
	88 5/1 23:53	5/2 4:51	298
	88 5/2 23:58	5/3 4:57	299
	88 5/4 0:02	5/4 5:03	300
	88 5/4 23:38	5/5 3:27	298
	88 5/4 5:25	5/4 5:38	13
	88 5/5 22:32	5/6 1:51	198
	88 5/6 22:40	5/7 2:17	217
	88 5/8 21:09	5/9 0:24	195
	88 5/10 19:42	5/10 22:38	175
	88 5/13 18:15	5/13 21:30	194
	88 5/17 18:35	5/17 20:46	130
	88 5/18 18:27	5/18 20:46	138
	88 6/1 9:43	6/1 13:15	211
	88 6/15 2:41	6/15 7:16	274
	88 6/21 23:49	6/22 3:07	198
	88 6/23 22:21	6/24 1:49	207
	88 6/26 20:53	6/27 1:43	289
	88 8/3 3:57	8/3 7:12	195
	88 9/8 15:45	9/8 17:25	100
	88 10/3 22:05	10/3 23:04	59
	88 10/4 0:40	10/4 3:42	181
	88 10/5 0:43	10/5 3:44	180
	88 10/18 14:21	10/19 14:14	1433
	88 11/5 8:55	11/7 5:05	2123
	88 12/7 14:40	12/9 13:44	2824
	88 12/16 9:32	12/17 1:31	958
	88 5/15 10:30	5/15 23:40	789
GX 339-4	88 9/3 13:36	9/7 10:40	512
	89 8/28 7:57	8/29 1:28	105
	89 9/28 14:12	10/1 1:39	356
	91 9/10 14:18	9/2 9:02	256
GS 1124-68	91 1/11 0:34	1/11 1:30	7
	91 1/11 19:16	1/12 1:30	37
	91 1/13 21:37	1/14 0:32	17
	91 1/14 19:30	1/15 0:04	27
	91 1/16 18:40	1/16 23:25	28
	91 1/17 16:22	1/17 22:44	38
	91 1/18 17:29	1/18 21:58	26
	91 1/20 14:58	1/20 17:59	18
	91 1/22 17:18	1/22 20:44	20
	91 1/24 13:04	1/24 14:38	9
	91 2/5 10:34	2/5 13:24	16
	91 2/6 6:39	2/6 13:00	38
	91 2/13 4:42	2/13 9:17	27
	91 2/14 4:11	2/14 7:23	19
	91 2/20 23:00	2/21 3:53	29
	91 2/25 20:26	2/26 1:41	31
	91 2/26 20:07	2/27 0:45	27
	91 3/8 14:27	3/8 19:59	33
	91 3/10 13:22	3/10 18:54	33
	91 3/12 12:57	3/12 18:39	34
	91 3/18 10:25	3/18 15:23	29
	91 3/19 9:53	3/19 16:37	40
	91 3/20 7:42	3/20 14:14	39
	91 3/28 5:13	3/28 9:45	27
	91 3/29 4:06	3/29 8:28	26
	91 3/30 3:29	3/30 10:13	40
	91 4/2 3:10	4/2 6:09	17
	91 4/19 17:24	4/19 21:21	23
	91 5/17 2:52	5/17 8:32	34
	91 5/18 2:15	5/18 5:51	21
	91 6/13 15:26	6/13 18:24	17
	91 6/21 9:01	6/21 15:20	37
	91 7/21 16:58	7/21 23:02	36
	91 7/22 16:21	7/22 17:36	7
	91 7/23 20:10	7/23 21:12	6
	91 8/9 7:30	8/9 1:12	22
	91 9/2 17:51	9/3 14:52	126
	91 9/24 7:20	9/25 1:36	109
	91 10/16 19:37	10/17 0:25	28
	91 10/17 4:01	10/17 21:26	104
1353-64	87 7/13 1:19	7/14 17:22	240
1826-24	88 9/9 14:14	9/9 15:33	7
	88 9/10 12:37	9/10 13:55	7
	88 9/15 7:37	9/15 11:00	20
	88 9/16 7:55	9/16 11:03	18
	88 9/16 7:40	9/16 7:54	1
1630-47	87 10/17 6:23	10/18 3:24	126
	88 4/10 12:57	4/11 4:45	94
	88 10/3 23:08	10/4 00:22	7
	88 10/4 23:08	10/5 00:25	7
CYG X-1	87 8/5 7:15	8/5 19:50	75
	87 8/6 10:15	8/8 14:01	310
	90 5/9 1:35	5/11 23:06	417
	91 6/5 17:13	6/6 21:12	167

[a] Format is year month/day time

B.2 Detailed Observation Times of Raw Data

This section contains tables listing the *Ginga* LAC data from which the raw data used in the power density spectral analyses for the black hole candidates (1354-64, 1826-24, 1630-47, LMC X-1, LMC X-3, GS 2000+25, GS 2023+33, GS 1124-68, Cyg X-1, and GX 339-4) were drawn. The observational periods are those contiguous periods for which a data file was produced.

This is a complete listing of the raw data, from which the data which were analyzed were selected. Periods which are not included below were not used in the analyses. Thus, observation periods which overlap with other observation periods (which were therefore later selected out) are listed, and still others may contain spikes, drop-outs, or other problems which cause them to be excluded from the final analyses.

The date is listed in tabular form, giving the start time (YY/DOY HH:MM:SS UT) and end time of the observational period, the total time of the observation (in seconds), the time resolution of the observation (in seconds), and the data mode during the observation (P1=MPC1, P2=MPC2, P3=MPC3).

Table B.2: Detailed Observation Times of Raw Data – 1/6

Start Time (UT)	End Time (UT)	Dur. (s)	Time Res. (s)	Mode
1826-24				
88/253 14:14:51	88/253 14:15:08	17	0.0625	P2
88/253 14:15:08	88/253 14:22:08	420	0.0625	P2
88/253 15:16:11	88/253 15:21:00	289	0.5000	P2
88/253 15:21:31	88/253 15:33:00	689	0.0625	P2
88/254 12:38:11	88/254 12:51:24	793	0.0625	P2
88/254 13:42:19	88/254 13:43:24	65	0.5000	P2
88/254 13:43:23	88/254 13:53:28	605	0.0625	P2
88/254 13:53:31	88/254 13:55:03	92	0.0625	P2
88/260 07:54:03	88/260 07:54:32	29	0.0078	P3
88/260 07:55:23	88/260 07:56:55	92	0.0078	P3
88/260 07:56:59	88/260 07:57:19	20	0.0078	P3
88/260 07:57:31	88/260 08:00:47	196	0.0078	P3
88/260 08:11:27	88/260 08:31:00	1173	0.0078	P3
88/260 09:09:07	88/260 09:20:24	677	0.0078	P3
88/260 09:22:55	88/260 09:23:03	8	0.0078	P3
88/260 09:23:23	88/260 09:29:00	337	0.0078	P3
88/260 09:31:07	88/260 09:34:32	205	0.0078	P3
88/260 09:34:35	88/260 09:42:56	501	0.0078	P3
88/260 09:41:31	88/260 10:06:59	1528	0.0078	P3
88/260 10:47:07	88/260 10:51:03	236	0.0078	P3
88/260 10:51:07	88/260 11:01:16	609	0.0078	P3
88/260 11:01:19	88/260 11:03:24	125	0.0625	P3
1354-64				
87/194 05:31:36	87/194 05:32:08	32	0.0625	P2
87/194 05:32:12	87/194 05:53:29	1277	0.5000	P2
87/194 07:02:16	87/194 07:27:53	1537	0.5000	P2
87/194 08:38:48	87/194 09:01:44	1376	0.5000	P2
87/194 10:14:48	87/194 10:38:17	1409	0.5000	P2
87/194 11:02:16	87/194 11:16:09	833	0.5000	P2
87/194 11:51:20	87/194 12:14:16	1376	0.5000	P2
87/194 12:40:24	87/194 12:52:40	736	0.5000	P2
87/194 13:27:52	87/194 13:50:17	1345	0.5000	P2
87/194 14:18:32	87/194 14:28:09	577	0.5000	P2
87/194 15:04:24	87/194 15:27:53	1409	0.5000	P2
87/194 15:55:04	87/194 16:06:16	672	0.5000	P2
87/194 16:44:08	87/194 17:00:08	960	0.5000	P2
87/194 17:32:08	87/194 17:42:17	609	0.5000	P2
87/194 19:08:08	87/194 19:18:17	609	0.5000	P2
87/194 22:24:24	87/194 22:30:49	385	0.5000	P2
87/194 23:06:00	87/194 23:24:09	1089	0.0625	P3
87/195 00:02:00	87/195 00:06:49	289	0.0625	P3
87/195 00:42:32	87/195 01:06:00	1408	0.0625	P3
87/195 01:40:40	87/195 01:43:20	160	0.0625	P3
87/195 02:19:04	87/195 02:47:21	1697	0.0625	P3
87/195 03:18:16	87/195 03:19:53	97	0.0625	P3
87/195 03:55:12	87/195 03:57:12	120	0.0078	P3
87/195 03:55:12	87/195 03:57:12	120	0.0078	P3
87/195 03:57:12	87/195 04:22:49	1537	0.0625	P3
87/195 05:33:32	87/195 05:34:31	59	0.0078	P3
87/195 05:34:32	87/195 05:39:00	268	0.0625	P2
87/195 05:41:12	87/195 05:59:20	1088	0.5000	P2
87/195 07:08:08	87/195 07:30:33	1345	0.5000	P2
87/195 07:56:08	87/195 07:58:49	161	0.5000	P2
87/195 08:44:40	87/195 09:07:05	1345	0.5000	P2
87/195 09:33:44	87/195 09:45:29	705	0.5000	P2
87/195 10:20:40	87/195 10:43:05	1345	0.5000	P2
87/195 11:07:04	87/195 11:22:01	897	0.5000	P2
87/195 11:57:12	87/195 12:19:05	1313	0.5000	P2
87/195 12:45:12	87/195 12:58:00	768	0.5000	P2
87/195 13:33:44	87/195 13:55:04	1280	0.5000	P2
87/195 14:23:20	87/195 14:34:32	672	0.5000	P2
87/195 15:10:16	87/195 15:28:57	1121	0.5000	P2
87/195 16:01:28	87/195 16:11:05	577	0.5000	P2
87/195 16:49:28	87/195 17:01:13	705	0.5000	P2
87/195 17:37:28	87/195 17:47:05	577	0.5000	P2
1630-47				
87/290 06:23:08	87/290 06:36:07	779	4.0000	P1
87/290 06:48:03	87/290 06:50:04	121	0.5000	P1
87/290 06:48:11	87/290 06:51:25	194	0.5000	P1
87/290 06:53:20	87/290 07:08:52	932	16.0000	P1
87/290 07:55:12	87/290 08:48:52	3220	16.0000	P1
87/290 09:33:20	87/290 10:25:16	3116	16.0000	P1
87/290 11:11:28	87/290 11:52:08	2440	16.0000	P1
87/290 12:53:52	87/290 13:34:32	2440	16.0000	P1
87/290 14:38:24	87/290 15:14:44	2180	16.0000	P1
87/290 16:18:40	87/290 16:35:56	1036	16.0000	P1
87/290 17:58:56	87/290 18:07:32	516	16.0000	P1
87/290 21:17:20	87/290 21:21:36	256	16.0000	P1
1630-47 (cont.)				
87/291 00:00:35	87/291 00:06:20	345	0.5000	P1
87/291 01:46:55	87/291 01:49:39	164	0.5000	P1
87/291 01:48:19	87/291 01:50:05	106	0.5000	P1
87/291 02:04:28	87/291 02:15:43	675	4.0000	P1
88/101 12:57:29	88/101 13:01:37	248	0.0625	P2
88/101 13:21:13	88/101 13:38:53	1060	0.0625	P2
88/101 14:34:17	88/101 14:35:25	68	0.0625	P2
88/101 14:37:41	88/101 14:47:29	588	0.0625	P2
88/101 14:47:21	88/101 15:00:17	776	0.0625	P2
88/101 15:00:29	88/101 15:16:49	980	0.0625	P2
88/101 16:10:01	88/101 16:14:57	296	0.0625	P2
88/101 16:16:41	88/101 16:19:17	156	0.0625	P2
88/101 16:19:29	88/101 16:53:53	2064	0.0625	P2
88/101 17:51:05	88/101 17:56:53	348	0.0625	P2
88/101 17:59:05	88/101 18:04:17	312	0.0625	P2
88/101 18:04:29	88/101 18:11:05	396	0.0625	P2
88/101 18:12:52	88/101 18:29:25	993	0.5000	P2
88/101 19:24:52	88/101 20:09:42	2690	0.5000	P2
88/101 21:06:44	88/101 21:36:37	1793	0.5000	P2
88/101 22:42:44	88/101 23:13:42	1858	0.5000	P2
88/102 00:23:00	88/102 00:49:41	1601	0.5000	P2
88/102 02:01:08	88/102 02:21:58	1250	0.5000	P2
Cyg X-1				
87/217 11:43:06	87/217 11:44:30	84	0.0625	P2
87/217 11:44:42	87/217 11:51:50	428	0.0625	P2
87/217 11:52:14	87/217 11:53:30	76	0.0625	P2
87/217 12:12:10	87/217 12:24:38	748	0.0625	P2
87/217 13:03:30	87/217 13:06:42	192	0.0625	P2
87/217 13:06:46	87/217 13:21:58	912	0.0625	P2
87/220 13:22:14	87/220 13:33:22	668	0.0625	P2
87/220 13:33:38	87/220 13:41:50	492	0.0625	P2
87/220 13:45:50	87/220 13:46:58	68	0.0625	P2
87/220 13:47:02	87/220 13:55:22	500	0.0625	P2
90/129 01:35:36	90/129 01:36:16	40	0.0078	P3
90/129 01:36:28	90/129 01:47:36	668	0.0078	P3
90/129 02:49:16	90/129 03:07:56	1120	0.0078	P3
90/129 03:13:12	90/129 03:14:12	60	0.0078	P3
90/129 03:15:15	90/129 03:20:13	298	0.5000	P1
90/129 03:20:20	90/129 03:25:16	296	0.0078	P3
90/129 03:25:24	90/129 03:25:48	24	0.0078	P3
90/129 04:25:24	90/129 04:48:48	1404	0.0078	P3
90/129 04:54:32	90/129 04:55:08	36	0.0078	P3
90/129 04:55:15	90/129 04:58:04	169	0.5000	P1
90/129 04:58:15	90/129 05:00:24	129	0.5000	P1
90/129 05:00:32	90/129 05:00:48	16	0.0078	P3
90/129 06:03:08	90/129 06:30:56	1668	0.0078	P3
90/129 06:35:20	90/129 06:35:44	24	0.0078	P3
90/130 01:22:24	90/130 01:26:56	272	0.0078	P3
90/130 02:32:12	90/130 02:50:56	1124	0.0078	P3
90/130 02:56:24	90/130 02:57:28	64	0.0078	P3
90/130 03:02:28	90/130 03:08:32	364	0.0078	P3
90/130 03:08:36	90/130 03:09:32	56	0.0078	P3
90/130 04:08:04	90/130 04:32:56	1492	0.0078	P3
90/130 04:37:12	90/130 04:38:04	52	0.0078	P3
90/130 04:38:11	90/130 04:43:25	314	0.5000	P1
90/130 04:44:12	90/130 04:44:28	16	0.0078	P3
90/130 05:44:28	90/130 06:14:08	1780	0.0078	P3
90/130 21:44:24	90/130 21:49:04	280	0.0078	P3
90/130 21:49:08	90/130 21:49:16	8	0.0078	P3
90/130 21:49:28	90/130 21:50:48	80	0.0078	P3
90/130 23:11:08	90/130 23:15:00	232	0.0078	P3
90/130 23:18:16	90/130 23:20:04	108	0.0078	P3
90/130 23:22:51	90/130 23:26:44	233	0.5000	P1
90/130 23:26:52	90/130 23:30:24	212	0.0078	P3
90/130 23:29:12	90/130 23:31:04	112	0.0078	P3
90/131 00:39:08	90/131 00:54:56	948	0.0078	P3
90/131 00:59:04	90/131 01:00:00	56	0.0078	P3
90/131 01:01:11	90/131 01:06:44	333	0.5000	P1
90/131 01:06:52	90/131 01:10:52	240	0.0078	P3
90/131 01:11:00	90/131 01:18:16	436	0.0078	P3
90/131 02:15:08	90/131 02:36:56	1308	0.0078	P3
90/131 02:39:36	90/131 02:40:52	76	0.0078	P3
90/131 02:40:59	90/131 02:42:45	106	0.5000	P1
90/131 02:42:55	90/131 02:47:40	285	0.5000	P1
90/131 02:47:48	90/131 02:51:56	248	0.0078	P3
90/131 02:50:12	90/131 02:53:08	176	0.0078	P3
90/131 03:52:12	90/131 04:18:00	1548	0.0078	P3
90/131 04:20:24	90/131 04:26:00	336	0.0078	P3

Table B.3: Detailed Observation Times of Raw Data – 2/6

Start Time (UT)	End Time (UT)	Dur. (s)	Time Res. (s)	Mode
Cyg X-1 (cont)				
90/131 04:26:12	90/131 04:28:04	112	0.0078	P3
91/156 18:00:26	91/156 19:32:54	5548	4.0000	P1
91/156 18:14:10	91/156 18:21:22	432	4.0000	P1
91/156 18:16:34	91/156 18:24:48	494	4.0000	P1
91/156 18:17:42	91/156 18:20:44	182	4.0000	P1
91/156 18:18:10	91/156 18:19:14	64	0.0078	P3
91/156 18:19:18	91/156 18:25:50	392	0.0078	P3
91/156 19:31:38	91/156 19:37:42	364	0.0078	P3
91/156 19:39:54	91/156 19:50:46	652	0.0078	P3
91/156 19:51:50	91/156 19:52:50	60	0.0078	P3
91/156 19:52:58	91/156 20:13:41	1243	4.0000	P1
91/156 19:55:42	91/156 20:23:42	1680	4.0000	P1
91/156 19:59:18	91/156 20:02:22	184	0.0078	P3
91/156 20:03:02	91/156 20:16:14	792	0.0078	P3
91/156 21:06:34	91/156 21:22:54	980	0.0078	P3
91/156 21:23:06	91/156 21:29:54	408	0.0078	P3
91/156 21:30:30	91/156 21:31:30	60	0.0078	P3
91/156 21:31:38	91/156 21:39:52	494	4.0000	P1
91/156 21:32:50	91/156 21:57:42	1492	4.0000	P1
91/156 21:35:58	91/156 21:51:29	931	4.0000	P1
91/156 21:38:02	91/156 21:41:04	182	4.0000	P1
91/156 21:38:30	91/156 21:40:50	140	0.0078	P3
91/156 21:41:06	91/156 21:52:10	664	0.0078	P3
91/156 22:40:22	91/156 23:07:54	1652	0.0078	P3
91/156 23:09:26	91/156 23:10:26	60	0.0078	P3
91/156 23:10:34	91/157 00:16:00	3926	4.0000	P1
91/157 15:51:22	91/157 15:59:36	494	4.0000	P1
91/157 15:52:30	91/157 16:14:15	1305	4.0000	P1
91/157 15:55:14	91/157 16:00:14	300	0.0078	P3
91/157 17:14:34	91/157 17:25:58	684	0.0078	P3
91/157 17:27:18	91/157 17:28:10	52	0.0078	P3
91/157 17:28:18	91/157 17:44:51	993	4.0000	P1
91/157 17:30:30	91/157 17:56:25	1555	4.0000	P1
91/157 17:33:46	91/157 17:37:50	244	4.0000	P1
91/157 17:34:18	91/157 17:36:58	160	0.0078	P3
91/157 18:49:26	91/157 18:51:58	152	0.0078	P3
91/157 18:53:30	91/157 18:53:46	16	0.0078	P3
91/157 19:02:10	91/157 19:04:58	168	0.0078	P3
91/157 19:05:18	91/157 19:06:26	68	0.0078	P3
91/157 19:06:34	91/157 19:16:53	619	4.0000	P1
91/157 19:07:58	91/157 19:28:41	1243	4.0000	P1
91/157 19:10:42	91/157 19:15:49	307	4.0000	P1
91/157 19:11:30	91/157 19:44:42	1992	4.0000	P1
91/157 19:17:10	91/157 21:40:36	8606	4.0000	P1
91/157 20:22:14	91/157 21:47:26	5112	4.0000	P1
91/157 20:32:54	91/157 22:02:15	5361	4.0000	P1
91/157 20:44:06	91/157 21:39:08	3302	4.0000	P1
91/157 20:51:10	91/157 23:06:17	8107	4.0000	P1
GS 1124-68				
91/011 00:51:28	91/011 01:16:44	1516	0.0625	P2
91/011 19:16:40	91/011 19:18:12	92	0.0625	P2
91/011 19:37:00	91/011 19:45:52	532	0.0625	P2
91/011 20:26:08	91/011 20:32:48	400	0.0625	P2
91/011 20:32:52	91/011 20:41:56	544	0.0625	P2
91/011 20:49:12	91/011 20:55:32	380	0.0078	P3
91/011 20:54:20	91/011 20:57:56	216	0.0078	P3
91/011 21:16:16	91/011 21:25:52	576	0.0078	P3
91/011 22:00:08	91/011 22:09:28	560	0.0078	P3
91/011 22:09:32	91/011 22:16:12	400	0.0078	P3
91/011 22:17:52	91/011 22:21:48	236	0.0078	P3
91/011 22:26:16	91/011 22:27:24	68	0.0078	P3
91/011 22:27:36	91/011 22:35:40	484	0.0078	P3
91/011 23:00:16	91/011 23:05:56	340	0.0078	P3
91/011 23:38:08	91/012 00:01:56	1428	0.0078	P3
91/012 00:03:40	91/012 00:05:12	92	0.0078	P3
91/013 21:33:15	91/013 21:43:24	609	0.5000	P1
91/013 21:37:43	91/013 21:51:04	801	0.5000	P1
91/013 21:52:31	91/013 23:36:33	6242	0.5000	P1
91/013 22:05:35	91/013 22:55:12	2977	0.5000	P1
91/013 22:52:15	91/014 00:41:35	6560	0.5000	P1
91/013 23:09:59	91/013 23:46:47	2208	0.5000	P1
91/013 23:14:47	91/013 23:49:29	2082	0.5000	P1
91/013 23:18:19	91/014 03:47:07	16128	0.5000	P1
91/014 19:48:16	91/014 20:03:56	940	0.0625	P2
91/014 20:40:28	91/014 20:50:28	600	0.0625	P2
91/014 20:55:16	91/014 20:57:44	148	0.0625	P2
91/014 20:58:52	91/014 21:00:08	76	0.0625	P2
91/014 21:02:36	91/014 21:04:48	132	0.0625	P2
91/014 21:05:00	91/014 21:11:08	368	0.0625	P2
91/014 22:41:08	91/014 22:45:36	268	0.0625	P2
91/014 22:45:48	91/014 22:50:56	308	0.0625	P2
91/014 23:05:36	91/014 23:11:16	340	0.0625	P2
91/014 23:11:28	91/014 23:24:56	808	0.0625	P2
91/016 18:46:16	91/016 19:06:32	1216	0.0625	P2
91/016 19:07:56	91/016 19:09:36	100	0.0625	P2
91/016 20:02:36	91/016 20:04:48	132	0.0625	P2
91/016 20:06:16	91/016 20:14:40	504	0.0625	P2
91/016 20:13:16	91/016 20:15:16	120	0.0625	P2
91/016 21:46:32	91/016 21:48:56	144	0.0625	P2
91/016 21:49:08	91/016 22:15:56	1608	0.0625	P2
91/016 22:16:00	91/016 22:21:08	308	0.0625	P2
91/016 23:23:08	91/016 23:25:04	116	0.0625	P2
91/016 23:25:16	91/016 23:26:36	80	0.0625	P2
91/017 16:22:31	91/017 16:25:56	205	0.0625	P2
91/017 17:58:31	91/017 18:00:48	137	0.0625	P2
91/017 18:01:11	91/017 18:06:11	300	0.0625	P2
91/017 18:05:15	91/017 18:08:28	193	0.0625	P2
91/017 18:16:47	91/017 18:36:52	1205	0.0625	P2
91/017 19:34:19	91/017 19:36:40	141	0.0625	P2
91/017 19:36:51	91/017 19:46:08	557	0.0625	P2
91/017 19:46:03	91/017 20:20:56	2093	0.0625	P2
91/017 21:14:19	91/017 21:19:04	285	0.0625	P2
91/017 21:19:15	91/017 21:20:40	85	0.0625	P2
91/017 21:20:43	91/017 21:26:00	317	0.0625	P2
91/017 21:24:27	91/017 21:48:40	1453	0.0625	P2
91/017 21:48:51	91/017 21:56:44	473	0.0625	P2
91/018 15:55:27	91/018 15:57:39	132	0.0625	P2
91/018 17:30:35	91/018 17:36:12	337	0.0625	P2
91/018 17:49:59	91/018 18:05:39	940	0.0625	P2
91/018 18:06:27	91/018 18:09:56	209	0.0625	P2
91/018 19:05:47	91/018 19:08:08	141	0.0625	P2
91/018 19:08:19	91/018 19:17:39	560	0.0625	P2
91/018 19:16:27	91/018 19:49:56	2009	0.0625	P2
91/018 20:46:03	91/018 20:50:36	273	0.0625	P2
91/018 20:50:47	91/018 20:57:35	408	0.0625	P2
91/018 20:56:27	91/018 21:17:59	1292	0.0625	P2
91/018 21:18:11	91/018 21:27:07	536	0.0625	P2
91/020 14:58:51	91/020 15:00:44	113	0.0625	P2
91/020 14:59:23	91/020 15:03:56	273	0.0625	P2
91/020 15:17:19	91/020 15:34:48	1049	0.0625	P2
91/020 16:30:03	91/020 16:31:32	89	0.0625	P2
91/020 16:34:31	91/020 16:40:51	380	0.0625	P2
91/020 16:39:23	91/020 16:43:47	264	0.0625	P2
91/020 16:50:07	91/020 17:08:20	1093	0.0625	P2
91/020 17:09:11	91/020 17:14:55	344	0.0625	P2
91/022 17:18:59	91/022 17:23:31	272	0.0078	P3
91/022 17:23:23	91/022 17:57:56	2073	0.0078	P3
91/022 18:24:11	91/022 18:31:56	465	0.0078	P3
91/022 19:03:23	91/022 19:35:55	1952	0.0078	P3
91/022 20:00:11	91/022 20:04:07	236	0.0078	P3
91/022 20:04:19	91/022 20:09:55	336	0.0078	P3
91/022 20:35:55	91/022 21:19:39	2624	0.5000	P1
91/024 13:23:39	91/024 13:38:55	916	0.0625	P2
91/024 14:15:27	91/024 14:26:55	688	0.0625	P2
91/025 12:48:31	91/025 12:56:43	492	0.0078	P3
91/025 12:56:51	91/025 13:09:55	784	0.0078	P3
91/025 13:46:35	91/025 13:55:55	560	0.0078	P3
91/036 10:34:55	91/036 11:01:15	1580	0.0078	P3
91/036 11:01:19	91/036 11:06:59	340	0.0078	P3
91/036 11:33:11	91/036 11:36:43	212	0.0078	P3
91/037 07:10:19	91/037 08:11:07	3648	0.5000	P1
91/037 07:52:11	91/037 08:47:40	3329	0.5000	P1
91/037 08:32:27	91/037 09:57:47	5120	0.5000	P1
91/037 08:43:27	91/037 08:59:27	960	0.5000	P1
91/037 08:46:35	91/037 10:01:15	4480	0.5000	P1
91/037 10:05:43	91/037 10:35:07	1764	0.0078	P3
91/037 10:35:19	91/037 10:36:55	96	0.0078	P3
91/037 11:05:11	91/037 11:07:07	116	0.0078	P3
91/037 11:39:43	91/037 11:41:31	108	0.0078	P3
91/037 11:42:19	91/037 11:44:51	152	0.0078	P3
91/037 11:45:03	91/037 12:13:31	1708	0.0078	P3
91/044 05:04:55	91/044 05:17:51	776	0.0625	P2
91/044 05:18:19	91/044 05:23:55	336	0.0625	P2
91/044 06:39:19	91/044 07:00:27	1268	0.0625	P2
91/044 07:00:35	91/044 07:04:55	260	0.0625	P2
91/044 08:12:59	91/044 08:20:19	440	0.0625	P2
91/044 08:20:23	91/044 08:38:03	1060	0.0625	P2
91/045 04:34:43	91/045 07:00:20	8737	0.5000	P1

Table B.4: Detailed Observation Times of Raw Data – 3/6

Start Time (UT)	End Time (UT)	Dur. (s)	Time Res. (s)	Mode
GS 1124-68 (cont.)				
91/045 05:30:03	91/045 05:49:15	1152	0.5000	P1
91/045 05:32:39	91/045 05:48:08	929	0.5000	P1
91/045 06:11:43	91/045 06:35:03	1400	0.0078	P3
91/045 07:01:15	91/045 07:05:03	228	0.0078	P3
91/045 07:07:03	91/045 07:08:55	112	0.0078	P3
91/045 07:43:03	91/045 07:49:55	412	0.0078	P3
91/045 07:50:35	91/045 08:06:11	936	0.0078	P3
91/045 08:06:31	91/045 08:07:47	76	0.0078	P3
91/045 08:08:43	91/045 08:10:03	80	0.0078	P3
91/051 23:29:55	91/051 23:37:03	428	0.0625	P2
91/052 00:23:23	91/052 00:30:35	432	0.0625	P2
91/052 01:03:51	91/052 01:15:35	704	0.0078	P3
91/052 01:15:39	91/052 01:17:55	136	0.0078	P3
91/052 01:58:19	91/052 02:03:55	336	0.0078	P3
91/052 02:37:51	91/052 02:57:55	1204	0.0078	P3
91/052 03:32:11	91/052 03:37:51	340	0.0078	P3
91/053 00:33:15	91/053 00:41:47	512	0.0625	P2
91/053 00:41:51	91/053 00:44:55	184	0.0625	P2
91/053 01:25:19	91/053 01:34:15	536	0.0625	P2
91/053 02:07:15	91/053 02:13:07	352	0.0078	P3
91/053 02:13:11	91/053 02:24:55	704	0.0078	P3
91/053 02:59:11	91/053 03:08:15	544	0.0078	P3
91/053 03:41:11	91/053 04:03:59	1368	0.0078	P3
91/053 04:32:31	91/053 04:42:11	580	0.0078	P3
91/056 20:56:31	91/056 20:59:55	204	0.0625	P2
91/056 21:36:11	91/056 21:51:59	948	0.0625	P2
91/056 23:30:23	91/056 23:31:55	92	0.0078	P3
91/057 00:04:11	91/057 00:20:55	1004	0.0078	P3
91/057 00:59:11	91/057 01:06:11	420	0.0078	P3
91/057 20:24:43	91/057 20:30:55	372	0.0625	P2
91/057 21:03:11	91/057 21:10:39	448	0.0625	P2
91/057 21:10:43	91/057 21:22:59	736	0.0625	P2
91/057 21:25:15	91/057 21:26:47	92	0.0625	P2
91/057 21:58:43	91/057 22:08:59	616	0.0078	P3
91/057 22:39:11	91/057 22:53:43	872	0.0078	P3
91/057 22:56:43	91/057 23:00:23	220	0.0078	P3
91/058 00:19:11	91/058 00:34:55	944	0.0078	P3
91/067 14:28:14	91/067 14:29:31	77	0.0625	P2
91/067 14:29:34	91/067 14:31:22	108	0.0625	P2
91/067 16:04:26	91/067 16:33:47	1761	0.0625	P2
91/067 16:37:54	91/067 16:39:54	120	0.0625	P2
91/067 17:42:26	91/067 17:44:50	144	0.0625	P2
91/067 17:45:50	91/067 17:50:19	269	0.0625	P2
91/067 17:52:58	91/067 18:00:31	453	0.0625	P2
91/067 18:00:42	91/067 18:21:06	1224	0.0625	P2
91/067 19:08:14	91/067 19:17:55	581	0.0625	P2
91/067 19:20:51	91/067 19:23:23	152	0.0078	P3
91/067 19:24:43	91/067 19:29:51	308	0.0078	P3
91/067 19:29:15	91/067 19:51:55	1360	0.0078	P3
91/067 19:51:59	91/067 19:54:55	176	0.0078	P3
91/069 13:22:51	91/069 13:25:11	140	0.0625	P2
91/069 14:54:35	91/069 14:56:07	92	0.0625	P2
91/069 14:57:11	91/069 15:01:19	248	0.0625	P2
91/069 15:01:23	91/069 15:04:59	216	0.0625	P2
91/069 15:03:23	91/069 15:27:31	1448	0.0625	P2
91/069 15:28:11	91/069 15:30:59	168	0.0625	P2
91/069 15:31:03	91/069 15:35:15	252	0.0625	P2
91/069 16:33:31	91/069 16:35:51	140	0.0625	P2
91/069 16:36:03	91/069 16:44:15	492	0.0625	P2
91/069 16:43:39	91/069 17:16:55	1996	0.0625	P2
91/069 18:13:15	91/069 18:15:31	136	0.0625	P2
91/069 18:16:43	91/069 18:18:31	108	0.0078	P3
91/069 18:18:39	91/069 18:23:51	312	0.0078	P3
91/069 18:22:19	91/069 18:51:35	1756	0.0078	P3
91/069 18:51:39	91/069 18:53:59	140	0.0078	P3
91/071 13:32:15	91/071 13:44:23	728	0.0078	P3
91/071 13:53:42	91/071 15:03:35	4193	0.5000	P1
91/071 15:26:34	91/071 15:43:39	1025	0.5000	P1
91/071 15:30:51	91/071 15:37:39	408	0.0078	P3
91/071 15:35:23	91/071 16:08:55	2012	0.0078	P3
91/077 10:28:26	91/077 10:34:30	364	0.0625	P2
91/077 10:34:18	91/077 10:36:02	104	0.0625	P2
91/077 10:54:22	91/077 11:07:34	792	0.0625	P2
91/077 11:40:10	91/077 12:01:54	1304	0.0625	P2
91/077 12:02:50	91/077 12:04:46	116	0.0625	P2
91/077 12:05:58	91/077 12:15:14	556	0.0625	P2
91/077 12:31:26	91/077 12:35:46	260	0.0625	P2
91/077 12:35:50	91/077 12:46:54	664	0.0625	P2
91/077 13:19:10	91/077 13:38:58	1188	0.0625	P2
91/077 13:45:14	91/077 13:54:50	576	0.0078	P3
91/077 14:17:34	91/077 14:26:58	564	0.0078	P3
91/077 14:53:10	91/077 15:20:58	1668	0.0078	P3
91/077 15:21:30	91/077 15:23:30	120	0.0078	P3
91/079 09:40:14	91/079 09:57:58	1064	0.0078	P3
91/079 10:32:10	91/079 10:38:34	384	0.0078	P3
91/079 10:38:38	91/079 10:44:58	380	0.0078	P3
91/079 12:38:34	91/079 12:44:02	328	0.0625	P2
91/079 12:44:06	91/079 13:16:54	1968	0.0625	P2
91/079 13:43:10	91/079 13:46:58	228	0.0625	P2
91/087 06:29:02	91/087 07:58:39	5377	0.5000	P1
91/087 06:40:26	91/087 08:36:11	6945	0.5000	P1
91/087 08:20:10	91/087 08:25:42	332	0.0078	P3
91/087 08:25:46	91/087 08:34:42	536	0.0078	P3
91/087 09:40:26	91/087 09:54:19	833	0.5000	P1
91/088 04:25:02	91/088 04:58:06	1984	0.5000	P1
91/088 04:30:22	91/088 05:38:38	4096	0.5000	P1
91/088 05:53:50	91/088 06:50:22	3392	0.5000	P1
91/088 06:01:10	91/088 06:31:02	1792	0.5000	P1
91/088 07:26:18	91/088 07:28:58	160	0.0078	P3
91/088 07:29:14	91/088 07:57:58	1724	0.0078	P3
91/089 03:48:37	91/089 05:43:18	6881	0.5000	P1
91/089 05:18:53	91/089 05:41:50	1377	0.5000	P1
91/089 05:22:29	91/089 06:13:42	3073	0.5000	P1
91/089 06:49:26	91/089 06:57:54	508	0.0078	P3
91/089 07:10:22	91/089 07:21:54	692	0.0078	P3
91/089 07:48:10	91/089 07:51:18	188	0.0078	P3
91/089 08:23:09	91/089 08:45:02	1313	0.5000	P1
91/089 08:38:21	91/089 11:22:06	9825	0.5000	P1
91/089 09:57:41	91/089 10:54:47	3426	0.5000	P1
91/089 10:06:17	91/089 10:25:29	1152	0.5000	P1
91/092 02:50:37	91/092 03:37:33	2816	0.5000	P1
91/092 03:29:09	91/092 06:15:02	9953	0.5000	P1
91/092 04:26:37	91/092 04:52:15	1538	0.5000	P1
91/092 05:02:49	91/092 08:31:22	12513	0.5000	P1
91/092 06:01:29	91/092 06:16:59	930	0.5000	P1
91/109 19:31:29	91/109 20:39:13	4064	0.5000	P1
91/109 20:13:17	91/109 22:38:54	8737	0.5000	P1
91/137 03:12:27	91/137 05:00:11	6464	0.5000	P1
91/137 04:59:35	91/137 05:24:07	1472	0.5000	P1
91/137 06:05:24	91/137 06:07:00	96	0.0078	P3
91/137 06:08:08	91/137 06:40:08	1920	0.0078	P3
91/137 07:38:36	91/137 07:40:40	124	0.0078	P3
91/137 07:40:52	91/137 07:42:28	96	0.0078	P3
91/137 07:42:35	91/137 08:06:04	1409	0.5000	P1
91/137 07:46:47	91/137 11:30:47	13440	0.5000	P1
91/138 05:25:23	91/138 08:57:07	12704	0.5000	P1
91/164 13:19:17	91/164 15:41:41	8544	0.5000	P1
91/164 13:37:41	91/164 13:59:34	1313	0.5000	P1
91/164 14:54:49	91/164 17:24:42	8993	0.5000	P1
91/164 16:28:17	91/164 18:55:31	8834	0.5000	P1
91/164 17:21:58	91/164 17:30:58	540	0.0078	P3
91/164 18:04:10	91/164 18:14:18	608	0.0078	P3
91/172 11:06:13	91/172 11:59:34	3201	0.5000	P1
91/172 12:37:37	91/172 13:40:34	3777	0.5000	P1
91/172 13:32:09	91/172 15:13:30	6081	0.5000	P1
91/202 17:15:44	91/202 18:45:53	5409	0.5000	P1
91/203 16:25:20	91/203 17:54:24	5344	0.5000	P1
91/203 17:58:12	91/203 18:38:12	2400	0.5000	P1
91/203 18:03:24	91/203 19:12:45	4161	0.5000	P1
91/203 19:30:32	91/203 19:49:00	1108	0.0078	P3
91/204 17:07:48	91/204 18:52:20	6272	0.5000	P1
91/204 17:54:44	91/204 18:20:52	1568	0.5000	P1
91/204 17:58:40	91/204 18:17:52	1152	0.5000	P1
91/204 18:41:28	91/204 18:44:24	176	0.0078	P3
91/204 18:44:28	91/204 18:48:56	268	0.0078	P3
91/204 18:49:00	91/204 18:57:12	492	0.0078	P3
91/204 20:12:56	91/204 20:22:16	560	0.0078	P3
91/204 20:25:08	91/204 20:29:44	276	0.0078	P3
91/204 21:04:28	91/204 21:08:40	252	0.0078	P3
GS 2000+25				
88/120 02:53:03	88/120 02:54:15	72	0.0625	P2
88/120 02:54:19	88/120 02:57:19	180	0.0625	P2
88/121 04:41:03	88/121 04:46:43	340	0.0625	P2
88/122 23:53:07	88/122 23:55:03	116	0.0078	P3
88/123 01:09:07	88/123 01:25:03	956	0.0078	P3
88/123 01:25:23	88/123 01:26:56	93	0.0078	P3
88/123 01:34:11	88/123 01:34:28	17	0.0625	P2
88/123 01:34:31	88/123 01:36:59	148	0.0078	P3

Table B.5: Detailed Observation Times of Raw Data – 4/6

Start Time (UT)	End Time (UT)	Dur. (s)	Time Res. (s)	Mode
GS 2000+25 (cont.)				
88/123 02:47:51	88/123 03:06:59	1148	0.0078	P3
88/123 03:08:19	88/123 03:09:31	72	0.0078	P3
88/123 03:09:31	88/123 03:11:35	124	0.0625	P2
88/123 03:11:39	88/123 03:14:11	152	0.0625	P2
88/123 23:58:39	88/124 00:01:03	144	0.0078	P3
88/124 01:12:59	88/124 01:30:03	1024	0.0078	P3
88/124 01:31:47	88/124 01:32:44	57	0.0078	P3
88/124 01:32:47	88/124 01:33:23	36	0.0625	P2
88/124 01:33:27	88/124 01:34:39	72	0.0625	P2
88/124 01:34:43	88/124 01:40:44	361	0.0625	P2
88/124 01:40:47	88/124 01:43:03	136	0.0078	P3
88/124 02:51:51	88/124 03:06:47	896	0.0078	P3
88/124 03:08:39	88/124 03:11:03	144	0.0078	P3
88/124 03:13:23	88/124 03:14:40	77	0.0078	P3
88/124 03:14:43	88/124 03:15:39	56	0.0625	P2
88/124 03:15:43	88/124 03:21:11	328	0.0625	P2
88/125 00:02:51	88/125 00:03:41	50	0.0625	P2
88/125 00:03:43	88/125 00:07:27	224	0.0078	P3
88/125 01:18:51	88/125 01:36:03	1032	0.0078	P3
88/125 01:37:27	88/125 01:38:30	63	0.0078	P3
88/125 01:38:31	88/125 01:40:23	112	0.0625	P2
88/125 01:40:27	88/125 01:46:41	374	0.0625	P2
88/125 01:46:43	88/125 01:49:03	140	0.0078	P3
88/125 02:57:07	88/125 03:17:03	1196	0.0078	P3
88/125 03:20:03	88/125 03:20:35	32	0.0078	P3
88/125 03:20:35	88/125 03:21:55	80	0.0625	P2
88/125 03:21:59	88/125 03:26:17	258	0.0625	P2
88/127 23:53:50	88/128 00:09:02	912	0.0078	P3
88/128 00:12:10	88/128 00:13:22	72	0.0078	P3
88/128 00:13:22	88/128 00:18:39	317	0.5000	P1
88/128 00:14:06	88/128 00:23:43	577	0.5000	P1
88/128 00:15:22	88/128 00:58:14	2572	0.5000	P1
88/128 00:20:46	88/128 00:21:14	28	0.0078	P3
88/128 01:31:50	88/128 01:50:58	1148	0.0078	P3
88/128 01:54:42	88/128 01:55:17	35	0.0078	P3
88/128 01:55:18	88/128 02:08:06	768	0.5000	P1
88/128 01:56:58	88/128 03:18:03	4865	0.5000	P1
88/128 02:05:06	88/128 02:43:27	2301	0.5000	P1
88/129 22:23:54	88/129 22:38:02	848	0.0078	P3
88/129 22:41:23	88/129 22:42:31	68	0.0078	P3
88/129 22:42:34	88/129 22:55:55	801	0.5000	P1
88/129 22:44:18	88/129 23:16:18	1920	0.5000	P1
88/130 00:01:42	88/130 00:20:58	1156	0.0078	P3
88/130 00:24:02	88/130 00:24:50	48	0.0078	P3
88/153 09:46:21	88/153 09:49:22	181	0.0625	P2
88/153 10:12:33	88/153 10:19:02	389	0.0625	P2
88/153 11:23:37	88/153 11:24:37	60	0.0625	P2
88/153 11:24:41	88/153 11:29:28	287	0.0625	P2
88/153 13:04:25	88/153 13:14:02	577	0.5000	P1
88/153 13:05:41	88/153 13:08:22	161	0.5000	P1
88/153 13:06:05	88/153 14:10:37	3872	0.5000	P1
88/153 13:13:05	88/153 13:27:57	892	0.5000	P1
88/153 13:14:13	88/153 13:15:18	65	0.5000	P1
88/178 22:28:16	88/178 22:29:56	100	0.0625	P2
88/178 22:30:00	88/178 22:32:43	163	0.0625	P2
88/179 00:10:24	88/179 00:12:32	128	0.0625	P2
88/179 00:12:36	88/179 00:14:28	112	0.0625	P2
88/252 15:45:59	88/252 15:50:52	293	0.0625	P2
88/252 15:50:59	88/252 15:52:12	73	0.0625	P2
88/252 15:51:08	88/252 16:01:55	647	0.0625	P2
88/252 15:52:15	88/252 15:52:40	25	0.0625	P2
88/252 16:53:07	88/252 17:21:04	1677	0.0625	P2
88/252 17:22:51	88/252 17:24:38	107	0.0625	P2
88/252 17:24:39	88/252 17:24:47	8	0.5000	P1
88/292 15:38:55	88/292 15:39:14	19	0.5000	P1
88/292 15:39:14	88/292 15:40:33	79	0.0078	P3
88/292 15:40:41	88/292 15:43:05	144	0.0078	P3
88/292 15:43:09	88/292 15:43:33	24	0.0078	P3
88/292 15:44:37	88/292 15:47:05	148	0.0078	P3
88/292 15:47:41	88/292 15:48:41	60	0.0625	P3
88/292 16:59:05	88/292 17:01:13	128	0.0625	P3
88/292 17:01:14	88/292 17:16:57	943	0.0078	P3
88/292 17:19:21	88/292 17:19:53	32	0.0078	P3
88/292 17:23:01	88/292 17:25:13	132	0.0078	P3
88/292 17:25:21	88/292 17:27:13	112	0.0078	P3
88/292 18:34:05	88/292 18:57:57	1432	0.0078	P3
88/292 19:00:57	88/292 19:03:29	152	0.0078	P3
88/292 19:39:45	88/292 19:41:05	80	0.0078	P3
88/292 20:14:05	88/292 20:28:57	892	0.0078	P3
88/292 20:36:17	88/292 20:39:41	204	0.0078	P3
88/292 21:53:27	88/292 22:16:57	1410	2.0000	P2
88/292 23:27:19	88/292 23:52:59	1540	2.0000	P2
88/293 00:50:31	88/293 01:28:58	2307	2.0000	P2
88/293 02:22:15	88/293 02:24:25	130	2.0000	P2
88/293 02:26:31	88/293 02:44:43	1092	2.0000	P2
88/293 03:03:51	88/293 03:04:56	65	2.0000	P2
88/293 04:00:23	88/293 04:22:16	1313	2.0000	P2
88/293 05:38:31	88/293 06:01:29	1378	2.0000	P2
88/293 07:15:37	88/293 07:38:33	1376	0.5000	P2
88/293 08:52:39	88/293 09:18:19	1540	2.0000	P2
88/293 10:28:39	88/293 10:54:19	1540	2.0000	P2
88/293 13:42:47	88/293 13:59:54	1027	2.0000	P2
88/293 14:00:09	88/293 14:03:30	201	0.0625	P2
88/310 09:36:02	88/310 09:55:10	1148	0.0078	P3
88/310 09:55:54	88/310 09:57:02	68	0.0078	P3
88/310 09:57:06	88/310 09:59:58	172	0.0078	P3
88/310 10:02:02	88/310 10:09:30	448	0.0078	P3
88/310 10:09:34	88/310 10:14:22	288	0.0078	P3
88/310 10:12:10	88/310 10:29:30	1040	0.0078	P3
88/310 11:20:06	88/310 11:42:02	1316	0.0078	P3
88/310 11:43:54	88/310 11:46:14	140	0.0078	P3
88/310 11:46:46	88/310 11:55:50	544	0.0625	P2
88/310 11:54:18	88/310 11:56:10	112	0.0625	P2
88/310 11:56:24	88/310 12:04:44	500	2.0000	P2
88/310 13:00:08	88/310 13:42:48	2560	2.0000	P2
88/310 14:34:00	88/310 15:18:50	2690	2.0000	P2
88/310 15:57:12	88/310 16:01:31	259	2.0000	P2
88/310 16:05:44	88/310 16:54:48	2944	2.0000	P2
88/310 17:33:12	88/310 17:46:05	773	2.0000	P2
88/310 18:05:44	88/310 18:30:51	1507	2.0000	P2
88/310 19:11:20	88/310 19:23:08	708	2.0000	P2
88/310 19:45:28	88/310 20:06:48	1280	2.0000	P2
88/310 20:47:20	88/310 21:02:16	896	2.0000	P2
88/310 21:23:36	88/310 21:42:52	1156	2.0000	P2
88/310 22:23:20	88/310 22:42:04	1124	2.0000	P2
88/310 23:03:52	88/310 23:16:45	773	2.0000	P2
88/310 23:59:20	88/311 00:18:36	1156	2.0000	P2
88/311 00:44:08	88/311 00:50:37	389	2.0000	P2
88/311 01:35:20	88/311 01:56:40	1280	2.0000	P2
88/311 02:22:16	88/311 02:26:35	259	2.0000	P2
88/311 03:11:20	88/311 03:34:50	1410	2.0000	P2
88/311 03:59:20	88/311 04:00:24	64	2.0000	P2
88/311 04:51:36	88/311 05:15:06	1410	2.0000	P2
88/311 05:30:00	88/311 05:40:43	643	2.0000	P2
88/311 06:31:52	88/311 06:53:12	1280	2.0000	P2
88/311 07:06:00	88/311 07:20:56	896	2.0000	P2
88/311 08:01:28	88/311 08:57:02	3334	2.0000	P2
88/311 09:41:44	88/311 10:32:58	3074	2.0000	P2
88/311 11:22:00	88/311 12:11:04	2944	2.0000	P2
88/311 13:00:08	88/311 13:44:58	2690	2.0000	P2
88/311 14:36:08	88/311 15:20:58	2690	2.0000	P2
88/311 16:01:28	88/311 16:59:05	3457	2.0000	P2
88/311 17:41:44	88/311 17:48:13	389	2.0000	P2
88/311 18:08:56	88/311 18:35:08	1572	2.0000	P2
88/311 19:13:28	88/311 19:26:21	773	2.0000	P2
88/342 14:41:28	88/342 14:44:08	160	0.0625	P3
88/342 15:22:32	88/342 15:38:00	928	0.0625	P3
88/342 16:11:16	88/342 16:22:00	644	0.0078	P3
88/342 17:00:08	88/342 17:12:44	756	0.0078	P3
88/342 17:13:16	88/342 17:16:32	196	0.0078	P3
88/342 17:47:40	88/342 18:06:00	1100	0.0078	P3
88/342 18:38:08	88/342 18:52:44	876	0.0078	P3
88/342 19:23:56	88/342 19:43:12	1156	0.0078	P3
88/342 20:19:08	88/342 20:21:12	124	0.0625	P3
88/342 20:21:12	88/342 20:29:00	468	0.0078	P3
88/343 14:00:24	88/343 14:02:05	101	0.0625	P2
88/343 14:02:08	88/343 14:04:20	132	0.0078	P3
88/343 14:04:24	88/343 14:07:48	204	0.0078	P3
88/343 15:22:08	88/343 15:42:00	1192	0.0078	P3
88/343 15:43:04	88/343 15:44:00	56	0.0078	P3
88/343 17:02:12	88/343 17:20:20	1088	0.0078	P3
88/343 19:28:24	88/343 19:44:24	960	0.0078	P3
88/343 20:19:08	88/343 20:32:52	824	0.0078	P3
88/344 12:22:20	88/344 12:24:40	140	0.0625	P2
88/344 12:24:40	88/344 12:26:28	108	0.5000	P1
88/344 12:26:31	88/344 12:34:04	453	0.5000	P1
88/344 12:33:15	88/344 12:35:04	109	0.5000	P1
88/344 12:35:04	88/344 12:35:42	38	4.0000	P1

Table B.6: Detailed Observation Times of Raw Data – 5/6

Start Time (UT)	End Time (UT)	Dur. (s)	Time Res. (s)	Mode
GS 2000+25 (cont.)				
88/344 13:07:32	88/344 13:09:15	103	4.0000	P1
88/351 09:32:31	88/351 09:33:39	68	0.5000	P1
88/351 09:33:11	88/351 09:34:40	89	0.5000	P1
88/351 10:44:35	88/351 10:57:34	779	4.0000	P1
88/351 10:57:27	88/351 11:01:00	213	0.5000	P1
88/351 11:03:03	88/351 11:04:03	60	0.5000	P1
88/351 11:08:47	88/351 11:13:44	297	0.5000	P1
88/351 12:22:43	88/351 12:29:12	389	4.0000	P1
88/351 12:29:11	88/351 12:38:56	585	0.5000	P1
88/351 12:45:11	88/351 12:49:19	248	0.5000	P1
88/351 12:49:23	88/351 12:56:51	448	0.5000	P1
88/351 14:01:03	88/351 14:24:59	1436	0.5000	P1
88/351 14:27:23	88/351 14:28:28	65	0.5000	P1
88/351 15:39:03	88/351 16:09:03	1800	0.5000	P1
88/351 17:17:59	88/351 17:46:31	1712	16.0000	P1
88/351 18:53:59	88/351 19:22:31	1712	16.0000	P1
88/351 20:12:55	88/351 20:57:55	2700	16.0000	P1
88/351 21:52:51	88/351 22:06:16	805	4.0000	P1
88/351 22:31:35	88/351 22:34:07	152	16.0000	P1
88/351 23:25:07	88/351 23:45:02	1195	4.0000	P1
88/352 00:10:15	88/352 00:11:55	100	16.0000	P1
88/352 01:03:15	88/352 01:24:41	1286	4.0000	P1
GS 2023+33				
89/143 09:28:10	89/143 09:32:06	236	0.0078	P3
89/143 10:15:38	89/143 10:26:38	660	0.0078	P3
89/143 11:33:26	89/143 11:36:42	196	0.0078	P3
89/143 11:38:10	89/143 11:39:22	72	0.0078	P3
89/150 04:31:17	89/150 04:32:41	84	0.0625	P2
89/150 04:32:53	89/150 04:36:09	196	0.0625	P2
89/150 05:07:13	89/150 05:13:18	365	0.0625	P2
89/150 05:47:09	89/150 06:10:58	1429	0.0625	P2
89/150 06:43:13	89/150 06:48:33	320	0.0625	P2
89/150 07:26:09	89/150 07:36:58	649	0.0625	P2
89/150 07:37:09	89/150 07:47:53	644	0.0625	P2
89/152 23:20:21	89/152 23:24:09	228	0.0625	P2
89/152 23:24:21	89/152 23:29:13	292	0.0625	P2
89/153 00:42:13	89/153 00:56:41	868	0.0625	P2
89/153 00:56:53	89/153 00:58:49	116	0.0625	P2
89/153 01:00:53	89/153 01:03:05	132	0.0625	P2
89/153 01:05:45	89/153 01:11:09	324	0.0625	P2
89/153 02:21:13	89/153 02:30:37	564	0.0625	P2
89/153 02:30:49	89/153 02:40:57	608	0.0625	P2
89/153 02:46:25	89/153 02:52:13	348	0.0078	P3
89/153 03:58:13	89/153 04:21:53	1420	0.0078	P3
89/153 04:26:25	89/153 04:28:33	128	0.0078	P3
89/153 05:36:09	89/153 06:03:57	1668	0.0078	P3
89/154 23:17:49	89/154 23:26:01	492	0.0625	P2
89/154 23:25:09	89/154 23:27:01	112	0.0625	P2
89/155 00:36:45	89/155 00:54:57	1092	0.0625	P2
89/155 00:56:53	89/155 01:00:01	188	0.0625	P2
89/155 01:00:13	89/155 01:00:34	21	0.0625	P2
89/155 01:00:35	89/155 01:07:33	418	0.0625	P2
89/155 02:14:13	89/155 02:35:49	1296	0.0625	P2
89/155 02:38:41	89/155 02:41:09	148	0.0625	P2
89/155 02:41:21	89/155 02:47:33	372	0.0625	P2
89/155 03:52:05	89/155 04:17:49	1544	0.0625	P2
89/155 04:19:41	89/155 04:23:17	216	0.0625	P2
89/155 05:32:05	89/155 05:57:57	1552	0.0625	P2
89/155 21:31:49	89/155 21:35:53	244	0.0625	P2
89/155 23:22:13	89/155 23:24:29	136	0.0625	P2
89/156 00:34:09	89/156 00:44:37	628	0.0625	P2
89/156 00:44:49	89/156 01:07:53	1384	0.0625	P2
89/156 02:35:49	89/156 02:38:53	184	0.0625	P2
89/156 02:39:05	89/156 02:44:49	344	0.0625	P2
89/156 03:49:09	89/156 04:04:57	948	0.0625	P2
89/160 19:43:25	89/160 19:48:01	276	0.0625	P2
89/160 21:00:13	89/160 21:16:57	1004	0.0625	P2
89/160 21:18:21	89/160 21:20:37	136	0.0625	P2
89/160 21:21:57	89/160 21:27:21	324	0.0625	P2
89/160 22:37:49	89/160 22:49:21	692	0.0625	P2
89/160 22:49:37	89/160 22:56:49	432	0.0625	P2
89/160 23:00:37	89/160 23:05:29	292	0.0625	P2
89/160 23:05:41	89/160 23:11:29	348	0.0625	P2
89/160 23:09:57	89/160 23:19:17	560	0.0625	P2
89/161 00:14:49	89/161 00:26:45	716	0.0625	P2
89/161 00:26:57	89/161 00:39:53	776	0.0625	P2
89/161 00:41:57	89/161 00:49:33	456	0.0625	P2
89/161 00:50:25	89/161 00:52:41	136	0.0625	P2
89/161 00:52:53	89/161 00:55:09	136	0.0625	P2
89/161 01:54:41	89/161 02:14:29	1188	0.0625	P2
GS 2023+33 (cont.)				
89/169 17:33:28	89/169 17:40:28	420	0.5000	P1
89/169 17:54:28	89/169 18:05:16	648	0.5000	P1
89/169 18:48:20	89/169 19:05:09	1009	0.5000	P1
89/169 19:08:00	89/169 19:09:48	108	0.5000	P1
89/169 22:36:08	89/169 22:40:40	272	0.0625	P2
89/169 22:40:52	89/169 22:45:52	300	0.0625	P2
89/170 15:44:52	89/170 15:47:24	152	0.0625	P2
89/170 16:16:40	89/170 16:27:12	632	0.5000	P1
89/170 17:15:12	89/170 17:24:48	576	0.5000	P1
89/170 17:26:44	89/170 17:28:13	89	0.5000	P1
89/171 14:39:16	89/171 14:45:56	400	0.0625	P2
89/171 15:42:36	89/171 15:47:32	296	0.0625	P2
89/171 15:47:44	89/171 15:53:40	356	0.0625	P2
89/171 16:10:36	89/171 16:23:56	800	0.0625	P2
89/171 17:12:20	89/171 17:18:56	396	0.0625	P2
89/171 17:19:32	89/171 17:21:48	136	0.0625	P2
89/171 19:26:16	89/171 19:35:48	572	0.0625	P2
89/171 20:26:28	89/171 20:46:00	1172	0.0625	P2
89/171 20:46:48	89/171 20:51:56	308	0.0625	P2
89/171 20:52:08	89/171 20:59:04	416	0.0625	P2
89/187 09:46:28	89/187 09:48:20	112	0.0625	P2
89/187 09:48:32	89/187 10:08:12	1180	0.0625	P2
89/187 11:36:20	89/187 11:50:04	824	0.0625	P2
89/187 13:10:24	89/187 13:12:48	144	0.0625	P2
89/187 13:13:00	89/187 13:17:36	276	0.0625	P2
89/203 02:26:31	89/203 02:43:55	1044	0.0625	P2
89/203 03:18:11	89/203 03:36:31	1100	0.0625	P2
89/203 04:05:23	89/203 04:24:35	1152	0.0625	P2
89/203 04:57:23	89/203 05:12:19	896	0.0625	P2
GX 339-4				
88/247 13:36:56	88/247 13:39:12	136	0.0625	P2
88/247 13:39:24	88/247 13:41:40	136	0.0625	P2
88/247 13:41:48	88/247 13:42:44	56	0.0078	P3
88/247 14:50:36	88/247 14:56:40	364	0.0078	P3
88/247 14:56:41	88/247 15:11:00	859	0.0078	P3
88/247 15:13:52	88/247 15:17:40	228	0.0078	P3
88/249 12:07:08	88/249 12:12:44	336	0.0078	P3
88/249 13:24:48	88/249 13:40:00	912	0.0078	P3
88/249 13:42:08	88/249 13:43:32	84	0.0078	P3
88/249 13:43:44	88/249 13:47:12	208	0.0078	P3
88/249 13:47:16	88/249 13:51:44	268	0.0078	P3
88/249 14:58:12	88/249 14:58:52	40	0.0078	P3
88/249 14:59:04	88/249 15:21:56	1372	0.0078	P3
88/249 15:24:16	88/249 15:26:28	132	0.0078	P3
88/249 15:26:40	88/249 15:27:32	52	0.0078	P3
88/249 15:27:48	88/249 15:28:04	16	0.0078	P3
88/249 16:02:52	88/249 16:09:04	372	0.0078	P3
88/249 16:38:12	88/249 17:04:00	1548	0.0078	P3
88/249 21:39:44	88/249 21:43:28	224	0.0625	P2
88/250 10:26:28	88/250 10:27:12	44	0.0078	P3
88/250 10:27:24	88/250 10:27:44	20	0.0078	P3
88/250 10:27:56	88/250 10:28:08	12	0.0078	P3
88/250 10:28:40	88/250 10:32:44	244	0.0078	P3
88/250 10:33:36	88/250 10:33:48	12	0.0078	P3
88/250 10:33:52	88/250 10:34:36	44	0.0078	P3
88/250 11:46:40	88/250 12:04:00	1040	0.0078	P3
88/250 12:05:36	88/250 12:09:08	212	0.0078	P3
88/250 12:09:20	88/250 12:09:44	24	0.0078	P3
88/250 12:09:48	88/250 12:11:52	124	0.0078	P3
88/250 12:12:28	88/250 12:16:36	248	0.0078	P3
88/250 13:23:12	88/250 13:35:24	732	0.0078	P3
88/250 13:35:40	88/250 13:36:32	52	0.0078	P3
88/250 13:36:36	88/250 13:45:00	504	0.0078	P3
88/250 13:46:56	88/250 13:47:08	12	0.0078	P3
88/250 13:48:40	88/250 13:49:36	56	0.0078	P3
88/250 13:49:48	88/250 13:51:12	84	0.0078	P3
88/250 13:51:20	88/250 13:56:20	300	0.0078	P3
88/250 14:30:24	88/250 14:35:00	276	0.0078	P3
88/250 15:03:08	88/250 15:07:12	244	0.0078	P3
88/250 15:07:16	88/250 15:27:00	1184	0.0078	P3
88/250 15:29:20	88/250 15:32:44	204	0.0078	P3
88/251 00:33:11	88/251 00:35:04	113	0.0625	P2
88/251 10:29:07	88/251 10:31:16	129	0.0625	P2
89/240 07:59:09	89/240 08:07:10	481	0.5000	P2
89/240 08:13:01	89/240 08:43:26	1825	0.5000	P2
89/240 09:14:25	89/240 09:37:54	1409	0.0625	P2
89/240 09:39:45	89/240 09:48:22	517	0.0625	P2
89/240 09:48:33	89/240 09:52:06	213	0.0625	P2

Table B.7: Detailed Observation Times of Raw Data – 6/6

Start Time (UT)	End Time (UT)	Dur. (s)	Time Res. (s)	Mode
GX 339-4 (cont.)				
89/240 09:51:13	89/240 10:19:37	1704	0.0625	P2
89/240 10:51:57	89/240 11:12:47	1250	0.5000	P2
89/240 11:13:21	89/240 11:18:54	333	0.0625	P2
89/240 11:21:21	89/240 11:29:06	465	0.0625	P2
89/240 11:33:33	89/240 11:52:14	1121	0.5000	P2
89/240 12:45:33	89/240 13:26:38	2465	0.5000	P2
89/240 14:30:05	89/240 14:58:21	1696	0.5000	P2
89/240 16:09:49	89/240 16:34:21	1472	0.5000	P2
89/240 17:02:05	89/240 17:17:02	897	0.5000	P2
89/240 17:45:17	89/240 18:10:22	1505	0.5000	P2
89/240 18:35:57	89/240 18:55:09	1152	0.5000	P2
89/240 19:21:17	89/240 19:44:13	1376	0.5000	P2
89/271 15:23:12	89/271 15:34:44	692	0.0625	P2
89/271 16:59:00	89/271 17:02:56	236	0.0625	P2
89/271 17:09:12	89/271 17:12:28	196	0.0625	P2
89/271 17:50:12	89/271 18:03:56	824	0.0625	P2
89/271 18:32:12	89/271 18:48:04	952	0.0625	P2
89/271 19:25:44	89/271 19:44:04	1100	0.0625	P2
89/271 20:11:12	89/271 20:23:36	744	0.0625	P2
89/271 21:01:32	89/271 21:19:40	1088	0.0625	P3
89/271 22:37:00	89/271 22:48:12	672	0.0625	P3
89/272 00:13:00	89/272 00:18:20	320	0.0625	P3
89/272 00:43:56	89/272 01:10:37	1601	0.0625	P3
89/272 01:48:28	89/272 01:54:52	384	0.0625	P3
89/272 02:15:08	89/272 02:36:28	1280	0.0625	P3
89/272 03:23:56	89/272 03:28:44	288	0.0625	P3
89/272 03:52:44	89/272 04:14:36	1312	0.0625	P3
89/272 04:59:24	89/272 05:05:17	353	0.0625	P3
89/272 05:30:20	89/272 05:52:44	1344	0.0625	P3
89/272 07:07:56	89/272 07:30:20	1344	0.0625	P3
89/272 08:47:08	89/272 09:07:24	1216	0.0625	P3
89/272 11:55:56	89/272 12:06:36	640	0.0625	P3
89/272 15:12:16	89/272 15:29:48	1052	0.0078	P3
89/272 17:44:16	89/272 17:56:04	708	0.0078	P3
89/272 18:26:08	89/272 18:42:04	956	0.0078	P3
89/272 19:21:46	89/272 19:36:42	896	2.0000	P2
89/272 20:06:34	89/272 20:17:17	643	2.0000	P2
89/272 20:59:54	89/272 21:12:47	773	2.0000	P2
89/272 23:01:30	89/272 23:25:00	1410	2.0000	P2
89/273 00:37:30	89/273 00:52:26	896	2.0000	P2
89/273 00:54:34	89/273 01:05:17	643	2.0000	P2
89/273 02:09:14	89/273 02:28:30	1156	2.0000	P2
89/273 03:47:22	89/273 04:06:38	1156	2.0000	P2
89/273 04:53:30	89/273 05:02:03	513	2.0000	P2
89/273 05:25:30	89/273 05:44:46	1156	2.0000	P2
89/273 07:03:38	89/273 07:20:44	1026	2.0000	P2
89/273 08:41:46	89/273 09:01:02	1156	2.0000	P2
89/273 10:13:30	89/273 10:37:00	1410	2.0000	P2
89/273 17:39:22	89/273 17:47:55	513	2.0000	P2
89/273 19:15:22	89/273 19:28:15	773	2.0000	P2
89/273 20:02:18	89/273 20:10:51	513	2.0000	P2
89/273 20:49:14	89/273 21:06:20	1026	2.0000	P2
89/273 22:25:14	89/273 22:35:57	643	2.0000	P2
89/273 22:57:14	89/273 23:20:44	1410	2.0000	P2
89/274 00:24:42	89/274 00:43:58	1156	2.0000	P2
91/254 15:53:14	91/254 15:56:42	208	0.0625	P2
91/254 15:57:38	91/254 16:06:42	544	0.0625	P2
91/254 16:06:54	91/254 16:12:54	360	0.0625	P2
LMC X-1				
87/197 04:18:00	87/197 04:34:00	960	0.5000	P2
87/197 05:30:00	87/197 06:10:32	2432	0.5000	P2
87/197 06:52:08	87/197 07:42:48	3040	0.5000	P2
87/197 08:31:20	87/197 09:18:48	2848	0.5000	P2
87/197 09:38:32	87/197 09:55:04	992	0.5000	P2
87/197 10:22:48	87/197 10:54:48	1920	0.5000	P2
87/197 11:16:40	87/197 11:22:32	352	0.5000	P2
87/273 15:02:29	87/273 15:04:45	136	0.5000	P1
87/274 07:55:13	87/274 08:08:09	776	16.0000	P1
LMC X-3				
89/258 21:54:24	89/258 21:58:22	238	0.5000	P1
89/258 21:58:32	89/258 22:05:53	441	0.5000	P1
89/258 23:39:49	89/258 23:59:49	1200	0.0625	P2
89/259 00:00:05	89/259 00:17:29	1044	0.0625	P2
89/259 01:18:09	89/259 01:25:29	440	0.0625	P2
89/259 01:26:25	89/259 01:53:53	1648	0.0625	P2
89/343 02:10:18	89/343 02:22:26	728	0.0078	P3
89/343 02:59:46	89/343 03:08:10	504	0.0078	P3
89/343 03:44:46	89/343 04:02:22	1056	0.5000	P1
89/343 04:36:50	89/343 04:42:47	357	0.5000	P1
89/343 05:21:22	89/343 05:40:55	1173	0.5000	P1
89/348 04:32:18	89/348 04:49:54	1056	0.5000	P1
89/355 01:41:02	89/355 01:59:58	1136	0.0078	P3
89/355 02:32:14	89/355 02:38:26	372	0.0078	P3
89/360 18:14:10	89/360 18:15:54	104	0.0078	P3
89/360 18:50:26	89/360 19:06:38	972	0.0078	P3
89/360 19:06:50	89/360 19:09:58	188	0.0078	P3
89/360 19:10:34	89/360 19:12:30	116	0.0078	P3
89/360 19:49:26	89/360 19:54:58	332	0.0078	P3
89/360 20:29:10	89/360 20:44:50	940	0.0078	P3
89/361 17:23:17	89/361 17:29:23	366	0.5000	P1
90/012 12:19:27	90/012 12:30:48	681	0.5000	P1
90/012 12:41:19	90/012 12:42:56	97	0.5000	P1
90/012 12:50:23	90/012 12:53:07	164	0.5000	P1
90/012 13:57:35	90/012 14:21:28	1433	0.5000	P1
90/012 14:27:39	90/012 14:32:48	309	0.5000	P1
90/012 15:36:11	90/012 15:51:55	944	0.5000	P1
90/028 01:46:38	90/028 01:57:51	673	0.5000	P1
90/028 02:34:10	90/028 02:38:38	268	0.5000	P1
90/028 03:14:26	90/028 03:37:58	1412	0.5000	P1
90/028 04:12:06	90/028 04:13:47	101	0.5000	P1
90/047 20:01:43	90/047 20:11:43	600	0.0078	P3
90/047 20:45:03	90/047 20:56:55	712	0.0078	P3
90/047 21:36:47	90/047 21:45:51	544	0.0078	P3
90/047 22:21:35	90/047 22:33:07	692	0.0078	P3
90/057 12:07:10	90/057 12:31:10	1440	0.0625	P2
90/057 14:01:42	90/057 14:04:34	172	0.5000	P1
90/057 14:04:46	90/057 14:07:10	144	0.5000	P1
90/057 15:28:14	90/057 15:39:59	705	0.5000	P1
90/057 15:41:30	90/057 15:44:02	152	0.5000	P1
90/057 16:10:50	90/057 16:23:58	788	0.5000	P1
90/071 05:59:33	90/071 06:04:09	276	0.5000	P1
90/071 06:04:25	90/071 06:06:25	120	0.5000	P1
90/071 06:28:29	90/071 06:37:54	565	0.5000	P1
90/071 07:10:13	90/071 07:17:46	453	0.5000	P1
90/071 07:28:17	90/071 07:31:58	221	0.5000	P1
90/071 07:33:13	90/071 07:36:37	204	0.5000	P1
90/074 10:19:05	90/074 10:23:46	281	0.5000	P1
90/077 03:03:09	90/077 03:30:42	1653	0.0078	P3
90/077 04:38:13	90/077 05:13:34	2121	0.0078	P3
90/077 06:14:49	90/077 06:52:54	2285	0.0078	P3
LMC X-3(cont.)				

B.3 Detailed Observation Times of Corrected Data

This section contains tables with a complete listing the *Ginga* LAC data from which the corrected data used in color-color diagram and hardness-intensity diagram analyses for the black hole candidates (1354-64, 1826-24, 1630-47, LMC X-1, LMC X-3, GS 2000+25, GS 2023+33, GS 1124-68, Cyg X-1, and GX 339-4) were drawn. The observational periods are those contiguous periods for which a data file was produced.

Periods which are not included below were not used in the analyses. Observation periods which overlap with other observation periods (which were therefore later selected out) are listed, and still others may contain spikes, drop-outs, or other problems which cause them to be excluded from the final analyses.

The date is listed in tabular form, giving the start time (YY/DOY HH:MM:SS UT) and end time of the observational period, the total time of the observation (in seconds), the time resolution of the data after rebinning and correction (in seconds), and the data mode during the observation (P1=MPC1, P2=MPC2, P3=MPC3).

Table B.8: Detailed Observation Times of Corrected Data – 1/10

Start Time (UT)	End Time (UT)	Dur. (s)	Time Res. (s)	Mode
1826-24				
88/253 14:14:51	88/253 14:15:07	16	4.0	P2
88/253 14:15:08	88/253 14:22:04	416	4.0	P2
88/253 15:16:11	88/253 15:20:59	288	4.0	P2
88/253 15:21:31	88/253 15:32:59	688	4.0	P2
88/253 15:21:52	88/253 15:32:48	656	16.0	P2
88/254 12:38:15	88/254 12:51:35	800	16.0	P2
88/254 13:43:23	88/254 13:53:27	604	4.0	P2
88/254 13:53:31	88/254 13:55:03	92	4.0	P2
88/254 13:53:32	88/254 13:54:52	80	16.0	P2
88/260 07:55:23	88/260 07:56:55	92	4.0	P3
88/260 07:55:27	88/260 07:56:15	48	16.0	P3
88/260 07:56:19	88/260 07:56:51	32	16.0	P3
88/260 07:56:59	88/260 07:57:19	20	4.0	P3
88/260 07:57:31	88/260 08:00:43	192	4.0	P3
88/260 07:58:04	88/260 07:58:36	32	16.0	P3
88/260 07:58:52	88/260 07:59:40	48	16.0	P3
88/260 09:09:11	88/260 09:20:19	668	4.0	P3
88/260 09:31:15	88/260 09:34:31	196	4.0	P3
88/260 09:32:03	88/260 09:33:23	80	16.0	P3
88/260 09:33:31	88/260 09:34:19	48	16.0	P3
88/260 09:34:35	88/260 09:38:51	256	16.0	P3
88/260 09:39:03	88/260 09:39:51	48	16.0	P3
88/260 09:39:55	88/260 09:40:43	48	16.0	P3
88/260 09:40:44	88/260 09:41:16	32	16.0	P3
88/260 09:41:31	88/260 09:42:19	48	16.0	P3
88/260 09:42:51	88/260 10:06:59	1448	4.0	P3
88/260 09:58:43	88/260 10:06:43	480	16.0	P3
88/260 10:51:07	88/260 11:00:59	592	16.0	P3
88/260 11:01:19	88/260 11:03:23	124	4.0	P3
1354-64				
87/194 05:25:48	87/194 05:26:36	48	16.0	P1
87/194 05:31:12	87/194 05:32:00	48	16.0	P1
87/194 05:32:40	87/194 05:52:40	1200	16.0	P1
87/194 07:02:16	87/194 07:27:20	1504	16.0	P1
87/194 08:38:48	87/194 09:01:44	1376	16.0	P1
87/194 10:15:52	87/194 10:35:04	1152	16.0	P1
87/194 10:36:08	87/194 10:37:28	80	16.0	P1
87/194 11:02:48	87/194 11:16:08	800	16.0	P1
87/194 11:51:52	87/194 12:13:44	1312	16.0	P1
87/194 12:40:56	87/194 12:52:40	704	16.0	P1
87/194 13:27:52	87/194 13:49:44	1312	16.0	P1
87/194 14:19:04	87/194 14:27:36	512	16.0	P1
87/194 15:04:56	87/194 15:24:56	1200	16.0	P1
87/194 15:55:04	87/194 16:05:12	608	16.0	P1
87/194 16:44:40	87/194 16:59:36	896	16.0	P1
87/194 17:32:40	87/194 17:41:44	544	16.0	P1
87/194 19:08:40	87/194 19:17:44	544	16.0	P1
87/194 22:24:56	87/194 22:30:48	352	16.0	P1
87/195 05:34:32	87/195 05:38:48	256	16.0	P1
1630-47				
87/290 06:22:40	87/290 06:36:00	800	16.0	P1
87/290 06:48:08	87/290 06:51:20	192	16.0	P1
87/290 06:53:20	87/290 07:08:16	896	16.0	P1
87/290 07:55:28	87/290 08:48:00	3152	16.0	P1
87/290 09:32:00	87/290 10:17:04	2704	16.0	P1
87/290 11:08:32	87/290 11:53:36	2704	16.0	P1
87/290 12:59:44	87/290 13:30:40	1856	16.0	P1
87/290 14:39:12	87/290 15:07:12	1680	16.0	P1
87/290 16:18:08	87/290 16:35:44	1056	16.0	P1
87/290 17:59:12	87/290 18:07:28	496	16.0	P1
87/290 19:38:08	87/290 19:41:20	192	16.0	P1
87/290 21:17:36	87/290 21:19:28	112	16.0	P1
87/291 00:01:00	87/291 00:06:20	320	16.0	P1
87/291 01:46:52	87/291 01:49:32	160	16.0	P1
87/291 01:50:16	87/291 01:51:36	80	16.0	P1
87/291 02:04:32	87/291 02:16:16	704	16.0	P1
87/291 03:13:52	87/291 03:16:00	128	16.0	P1
87/291 03:20:16	87/291 03:21:04	48	16.0	P1
88/101 12:57:33	88/101 12:59:41	128	16.0	P2
88/101 12:59:53	88/101 13:00:05	12	4.0	P2
88/101 13:00:13	88/101 13:00:45	32	16.0	P2
88/101 13:21:29	88/101 13:38:53	1044	4.0	P2
88/101 14:34:25	88/101 14:35:25	60	4.0	P2
88/101 14:34:29	88/101 14:35:17	48	16.0	P2
88/101 14:36:33	88/101 14:37:21	48	16.0	P2
88/101 14:37:41	88/101 14:47:29	588	4.0	P2
88/101 15:00:29	88/101 15:15:53	924	4.0	P2
88/101 15:15:57	88/101 15:16:09	12	4.0	P2
88/101 16:10:09	88/101 16:14:57	288	16.0	P2
88/101 16:16:53	88/101 16:19:17	144	16.0	P2
88/101 16:19:29	88/101 16:26:29	420	4.0	P2
88/101 16:26:33	88/101 16:52:17	1544	4.0	P2
88/101 16:28:41	88/101 16:30:01	80	16.0	P2
88/101 17:46:45	88/101 17:51:01	256	16.0	P2
88/101 17:51:21	88/101 17:56:53	332	4.0	P2
88/101 17:59:09	88/101 18:04:17	308	4.0	P2
88/101 18:04:29	88/101 18:10:57	388	4.0	P2
88/101 18:12:49	88/101 18:27:13	864	16.0	P2
88/101 19:24:53	88/101 20:08:05	2592	16.0	P2
88/101 21:06:45	88/101 21:35:17	1712	16.0	P2
88/101 22:42:45	88/101 23:12:05	1760	16.0	P2
88/102 00:23:01	88/102 00:48:37	1536	16.0	P2
88/102 02:01:09	88/102 02:21:57	1248	16.0	P2
88/278 23:26:02	88/278 23:51:38	1536	16.0	P1
Cyg X-1				
87/217 11:41:18	87/217 11:43:58	160	16.0	P1
87/217 11:44:38	87/217 11:51:18	400	16.0	P2
87/217 11:52:22	87/217 11:53:30	68	4.0	P2
87/217 12:15:38	87/217 12:15:50	12	4.0	P2
87/217 12:16:34	87/217 12:17:34	60	4.0	P2
87/217 12:18:02	87/217 12:24:26	384	16.0	P2
87/217 13:03:30	87/217 13:06:42	192	4.0	P2
87/217 13:03:58	87/217 13:06:38	160	16.0	P1
87/217 13:06:46	87/217 13:21:58	912	4.0	P2
87/217 13:06:50	87/217 13:21:46	896	16.0	P1
87/217 13:24:18	87/217 13:25:22	64	16.0	P1
87/217 18:31:25	87/217 18:34:53	208	16.0	P2
87/217 18:34:58	87/217 18:35:30	32	16.0	P2
87/217 18:35:46	87/217 18:36:18	32	16.0	P2
87/217 18:36:34	87/217 18:40:50	256	16.0	P2
87/217 19:48:38	87/217 19:50:14	96	16.0	P1
87/218 11:48:10	87/218 11:49:14	64	16.0	P1
87/218 11:49:26	87/218 11:50:30	64	16.0	P3
87/218 11:50:58	87/218 11:55:46	288	16.0	P3
87/218 11:55:54	87/218 11:56:42	48	16.0	P3
87/218 11:56:46	87/218 11:57:18	32	16.0	P3
87/218 11:57:30	87/218 11:58:18	48	16.0	P3
87/218 11:58:19	87/218 11:58:51	32	16.0	P3
87/218 12:20:06	87/218 12:20:38	32	16.0	P3
87/218 12:20:54	87/218 12:21:26	32	16.0	P3
87/218 12:22:30	87/218 12:23:50	80	16.0	P3
87/218 12:23:58	87/218 12:30:38	400	16.0	P3
87/218 13:09:38	87/218 13:14:58	320	16.0	P3
87/218 13:15:10	87/218 13:27:58	768	16.0	P3
87/218 13:30:14	87/218 13:31:50	96	16.0	P3
87/218 13:31:50	87/218 13:33:26	96	16.0	P3
87/218 13:33:30	87/218 13:36:58	208	16.0	P3
87/218 13:37:02	87/218 13:37:50	48	16.0	P3
87/218 13:37:54	87/218 13:38:26	32	16.0	P3
87/218 13:38:38	87/218 13:39:10	32	16.0	P3
87/218 13:39:22	87/218 13:39:54	32	16.0	P3
87/218 13:40:06	87/218 13:40:38	32	16.0	P3
87/218 13:40:50	87/218 13:41:22	32	16.0	P3
87/218 13:44:30	87/218 13:46:06	96	16.0	P3
87/218 13:46:22	87/218 13:46:54	32	16.0	P3
87/218 13:53:34	87/218 13:54:22	48	16.0	P3
87/218 13:54:38	87/218 13:55:10	32	16.0	P3
87/218 13:55:42	87/218 13:56:14	32	16.0	P3
87/218 13:58:06	87/218 13:58:54	48	16.0	P3
87/218 13:59:10	87/218 14:03:58	288	16.0	P3
87/218 14:50:10	87/218 14:57:06	416	16.0	P3
87/218 14:57:10	87/218 15:09:42	752	16.0	P3
87/218 15:26:22	87/218 15:27:58	96	16.0	P3
87/218 15:28:46	87/218 15:30:54	128	16.0	P3
87/218 15:31:58	87/218 15:33:34	96	16.0	P3
87/218 15:33:50	87/218 15:42:06	496	16.0	P3
87/218 15:42:22	87/218 15:42:54	32	16.0	P3
87/218 16:31:14	87/218 16:52:50	1296	16.0	P3
87/218 17:09:26	87/218 17:19:02	576	16.0	P3
87/218 18:05:10	87/218 18:34:46	1776	16.0	P3
87/218 18:38:14	87/218 18:39:02	48	16.0	P3
87/218 18:39:18	87/218 18:40:06	48	16.0	P3
87/218 18:40:22	87/218 18:44:54	272	16.0	P3
87/218 18:44:55	87/218 18:45:59	64	16.0	P3
87/218 18:46:02	87/218 18:46:50	48	16.0	P3
87/218 19:45:26	87/218 20:32:22	2816	16.0	P3
87/218 21:17:42	87/218 22:06:46	2944	16.0	P3
87/218 22:49:58	87/218 22:59:02	544	16.0	P3

Table B.9: Detailed Observation Times of Corrected Data – 2/10

Start Time (UT)	End Time (UT)	Dur. (s)	Time Res. (s)	Mode	Start Time (UT)	End Time (UT)	Dur. (s)	Time Res. (s)	Mode
Cyg X-1 (cont.)					Cyg X-1 (cont.)				
87/218 23:16:06	87/218 23:44:22	1696	16.0	P3	87/220 06:57:58	87/220 07:12:06	848	16.0	P3
87/219 01:00:06	87/219 01:20:22	1216	16.0	P3	87/220 08:33:58	87/220 08:52:22	1104	16.0	P3
87/219 02:01:58	87/219 02:12:22	624	16.0	P3	87/220 10:22:10	87/220 10:22:58	48	16.0	P3
87/219 02:37:42	87/219 02:57:10	1168	16.0	P3	87/220 10:23:14	87/220 10:28:18	304	16.0	P3
87/219 03:40:06	87/219 03:50:14	608	16.0	P3	87/220 10:28:22	87/220 10:29:10	48	16.0	P3
87/219 04:17:58	87/219 04:31:50	832	16.0	P3	87/220 10:29:18	87/220 10:30:06	48	16.0	P3
87/219 05:13:58	87/219 05:27:34	816	16.0	P3	87/220 10:30:07	87/220 10:30:39	32	16.0	P3
87/219 06:52:06	87/219 07:06:30	864	16.0	P3	87/220 10:54:30	87/220 10:55:50	80	16.0	P3
87/219 10:15:58	87/219 10:17:02	64	16.0	P3	87/220 10:56:06	87/220 10:56:38	32	16.0	P3
87/219 10:17:18	87/219 10:19:42	144	16.0	P3	87/220 10:56:54	87/220 10:57:42	48	16.0	P3
87/219 10:19:58	87/219 10:21:02	64	16.0	P3	87/220 10:58:46	87/220 11:04:22	336	16.0	P3
87/219 10:21:30	87/219 10:22:18	48	16.0	P3	87/220 11:45:42	87/220 12:00:54	912	16.0	P3
87/219 10:22:19	87/219 10:23:07	48	16.0	P3	87/220 12:27:02	87/220 12:27:34	32	16.0	P1
87/219 10:48:54	87/219 10:49:26	32	16.0	P3	87/220 12:27:50	87/220 12:29:42	112	16.0	P1
87/219 10:51:02	87/219 10:51:34	32	16.0	P3	87/220 12:31:50	87/220 12:41:10	560	16.0	P1
87/219 10:52:22	87/219 10:58:30	368	16.0	P3	87/220 12:41:42	87/220 12:42:14	32	16.0	P1
87/219 11:39:26	87/219 11:53:50	864	16.0	P3	87/220 13:22:14	87/220 13:33:22	668	4.0	P2
87/219 11:55:10	87/219 11:55:58	48	16.0	P3	87/220 13:33:38	87/220 13:41:50	492	4.0	P2
87/219 11:56:02	87/219 11:57:22	80	16.0	P3	87/220 13:45:50	87/220 13:46:58	68	4.0	P2
87/219 11:58:30	87/219 12:02:14	224	16.0	P3	87/220 13:47:02	87/220 13:55:22	500	4.0	P2
87/219 12:02:15	87/219 12:03:03	48	16.0	P3	90/129 01:35:16	90/129 01:36:20	64	16.0	P3
87/219 12:03:06	87/219 12:03:54	48	16.0	P3	90/129 01:35:36	90/129 01:36:16	40	4.0	P3
87/219 12:03:58	87/219 12:04:30	32	16.0	P3	90/129 01:36:24	90/129 01:40:40	256	16.0	P3
87/219 12:04:42	87/219 12:05:30	48	16.0	P3	90/129 01:40:48	90/129 01:41:36	48	16.0	P3
87/219 12:05:31	87/219 12:06:03	32	16.0	P3	90/129 01:43:13	90/129 01:43:45	32	16.0	P3
87/219 12:22:38	87/219 12:23:10	32	16.0	P3	90/129 02:49:12	90/129 02:52:08	176	16.0	P3
87/219 12:24:30	87/219 12:25:02	32	16.0	P3	90/129 02:52:56	90/129 02:53:44	48	16.0	P3
87/219 12:25:18	87/219 12:25:50	32	16.0	P3	90/129 02:54:00	90/129 02:58:16	256	16.0	P3
87/219 12:26:22	87/219 12:27:10	48	16.0	P3	90/129 02:58:48	90/129 03:02:32	224	16.0	P3
87/219 12:27:42	87/219 12:35:58	496	16.0	P3	90/129 03:02:48	90/129 03:04:08	80	16.0	P3
87/219 12:36:14	87/219 12:36:46	32	16.0	P3	90/129 03:04:24	90/129 03:07:52	208	16.0	P3
87/219 13:15:50	87/219 13:26:30	640	16.0	P3	90/129 03:13:12	90/129 03:14:12	60	4.0	P3
87/219 13:28:54	87/219 13:34:46	352	16.0	P3	90/129 03:14:13	90/129 03:15:01	48	16.0	P1
87/219 13:36:54	87/219 13:37:42	48	16.0	P3	90/129 03:20:20	90/129 03:23:19	179	4.0	P3
87/219 13:37:42	87/219 13:38:46	64	16.0	P3	90/129 03:24:20	90/129 03:25:08	48	16.0	P3
87/219 13:39:02	87/219 13:39:50	48	16.0	P3	90/129 04:28:00	90/129 04:28:48	48	16.0	P3
87/219 13:39:58	87/219 13:42:06	128	16.0	P3	90/129 04:29:04	90/129 04:31:28	144	16.0	P3
87/219 13:42:34	87/219 13:43:54	80	16.0	P3	90/129 04:31:44	90/129 04:39:28	464	16.0	P3
87/219 13:43:55	87/219 13:44:43	48	16.0	P3	90/129 04:39:44	90/129 04:45:04	320	16.0	P3
87/219 13:44:46	87/219 13:45:34	48	16.0	P3	90/129 04:45:20	90/129 04:48:48	208	16.0	P3
87/219 13:45:38	87/219 13:46:10	32	16.0	P3	90/129 04:54:32	90/129 04:55:04	32	16.0	P3
87/219 13:46:22	87/219 13:47:10	48	16.0	P3	90/129 04:56:14	90/129 04:57:02	48	16.0	P1
87/219 13:47:11	87/219 13:47:43	32	16.0	P3	90/129 04:59:00	90/129 04:59:32	32	16.0	P1
87/219 13:52:30	87/219 13:54:06	96	16.0	P3	90/129 06:03:20	90/129 06:04:24	64	16.0	P3
87/219 13:54:22	87/219 13:55:10	48	16.0	P3	90/129 06:04:40	90/129 06:10:48	368	16.0	P3
87/219 13:55:58	87/219 13:56:46	48	16.0	P3	90/129 06:11:04	90/129 06:14:48	224	16.0	P3
87/219 13:57:18	87/219 13:58:22	64	16.0	P3	90/129 06:15:04	90/129 06:22:00	416	16.0	P3
87/219 13:58:38	87/219 13:59:58	80	16.0	P3	90/129 06:22:16	90/129 06:22:48	32	16.0	P3
87/219 14:02:54	87/219 14:10:38	464	16.0	P3	90/129 06:23:04	90/129 06:23:36	32	16.0	P3
87/219 14:57:06	87/219 15:16:50	1184	16.0	P3	90/129 06:23:52	90/129 06:29:28	336	16.0	P3
87/219 15:19:18	87/219 15:20:22	64	16.0	P3	90/129 06:29:44	90/129 06:30:48	64	16.0	P3
87/219 15:20:30	87/219 15:21:02	32	16.0	P3	90/130 01:19:56	90/130 01:21:48	112	16.0	P1
87/219 15:21:06	87/219 15:21:54	48	16.0	P3	90/130 01:23:04	90/130 01:23:52	48	16.0	P3
87/219 15:22:02	87/219 15:26:50	288	16.0	P3	90/130 01:24:00	90/130 01:24:48	48	16.0	P3
87/219 15:27:02	87/219 15:27:50	48	16.0	P3	90/130 01:24:52	90/130 01:25:40	48	16.0	P3
87/219 15:27:51	87/219 15:28:23	32	16.0	P3	90/130 01:25:44	90/130 01:26:32	48	16.0	P3
87/219 15:28:38	87/219 15:29:26	48	16.0	P3	90/130 02:32:08	90/130 02:42:16	608	16.0	P3
87/219 15:30:30	87/219 15:31:02	32	16.0	P3	90/130 02:43:04	90/130 02:50:48	464	16.0	P3
87/219 15:33:14	87/219 15:34:02	48	16.0	P3	90/130 02:57:31	90/130 02:58:19	48	16.0	P1
87/219 15:34:34	87/219 15:35:06	32	16.0	P3	90/130 02:59:00	90/130 03:02:12	192	16.0	P1
87/219 15:36:10	87/219 15:37:46	96	16.0	P3	90/130 03:03:04	90/130 03:04:08	64	16.0	P3
87/219 15:38:34	87/219 15:46:50	496	16.0	P3	90/130 03:04:12	90/130 03:05:00	48	16.0	P3
87/219 16:33:06	87/219 16:58:58	1552	16.0	P3	90/130 03:05:56	90/130 03:06:44	48	16.0	P3
87/219 17:01:14	87/219 17:02:50	96	16.0	P3	90/130 03:06:44	90/130 03:07:32	48	16.0	P3
87/219 17:02:54	87/219 17:04:46	112	16.0	P3	90/130 03:08:08	90/130 03:08:56	48	16.0	P3
87/219 17:05:06	87/219 17:06:10	64	16.0	P3	90/130 04:10:40	90/130 04:11:12	32	16.0	P3
87/219 17:06:26	87/219 17:07:30	64	16.0	P3	90/130 04:11:28	90/130 04:15:28	240	16.0	P3
87/219 17:07:50	87/219 17:09:10	80	16.0	P3	90/130 04:15:44	90/130 04:22:40	416	16.0	P3
87/219 17:09:11	87/219 17:09:59	48	16.0	P3	90/130 04:22:56	90/130 04:25:20	144	16.0	P3
87/219 17:11:02	87/219 17:11:50	48	16.0	P3	90/130 04:26:40	90/130 04:27:28	48	16.0	P3
87/219 17:11:58	87/219 17:12:30	32	16.0	P3	90/130 04:27:44	90/130 04:30:40	176	16.0	P3
87/219 18:13:42	87/219 19:00:38	2816	16.0	P3	90/130 04:31:12	90/130 04:32:00	48	16.0	P3
87/219 19:49:42	87/219 20:38:46	2944	16.0	P3	90/130 04:32:16	90/130 04:32:48	32	16.0	P3
87/219 21:25:42	87/219 22:14:46	2944	16.0	P3	90/130 04:37:32	90/130 04:38:04	32	16.0	P3
87/219 23:27:50	87/219 23:50:46	1376	16.0	P3	90/130 04:39:57	90/130 04:41:33	96	16.0	P1
87/220 01:05:58	87/220 01:26:46	1248	16.0	P3	90/130 04:41:49	90/130 04:42:53	64	16.0	P1
87/220 02:44:06	87/220 03:01:10	1024	16.0	P3	90/130 04:43:32	90/130 04:44:04	32	16.0	P1
87/220 03:45:58	87/220 03:56:06	608	16.0	P3	90/130 05:45:20	90/130 05:46:08	48	16.0	P3
87/220 05:21:58	87/220 05:33:58	720	16.0	P3	90/130 05:46:24	90/130 05:48:00	96	16.0	P3

Table B.10: Detailed Observation Times of Corrected Data – 3/10

Start Time (UT)	End Time (UT)	Dur. (s)	Time Res. (s)	Mode
Cyg X-1 (cont.)				
90/130 05:49:52	90/130 05:51:28	96	16.0	P3
90/130 05:51:44	90/130 05:52:48	64	16.0	P3
90/130 05:53:04	90/130 05:56:00	176	16.0	P3
90/130 05:56:48	90/130 06:02:24	336	16.0	P3
90/130 06:02:40	90/130 06:04:48	128	16.0	P3
90/130 06:05:04	90/130 06:06:24	80	16.0	P3
90/130 06:06:40	90/130 06:09:20	160	16.0	P3
90/130 06:09:36	90/130 06:14:08	272	16.0	P3
90/130 21:39:44	90/130 21:41:36	112	16.0	P1
90/130 21:41:52	90/130 21:44:16	144	16.0	P1
90/130 21:44:18	90/130 21:44:50	32	16.0	P3
90/130 21:45:22	90/130 21:46:10	48	16.0	P3
90/130 21:46:24	90/130 21:47:12	48	16.0	P3
90/130 21:47:44	90/130 21:48:48	64	16.0	P3
90/130 23:02:28	90/130 23:10:28	480	16.0	P3
90/130 23:11:04	90/130 23:14:32	208	16.0	P3
90/130 23:18:20	90/130 23:19:08	48	16.0	P3
90/130 23:19:08	90/130 23:19:56	48	16.0	P3
90/130 23:20:07	90/130 23:21:59	112	16.0	P1
90/130 23:23:36	90/130 23:24:08	32	16.0	P1
90/130 23:24:40	90/130 23:25:12	32	16.0	P1
90/130 23:25:28	90/130 23:26:32	64	16.0	P1
90/130 23:27:08	90/130 23:27:40	32	16.0	P3
90/131 00:39:08	90/131 00:40:44	96	16.0	P3
90/131 00:41:16	90/131 00:42:04	48	16.0	P3
90/131 00:42:20	90/131 00:44:44	144	16.0	P3
90/131 00:45:00	90/131 00:47:24	144	16.0	P3
90/131 00:47:40	90/131 00:49:16	96	16.0	P3
90/131 00:49:32	90/131 00:54:20	288	16.0	P3
90/131 00:59:16	90/131 00:59:48	32	16.0	P3
90/131 01:00:03	90/131 01:00:35	32	16.0	P1
90/131 01:02:12	90/131 01:03:48	96	16.0	P1
90/131 01:04:04	90/131 01:04:52	48	16.0	P1
90/131 01:05:40	90/131 01:06:12	32	16.0	P1
90/131 01:12:08	90/131 01:16:24	256	16.0	P3
90/131 01:16:40	90/131 01:17:44	64	16.0	P3
90/131 02:15:08	90/131 02:18:20	192	16.0	P3
90/131 02:18:36	90/131 02:20:28	112	16.0	P3
90/131 02:20:44	90/131 02:30:36	592	16.0	P3
90/131 02:30:52	90/131 02:36:44	352	16.0	P3
90/131 02:43:08	90/131 02:44:12	64	16.0	P1
90/131 02:45:00	90/131 02:45:32	32	16.0	P1
90/131 02:45:48	90/131 02:46:20	32	16.0	P1
90/131 02:48:20	90/131 02:49:08	48	16.0	P3
90/131 02:49:12	90/131 02:49:44	32	16.0	P3
90/131 02:50:00	90/131 02:50:48	48	16.0	P3
90/131 02:50:52	90/131 02:51:40	48	16.0	P3
90/131 02:51:52	90/131 02:52:56	64	16.0	P3
90/131 03:53:00	90/131 03:54:52	112	16.0	P3
90/131 03:55:56	90/131 04:03:08	432	16.0	P3
90/131 04:05:00	90/131 04:06:52	112	16.0	P3
90/131 04:07:24	90/131 04:07:56	32	16.0	P3
90/131 04:08:12	90/131 04:09:32	80	16.0	P3
90/131 04:10:20	90/131 04:14:20	240	16.0	P3
90/131 04:14:36	90/131 04:15:40	64	16.0	P3
90/131 04:15:56	90/131 04:17:32	96	16.0	P3
90/131 04:20:20	90/131 04:21:08	48	16.0	P3
90/131 04:21:16	90/131 04:22:52	96	16.0	P3
90/131 04:22:52	90/131 04:24:44	112	16.0	P3
90/131 04:25:00	90/131 04:26:04	64	16.0	P3
90/131 04:26:08	90/131 04:26:56	48	16.0	P3
90/131 04:26:56	90/131 04:27:28	32	16.0	P3
90/131 07:07:16	90/131 07:37:40	1824	16.0	P1
90/131 08:41:08	90/131 09:12:36	1888	16.0	P1
90/131 09:54:44	90/131 09:55:48	64	16.0	P1
90/131 10:00:04	90/131 10:13:56	832	16.0	P1
90/131 11:31:16	90/131 11:51:00	1184	16.0	P1
90/131 13:07:16	90/131 13:20:36	800	16.0	P1
91/156 17:58:42	91/156 17:59:46	64	16.0	P1
91/156 18:00:18	91/156 18:03:46	208	16.0	P1
91/156 18:04:34	91/156 18:06:26	112	16.0	P1
91/156 18:06:42	91/156 18:11:46	304	16.0	P1
91/156 18:14:19	91/156 18:14:51	32	16.0	P1
91/156 18:16:30	91/156 18:17:34	64	16.0	P1
91/156 18:18:04	91/156 18:18:36	32	16.0	P3
91/156 18:18:52	91/156 18:19:40	48	16.0	P3
91/156 18:19:46	91/156 18:20:34	48	16.0	P3
91/156 18:20:38	91/156 18:21:26	48	16.0	P3
91/156 18:21:30	91/156 18:22:18	48	16.0	P3
91/156 18:22:18	91/156 18:22:50	32	16.0	P3
91/156 18:23:02	91/156 18:23:50	48	16.0	P3
91/156 18:24:59	91/156 18:25:31	32	16.0	P3
91/156 18:45:06	91/156 18:46:10	64	16.0	P3
91/156 19:29:54	91/156 19:30:58	64	16.0	P3
91/156 19:31:34	91/156 19:32:06	32	16.0	P3
91/156 19:32:22	91/156 19:32:54	32	16.0	P3
91/156 19:36:06	91/156 19:36:54	48	16.0	P3
91/156 19:40:22	91/156 19:41:10	48	16.0	P3
91/156 19:42:30	91/156 19:45:10	160	16.0	P3
91/156 19:45:26	91/156 19:45:58	32	16.0	P3
91/156 19:47:02	91/156 19:47:50	48	16.0	P3
91/156 19:48:06	91/156 19:49:26	80	16.0	P3
91/156 19:49:58	91/156 19:50:30	32	16.0	P3
91/156 19:51:51	91/156 19:52:23	32	16.0	P3
91/156 19:52:53	91/156 19:54:29	96	16.0	P1
91/156 19:54:45	91/156 19:55:33	48	16.0	P1
91/156 19:55:38	91/156 19:59:06	208	16.0	P1
91/156 19:59:13	91/156 19:59:45	32	16.0	P3
91/156 19:59:46	91/156 20:00:18	32	16.0	P3
91/156 20:03:14	91/156 20:03:46	32	16.0	P3
91/156 20:05:22	91/156 20:05:54	32	16.0	P3
91/156 20:06:42	91/156 20:07:30	48	16.0	P3
91/156 20:07:46	91/156 20:08:50	64	16.0	P3
91/156 20:09:06	91/156 20:09:38	32	16.0	P3
91/156 20:09:54	91/156 20:15:14	320	16.0	P3
91/156 20:15:30	91/156 20:16:18	48	16.0	P3
91/156 20:17:22	91/156 20:17:54	32	16.0	P3
91/156 20:18:10	91/156 20:18:58	48	16.0	P3
91/156 21:05:22	91/156 21:05:54	32	16.0	P3
91/156 21:06:30	91/156 21:07:34	64	16.0	P3
91/156 21:08:06	91/156 21:09:26	80	16.0	P3
91/156 21:09:42	91/156 21:10:14	32	16.0	P3
91/156 21:10:30	91/156 21:11:02	32	16.0	P3
91/156 21:11:50	91/156 21:15:18	208	16.0	P3
91/156 21:16:38	91/156 21:17:26	48	16.0	P3
91/156 21:17:42	91/156 21:18:30	48	16.0	P3
91/156 21:20:06	91/156 21:23:34	208	16.0	P3
91/156 21:24:22	91/156 21:25:42	80	16.0	P3
91/156 21:25:58	91/156 21:26:30	32	16.0	P3
91/156 21:27:18	91/156 21:27:50	32	16.0	P3
91/156 21:28:54	91/156 21:29:58	64	16.0	P3
91/156 21:30:35	91/156 21:31:23	48	16.0	P3
91/156 21:31:31	91/156 21:32:03	32	16.0	P1
91/156 21:32:46	91/156 21:34:38	112	16.0	P1
91/156 21:34:54	91/156 21:37:18	144	16.0	P1
91/156 21:38:26	91/156 21:38:58	32	16.0	P3
91/156 21:38:58	91/156 21:39:46	48	16.0	P3
91/156 21:41:43	91/156 21:42:15	32	16.0	P3
91/156 21:43:03	91/156 21:44:07	64	16.0	P3
91/156 21:44:23	91/156 21:46:31	128	16.0	P3
91/156 21:46:47	91/156 21:47:35	48	16.0	P3
91/156 21:47:51	91/156 21:48:23	32	16.0	P3
91/156 21:48:55	91/156 21:50:31	96	16.0	P3
91/156 21:51:19	91/156 21:52:07	48	16.0	P3
91/156 22:40:18	91/156 22:40:50	32	16.0	P3
91/156 22:41:06	91/156 22:41:38	32	16.0	P3
91/156 22:41:54	91/156 22:43:30	96	16.0	P3
91/156 22:43:46	91/156 22:44:18	32	16.0	P3
91/156 22:45:06	91/156 22:45:38	32	16.0	P3
91/156 22:45:54	91/156 22:46:42	48	16.0	P3
91/156 22:46:58	91/156 22:47:30	32	16.0	P3
91/156 22:47:46	91/156 22:49:54	128	16.0	P3
91/156 22:50:42	91/156 22:53:38	176	16.0	P3
91/156 22:54:26	91/156 22:54:58	32	16.0	P3
91/156 22:56:02	91/156 22:58:58	176	16.0	P3
91/156 22:59:14	91/156 23:00:50	96	16.0	P3
91/156 23:01:38	91/156 23:04:02	144	16.0	P3
91/156 23:04:18	91/156 23:05:54	96	16.0	P3
91/156 23:06:58	91/156 23:07:30	32	16.0	P3
91/156 23:13:26	91/156 23:16:06	160	16.0	P1
91/156 23:17:10	91/156 23:18:30	80	16.0	P1
91/157 00:18:26	91/157 00:23:30	304	16.0	P1
91/157 00:23:46	91/157 00:35:30	704	16.0	P1
91/157 04:43:30	91/157 04:56:02	752	16.0	P1
91/157 04:56:18	91/157 04:57:22	64	16.0	P1
91/157 05:14:58	91/157 05:15:30	32	16.0	P1
91/157 11:02:42	91/157 11:04:50	128	16.0	P1
91/157 11:05:06	91/157 11:12:50	464	16.0	P1

Table B.11: Detailed Observation Times of Corrected Data – 4/10

Start Time (UT)	End Time (UT)	Dur. (s)	Time Res. (s)	Mode
Cyg X-1 (cont.)				
91/157 12:29:06	91/157 12:47:46	1120	16.0	P1
91/157 14:02:58	91/157 14:03:30	32	16.0	P1
91/157 14:04:02	91/157 14:06:42	160	16.0	P1
91/157 14:06:58	91/157 14:12:34	336	16.0	P1
91/157 14:12:50	91/157 14:15:46	176	16.0	P1
91/157 14:16:02	91/157 14:19:14	192	16.0	P1
91/157 14:19:30	91/157 14:24:02	272	16.0	P1
91/157 15:51:34	91/157 15:52:22	48	16.0	P1
91/157 15:52:26	91/157 15:55:06	160	16.0	P1
91/157 15:56:22	91/157 15:57:26	64	16.0	P3
91/157 15:58:27	91/157 15:58:59	32	16.0	P3
91/157 15:59:31	91/157 16:00:03	32	16.0	P3
91/157 16:26:26	91/157 16:29:06	160	16.0	P3
91/157 17:12:50	91/157 17:13:54	64	16.0	P3
91/157 17:14:30	91/157 17:15:34	64	16.0	P3
91/157 17:15:50	91/157 17:17:26	96	16.0	P3
91/157 17:17:58	91/157 17:19:02	64	16.0	P3
91/157 17:19:34	91/157 17:20:38	64	16.0	P3
91/157 17:20:54	91/157 17:21:42	48	16.0	P3
91/157 17:21:58	91/157 17:22:46	48	16.0	P3
91/157 17:23:02	91/157 17:23:34	32	16.0	P3
91/157 17:23:50	91/157 17:24:38	48	16.0	P3
91/157 17:29:49	91/157 17:30:21	32	16.0	P1
91/157 17:30:26	91/157 17:30:58	32	16.0	P1
91/157 17:31:30	91/157 17:34:10	160	16.0	P1
91/157 17:34:34	91/157 17:35:22	48	16.0	P3
91/157 17:35:23	91/157 17:35:55	32	16.0	P3
91/157 17:36:06	91/157 17:36:54	48	16.0	P3
91/157 18:47:46	91/157 18:48:50	64	16.0	P3
91/157 18:49:22	91/157 18:49:54	32	16.0	P3
91/157 18:50:10	91/157 18:50:42	32	16.0	P3
91/157 18:51:30	91/157 18:52:02	32	16.0	P3
91/157 19:02:22	91/157 19:05:02	160	16.0	P3
91/157 19:05:47	91/157 19:06:19	32	16.0	P3
91/157 19:06:31	91/157 19:07:35	64	16.0	P1
91/157 19:07:54	91/157 19:09:46	112	16.0	P1
91/157 19:10:02	91/157 19:10:34	32	16.0	P1
91/157 19:10:38	91/157 19:11:10	32	16.0	P1
91/157 19:11:26	91/157 19:14:54	208	16.0	P1
91/157 19:15:10	91/157 19:15:42	32	16.0	P1
91/157 19:21:54	91/157 19:22:26	32	16.0	P1
91/157 19:22:42	91/157 19:24:02	80	16.0	P1
91/157 19:25:06	91/157 19:27:14	128	16.0	P1
91/157 19:27:30	91/157 19:29:06	96	16.0	P1
91/157 19:29:54	91/157 19:34:26	272	16.0	P1
91/157 20:22:42	91/157 20:27:46	304	16.0	P1
91/157 20:28:02	91/157 20:29:22	80	16.0	P1
91/157 20:29:54	91/157 20:30:26	32	16.0	P1
91/157 20:30:42	91/157 20:32:02	80	16.0	P1
91/157 20:32:18	91/157 20:35:30	192	16.0	P1
91/157 20:35:46	91/157 20:37:22	96	16.0	P1
91/157 20:37:38	91/157 20:40:18	160	16.0	P1
91/157 20:40:50	91/157 20:44:02	192	16.0	P1
91/157 20:44:15	91/157 20:46:55	160	16.0	P1
91/157 20:47:11	91/157 20:47:43	32	16.0	P1
91/157 20:47:59	91/157 20:48:31	32	16.0	P1
91/157 20:48:47	91/157 20:49:35	48	16.0	P1
91/157 20:50:23	91/157 20:50:55	32	16.0	P1
91/157 20:54:43	91/157 21:01:39	416	16.0	P1
91/157 21:01:55	91/157 21:04:19	144	16.0	P1
91/157 21:04:35	91/157 21:05:23	48	16.0	P1
91/157 21:05:39	91/157 21:07:31	112	16.0	P1
GS 1124-68				
91/011 00:55:04	91/011 01:15:04	1200	4.0	P2
91/011 19:42:24	91/011 19:45:52	208	4.0	P2
91/011 20:26:04	91/011 20:41:48	944	16.0	P1
91/011 20:26:08	91/011 20:32:48	400	4.0	P2
91/011 20:43:56	91/011 20:44:44	48	16.0	P1
91/011 20:55:28	91/011 20:56:04	36	4.0	P3
91/011 21:17:04	91/011 21:25:52	528	4.0	P3
91/011 22:00:08	91/011 22:09:28	560	4.0	P3
91/011 22:09:32	91/011 22:16:12	400	4.0	P3
91/011 22:17:52	91/011 22:21:48	236	4.0	P3
91/011 22:26:16	91/011 22:27:20	64	16.0	P3
91/011 22:27:32	91/011 22:28:36	64	16.0	P3
91/011 22:28:44	91/011 22:29:48	64	16.0	P3
91/011 22:29:48	91/011 22:30:20	32	16.0	P3
91/011 23:00:16	91/011 23:05:56	340	4.0	P3
91/011 23:38:04	91/011 23:45:32	448	16.0	P3
91/011 23:45:48	91/011 23:48:44	176	16.0	P3
91/011 23:49:00	91/012 00:01:48	768	16.0	P3
91/012 00:03:48	91/012 00:04:44	56	4.0	P3
91/014 19:48:12	91/014 20:03:56	944	16.0	P1
91/014 20:40:28	91/014 20:50:28	600	4.0	P2
91/014 20:55:16	91/014 20:57:44	148	4.0	P2
91/014 20:59:04	91/014 21:00:08	64	4.0	P2
91/014 21:01:24	91/014 21:02:28	64	16.0	P1
91/014 21:02:36	91/014 21:04:48	132	4.0	P2
91/014 21:05:00	91/014 21:11:08	368	4.0	P2
91/014 22:41:04	91/014 22:45:36	272	16.0	P1
91/014 23:05:28	91/014 23:11:04	336	16.0	P1
91/014 23:11:28	91/014 23:22:24	656	16.0	P1
91/016 18:46:12	91/016 19:06:28	1216	16.0	P1
91/016 20:02:48	91/016 20:04:40	112	16.0	P1
91/016 20:04:56	91/016 20:06:00	64	16.0	P1
91/016 20:06:12	91/016 20:12:36	384	16.0	P1
91/016 20:12:48	91/016 20:14:40	112	16.0	P1
91/016 21:46:28	91/016 21:48:52	144	16.0	P1
91/016 21:49:04	91/016 21:52:32	208	16.0	P1
91/016 21:54:04	91/016 22:21:00	1616	16.0	P1
91/016 23:23:08	91/016 23:25:00	112	16.0	P1
91/016 23:25:16	91/016 23:26:36	80	4.0	P2
91/017 16:22:52	91/017 16:25:48	176	16.0	P1
91/017 17:58:28	91/017 18:00:36	128	16.0	P1
91/017 18:01:08	91/017 18:04:04	176	16.0	P1
91/017 18:06:04	91/017 18:08:28	144	16.0	P1
91/017 18:16:44	91/017 18:36:44	1200	16.0	P1
91/017 19:34:32	91/017 19:36:40	128	16.0	P1
91/017 19:36:48	91/017 19:45:52	544	16.0	P1
91/017 19:46:04	91/017 19:53:48	464	16.0	P1
91/017 19:54:04	91/017 20:17:48	1424	16.0	P1
91/017 21:14:16	91/017 21:17:12	176	16.0	P1
91/017 21:17:12	91/017 21:19:04	112	16.0	P1
91/017 21:19:12	91/017 21:23:44	272	16.0	P1
91/017 21:25:52	91/017 21:48:32	1360	16.0	P1
91/018 15:55:27	91/018 15:57:35	128	4.0	P2
91/018 17:30:35	91/018 17:32:59	144	4.0	P2
91/018 17:33:03	91/018 17:36:11	188	4.0	P2
91/018 17:50:11	91/018 18:05:39	928	4.0	P2
91/018 18:06:27	91/018 18:09:55	208	4.0	P2
91/018 19:05:59	91/018 19:08:07	128	4.0	P2
91/018 19:08:19	91/018 19:17:39	560	4.0	P2
91/018 20:46:03	91/018 20:50:35	272	4.0	P2
91/018 20:50:47	91/018 20:57:35	408	4.0	P2
91/018 21:18:11	91/018 21:27:07	536	4.0	P2
91/020 15:00:39	91/020 15:03:55	196	4.0	P2
91/020 15:17:19	91/020 15:34:47	1048	4.0	P2
91/020 16:30:11	91/020 16:31:31	80	4.0	P2
91/020 16:34:31	91/020 16:40:39	368	4.0	P2
91/020 16:40:47	91/020 16:43:47	180	4.0	P2
91/020 16:50:07	91/020 17:08:19	1092	4.0	P2
91/020 17:09:11	91/020 17:14:55	344	4.0	P2
91/022 17:19:15	91/022 17:20:03	48	16.0	P3
91/022 17:20:04	91/022 17:20:36	32	16.0	P3
91/022 17:20:51	91/022 17:21:39	48	16.0	P3
91/022 17:21:40	91/022 17:22:12	32	16.0	P3
91/022 17:22:27	91/022 17:22:59	32	16.0	P3
91/022 17:23:19	91/022 17:55:03	1904	16.0	P3
91/022 18:26:19	91/022 18:31:55	336	4.0	P3
91/022 19:03:19	91/022 19:20:55	1056	16.0	P3
91/022 19:21:11	91/022 19:35:51	880	16.0	P3
91/022 20:00:27	91/022 20:04:07	220	4.0	P3
91/022 20:04:19	91/022 20:08:35	256	4.0	P3
91/025 12:48:31	91/025 12:56:43	492	4.0	P3
91/025 12:56:51	91/025 13:09:55	784	4.0	P3
91/025 13:46:35	91/025 13:52:23	348	4.0	P3
91/036 10:39:11	91/036 10:39:59	48	16.0	P3
91/036 10:40:15	91/036 11:04:31	1456	16.0	P3
91/036 11:01:19	91/036 11:04:27	188	4.0	P3
91/037 10:10:19	91/037 10:34:19	1440	16.0	P3
91/037 11:41:15	91/037 11:41:31	16	4.0	P3
91/037 11:42:27	91/037 11:44:51	144	4.0	P3
91/037 11:45:03	91/037 12:08:31	1408	16.0	P3
91/037 12:08:47	91/037 12:09:35	48	16.0	P3
91/037 12:08:59	91/037 12:09:11	12	4.0	P3
91/044 05:15:15	91/044 05:17:51	156	4.0	P2
91/044 05:18:19	91/044 05:23:55	336	4.0	P2
91/044 06:49:15	91/044 07:00:27	672	4.0	P2

Table B.12: Detailed Observation Times of Corrected Data – 5/10

Start Time (UT)	End Time (UT)	Dur. (s)	Time Res. (s)	Mode
GS 1124-68 (cont.)				
91/044 07:00:35	91/044 07:01:59	84	4.0	P2
91/044 08:23:27	91/044 08:34:55	688	4.0	P2
91/045 06:11:39	91/045 06:31:23	1184	16.0	P3
91/045 07:02:31	91/045 07:04:55	144	16.0	P3
91/045 07:07:03	91/045 07:07:11	8	4.0	P3
91/045 07:44:03	91/045 07:49:55	352	4.0	P3
91/045 07:50:35	91/045 08:05:47	912	16.0	P3
91/045 08:06:31	91/045 08:06:39	8	4.0	P3
91/051 23:31:15	91/051 23:36:55	340	4.0	P2
91/052 00:23:27	91/052 00:29:03	336	4.0	P2
91/052 01:05:19	91/052 01:17:51	752	16.0	P3
91/052 01:58:19	91/052 02:02:59	280	4.0	P3
91/052 02:38:55	91/052 02:55:43	1008	16.0	P3
91/052 02:39:15	91/052 02:55:39	984	4.0	P3
91/052 03:32:11	91/052 03:37:03	292	4.0	P3
91/053 00:34:39	91/053 00:41:47	428	4.0	P2
91/053 00:41:51	91/053 00:44:55	184	4.0	P2
91/053 01:25:19	91/053 01:32:39	440	4.0	P2
91/053 02:08:39	91/053 02:13:07	268	4.0	P3
91/053 02:13:11	91/053 02:24:31	680	4.0	P3
91/053 02:59:11	91/053 03:06:39	448	4.0	P3
91/053 03:42:39	91/053 04:00:35	1076	4.0	P3
91/053 04:00:55	91/053 04:01:03	8	4.0	P3
91/053 04:32:31	91/053 04:40:39	488	4.0	P3
91/056 20:57:27	91/056 20:59:55	148	4.0	P2
91/056 23:30:23	91/056 23:30:51	28	4.0	P3
91/057 00:05:23	91/057 00:09:23	240	16.0	P3
91/057 00:09:39	91/057 00:19:15	576	16.0	P3
91/057 00:59:15	91/057 01:03:47	272	16.0	P3
91/057 20:26:23	91/057 20:30:55	272	4.0	P2
91/057 21:25:15	91/057 21:26:11	56	4.0	P2
91/057 22:00:03	91/057 22:08:51	528	16.0	P3
91/057 22:39:39	91/057 22:53:31	832	16.0	P3
91/057 22:56:43	91/057 23:00:15	212	4.0	P3
91/058 00:19:11	91/058 00:33:19	848	16.0	P3
91/067 19:20:46	91/067 19:22:06	80	16.0	P3
91/067 19:20:51	91/067 19:21:31	40	4.0	P3
91/067 19:22:11	91/067 19:22:59	48	16.0	P3
91/067 19:37:47	91/067 19:51:55	848	4.0	P3
91/067 19:51:59	91/067 19:54:55	176	4.0	P3
91/069 18:15:34	91/069 18:16:22	48	16.0	P3
91/069 18:19:59	91/069 18:20:47	48	16.0	P3
91/069 18:20:47	91/069 18:21:19	32	16.0	P3
91/069 18:21:35	91/069 18:22:07	32	16.0	P3
91/069 18:22:19	91/069 18:22:51	32	16.0	P3
91/069 18:23:03	91/069 18:23:35	32	16.0	P3
91/069 18:24:03	91/069 18:53:55	1792	16.0	P3
91/077 12:31:26	91/077 12:35:46	260	4.0	P2
91/077 13:37:50	91/077 13:38:58	68	4.0	P2
91/077 13:45:11	91/077 13:46:31	80	16.0	P3
91/077 13:46:38	91/077 13:47:58	80	16.0	P3
91/077 13:48:10	91/077 13:48:58	48	16.0	P3
91/077 13:49:10	91/077 13:49:58	48	16.0	P3
91/077 13:50:02	91/077 13:50:50	48	16.0	P3
91/077 13:50:51	91/077 13:51:23	32	16.0	P3
91/077 13:51:38	91/077 13:52:10	32	16.0	P3
91/077 13:52:22	91/077 13:53:10	48	16.0	P3
91/077 13:53:22	91/077 13:54:50	88	4.0	P3
91/077 13:53:26	91/077 13:54:46	80	16.0	P3
91/077 14:17:34	91/077 14:21:50	256	16.0	P3
91/077 14:22:06	91/077 14:26:54	288	16.0	P3
91/077 15:11:54	91/077 15:20:58	544	4.0	P3
91/077 15:21:42	91/077 15:23:30	108	4.0	P3
91/077 15:21:46	91/077 15:22:18	32	16.0	P3
91/079 09:40:14	91/079 09:57:50	1056	16.0	P3
91/079 13:16:22	91/079 13:16:54	32	4.0	P2
91/087 08:20:10	91/087 08:25:42	332	4.0	P3
91/087 08:20:14	91/087 08:25:34	320	16.0	P3
91/087 08:25:46	91/087 08:33:06	440	4.0	P3
91/087 08:25:50	91/087 08:27:42	112	16.0	P3
91/087 08:27:58	91/087 08:33:02	304	16.0	P3
91/087 09:40:26	91/087 09:42:10	104	4.0	P1
91/088 04:30:22	91/088 04:38:54	512	16.0	P1
91/088 05:56:46	91/088 06:00:54	248	4.0	P1
91/088 06:01:10	91/088 06:04:54	224	16.0	P1
91/088 07:26:26	91/088 07:28:58	152	4.0	P3
91/088 07:29:14	91/088 07:57:10	1676	4.0	P3
91/089 05:18:46	91/089 05:21:42	176	16.0	P1
91/089 07:10:22	91/089 07:20:46	624	4.0	P3
91/089 08:24:46	91/089 08:25:50	64	16.0	P1
91/089 08:53:29	91/089 08:53:45	16	4.0	P1
91/089 08:53:53	91/089 08:54:17	24	4.0	P1
91/089 08:54:37	91/089 08:54:45	8	4.0	P1
91/092 06:01:29	91/092 06:02:01	32	4.0	P1
91/164 13:19:37	91/164 13:19:45	8	4.0	P1
91/164 13:19:49	91/164 13:37:05	1036	4.0	P1
91/164 13:37:41	91/164 13:39:13	92	4.0	P1
91/164 13:39:17	91/164 13:40:25	68	4.0	P1
91/164 14:54:49	91/164 15:13:33	1124	4.0	P1
91/164 16:28:17	91/164 16:46:41	1104	4.0	P1
91/164 17:21:58	91/164 17:30:58	540	4.0	P3
91/164 18:05:10	91/164 18:18:46	816	16.0	P3
91/172 11:06:13	91/172 11:12:53	400	4.0	P1
91/172 12:37:37	91/172 12:45:29	472	4.0	P1
91/172 13:32:09	91/172 13:44:49	760	4.0	P1
91/202 17:15:44	91/202 17:27:00	676	4.0	P1
91/203 17:59:16	91/203 18:03:12	236	4.0	P1
91/203 18:03:24	91/203 18:11:20	476	4.0	P1
91/203 18:11:24	91/203 18:12:04	40	4.0	P1
91/203 19:31:44	91/203 19:47:16	932	4.0	P3
91/204 17:08:36	91/204 17:20:52	736	4.0	P1
91/204 17:55:12	91/204 17:58:00	168	4.0	P1
91/204 18:41:32	91/204 19:00:12	1120	16.0	P3
91/204 20:13:52	91/204 20:32:16	1104	16.0	P3
91/204 20:32:32	91/204 20:33:04	32	16.0	P3
91/204 21:05:32	91/204 21:08:40	188	4.0	P3
GS 2000+25				
88/120 02:53:03	88/120 02:54:15	72	4.0	P2
88/120 02:54:19	88/120 02:57:15	176	16.0	P1
88/121 04:41:03	88/121 04:46:43	340	4.0	P2
88/123 01:34:11	88/123 01:34:27	16	4.0	P2
88/123 03:09:35	88/123 03:11:31	116	4.0	P2
88/123 03:11:39	88/123 03:14:03	144	16.0	P1
88/124 01:32:47	88/124 01:33:23	36	4.0	P2
88/124 01:33:27	88/124 01:34:39	72	4.0	P2
88/124 01:34:43	88/124 01:35:43	60	4.0	P2
88/124 01:35:47	88/124 01:40:43	296	4.0	P2
88/124 03:14:43	88/124 03:15:39	56	4.0	P2
88/124 03:15:43	88/124 03:21:11	328	4.0	P2
88/125 00:02:51	88/125 00:03:39	48	4.0	P2
88/125 01:38:31	88/125 01:40:23	112	4.0	P2
88/125 01:40:27	88/125 01:44:59	272	16.0	P1
88/125 01:45:15	88/125 01:46:03	48	16.0	P1
88/125 01:46:07	88/125 01:46:19	12	4.0	P2
88/125 01:46:31	88/125 01:46:39	8	4.0	P2
88/125 03:20:35	88/125 03:21:39	64	16.0	P1
88/125 03:20:39	88/125 03:20:51	12	4.0	P2
88/125 03:21:59	88/125 03:26:15	256	4.0	P2
88/153 09:46:21	88/153 09:49:17	176	4.0	P2
88/153 10:13:13	88/153 10:13:29	16	4.0	P2
88/153 10:13:41	88/153 10:16:17	156	4.0	P2
88/153 10:16:29	88/153 10:16:57	28	4.0	P2
88/153 10:17:09	88/153 10:17:17	8	4.0	P2
88/153 10:17:29	88/153 10:17:45	16	4.0	P2
88/153 11:24:41	88/153 11:29:25	284	4.0	P2
88/252 15:45:59	88/252 15:50:23	264	4.0	P2
88/252 15:50:27	88/252 15:50:39	12	4.0	P2
88/252 15:51:03	88/252 15:52:11	68	4.0	P2
88/252 15:52:32	88/252 16:01:52	560	4.0	P2
88/252 16:53:11	88/252 17:20:59	1668	4.0	P2
88/252 17:23:03	88/252 17:24:35	92	4.0	P2
88/252 17:24:39	88/252 17:24:47	8	4.0	P1
88/292 15:38:55	88/292 15:39:11	16	4.0	P1
88/292 15:39:18	88/292 15:40:30	72	4.0	P3
88/292 15:40:45	88/292 15:43:05	140	4.0	P3
88/292 15:43:09	88/292 15:43:33	24	4.0	P3
88/292 15:44:37	88/292 15:47:01	144	4.0	P3
88/292 16:59:37	88/292 17:01:13	96	4.0	P3
88/292 17:01:18	88/292 17:16:54	936	4.0	P3
88/292 17:19:21	88/292 17:19:53	32	4.0	P3
88/292 17:23:01	88/292 17:25:09	128	4.0	P3
88/292 17:25:25	88/292 17:27:13	108	4.0	P3
88/292 18:34:09	88/292 18:57:57	1428	4.0	P3
88/292 19:01:01	88/292 19:03:29	148	4.0	P3
88/292 20:14:09	88/292 20:28:57	888	4.0	P3
88/292 20:36:21	88/292 20:39:41	200	4.0	P3
88/292 21:55:35	88/292 22:16:55	1280	4.0	P2
88/292 23:29:27	88/292 23:52:55	1408	4.0	P2

Table B.13: Detailed Observation Times of Corrected Data – 6/10

Start Time (UT)	End Time (UT)	Dur. (s)	Time Res. (s)	Mode
GS 2000+25 (cont.)				
88/293 00:52:39	88/293 01:05:27	768	4.0	P2
88/293 01:07:35	88/293 01:28:55	1280	4.0	P2
88/293 02:28:39	88/293 02:44:39	960	4.0	P2
88/293 03:03:51	88/293 03:04:55	64	4.0	P2
88/293 04:00:23	88/293 04:21:43	1280	4.0	P2
88/293 05:38:31	88/293 05:59:51	1280	4.0	P2
88/293 08:52:39	88/293 09:13:59	1280	4.0	P2
88/293 10:28:39	88/293 10:52:07	1408	4.0	P2
88/293 13:44:55	88/293 13:57:43	768	4.0	P2
88/293 14:00:21	88/293 14:03:29	188	4.0	P2
88/310 09:55:58	88/310 09:57:02	64	4.0	P3
88/310 09:57:06	88/310 09:59:58	172	4.0	P3
88/310 10:02:06	88/310 10:07:58	352	4.0	P3
88/310 10:08:02	88/310 10:09:30	88	4.0	P3
88/310 10:14:18	88/310 10:29:30	912	4.0	P3
88/310 11:44:10	88/310 11:46:10	120	4.0	P3
88/310 11:46:46	88/310 11:48:54	128	4.0	P2
88/310 11:48:58	88/310 11:55:50	412	4.0	P2
88/310 11:58:16	88/310 12:04:40	384	4.0	P2
88/310 13:02:16	88/310 13:40:40	2304	4.0	P2
88/310 14:36:08	88/310 15:16:40	2432	4.0	P2
88/310 16:07:52	88/310 16:52:40	2688	4.0	P2
88/310 17:35:20	88/310 17:43:52	512	4.0	P2
88/310 18:05:44	88/310 18:28:40	1376	4.0	P2
88/310 19:13:28	88/310 19:19:52	384	4.0	P2
88/310 19:45:28	88/310 20:06:48	1280	4.0	P2
88/310 20:49:28	88/310 21:00:08	640	4.0	P2
88/310 21:23:36	88/310 21:40:40	1024	4.0	P2
88/310 22:23:20	88/310 22:38:16	896	4.0	P2
88/310 23:03:52	88/310 23:14:32	640	4.0	P2
88/311 00:01:28	88/311 00:16:24	896	4.0	P2
88/311 00:44:08	88/311 00:48:24	256	4.0	P2
88/311 02:22:16	88/311 02:24:24	128	4.0	P2
88/311 03:13:28	88/311 03:32:40	1152	4.0	P2
88/311 04:53:44	88/311 05:12:56	1152	4.0	P2
88/311 05:32:08	88/311 05:38:32	384	4.0	P2
88/311 06:34:00	88/311 06:51:04	1024	4.0	P2
88/311 07:08:08	88/311 07:18:48	640	4.0	P2
88/311 08:03:36	88/311 08:54:48	3072	4.0	P2
88/311 09:43:52	88/311 10:30:48	2816	4.0	P2
88/311 16:03:36	88/311 16:56:56	3200	4.0	P2
88/311 17:43:52	88/311 17:46:00	128	4.0	P2
88/311 18:08:56	88/311 18:32:56	1440	4.0	P2
88/311 19:13:28	88/311 19:24:08	640	4.0	P2
88/342 15:22:32	88/342 15:37:28	896	16.0	P3
88/342 16:11:16	88/342 16:21:56	640	16.0	P3
88/342 17:47:40	88/342 18:05:56	1096	4.0	P3
88/342 18:38:08	88/342 18:52:48	880	16.0	P3
88/342 19:23:56	88/342 19:43:08	1152	4.0	P3
88/342 20:19:36	88/342 20:21:12	96	4.0	P3
88/342 21:03:20	88/342 21:16:40	800	16.0	P1
88/342 21:56:08	88/342 22:05:12	544	16.0	P1
88/342 22:36:40	88/342 22:48:24	704	16.0	P1
88/342 23:12:24	88/342 23:14:32	128	16.0	P1
88/342 23:30:00	88/342 23:41:44	704	16.0	P1
88/343 00:13:12	88/343 00:20:40	448	16.0	P1
88/343 00:49:28	88/343 01:02:16	768	16.0	P1
88/343 01:49:12	88/343 01:58:16	544	16.0	P1
88/343 02:26:32	88/343 02:42:32	960	16.0	P1
88/343 03:25:12	88/343 03:34:16	544	16.0	P1
88/343 04:02:00	88/343 04:20:40	1120	16.0	P1
88/343 05:01:44	88/343 05:10:16	512	16.0	P1
88/343 05:40:40	88/343 05:59:36	1136	16.0	P1
88/343 06:38:48	88/343 06:44:40	352	16.0	P1
88/343 07:19:20	88/343 07:37:44	1104	16.0	P1
88/343 08:56:24	88/343 09:14:32	1088	16.0	P1
88/343 10:32:24	88/343 10:54:16	1312	16.0	P1
88/343 14:00:32	88/343 14:02:04	92	4.0	P2
88/343 19:28:24	88/343 19:44:20	956	4.0	P3
88/343 20:19:12	88/343 20:32:52	820	4.0	P3
88/343 23:38:32	88/343 23:44:56	384	16.0	P1
88/344 00:19:04	88/344 00:25:28	384	16.0	P1
88/344 00:51:04	88/344 01:06:16	912	16.0	P1
88/344 01:09:12	88/344 01:12:24	192	16.0	P1
88/344 01:53:28	88/344 02:00:56	448	16.0	P1
88/344 02:28:40	88/344 02:44:56	976	16.0	P1
88/344 03:31:04	88/344 03:37:12	368	16.0	P1
88/344 04:02:32	88/344 04:23:20	1248	16.0	P1
88/344 05:07:04	88/344 05:11:52	288	16.0	P1
88/344 05:41:44	88/344 06:02:16	1232	16.0	P1
GS 2000+25(cont.)				
88/344 07:21:28	88/344 07:40:08	1120	16.0	P1
88/344 10:34:00	88/344 10:56:56	1376	16.0	P1
88/344 12:10:00	88/344 12:21:44	704	16.0	P1
88/344 12:22:36	88/344 12:24:36	120	4.0	P2
88/344 12:22:40	88/344 12:24:32	112	16.0	P1
88/344 12:24:44	88/344 12:26:24	100	4.0	P1
88/344 12:26:32	88/344 12:34:00	448	16.0	P1
88/344 13:07:32	88/344 13:08:36	64	4.0	P1
88/351 09:32:31	88/351 09:33:27	56	4.0	P1
88/351 09:33:31	88/351 09:33:39	8	4.0	P1
88/351 10:45:11	88/351 11:00:55	944	16.0	P1
88/351 11:03:15	88/351 11:04:03	48	4.0	P1
88/351 11:08:47	88/351 11:11:59	192	16.0	P1
88/351 12:29:15	88/351 12:38:55	580	4.0	P1
88/351 12:45:11	88/351 12:49:19	248	4.0	P1
88/351 12:45:15	88/351 12:49:15	240	16.0	P1
88/351 12:49:23	88/351 12:52:23	180	4.0	P1
88/351 14:01:07	88/351 14:24:55	1428	4.0	P1
88/351 14:27:35	88/351 14:28:23	48	4.0	P1
88/351 15:40:03	88/351 16:08:59	1736	4.0	P1
88/351 15:40:07	88/351 16:08:55	1728	16.0	P1
88/351 17:20:07	88/351 17:45:43	1536	16.0	P1
88/351 18:56:07	88/351 19:21:43	1536	16.0	P1
88/351 20:15:03	88/351 20:27:51	768	16.0	P1
88/351 20:29:59	88/351 20:57:43	1664	16.0	P1
88/351 22:31:51	88/351 22:33:59	128	16.0	P1
88/352 01:05:59	88/352 01:23:51	1072	16.0	P1
89/135 16:37:38	89/135 16:44:34	416	16.0	P1
GS 2023+33				
89/143 09:28:38	89/143 09:32:22	224	16.0	P3
89/143 10:15:34	89/143 10:26:30	656	16.0	P3
89/143 11:02:26	89/143 11:04:02	96	16.0	P3
89/143 11:33:42	89/143 11:36:42	180	4.0	P3
89/143 11:38:10	89/143 11:39:22	72	4.0	P3
89/143 13:12:22	89/143 13:34:46	1344	16.0	P1
89/143 14:45:38	89/143 15:09:06	1408	16.0	P1
89/143 16:22:42	89/143 16:23:30	48	16.0	P1
89/143 19:34:10	89/143 19:57:06	1376	16.0	P1
89/143 20:26:26	89/143 20:43:30	1024	16.0	P1
89/143 21:12:18	89/143 21:26:42	864	16.0	P1
89/149 18:29:05	89/149 18:46:41	1056	16.0	P1
89/149 20:06:41	89/149 20:23:45	1024	16.0	P1
89/149 21:42:09	89/149 22:02:57	1248	16.0	P1
89/149 23:17:37	89/149 23:30:25	768	16.0	P1
89/150 00:54:41	89/150 01:06:57	736	16.0	P1
89/150 01:08:02	89/150 01:09:22	80	16.0	P1
89/150 02:56:22	89/150 02:59:18	176	16.0	P1
89/150 05:08:37	89/150 05:09:25	48	16.0	P1
89/150 05:47:05	89/150 05:56:25	560	16.0	P1
89/150 05:56:37	89/150 05:56:49	12	4.0	P2
89/150 05:59:21	89/150 06:00:41	80	16.0	P1
89/150 06:02:01	89/150 06:09:29	448	16.0	P1
89/150 06:09:53	89/150 06:10:29	36	4.0	P2
89/150 06:43:25	89/150 06:48:05	280	4.0	P2
89/150 06:43:29	89/150 06:48:01	272	16.0	P1
89/150 07:26:05	89/150 07:37:01	656	16.0	P1
89/150 07:37:05	89/150 07:48:01	656	16.0	P1
89/150 08:19:29	89/150 08:22:57	208	16.0	P1
89/150 09:05:21	89/150 09:24:01	1120	16.0	P1
89/150 09:55:29	89/150 09:56:49	80	16.0	P1
89/150 10:41:21	89/150 10:59:29	1088	16.0	P1
89/152 15:01:05	89/152 15:22:25	1280	16.0	P1
89/152 16:40:17	89/152 16:59:45	1168	16.0	P1
89/152 18:20:01	89/152 18:36:33	992	16.0	P1
89/152 19:55:29	89/152 20:15:13	1184	16.0	P1
89/152 23:05:53	89/152 23:18:09	736	16.0	P1
89/152 23:20:21	89/152 23:23:49	208	16.0	P1
89/152 23:24:17	89/152 23:29:21	304	16.0	P1
89/153 00:42:25	89/153 00:56:41	856	4.0	P2
89/153 00:56:49	89/153 00:58:57	128	16.0	P1
89/153 01:01:01	89/153 01:03:05	124	4.0	P2
89/153 01:01:05	89/153 01:02:57	112	16.0	P1
89/153 01:05:41	89/153 01:11:01	320	16.0	P1
89/153 02:21:09	89/153 02:30:29	560	16.0	P1
89/153 02:30:45	89/153 02:40:53	608	16.0	P1
89/153 02:42:41	89/153 02:45:21	160	16.0	P1
89/153 02:46:25	89/153 02:52:13	348	4.0	P3
89/153 02:52:13	89/153 02:53:01	48	16.0	P3

Table B.14: Detailed Observation Times of Corrected Data – 7/10

Start Time (UT)	End Time (UT)	Dur. (s)	Time Res. (s)	Mode
GS 2023+33 (cont.)				
89/153 03:58:17	89/153 04:21:53	1416	4.0	P3
89/153 04:24:53	89/153 04:25:41	48	16.0	P3
89/153 04:26:25	89/153 04:28:33	128	4.0	P3
89/153 05:37:21	89/153 06:03:57	1596	4.0	P3
89/153 11:50:09	89/153 12:02:09	720	16.0	P1
89/153 12:05:05	89/153 12:06:09	64	16.0	P1
89/153 12:24:17	89/153 12:28:01	224	16.0	P1
89/153 13:27:45	89/153 13:38:57	672	16.0	P1
89/153 14:58:25	89/153 15:19:29	1264	16.0	P1
89/153 16:38:09	89/153 16:56:33	1104	16.0	P1
89/153 18:16:49	89/153 18:33:05	976	16.0	P1
89/153 19:51:13	89/153 20:10:41	1168	16.0	P1
89/153 21:27:13	89/153 21:50:41	1408	16.0	P1
89/154 11:46:25	89/154 11:58:41	736	16.0	P1
89/154 13:23:29	89/154 13:37:05	816	16.0	P1
89/154 14:58:25	89/154 15:14:25	960	16.0	P1
89/154 16:35:29	89/154 16:52:01	992	16.0	P1
89/154 18:13:05	89/154 18:30:25	1040	16.0	P1
89/154 19:47:29	89/154 20:06:57	1168	16.0	P1
89/154 20:07:13	89/154 20:08:33	80	16.0	P1
89/154 21:23:29	89/154 21:46:57	1408	16.0	P1
89/154 22:59:29	89/154 23:13:53	864	16.0	P1
89/154 23:14:49	89/154 23:16:09	80	16.0	P1
89/154 23:16:17	89/154 23:17:05	48	16.0	P1
89/154 23:17:49	89/154 23:20:49	180	4.0	P2
89/154 23:20:53	89/154 23:25:53	300	4.0	P2
89/155 00:36:49	89/155 00:54:57	1088	4.0	P2
89/155 00:56:57	89/155 01:00:01	184	4.0	P2
89/155 01:00:13	89/155 01:00:33	20	4.0	P2
89/155 01:00:35	89/155 01:07:31	416	4.0	P2
89/155 02:14:17	89/155 02:35:37	1280	16.0	P1
89/155 02:38:41	89/155 02:38:57	16	4.0	P2
89/155 02:39:01	89/155 02:41:09	128	4.0	P2
89/155 02:41:21	89/155 02:47:33	372	4.0	P2
89/155 03:53:53	89/155 04:17:49	1436	4.0	P2
89/155 03:53:57	89/155 04:17:41	1424	16.0	P1
89/155 04:19:49	89/155 04:21:33	104	4.0	P2
89/155 04:21:49	89/155 04:23:17	88	4.0	P2
89/155 05:32:17	89/155 05:36:09	232	4.0	P2
89/155 05:36:13	89/155 05:57:57	1304	4.0	P2
89/155 10:07:45	89/155 10:15:13	448	16.0	P1
89/155 10:20:49	89/155 10:21:37	48	16.0	P1
89/155 10:25:53	89/155 10:46:09	1216	16.0	P1
89/155 11:42:09	89/155 11:55:45	816	16.0	P1
89/155 12:18:57	89/155 12:22:41	224	16.0	P1
89/155 13:18:41	89/155 13:34:09	928	16.0	P1
89/155 13:57:05	89/155 13:58:09	64	16.0	P1
89/155 14:54:41	89/155 15:11:29	1008	16.0	P1
89/155 16:32:49	89/155 16:48:49	960	16.0	P1
89/155 18:08:49	89/155 18:26:57	1088	16.0	P1
89/155 19:43:45	89/155 20:05:05	1280	16.0	P1
89/155 21:20:49	89/155 21:29:53	544	16.0	P1
89/155 21:31:53	89/155 21:35:53	240	4.0	P2
89/155 23:16:34	89/155 23:17:22	48	16.0	P1
89/155 23:17:33	89/155 23:22:05	272	16.0	P1
89/155 23:22:21	89/155 23:22:57	36	4.0	P2
89/156 00:34:05	89/156 00:44:29	624	16.0	P1
89/156 00:44:45	89/156 01:07:09	1344	16.0	P1
89/156 02:11:29	89/156 02:33:21	1312	16.0	P1
89/156 02:35:49	89/156 02:38:29	160	16.0	P1
89/156 02:39:01	89/156 02:44:53	352	16.0	P1
89/156 03:49:53	89/156 04:04:33	880	16.0	P1
89/160 19:43:41	89/160 19:47:25	224	16.0	P1
89/160 21:00:29	89/160 21:16:57	988	4.0	P2
89/160 21:18:33	89/160 21:20:37	124	4.0	P2
89/160 21:18:37	89/160 21:20:29	112	16.0	P1
89/160 21:20:45	89/160 21:21:49	64	16.0	P1
89/160 21:21:53	89/160 21:25:53	240	16.0	P1
89/160 22:38:05	89/160 22:49:17	672	16.0	P1
89/160 22:49:37	89/160 22:56:49	432	16.0	P1
89/160 23:00:41	89/160 23:03:21	160	16.0	P1
89/160 23:03:25	89/160 23:05:01	96	16.0	P1
89/160 23:09:57	89/160 23:10:05	8	4.0	P2
89/160 23:11:21	89/160 23:11:53	32	16.0	P1
89/160 23:13:13	89/160 23:13:21	8	4.0	P2
89/160 23:13:29	89/160 23:19:21	352	16.0	P1
89/161 00:14:45	89/161 00:26:45	720	16.0	P1
89/161 00:26:53	89/161 00:39:57	784	16.0	P1
89/161 00:42:09	89/161 00:42:57	48	16.0	P1
89/161 00:43:13	89/161 00:44:17	64	16.0	P1
89/161 00:44:29	89/161 00:49:33	304	16.0	P1
89/161 00:49:41	89/161 00:50:13	32	16.0	P1
89/161 00:50:21	89/161 00:52:29	128	16.0	P1
89/161 00:52:49	89/161 00:54:57	128	16.0	P1
89/161 01:54:37	89/161 02:14:21	1184	16.0	P1
89/169 17:33:28	89/169 17:40:24	416	16.0	P1
89/169 17:54:44	89/169 17:57:40	176	16.0	P1
89/169 17:57:56	89/169 18:05:24	448	16.0	P1
89/169 18:48:32	89/169 18:57:36	544	16.0	P1
89/169 18:57:52	89/169 19:00:48	176	16.0	P1
89/169 19:01:04	89/169 19:05:04	240	16.0	P1
89/169 19:11:00	89/169 19:13:56	176	16.0	P1
89/169 22:36:16	89/169 22:40:40	264	4.0	P2
89/169 22:40:48	89/169 22:45:36	288	16.0	P1
89/169 22:47:44	89/169 22:48:48	64	16.0	P1
89/169 22:50:56	89/169 22:53:04	128	16.0	P1
89/170 00:03:28	89/170 00:26:56	1408	16.0	P1
89/170 01:18:08	89/170 01:41:36	1408	16.0	P1
89/170 01:42:08	89/170 02:04:32	1344	16.0	P1
89/170 02:43:28	89/170 02:55:12	704	16.0	P1
89/170 02:58:24	89/170 03:10:40	736	16.0	P1
89/170 03:16:00	89/170 03:19:44	224	16.0	P1
89/170 03:22:24	89/170 03:40:32	1088	16.0	P1
89/170 04:19:28	89/170 04:30:40	672	16.0	P1
89/170 04:55:12	89/170 04:57:52	160	16.0	P1
89/170 04:58:24	89/170 05:16:00	1056	16.0	P1
89/170 05:55:28	89/170 06:08:48	800	16.0	P1
89/170 06:33:20	89/170 06:36:00	160	16.0	P1
89/170 06:38:40	89/170 06:52:00	800	16.0	P1
89/170 07:32:00	89/170 07:44:16	736	16.0	P1
89/170 08:12:00	89/170 08:26:56	896	16.0	P1
89/170 09:06:56	89/170 09:23:44	1008	16.0	P1
89/170 09:52:16	89/170 10:02:56	640	16.0	P1
89/170 10:42:56	89/170 11:00:48	1072	16.0	P1
89/170 11:30:24	89/170 11:34:40	256	16.0	P1
89/170 12:18:24	89/170 12:37:04	1120	16.0	P1
89/170 12:37:20	89/170 12:39:12	112	16.0	P1
89/170 15:44:52	89/170 15:45:56	64	16.0	P1
89/170 15:46:08	89/170 15:47:24	76	4.0	P2
89/170 15:47:32	89/170 15:49:56	144	16.0	P1
89/170 15:50:04	89/170 15:52:12	128	16.0	P1
89/170 15:52:16	89/170 15:57:20	304	16.0	P1
89/170 16:17:08	89/170 16:23:48	400	16.0	P1
89/170 16:24:04	89/170 16:26:44	160	16.0	P1
89/170 17:23:44	89/170 17:24:32	48	16.0	P1
89/171 14:09:28	89/171 14:10:32	64	16.0	P1
89/171 14:10:48	89/171 14:12:08	80	16.0	P1
89/171 14:39:32	89/171 14:40:12	40	4.0	P2
89/171 14:40:16	89/171 14:45:56	340	4.0	P2
89/171 15:37:20	89/171 15:41:36	256	16.0	P1
89/171 15:42:40	89/171 15:43:12	32	16.0	P1
89/171 15:43:28	89/171 15:46:08	160	16.0	P1
89/171 15:46:20	89/171 15:47:24	64	16.0	P1
89/171 15:47:40	89/171 15:51:56	256	16.0	P1
89/171 15:52:08	89/171 15:53:44	96	16.0	P1
89/171 16:11:36	89/171 16:23:04	688	16.0	P1
89/171 17:12:36	89/171 17:18:12	336	16.0	P1
89/171 17:19:29	89/171 17:21:37	128	16.0	P1
89/171 19:26:16	89/171 19:34:48	512	16.0	P1
89/171 20:26:48	89/171 20:46:00	1152	16.0	P1
89/171 20:46:56	89/171 20:51:56	300	4.0	P2
89/171 20:52:08	89/171 20:59:04	416	4.0	P2
89/171 21:03:44	89/171 21:10:40	416	16.0	P1
89/171 22:02:56	89/171 22:46:08	2592	16.0	P1
89/171 23:35:44	89/172 00:22:08	2784	16.0	P1
89/172 01:34:08	89/172 01:51:28	1040	16.0	P1
89/172 01:53:20	89/172 01:54:24	64	16.0	P1
89/172 01:54:40	89/172 01:56:32	112	16.0	P1
89/172 03:11:44	89/172 03:33:36	1312	16.0	P1
89/187 06:32:56	89/187 06:36:24	208	16.0	P1
89/187 06:59:48	89/187 07:08:20	512	16.0	P1
89/187 08:07:04	89/187 08:08:08	64	16.0	P1
89/187 09:46:28	89/187 09:48:20	112	4.0	P2
89/187 09:48:32	89/187 09:55:20	408	4.0	P2
89/187 09:55:32	89/187 09:57:52	140	4.0	P2
89/187 09:57:56	89/187 09:58:24	28	4.0	P2
89/187 09:58:28	89/187 10:00:24	116	4.0	P2
89/187 10:00:28	89/187 10:00:48	20	4.0	P2

Table B.15: Detailed Observation Times of Corrected Data – 8/10

Start Time (UT)	End Time (UT)	Dur. (s)	Time Res. (s)	Mode
GS 2023+33 (cont.)				
89/187 10:00:52	89/187 10:01:44	52	4.0	P2
89/187 10:01:48	89/187 10:06:32	284	4.0	P2
89/187 10:06:36	89/187 10:07:20	44	4.0	P2
89/187 10:07:28	89/187 10:08:12	44	4.0	P2
89/187 10:08:40	89/187 10:27:20	1120	16.0	P1
89/187 11:18:40	89/187 11:44:16	1536	16.0	P1
89/187 11:44:32	89/187 11:50:08	336	16.0	P1
89/187 11:50:40	89/187 12:03:28	768	16.0	P1
89/187 12:54:40	89/187 13:05:52	672	16.0	P1
89/187 13:10:24	89/187 13:12:48	144	4.0	P2
89/187 13:13:00	89/187 13:15:00	120	4.0	P2
89/187 13:15:12	89/187 13:15:48	36	4.0	P2
89/187 13:15:52	89/187 13:17:36	104	4.0	P2
89/187 13:18:12	89/187 13:19:16	64	16.0	P1
89/187 13:19:48	89/187 13:38:12	1104	16.0	P1
89/187 14:36:00	89/187 15:08:32	1952	16.0	P1
89/187 16:12:00	89/187 16:48:16	2176	16.0	P1
89/201 00:56:47	89/201 01:09:03	736	16.0	P1
89/201 01:47:59	89/201 01:53:51	352	16.0	P1
89/201 02:31:11	89/201 02:48:47	1056	16.0	P1
89/201 03:25:03	89/201 03:29:19	256	16.0	P1
89/201 04:05:35	89/201 04:29:35	1440	16.0	P1
89/201 05:02:07	89/201 05:05:51	224	16.0	P1
89/202 00:51:59	89/202 01:03:43	704	16.0	P1
89/202 01:41:35	89/202 01:50:39	544	16.0	P1
89/202 02:27:59	89/202 02:43:27	928	16.0	P1
89/202 03:19:43	89/202 03:26:39	416	16.0	P1
89/203 02:26:31	89/203 02:43:55	1044	4.0	P2
89/203 03:18:27	89/203 03:22:51	264	4.0	P2
89/203 04:05:23	89/203 04:24:35	1152	4.0	P2
89/203 04:57:23	89/203 04:58:35	72	4.0	P2
89/305 00:21:30	89/305 00:49:46	1696	16.0	P1
89/305 01:58:02	89/305 02:28:26	1824	16.0	P1
89/305 03:19:38	89/305 03:24:58	320	16.0	P1
89/305 03:28:02	89/305 03:32:18	256	16.0	P1
89/305 03:32:34	89/305 03:38:58	384	16.0	P1
89/305 03:39:54	89/305 04:01:46	1312	16.0	P1
89/305 04:55:38	89/305 05:14:34	1136	16.0	P1
89/305 05:23:22	89/305 05:38:02	880	16.0	P1
89/305 06:31:38	89/305 07:10:34	2336	16.0	P1
89/305 08:07:38	89/305 08:41:30	2032	16.0	P1
89/305 09:45:46	89/305 10:17:30	1904	16.0	P1
89/305 11:24:26	89/305 11:53:30	1744	16.0	P1
89/305 13:04:10	89/305 13:25:14	1264	16.0	P1
89/305 14:41:30	89/305 14:59:06	1056	16.0	P1
89/305 22:51:54	89/305 23:00:58	544	16.0	P1
90/228 00:50:07	90/228 01:02:23	736	16.0	P1
90/228 01:34:23	90/228 01:55:43	1280	16.0	P1
90/228 02:25:03	90/228 02:39:27	864	16.0	P1
90/228 03:13:03	90/228 03:30:07	1024	16.0	P1
90/228 03:58:55	90/228 04:14:39	944	16.0	P1
90/228 04:51:11	90/228 05:03:43	752	16.0	P1
90/228 05:31:43	90/228 05:49:51	1088	16.0	P1
90/228 06:26:55	90/228 06:40:15	800	16.0	P1
90/228 07:05:51	90/228 07:24:47	1136	16.0	P1
90/228 07:50:55	90/228 07:51:43	48	16.0	P1
90/228 07:56:31	90/228 08:15:11	1120	16.0	P1
90/228 08:40:47	90/228 08:55:11	864	16.0	P1
90/228 09:30:39	90/228 09:39:59	560	16.0	P1
90/228 09:46:23	90/228 09:50:07	224	16.0	P1
90/228 10:15:43	90/228 10:30:07	864	16.0	P1
90/228 11:00:47	90/228 11:10:39	592	16.0	P1
90/228 11:50:39	90/228 12:04:31	832	16.0	P1
90/228 13:27:27	90/228 13:37:51	624	16.0	P1
90/228 14:10:39	90/228 14:22:39	720	16.0	P1
90/228 15:48:15	90/228 15:58:39	624	16.0	P1
90/228 17:21:35	90/228 17:36:47	912	16.0	P1
GX 339-4				
88/247 13:36:56	88/247 13:39:12	136	4.0	P2
88/247 13:39:20	88/247 13:41:28	128	16.0	P1
88/247 14:51:20	88/247 14:56:40	320	16.0	P3
88/247 14:56:48	88/247 15:04:16	448	16.0	P3
88/247 15:04:20	88/247 15:11:00	400	16.0	P3
88/247 15:13:48	88/247 15:14:52	64	16.0	P3
88/249 12:07:04	88/249 12:07:52	48	16.0	P3
88/249 12:08:04	88/249 12:08:52	48	16.0	P3
88/249 12:09:00	88/249 12:09:48	48	16.0	P3
88/249 12:09:56	88/249 12:10:44	48	16.0	P3
88/249 12:10:48	88/249 12:11:36	48	16.0	P3
GX 339-4(cont.)				
88/249 13:24:48	88/249 13:40:00	912	16.0	P3
88/249 13:42:12	88/249 13:43:00	48	16.0	P3
88/249 13:43:00	88/249 13:43:32	32	16.0	P3
88/249 13:43:40	88/249 13:44:28	48	16.0	P3
88/249 13:44:32	88/249 13:46:08	96	16.0	P3
88/249 13:46:16	88/249 13:47:04	48	16.0	P3
88/249 13:47:20	88/249 13:49:44	144	16.0	P3
88/249 13:50:04	88/249 13:50:36	32	16.0	P3
88/249 13:51:00	88/249 13:51:32	32	16.0	P3
88/249 14:59:00	88/249 15:21:56	1376	16.0	P3
88/249 15:24:12	88/249 15:25:00	48	16.0	P3
88/249 15:25:04	88/249 15:26:24	80	16.0	P3
88/249 15:26:36	88/249 15:27:24	48	16.0	P3
88/249 15:27:40	88/249 15:28:12	32	16.0	P3
88/249 16:02:52	88/249 16:08:44	352	16.0	P3
88/249 16:39:00	88/249 17:04:04	1504	16.0	P3
88/249 21:39:44	88/249 21:43:28	224	4.0	P2
88/250 10:08:28	88/250 10:23:24	896	16.0	P1
88/250 10:24:16	88/250 10:24:48	32	16.0	P1
88/250 10:24:56	88/250 10:25:28	32	16.0	P1
88/250 10:26:21	88/250 10:27:09	48	16.0	P3
88/250 10:28:36	88/250 10:30:44	128	16.0	P3
88/250 10:30:48	88/250 10:32:08	80	16.0	P3
88/250 10:32:12	88/250 10:32:44	32	16.0	P3
88/250 10:34:16	88/250 10:34:48	32	16.0	P3
88/250 11:46:56	88/250 12:03:12	976	16.0	P3
88/250 12:03:12	88/250 12:04:00	48	16.0	P3
88/250 12:05:52	88/250 12:06:56	64	16.0	P3
88/250 12:07:04	88/250 12:08:40	96	16.0	P3
88/250 12:08:40	88/250 12:09:12	32	16.0	P3
88/250 12:09:16	88/250 12:11:56	160	16.0	P3
88/250 12:12:28	88/250 12:13:16	48	16.0	P3
88/250 12:13:16	88/250 12:14:04	48	16.0	P3
88/250 12:14:12	88/250 12:15:00	48	16.0	P3
88/250 12:15:00	88/250 12:15:48	48	16.0	P3
88/250 12:15:52	88/250 12:16:24	32	16.0	P3
88/250 13:24:32	88/250 13:35:28	656	16.0	P3
88/250 13:35:36	88/250 13:36:24	48	16.0	P3
88/250 13:36:40	88/250 13:44:56	496	16.0	P3
88/250 13:48:40	88/250 13:49:28	48	16.0	P3
88/250 13:49:44	88/250 13:50:48	64	16.0	P3
88/250 13:50:48	88/250 13:54:32	224	16.0	P3
88/250 13:54:48	88/250 13:55:20	32	16.0	P3
88/250 13:55:40	88/250 13:56:12	32	16.0	P3
88/250 14:30:24	88/250 14:34:24	240	16.0	P3
88/250 15:03:08	88/250 15:26:52	1424	16.0	P3
88/250 15:29:20	88/250 15:30:08	48	16.0	P3
88/250 15:30:12	88/250 15:30:44	32	16.0	P3
88/251 00:33:08	88/251 00:35:00	112	16.0	P1
88/251 06:58:04	88/251 07:22:36	1472	16.0	P1
88/251 08:35:40	88/251 09:01:16	1536	16.0	P1
88/251 10:15:56	88/251 10:26:36	640	16.0	P1
88/251 10:29:08	88/251 10:31:16	128	16.0	P1
89/240 07:59:10	89/240 08:07:10	480	16.0	P1
89/240 09:13:50	89/240 09:14:22	32	16.0	P1
89/240 09:14:38	89/240 09:37:50	1392	16.0	P1
89/240 09:39:54	89/240 09:42:34	160	16.0	P1
89/240 09:42:42	89/240 09:46:42	240	16.0	P1
89/240 09:46:58	89/240 09:48:18	80	16.0	P1
89/240 09:48:30	89/240 09:51:26	176	16.0	P1
89/240 09:51:30	89/240 09:52:02	32	16.0	P1
89/240 09:52:34	89/240 10:19:30	1616	16.0	P1
89/240 10:52:30	89/240 11:18:54	1584	16.0	P1
89/240 11:13:21	89/240 11:18:53	332	4.0	P2
89/240 11:21:30	89/240 11:24:42	192	16.0	P1
89/240 11:24:46	89/240 11:29:02	256	16.0	P1
89/240 11:32:46	89/240 11:33:18	32	16.0	P1
89/240 11:33:34	89/240 11:52:46	1152	16.0	P1
89/240 12:36:30	89/240 12:45:02	512	16.0	P1
89/240 12:45:34	89/240 13:26:38	2464	16.0	P1
89/240 14:30:06	89/240 14:58:22	1696	16.0	P1
89/240 16:09:50	89/240 16:34:22	1472	16.0	P1
89/240 17:02:06	89/240 17:16:30	864	16.0	P1
89/240 17:45:50	89/240 18:10:22	1472	16.0	P1
89/240 18:35:58	89/240 18:54:38	1120	16.0	P1
89/240 19:21:50	89/240 19:44:46	1376	16.0	P1
89/240 20:19:26	89/240 20:32:14	768	16.0	P1
89/240 21:57:02	89/240 22:08:14	672	16.0	P1
89/240 22:44:30	89/240 22:55:10	640	16.0	P1

Table B.16: Detailed Observation Times of Corrected Data – 9/10

Start Time (UT)	End Time (UT)	Dur. (s)	Time Res. (s)	Mode
GX 339-4 (cont.)				
89/240 23:33:34	89/240 23:46:22	768	16.0	P1
89/241 01:10:06	89/241 01:24:30	864	16.0	P1
89/271 15:23:16	89/271 15:34:44	688	16.0	P1
89/271 16:59:12	89/271 17:02:56	224	16.0	P1
89/271 17:10:00	89/271 17:12:24	144	16.0	P1
89/271 17:50:24	89/271 18:01:04	640	16.0	P1
89/271 18:01:12	89/271 18:01:20	8	4.0	P2
89/271 18:01:24	89/271 18:01:52	28	4.0	P2
89/271 18:02:08	89/271 18:02:56	48	16.0	P1
89/271 18:35:04	89/271 18:48:08	784	16.0	P1
89/271 19:25:56	89/271 19:37:28	692	4.0	P2
89/271 19:37:36	89/271 19:38:08	32	4.0	P2
89/271 19:38:44	89/271 19:38:52	8	4.0	P2
89/271 20:11:12	89/271 20:23:36	744	4.0	P2
89/272 00:12:28	89/272 00:18:20	352	16.0	P3
89/272 00:43:56	89/272 01:10:36	1600	16.0	P3
89/272 01:48:28	89/272 01:54:20	352	16.0	P3
89/272 02:19:40	89/272 02:37:00	1040	16.0	P3
89/272 03:23:56	89/272 03:28:44	288	16.0	P3
89/272 03:53:16	89/272 04:14:36	1280	16.0	P3
89/272 04:59:24	89/272 05:04:44	320	16.0	P3
89/272 05:30:52	89/272 05:53:16	1344	16.0	P3
89/272 06:34:52	89/272 06:37:00	128	16.0	P3
89/272 07:10:36	89/272 07:30:20	1184	16.0	P3
89/272 08:47:08	89/272 09:07:40	1232	16.0	P3
89/272 17:44:16	89/272 17:52:32	496	16.0	P3
89/272 17:53:20	89/272 17:53:52	32	16.0	P3
89/272 18:28:00	89/272 18:42:08	848	16.0	P3
89/272 19:23:56	89/272 19:30:52	416	16.0	P1
89/272 20:06:36	89/272 20:17:16	640	16.0	P1
89/272 20:57:48	89/272 21:06:52	544	16.0	P1
89/272 20:59:54	89/272 21:06:18	384	4.0	P2
89/272 23:05:48	89/272 23:09:00	192	16.0	P1
89/272 23:12:44	89/272 23:25:00	736	16.0	P1
89/273 00:40:44	89/273 00:50:20	576	16.0	P1
89/273 00:41:46	89/273 00:50:18	512	4.0	P2
89/273 00:56:42	89/273 01:04:42	480	4.0	P2
89/273 01:42:04	89/273 01:49:00	416	16.0	P1
89/273 02:13:00	89/273 02:28:28	928	16.0	P1
89/273 02:13:30	89/273 02:28:26	896	4.0	P2
89/273 03:18:04	89/273 03:24:28	384	16.0	P1
89/273 03:46:20	89/273 04:06:36	1216	16.0	P1
89/273 03:47:22	89/273 04:06:34	1152	4.0	P2
89/273 04:53:30	89/273 05:02:02	512	4.0	P2
89/273 05:31:56	89/273 05:44:44	768	16.0	P1
89/273 07:05:48	89/273 07:22:52	1024	16.0	P1
89/273 08:41:48	89/273 08:58:52	1024	16.0	P1
89/273 10:14:36	89/273 10:37:00	1344	16.0	P1
89/273 10:15:38	89/273 10:36:58	1280	4.0	P2
89/273 17:38:20	89/273 17:47:56	576	16.0	P1
89/273 17:39:22	89/273 17:47:54	512	4.0	P2
89/273 19:15:24	89/273 19:23:56	512	16.0	P1
89/273 20:02:20	89/273 20:10:52	512	16.0	P1
89/273 20:49:16	89/273 20:59:24	608	16.0	P1
89/273 21:38:20	89/273 21:44:44	384	16.0	P1
89/273 22:25:16	89/273 22:33:48	512	16.0	P1
89/273 22:57:16	89/273 23:20:44	1408	16.0	P1
89/274 00:01:16	89/274 00:06:36	320	16.0	P1
89/274 00:29:00	89/274 00:43:56	896	16.0	P1
91/253 15:24:30	91/253 15:40:30	960	16.0	P3
91/253 16:22:06	91/253 16:25:50	224	16.0	P3
91/253 16:58:26	91/253 17:08:34	608	16.0	P3
91/253 17:08:58	91/253 17:14:18	320	16.0	P3
91/253 19:26:10	91/253 19:33:22	432	16.0	P3
91/253 20:08:14	91/253 20:18:06	592	16.0	P3
91/254 03:35:10	91/254 03:51:10	960	16.0	P1
91/254 05:09:02	91/254 05:26:06	1024	16.0	P1
91/254 14:21:02	91/254 14:36:46	944	16.0	P3
91/254 14:38:50	91/254 14:39:54	64	16.0	P3
91/254 15:53:26	91/254 15:56:38	192	16.0	P1
91/254 15:57:34	91/254 16:12:46	912	16.0	P1
91/254 15:57:38	91/254 16:06:42	544	4.0	P2
91/254 16:51:10	91/254 16:57:50	400	16.0	P3
91/254 17:26:06	91/254 17:44:46	1120	16.0	P3
91/255 00:53:02	91/255 01:12:46	1184	16.0	P1
LMC X-1				
87/112 22:55:43	87/112 23:08:47	784	16.0	P1
87/113 00:34:23	87/113 00:42:39	496	16.0	P1
87/113 02:08:47	87/113 02:18:39	592	16.0	P1
87/113 02:55:27	87/113 03:01:11	344	16.0	P1
87/113 03:45:19	87/113 03:54:39	560	16.0	P1
87/113 04:26:39	87/113 04:38:55	736	16.0	P1
87/113 05:24:31	87/113 05:30:39	368	16.0	P1
87/113 06:04:47	87/113 06:15:59	672	16.0	P1
87/113 06:58:23	87/113 07:06:39	496	16.0	P1
87/113 07:42:55	87/113 07:57:51	896	16.0	P1
87/113 08:34:23	87/113 08:40:31	368	16.0	P1
87/113 09:21:19	87/113 09:35:11	832	16.0	P1
87/113 10:57:03	87/113 11:09:51	768	16.0	P1
87/113 12:33:03	87/113 12:47:59	896	16.0	P1
87/113 14:11:11	87/113 14:19:43	512	16.0	P1
87/197 04:18:00	87/197 04:33:28	928	16.0	P2
87/197 05:30:00	87/197 06:10:32	2432	16.0	P2
87/197 06:52:08	87/197 07:42:48	3040	16.0	P2
87/197 08:31:52	87/197 09:18:48	2816	16.0	P2
87/197 09:38:32	87/197 09:54:32	960	16.0	P2
87/197 10:22:48	87/197 10:43:36	1248	16.0	P2
87/197 11:16:40	87/197 11:22:32	352	16.0	P2
87/273 15:02:29	87/273 15:04:37	128	16.0	P1
87/273 15:18:57	87/273 15:26:25	448	16.0	P1
87/273 16:38:41	87/273 17:06:57	1696	16.0	P1
87/273 18:15:13	87/273 18:38:41	1408	16.0	P1
87/273 19:51:45	87/273 20:11:45	1200	16.0	P1
87/273 20:37:53	87/273 20:49:37	704	16.0	P1
87/273 21:27:45	87/273 21:48:17	1232	16.0	P1
87/273 22:12:17	87/273 22:29:37	1040	16.0	P1
87/273 23:04:17	87/273 23:24:49	1232	16.0	P1
87/273 23:50:09	87/274 00:05:37	928	16.0	P1
87/274 00:40:49	87/274 00:54:57	848	16.0	P1
87/274 01:29:05	87/274 01:42:09	784	16.0	P1
87/274 02:16:49	87/274 02:30:57	848	16.0	P1
87/274 03:06:09	87/274 03:18:41	752	16.0	P1
87/274 03:56:17	87/274 04:02:41	384	16.0	P1
87/274 04:42:09	87/274 04:54:41	752	16.0	P1
87/274 05:35:29	87/274 05:38:41	192	16.0	P1
87/274 06:18:25	87/274 06:27:45	560	16.0	P1
LMC X-3				
88/008 07:49:33	88/008 07:50:53	80	16.0	P3
88/008 07:50:53	88/008 07:52:45	112	16.0	P3
88/008 07:54:33	88/008 07:55:21	48	16.0	P3
88/008 08:24:05	88/008 08:31:49	464	16.0	P3
88/008 09:10:05	88/008 09:25:49	944	16.0	P3
88/008 09:28:21	88/008 09:29:25	64	16.0	P3
88/008 09:29:29	88/008 09:30:49	80	16.0	P3
88/008 09:30:53	88/008 09:31:41	48	16.0	P3
88/008 09:31:53	88/008 09:33:45	112	16.0	P3
88/008 09:34:01	88/008 09:35:21	80	16.0	P3
88/008 09:35:21	88/008 09:36:09	48	16.0	P3
88/008 09:36:13	88/008 09:37:01	48	16.0	P3
88/008 11:02:45	88/008 11:07:49	304	16.0	P3
88/008 11:10:33	88/008 11:11:37	64	16.0	P3
88/008 11:11:49	88/008 11:13:09	80	16.0	P3
88/008 11:13:21	88/008 11:17:53	272	16.0	P3
88/008 11:20:21	88/008 11:33:09	768	16.0	P3
88/008 11:33:25	88/008 11:45:57	752	16.0	P3
88/008 12:34:05	88/008 12:37:01	176	16.0	P3
88/008 12:37:13	88/008 12:50:01	768	16.0	P3
88/008 12:52:37	88/008 12:53:25	48	16.0	P3
88/008 12:53:37	88/008 12:54:57	80	16.0	P3
88/008 12:55:09	88/008 12:57:01	112	16.0	P3
88/008 12:57:01	88/008 12:58:21	80	16.0	P3
88/008 12:58:41	88/008 12:59:29	48	16.0	P3
88/008 12:59:29	88/008 13:00:17	48	16.0	P3
88/008 13:00:21	88/008 13:01:09	48	16.0	P3
88/008 13:03:01	88/008 13:03:33	32	16.0	P3
88/008 14:09:05	88/008 14:30:25	1280	16.0	P3
88/008 14:30:33	88/008 14:32:57	144	16.0	P3
88/008 14:34:37	88/008 14:35:41	64	16.0	P3
88/008 14:35:49	88/008 14:36:21	32	16.0	P3
88/009 07:59:57	88/009 08:00:45	48	16.0	P3
88/009 08:00:57	88/009 08:01:45	48	16.0	P3
88/009 08:26:17	88/009 08:37:45	688	16.0	P3
88/009 09:15:05	88/009 09:23:37	512	16.0	P3
88/009 09:36:29	88/009 09:37:17	48	16.0	P3
88/009 09:37:29	88/009 09:38:49	80	16.0	P3
88/009 09:41:01	88/009 09:41:49	48	16.0	P3
89/258 21:54:21	89/258 21:56:45	144	16.0	P1
89/258 21:58:29	89/258 22:05:57	448	16.0	P1

Table B.17: Detailed Observation Times of Corrected Data – 10/10

Start Time (UT)	End Time (UT)	Dur. (s)	Time Res. (s)	Mode
LMC X-3 (cont.)				
89/258 21:58:32	89/258 22:05:52	440	4.0	P1
89/258 22:18:21	89/258 22:40:45	1344	16.0	P1
89/258 23:13:49	89/258 23:34:05	1216	16.0	P1
89/258 23:36:45	89/258 23:39:09	144	16.0	P1
89/258 23:39:49	89/258 23:47:21	452	4.0	P2
89/259 00:00:05	89/259 00:17:29	1044	4.0	P2
89/259 00:53:01	89/259 01:14:53	1312	16.0	P1
89/259 01:18:13	89/259 01:25:29	436	4.0	P2
89/259 01:25:37	89/259 01:26:09	32	16.0	P1
89/259 01:26:21	89/259 01:29:01	160	16.0	P1
89/259 01:29:53	89/259 01:53:53	1440	16.0	P1
89/259 02:30:05	89/259 02:56:45	1600	16.0	P1
89/259 03:00:13	89/259 03:01:49	96	16.0	P1
89/293 14:01:31	89/293 14:18:51	1040	16.0	P1
89/293 14:55:39	89/293 15:08:43	784	16.0	P1
89/293 15:34:19	89/293 15:54:03	1184	16.0	P1
89/293 16:33:47	89/293 16:40:43	416	16.0	P1
89/293 17:08:27	89/293 17:30:19	1312	16.0	P1
89/343 03:44:42	89/343 04:02:18	1056	16.0	P1
89/343 03:44:46	89/343 03:53:14	508	4.0	P1
89/343 04:36:54	89/343 04:42:30	336	16.0	P1
89/343 05:20:10	89/343 05:40:58	1248	16.0	P1
89/343 05:21:22	89/343 05:28:46	444	4.0	P1
89/343 06:14:02	89/343 06:18:18	256	16.0	P1
89/348 04:32:18	89/348 04:44:50	752	4.0	P1
89/348 04:47:22	89/348 04:47:54	32	16.0	P1
89/348 04:48:10	89/348 04:50:02	112	16.0	P1
89/355 01:40:58	89/355 01:57:46	1008	16.0	P3
89/355 02:32:10	89/355 02:39:38	448	16.0	P3
89/361 00:35:22	89/361 00:41:30	368	16.0	P1
89/361 02:11:22	89/361 02:19:38	496	16.0	P1
89/361 04:17:14	89/361 04:46:50	1776	16.0	P1
89/361 05:52:58	89/361 06:10:34	1056	16.0	P1
89/361 06:56:10	89/361 06:59:06	176	16.0	P1
89/361 07:24:58	89/361 07:46:02	1264	16.0	P1
89/361 08:31:38	89/361 08:35:06	208	16.0	P1
89/361 09:01:46	89/361 09:22:02	1216	16.0	P1
89/361 10:39:38	89/361 10:58:02	1104	16.0	P1
89/361 12:19:06	89/361 12:36:10	1024	16.0	P1
89/361 13:52:58	89/361 14:06:02	784	16.0	P1
89/361 14:08:10	89/361 14:12:10	240	16.0	P1
89/361 17:22:26	89/361 17:22:58	32	16.0	P1
89/361 17:23:14	89/361 17:29:06	352	16.0	P1
90/012 14:27:39	90/012 14:32:47	308	4.0	P1
90/012 15:36:11	90/012 15:51:55	944	4.0	P1
90/028 01:46:35	90/028 01:57:47	672	16.0	P1
90/028 02:34:07	90/028 02:38:07	240	16.0	P1
90/028 03:15:59	90/028 03:37:51	1312	16.0	P1
90/028 04:12:03	90/028 04:13:07	64	16.0	P1
90/047 23:13:58	90/047 23:18:14	256	16.0	P1
90/048 00:45:42	90/048 00:57:10	688	16.0	P1
90/048 02:19:34	90/048 02:27:50	496	16.0	P1
90/048 02:55:50	90/048 03:02:14	384	16.0	P1
90/048 03:10:46	90/048 03:17:10	384	16.0	P1
90/048 03:55:34	90/048 04:03:02	448	16.0	P1
90/048 04:29:42	90/048 04:40:22	640	16.0	P1
90/048 05:29:42	90/048 05:37:58	496	16.0	P1
90/048 06:04:06	90/048 06:18:30	864	16.0	P1
90/048 07:36:54	90/048 07:56:38	1184	16.0	P1
90/048 08:40:06	90/048 08:41:26	80	16.0	P1
90/057 12:07:10	90/057 12:30:54	1424	16.0	P1
90/057 13:59:58	90/057 14:04:30	272	16.0	P1
90/057 14:04:42	90/057 14:07:06	144	16.0	P1
90/057 14:07:46	90/057 14:08:34	48	16.0	P1
90/057 14:35:50	90/057 14:43:18	448	16.0	P1
90/057 15:20:38	90/057 15:27:34	416	16.0	P1
90/057 15:28:10	90/057 15:38:02	592	16.0	P1
90/057 15:41:30	90/057 15:43:54	144	16.0	P1
90/057 16:10:58	90/057 16:23:46	768	16.0	P1
90/057 16:57:10	90/057 17:07:18	608	16.0	P1
90/071 05:59:29	90/071 06:04:01	272	16.0	P1
90/071 06:04:21	90/071 06:06:29	128	16.0	P1
90/071 06:15:01	90/071 06:27:49	768	16.0	P1
90/071 06:28:25	90/071 06:37:45	560	16.0	P1
90/071 07:25:53	90/071 07:26:41	48	16.0	P1
90/071 07:28:13	90/071 07:31:57	224	16.0	P1
90/071 07:33:25	90/071 07:36:37	192	16.0	P1
90/077 03:03:09	90/077 03:30:41	1652	4.0	P3
90/077 04:38:13	90/077 04:41:49	216	4.0	P3
90/077 06:14:49	90/077 06:22:41	472	4.0	P3
90/077 06:22:41	90/077 06:49:33	1612	4.0	P3
90/077 08:00:14	90/077 08:02:38	144	16.0	P1
90/077 08:09:25	90/077 08:23:17	832	16.0	P1
90/077 09:28:37	90/077 09:59:49	1872	16.0	P1
90/077 11:00:05	90/077 11:28:53	1728	16.0	P1
90/077 11:30:29	90/077 11:31:01	32	16.0	P1
90/077 11:57:41	90/077 12:03:17	336	16.0	P1
90/077 12:33:41	90/077 13:03:17	1776	16.0	P1
90/077 13:31:49	90/077 13:38:13	384	16.0	P1
90/077 14:08:37	90/077 14:38:13	1776	16.0	P1
90/077 15:12:05	90/077 15:13:09	64	16.0	P1
90/077 15:45:25	90/077 16:12:37	1632	16.0	P1
90/077 16:39:17	90/077 16:48:05	528	16.0	P1
90/077 17:23:33	90/077 17:43:17	1184	16.0	P1
90/077 18:17:25	90/077 18:23:33	368	16.0	P1
90/077 19:02:29	90/077 19:17:09	880	16.0	P1
90/078 01:28:21	90/078 01:40:05	704	16.0	P1
90/078 10:47:17	90/078 11:10:45	1408	16.0	P1

Bibliography

Arnaud, K., 1995, *XSPEC v9.0*, Self-published Manual

Avni, Y., 1976, *ApJ*, **210**, 642

Baade, W. & Zwicky, F., 1934, *Proc. Nat. Acad Sci. U.S.* **20**, 254

Babul, A., Paczyński, B., & Spergel, D., 1987, *ApJLett*, **316**, L49

Band, D., Matteson, J., Ford, L., Schaefer, B., Palmer, D., Teegarden, B., Cline, T., Briggs, M., Paciesas, W., Pendleton, G., Fishman, G., Kouveliotou, C., Meegan, C., Wilson, R., & Lestrade, P., 1993, *ApJ*, **413**, 281

Band, D. L., 1994, *ApJLett*, **432**, L23

Belian, R. D., Conner, J. P., & Evans, W. D., 1976, *ApJLett*, **206**, L135

Belloni, T. & Hasinger, G., 1989, in (Hunt & Battrick 1989), p. 283

Belloni, T., van der Klis, M., Lewin, W., Van Paradijs, V., Dotani, T., Mitsuda, K., & S., M., 1996, *A&A*, 448

Bevington, P. R., 1969, *Data Reduction and Error Analysis for the Physical Sciences*, McGraw-Hill

Bolton, C. T., 1972, *Nat*, **235**, 271

Bradt, H., Rappaport, S., Mayer, W., Nather, R., Warner, B., MacFarlane, M., & Kristian, J., 1969, *Nat*, **222**, 728

Brainerd, J. J., 1994, *ApJLett*, **428**, L1

Caditz, D., 1995, *ApJ*, **452**, 140

Casares, J., Charles, P. A., & Naylor, T., 1992, *Nat*, **355**, 614

Chandrasekhar, S., 1935, *MNRAS*, **444**, L25

Cohen, E. & Piran, T., 1995, *ApJLett*, **444**, L25

Davis, S., 1995, *Ph.D. thesis*, The Catholic University of America

Davis, S., Norris, J., Kouveliotou, C., Fishman, G., Meegan, C., & Paciesas, W., 1994, in (Fishman et al. 1994), p. 182

Dermer, C. D., 1992, *Physical Review Letters* **68**, 1799

Dingus, B. & et al. , 1994, in (Fishman et al. 1994), p. 22

Dotani, T., 1988, *Ph.D. thesis*, University of Tokyo

Dotani, T., 1992, in Y. Tanaka & K. Koyama (eds.), *Frontiers of X-ray Astronomy*, No. 2 in Frontiers Science Series, p. 151, Universal Academy Press

Ebisawa, K., 1991, *Ph.D. thesis*, University of Tokyo

Ebisawa, K., Mitsuda, K., & Inoue, H., 1989, *PASJ*, **41**, 519

Efstathiou, G., Ellis, R. S., & Peterson, B. A., 1988, *MNRAS*, **232**, 431

Elvis, M. & et al. , 1975, *Nat*, **257**, 656

Eyles, C. J., Skinner, G. K., Willmore, A. P., & Rosenberg, F. D., 1975, *MNRAS*, **173**, 63P

Fenimore, E. E., Epstein, R. I., Ho, C., Klebesadel, R. W., Lacey, C., Laros, J. G., Meier, M., Strohmayer, T., Pendleton, G., Fishman, G., Kouveliotou, C., & Meegan, C., 1993, *Nat*, **366**, 40

Fenimore, E. E., In'T Zand, J. J. M., Norris, J. P., Bonnell, J. T., & Nemiroff, R. J., 1995, *ApJLett*, **448**, L101

Fishman, G., Brainered, J., & Hurley, K. (eds.), 1994, *Gamma Ray Bursts: Second Workshop, Huntsville, AL 1993*, No. 307 in AIP Conference Proceedings, American Institute of Physics

Fishman, G. & et al. , 1989, in W. N. Johnson (ed.), *Proc. Gamma Ray Observatory Science Workshop*, pp 2–39, NASA: Greenbelt

Fishman, G., Meegan, C., Wilson, R., Paciesas, W., Pendleton, G., & for the BATSE Science Team, 1992, in C. Shrader, N. Gehrels, & B. Dennis (eds.), *The Compton Observatory Science Workshop: Proc. for a workshop held in Annapolis, Maryland September 23-25, 1991*, No. 3137 in NASA Conference Publication, p. 26, NASA

Fishman, G. J. & Meegan, C. A., 1995, Vol. 33 of *Annual Review of Astronomy and Astrophysics*, p. 415, Annual Reviews Inc.

Fishman, G. J., Meegan, C. A., Wilson, R. B., Brock, M. N., Horack, J. M., Kouve-

liotou, C., Howard, S., Paciesas, W. S., Briggs, M. S., Pendleton, G. N., Koshut, T. M., Mallozzi, R. S., Stollberg, M., & Lestrade, J. P., 1994, *ApJS*, **92**, 229

Forman, W., Jones, C., & Tananbaum, H., 1976, *ApJ*, **208**, 849

Fritz, G. & et al. , 1969, *Science* **164**, 709

Giacconi, R. & et al. , 1962, *Phys. Rev. Lett.* **9**, 439

Grebenev, S. A., Siuniaev, R. A., Pavlinskii, M. N., & Dekhanov, I. A., 1991, *Soviet Astronomy Letters* **17**, 985

Grindlay, J., Gursky, H., Schnopper, H., Parsignault, D. R., Heise, J., Brinkman, A. C., & Schrijver, J., 1976, *ApJLett*, **205**, L127

Gursky et al. , H., 1975, *I.A.U. Circ.*, # 2778

Hakkila, J., Meegan, C. A., Pendleton, G. N., Fishman, G. J., Wilson, R. B., Paciesas, W. S., Brock, M. N., & Horack, J. M., 1994, *ApJ*, **422**, 659

Hakkila, J., Meegan, C. A., Pendleton, G. N., Horack, J. M., Briggs, M. S., Paciesas, W. S., & Emslie, A. G., 1995, *ApJ*, **454**, 134+

Hasinger, G. & Van Der Klis, M., 1989, *A&A*, **225**, 79

Hayashida, K., Inoue, H., Koyama, K., Awaki, H., & Takano, S., 1989, *PASJ*, **41**, 373

Heise, J., Mewe, R., Brinkman, A. C., Den Boggende, A., Schrijver, J., Gronenschild, E., Parsignault, D., Grindlay, J., Schreier, E., & Schnopper, H., 1975, *Nat*, **256**, 107+

Hewish, A., Bell, J., Pilkington, J., Scott, P., & Collins, R., 1967, *Nat*, **217**, 709

Holt, S. S., Boldt, E. A., Kaluzienski, L. J., & Serlemitsos, P. J., 1975, *Nat*, **256**, 108+

Hones, E. W. & Higbie, P. R., 1989, *Science* **244**, 448

Horack, J. M., Emslie, A. G., & Hartmann, D. H., 1995, *ApJ*, **447**, 474+

Horack, J. M., Mallozzi, R. S., & Koshut, T. M., 1996, *ApJ*, **466**, 21+

Hunt, J. & Battrick, B. (eds.), 1989, *Proc. 23rd ESLAB Symp. on Two Topics in X-ray Astronomy*, Vol. 1, ESTEC, Noordwijk, The Netherlands, ESA Publications Division

Jones, C., 1977, *ApJ*, **214**, 856

Kitamoto, S., 1989, in (Hunt & Battrick 1989), p. 231

Klebesadel, R., Strong, I., & Olson, R., 1973, *ApJLett*, **182**, L85

Kniffen, D., 1989, in W. N. Johnson (ed.), *Proc. Gamma Ray Observatory Science Workshop*, pp 2–39, NASA: Greenbelt

Koshut, T. M., 1995, *Ph.D. thesis*, University of Alabama, Huntsville

Koshut, T. M., Kouveliotou, C., Paciesas, W. S., Van Paradijs, J., Pendleton, G. N., Briggs, M. S., Fishman, G. J., & Meegan, C. A., 1995, *ApJ*, **452**, 145+

Kouveliotou, C., 1995, *Astrophysics & Space.Sci.* **231**, 49

Kouveliotou, C., 1996, in (Kouveliotou et al. 1996), in press

Kouveliotou, C. & et al. , 1994, in (Fishman et al. 1994), p. 167

Kouveliotou, C., Meegan, C. A., Fishman, G. J., Bhat, N. P., Briggs, M. S., Koshut, T. M., Paciesas, W. S., & Pendleton, G. N., 1993, *ApJLett*, **413**, L101

Kouveliotou, C., Van Paradijs, J., Fishman, G. J., Briggs, M. S., Kommers, J., Harmon, B. A., Meegan, C. A., & Lewin, W. H. G., 1996, *Nat*, **379**, 799+

Kouveliotou, C. K., Briggs, M., & Fishman, J. (eds.), 1996, *Gamma Ray Bursts: Third Workshop, Huntsville, AL 1995*, AIP Conference Proceedings, American Institute of Physics, in press

Kwok, P. & et al. , 1993, in *Compton Gamma-Ray Observatory*, No. 280 in AIP Conference Proceedings, p. 855, American Institute of Physics, High Energy Photons detected from GRBs

Lamb, D. Q., Graziani, C., & Smith, I. A., 1993, *ApJLett*, **413**, L11

Landau, L., 1932, *Phys. Z. Sowjetunion* **1**, 285

Leahy, D. A., Darbro, W., Elsner, R. F., Weisskopf, M. C., Kahn, S., Sutherland, P. G., & Grindlay, J. E., 1983, *ApJ*, **266**, 160

Lestrade, J. P., Dezalay, J. P., Atteia, J. L., Barat, C., Talon, R., Siuniaev, R. A., Kuznetsov, A., Terekhov, O., D'Iachkov, A., & Khavenson, N., 1993, *Astronomy and Astrophysics Supplement Series* **97**, 79+

Lewin, W., Van Paradijs, J., & Taam, R., 1993, *SSR*, **62**, 223

Lewin, W., van Paradijs, J., & van den Heuvel, E. (eds.), 1995, *X-Ray Binaries*, Vol. 1, Cambridge University Press

Lewin, W. H. G., 1994, in S. Holt & C. Day (eds.), *The Evolution of X-ray Binaries*, No. 308 in AIP Conference Proceedings, p. 3, American Institute of Physics

Lewin, W. H. G., Van Paradijs, J., & Van Der Klis, M., 1988, *Space Science Reviews* **46**, 273

Lubin, L. M. & Wijers, R. A. M. J., 1993, *ApJLett*, **418**, L9

Luminet, J.-P., 1992, *Black Holes*, Cambridge University Press

Makino, F. & Nagase, F. (eds.), 1992, *Ginga Memorial Symposium: Feb 4-5 1992*, Sagamihara, Japan, The Institute of Space and Astronautical Science

Makishima, K. & Miyamoto, S., 1988, *I.A.U. Circ.*, # 4653

Mallozzi, R. S., Paciesas, W. S., Pendleton, G. N., Briggs, M. S., Preece, R. D., Meegan, C. A., & Fishman, G. J., 1995, *ApJ*, **454**, 597+

Mao, S. & Paczynski, B., 1992, *ApJLett*, **388**, L45

Mao, S. & Yi, I., 1994, *ApJLett*, **424**, L131

Markert, T. & et al. , 1973, *ApJLett*, **184**, L67

McClintock, J. E. & Remillard, R. A., 1986, *ApJ*, **308**, 110

Meegan, C. & et al. , 1994, *The Second BATSE Gamma Ray Burst Catalog*, Available Electronically from GROSSC, NASA/GSFC

Meegan, C. A., Fishman, G. J., Wilson, R. B., Horack, J. M., Brock, M. N., Paciesas, W. S., Pendleton, G. N., & Kouveliotou, C., 1992, *Nat*, **355**, 143

Meegan, C. A., Pendleton, G. N., Briggs, M. S., Kouveliotou, C., Koshut, T. M., Lestrade, J. P., Paciesas, W. S., McCollough, M. L., Brainerd, J. J., Horack, J. M., Hakkila, J., Henze, W., Preece, R. D., Mallozzi, R. S., & Fishman, G. J., 1996, *ApJS*, **106**, 65+

Mitrofanov et al. , I., 1994, in (Fishman et al. 1994), p. 187

Mitsuda, K. & Dotani, T., 1989, *PASJ*, **41**, 557

Mitsuda, K., Inoue, H., Koyama, K., Makishima, K., Matsuoka, M., Ogawara, Y., Suzuki, K., Tanaka, Y., Shibazaki, N., & Hirano, T., 1984, *PASJ*, **36**, 741

Miyamoto, S., Iga, S., Kitamoto, S., & Kamado, Y., 1993, *ApJLett*, **403**, L39

Miyamoto, S., Iga, S., Terada, K., Kitamoto, S., Hayashida, K., & Negoro, H., 1992, in (Makino & Nagase 1992), p. 37

Miyamoto, S., Kimura, K., Kitamoto, S., Dotani, T., & Ebisawa, K., 1991, *ApJ*, **383**, 784

Miyamoto, S., Kitamoto, S., Hayashida, K., & Egoshi, W., 1995, *ApJLett*, **442**, L13

Miyamoto, S., Kitamoto, S., Iga, S., Hayashida, K., & Terada, K., 1994, *ApJ*, **435**, 398

Miyamoto, S., Kitamoto, S., Iga, S., Negoro, H., & Terada, K., 1992, *ApJLett*, **391**, L21

Miyamoto, S., Kitamoto, S., & Kimura, K., 1989, in (Hunt & Battrick 1989), p. 531

Norris, J. P., Bonnell, J. T., Nemiroff, R. J., Scargle, J. D., Kouveliotou, C., Paciesas, W. S., Meegan, C. A., & Fishman, G. J., 1995, *ApJ*, **439**, 542

Norris, J. P., Nemiroff, R. J., Scargle, J. D., Kouveliotou, C., Fishman, G. J., Meegan, C. A., Paciesas, W. S., & Bonnel, J. T., 1994, *ApJ*, **424**, 540

Oppenheimer, J. R. & Serber, R., 1938, *Phys. Rev.* **54**, 540

Oppenheimer, J. R. & Volkoff, G. M., 1939, *Phys. Rev.* **55**, 374

Paczynski, B., 1992, *Nat*, **355**, 521+

Piran, T., 1992, *ApJLett*, **389**, L45

Press, W., Flannery, B., Teukolsky, S., & Vetterling, W., 1995, *Numerical Recipies in C*, Cambridge University Press

Remillard, R. A., McClintock, J. E., & Bailyn, C. D., 1992, *ApJLett*, **399**, L145

Rieger, E. & et al. , 1989, *Science* **244**, 441

Rutledge, R., Hui, L., & Lewin, W., 1995, *MNRAS*, **276**, 753

Rutledge, R. & Lewin, W., 1993, *MNRAS*, **265**, L51

Rutledge, R., Lewin, W., Hakkila, J., Pendleton, G., Lestrade, J., Kouveliotou, C., & Meegan, C., 1996a, in (Kouveliotou et al. 1996), in press

Rutledge, R., Lewin, W., Pendleton, G., Lestrade, J., Kouveliotou, C., & Meegan, C., 1996b, in (Kouveliotou et al. 1996), in press

Samimi, J., Share, G. H., Wood, K., Yentis, D., Meekins, J., Evans, W. D., Shulman, S., Byram, E. T., Chubb, T. A., & Friedman, H., 1979, *Nat*, **278**, 434

Sanford, P. W., Ives, J. C., Burnell, S. J. B., Mason, K. O., & Murdin, P., 1975, *Nat*, **256**, 109

Schaefer, B. E., Teegarden, B. J., Fantasia, S. F., Palmer, D., Cline, T. L., Matteson, J. L., Band, D. L., Ford, L. A., Fishman, G. J., Meegan, C. A., Wilson, R. B., Paciesas, W. S., Pendleton, G. N., Briggs, M. S., & Lestrade, J. P., 1994, *ApJS*, **92**, 285

Schmidt, M., Higdon, J. C., & Hueter, G., 1988, *ApJLett*, **329**, L85

Schneid, E. J., Bertsch, D. L., Fichtel, C. E., Hartman, R. C., Hunter, S. D., Kanbach, G., Kniffen, D. A., Kwok, P. W., Lin, Y. C., & Mattox, J. R., 1992, *A&A*, **255**, L13

Schreier, E. & et al. , 1972, *ApJLett*, **172**, L79

Share, G., Kurfess, J., Marlow, K., & Messina, D., 1989, *Science* **244**, 444

Sommer, M., Bertsch, D. L., Dingus, B. L., Fichtel, C. E., Fishman, G. J., Harding, A. K., Hartman, R. C., Hunter, S. D., Hurley, K., Kanbach, G., Kniffen, D. A., Kouveliotou, C., Lin, Y. C., Mattox, J. R., Mayer-Hasselwander, H. A., Michelson, P. F., Von Montigny, C., Nolan, P. L., Schneid, E., Sreekumar, P., & Thompson, D. J., 1994, *ApJLett*, **422**, L63

Takizawa, M., Dotani, T., Mitsuda, K., Matsuba, E., Ogawa, M., Aoki, T., Asai, K., Ebisawa, K., Makishima, K., Miyamoto, S., Iga, S., Vaughan, B., Rutledge, R., & Lewin, W., 1996, *Spectral and Temporal Variability in the X-ray flux of Nova Muscae 1991*, in preparation

Tamblyn, P. & Melia, F., 1993, *ApJLett*, **417**, L21

Tanaka, Y., 1992, in (Makino & Nagase 1992), p. 19

Tanaka, Y. & Lewin, W., 1995, in (Lewin et al. 1995), p. 126

Tananbaum, H., Gursky, H., Kellogg, E., & Giacconi, R., 1972, *ApJLett*, **177**, L5

Tennant, A. F., Fabian, A. C., & Shafer, R. A., 1986a, *MNRAS*, **219**, 871

Tennant, A. F., Fabian, A. C., & Shafer, R. A., 1986b, *MNRAS*, **221**, 27P

Tolman, R. C., 1939, *Phys. Rev.* **55**, 364

Turner, M., Thomas, H., Patchett, B., Reading, D., Makishima, K., Ohashi, T., Dotani, T., Hayashida, K., Inoue, H., Kondo, H., Koyama, K., Mitsuda, K., Ogawara, Y., Takano, S., Awak, H., Tawara, Y., & Nakamura, N., 1989, *PASJ*, **41**, 345

Van der Klis, M., 1989, in H. Ögelman & E. van den Heuvel (eds.), *Timing Neutron Stars*, No. 330 in Lecture Notes in Physics, pp 27–69, Kluwer Academic Publishers

Van der Klis, M., 1994a, *A&A*, **283**, 469

Van der Klis, M., 1994b, *ApJS*, **92**, 511

Van der Klis, M., 1995, in (Lewin et al. 1995), p. 252

Van der Klis, M., Jansen, F., Van Paradijs, J., Van den Heuvel, E. P. J., & Lewin, W. H. G., 1985, *Nat*, **316**, 225

Van Paradijs, J., 1995, in (Lewin et al. 1995), p. 536

Webster, B. L. & Murdin, P., 1972, *Nat*, **235**, 37

Weinberg, S., 1972, *Gravitation and Cosmology*, John Wiley & Sons

White, N. & Marshall, F., 1984, *ApJ*, **281**, 354

White, N., Nagase, F., & Parmar, A., 1995, in (Lewin et al. 1995), p. 1

Wickramasinghe, W. A. D. T., Nemiroff, R. J., Norris, J. P., Kouveliotou, C., Fishman, G. J., Meegan, C. A., Wilson, R. B., & Paciesas, W. S., 1993, *ApJLett*, **411**, L55

Wijers, R. A. M. J. & Paczynski, B., 1994, *ApJLett*, **437**, L107

Zhang et al. , S., 1996, *I.A.U. Circ.*, # 6462